Asteroid differentiation from Gaia reflectance spectroscopy

Marjorie Galinier

To cite this version:

Marjorie Galinier. Asteroid differentiation from Gaia reflectance spectroscopy. Sciences of the Universe [physics]. Université Côte d'Azur, 2024. English. NNT : 2024COAZ5046 . tel-04814227

HAL Id: tel-04814227

https://theses.hal.science/tel-04814227v1

Submitted on 2 Dec 2024

UNIVERSITÉ
CÔTE D'AZUR

ÉCOLE DOCTORALE
SCIENCES
FONDAMENTALES
ET APPLIQUÉES

THÈSE DE DOCTORAT

Étude spectroscopique de la différentiation des astéroïdes avec Gaia

Marjorie Galinier

Laboratoire J.-L. Lagrange · Observatoire de la Côte d'Azur

Présentée en vue de l'obtention
du grade de docteur en
Sciences de la Planète et de l'Univers
d' Université Côte d'Azur

Dirigée par : Marco Delbo et Laurent Galluccio

Soutenue le : 26 septembre 2024

Devant le jury composé de :
Pierre Beck, *Professeur, IPAG, Grenoble*
Sonia Fornasier, *Professeure, Université Paris Cité, LESIA*
Audrey Bouvier, *Professor, Bayerisches Geoinstitut, Universität Bayreuth*
Marcel Popescu, *scientific researcher II, Astronomical Institute of the Romanian Academy*
Marco Delbo, *Directeur de recherche, Laboratoire Lagrange, OCA*
Laurent Galluccio, *Ingénieur de recherche, Laboratoire Lagrange, OCA*

Étude spectroscopique de la différentiation des astéroïdes avec Gaia

Asteroid differentiation from Gaia reflectance spectroscopy

Rapporteurs

Pierre Beck
Professeur, Institut d'astrophysique et de planétologie, Grenoble, France

Sonia Fornasier
Professeure, Université Paris Cité - LESIA, Paris - Meudon, France

Examinateurs

Audrey Bouvier
Professor, Bayerisches Geo-Institut, Bayreuth, Allemagne

Marcel Popescu
Scientific researcher II, Astronomical Institute of the Romanian Academy, Bucharest, Roumanie

Marco Delbo
Directeur de recherches, Observatoire de la Côte d'Azur, Nice, France

Laurent Galluccio
Ingénieur de Recherches, Université Côte d'Azur, Nice, France

Membre invité

Chrysa Avdellidou
Lecturer, University of Leicester, UK

That's the trouble with science. It's never done. Always upending itself. Ruining perfect systems for the little inconvenience of them being wrong.

C'est tout le problème avec la science : ce n'est jamais fini. Elle se chamboule elle-même en permanence. Elle gâche des systèmes parfaits au motif futile qu'ils sont faux.

— Brandon Sanderson, The Stormlight Archive - Rhythm of War, 2020

RESUMÉ Les planétésimaux se sont formés par accrétion de poussières dans le disque protoplanétaire du Soleil, et leur agglomération a conduit à la formation des planètes. Les planétésimaux larges et accrétés tôt se sont partiellement ou complètement différenciés, s'organisant en couches de densités et compositions différentes : noyau métallique, manteau riche en olivine et croûte magmatique. Des traces de ce processus sont observables dans la composition des météorites, et devraient l'être dans celle des astéroïdes.

La destruction catastrophique d'un corps différencié produit une famille collisionnelle d'astéroïdes, dont les membres devraient présenter une gamme de compositions reflétant chaque couche du corps d'origine. Aucune famille présentant cette caractéristique n'a été clairement identifiée à ce jour. En outre, des années d'études spectroscopiques ont mis en évidence une déplétion en corps riches en olivine dans la ceinture principale. Avant ces travaux, aucune concentration significative d'astéroïdes riches en olivine n'avait été détectée au sein des familles d'astéroïdes.

La spectroscopie permet de caractériser la composition de surface des astéroïdes. La Data Release 3 (DR3) de la mission Gaia de l'ESA a publié plus de 60 000 spectres de réflectance de petits corps, offrant une occasion unique de rechercher des traces de différenciation dans la ceinture principale. En exploitant ces données spectrales et en classifiant les astéroïdes au sein de classes taxonomiques connues, j'ai découvert que la famille (36256) 1999XT17 contient un nombre significatif de membres dont le spectre correspond à celui de l'olivine. Ils pourraient être des fragments d'un corps formé dans le manteau d'un planétésimal différencié, puis implanté dans la ceinture principale a posteriori. Cette famille est la première famille d'astéroïdes potentiellement riche en olivine identifiée.

Les météorites présentent une large gamme de compositions, caractéristiques des astéroïdes dont elles proviennent. Certaines sont des produits de la différenciation, comme l'andésite Erg Chech 002 (EC002). Connue comme la "plus ancienne achondrite du système solaire", cette météorite s'est vraisemblablement formée dans la croûte partiellement fondue d'un planétésimal différencié. En exploitant les données spectrales de la DR3, j'ai cherché à identifier des analogues potentiels à cette météorite dans la ceinture principale. En utilisant des méthodes de comparaison de spectres, j'ai identifié 142 astéroïdes avec un spectre visible semblable à celui de la météorite. Vingt de ces analogues potentiels ont été observés dans la gamme de longueur d'onde proche infrarouge, et aucun n'a été confirmé. Cependant, l'astéroïde (10537) 1991 RY16, dont le spectre a été publié dans la littérature, semble de composition similaire à celle de la météorite. Ainsi, les astéroïdes présentant des compositions andésitiques pourraient être extrêmement rares.

Un aspect important de cette thèse de doctorat a été l'analyse générale des spectres de réflectance des petits corps publiés lors de la DR3. En tant que membre du consortium de production et d'analyse des données (DPAC), j'ai identifié des problèmes potentiels dans les spectres d'astéroïdes et proposé des corrections afin de les améliorer, pour préparer la DR4. J'ai également classifié ces spectres, afin d'évaluer les limites du jeu de données et pour identifier de nouveaux astéroïdes riches en olivine. J'ai découvert 78 astéroïdes potentiellement riches en olivine qui n'avaient encore jamais été caractérisés par spectroscopie, constituant une concentration d'objets riches en olivine dans la ceinture principale cinq fois plus importante que précédemment évalué. Ces études montrent que, bien que les preuves de différenciation semblent rares dans la ceinture principale, l'interprétation des études précédentes devrait être révisée à la lumière de bases de données spectroscopiques telles que celles fournies par la mission Gaia.

Mots clés Astéroïdes · spectroscopie · Gaia

ABSTRACT Planetesimals are the "building blocks of planets" that formed from dust accretion in the Sun's protoplanetary disk. It is established that the largest and early-formed planetesimals partially or completely differentiated, organizing into layers of distinct densities and compositions: an iron-rich core, an olivine-rich mantle, and an igneous crust. Evidence of differentiation is given by meteorites and should be observable today in the composition of asteroids. The catastrophic disruption of a differentiated body should produce a family of fragments with a range of compositions reflecting each layer of the original body. Evidence of differentiation should therefore be detected in asteroid collision families, but no such family has been clearly identified to date. In addition, extensive spectroscopic studies have highlighted a lack of olivine-rich bodies in the Main Belt, known as the "missing mantle problem". Prior to my work, no significant concentration of olivine-rich asteroids had been detected in any asteroid family.

Spectroscopy is a powerful tool for probing the surface composition of asteroids. The Data Release 3 (DR3) of ESA's Gaia mission includes over 60,000 reflectance spectra of small bodies and presents a unique opportunity to search for evidence of differentiation in the Main Belt. By exploiting this dataset and classifying asteroids using well known taxonomic schemes, I discovered that the family (36256) 1999 XT17 contains a significant number of asteroids likely to exhibit olivine-rich compositions. This is the first family of potentially olivine-rich asteroids ever identified. It could result from the breakup of an olivine-rich parent body, that could have formed in the mantle of a differentiated planetesimal. This planetesimal could have been catastrophically disrupted in another region of the Solar System, and one of its fragments - the parent body of the family - could have been implanted into the Main Belt.

Meteorites display a wide range of compositions, characteristic of the asteroid from which they derive. Establishing a link between these objects and asteroids provides a better understanding of their formation and evolutionary processes. Some meteorites are products of differentiation, such as the andesite Erg Chech 002 (EC002), understood to have formed in the partially molten crust of a differentiated planetesimal and known as the "oldest achondrite of the Solar System".

I searched for potential spectral analogues of this meteorite in the Main Belt, exploiting the Gaia DR3 dataset. Using spectral parameter comparisons and a curve-matching method, I identified 142 asteroids with Gaia DR3 visible spectra potentially alike those of the meteorite. Twenty of these potential analogues were observed in the near-infrared wavelength range, but none presented an EC002-like spectrum. Studying literature spectra, asteroid (10537) 1991 RY16 appears a possible compositional match to this meteorite. Overall, asteroids presenting andesitic compositions might be extremely rare.

An important aspect of this PhD thesis work was devoted to the general analysis of the Gaia DR3 reflectance spectra of small bodies, as I am a member of the Data Production and Analysis Consortium. I identified potential issues in the spectra and proposed corrections to improve them, to prepare for the DR4. Additionally, I worked on a classification of Gaia DR3 reflectance spectra both to assess the limitations of this dataset, and to look for olivine-rich asteroids in the Main Belt. I discovered 78 potentially olivine-rich asteroids never characterized with spectroscopy before, and a concentration of olivine-rich objects in the belt five times larger than previously assessed. These studies lead to the conclusion that, although evidence of differentiation appears rare in the Main Belt, the interpretation of previous studies should be revised in the light of large-scale spectroscopic surveys such as Gaia.

Keywords Asteroids · spectroscopy · Gaia

ACKNOWLEDGEMENTS

Quand j'étais petite, je voulais être bibliothécaire. Puis j'ai voulu être écrivain, mais mes parents m'ont dit que ce n'était pas un métier très stable. Du coup, j'ai choisi un autre métier instable : astrophysicienne.

Je n'aurais jamais découvert ce métier sans Bertrand Plez, notre voisin dans la petite ville de Prades-le-Lez où j'ai grandi. Bertrand, merci d'être passé chez nous à chaque éclipse avec les lunettes spéciales, et d'être venu à l'école nous parler de la comète de Halley. Merci aussi de m'avoir permis de faire mon stage de troisième au LUPM, ce qui a définitivement confirmé mon intérêt pour l'astrophysique et a guidé mes pas jusqu'à l'achèvement de cette thèse. Je ne serais sans doute pas là aujourd'hui sans toi.

Je n'y serais pas non plus arrivée sans mes directeurs de thèse. Marco, grazie mille pour l'enthousiasme contagieux que tu montres envers la science et ta confiance vis à vis de mon travail. Cette thèse ne serait pas la même sans tes précieux conseils tout au long de ces trois ans, et ta lecture attentive de ce manuscrit. Laurent, merci pour la manière que tu as eu de guider mes pas quand nous explorions les données Gaia ensemble, et pour ton écoute, tes mots rassurants et tes conseils avisés tout au long de la thèse. Merci à tous les deux pour votre présence et votre réactivité sans faille, même lorsqu'il a fallu relire des abstracts ou chapitres de la thèse à la dernière minute (certaines conclusions donnent des torticolis). Vous avez fait de moi une jeune chercheuse indépendante et je vous dois de m'avoir permis de m'épanouir dans la planétologie.

I want to thank as well Chrysa, who was in a way my third supervisor. Thank you for offering your expertise and help throughout this PhD, and for always providing expert advice on scientific matters. You taught me and enabled me to observe asteroids, and you were always there to help me with the IRTF and diverse other matters. Your rigour and determination are examples that I look up to.

I would like to thank the members of my jury Pierre Beck, Audrey Bouvier, Sonia Fornasier and Marcel Popescu, for their time and kind words during my defense. I enjoyed discussing with each of you before and during the defense, and I highly appreciated your coming to Nice for this special day. To my rapporteurs Pierre Beck and Sonia Fornasier, thank you for your detailed reports and your thorough reading of this thesis. These reports, together with additional great insights of Audrey Bouvier and Marcel Popescu, have enabled me to further improve this manuscript. I would be delighted to collaborate with each of you in the future.

Before starting this PhD, my interest for astrophysics was confirmed and strengthened during internships under the excellent supervision of Gianrico Filacchione, Kévin Baillie, Valéry Lainey and Florian Debras. Thank you all for having been encouraging and caring supervisors, who made me want to continue in this path.

Of course, this PhD would not have been the same in another lab. When I chose to come to Nice, I did not know that I was about to meet such incredible friends. I had the chance of starting the PhD at the same time as Fabiola, Marie and Philippine. Your presence made the Observatory a welcoming place, and knowing that you were there always helped me wake up in the morning (not too early however). All the coffee breaks, conversations, sun breaks, afternoons at the beach or evenings playing games or chatting that we shared will remain bright memories in my heart forever. Fabi, your constant presence in the office next door has been a comfort for three years, and I could not imagine this PhD without you. Thank you for all the time spent together, for all the laughs and the singing, for the empathy and caring that you radiate and for your ability to bring light wherever you go. Marie, je n'oublierai jamais toutes ces douces soirées passées chez toi, et toutes nos conversations autour de la vie et de livres. En attendant d'ouvrir notre club de lecture, je sais que je trouverai toujours chez toi une oreille attentive et des conseils avisés. Merci pour ton amitié et ton immense capacité d'écoute. Philou, ton soutien inébranlable et ta confiance ont été des piliers pendant ces trois ans. Tu as toujours su trouver les mots pour me rassurer quand j'en avais besoin, et la passion que tu montres pour ton sujet de recherche est un exemple. Merci pour tous les partages de séries, de bonnes adresses, de thés et de conseils sur les plantes (also Fabi and Philou, thanks for all the rides down the hill). Merci pour tout les Princesses.

Many other people at this lab had a major impact in my life during this PhD. When I started, I had the chance of meeting Max, Nico, Sab, Julia and Camille. Max, you have been taking care of me since my first day at the obs, thank you for being such a mentor in asteroid science. Nico, Sab, Julia and Camille, thank you for your warm welcome and for paving the way for us in this academic life. Thank you Marco (of Nico) for integrating so well and bringing your kindness to this group of astrophysicists.

Luana, you were here at the beginning of my PhD, and you are here again at the end, as you should. I missed your laugh and sense of humour while you were away, and I am delighted to be in the same field as you, so we can meet at every conference. I look forward to seeing you again, so we can keep on sharing great moments and songs.

Early in my first year I met as well Lucas, Tristan and Paul, who brought a lot of laughters and good memories in these three years. Paulina and Joe arrived later, and they generated many fun moments and parties at their flats. Joe, thank you for all the music and conversations shared, and Pauli for always being so chill and welcoming.

When I met Raphael, I did not know I had just encountered a molkky rule and 3D printer master. Thank you for your sense of humour, your creativity and your sweetness. I discovered Kate during summer, whom I had the pleasure of seeing stay for her PhD. Thank you for the unique fairy vibe you bring to this Observatory. Among the new PhD students, Adrien, Daniele and Isaure added some fun in the PhD team, with their ability to speak and share, their sense of humour, and their skills (or lack thereof) at molkky and Time's Up. Thanks for all the good moments. Katherine became my new office mate, with whom I have the pleasure of sharing a fantasy world. Journey before destination, Katherine.

At the end of my second year I discovered Rob, who managed to stay in Nice for his PhD and bring his craziness and friendship to my life. Grazie per tutti i risotti Bobby. Among the more permanent members of the Observatory, the Americans, such as Harrison and Max, started populating the lab and (unfortunately) winning at molkky.

Some other friends came and left during these three years, such as Steve, Fernando, Federico, Pietro, Cyril, Oliver, Camille C., Maya, Gabe and Lapo. Some of you became very dear to me, thank you for passing by the obs and settling in my life. This academic life lead me to make friends at conferences too, such as Lucas McClure and David Morate, or the awesome group from the CNES days. These experiences showed me that the shortest encounters can lead to the greatest friendships.

Overall, this whole PhD would have been very different without each of the wonderful people named above and the healthy and joyful work environment they provide.

If this lab is that nice, it's also thanks to the great permanent researchers that are part of it. Thank you to the TOP team for being such a good place where young researchers can evolve and thrive. I would like to thank especially Aurélien, Benoit, Paolo, Elena, Roxane and Emanuele for all the fun moments and conversations. Un merci spécial aux membres de mon comité de suivi de thèse, Héloïse Méheut et Mathieu Vincendon, pour avoir toujours été à l'écoute et de bon conseil. Merci au chef Khaled et à toute l'équipe de la cantine, qui est parfois la motivation principale pour venir à l'Observatoire.

Enfin, j'aimerais remercier toutes les personnes qui n'étaient pas présentes directement au labo, mais qui m'ont guidée et soutenue pendant ces 3 ans. Tout d'abord, merci à ma famille qui fait preuve d'une bienveillance, d'un amour et d'un soutien indéfectible depuis toujours. Merci à mon super petit frère et à Matthieu d'être venus pour ce jour si spécial, et merci à mes grands parents, oncles, tantes et cousines d'avoir été nombreux sur zoom et de m'avoir soutenue à distance. Merci aussi à mes amis : Cassandre, Lucile, Xavier et Coline pour être venus et avoir suivi les étapes majeures de ma thèse depuis Paris, et de manière plus générale, merci d'être toujours présents et d'être les amis incroyables que vous êtes. Parmi la clique du M2, merci aussi aux Bruno et aux Raph, et à Maud. Merci à Julien, Théophile, Raphael, Emrys and co pour tous les bons moments et les péripéties depuis la L3. Merci au gang de la prépa Valou, Lucie et Floriane, qui me soutiennent et me suivent depuis toutes ces années. Finally, I would like to thank the friends I made during the internship before starting my PhD and that I kept to this day, Stefano and Anthony. Thanks for all the laughs and good memories, and thank you Ste for being such a guide and an example in science and life.

Since this thesis would not have been the same without all of these people, I dedicate it to them.

CONTENTS

I ASTEROID DIFFERENTIATION FROM GAIA REFLECTANCE SPECTROSCOPY 1

1 ASTEROIDS, FROM THE SOLAR NEBULA TO TODAY 3
- 1.1 Formation and evolution . . . 3
  - 1.1.1 Reservoirs of small bodies in the Solar System . . . 3
  - 1.1.2 From the solar nebula... . . . 5
  - 1.1.3 ... to today's Main Belt . . . 7
- 1.2 Dynamical asteroid families . . . 9
  - 1.2.1 Hierarchical clustering method . . . 9
  - 1.2.2 V-shape . . . 12
- 1.3 Asteroids composition . . . 14
  - 1.3.1 Spectroscopy, photometry and albedo . . . 14
  - 1.3.2 Asteroid classification . . . 16
  - 1.3.3 Spectral types and composition . . . 20
  - 1.3.4 Spectral ambiguity and space weathering . . . 21
- 1.4 Meteorites . . . 23
  - 1.4.1 Short history . . . 24
  - 1.4.2 Finding meteorites today . . . 24
  - 1.4.3 Meteorite classification . . . 25
- 1.5 Linking meteorites with asteroids . . . 29
- 1.6 Differentiation: current questions and open problems . . . 33
- 1.7 The Gaia mission . . . 35
  - 1.7.1 The Gaia satellite . . . 36
  - 1.7.2 The BP and RP spectrophotometers . . . 38
  - 1.7.3 Gaia DR3 mean reflectance spectra . . . 39
- 1.8 Outline of the thesis . . . 41

2 GAIA DR3 BP-RP SPECTRA 43
- 2.1 Identified issues of asteroids mean reflectance spectra . . . 44
  - 2.1.1 BP-RP epoch reflectance spectra mismatch . . . 44
  - 2.1.2 "Fake band" around 650 nm . . . 44
  - 2.1.3 Solar analogue and near-UV . . . 45
  - 2.1.4 "RP reddening" . . . 45
  - 2.1.5 Comparison with the SDSS . . . 46
  - 2.1.6 Comparison with SMASS . . . 47
- 2.2 Epoch reflectance spectra analysis . . . 49
  - 2.2.1 Analysis of the BP-RP epoch reflectance spectra mismatch . . . 52
  - 2.2.2 "Wiggly BP" . . . 53
  - 2.2.3 High frequency variations . . . 54
  - 2.2.4 Analysis of the "RP reddening" . . . 55
- 2.3 "RP reddening" analysis: C-, X-, and S-complex study . . . 56
  - 2.3.1 "Red slope" . . . 57
  - 2.3.2 Payload decontamination . . . 58

2.3.3 Comparison with the literature 60
2.4 Solar Analogue 61
2.4.1 Red slope 62
2.4.2 NUV slope 63
2.5 Filtering method study: MAD-clipping procedure 64
2.6 Conclusions and perspectives 66
3 THE METEORITE ERG CHECH 002 71
3.1 The ungrouped achondrite Erg Chech 002 71
3.2 Data 74
3.3 Methods 75
3.3.1 Identification of potential analogues of EC 002 with spectral parameters comparison 75
3.3.2 Identification of potential analogues of EC 002 with a curve matching method 79
3.4 Results 80
3.4.1 Spectral parameters comparison 81
3.4.2 Curve matching method 83
3.5 Discussion of the study in the visible wavelength range 83
3.5.1 Choice of curve matching coefficient 84
3.5.2 Proper orbital elements and asteroid families 85
3.5.3 The band around 650 nm 88
3.6 Observations in the NIR wavelength range 89
3.6.1 Target selection 91
3.6.2 Instruments 92
3.6.3 Reduction 92
3.7 Analysis of the Observations 94
3.7.1 Classification of the observed spectra 94
3.7.2 Producing VISNIR spectra 97
3.7.3 Spectral features analysis: BIC and BAR 97
3.8 Discussion 105
3.9 Conclusions and perspectives 108
4 THE FAMILY (36256) 1999 XT17 111
4.1 Family selection 111
4.2 Characterisation of the (36256) 1999 XT17 family 113
4.2.1 NIR observation of (33763) 1999 RB84 114
4.2.2 Classification of family members 115
4.2.3 Comparison with meteorites 116
4.3 Discussion on the methods 120
4.3.1 Family selection 120
4.3.2 Classification algorithm 121
4.4 Dynamical aspects and family formation scenarios 122
4.5 Conclusions 127
5 CLASSIFICATION OF GAIA DR3 SPECTRA 129
5.1 Data 130
5.2 Methods 130
5.2.1 Classification algorithm: curve matching 130
5.2.2 Confusion matrix 131

5.2.3 Principal Component Analysis 132
5.3 Building the classification 132
5.3.1 Testing the algorithm: classification of SMASS spectra using Bus templates 133
5.3.2 Study of the templates: classification of Gaia DR3 spectra 134
5.3.3 "True" classes on the basis of VISNIR and NIR spectroscopy . . . 140
5.4 Final classification 143
5.5 Improving the classification of A-types 145
5.5.1 A-types and BP slope 145
5.5.2 BP classification 147
5.6 Application of the classification method 148
5.6.1 Gaia classification of the (36256) 1999 XT17 family 149
5.6.2 Classification of Gaia DR3 asteroid spectra 150
5.6.3 Gaia A-type asteroids 152
5.7 Perspectives and conclusions 156
6 CONCLUSIONS AND PERSPECTIVES 159
6.1 Conclusions 160
6.2 Perspectives 162

II APPENDIX 165
A GAIA DR3 BP-RP SPECTRA 167
B THE METEORITE ERG CHECH 002 171
C CLASSIFICATION OF GAIA DR3 SPECTRA 195
C.1 Building the NIR list 195
C.1.1 B-types 211
C.1.2 K-types 212
C.2 Validation and discussion 215
C.2.1 Templates 215
C.2.2 SNR limit 217
C.2.3 Principal Component Analysis and curve matching 218
C.3 A-types 222

BIBLIOGRAPHY 227

LIST OF FIGURES

Figure 1.1 Scheme of the main reservoirs of asteroids in the Solar System. 4

Figure 1.2 Scheme of the orbits of the three groups of Near-Earth Asteroids: the Amors, Apollos, Atens and Atiras. Inspired from a scheme by Shamil Biktimirov. 5

Figure 1.3 Simplified scheme illustrating the different stages of planet formation in a protoplanetary disk. Inspired from a scheme of Takayuki Tanigawa. 6

Figure 1.4 Schematic representation of planetesimal differentiation. 6

Figure 1.5 Dynamical structure of the Main Belt seen from its proper orbital elements. Mean motion resonances with Jupiter are displayed in dashed lines, as well as the secular resonance ν_6. The Inner, Middle and Outer Main Belt are highlighted, and the "pristine zone" is indicated as well as the Hungaria, Cybele and Hilda groups. This figure is inspired from Figure 1.3 from Max Mahlke's PhD thesis. 8

Figure 1.6 Simplified illustration of three possible outcomes of a catastrophic collision. The fragments orbiting around what remains of the parent body are likely to accrete and form rubble-pile bodies. Scheme inspired from the course of Alain Doressoundiram. 9

Figure 1.7 Simplified illustration of the steps of the HCM applied to the proper orbital elements space of asteroids. The proper inclination versus eccentricity space is taken as an example for clarity, the HCM being applied to the 3D space including the proper semi-major axis. 10

Figure 1.8 Proper inclination versus proper eccentricity scatter plots showing the Vesta (green), Flora (cyan), Baptistina (orange), Massalia (blue) and Nysa–Polana–Eulalia (magenta) families in the Inner Main Belt (left panel). The right panel shows the same proper elements plot after removal of these families. Black dots corresponds to non family asteroids in Nesvorny et al. (2015), and the red dots in the right panel coloured for a specificity of Dermott et al. (2018) are here considered as non-family members as well. Figure taken from Fig.1 of Dermott et al. (2018). 11

Figure 1.9 Illustration of the diurnal Yarkovsky effect, in the case of a prograde and retrograde rotator. The direction of the thermal force generated by the emission of heat is represented by wide orange arrows. 13

Figure 1.10 Inverse diameter versus semi-major axis plot of the Massalia family. Two V-shapes are shown according to different V-shape parameters, α and C (see Bolin et al. (2018) for a full description). Figure taken from Bolin et al. (2018). 13

Figure 1.11 Figure 3 of Gaffey (2011), showing the reflectance spectra in the visible and near-infrared wavelength range of four major anhydrous mineral phases in meteorites and asteroids. Olivine and pyroxene show deep absorption bands, while the iron metal spectrum is featureless. Spinel is an aluminum magnesium oxide (AlMg), showing an almost featureless spectrum in the visible wavelength range. The curves have been offset for clarity. . 15
Figure 1.12 Panel (a): Fig.2 of Morrison (1977), showing the distribution of measured geometric visual albedo obtained for his dataset of asteroids. The numbers and designations inside the histogram are those of each of the 187 considered asteroid. The low-albedo peak corresponds to carbonaceous asteroids, and the higher-albedo peak to silicaceous asteroids. Panel (b): same histogram considering the 41 468 asteroids having a spectrum in the Gaia Data Release 3 catalogue and albedo values in MP3C. 16
Figure 1.13 Fig.15 from Bus and Binzel (2002a) showing the 26 taxonomic classes defined from SMASSII survey, developed from spectra spanning the visible wavelength range. The horizontal and vertical scaling are constant, and the horizontal line plotted with each spectrum represents a reflectance of 1.0. 17
Figure 1.14 Fig.15 from DeMeo et al. (2009) showing the extension of the Bus and Binzel (2002a) taxonomy in 24 taxonomic classes, from observations in the NIR. The spectra cover the wavelength range from 450 to 2450 nm. The horizontal and vertical scaling are constant, and the horizontal line plotted with each spectrum represents a reflectance of 1. 18
Figure 1.15 Combination of the Fig.9, 12 and 15 from Mahlke et al. (2022) showing the mean (solid line) and standard deviation (shaded area) of the reflectance spectra for each of the 17 taxonomic classes, along with the mean, lower and upper quartiles, and the 5 and 95 percentiles of the distribution of visual geometric albedo within each class. The classes are grouped into the S, M and C-complexes. 19
Figure 1.16 Scheme illustrating the global evolution of taxonomy, from Chapman et al. (1975) to Mahlke et al. (2022). Each letters refers to a taxonomic class defined in each scheme, and the classes are grouped in complexes: the S (green), C (blue), X (pink) or M (orange) complexes. The U class in Chapman et al. (1975) taxonomy indicates an "undefined" class. The core and end-members are not indicated prior to Bus and Binzel (2002a), as these designations were not introduced at the time. 20
Figure 1.17 Scheme illustrating the phase angle of an observation. 22

Figure 1.18 Schematic view of the possible delivery of Main Belt fragments of asteroids to Earth, inspired from Fig.1 of Greenwood et al. (2020). The Main Belt is represented in the proper inclinations versus proper semi-major axis space. A differentiated body that undergoes a collision is illustrated, generating a family of fragments. One of these fragments, by the combined actions of collisions, gravitational perturbations and non-gravitational forces, falls in a resonance (here the 3:1 MMR with Jupiter). Once in the resonance, the fragment enters the Near-Earth space and can either fall directly on Earth in the form of a meteoroid, or become a NEO. NEOs or fragments of them can eventually fall on Earth and be found as meteorites. 23

Figure 1.19 Carbonaceous chondrite Allende, on which are indicated Calcium-Aluminium-rich Inclusions (CAIs), chondrules, and the matrix. Image credit: Matteo Chinellato. 26

Figure 1.20 Scheme of the classification of meteorites. Inspired from schemes by Laurette Piani and in Ruf et al. (2018). 27

Figure 1.21 Reflectance spectra of (4) Vesta and some vestoids, along with the spectra of howardite Le Teilleul, eucrite Juvinas, and diogenite Johnstown acquired by Gaffey, 1976. Figure taken from Burbine et al., n.d. 30

Figure 1.22 Reflectance spectra of various asteroid spectroscopic types, along with the spectra of meteorite types they are linked with. Figure taken from Vernazza and Beck, 2016. Spectra are all normalized to unity at 550 nm and are offset vertically for clarity. The V, K, A, Xc, and Cgh spectra are the average template spectra of the taxonomic scheme of DeMeo et al., 2009. The two S-type spectra are averages of S-type asteroids spectra presenting H-like (top) and LL-like (bottom) compositions according to Vernazza et al., 2014. The diogenite and eucrite spectra are averages of all the spectra of meteorites in these families available in the RELAB database at the time of the publication of Vernazza and Beck, 2016, as well as the spectra of The H, LL, CR, CO, CV, EC, CM and iron meteorite spectra. The howardite spectrum is the one of meteorite EET 87503 (25-25 µm size fraction), the pallasite is Thiel Mountain's spectrum (Sunshine et al., 2007), the brachinite is Brachina's spectrum (Reflectance Experiment LABoratory (RELAB)), and the aubrite's spectrum is the one of Mayo Belwa (RELAB). 32

Figure 1.23 Orbital distribution of A-types in the Main Belt, from Fig.4 of DeMeo et al. (2019). Green full circles show A-types confirmed with near-infrared data in DeMeo et al. (2019), and A-types known previously from this work are plotted as empty green circles. 35

Figure 1.24 Gaia motion and scanning law at the L2 Lagrange point. Image credit: ESA. 36

Figure 1.25 Gaia focal plane. The wave-front sensor and basic-angle monitor have for function the realignment of the telescopes in orbit, while the sky mapper (SM) is made for detecting objects entering the fields of view down to magnitude 21 and communicating to the on-board electronics. The main astrometric field (AF), the blue and red spectrophotometers (BP and RP) and the radial velocity spectrometer (RVS) are briefly described in the text. Image credit: ESA. 37

Figure 1.26 DR3 epoch spectrum and epoch reflectance spectrum of a transit of asteroid (90) Antiope. 40

Figure 1.27 Mean reflectance spectrum of asteroid (90) Antiope published in the DR3. Every data point is flagged with a 0 digit for this spectrum. 40

Figure 2.1 Figure extracted from Gaia Collaboration et al. (2023), showing the epoch reflectance spectra of asteroid (61) Danae. The grey points are epoch reflectance values filtered out by the σ-clipping procedure, and the accepted values are coloured in light blue for the BP and light red for the RP. The large empty circles correspond to the 16 data bands chosen to produce the mean reflectance spectra of the DR3. 44

Figure 2.2 Normalised reflectance spectra of asteroid (4) Vesta from the DR3, compared with the spectrum of Xu et al. (1995). The 16 data bands of the Gaia DR3 spectrum are given a colour and a symbol according to the value of the flag associated to the band: blue circle if flag=0, orange diamond if flag=1 and red star if flag=2. The literature spectrum is displayed as grey dots. 45

Figure 2.3 Comparison of the gri slope and $z-i$ parameter for the subsample of 14 129 asteroids observed both by Gaia and SDSS. . 47

Figure 2.4 Normalised reflectance spectrum of asteroid (25) Phocaea from the DR3 (blue dots), and from Bus and Binzel (2002b) (grey). Every band of this DR3 spectrum is associated to a null flag. . . 48

Figure 2.5 Histogram of the global slope (calculated between 462 and 946 nm) and the BP slope (calculated between 462 and 726 nm) for the 1187 asteroids both included in a filtered Gaia DR3 dataset and in SMASS. The Gaia DR3 data are represented in red colors, and the SMASS data in blue. 48

Figure 2.6 Example of normalised epoch reflectance spectra showing flagged issues. In grey dots are displayed every epoch reflectance spectra of a given object, and the BP and RP analysed epoch reflectance spectra are plotted as blue and red dots respectively. Each highlighted epoch spectrum is associated to a transit_id and corresponds to a given asteroid, which number and name are given in the title of each figure. 51

Figure 2.7 Every epoch reflectance spectra of asteroid (13) Egeria, colour-coded with the absolute value of the across scan velocity (left panel) and along scan velocity (right panel). the error bars are not represented here. 52

Figure 2.8 Proportion of matched (black) and mismatched (grey) BP-RP epoch reflectance spectra with respect to the absolute value of the across scan velocity. 53
Figure 2.9 DR3 mean reflectance spectra of asteroids (40244) 1998 WP4 and (42531) McKenna, that get filtered out because of the high across scan velocity values at which were acquired their respective epoch spectra. The 16 data bands of the Gaia DR3 spectrum are given a colour and a symbol according to the value of the flag associated to the band: blue circle if flag=0, orange diamond if flag=1 and red star if flag=2. The colours and symbols of the DR3 spectra data bands will respect this same convention in the following. 54
Figure 2.10 BP (blue) and RP (red) epoch spectrum of asteroid (588) Achilles, on which the effect of a cosmic ray is visible in the BP part. . . 55
Figure 2.11 Histogram of the transits showing a RP reddening phenomenon (black colour) compared to all analysed transits (grey colour), with respect to the date at which the spectra were acquired. 266 transits were flagged as affected by a RP reddening. 55
Figure 2.12 BP and RP epoch reflectance spectra of asteroid (5) Astraea, taken respectively on November 6, 2014 and on May 10, 2017. The linear spline fitting the red slope is displayed in black colors. 56
Figure 2.13 Study of the slope of the linear regression fit of the epoch reflectance spectra from 900 to 1070 nm (red slope) for the S, C and X-complexes, after outliers rejection. The rejected outliers are displayed as grey dots, the accepted values as black dots, and the moving average as a blue line. 57
Figure 2.14 Superposition of the smoothed moving average of the red slope, for each taxonomic complex considered. The smoothed moving average corresponding to the S, C and X-complexes is displayed in green, blue and orange colours, respectively. 58
Figure 2.15 Study of the influence of the phase angle on the red slope. The median slope calculated on phase angle bins is displayed as red dots. 59
Figure 2.16 BP and RP epoch reflectance spectra of asteroid (192) Nausikaa, taken before (panel a) and after (panel b) the third payload decontamination. 59
Figure 2.17 Gaussian fit of the histogram of the calculated red slope on asteroids members of the S, the C and the X-complex, displayed on panels a), b) and c) respectively. In black, gaussian fit of the histogram of red slope difference between the one calculated on literature spectra from DeMeo et al. (2009) and the one calculated on Gaia DR3 mean reflectance spectra. In orange, red slope difference calculated between the red slope of DeMeo et al. (2009) spectra and the one calculated on filtered Gaia spectra. A line at 0 nm is highlighted in red, and the legend displayed in panel a) applies for panels b) and c). 60

Figure 2.18 Gaussian fit of the histogram of the calculated red slope on asteroids members of the S, the C and the X-complex, displayed on panels a), b) and c) respectively. In black, Gaussian fit of the histogram of the red slope difference between the one calculated on literature spectra from DeMeo et al. (2009) and the one calculated on Gaia DR3 mean reflectance spectra. In orange, red slope difference calculated between the red slope of DeMeo et al. (2009) spectra and the one of filtered Gaia spectra. In blue, same difference calculated on filtered Gaia DR3 spectra produced with the new mean solar analogue. A line at 0 nm is highlighted in red, and the legend displayed in panel a) applies for panels b) and c). 62

Figure 2.19 Gaussian fit of the histogram of the calculated NUV slope on the 154 asteroids having spectra in the filtered DR3 and in Tinaut-Ruano et al. (2023). In black is displayed the Gaussian fit of the histogram of the NUV slope difference between the one calculated on spectra from the ECAS database and the one calculated on Gaia DR3 mean reflectance spectra, in orange the red slope difference calculated between the red slope of ECAS spectra and the one calculated on filtered Gaia spectra, and in blue the same difference calculated on filtered Gaia DR3 spectra produced with the new mean solar analogue. In green is displayed the Gaussian fit of the histogram of the NUV slope difference between ECAS and the Gaia mean reflectance spectra calculated using Hyades 64 as solar analogue. A line at 0 nm is highlighted in red. 63

Figure 2.20 Illustration of the Gaia bins chosen for the DR3, on asteroid (29) Amphitrite. Each bin is colour-coded with a colour different from the one of its two direct neighbouring bins. 65

Figure 2.21 Comparison of the results of the med+mad filtering method applied to (29) Amphitrite, without transits filtering (left panel) and computed using only the filtered spectra (right panel). On orange is overplotted the derived mean Gaia reflectance spectrum. 66

Figure 2.22 Effects of the filtering procedure on the epoch reflectance spectra of (13) Egeria and (29) Amphitrite. Panels a and b: every epoch reflectance spectra colour-coded with the absolute value of the across scan velocity. Panels c and d: epoch reflectance spectra accepted after the first two steps of our filtering procedure. Panels e and f: data points accepted after filtering out spectra acquired after the third decontamination period. The error bars are not represented for clarity. 67

Figure 2.23 Effects of the filtering procedure on the mean reflectance spectra of (13) Egeria and (29) Amphitrite. Produced mean reflectance spectra after filtering (orange dots), DR3 spectrum (black dots) and literature spectrum from Bus and Binzel (2002a) (grey dots). 68

Figure 3.1 Fragment of the meteorite Erg Chech 002. *Credit*: Anthony Irving (University of Washington), The Meteoritical Society. 72

Figure 3.2 Figure from the supplementary material of Barrat et al. (2021), showing the reflectance spectrum of a powder sample of EC 002 compared to the spectra of the V and O-types of DeMeo et al. (2009). 73

Figure 3.3 VISNIR spectra of the powder (black lines) and three slabs samples (red lines) of EC 002 acquired by Barrat et al. (2021), along with the modelled space weathered spectra of the powder sample (from light to dark blue with increasing space weathering) corresponding to SW low, medium and high. 74

Figure 3.4 Gri-slope and $R_z - R_i$ parameters on the Gaia DR3 reflectance spectrum of (1459) Magnya (black dots). The cubic smoothing spline of the DR3 spectrum is in grey lines. The reflectance values at wavelengths corresponding to the central wavelength of the SDSS filters are indicated as coloured diamonds, with $R_g = R(\lambda = 468.6 \text{ nm})$ the normalisation wavelength, $R_r = R(\lambda = 616.6 \text{ nm})$, $R_i = R(\lambda = 748.0 \text{ nm})$, and $R_z = R(\lambda = 893.2 \text{ nm})$. . 76

Figure 3.5 Distribution of depth of the band around 1000 nm with respect to the spectral slope of every Gaia asteroid (grey dots). Red squares: raw slabs of the meteorite EC 002. Purple square : powder sample of the meteorite. Full orange diamond: barycentre of these 4 samples, and empty orange diamond: shifted barycentre along the "space weathering line". The squares going from light blue to dark blue represent the modelled space-weathered spectra of EC 002, with different space weathering intensity. The orange ellipses are the 3-σ ellipse respectively around the barycentre and shifted following the space weathering behaviour of EC 002. The two dashed blue lines delimit a "possible matches area", within which can be found candidate asteroids matching EC 002. 78

Figure 3.6 Spectra of a powder, three raw slab samples and three modelled spectra of space-weathered of EC 002 sampled and normalised as Gaia data, not taking into account the first and last Gaia bands. 80

Figure 3.7 Distribution of depth of the band around 1000 nm with respect to the spectral slope of every Gaia asteroid (grey dots). See Fig.3.5 for the legend. Pink stars: asteroids matching the raw slabs and powder sample of EC 002, found within the "possible matches area". Cyan stars: asteroids matching the space-weathered samples, found within the "possible matches area". Dark red stars (resp. green stars): asteroids matching EC 002 (resp. the space-weathered modelled spectra of EC 002) according to the curve matching method. 82

Figure 3.8 Proper orbital element plots of Gaia asteroids with absolute magnitude H<14.5 (light grey dots). Vesta and Flora family members are indicated respectively with black and blue dots. Asteroids that were found to be spectroscopically matching with EC 002 after visual inspection are plotted with dots circles indicated in the legend above. Proper orbital elements retrieved from the Belgrade catalogue `http://asteroids.matf.bg.ac.rs/fam/properelements.php`. 86

Figure 3.9 Same as Fig. 3.8, but with cyan dots indicating asteroids that have spectral parameters compatible with the space-weathered models of EC 002 derived by Barrat et al. (2021) in the spectral parameters space. The green dots are asteroids matching the weathered models of the meteorite spectra using the curve matching method. 87

Figure 3.10 VISNIR spectra of the powder sample of EC 002 (black lines) and of asteroid (10537) 1991 RY16 (orange lines) retrieved from Fig.1 of Moskovitz et al. (2008). Both spectra were normalised at 550 nm. The two spectra show a similar shape, both showing a band around 650 nm and similar Band I centre. Their Band II centre appears shifted. 89

Figure 3.11 Observable asteroids with the IRTF on the night of November 11, 2023. This is a snapshot of the sky as seen by the IRTF at the beginning of our observation run, the date and time being indicated in UTC on the top right corner. The potential analogues of EC 002 without space weathering observable on that night are displayed as red dots, and their numbers are indicated in yellow boxes. In the white box is indicated the name of the pointed target, along with its V magnitude, and an idea of the seeing of the observation. 90

Figure 3.12 Distribution of depth of the band around 1000 nm with respect to the spectral slope of every Gaia asteroid (grey dots). See Fig.3.5 for the legend. The asteroids classified here as V-types are highlighted with a magenta V, and the asteroids respectively classified as S and A are shown with a green S and a red A. The two asteroids (12551) 1998 QQ39 and (27884) 1996 EZ1 are shown as black dots, as their NIR spectra did not allow a good classification. 96

Figure 3.13 NIR (grey lines) and DR3 spectra of the observed asteroids. Their designation is in the title, and the multiplicative factor applied to each NIR spectrum to align it with the VIS spectrum is in the legend of each sub-figure. The 16 bands of Gaia spectra are assigned a colour and symbol according to their flag value: blue circle if flag=0,orange diamond if flag=1 and red star if flag=2. 98

Figure 3.14 VISNIR spectrum of (1643) Brown, before and after continuum removal with a convex hull fit. The spectrum is displayed in grey dots, the continuum fit in orange lines. 100

Figure 3.15 Second order polynomial fit of the 1 micron band on the continuum-removed spectrum of (1643) Brown. The polynomial fit parameters are displayed in the red box, the equation of the fit being $y = ax^2 + bx + c$. 100
Figure 3.16 Band areas of the first and second bands of the continuum-removed spectrum of (1643) Brown. 101
Figure 3.17 Illustration of the continuum-removal (panels a and b), the Band I Center calculation with polynomial fitting (panels c and d) and the and Band Area Ratio calculation (panels e and f)for asteroids (18780) Kuncham (left panels) and (31060) 1996 TB6 (right panels). 102
Figure 3.18 Band I Center as a function of the BII/BI area ratio. The BIC and BAR of the meteorite powder and slab spectra are displayed as black and grey stars respectively, and the observed asteroids as black dots. The numbers of asteroids (18780) Kuncham and (31060) 1996 TB6 are highlighted next to their corresponding data point. The BIC and BAR of the taxonomic end-members of DeMeo et al. (2009) are highlighed in colours, the letter corresponding to the taxonomic type. Finally, asteroid (10537) 1991 RY16 is plotted as a black diamond. 104
Figure 3.19 Proper orbital element plots of Gaia asteroids with absolute magnitude H<14.5 (light grey dots). Vesta and Flora family members are indicated respectively with black and blue dots. Asteroids potential analogues of the meteorite EC 002 that we observed are highlighted as red diamonds. 106
Figure 3.20 Literature (grey dots) and Gaia DR3 spectra of asteroids (10537) 1991 RY16, (7472) Kumakiri and (14390) 1990 QP10. The 16 bands of the Gaia asteroid spectra are given a colour and a symbol according to the value of the flag associated to the band: blue circle if flag=0, orange diamond if flag=1 and red star if flag=2. 108
Figure 4.1 Proper orbital elements plots where are highlighted the pristine zone (black dots) and the family (36256) 1999 XT17 (orange diamonds). 114
Figure 4.2 Full VISNIR spectrum of (33763) 1999 RB84. The coloured part is the VIS Gaia DR3 spectrum, and in grey is displayed the acquired NIR spectrum. 115
Figure 4.3 Available data of the members of the family (36256) 1999 XT17 in the Gaia DR3: Gaia spectra (black dots), SDSS data from DeMeo and Carry (2013) (red dots), MOVIS data from Popescu et al. (2018a) (black squares), and NIR spectra from DeMeo et al. (2019) and from our own observations (grey stars). The shaded coloured areas represent the reflectance spectra from the A and S-type taxonomic templates of the Bus-DeMeo scheme (DeMeo et al., 2009), and the grey areas represent zones affected by telluric lines. 118

Figure 4.4 Proper orbital elements plots of the pristine zone (black dots) on which are highlighted S-complex families identified by Nesvorny et al. (2015). Only the asteroids having a Gaia DR3 spectrum are highlighted in this plot. 123

Figure 4.5 Figure 3 from Tsirvoulis et al. (2018): (221) Eos family V-shape and identified population of Eos fugitives in the pristine zone. The Eos family core as identified by Milani et al. (2014) is displayed in purple dots, and the asteroids in the pristine zone in the region delimited by $2.82 < a_p < 2.96$, $0.03 < e_p < 0.1$ and $0.12 < \sin(i_p) < 0.2$ in green dots. 124

Figure 4.6 V-shape (down panel) and proper orbital elements plots (top panels) of the (36256) 1999 XT17 and the (221) Eos family, according to Nesvorny et al. (2015). The Eos family members are displayed as grey crosses, and those of the 1999 XT17 family as circles. Black filled circles are 1999 XT17 family members that were classified as A-types by our algorithm, while the empty circles are members that were not classified as A. Family members that were classified A-types in the literature and have no DR3 spectra are marked with a red "X". Among the latter group, asteroid 76627 overlaps in the plot with asteroid 88052 (non A-type), due to their similar proper orbital elements and H magnitudes. The position of the 7:3 mean motion resonance with Jupiter is highlighted with a shade of light-grey. The V-shapes of the two families are drawn by eye following the equation $H = 5\log_{10}(|a - a_c|/C_0)$ with $a_C = 2.942$ au and $C_0 = 1.8 \times 10^{-5}$ au for the 1999 XT17 family, and $a_C = 3.017$ au and $C_0 = 2.25 \times 10^{-4}$ au for the Eos family. 125

Figure 5.1 Confusion matrix corresponding to the classification of SMASS spectra, using Bus and Binzel (2002a) templates. 133

Figure 5.2 Confusion matrix corresponding to the classification of Gaia DR3 spectra, using Bus and Binzel (2002a) templates. 135

Figure 5.3 Gaia templates (black dots), defined as the average of the prototypes of each taxonomic class of Bus and Binzel (2002a). The Bus templates are displayed as red dots for comparison. The type corresponding to each template spectrum is indicated on the top left of each sub-figure. 137

Figure 5.4 Confusion matrix corresponding to the classification of Gaia DR3 spectra using Gaia templates. 139

Figure 5.5 Confusion matrix corresponding to the classification of Gaia DR3 spectra using Gaia templates, with sub-classes grouped as complexes. 140

Figure 5.6 Confusion matrix corresponding to the classification of Gaia DR3 spectra of asteroids classified in the literature from VISNIR and NIR spectroscopy, using Gaia templates. The sub-classes are grouped as complexes. 142

Figure 5.7 Confusion matrix corresponding to the classification of Gaia DR3 spectra of asteroids classified in the literature from VISNIR and NIR spectroscopy, using Gaia templates. The sub-classes are grouped as complexes and the B-class is included in the C-complex. An exception is the Ch-class, considered here outside of the C-complex. The templates of the classes Sr, Sl, Q, R, O, Ld, T, Xc, Xe, and Cgh are not considered. 144
Figure 5.8 Proportion of asteroids in the NIR list classified as A or S-complex from the literature, depending on their Global spectral slope of BP slope value. Ranges of slopes go from 0 to a 2.6 by steps of 0.2. No asteroid shows BP slope values between 0.4 and 0.6 % $(100\ \mathrm{nm})^{-1}$ and between 2.2 and 2.4 % $(100\ \mathrm{nm})^{-1}$ in the chosen sample, which is why these regions are white in panel (B). 146
Figure 5.9 Plot of the principal component PC2′ with respect to the global spectral slope, calculated for the 18 739 filtered Gaia DR3 asteroids. The eight asteroids of family 36256 having a SNR$\leqslant$30 are highlighted as black diamonds, and their names are given in panel (B). Panel (B) is a zoom of panel (A) 150
Figure 5.10 Histograms of the proportion of asteroids of each taxonomic type according to the Gaia classification, normalised by the total number of asteroids considered (18 739); in the inner, middle and outer Main Belt. The interval of semi-major axis considered for each part are given. 151
Figure 5.11 Flow chart of the classification of A-type asteroids, after the two steps classification using Gaia templates. 153
Figure 5.12 Proper orbital elements plot of the 40 best potential A-types (asteroids found A as best first class after both classification steps, red dots) and 58 potential A-types (asteroids found A as first best class after one of the two classification steps, orange squares). The 71 asteroids having a spectrum in the DR3 and found A with spectroscopy in the literature are highlighted as black diamonds. 154
Figure 5.13 V-shape of the Flora family, using the membership of Nesvorny et al. (2015). Only the asteroids classified are considered, each taxonomic type is given a colour and a symbol corresponding to the type. Best potential A-types asteroids, potential A-types and A-types from spectroscopy in the literature are highlighted in black colour. 155
Figure B.1 Spectra of the 41 asteroids found in the 'possible matches area', validated as matches of EC 002 after visual inspection. The spectra are normalised at 550 nm. Black continuous line: spectrum of the powder sample of the meteorite, grey lines: spectra of the raw slab samples. The 16 bands of the Gaia asteroid spectra are given a colour and a symbol according to the value of the flag associated to the band: blue circle if flag=0, orange diamond if flag=1 and red star if flag=2. This way of showing the asteroid spectra applies for every figure hereafter. 186
Figure B.1 continued. 187

Figure B.2 Same as Fig. B.1 but with the 56 asteroids visually validated as matches of the low space-weathered EC 002. The space-weathered spectra of EC 002 are shown in grey lines. 188
Figure B.2 continued. 189
Figure B.3 Same as Fig. B.2 but with the 12 asteroids visually validated as matches of the medium space-weathered EC 002. 190
Figure B.4 Same as Fig. B.2 but with the two asteroids visually validated as matches of the high space-weathered EC 002. 190
Figure B.5 Spectra of the ten asteroids found with the curve matching method only, validated as matches of EC 002 after visual inspection. The spectra are normalised with a scaling factor f, here the meteorite spectrum was divided by the scaling factor. The spectra of the powder sample of the meteorite is shown in black continuous line, and the raw slab samples spectra are shown in grey lines. As previously, the 16 bands of the Gaia asteroid spectra are shown with a colour and a symbol associated to their flag number. 191
Figure B.6 Same as Fig. B.5 but with the 15 asteroids visually validated as matches of the low space-weathered EC 002. Here the spectra of the powder sample of the meteorite is shown in black continuous line, and the space-weathered spectra are shown in grey lines. 192
Figure B.7 Same as Fig. B.6 but with the 8 asteroids visually validated as matches of the medium space-weathered EC 002. 193
Figure B.8 Same as Fig. B.6 but with the asteroid visually validated as match of the high space-weathered EC 002. 193
Figure B.9 Fig.S13 from Barrat et al. (2021), showing the Band I Center (BIC) as a function of the Band Area Ratio (BAR) of the silicate features of the spectra. The BIC and BAR were calculated for EC 002 laboratory samples, for Ordinary Chondrite meteorites, for HEDs, and for some of the DeMeo et al. (2009) taxonomic end-members showing silicate features. Trends calculated based on mixtures of EC 002 with olivine or mantle material, and calculated on modelled space-weathered spectra are shown. . . . 194
Figure B.9 Confusion matrix corresponding to the classification of Gaia DR3 spectra of asteroids classified in the literature from VISNIR and NIR spectroscopy, using Gaia templates. The sub-classes are grouped as complexes, and only the templates of the A, Sa, Sq, Sk, S, V, K, L, D, Xk, X, C, Cg, Ch, Cb, and B classes are considered. 211
Figure B.9 Gaia DR3 spectra of the three B-type asteroids contained in the NIR list (black dots). The Gaia B-type template is displayed as blue dots, for reference. 212

Figure B.9 Confusion matrix corresponding to the classification of Gaia DR3 spectra of asteroids classified in the literature from VIS-NIR and NIR spectroscopy, using Gaia templates of the A, S, V, K, L, D, X, C, Ch, and B-classes only. The sub-classes are not considered in the classification, and the B-class is merged into the C-complex. 216

Figure B.9 Proportion of well and badly classified asteroids with my classification algorithm for ranges of SNR going from 10 to a hundred by steps of 10. 218

Figure B.9 Plot of the principal component PC2′ with respect to the global spectral slope, calculated for the 18 739 filtered Gaia DR3 asteroids. The 517 asteroids highlighted are the objects classified from NIR observations. Each coloured letter represents the assigned spectral type from the literature in panel (A), and the first best spectral type assigned with the Gaia classification in panel (B). 219

Figure B.9 Plot of the principal component PC2′ with respect to the global spectral slope, calculated for the 18 739 filtered Gaia DR3 asteroids. The classes and positions of Eos family members according to Nesvorny et al. (2015), that have a spectrum in the filtered Gaia DR3 dataset, are highlighted. Each coloured letter represents the spectral type assigned to the family members from the Gaia classification. 220

Figure B.9 Plot of the principal component PC2′ with respect to the global slope, calculated for the 14 132 filtered Gaia DR3 asteroids with 20⩽SNR⩽30. The 36 asteroids highlighted are the objects classified from NIR observations. Each coloured letter represents the assigned spectral type from the literature in panel (A), and the first best spectral type assigned with the Gaia classification in panel (B). 221

Figure B.9 Plot of the principal component PC2′ with respect to the global slope, calculated for the 22 066 filtered Gaia DR3 asteroids with SNR⩽20. The 33 asteroids highlighted are the objects classified from NIR observations. Each coloured letter represents the assigned spectral type from the literature in panel (A), and the first best spectral type assigned with the Gaia classification in panel (B). 221

LIST OF TABLES

Table 3.1 Accepted asteroids as candidate matches for the different samples of EC 002, according to the method used. 81
Table 3.2 Spectral slope and Band I depth evaluated for different samples of EC 002. 81
Table 3.3 Table of observations of potential analogues of EC 002. Thee table includes object number, the match type (space weathering or not), the proper orbital elements of the asteroids (semi-major axis, eccentricity and inclination), the geometric albedo, the magnitude in the V band, the date of the observations, and the airmass. 93
Table 3.4 Classification of the observed asteroids with online classifiers, M4AST and *classy*. The first best three classes given by M4AST are indicated, the first class written being the best one. The two observed spectra of (24286) 1999 XU188 are designated as (a) and (b). 95
Table 3.5 BIC and BAR calculated for every considered asteroid. (a) and (b) designate the two acquired spectra of asteroid (24286) 1999 XU188. 103
Table 3.6 Considered wavelength range (Range) for the second degree polynomial fit of the first absorption band, and wavelength limit (Limit) considered to calculate the band area ratio of each taxonomic end-member of DeMeo et al. (2009) considered. The BIC and BAR obtained for each template are given. 103
Table 4.1 Members of the (36256) 1999 XT17 family with a Gaia DR3 spectrum. Here is given the diameter D of family members, their geometric visible albedo p_V, the average signal-to-noise ratio of their DR3 spectrum, their H magnitude, and the two best spectral classes given by our classification algorithm. The physical properties data were obtained from `mp3c.oca.eu`. 117
Table 4.2 Confusion matrix of the classification of A-type asteroids by our algorithm. The list of 389 asteroids both classified by DeMeo et al. (2009), DeMeo et al. (2014), and DeMeo et al. (2019) and having a DR3 spectrum considered for this study contains 21 A-type asteroids. 122
Table 5.1 Asteroids used in the definition of Gaia templates, defined as classes prototypes in the Bus and Binzel (2002a) taxonomy. . . 136
Table 5.2 Members of the (36256) 1999 XT17 family with a Gaia DR3 spectrum having a SNR⩾21. 149
Table A.1 Asteroids selected among the class prototypes of Mahlke et al. (2022). 167
Table A.2 Selected S-type asteroids. 169

Table B.1 Accepted asteroids as candidate matches for the different samples of EC 002 . . . 171
Table B.2 Asteroids within the "possible matches area". . . . 175
Table B.3 Asteroids found as a match to the powder and raw slab samples of EC 002 with a curve-matching method. . . . 182
Table B.4 Accepted asteroids as candidate matches to the three space-weathered modelled samples of EC 002. . . . 185
Table C.1 Asteroids observed in the NIR or VISNIR wavelength range, used to test my classification algorithm. The MPC number of the asteroids along with their spectroscopic type is given, with the associated reference. When an asteroid was classified differently by different authors, the different classes and the associated reference are displayed in the last column. . . . 196
Table C.2 K-type asteroids classified with the Gaia classification algorithm. Their assigned class is given in the Type column, and their literature class in the Class column, along with the wavelength range and associated reference (Ref. column). The taxonomic schemes used in the literature are the Bus (Bus and Binzel, 2002a), Bus-DeMeo (DeMeo et al., 2009), or Mahlke (Mahlke et al., 2022) schemes. . . . 213
Table C.3 List of the 40 asteroids found A-type as first best class after the Gaia classification, and after the BP classification. The asteroid number and name is given in the first column, accompanied with its assigned type from the literature, the method and wavelength range used, and the corresponding reference, when existing. The python package *rocks* was used to produce this table. . . . 222
Table C.4 List of the 58 potential A-type asteroids found after the Gaia and the BP classification. The asteroid number and name is given in the first column, accompanied with its assigned type from the literature, the method and wavelength range used, and the corresponding reference. The python package *rocks* was used to produce this table. . . . 223

ACRONYMS

au	astronomical units
TNOs	Trans Neptunian Objects
KBOs	Kuiper Belt Objects
NEOs	Near-Earth Objects
NEAs	Near-Earth Asteroids
MMR	Mean Motion Resonance
IMB	Inner Main Belt
MMB	Middle Main Belt
OMB	Outer Main Belt
HCM	Hierarchical Clustering Method
ECAS	Eight-Color Asteroid Survey
CCD	charge-coupled device
SMASS	Small Main belt Asteroid Spectroscopic Survey
UV	ultraviolet
VIS	visible
NIR	near-infrared
FRIPON	Fireball Recovery and InterPlanetary Observation Network
PRISMA	Prima Rete Italiana per la Sorveglianza sistematica di Meteore e Atmosfera
SPN	Spanish Meteor Network
EFN	European Fireball Network
CAMO	Canadian Automated Meteor Observatory
AMOS	All-sky Meteor Orbit System
GFO	Global Fireball Observatory
DFN	Desert Fireball Network
CAIs	Calcium Aluminium-rich Inclusions
OC	Ordinary Chondrite

PT	petrologic type
HED	Howardite, Eucrite, Diogenite
CC	Carbonaceous Chondrites
NC	Non-Carbonaceous
RELAB	Reflectance Experiment LABoratory
BAR	Band Area Ratio
SNC	Shergottites, Nakhlites, Chassignites
Hipparcos	HIgh Precision PARallax COllecting Satellite
DR3	Gaia Data Release 3
DR4	Gaia Data Release 4
FoV	Field of View
RVS	Radial Velocity Spectrometer
AL	along scan
AC	across scan
TDI	Time Delay Integration
SM	SkyMapper
AF	Astrometric Field
BP	Blue spectroPhotometer
RP	Red spectroPhotometer
LSF	Line Spread Function
SSOs	Solar System Objects
MAD	median absolute deviation
SNR	Signal-to-Noise Ratio
EC 002	Erg Chech 002 meteorite
SSO	Solar System Object
DPAC	Data Production and Analysis Consortium
SDSS	Sloan Digital Sky Survey
ska	a Spectral Kit for Asteroids
IRTF	Infrared Telescope Facility
NWA	North-West Africa

MORIS	MIT Optical Rapid Imaging System
IDL	Interactive Data Language
M4AST	Modeling for ASTeroids
classy	CLAssification of a Solar System bodY
BIC	Band I Centre
BIIC	Band II Centre
FIN	Family Identifier Number
MOVIS	Moving Objects VISTA
VHS	VISTA Hemisphere Survey
VISTA	Visible and Infrared Survey Telescope for Astronomy
SsODNet	Solar system Open Database Network
FPR	False Positive Rate
TPR	True Positive Rate
PCA	Principal Component Analysis

Part I

ASTEROID DIFFERENTIATION FROM GAIA REFLECTANCE SPECTROSCOPY

1

ASTEROIDS, FROM THE SOLAR NEBULA TO TODAY

1.1 FORMATION AND EVOLUTION

In the dictionary, asteroids are defined as small rocky bodies orbiting the Sun. While he was trying to observe a star, priest Giuseppe Piazzi discovered Ceres in 1801 (Piazzi, 1801). He thought at first that this new object could be a comet, as comets were already known, but measures of its positions and motion made him realise that it was "better than a comet". Ceres was later confirmed not to be a comet, and was first designated as a planet (Bottke, 2002). With time were discovered increasingly more objects in its vicinity, which made astronomers review this designation: Ceres became the first discovered member of a complete new class of astronomical objects. Their small size made them difficult to distinguish from stars using early 19th-century telescopes, so William Herschel invented in 1802 the term of "asteroids" to designate them, coming from the Greek *asteroides*, "star-like" (Herschel, 1832).

As Ceres was the first asteroid discovered, it was given the number one (Encke, 2023), and is now designated as (1) Ceres in the asteroids numeration systems. Every time a new asteroid is discovered, it is given a provisional designation before being assigned the number following the previous asteroid discovered (Hilton, 2007).

1.1.1 Reservoirs of small bodies in the Solar System

(1) Ceres, with its diameter of about a thousand kilometres, is the largest body orbiting in the Main Belt. This reservoir of asteroids located between 1.7 and 4.5 astronomical units (au), between the orbits of Mars and Jupiter, holds more than 10^6 known objects. The total number of objects it contains should be around one million with diameters larger than or equal to one kilometre, and as the number of asteroids decreases with increasing size, only over 200 asteroids are known to have diameters larger than a hundred kilometres.

Contrary to the science-fiction image of a crowded asteroid belt, the Main Belt is mostly empty. The mean distance between two asteroids in this reservoir is of the order of the million of kilometres, so the chase of the Millenium Falcon in Star Wars episode V would have been much less dangerous in the real Main Belt (but probably less fun to watch). The total mass of the Main Belt today represents a mere 3% of the mass of the Moon (Pitjeva and Pitjev, 2018), an about 60% of this mass is hold by the four largest asteroids alone: (1) Ceres, (4) Vesta, (2) Pallas, and (10) Hygeia.

Other reservoirs of small bodies exist in the Solar System, and most will be presented but not be detailed here. The largest reservoir is the Kuiper Belt, located beyond the orbit of Neptune, between 30 and 55 au (Stern and Colwell, 1997). This extended and 20 to 200 times more massive reservoir than the Main Belt is where Pluto orbits, along with many other minor bodies (Delsanti and Jewitt, 2006). The Kuiper Belt is part of a larger group of Trans Neptunian Objects (TNOs), orbiting beyond the orbit of Neptune. Some objects that were originally TNOs but that got scattered inwards by interaction with Neptune are today found orbiting between Jupiter and Neptune, and are designated as Centaurs (Duncan and Levison, 1997).

Going from the outer to the inner Solar System, another population of small bodies is found located at the stable L4 and L5 Lagrange points of the Sun-Jupiter gravitational system: the Jupiter Trojans (Emery et al., 2011). These objects show compositions closer to the ones of outer Solar System objects, supporting the theory that they formed in the same region of the solar nebula as Kuiper Belt Objects (KBOs) (Morbidelli et al., 2005). The Main Belt, the Kuiper Belt and Jupiter trojans are represented in the sketch of Fig.1.1.

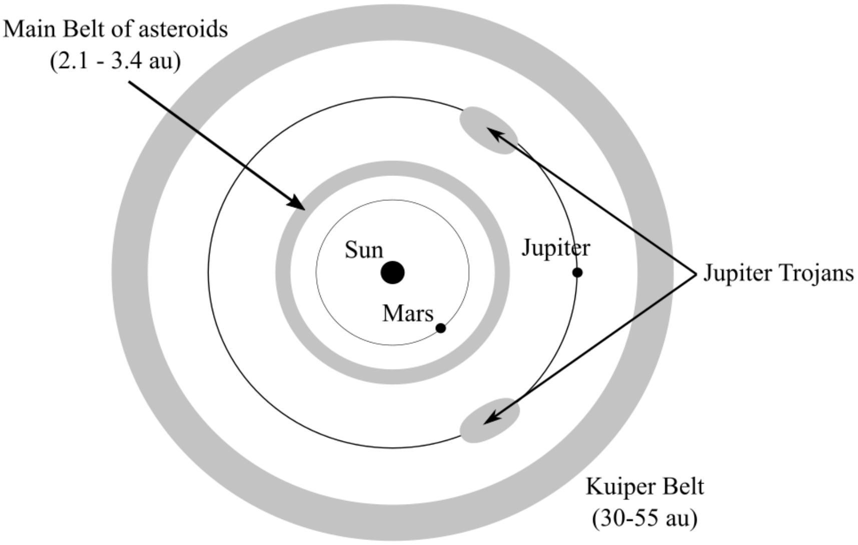

Figure 1.1: Scheme of the main reservoirs of asteroids in the Solar System.

In the inner Solar System, some asteroids have orbits crossing those of terrestrial planets. As suggested by their name, Mars Crossers cross the orbit of Mars (Michel et al., 2000), and vatiras orbits between those of Venus and the Sun. There is, to date, only one vatira known, and the vulcanoids are a hypothetical population of asteroids orbiting inside the orbit of the planet Mercury (Greenstreet et al., 2012).

An interesting reservoir of asteroids with planet-crossing orbits is the population of Near-Earth Asteroids (NEAs) - also called Near-Earth Objects (NEOs) (Lazzarin et al., 2004; Lazzarin et al., 2005; Perna et al., 2018; Devogèle et al., 2019). These bodies have Earth-crossing orbits, and are characterised by a periapsis distance $q < 1.3$ au. They are separated into four groups, depending on the characteristics of their orbits: the Amor (semi-major axis $a > 1$ au, $1.017 < q < 1.3$ au), Apollo ($a > 1$ au, $q < 1.017$ au), Aten ($a < 1$ au, apoapsis distance $Q > 0.983$ au) and Atira groups ($a < 1$ au, $Q < 0.983$ au). The orbits of these groups are represented in Fig.1.2. Most NEAs are contained in the Apollo and Amor groups, while the Atira contains only a few tens of bodies (Sokolova et al., 2018). The dynamical lifetimes of NEAs is estimated to be of the order of 10^7 years (Morbidelli et al., 2022), and these objects are understood to come mostly from the Main Belt, as will be explained in the following.

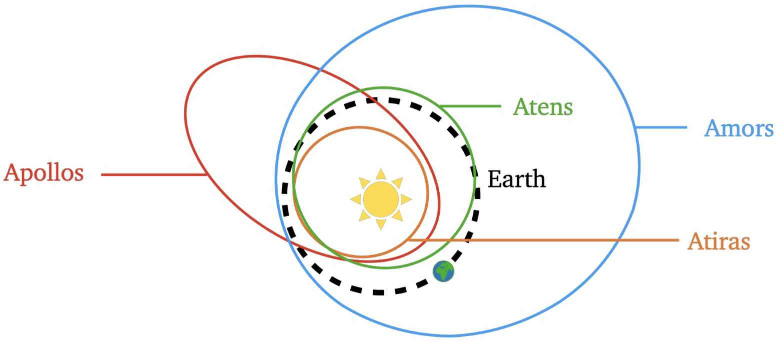

Figure 1.2: Scheme of the orbits of the three groups of Near-Earth Asteroids: the Amors, Apollos, Atens and Atiras. Inspired from a scheme by Shamil Biktimirov.

1.1.2 From the solar nebula...

The fact that small bodies are located in such reservoirs today goes back to the formation of the Solar System. The Solar System formed about 4.6 billion years ago, from the gravitational collapse of an interstellar cloud of gas and dust, that lead to the formation of our Sun (Bouvier and Wadhwa, 2010). At this stage, the young Sun was surrounded by a protoplanetary disk composed of 99% of gas and of a mere 1% of dust (Armitage, 2019). The dust grains accreted with the effect of the rotating disk, and they formed larger dust grains, that eventually lead to the formation of planetesimals (Armitage, 2011).

Planetesimals are several hundred kilometres-size bodies (Morbidelli et al., 2009; Delbo et al., 2017; Ferrone et al., 2023; Klahr and Schreiber, 2015) that are designated as the "building blocks" of planets. Indeed, some of these large bodies accreted to form even larger bodies, the protoplanets, that then evolved into the core of giant planets (Kokubo and Ida, 2000; D'Angelo et al., 2014), and terrestrial-type planets. In Fig.1.3 is displayed a scheme illustrating the different stages of planet formation the a protoplanetary disk. The final stage shows fully formed planets after the dissipation of the gas, with no leftover planetesimal. In reality, due to complex planet-disk interactions between the forming giant planets and the gas of the disk, some planetesimals never accreted into planets and remained as they formed in the Solar System (Klahr and Schreiber, 2015).

Theories state that some planetesimals have differentiated, i.e. organising into layers of different densities and compositions (Neumann et al., 2012). The differentiation steps and the layers of a differentiated planetesimal are illustrated in Fig.1.4. At the beginning of the Solar System, a significant quantity of $^{26}\mathrm{Al}$ was available in the forming planetesimals. This radioactive isotope of aluminium has a half-life of about 700 000 years (Overholt and Melott, 2013), and its radioactive decay produces heat. Because of it, some planetesimals must have melted partially or completely (Bizzarro et al., 2005), leading denser elements to sink through lighter materials and to congregate at the centre of bodies. Iron being the most common element likely to form a dense molten metal phase, differentiated planetesimals should show an iron-rich

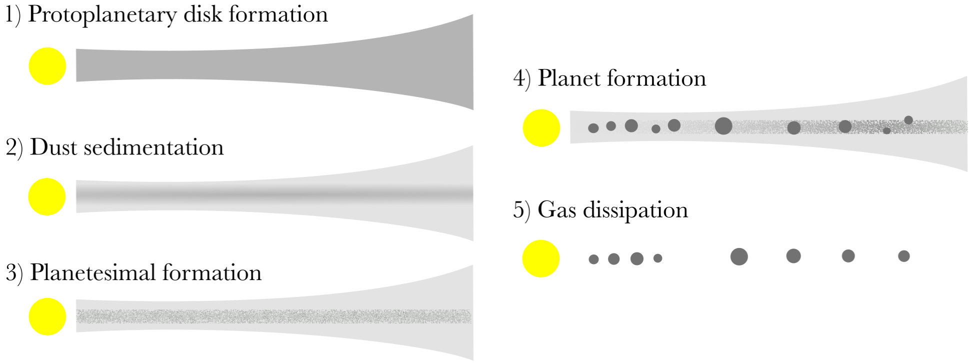

Figure 1.3: Simplified scheme illustrating the different stages of planet formation in a protoplanetary disk. Inspired from a scheme of Takayuki Tanigawa.

metallic core. On the contrary, lighter materials tend to rise to the surface of differentiating bodies,forming igneous crusts. An olivine-rich mantle should separate the crust from the core (McConnell et al., 1967). Olivine is a mineral made of magnesium, iron and silicates of chemical formula $(Mg, Fe)_2SiO_4$, and it is the most abundant constituent of the upper mantle of the Earth (Mainprice et al., 2005), along with pyroxene $(Fe, Mg, Ca)_2(SiO_6)$.

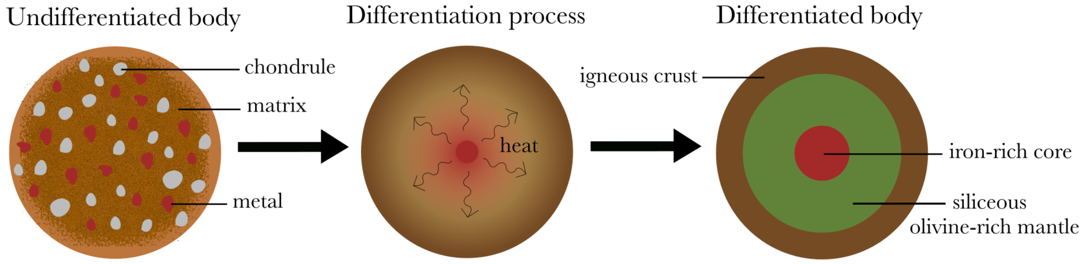

Figure 1.4: Schematic representation of planetesimal differentiation.

According to some theories, differentiation should only have occurred most likely to sufficiently large bodies (larger than 20 km in diameter), since radioactive decay heats up bodies from the inside and they cool down through their surface (Moskovitz and Gaidos, 2011). Taking into account the gradual disappearance of ^{26}Al in the early Solar System, a body should therefore have a volume/surface ratio large enough to remain heated long enough for differentiation to occur.

Other studies lead to the conclusion that planetesimals differentiation depends on several parameters, such as the time of formation, the accretion law, and the duration of accretion (Neumann et al., 2012). Differentiation is not an instantaneous process, and its degree may vary from a body to another. A small body accreted early (i.e. when the first solids condensed in the solar nebula (Wadhwa et al., 2006)) could have differentiated as efficiently as a larger body accreted late (i.e. accreted ~1.5 Ma after the first condensates, with a radius greater than 200 km (Elkins-Tanton et al., 2011)), due to the high ^{26}Al content in the early stages of solar system formation. Some objects accreted late might have differentiated only partially, and thus could show an iron core and a silicaceous mantle but covered by an undifferentiated layer (Elkins-Tanton et al., 2011; Neumann et al., 2012).

Planetesimals evolved very little from a chemical and thermal point of view since their formation. What is left of these bodies can be studied as today's asteroids.

The study of today's asteroids population lead to the conclusion that planetesimals were born big (Morbidelli et al., 2009). Indeed, in order to reproduce today's size-frequency distribution of the asteroids in the Main Belt, planet formation models suggest that most planetesimals formed with diameters ~ 120 km and subsequently got fragmented by an intense collisional period (Bottke et al., 2005). This evidence is corroborated by Klahr and Schreiber (2020), who observed a peak in the size distribution of asteroids and Kuiper Belt objects around ~ 100 km. They found that a critical mass is needed for pebbles to clump and form a planetesimal in the protoplanetary disk, because turbulent diffusion in the disk tends to disperse pebbles before their accretion, due to their low self-gravity. The critical mass they found suggests that planetesimals formed with diameters around ~ 100 km, showing that larger planetesimals are more likely to be formed. The Main Belt should thus be populated by fragmentation by-products of planetesimals with ~ 100 km in diameter (Bottke et al., 2005; Morbidelli et al., 2009; Klahr and Schreiber, 2020), leaving few whole planetesimals in the Main Belt nowadays (Delbo et al., 2017; Delbo et al., 2019; Ferrone et al., 2023; Bourdelle de Micas et al., 2022). Evidence of differentiation should therefore be found in today's population of asteroids, and studying the composition of bodies in the Main Belt is a tool to retrace the origin and evolution of planetesimals in the early Solar System.

1.1.3 ... to today's Main Belt

Today's Main Belt is shaped by the gravitational influence of planets on the orbits of asteroids, which can be observed through Kirkwood gaps (Henrard and Lemaitre, 1983). These gaps were first noticed in 1866 by Daniel Kirkwood, who explained their existence by the influence of orbital resonances with Jupiter (Kirkwood, 1891). A Mean Motion Resonance (MMR) happens when two celestial bodies that are revolving around a common barycentre, have the ratio of the revolution periods that is a rational number. For example, an asteroid in a 3:1 MMR with Jupiter does three revolutions around the Sun when Jupiter does one. Some of the MMRs with Jupiter destabilise the asteroids' orbits by increasing the eccentricity of the objects, which can result in their ejection from the Main Belt, creating visible empty gaps. The 3:1, 5:2 and 2:1 MMRs with Jupiter are efficient to eject objects from the Main Belt into the near-Earth space (Morbidelli et al., 2002), feeding the NEA population.

Another type of resonance efficient to deliver material into the near-Earth space is the ν_6 secular resonance. Typically, a secular resonance occurs when two bodies have the precession of their orbits synchronised (the precession being the gradual change of orientation of their axis of rotation). This happens when the argument of periapsis or the ascending node of two bodies evolve in a synchronous manner. The ν_6 secular resonance happens between Main Belt asteroids and Saturn: asteroids entering the region of the ν_6 resonance see their orbital eccentricity excited, eventually leading to their ejection of the belt (Morbidelli and Henrard, 1991; Morbidelli et al., 2002). It is the most efficient resonance for the delivery of Main Belt asteroids to Earth-crossing orbits (Granvik et al., 2016)

These resonances shape the Main Belt into separate regions, called the Inner Main Belt (IMB), Middle Main Belt (MMB), the so-called "pristine zone", and the Outer Main

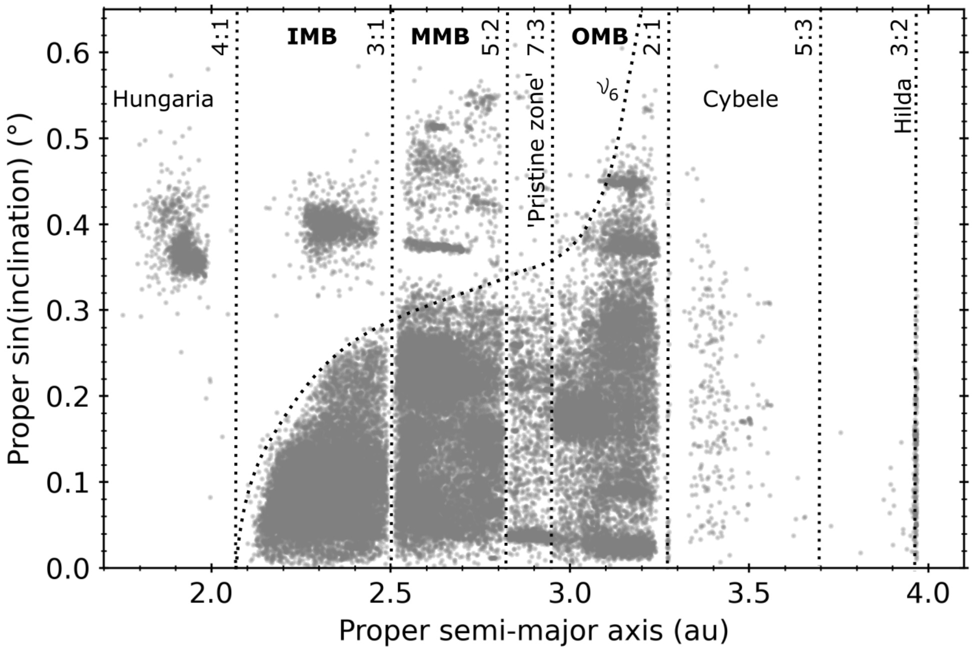

Figure 1.5: Dynamical structure of the Main Belt seen from its proper orbital elements. Mean motion resonances with Jupiter are displayed in dashed lines, as well as the secular resonance ν_6. The Inner, Middle and Outer Main Belt are highlighted, and the "pristine zone" is indicated as well as the Hungaria, Cybele and Hilda groups. This figure is inspired from Figure 1.3 from Max Mahlke's PhD thesis.

Belt (OMB). The effect of these resonances on the Main Belt can be observed in the proper orbital elements space. The proper orbital elements of an object are quasi-stable constants of movement that are conserved during orbital evolution. These synthetic elements are calculated for asteroids by integrating the asteroids' orbits over long timescales with the use of a dynamical model, while filtering out the short periodic perturbations affecting their orbital motion (Knežević and Milani, 2003). Bodies of the Solar System are dynamically characterised by their proper semi-major axis a_p, the proper eccentricity of their orbit e_p, and the proper inclination of their orbit i_p (the sinus of the inclination $\sin(i_p)$ is often considered for this quantity).

In Fig.1.5 is represented the Main Belt in the proper orbital elements space, divided in the Inner, Middle and Outer Main Belt. These regions are all clearly bounded by the actions of the MMRs with Jupiter and by the strong ν_6 secular resonance. Regions populated by groups of asteroids such as the Hungaria, Cybele or Hilda groups are represented, and we can note that the Hilda group is located inside a stable MMR (Terai and Yoshida, 2018; Brož and Vokrouhlický, 2008). The Hungaria group is shaped by the gravitational influence of Mars, that lead only high inclination asteroids to survive inward the 4:1 MMR (McEachern et al., 2010; Forgács-Dajka et al., 2022).

The proper orbital elements space is useful to detect the existence of potential stable groupings in the Main Belt (Novaković et al., 2011). We can also observe in Fig.1.5 zones of higher densities, corresponding to asteroid families.

1.2 DYNAMICAL ASTEROID FAMILIES

Despite the large distance between asteroids, collisions happen. When a catastrophic collision occurs, an asteroid can get partially or completely disrupted. The fragments resulting from this disruption can either get ejected far from the body that underwent the collision (designated as the "parent body"), they can fall back on the asteroid, or they can remain dynamically linked to the parent body and keep similar orbital elements (Michel et al., 2004b; Michel et al., 2004a). The outcomes of a catastrophic collision are illustrated in Fig.1.6. Rubble-pile asteroids are gravitational aggregates of fragments ejected from a body with small differential velocities, and which self-gravity is enough to make them accrete back together. This does not necessarily happen on the parent body, but can happen to fragments ejected from it. Therefore, it is possible that most family members are rubble-pile asteroids (Michel et al., 2004a).

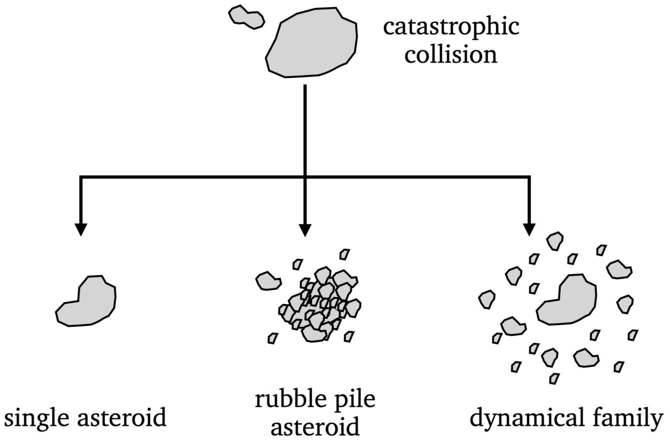

Figure 1.6: Simplified illustration of three possible outcomes of a catastrophic collision. The fragments orbiting around what remains of the parent body are likely to accrete and form rubble-pile bodies. Scheme inspired from the course of Alain Doressoundiram.

Different methods exist to detect and define asteroid families in the Main Belt, all extensively described in Nesvorný et al. (2015) and Novaković et al. (2022). Only two widely used methods relevant for this thesis will be presented in the following: the Hierarchical Clustering Method (HCM), and the V-shape technique.

1.2.1 Hierarchical clustering method

The HCM was first introduced by Zappala et al. (1990) and is the most often used technique to define asteroid families. This method is based on an agglomerative clustering approach, where each observation is considered at first as an independent cluster. At each step, the hierarchical clustering algorithm calculates the distance between each cluster, and merges the two clusters that contain the closest pairs of elements. This grouping is reproduced at each step, considering the newly defined clusters. To define asteroid families, the HCM is often applied to the 3D proper orbital elements space of the objects (Milani et al., 2014; Nesvorny et al., 2015).

The definition of asteroid families is mainly influenced by the choice of the distance at which two objects are considered to belong to the same cluster. Commonly, the distance in the proper orbital elements space is determined using the metric defined in Zappala et al. (1990):

$$d = na_P \sqrt{\left(\frac{5}{4}\left(\frac{\Delta a_P}{a_P}\right)^2 + 2(\Delta e_P)^2 + 2(\Delta \sin(i_P))^2\right)}, \tag{1.1}$$

with na_P the orbital velocity of an asteroid on a circular heliocentric orbit, and $a_P = \frac{(a_{P,1}+a_{P,2})}{2}$ its proper semi-major axis, with $a_{P,1}$ and $a_{P,2}$ the proper semi major axis of the two bodies considered in the calculation of the mutual distance. Δa_P, Δe_P and $\Delta \sin(i_P)$ represent the separation vectors between two orbits in the 3D space, hence between the proper semi major axis, the proper eccentricity and the proper inclination of the two bodies considered in the clustering. d is usually in $m.s^{-1}$.

A cutoff distance d_{cut} is defined so that the distance between two neighbouring orbits that are clustered by the algorithm is $d(a_P, e_P, i_P) < d_{cut}$. The choice of d_{cut} impacts the amount of asteroids joined in a single cluster, and hence the amount of families defined. A simplified illustration of the different steps of the HCM is displayed in Fig.1.7.

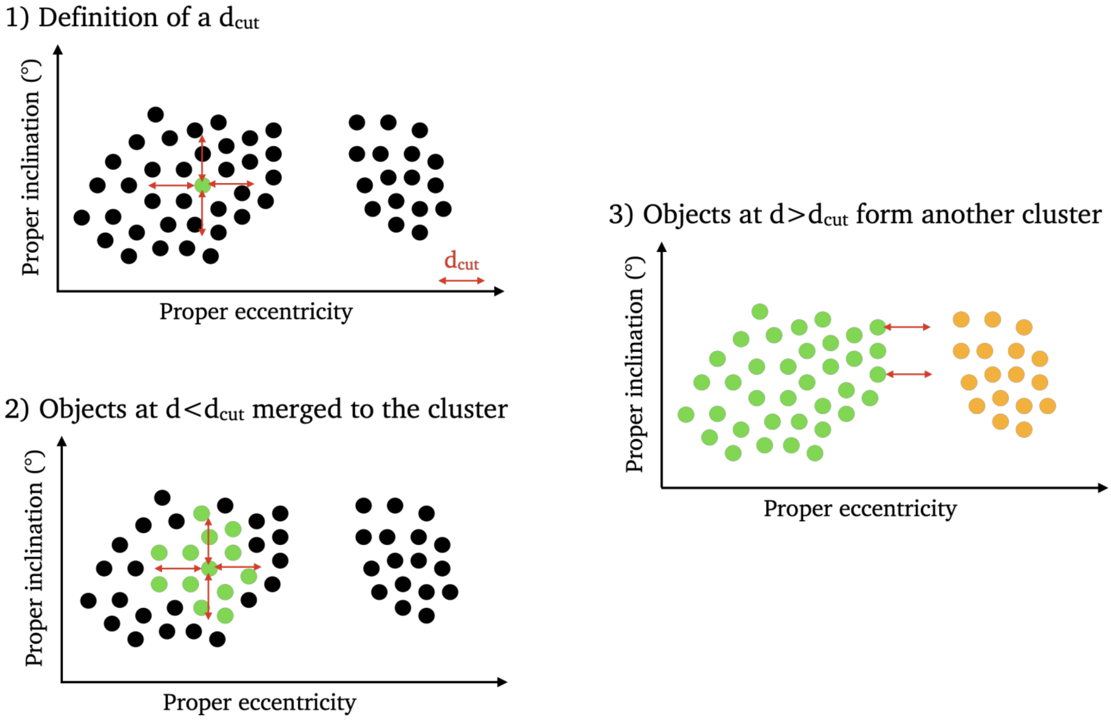

Figure 1.7: Simplified illustration of the steps of the HCM applied to the proper orbital elements space of asteroids. The proper inclination versus eccentricity space is taken as an example for clarity, the HCM being applied to the 3D space including the proper semi-major axis.

An advantage of the HCM is that it does not assume the shape of the clusters it defines, enabling the detection of irregularly shaped families (Nesvorny et al., 2015; Novaković et al., 2022). Its main issue is the chaining effect: in order to merge two clusters together, a single pair of close points is enough. Therefore, if a too large d_{cut} is used, the algorithm tends to incorporate groups of asteroids within already defined clusters, forming a chain that can merge families together and prevent from distinguishing them. This problem can arise because some fragments of asteroids ejected from the family after a catastrophic collision orbit far away from the family core. Linking these objects to the family can create artificial links between clusters (Novaković et al., 2022), which can lead to the integration in the families of background asteroids (Nesvorny et al., 2015; Novaković et al., 2022). If a too small d_{cut} is used instead, several issues can arise: (i) some families can be divided into different clusters, (ii) some family members can be lost in the background, or (iii) some small families can remain undetected (Nesvorny et al., 2015). Hence, the choice of d_{cut} is of major importance to define asteroid families (Nesvorny et al., 2015).

This statistical identification of families can lead to the inclusion of asteroids that are not actually part of the family, but which share similar orbital characteristics to family members. Such intruders inside the families are called interlopers (Migliorini et al., 1995). These objects need to be identified, to study asteroid families formation and evolution accurately.

A way of identifying interlopers is to use asteroid compositional data, such as surface reflectance spectra, colour or albedo information (see section 1.3). Indeed, asteroid families are thought to be mostly homogeneous in composition (Parker et al., 2008), as they come from the break up of a common parent body. Therefore, interlopers should show a different surface composition from family members, in most cases. However, an asteroid family generated from the breakup of a differentiated parent body should show members with different surface compositions, representative of the compositional layers of such parent body. Interloper removal methods based only on the composition of asteroids could thus prevent the discovery of heterogeneous families, and therefore the detection of differentiated families in the Main Belt (Novaković et al., 2022). To avoid this issue, Migliorini et al. (1995) calculated that the fraction of interlopers in a family identified with the HCM should be up to around 10%. That way, any fraction of family members having a composition different from the main one, but significantly more abundant than 10%, could point out to a differentiated family, or to different families overlapping.

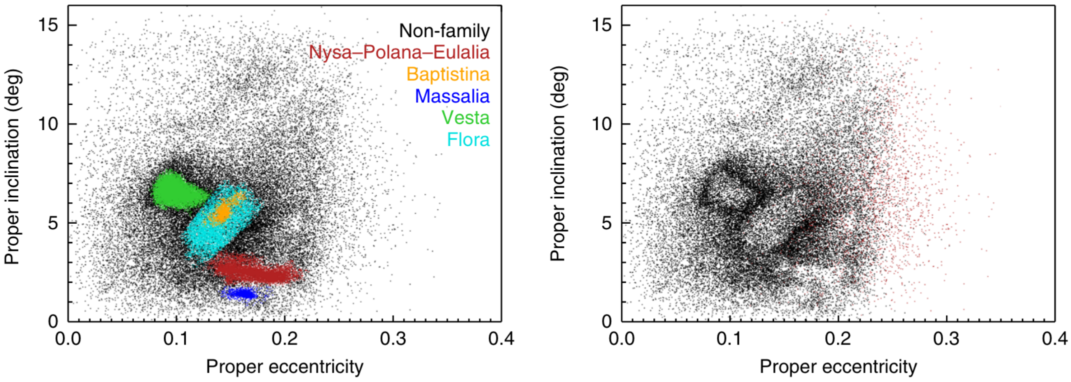

Figure 1.8: Proper inclination versus proper eccentricity scatter plots showing the Vesta (green), Flora (cyan), Baptistina (orange), Massalia (blue) and Nysa–Polana–Eulalia (magenta) families in the Inner Main Belt (left panel). The right panel shows the same proper elements plot after removal of these families. Black dots corresponds to non family asteroids in Nesvorny et al. (2015), and the red dots in the right panel coloured for a specificity of Dermott et al. (2018) are here considered as non-family members as well. Figure taken from Fig.1 of Dermott et al. (2018).

Another issue of this method is the so-called halo effect (Nesvorny et al., 2015). Some asteroid, that are true family members, are not clustered together with their family by the HCM, because they orbit at a distance larger than the defined d_{cut} from the family core. When identified dynamical families are artificially removed from the Main Belt, they leave holes in the proper elements space surrounded by zones of high asteroid density: the family halos. Such halos are visible in Fig.1.8, taken from Dermott et al. (2018) and using the families defined by Nesvorny et al. (2015) with the HCM. The number density of asteroids in the halo is similar to the background number density (Nesvorny et al., 2015; Novaković et al., 2022), thus if asteroids from the halos are integrated into the families with the HCM, background asteroids will be too. Assigning these halo objects to families and distinguishing them from interlopers is a difficult task that requires compositional studies. Thus, the HCM is powerful for detecting groupings in the proper orbital elements space, but assigning asteroids to collisional families accurately requires the use of complementary methods.

1.2.2 V-shape

Another method used to identify and study asteroid families is the V-shape method (Walsh et al., 2013; Bolin et al., 2017; Delbo et al., 2017). When a parent body undergoes a catastrophic collision, it breaks into fragments of different sizes, that are each subject to the Yarkovsky force. This force is a consequence of the non-zero thermal inertia of rotating objects heated up by radiation in space (Bottke et al., 2006a). When subject to solar radiations, the surface of an asteroid heats up slowly, and takes time to cool down once in the shadow. The thermal properties of the surface cause a time lag between when solar radiation is absorbed and when heat is emitted. The difference between the directions of absorption and emission of photons creates a non-gravitational force along the direction of motion of the orbit, making the asteroid speed up or slow down, depending on its prograde or retrograde rotation. Hence, the asteroids see their orbits increase (if they are prograde rotators) or decrease (if they are retrograde) due to the diurnal Yarkovsky effect (e.g Bottke et al., 2006a). This phenomenon is illustrated in Fig.1.9. The smaller the asteroid, the most effective the effect.

Because of the increase or decrease of their orbit, Main Belt asteroids can fall in MMRs or in secular resonances, which makes their eccentricity increase. This can lead to their ejection out of the belt, participating to the injection of objects into Earth crossing orbits (Bottke et al., 2006b; O'Brien and Greenberg, 2005).

The Yarkovsky effect leaves its trail in the proper orbital elements space. Since smaller asteroid are more effectively affected by this effect, they see their proper semi major axis increase or decrease proportionally to their size; hence to their absolute magnitude, as it is size-dependent. Evolved asteroid families are composed of bodies of different sizes, resulting from the fragmentation of the parent body (Michel et al., 2004a). These bodies see their semi-major axis impacted by the Yarkovsky force inversely proportionally to their diameter, leading evolved families to form a "V-shape" in the inverse diameter (or absolute magnitude) versus proper semi major axis space (Bolin et al., 2017; Delbo et al., 2017; Bolin et al., 2018). Such V-shape is shown in Fig.1.10 for the (20) Massalia family. The older the family, the wider the V-shape (Delbo et al., 2017; Ferrone et al., 2023). This spatial distribution of family members allows to

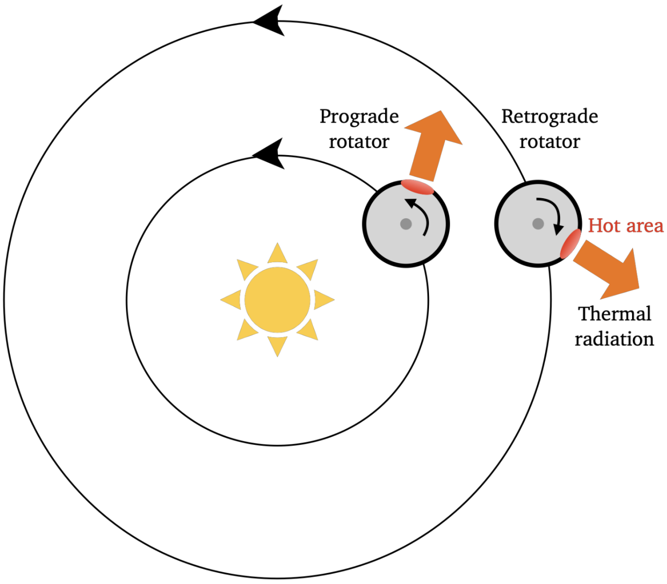

Figure 1.9: Illustration of the diurnal Yarkovsky effect, in the case of a prograde and retrograde rotator. The direction of the thermal force generated by the emission of heat is represented by wide orange arrows.

detect and characterise families, and to try identifying interlopers when their size or magnitude puts them outside of a family's V-shape (Bolin et al., 2017).

Finally, the development of a V-shape-constrained HCM method by Ferrone et al. (2023) showed good results in the identification of asteroid families, as it allowed to link family halos with their cores, and it revealed an unknown old collisional family in

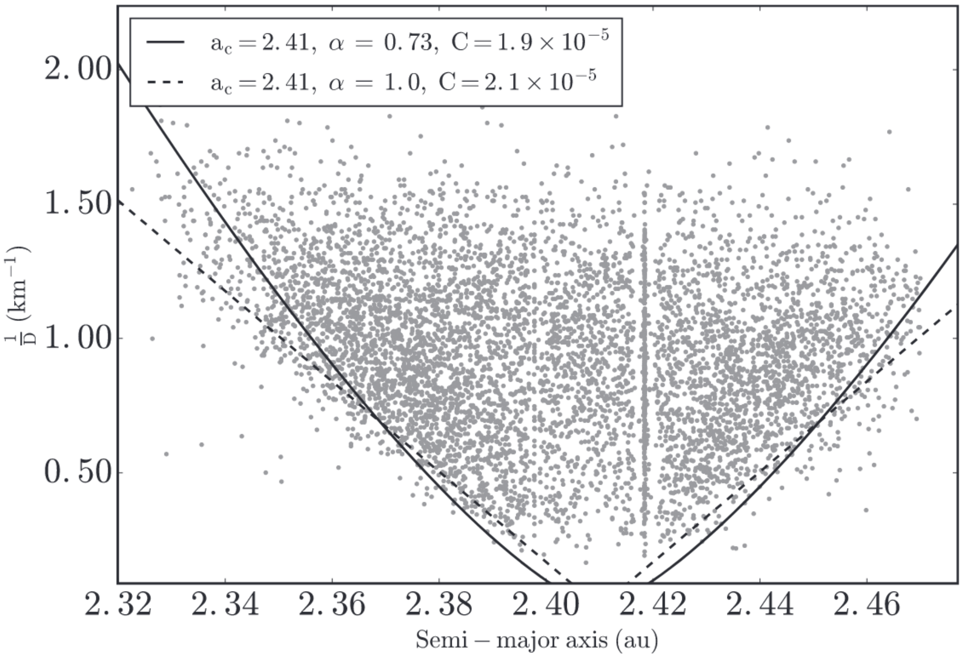

Figure 1.10: Inverse diameter versus semi-major axis plot of the Massalia family. Two V-shapes are shown according to different V-shape parameters, α and C (see Bolin et al. (2018) for a full description). Figure taken from Bolin et al. (2018).

the IMB. This work contributes to the argument that the Main Belt is mainly composed of planetesimals and their collision fragments.

As mentioned earlier, characterising asteroids and their dynamical families requires compositional studies. Unveiling the composition of these objects allows to go back to their formation mechanisms and evolution, which can give us evidence corroborating the differentiation theories.

1.3 ASTEROIDS COMPOSITION

1.3.1 Spectroscopy, photometry and albedo

The most commonly used technique to learn information about the composition of asteroids is spectrophotometry. This technique relies on the fact that all materials interact with light: they can absorb it, reflect it, or transmit it. The interaction between light and matter leads to the transition of ions in the material's crystal lattice, manifested by the presence of electronic bands in the electromagnetic spectrum characteristic of the ionic transition in the visible and near-infrared wavelength range (Burns, 1993).

Reflectance is the effectiveness with which the surface of a given material reflects light. It depends on the response of the electronic structure of the material when hit by light, and it varies with the wavelength, the polarisation, and the angle of incidence or emission of the light. A reflectance spectrum is a curve representing the dependence of reflectance on the wavelength. Studying the reflectance spectrum of an object therefore gives information about the mineralogical composition of this object. For example, opaque minerals such as graphite or other carbon-rich objects only absorb light, leading these materials to have a mostly featureless reflectance spectrum (Cloutis et al., 2012; Gaffey et al., 2002). Metal-rich materials show a spectrum where reflectivity increases with wavelength (Cloutis et al., 1990; Cloutis et al., 2010), while silicate-rich minerals, such as olivine and pyroxene, lead to the presence of strong characteristic absorption bands in their spectra (Gaffey et al., 1993; Cloutis, 2002; Cloutis et al., 2004; Gaffey, 2011). Spectra of different minerals found to compose asteroids surfaces are displayed in Fig.1.11.

Spectrophotometry and multi-band photometry are other techniques widely used to study asteroids. They rely on the observed magnitude of a celestial body, and are based on colour indices. These indices have been built with respect to the colour of the Sun, and objects can therefore be "bluer" (or "redder") than the Sun, if they absorb more the red (respectively the blue) than the Sun, on a given wavelength range. Colour indices can be used as well to draw an approximation of the reflectance spectrum of an object (e.g. Ivezic et al., 2002; Carvano et al., 2010; DeMeo and Carry, 2013).

The albedo of asteroids is also indicative of their surface composition. The Bond albedo of an object is a physical parameter that takes values between 0 and 1, and that varies with the quantity of light globally reflected by a given material. If the light gets entirely reflected by the material, its albedo value is one (a perfect mirror would have such albedo). On the contrary, if the material absorbs all the light, its albedo is zero and the object is not visible (a perfect black body would have an albedo of zero). The Bond albedo is to be distinguished from the geometric visible albedo, noted p_V. This geometric visible albedo is defined as the ratio between the radiance of an object observed from the light source, and the radiance of a perfectly lambertian surface

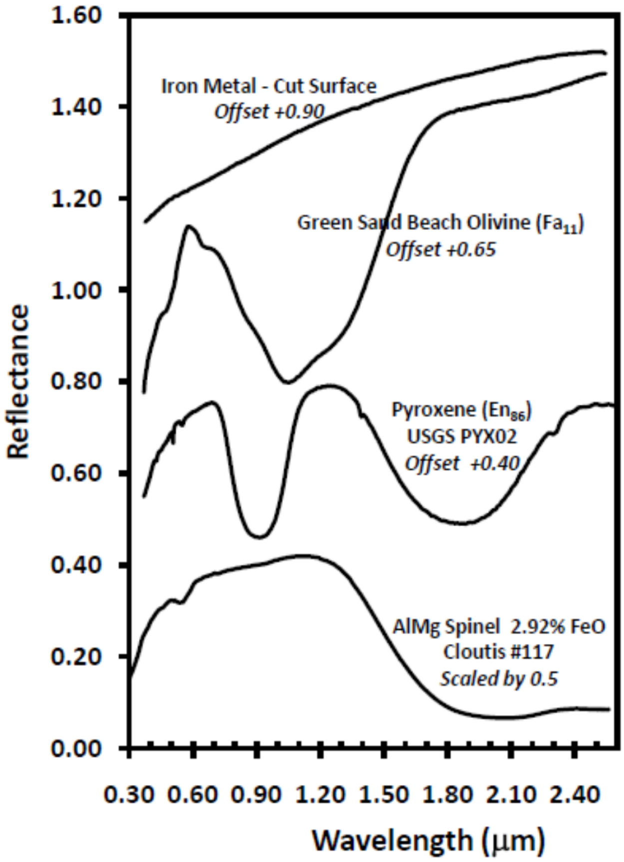

Figure 1.11: Figure 3 of Gaffey (2011), showing the reflectance spectra in the visible and near-infrared wavelength range of four major anhydrous mineral phases in meteorites and asteroids. Olivine and pyroxene show deep absorption bands, while the iron metal spectrum is featureless. Spinel is an aluminum magnesium oxide (AlMg), showing an almost featureless spectrum in the visible wavelength range. The curves have been offset for clarity.

(an idealised flat, fully reflecting and diffusely scattering surface) of the same cross-section, at zero phase angle. For p_V, the radiance ratio is measured in the photometric V band (corresponding to the maximum sensitivity of the human eye in the visible wavelength range), and it can take values above 1.

Studying the equivalent geometric albedo distribution of a large number of asteroids, a bimodal distribution has been identified by Zellner (1973). He distinguished two main types of asteroids, dark "carbonaceous" types with albedo values around 0.05, and brighter "stony" types with albedo values around 0.18. Morrison (1977) conducted a study of 187 asteroids down to 80 km, and came to the same conclusion. His figure showing the bimodal distribution of albedos is displayed in panel (a) of Fig.1.12. This figure evolved since 1977 with the increase in the number of observed objects. The albedo histogram considering the 41 468 asteroids having a spectrum in the Gaia Data Release 3 catalogue and an having albedo value in MP3C[1] is displayed in panel (b) of Fig.1.12. The bimodal distribution is still observable.

---

[1] `https://mp3c.oca.eu/`

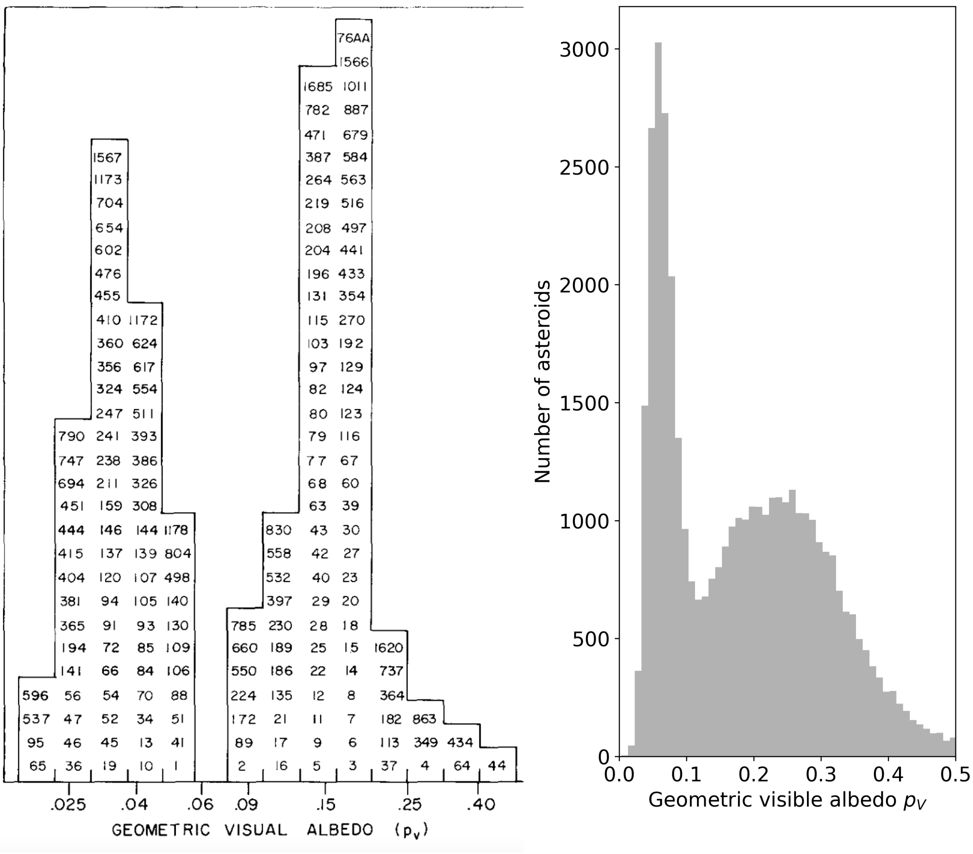

(a) (b)

Figure 1.12: Panel (a): Fig.2 of Morrison (1977), showing the distribution of measured geometric visual albedo obtained for his dataset of asteroids. The numbers and designations inside the histogram are those of each of the 187 considered asteroid. The low-albedo peak corresponds to carbonaceous asteroids, and the higher-albedo peak to silicaceous asteroids. Panel (b): same histogram considering the 41 468 asteroids having a spectrum in the Gaia Data Release 3 catalogue and albedo values in MP3C.

The low-albedo peak in Fig.1.12 around 0.03 corresponds to carbonaceous asteroids, and the peak around 0.2 to silicaceous asteroids. On the spectral side, silicaceous asteroids show characteristic absorption bands in their reflectance spectra, while carbonaceous asteroids show more featureless spectra. In fact, a gradient of composition exists between these two groups, representative of the gradient of composition of the primordial solar nebula. This gradient is more visible in panel (b) of Fig.1.12: no gap exists between the two asteroid groups, as many more objects than in Morrison (1977) are included in this plot.

1.3.2 Asteroid classification

With time, the number of asteroids discovered and observed increased. Astronomers started grouping them into spectral classes based on their observed features, which lead to the development of taxonomies.

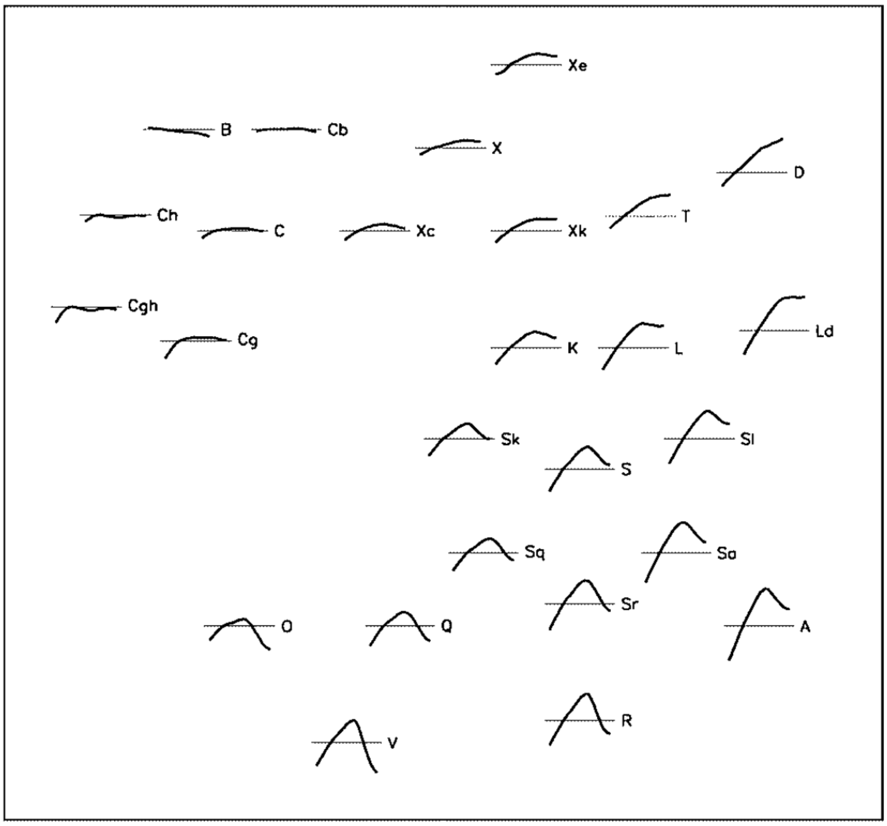

Figure 1.13: Fig.15 from Bus and Binzel (2002a) showing the 26 taxonomic classes defined from SMASSII survey, developed from spectra spanning the visible wavelength range. The horizontal and vertical scaling are constant, and the horizontal line plotted with each spectrum represents a reflectance of 1.0.

The evolution of the asteroid taxonomy followed the development of observational methods and instrumentation techniques. Chapman et al. (1975) proposed a first taxonomy, based on observations in narrow band spectrophotometry and albedo measurements. They distinguished three types of asteroids using a system of letters: the two aforementioned types of silicaceous and carbonaceous asteroids were designated respectively as S and C-types, and a additional U-type (for "Undetermined") was added for objects showing characteristics not fitting in either of these categories.

Years later, following the growth of asteroid databases and diverse attempts to improve the taxonomy of Chapman et al. (1975), Tholen (1989) proposed an extended taxonomy based on broad band spectrophotometry obtained with the Eight-Color Asteroid Survey (ECAS) (Zellner et al., 1985), and making use of albedo measurements. This taxonomy is composed of 14 classes, allowing a greater distinction between asteroids and thus a finer study of their composition. Each class is designated by a letter, each designating a specificity of the objects' spectrum or albedo, representative of the asteroids' mineralogical composition.

Another major evolution of the taxonomy happened with the arrival of charge-coupled device (CCD) spectroscopy. Facing the impossibility of classifying asteroids of the Small Main belt Asteroid Spectroscopic Survey (SMASS) in the Tholen taxonomy, Bus and Binzel (2002a) developed a new taxonomic scheme taking advantage of the information contained in spectra acquired with CCD spectroscopy. These spectra cov-

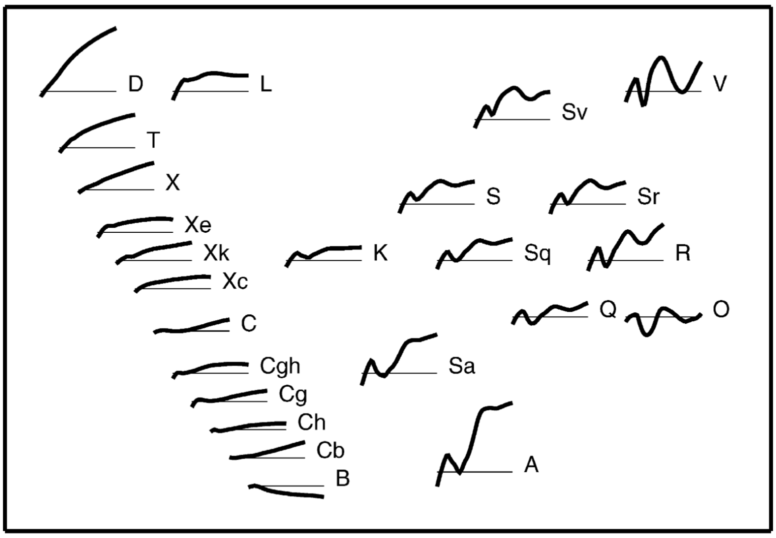

Figure 1.14: Fig.15 from DeMeo et al. (2009) showing the extension of the Bus and Binzel (2002a) taxonomy in 24 taxonomic classes, from observations in the NIR. The spectra cover the wavelength range from 450 to 2450 nm. The horizontal and vertical scaling are constant, and the horizontal line plotted with each spectrum represents a reflectance of 1.

ered a smaller wavelength range than the one covered in ECAS (440 - 920 nm), but were of higher resolution, and allowed to discover shallow absorption features not detectable with ECAS (Vilas et al., 1993; Hiroi et al., 1996; Bus and Binzel, 2002a). Bus and Binzel (2002a) defined three major groupings from the study of the spectra: the C, S and X-complexes. These complexes were subdivided in 26 classes, based on the presence and strength of spectral features. Each asteroid type and its associated average spectrum in this taxonomic scheme is displayed in Fig.1.13, extracted from Fig.15 of Bus and Binzel (2002a).

The Bus taxonomic scheme was extended to the near-infrared (NIR) wavelength range by DeMeo et al. (2009), following the development of instruments covering this range, such as SpeX on NASA's Infrared Telescope Facility (IRTF) (Rayner et al., 2003). DeMeo et al. (2009) defined 24 classes, refining the classification of Bus and Binzel (2002a) according to what they discovered in the range from 450 to 2450 nm. The 24 classes are displayed in Fig.1.14, extracted from Fig.15 of DeMeo et al. (2009). The S, C and X-complexes are also defined in this taxonomic scheme, and the groupings of more carbonaceous and more silicaceous objects are distinguishable in Fig.1.14. The first ones have mostly featureless spectra, and the seconds show more or less prominent silicate absorption bands around 1000 and 2000 nm in their spectra. Some types of Bus and Binzel (2002a) were abandoned by DeMeo et al. (2009), such as the Ld class, as objects belonging to this class in the Bus system separated well into the L and D classes in the NIR.

Finally, following the increase of asteroids spectra available and the development of new classification techniques, Mahlke et al. (2022) proposed a new iteration of the asteroids taxonomy based on visible, near-infrared, and visible-near-infrared spectroscopy, and re-introducing the albedo as an observable for the classification. In this scheme, the objects are assigned to three main complexes divided into 17 classes in a probabilistic way. The S and C-complexes are still defined, but the X-complex is

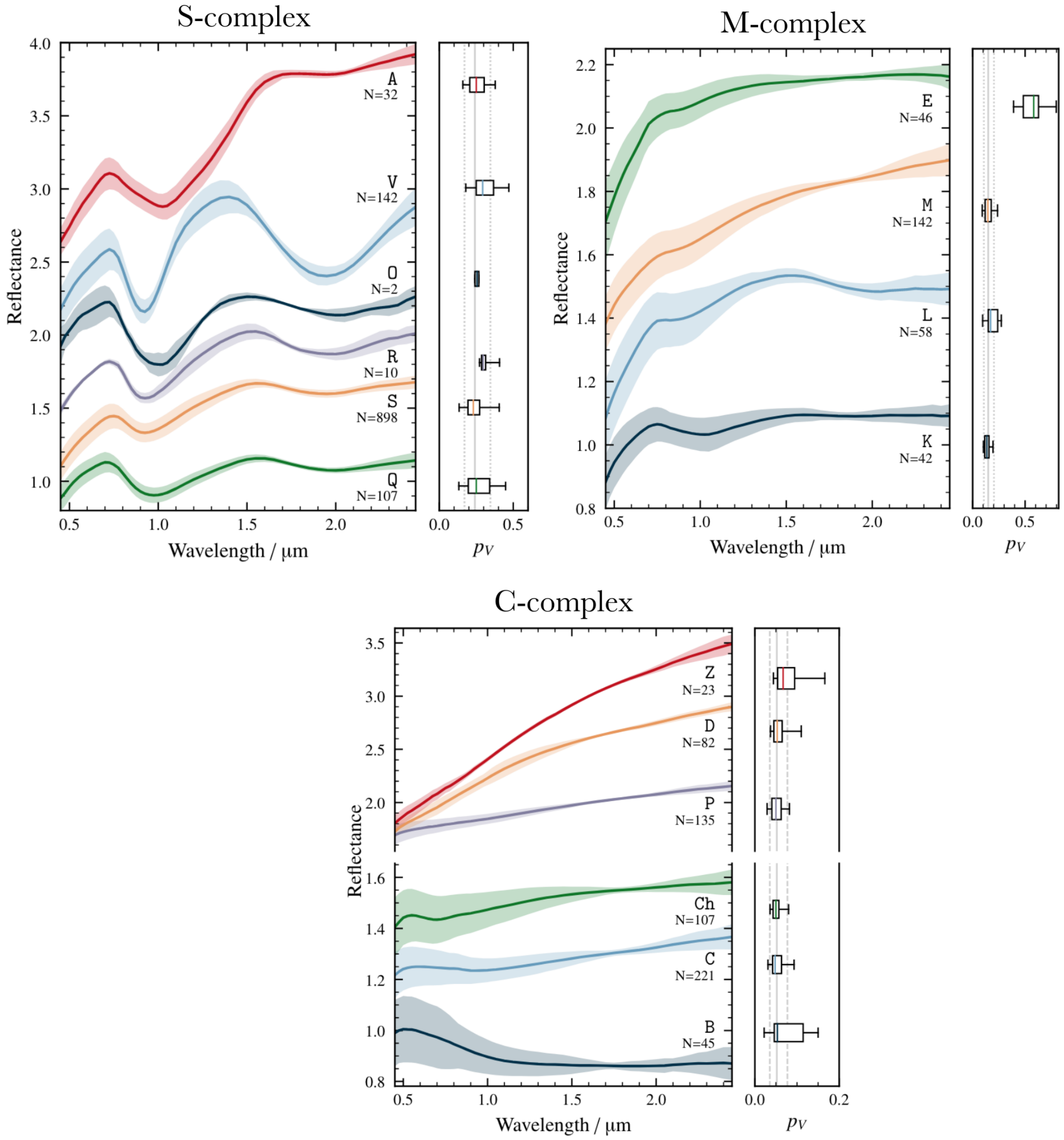

Figure 1.15: Combination of the Fig.9, 12 and 15 from Mahlke et al. (2022) showing the mean (solid line) and standard deviation (shaded area) of the reflectance spectra for each of the 17 taxonomic classes, along with the mean, lower and upper quartiles, and the 5 and 95 percentiles of the distribution of visual geometric albedo within each class. The classes are grouped into the S, M and C-complexes.

replaced by the M-complex, as taking the albedo into account enables to distinguish objects with similar spectral properties. The spectra and albedo range corresponding to each class defined in the Mahlke et al. (2022) taxonomic scheme are displayed in Fig.1.15.

The evolution of the most used taxonomic schemes presented here is illustrated in Fig.1.16. Every class defined in each scheme is indicated as a letter, and the S, C, X and M-complexes are indicated in a different colour. Some asteroid types show characteristics not matching with the C-, X-, and S-complexes, corresponding to intermediate or end-member compositions. Among them, the O-type was created to represent the peculiar spectrum of a single asteroid, (3628) Boznemcova.

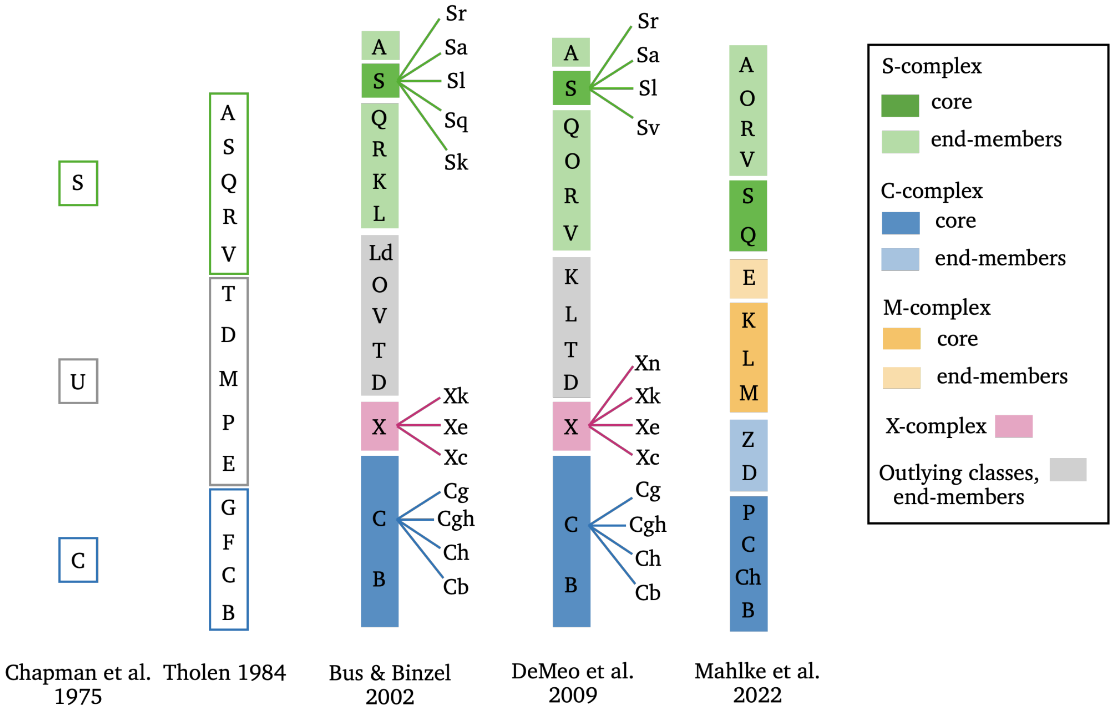

Figure 1.16: Scheme illustrating the global evolution of taxonomy, from Chapman et al. (1975) to Mahlke et al. (2022). Each letters refers to a taxonomic class defined in each scheme, and the classes are grouped in complexes: the S (green), C (blue), X (pink) or M (orange) complexes. The U class in Chapman et al. (1975) taxonomy indicates an "undefined" class. The core and end-members are not indicated prior to Bus and Binzel (2002a), as these designations were not introduced at the time.

1.3.3 Spectral types and composition

In every taxonomic scheme, spectroscopic classes are built on observables representative of the asteroids' surface composition, such as the presence and strength of features in their spectra and their albedo. Classifying asteroids is thus an efficient way to characterise them. In the following, the main complexes and types of asteroids relevant to this thesis are described.

Asteroids belonging to the C-complex show mostly featureless spectra, characteristic of carbonaceous objects. These low-albedo asteroids are considered primitive, and they are found mostly populating the OMB. In this complex, Cgh and Ch-types show a shallow absorption feature around 700 nm, thought to be diagnostic of the presence of oxidized iron in phyllosilicates, generated by aqueous alteration (Vilas and Gaffey, 1989). Studying them is of great interest, as they contain information about the early Solar System and might be the objects that brought water to Earth (Trigo-Rodríguez et al., 2019).

Asteroids belonging to the S-complex show spectra with moderate to steep slopes extending from the ultraviolet (UV) part to about 700 nm, and a more or less deep absorption feature around 1000 nm, diagnostic of silicate minerals and varying mostly with the pyroxene and olivine content (Bus and Binzel, 2002a). These objects are thought to be undifferentiated (Feierberg et al., 1982), and populate mostly the IMB (Gradie et al., 1989).

Among the end-members of this complex, A or Sa-types are characterised by a spectrum showing a strong absorption feature at about 1000 nm, an absent or weak absorption feature at 2000 nm, an extremely reddish slope short-wards of 700 nm, and a moderately high albedo (DeMeo et al., 2009; Mahlke et al., 2022). These are diagnostic of an olivine-rich composition (Cruikshank and Hartmann, 1984; DeMeo et al., 2019), that can be generated in the mantle of differentiated planetesimals (Burbine et al., 1996).

Asteroids belonging to the X-complex are slightly redder than C-complex asteroids in colour, and show shallow absorption features in their mostly featureless spectra, that can indicate the presence of troilite (FeS) (Bus and Binzel, 2002a). The use of albedo allowed to distinguish between different spectral types in this complex, and M-type asteroids are understood to be of metallic-rich composition with traces of silicates. They are the remnants of cores of differentiated planetesimals (Lupishko and Belskaya, 1989).

Finally, V-type asteroids show a strong silicate absorption feature around 1000 nm, characteristic of a basaltic or gabbroic composition (Barrat et al., 2010). Such mineralogy is the product of magmatic processes, and V-type asteroids are understood as remnants of the crust of differentiated planetesimals (Russell et al., 2012; Oszkiewicz et al., 2014).

1.3.4 Spectral ambiguity and space weathering

Deducing the composition of an asteroid from their spectrum and albedo is made difficult by various phenomena affecting the spectral response of objects. In space, bodies are subject to meteoroids and micrometeoroids impacts, to the irradiation, implantation and sputtering of solar wind particles, and to galactic and solar cosmic rays bombardment (Clark et al., 2002). The effect these phenomena have on asteroids surfaces is called space weathering (Hapke, 2001; Pieters and Noble, 2016). One of its known effects is the injection of nanophase iron $npFe^0$ inside a silicate host medium, as discovered from the study of lunar soils returned by the Apollo missions (Pieters et al., 2000; Hapke, 2001). Nanophase iron inclusions change the physical properties of a surface, and induce visible effects on the spectra of silicate materials in the UV, VIS, and NIR wavelengths range: the spectral slope is increased (reddened), the silicate bands become shallower and less recognisable, and the albedo of the object is darkened (Adams and McCord, 1971; Brunetto et al., 2015). However, silicate band centres were found not to (or little) be affected by this phenomenon (Gaffey et al., 2002).

Solar-wind ion bombardment was found the main agent of space weathering, since it alters surfaces on a timescale of 10^4 to 10^6 years (Vernazza et al., 2009a). It is responsible for the spectral reddening of silicate materials in the UV, VIS, and NIR wavelengths range, while micrometeoroids impacts induce a spectral darkening (Hapke, 2001; Brunetto et al., 2006; Vernazza et al., 2009a; Brunetto et al., 2015).

Models of space weathering have been made to study its effect on asteroids surfaces. The Hapke (2001) model was derived from the study of lunar samples, and is based on the calculation of the absorption coefficient of a silicate host medium in which small nanophase iron spheres are included (see Brunetto et al. (2007) for further details). The model of Brunetto et al. (2006), based on previously developed models, focuses on modelling the reddening effect of solar wind ion bombardment, considering it is the main space weathering agent.

The effects of space weathering on non-silicate material are poorly understood so far and are still under study (Brunetto et al., 2015). Laser-irradiation experiments have been performed on samples of different compositions to mimic the effect of solar-wind ions bombardment on an object in space. It was found that more metallic objects get brightened and reddened, while a low exposure to space weathering darkens and bluens the spectra of volatile rich carbonaceous objects. The more this material gets exposed to weathering agents, the brighter and bluer it becomes (Zhang et al., 2022; Nesvorný et al., 2005; Lazzarin et al., 2006). Therefore, the effects of space weathering depend on the composition of bodies, and can differ from the ones observed on silicate material.

Space weathering is not the only non-compositional cause of variations in asteroids spectra. Grain size affects the slope and band depth of reflectance spectra (MacLennan et al., 2024), as the optical path taken by the light depends on the particles' size. Smallest grains dominate the spectral appearance of an object, and can lead to less distinguishable absorption features (Mustard and Hays, 1997; Vernazza et al., 2010). Asteroid surfaces are covered in grains that vary in size from one order of magnitude to another, partly anti-correlated to the asteroids diameter, and their production can result from the action of space weathering or thermal fatigue (Delbo' et al., 2007; Delbo' and Tanga, 2009; Delbo et al., 2014; Vernazza and Beck, 2016). A variation in grain size can, for example, affect the spectral slope of carbonaceous objects (Johnson and Fanale, 1973), and the albedo of silicaceous asteroids (Cloutis et al., 1986). In some cases, grain size can affect the taxonomic classification of asteroids, for example of low-albedo NEOs (Cantillo et al., 2023).

Other non-compositional factors affect asteroids' reflectance spectra, such as the shape of a body or its temperature. Indeed, minerals' absorption features see their position move to shorter wavelengths with temperature, and their width decrease (Lucey et al., 1998; Sunshine et al., 2007; Reddy et al., 2015).

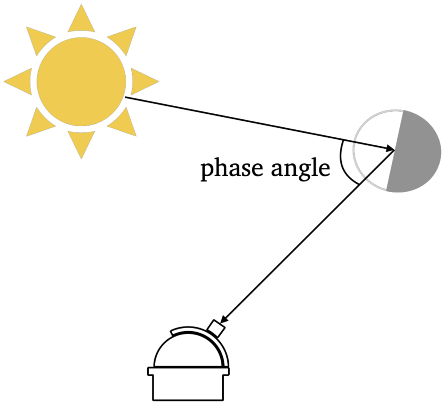

Figure 1.17: Scheme illustrating the phase angle of an observation.

Finally, the geometry of the observations is also known to have an effect on spectra. The phase angle of an observation is the angle made between the observer line of sight and the Sun's direction of illumination, as illustrated in Fig.1.17. Spectral slope increases with phase angle (Fornasier et al., 2020), and this phase reddening also increase the depth of absorption bands (Sanchez et al., 2012) and affects the asteroids' colour (Carvano and Davalos, 2015). These modifications can lead to an ambiguous classification of asteroids (Sanchez et al., 2012; Carvano and Davalos, 2015). All the mentioned phenomena have to be considered and disentangled to get an accurate idea of the composition of a body, to correctly interpret remotely sensed data, and to successfully link asteroids with meteorites.

1.4 METEORITES

Meteorites are fragments of celestial bodies that have landed on Earth. They can come from different bodies, such as Mars or the Moon, but the vast majority of them are fragments of asteroids. As explained earlier, some asteroids see their orbits drift inside the Kirkwood gaps and get ejected out of the Main Belt to Near Earth orbits, by the combined action of collisions, gravitational perturbations, and non-gravitational forces such as the Yarkovsky effect (Greenwood et al., 2020). In some cases, these objects fall on Earth. Such case is illustrated in the schematic view in Fig.1.18, inspired from Greenwood et al. (2020). This scheme represents an asteroid of the Inner Main Belt that undergoes a collision, and a fragment of it gets ejected out of the Main Belt through the 3:1 MMR with Jupiter. Such object falling on Earth is designated as a meteor while it burns in the atmosphere, and as a meteorite once it can be found on the ground.

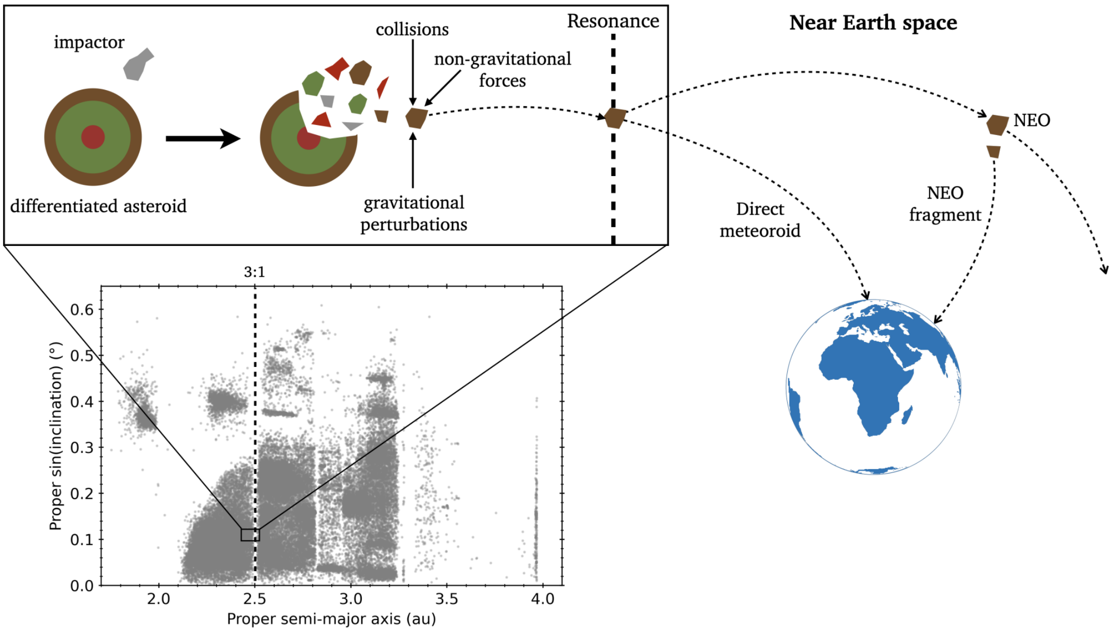

Figure 1.18: Schematic view of the possible delivery of Main Belt fragments of asteroids to Earth, inspired from Fig.1 of Greenwood et al. (2020). The Main Belt is represented in the proper inclinations versus proper semi-major axis space. A differentiated body that undergoes a collision is illustrated, generating a family of fragments. One of these fragments, by the combined actions of collisions, gravitational perturbations and non-gravitational forces, falls in a resonance (here the 3:1 MMR with Jupiter). Once in the resonance, the fragment enters the Near-Earth space and can either fall directly on Earth in the form of a meteoroid, or become a NEO. NEOs or fragments of them can eventually fall on Earth and be found as meteorites.

1.4.1 Short history

In history, meteorites were not always linked to asteroids. At the end of the third millennium, a mention of a stone falling from the sky is made in *The Epic of Gilgamesh*, a poem from ancient Mesopotamia and one of the first literary piece ever written. This stone is described as being so heavy that not even the strong Gilgamesh could lift it, making it an object of worship for the local population. This association between meteorites and a deity remained for centuries, with multiple examples across time: for example, around 220 a.c, Roman emperor Heliogabalus tried to turn a "black stone fallen from the sky" into a main divinity (unsuccessfully). The iron found in meteorites has also been used in practical ways, as Tutankhamen's dagger is known to be made of meteoritic iron. Eventually, the link between observed meteors and iron rocks found on the ground was made in the 1770s by Ernst Chladni, a german physicist who published a pamphlet stating that meteorites come from space.

Many meteorites have been found and collected since the 1770s. A distinction is made between two types of meteorites discoveries: the falls, and the finds. A fall is a meteorite found following the observation of a meteor, while a find is a meteorite found directly on land, without observing the fall. Finds can therefore remain on Earth for long periods of time before being discovered. In 1985, the number of falls was of about a thousand, while the number of finds was of 1706. Today, these numbers increased drastically, with the observation of 1390 falls and a total number of about 75 000 meteorites recorded in the Meteoritical Bulletin Database.

1.4.2 Finding meteorites today

Today, 97% of meteorites are searched for and found in hot and cold deserts, with 72% of meteorites found in Antarctica, and 25% found in hot deserts such as the Atacama or African deserts (data from the Meteoritical Bulletin Database). These deserts are places of choice to look for meteorites, because their dark colour contrasts with the desert's soil or with snow, making them easier to identify.

All over the world, networks have been put in place to detect meteors, such as the French network Fireball Recovery and InterPlanetary Observation Network (FRIPON) (Colas et al., 2020), the associated Italian Prima Rete Italiana per la Sorveglianza sistematica di Meteore e Atmosfera (PRISMA) (Gardiol et al., 2016), the Spanish Meteor Network (SPN) (Trigo-Rodríguez et al., 2004), the Czech European Fireball Network (EFN) (Ceplecha and Rajchl, 1965), the Canadian Automated Meteor Observatory (CAMO) (Weryk et al., 2013), the slovak All-sky Meteor Orbit System (AMOS) (Tóth et al., 2015), the Global Fireball Observatory (GFO) (Devillepoix et al., 2020) bringing together multiple countries, or the Australian Desert Fireball Network (DFN) (Bland, 2004). All these networks are composed of all-sky cameras and radio receptors observing the sky continuously in order to detect meteors (also called fireballs). These cameras can be located anywhere, on the roof of observatories and universities, but also on top of museums or in the middle of deserts. They are connected to programs able to detect bright flashes, characteristic of the entry of a meteor in the atmosphere. The goal of these networks is to determine the orbit of the meteoroids before their fall to trace the origin of the body, and to delimit an area of research on land to try recovering the meteorite (or fragments of meteorite) resulting from the fall.

Indeed, recovering meteorites right after their fall allows to analyse extraterrestrial material only mildly contaminated by the terrestrial environment. Once on the ground, meteorites experience a terrestrial weathering dependent on the environment they fall in: chemical weathering by the actions of water, oxygen and chlorine; and physical weathering if they fall in a cold and wet environment (Pentikäinen et al., 2014). Depending on where they fall, meteorites can survive a more or less long time, and Antarctica is known to preserve meteorites better (Bland et al., 2006). Thus, recovering a meteorite right after its fall allows to study primitive material of the Solar System little altered by Earth.

1.4.3 Meteorite classification

Before the development of such networks, meteorites have long been analysed and exhibited in museums. In 1867, Professor at the Natural History Museum Gabriel Auguste Daubrée published a classification for the meteorites of the museum (Daubrée, 1867). His classification is based on the abundance of metal in the meteorite, and he distinguished mostly iron-rich and stony meteorites.

More advanced classifications make a distinction between differentiated and non-differentiated meteorites (Weisberg et al., 2006). Non differentiated meteorites are designated as chondrites. These meteorites are the most primitive kind, they evolved little since their formation in the protoplanetary disk (Sears and Dodd, 1988). Chondrites contain chondrules, millimetre-size spherical grains rich in silicates made by the condensation of the solar nebula (see for example Woitke et al., 2024, and references therein), as well as Calcium Aluminium-rich Inclusions (CAIs). These inclusions are the first refractory elements that condensed in the solar nebula. They formed at very high temperature more than 4.567 billion years ago (Amelin et al., 2010; Connelly et al., 2012; Piralla et al., 2023), and the age of the cosmochemical origin the Solar System has been estimated from their datation (Kita and Ushikubo, 2012; Kruijer et al., 2017; Woitke et al., 2024). These objects are essential for constraining the formation and evolution of the Solar System.

1.4.3.1 *Chondrites*

Chondrites are divided in classes representative of their chemical and isotopic composition, and of their mineralogy. More than 80% of the meteorites found on Earth correspond to the Ordinary Chondrite (OC) group (the Meteoritical Bulletin Database). These meteorites are mostly composed of silicate minerals and metal, and they are divided in three categories depending on the metal, iron, and iron oxide (fayalite) content in their silicates: the H, L, and LL groups (Weisberg et al., 2006). H chondrites show the highest content in iron and metal, and a lower content in iron oxide. L chondrites show lower iron and metal content, but higher iron oxide content. Finally, LL chondrites show the highest iron oxide content and a low iron and metal content. These slightly different compositions lead to think that the OCs could originate from three different parent bodies (Yomogida and Matsui, 1984), or could be due to thermal metamorphism instead (Dodd, 1969).

The carbonaceous chondrites and enstatite chondrites represent respectively about 4.5% and 1% of the meteorites collection on Earth (The Meteoritical Bulletin Database). The carbonaceous chondrites are divided into eight groups depending on their mineralogical composition, elemental ratios, and oxygen isotopic ratios (Weisberg et al., 2006). The designations of these groups are given in Fig.1.20. These meteorites contain CAIs and chondrules embedded in a matrix of olivine, pyroxene, and Fe-Ni metal (see Woitke et al., 2024, and references therein), as can be seen in Fig.1.19 with a photo of Allende, the largest carbonaceous chondrite found on Earth.

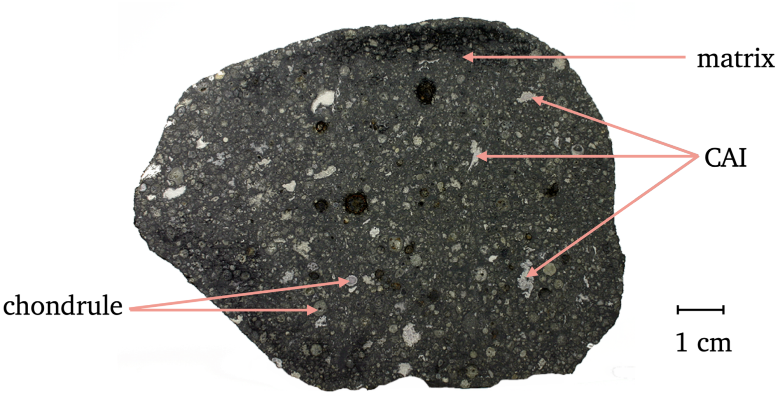

Figure 1.19: Carbonaceous chondrite Allende, on which are indicated Calcium-Aluminium-rich Inclusions (CAIs), chondrules, and the matrix. Image credit: Matteo Chinellato.

The enstatite chondrites are mostly made of pyroxene and iron metal, and can be divided in two groups depending on their iron content (high H or low L (Weisberg et al., 2006)). They are the most reduced chondrites, and are thought to be representative of the primordial objects that built the Earth in composition (Javoy et al., 2010).

Another rare type of chondrite are the R- and K-chondrite groups, names after the meteorites Rumuruti and Kakangari. The R-chondrite group contains less than five members, which are highly oxidized. They show a chemical composition consistent with a production by the accretion of grains from an oxidised region of the solar nebula, without significant heating after the accretion (Schulze et al., 1994). It seems therefore possible to form olivine material outside of differentiation processes. K-chondrites are similar to OCs, except for their oxygen isotopic composition (Weisberg et al., 2006).

A secondary step in the classification of meteorites is the indication of their petrologic type (PT). Six petrologic types exist, indicating the degree of aqueous alteration and thermal metamorphism of a meteorite. A PT between 1 and 2 indicates an aqueously altered meteorite (PT=1 being the highest alteration), and a PT between 4 and 6 is indicative of an increasing thermal metamorphism. A PT=3 should represent pristine material, according to the first classification of chondrites by Van Schmus and Wood (1967).

In total, 14 groups of chondrites have been identified to date, leaving a large number of chondrites ungrouped. At least five objects sharing characteristics are required to create a new group, and ungrouped objects show too different characteristics to be classified in any existing group. This gives an idea of the compositional diversity of undifferentiated objects.

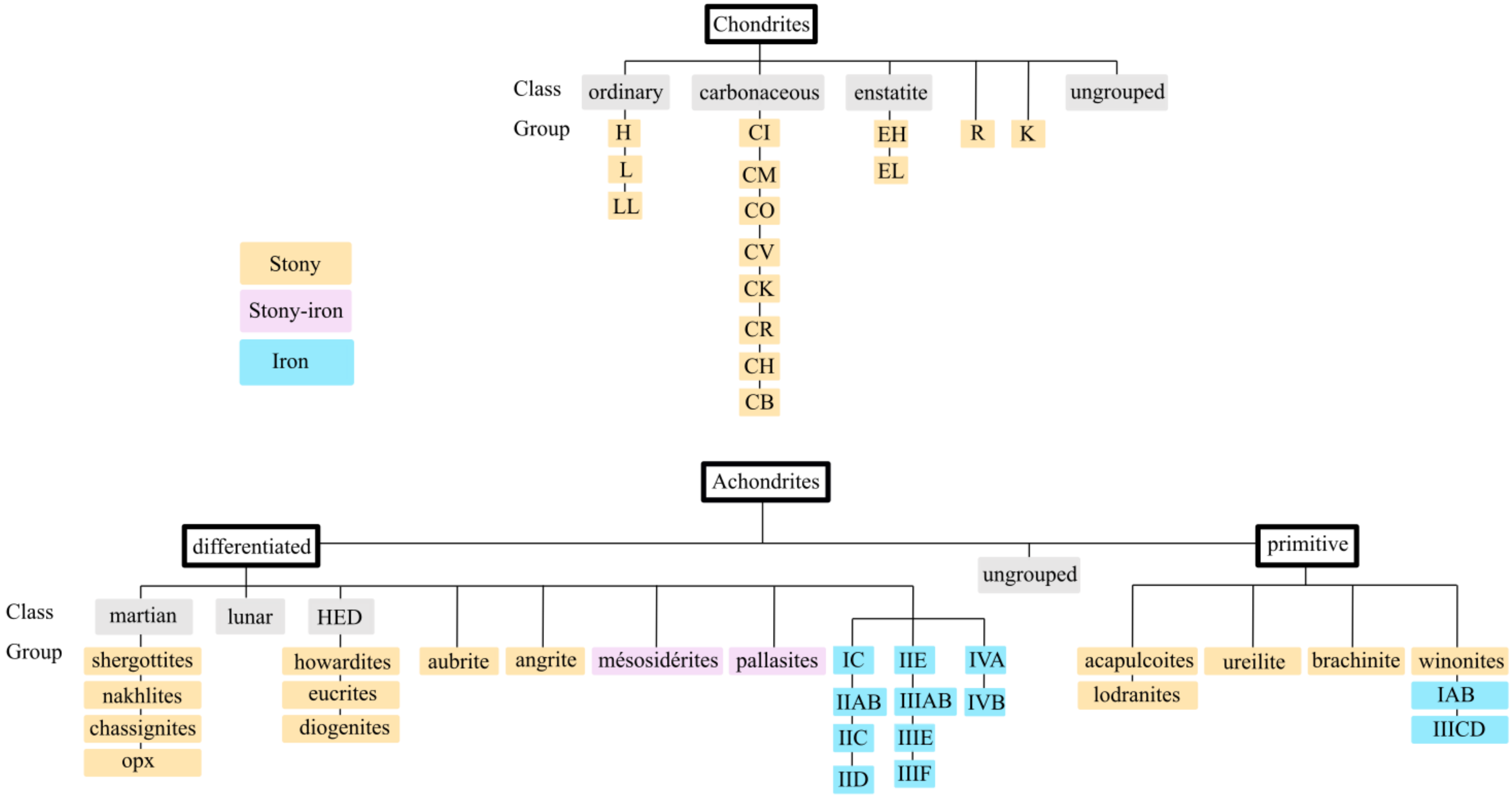

Figure 1.20: Scheme of the classification of meteorites. Inspired from schemes by Laurette Piani and in Ruf et al. (2018).

1.4.3.2 *Differentiated meteorites*

Differentiated meteorites, that represent about 8% of the total meteorite collection (the Meteoritical Bulletin Database), can be assigned to three categories: achondrites (meaning "that do not contain chondrules"), iron-meteorites, and stony-iron meteorites. These objects are the ones of interest for this thesis, as they are products of differentiation.

As displayed in the scheme of Fig.1.20, many sub-categories exist among the achondrites. Martian and lunar meteorites show petrologies, mineralogies and ages compatible with Mars and the Moon (see Papike et al., 2009; Demidova et al., 2007, and references therein), while the other groups of meteorites are understood to come from asteroids.

The Howardite, Eucrite, Diogenite (HED) group of meteorites are magmatic rocks (Burbine et al., n.d.) that represent the most abundant class of the achondrite grouping. They are mostly made of pyroxene and plagioclase cristals, and the difference between these three types comes from the size of their crystals and from the quantity of olivine they contain. Eucrites are basaltic, diogenites are cumulates of various quantities of orthopyroxene and olivine (McSween et al., 2013), and Howardites are breccias containing clasts of eucrites and diogenites (Beck et al., 2012). They correspond to crustal material of a differentiated body.

Meteorites corresponding to the core of differentiated planetesimals are iron meteorites (Goldstein et al., 2009). They are made of iron-nickel alloys, and are classified in subgroups based on their chemical heterogeneities (Scott and Wasson, 1975; Goldstein et al., 2009), which names are given in Fig.1.20.

Some meteorites show a high content in olivine, such as pallasites and brachinites. Pallasites are highly differentiated meteorites composed of olivine crystals included in a iron-nickel matrix (Buseck, 1977). Their petrology and mineralogy suggest a formation in the core-mantle boundary of differentiated bodies (Buseck, 1977), or by an impact between an iron-rich asteroid and an olivine-rich body (Tarduno et al., 2012; Windmill et al., 2022). Brachinites are primitive achondrites that correspond to an olivine-rich residue obtained after the extraction of basaltic material by partial melting of an Fe-O rich parent body (Keil, 2014).

Among the other differentiated meteorites, aubrites mostly contain enstatite (iron-poor magnesium-rich orthopyroxene) (Watters and Prinz, 1979), while angrites are among the oldest magmatic rocks, with crystallisation ages of about 4.56 Myr (Kleine et al., 2012). Mesosiderites are rare meteorites, made of silicates and of an iron-nickel allow, mostly presenting traces of thermal metamorphism (Rubin and Mittlefehldt, 1993).

Among primitive achondrites, ureilites are mostly made of olivine and pyroxene, with presence of graphite or diamonds (Goodrich, 1992). Acapulcoites and lodranites show traces of chondrules and chondritic textures, and they can be described as chondrites that partially melted (Keil and McCoy, 2018). Winonaites also show chondrules vestiges, and show traces of partial fusion and metamorphism (Benedix et al., 1998).

Finally, achondrites showing compositions and a petrology that do not correspond to any of these groupings are classified as "ungrouped achondrites". The meteorite Erg Chech 002, that is of major importance for this thesis, is part of this group (Barrat et al., 2021).

The classification of meteorites is based on the precise study of their chemical and mineralogical composition from laboratory measurements. The amount of information obtained from the study of meteorites is therefore much more important than what we obtain from remote observations of asteroids. For this reason, establishing links between asteroids and meteorites is interesting to probe the asteroid population with an increased precision.

1.5 LINKING METEORITES WITH ASTEROIDS

Classical techniques used to link asteroids with meteorites consist in comparing their spectral characteristics. Curve-matching techniques rely on the calculation of a similarity coefficient between spectra (see e.g Popescu et al., 2012). However, non-compositional phenomena affecting reflectance spectra, such as space weathering or grain size, make the establishment of a satisfactory link between asteroids and meteorites difficult, in most cases (Brunetto et al., 2006; Gaffey, 2011).

Basaltic V-type asteroids, such as asteroid (4) Vesta and its family members, have however been successfully linked to the group of Howardite, Eucrite and Diogenite meteorites (HEDs) from the direct comparison of their reflectance spectra (McCord et al., 1970; Russell et al., 2012). (4) Vesta shows two craters, the large basins Rheasilvia and Veneneia (Marchi et al., 2012), that are traces of two violent impacts that ejected parts of its crust. These collisions produced a family of fragments designated as vestoids, showing spectra matching the one of (4) Vesta and indicating a basaltic composition (Mansour et al., 2020). Such mineralogy matches that of the crust of differentiated planetesimals, indicating that Vesta is a differentiated asteroid that accreted and melted during the first million years of the Solar System (see Bizzarro et al., 2005; Turrini et al., 2016, and references therein).

Dynamically, there is a high probability that some vestoids got ejected of the Main Belt to later land on Earth, because of the family's proximity with the 3:1 MMR and the ν_6 secular resonance (see Fig.1.5 for the position of the Vesta family in the belt) (Migliorini et al., 1997). The petrology of eucrites suggests that they have been formed by rapid cooling, linking them to the superior crust of Vesta; while diogenites should come from deeper crustal or upper mantle parts (McSween et al., 2013). Howardites, as it comprises Vesta's regolith, could be the result of impacts between eucrite and diogenite-type material, compacting fragments created at different depths (McSween et al., 2013).

In Fig.1.21 are displayed the reflectance spectra of asteroid (4) Vesta and of some vestoids, along with the spectra of howardite Le Teilleul, eucrite Juvinas, and diogenite Johnstown (figure extracted from Burbine et al., n.d.). Their spectra shows great similarity, with (4) Vesta being the most similar to the meteorites. Indeed, this asteroid does not show the significant darkening and reddening implied by space weathering (McCord et al., 1970), which is further confirmed by the asteroid's high $p_V \simeq 0.38$ (Li et al., 2013). It appears that there is no accumulation of nanophase iron on the surface of Vesta (Pieters et al., 2012), while ion irradiation experiments on pyroxenes and HEDs show such phenomenon (Vernazza et al., 2006; Fulvio et al., 2012; Marchi et al., 2010). Vestoids actually show a darker and redder surface than Vesta, as can be seen in Fig.1.21, implying that they are affected by space weathering (Burbine et al., n.d.).

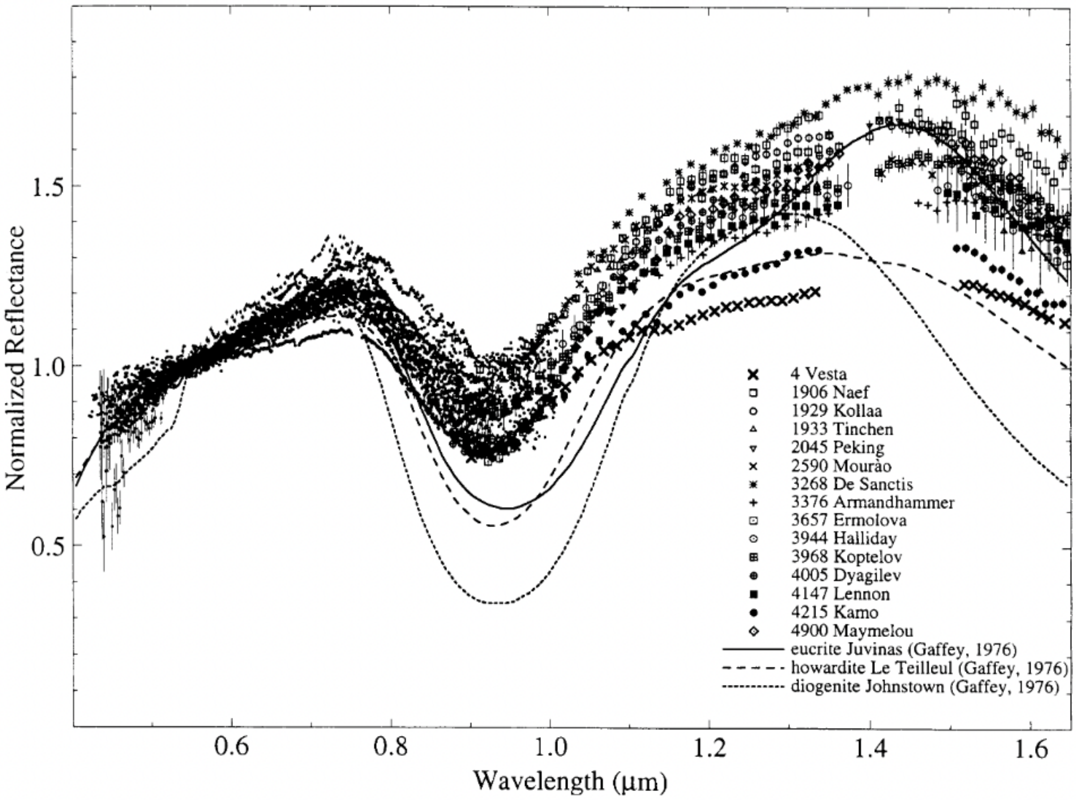

Figure 1.21: Reflectance spectra of (4) Vesta and some vestoids, along with the spectra of howardite Le Teilleul, eucrite Juvinas, and diogenite Johnstown acquired by Gaffey, 1976. Figure taken from Burbine et al., n.d.

Several possibilities could explain the observed differences between Vesta, the vestoids and HED meteorites. First, the vestoids could be covered in finer grains than Vesta, leading to their observed reddening (Burbine et al., n.d.). Second, nanophase iron and FeS that participate to space weathering could not be available in large quantities on Vesta, limiting its weathering (McSween et al., 2013). Third, pyroxene, dominating on Vesta's surface, could be more resistant than olivine to the effects of space weathering (Vernazza et al., 2009a). Finally, the large Vesta could be protected by a magnetic field deflecting the solar wind ions, a suggested from the analysis of the paleomagnetism of an eucrite (Vernazza et al., 2006; Starukhina and McCord, 2012; Fu et al., 2012).

Vesta being resistant to space weathering allowed to link it and its family to the HEDs from direct spectral comparison, which is not the case for other meteorites. Indeed, laboratory space weathering experiments and the use of space weathering models is often needed to successfully link asteroids and meteorites (Brunetto et al., 2006; Brunetto et al., 2007). Ordinary chondrites, the most abundant type of meteorite, have been successfully associated with a subset of S-type asteroids thanks to these studies (Chapman, 1996; Pieters et al., 2000). These meteorites are undifferentiated, leading to think that S-type asteroids are not products of differentiation.

On the other hand, A and Sa-type asteroids present spectral similarities with brachinites and pallasites (DeMeo et al., 2019), after correcting them from the effects of space weathering reddening their spectral slopes (Brunetto et al., 2006; Brunetto et al., 2007). These olivine-rich meteorites are products of differentiation (Buseck, 1977; Burbine and Binzel, 2002; Keil, 2014), suggesting that some objects in the Main Belt completely or partially differentiated, before going through catastrophic collisions that exposed their inner layers (Sanchez et al., 2014). However, the observation of spectral similarities between A-types and R-chondrites, that are understood to be formed through nebular processes (Schulze et al., 1994), suggests that not all A-type asteroids are products of differentiation (Sanchez et al., 2014; DeMeo et al., 2019; Sunshine et al., 2007).

Olivine is also a major constituent of the planet Mars' upper mantle (Bertka and Fei, 1997; Zuber, 2001; Hyodo and Genda, 2018). The Shergottites, Nakhlites, Chassignites (SNC) meteorites, amongst others, have been successfully linked to the planet from analyses of the gas they contain, and from their extremely young age of less than 1.3 billion years. These meteorites are olivine-rich, and they show spectral signatures similar to those of A-type asteroids. With a petrologic and spectroscopic analysis only, it is difficult to distinguish a martian from an olivine-rich meteorite of a different origin. Therefore, it has been hypothesised that a mega impact on Mars could have implanted martian material in the Mars Trojans group, in the Hungaria region, and in the Main Belt (Polishook et al., 2017; Hyodo and Genda, 2018). This would make A-type asteroids observed in the Main Belt potential fragments of an early Mars' crust (Polishook et al., 2017; Hyodo and Genda, 2018). However, the fact that some olivine-rich meteorites, such as the brachinites and pallasites, have not been linked to Mars leads us to believe that another origin is necessary to explain their existence. Thus, A-type asteroids in the Main Belt can still be evidence of differentiation processes.

Other meteorites have been successfully linked to asteroids. Indeed, the effect of space weathering on silicate material was found to affect mostly the slopes and the continuum of their VISNIR spectra, and not the position of their bands and their relative area ratio (Gaffey, 2011). Therefore, methods based on the measure of absorption band centres, Band Area Ratio (BAR), or reflectance values and ratios at given wavelengths, have been developed to succesfully link asteroids of various taxonomic types with meteorites (Cloutis et al., 2010; Gaffey, 2011; Avdellidou et al., 2022).

Fig.1.22 shows the spectra corresponding to different asteroid types, along with the spectra of meteorite types they have been linked with . The spectral similarities between asteroids and meteorites is clear, and the reddening effect induced by space weathering is especially noticeable on asteroids' spectra presenting features, such as those of S and A-type asteroids.

The collection of meteorites available today was however found to be biased, and not representative of all Main Belt asteroids. With a clear dominance of OCs in the collections, many meteorites and asteroids are yet to be linked. Despite this, the study of meteorites provides clues as to where planetesimals formed in the early Solar System and how they evolved.

Indeed, an isotopic dichotomy has been discovered between Carbonaceous Chondrites (CC) and Non-Carbonaceous (NC) meteorites (Warren, 2011), regardless of their belonging to the chondrite or achondrite grouping. This dichotomy is valid for all known meteorites, indicating that CC and NC meteorites came from two genetically distinct reservoirs in the early Solar System. These reservoirs are understood to have formed at different locations (rather than at different times), that remained isolated from each other for the first few million years of the Solar System, possibly because of the presence of the forming Jupiter (Warren, 2011; Morbidelli et al., 2016; Kruijer

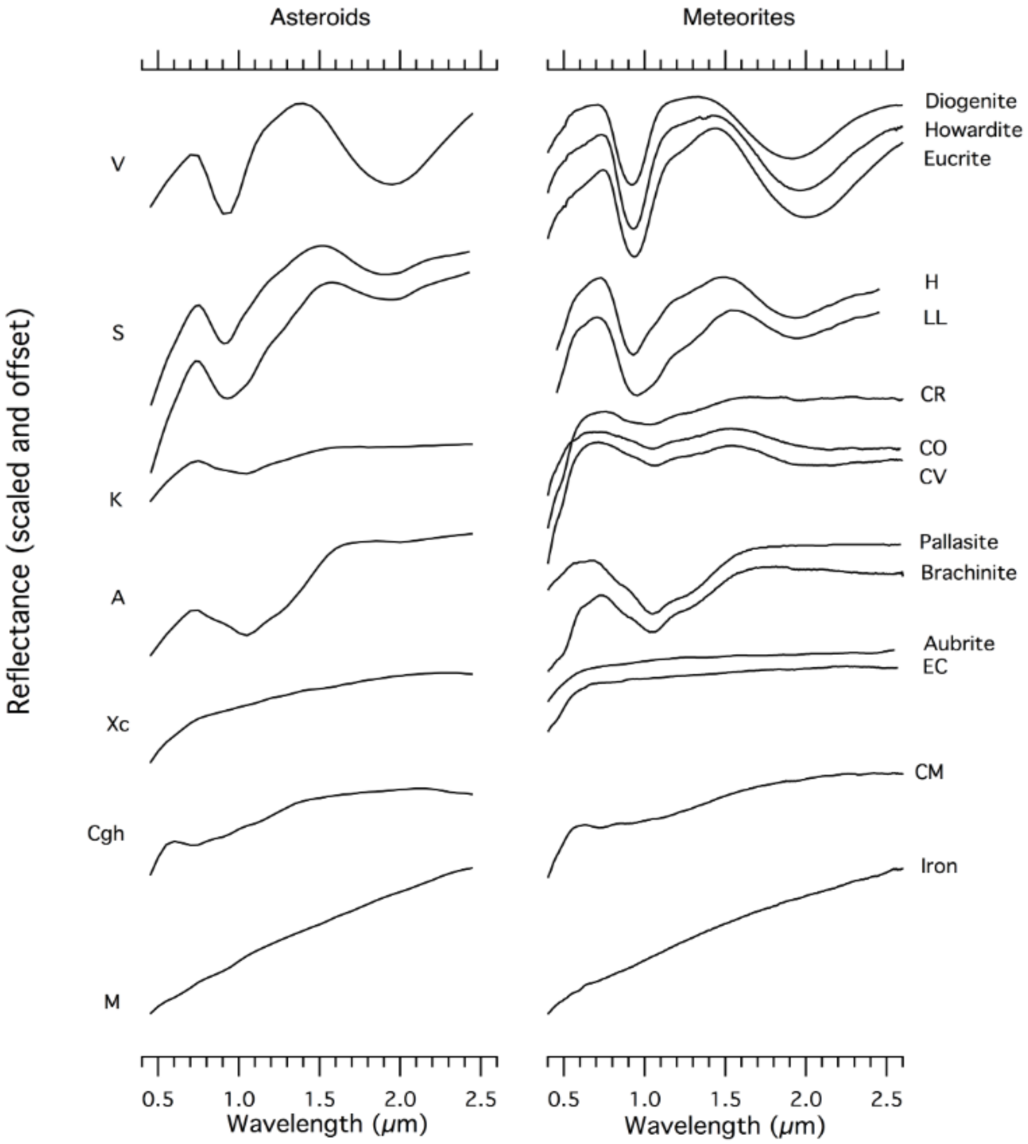

Figure 1.22: Reflectance spectra of various asteroid spectroscopic types, along with the spectra of meteorite types they are linked with. Figure taken from Vernazza and Beck, 2016. Spectra are all normalized to unity at 550 nm and are offset vertically for clarity. The V, K, A, Xc, and Cgh spectra are the average template spectra of the taxonomic scheme of DeMeo et al., 2009. The two S-type spectra are averages of S-type asteroids spectra presenting H-like (top) and LL-like (bottom) compositions according to Vernazza et al., 2014. The diogenite and eucrite spectra are averages of all the spectra of meteorites in these families available in the RELAB database at the time of the publication of Vernazza and Beck, 2016, as well as the spectra of The H, LL, CR, CO, CV, EC, CM and iron meteorite spectra. The howardite spectrum is the one of meteorite EET 87503 (25-25 μm size fraction), the pallasite is Thiel Mountain's spectrum (Sunshine et al., 2007), the brachinite is Brachina's spectrum (RELAB), and the aubrite's spectrum is the one of Mayo Belwa (RELAB).

et al., 2017). This observation lead to the conclusion that S-type asteroids and NC meteorites were generated in the inner Solar System, while C-type asteroids and CC meteorites were implanted from the outer Solar System. The study of meteorites is therefore fundamental to constrain models of Solar System evolution.

1.6 DIFFERENTIATION: CURRENT QUESTIONS AND OPEN PROBLEMS

Spectroscopic surveys and the classification of asteroids lead to the discovery that most collisional families of asteroids detected in the Main Belt are homogeneous, showing members sharing the same or similar spectral characteristics, photometric parameters and albedos (Mothé-Diniz et al., 2005a; Jurić et al., 2002; Parker et al., 2008; Masiero et al., 2011; Oszkiewicz et al., 2014). This homogeneity suggests that the parent body at the origin of the family was homogeneous, leading to a family of fragments showing similar composition (Oszkiewicz et al., 2014). However, the catastrophic disruption of differentiated parent bodies should have produced families with members showing compositions characteristic of the different layers of the parent body (Galinier et al., 2024). No such family has been detected so far.

The only family confirmed to be differentiated is the Vesta family, because of the basaltic composition of its members and their confirmed link with HEDs (McCord et al., 1970; Russell et al., 2012). (4) Vesta went through cratering events that ejected parts of its crust, but that did not reveal its internal layers. NASA's Dawn spacecraft visited Vesta and performed gravitational field measurements, confirming the presence of an iron core (Russell et al., 2012). Magma-ocean models and the study of HEDs suggest that Vesta could be completely differentiated, showing an eucritic crust on top of a diogenite layer, an olivine-rich mantle, and a metallic core (Righter and Drake, n.d.). Other models suggest that diogenites formed after eucrites, and rather within the eucritic crust than in a lower layer (Barrat et al., 2010). The issue with these differentiation models is that only a small amount of olivine material has been detected on the surface of Vesta, and it has been found located at near surface and not within deep basins, that should show excavated mantle (Ammannito et al., 2013). This olivine could be exogenous contaminants brought by impacts, as it is exposed in crater walls (Ammannito et al., 2013), which would suggest that Vesta has a thick crust, keeping its internal layers from being exposed by impacts (Turrini et al., 2016). No vestoid appears to show olivine-rich compositions, so the existence of Vesta's olivine-rich mantle has not been confirmed thus far.

Other families have been suggested as potentially differentiated, such as the Hungaria (Gaffey et al., 1992), Merxia, Agnia (Sunshine et al., 2004; Vernazza et al., 2014), and Maria families (Fieber-Beyer et al., 2011), but none of them has been confirmed to date.

Finding differentiated bodies in the Main Belt can be done by measuring their density, as was performed with Dawn for Vesta. In the last decades, improvements were made in the measurement of asteroid sizes and volumes (Durech et al., 2010; Ďurech et al., 2011; Vernazza et al., 2021), but the estimation of asteroid masses is still limited (Fienga et al., 2020) and might lead to large uncertainties in the determination of an object's density (Carry, 2012). Therefore, detecting a high density object is not necessarily proof of differentiation.

However, such measurements performed on chondritic asteroid (21) Lutetia suggest that partial differentiation occurred, leading to the production of a metallic core on (21) Lutetia while preserving a primitive chondritic crust (Weiss and Elkins-Tanton, 2013). Hence, evidence of differentiation can be hidden in the asteroid population, and would not be detected by studying the surface composition of asteroids only. Further evidence of partial differentiation is given by the CV carbonaceous chondrite Allende. This undifferentiated meteorite shows a remnant magnetic field, trace of the core dynamo of the partially differentiated planetesimal it is derived from (Carporzen et al., 2011). Other asteroids showing chondritic surfaces might thus be partially differentiated (Weiss and Elkins-Tanton, 2013).

The meteorite record suggests that there should exist about a hundred parent bodies for the whole meteoritical collection (Greenwood et al., 2020). Among differentiated meteorites, pallasites are understood to originate from six to nine parent bodies (Greenwood et al., 2017; Ruzicka et al., 2017). Three parent bodies are thought to be the source of aubrites (Keil, 2012; Barrat et al., 2016), while other differentiated meteorite groups, such as angrites, mesosiderites, and HEDs, are each considered to derive from a single parent body (Keil, 2012; McSween et al., 2013). The ~hundred of ungrouped achondrites have been found by Greenwood et al. (2017) to come from about 16 parent bodies, even if many of these objects are yet to be linked to asteroids. Evidence of differentiated parent bodies at the origin of these meteorites should therefore be observable in the Main Belt.

Basaltic objects have been detected in the Main Belt outside the Vesta family as well (Moskovitz et al., 2008; Solontoi et al., 2012; Leith et al., 2017; Oszkiewicz et al., 2023), remnants of the crust of other differentiated planetesimals. Metallic (Fornasier et al., 2010; Harris and Drube, 2014) and olivine-rich asteroids (DeMeo et al., 2019) have been found, but no evidence of full differentiation has been detected in the Main Belt, in the form of an asteroid family showing basaltic, olivine-rich and metallic members (DeMeo et al., 2019). Moreover, there is an observed scarcity of olivine-rich asteroids known as the "missing-mantle problem" (Chapman, 1986; Burbine et al., 1996). DeMeo et al. (2019) derived from NIR spectroscopic observations that A-type asteroids account for less than 0.16% of the Main Belt, for asteroids with a diameter above 2 km. They estimate the number of A-type asteroids above that size to be of around 600. They find these objects evenly distributed throughout the Main Belt, showing no statistically significant concentration in any asteroid family, as can be seen in Fig.1.23 (extracted from Fig.4 of DeMeo et al. (2019)).

Several explanations have been proposed to account for the absence of olivine-rich bodies in the Main Belt. One hypothesis suggests that collisions cause olivine-rich objects to break into fragments too small to be detected by current observational techniques (Sanchez et al., 2014; Popescu et al., 2018b). Another theory proposes that olivine may exist in the mantle of asteroids, but is concealed beneath a covering of another material, as mentioned earlier (Elkins-Tanton et al., 2011). This could be the case for asteroid (4) Vesta. Another explanation could be that differentiated planetesimals formed early and mostly accreted to planets, leaving few differentiated bodies to be implanted in the Main Belt, in the form of intact bodies or fragments (Delbo et al., 2017; Delbo et al., 2019; Ferrone et al., 2023; Bourdelle de Micas et al., 2022). An alternative hypothesis challenges current understanding by proposing that the formation of thick olivine mantles during planetesimal differentiation might not occur as conventionally thought (DeMeo et al., 2019). Finally, it is possible that olivine material is highly sensitive to space-weathering processes, potentially causing olivine fragments to weather to the point where they are no longer detectable (DeMeo et al., 2019).

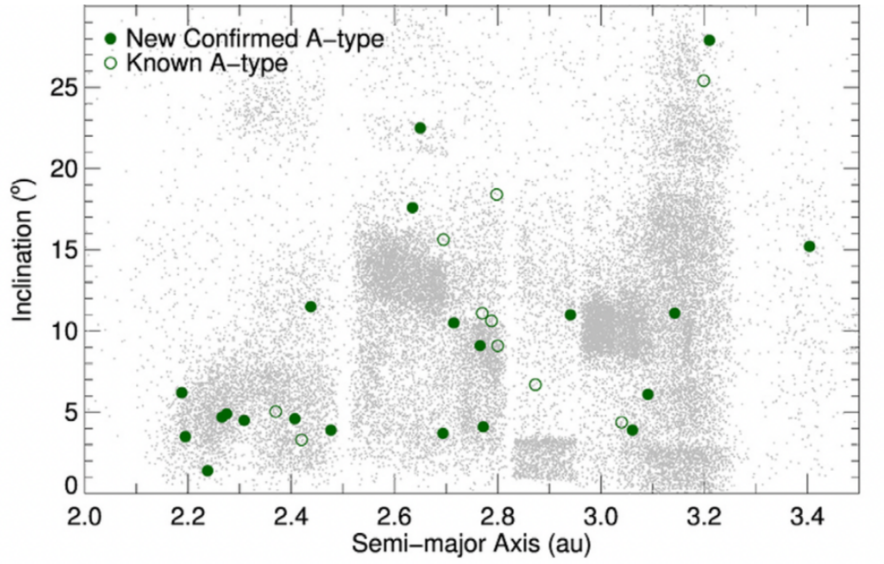

Figure 1.23: Orbital distribution of A-types in the Main Belt, from Fig.4 of DeMeo et al. (2019). Green full circles show A-types confirmed with near-infrared data in DeMeo et al. (2019), and A-types known previously from this work are plotted as empty green circles.

Years of spectroscopic, spectrophotometric and laboratory study of meteorites and asteroids therefore lead to the following questions: where is evidence of differentiation in the Main Belt? Where are olivine-rich bodies, and what happened to the first population of planetesimals?

Evidence of differentiation in the Main Belt can be searched for by linking differentiated meteorites with asteroids, and by detecting olivine-rich bodies within asteroid families. Large spectroscopic surveys allowing to characterise numerous bodies in an homogeneous way is a powerful tool to study asteroid populations.

Ground based spectroscopy allows the characterisation of asteroids, but can be limited in wavelength range by the opaque regions of the atmosphere, by atmospheric turbulence, or by weather conditions. The development and use of space telescopes insures stable conditions to characterise astronomical targets, and they can observe the sky continuously. Visible-light observations is the most ancient form of astronomy, as it covers the wavelength range detectable by the human eye, from approximately 400 to 800 nm. The first space telescope to have done observations in visible light is ESA's HIgh Precision PARallax COllecting Satellite (Hipparcos), which provided data for four years after a launch in August 1989. It measured the position, parallax and proper motion of more than 2.5 millions of stars, allowing to produce three catalogues (Perryman, 2009). The Gaia mission is its successor.

1.7 THE GAIA MISSION

Gaia is an ESA astrometric mission that was launched in December 2013, designed to primarily measure the position, the distance and the motion of stars (Gaia Collaboration et al., 2016). One of the main scientific objectives of this mission is to measure the physical characteristics of over a billion objects (stars, galaxies, asteroids...) going down to magnitude 21, to improve our knowledge of the structure, the formation and the evolution of the Milky Way (Carrasco et al., 2021). Initially scheduled to last five years, the observational phase of the mission has been extended to January 2025. The Gaia Data Release 3 (DR3), released in June 2022, published 60 518 reflectance spectra of Solar System small bodies acquired by Gaia between August 5, 2014 and May 28, 2017.

1.7.1 The Gaia satellite

Gaia is a two tons satellite placed on a orbit around the L2 Lagrange point of the Earth-Sun system, located at 1.5 million kilometres from the Earth (Crowley et al., 2016). The L2 point provides a stable orbit, and keeps the satellite away from possible perturbations from the Earth or the Moon. It is a position of choice for astronomic observations, as a spacecraft placed there is constantly in the Earth's shadow, and thus does not suffer from temperature effects that can damage it and its observations. Gaia scans the entire celestial sphere, combining slow motion around a main rotation axis, a precession axis, and the Earth's revolution around the Sun. The precession of its axis if of 63.12 days, and Gaia spins around its axis at a constant speed of 60 arcsec.sec^{-1}. It therefore completes a full rotation in six hours (Gaia Collaboration et al., 2016), scanning across every object located along a given "great circle" illustrated in Fig.1.24. The satellite scans the sky using two telescopes simultaneously, which lines of sights are separated by a basic angle of 106.5 deg, as illustrated in Fig.1.24. An object observed by the first telescope - the first Field of View (FoV) - is thus observed by the second telescope 106 minutes and 30 seconds later (second FoV) (Gaia Collaboration et al., 2016).

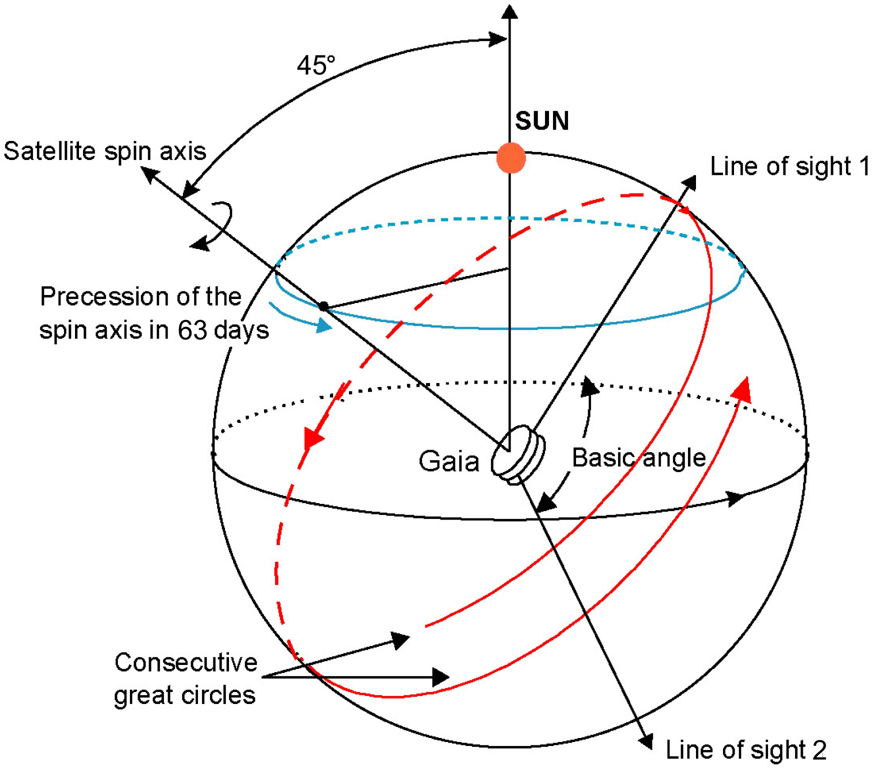

Figure 1.24: Gaia motion and scanning law at the L2 Lagrange point. Image credit: ESA.

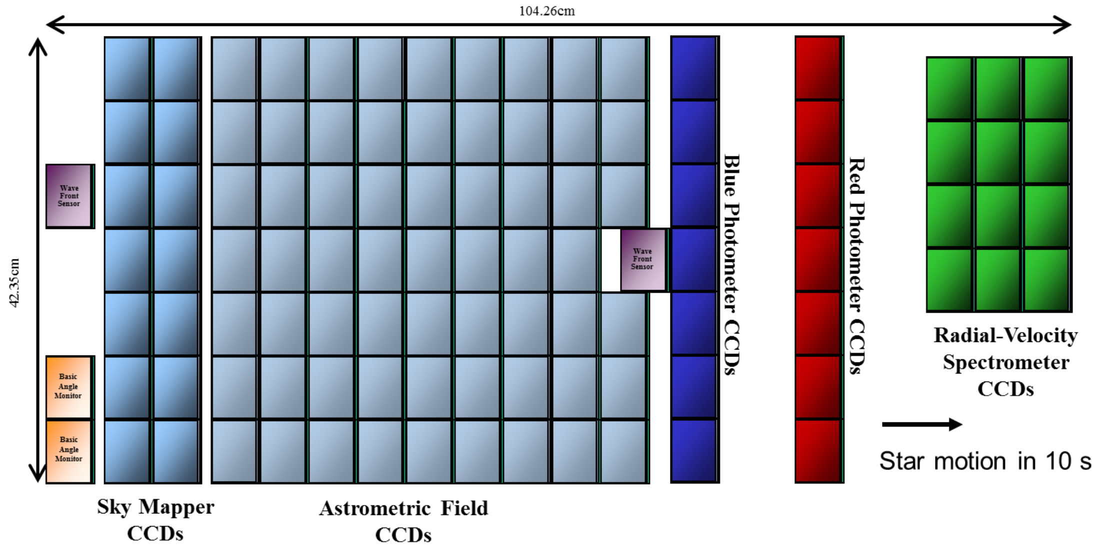

Figure 1.25: Gaia focal plane. The wave-front sensor and basic-angle monitor have for function the realignment of the telescopes in orbit, while the sky mapper (SM) is made for detecting objects entering the fields of view down to magnitude 21 and communicating to the on-board electronics. The main astrometric field (AF), the blue and red spectrophotometers (BP and RP) and the radial velocity spectrometer (RVS) are briefly described in the text. Image credit: ESA.

The two telescopes share the same focal plane illustrated in Fig.1.25, composed of 106 CCD detectors (Kohley et al., 2012; Crowley et al., 2016). Gaia has three instruments on this focal plane: an astrometric instrument, designed to measure the position and proper motion of stars and other celestial bodies (Lindegren et al., 2018); two spectrophotometers collecting the light of objects in two distinct spectral bands (Carrasco et al., 2021); and the Radial Velocity Spectrometer (RVS), a high resolution spectrometer designed to compute the radial velocity of the brightest objects (David et al., 2014; Recio-Blanco et al., 2016). Due to the rotation of the spacecraft, an observed source transits the focal plane during the observation (Gaia Collaboration et al., 2016). The direction of the transit is referred to as the along scan (AL) direction, while the perpendicular direction is designated as the across scan (AC) direction (Crowley et al., 2016). To compensate for Gaia's spinning effect, the CCDs are operated in Time Delay Integration (TDI) mode (Crowley et al., 2016). This mode consists of reading the image at a chosen rate continuously, instead of reading each time at the end of a defined time exposure. The transfer of charges inside the CCD are timed at a constant rate in the AL direction, and Gaia's rotation is constantly adjusted so that the movement of the images is simultaneous with the reading. Thanks to this procedure, the light of every object is integrated over every CCD while the object is transiting (Carrasco et al., 2021). The transit of the source on the focal plane leads it to be observed by the different instruments onboard Gaia. The first ones are the SkyMapper (SM) instruments, used to detect sources by the on-board electronics. The nine Astrometric Field (AF) CCDs then measure the source light, before it gets dispersed by two different slit-less prisms. The dispersed light is then collected by each spectrophotometer (Carrasco et al., 2021).

1.7.2 The BP and RP spectrophotometers

The instrument designed for spectrophotometry is composed of two low-resolution, slit-less spectrophotometers, the blue and red spectrophotometers (BP and RP, or more generically XP). These instruments are respectively optimised for the blue part (wavelength range from 330 to 680 nm) and the red part (from 640 to 1050 nm) of the spectrum (Jordi et al., 2010; Carrasco et al., 2016). They are each made of a slit-less prism that disperses the light in the direction of motion (AL direction) on two different sets of CCDs, corresponding to around 45 pixels. Each CCD is made of 4500 lines x 1996 columns, and only 4.42 seconds are needed for a source to cross the 4500 columns of the AL direction of a CCD, this time being the maximum exposure time for each crossing of the CCDs (Carrasco et al., 2021).

The pixels in the AC direction are binned simultaneously as they are being read, for observations fainter than G = 11.5 mag, in order to produce 1D spectra from the 2D image generated by the BP and RP spectra. The 1D spectra are composed of 60 "samples", groups of 12 pixels combined in the AC direction (Carrasco et al., 2021). However, the approximately outermost 10 samples on both sides of the window are not considered, given that these regions are characterised by a negligible instrumental response and a signal dominated by background flux and the contamination (smearing effects) of the Line Spread Function (LSF) (Carrasco et al., 2021).

For each object transiting the focal plane of the instrument, an "epoch spectrum" is acquired by the BP and RP (Gaia Collaboration et al., 2023). For each XP, only a small window of 60 × 12 pixels (3.5 arcsec × 2.1 arcsec) centred on each detected position of the source is considered by the on-board electronics, to reduce the telemetry (process of recording and transmitting the readings) of the satellite (Carrasco et al., 2021). The size of this window was selected to be wide enough to include most of the source flux after dispersion by the prisms, and to allow background flux determination (Carrasco et al., 2021).

The observed raw pixel data are internally calibrated (Carrasco et al., 2021; Montegriffo et al., 2023), and corrected from instrumental and astrophysical effects such as geometry effects, differential dispersion, variation in the LSF across the focal plane, sensitivity, and flux loss (Gaia Collaboration et al., 2023). The main product of this calibration process is a set of internally calibrated epoch spectra, corresponding to each transit of each source (Carrasco et al., 2021; Montegriffo et al., 2023). A unique identifier called a transit_id is associated to each single transit of an object (Gaia Collaboration et al., 2023).

Once the epoch spectra are internally calibrated, an internal reference scale is defined: the "pseudo-wavelength" (Carrasco et al., 2021). This scale is measured in units of sample and not in wavelength units, as it is measured in an arbitrarily chosen reference location in the focal plane. This scale allows to align the observed epoch spectra of a given source obtained from observations at different FoV, time, and locations of the focal plane (Gaia Collaboration et al., 2023). Internally calibrated epoch spectra are thus arrays of 60×1 flux values along with their uncertainty, corresponding to the 60 samples of the 1D spectra. The transformation to the physical wavelength unit is then done by external calibration (Carrasco et al., 2021).

In the case of stars and other distant bright objects, the pseudo-wavelength scale is used to produce mean spectra. In the case of Solar System Objects (SSOs), the calculation of their mean spectra is performed differently, because of their proper motion and intrinsic variability (Carrasco et al., 2021). As the CCDs are operated in TDI mode, the image formation is dispersed. Consequently, the dispersion function is defined by a relation between real wavelengths, and an offset in the data space relative to a reference point in the dispersed image. For each transit of a SSO, the use of the object's sky-plane motion predicted from its ephemerides, and of data from the astrometric field allow to determine its angular coordinates on the focal plane (field angles) as a function of time. This allows to predict the object's sky-plane motion and the location of the reference point with a high accuracy, allowing to produce mean SSO spectra (Gaia Collaboration et al., 2023).

For each transit of each object, the nominal dispersion function determined before the launch of Gaia is used to convert pseudo-wavelengths to physical wavelengths (Gaia Collaboration et al., 2023). A geometric calibration is also needed at that stage, to estimate potential shifts of the source position in the AL direction affecting the wavelength calibration. Indeed, the observed source can be imperfectly centred inside a CCD window, due to the imprecise propagation of the position of the window because of the different position of each CCD on the focal plane, and because of the slightly different focal length of each telescope (Carrasco et al., 2016). These calibrations allow the production of epoch spectra expressed in terms of physical wavelengths, in the form of 60 flux values with their associated uncertainty (Gaia Collaboration et al., 2023).

1.7.3 Gaia DR3 mean reflectance spectra

As explained in Gaia Collaboration et al. (2023), epoch reflectance spectra are calculated for each SSO epoch spectra, by dividing the flux of the epoch spectrum by the one of a reference solar analogue. The solar analogue spectrum used to produce the DR3 mean reflectance spectra is an average of 19 known solar analogue stars used for asteroid spectroscopy. For the complete list of solar analogues, refer to Table C.1 of Appendix C in Gaia Collaboration et al. (2023), knowing that the star designated as 16CygB is in fact 16CygA (Tinaut-Ruano et al., 2023). The spectra of these solar analogues are normalised by dividing them by the sum of the fluxes of the BP and RP, before calculating their average spectrum and its associated uncertainty. A mean solar analogue spectrum is calculated independently for the BP and the RP.

An epoch spectrum and a produced epoch reflectance spectrum of asteroid (90) Antiope (published as well in Gaia Collaboration et al. (2023)) is displayed in Fig.1.26, corresponding to the transit_id 50299852816031 97. This asteroid is expected to show a featureless spectrum, as it has been classified as a C-type by DeMeo et al. (2009) and as a M-type by Mahlke et al. (2022). Its Gaia DR3 epoch reflectance spectrum shown here is coherent with the literature.

For each SSO, a unique mean reflectance spectrum spanning the visible wavelength range from 374 to 1034 nm is then calculated. Only BP and RP epoch reflectance spectra in the respective wavelength ranges [325, 650] nm and [650, 1125] nm are used to generate the mean reflectance spectra. Bins 44 nm wide centred on 16 wavelength bands spanning the range from 325 to 1125 nm every 44 nm are defined to calculate the mean reflectance spectra. In each bin, the median and median absolute deviation (MAD) of the reflectance values are calculated. Then, a MAD-clipping approach is used to remove possible outliers before calculating the weighted average of the ac-

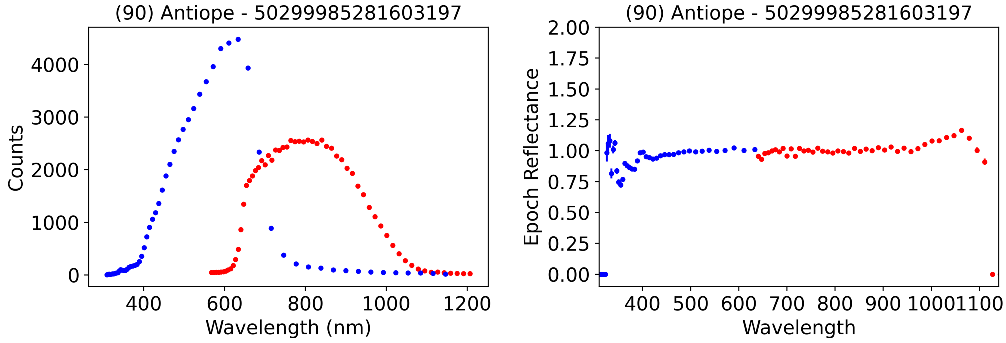

(a)

(b)

Figure 1.26: DR3 epoch spectrum and epoch reflectance spectrum of a transit of asteroid (90) Antiope.

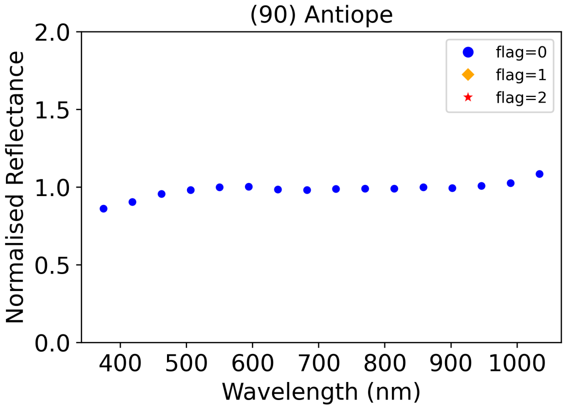

Figure 1.27: Mean reflectance spectrum of asteroid (90) Antiope published in the DR3. Every data point is flagged with a 0 digit for this spectrum.

cepted reflectance values in each bin. Finally, the obtained mean reflectance spectrum is normalised at 550 nm. As an example, the mean reflectance spectrum of (90) Antiope published in the DR3 is displayed in Fig.1.27.

For the Gaia DR3, the published mean reflectance spectra were limited to an average Signal-to-Noise Ratio (SNR) > 13 (Gaia Collaboration et al., 2023). The average SNR is calculated as

$$\mathrm{SNR} = \frac{1}{12}\sum_{i=3}^{14}\frac{\overline{R}(\lambda_i)}{\sigma_{\overline{R}(\lambda_i)}} \tag{1.2}$$

with $\overline{R}(\lambda_i)$ the weighted average of the accepted reflectance values in the i bin, and $\sigma_{\overline{R}(\lambda_i)}$ its associated calculated uncertainty. The first two and last two wavelength bands, respectively centred at 374, 418, 990, and 1034 nm, were not considered in the calculation of the SNR, as they are often affected by random systematic errors (Gaia Collaboration et al., 2023).

This filtering in SNR does not guarantee the quality of each produced mean reflectance spectrum in the DR3 (Gaia Collaboration et al., 2023). To each wavelength band was therefore associated a "spectral_validation_flag" (hereafter flag) number, assessing the estimated quality of the band. A flag value of 2 indicates that the corresponding band is of low quality, a flag=1 indicates a suspected issue, and validated bands are associated to null flag values. Several other filters were put in place, in order to clean up the catalogue from anomalous mean reflectance spectra (see Gaia Collaboration et al., 2023, for details).

Overall, the DR3 contains a majority of objects having magnitudes between 18 and 20, making it an unprecedented dataset of objects usually too faint to be observed from ground-based telescopes. Many objects have been characterised for the first time, making the DR3 a survey of choice to study asteroid families and to search for evidence of differentiation in the Main Belt.

1.8 OUTLINE OF THE THESIS

This thesis has for objectives the analysis and exploitation of the Gaia DR3 catalogue of reflectance spectra of Solar System small bodies, to search for evidence of differentiation in the Main Belt. In Chapter 2, a detailed analysis of the asteroids' epoch and mean reflectance spectra is provided. The goal was to try detecting and correcting potential issues in the spectra, to prepare for the DR4.

In Chapter 3 is presented the search for analogues of the achondrite meteorite Erg Chech 002, designated as the "oldest andesite of the Solar System" (Barrat et al., 2021) and that likely formed in the crust of a differentiated planetesimal (Barrat et al., 2021; Neumann et al., 2012; Sturtz et al., 2022). A curve matching method and a spectral parameters exploration were used to search for spectral analogues of this meteorite among the asteroids having a spectrum in the Gaia DR3, and some of the potential matches found were then characterised from spectroscopic observations in the NIR.

In Chapter 4, I present a study of the collisional asteroid family (36256) 1999 XT17, searching for a potential concentration of olivine-rich asteroids. The family members were classified and characterised from their DR3 spectra, from available literature data, and from a new observed NIR spectrum. Finally, in Chapter 5, a global study of the classification of Gaia DR3 spectra is presented. The aim of this study was to classify asteroids from their DR3 spectra, both to prepare for the DR4 that is planned to contain a Gaia classification scheme, and to study the Main Belt as a whole, taking advantage of the large homogeneous DR3 dataset. In particular, the classification method has been optimised to detect A-type asteroids, to search for potential new olivine-rich bodies in the Main Belt and to try detecting differentiated asteroid families.

2

GAIA DR3 BP-RP SPECTRA

In June 2022, the mean reflectance spectra of 60 518 Solar System objects were published as part of the Gaia DR3 (Gaia Collaboration et al., 2023) after ~34 months of observations. To each Solar System Object (SSO) was associated a single mean reflectance spectrum, obtained from the averaging of several epoch reflectance spectra acquired by the blue and red photometers (Blue spectroPhotometer (BP) and Red spectroPhotometer (RP)) each time the object was transiting Gaia's focal plane. The data production is presented in Chapter 1.

This data release was orchestrated by the Data Production and Analysis Consortium (DPAC). The DPAC is a European consortium made of an international community of over 400 scientists and software engineers, responsible for collecting, analysing, treating, validating, producing and releasing the Gaia data (see `https://www.cosmos.esa.int/web/gaia/dpac/consortium` for details). Indeed, the observations and scientific measurements made by the various instruments of Gaia are sent to Earth in a continuous stream of data, that need to go through complex data analysis and calibration processes to be scientifically exploitable. The DPAC is in charge of the processing of data, the testing and implementation of algorithms, and the verification of the science products before making it available to the community.

As a member of the DPAC, I devoted part of my thesis time to analysing the mean reflectance spectra of SSOs in order to identify and try to resolve potential issues. This work aims to prepare for the Gaia Data Release 4 (DR4), that should be released in 2026 and will account for 66 months of observations.

In this chapter I present an analysis of potential issues identified in the mean reflectance spectra of SSOs. In section 2.1, issues identified by various authors (Hasegawa et al., 2022; Tinaut-Ruano et al., 2023; Galinier et al., 2023; Bourdelle de Micas, 2022) on the DR3 spectra of SSOs are presented. In section 2.2, the asteroids' epoch reflectance spectra used to produce the DR3 mean reflectance spectra are analysed, allowing to identify and propose solutions to issues that could potentially affect the quality of the spectra. A specific reddening issue is extensively studied in 2.3, and the impact of the choice of solar analogue and of the filtering method used to produce the DR3 dataset are presented in sections 2.4 and 2.5, respectively. Finally, the improvements of the spectra for the DR4 that can be achieved using filtering procedures we propose are presented, and we conclude that, despite identified potential issues, the homogeneous DR3 dataset remains a unique opportunity to study the Main Belt as a whole.

2.1 IDENTIFIED ISSUES OF ASTEROIDS MEAN REFLECTANCE SPECTRA

2.1.1 BP-RP epoch reflectance spectra mismatch

During the production of Gaia DR3 mean reflectance spectra, Gaia Collaboration et al. (2023) identified some cases of badly aligned BP and RP epoch reflectance spectra. Such case is shown in their Fig.6, with the epoch reflectance spectra of asteroid (61) Danae displayed here Fig.2.1. Asteroid (61) Danae shows some RP epoch reflectance spectra badly aligned to the BP epoch spectra, having reflectance values too high or too low. As such mismatch can degrade the production of mean reflectance spectra, filters described in Gaia Collaboration et al. (2023) have been put in place. For most asteroids, these filters were found efficient at producing good spectra. This can be seen with the good quality mean reflectance spectrum of (61) Danae, over-plotted on the epoch reflectance spectra in Fig.2.1. We examined the mismatch issue here in an effort to improve the spectra for which the issue is too significant for the filters to be efficient, to prepare for the DR4.

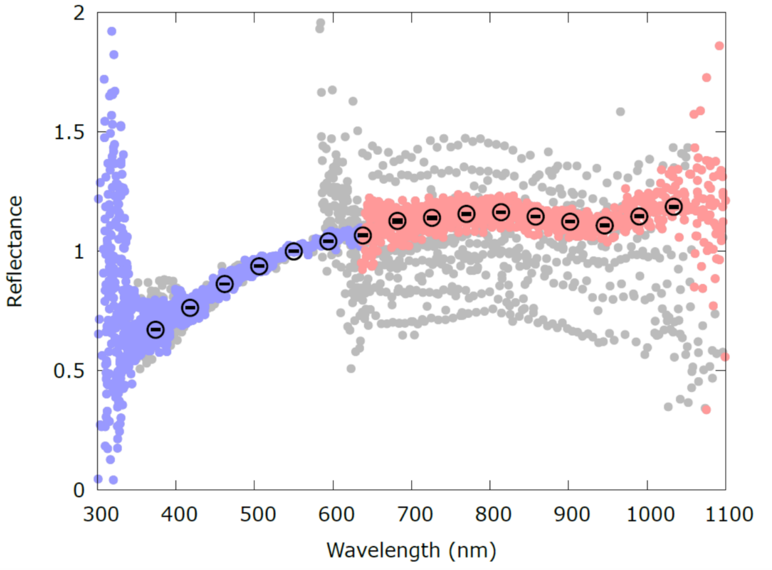

Figure 2.1: Figure extracted from Gaia Collaboration et al. (2023), showing the epoch reflectance spectra of asteroid (61) Danae. The grey points are epoch reflectance values filtered out by the σ-clipping procedure, and the accepted values are coloured in light blue for the BP and light red for the RP. The large empty circles correspond to the 16 data bands chosen to produce the mean reflectance spectra of the DR3.

2.1.2 "Fake band" around 650 nm

Another issue identified by Gaia Collaboration et al. (2023) is the potential presence of a "fake band" around 650 nm for some of the brightest asteroids. An example of such drop in reflectance around 650 nm is displayed in Fig.2.2, with the DR3 mean reflectance spectrum of asteroid (4) Vesta, compared to Vesta's spectrum from Xu et al.

(1995). This issue has to be understood, as this band could be wrongly interpreted as a feature characteristic of the surface mineralogy of asteroids.

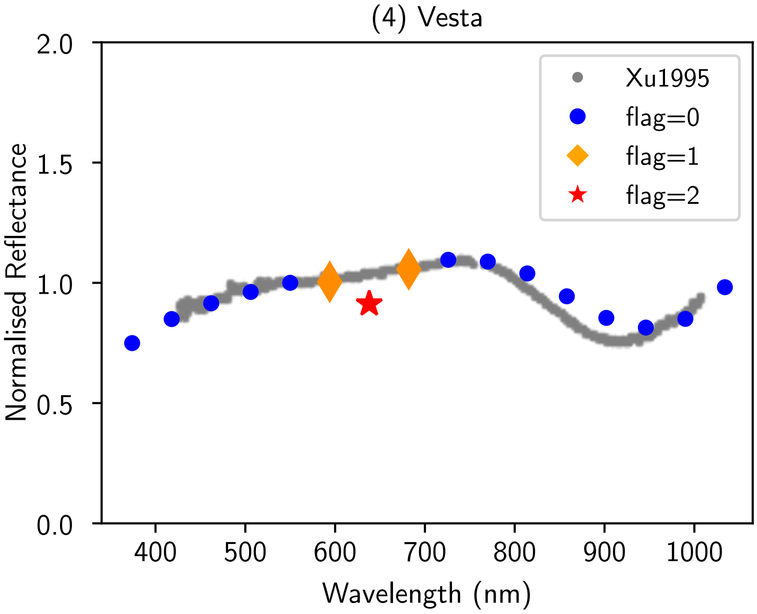

Figure 2.2: Normalised reflectance spectra of asteroid (4) Vesta from the DR3, compared with the spectrum of Xu et al. (1995). The 16 data bands of the Gaia DR3 spectrum are given a colour and a symbol according to the value of the flag associated to the band: blue circle if flag=0, orange diamond if flag=1 and red star if flag=2. The literature spectrum is displayed as grey dots.

2.1.3 Solar analogue and near-UV

Tinaut-Ruano et al. (2023) identified an issue related to the choice of solar analogue stars in the production of the reflectance spectra. They compared the mean DR3 solar analogue with two well-studied solar analogues, Hyades 64 (HD 28099) and 16 Cyg B (HD 186427), found to show a spectrum similar to the solar spectrum in the 360 to 550 nm wavelength range (Tatsumi et al., 2022). Tinaut-Ruano et al. (2023) found that the mean solar analogue used in the production of Gaia DR3 spectra induces a change of slope in the near-UV for most asteroid spectra. They suggest to apply correction factors to the near-UV wavelengths bands of the published Gaia DR3 spectra, to compensate this change of slope.

2.1.4 "RP reddening"

A systematic deviation of the reflectance in the last wavelength bands of some DR3 spectra has been identified as well (for example by Anti Penttilä, DPAC communication). This issue has been investigated in the Master thesis of R. Balossi (1). These deviations have been found to increase with the wavelength, and to be independent from the magnitude and from other physical parameters of the asteroids. However, this reddening effect seems to vary with the object's taxonomic type. R. Balossi compared

---

[1] https://hdl.handle.net/20.500.12608/51823

Gaia DR3 spectra to literature spectra classified in the Mahlke et al. (2022) taxonomic scheme, and found that objects classified as A-, S-, K- or L-types deviate more from the literature spectra than objects classified as C-, Ch-, M- or P-. It thus seems that non-featureless and featureless spectra are not affected the same way by this reddening issue. An exception was found with V-type asteroids, that appear to deviate more from literature spectra around 900 nm, as noticeable in Fig.2.2 with the spectrum (4) Vesta. The band centre of its DR3 spectrum is slightly shifted towards longer wavelengths compared to the spectrum from Xu et al. (1995), and its band depth appears slightly reduced. This band shift effect will not be studied in the following.

2.1.5 Comparison with the SDSS

In Galinier et al. (2023), we did a comparison of the spectral parameters of Gaia and the Sloan Digital Sky Survey (SDSS) asteroid spectrophotometric data, to investigate potential differences between these datasets. The measured parameters are the slope of the reflectance spectrum between 468.6 and 748 nm, and a measure of the depth of the silicate band centred around 950 nm. DeMeo and Carry (2013) used the z-i parameter to characterise asteroids from SDSS data. To do so, the SDSS observed magnitudes of asteroids were converted into reflectance values at the centre of each SDSS filter, and the $z-i$ parameter was defined as $z-i = R(\lambda = 893.2 \text{ nm}) - R(\lambda = 748.0 \text{ nm})$.

To compare Gaia with the SDSS, we evaluated the gri-slope and the $z-i$ parameter for every object contained in both datasets in Galinier et al. (2023). No selection criteria was applied to filter out noisy SDSS data or low SNR Gaia DR3 spectra. For SDSS data, the spectral slope was computed by linearly fitting the three SDSS equivalent reflectance data points in the g, r and i SDSS filters using a one-degree polynomial fit (numpy polynomial.polyfit). For the Gaia data, each Gaia DR3 spectrum was interpolated using a cubic smoothing spline (python package *csaps*, default smoothing parameter) and re-sampled between 450 and 900 nm. For this procedure, only Gaia bands with a flag equal to zero (good quality bands) were considered, and the first and last Gaia bands were not taken into account to limit the impact of low quality bands on the calculated reflectance values. The re-sampled Gaia spectra were then normalised at 468.6 nm, and the spectral gri-slope was computed by linearly fitting the spectrum between 468.6 and 748.0 nm (first-degree polynomial fit, numpy package *polyfit*).

Then, an equivalent of the $z-i$ parameter was calculated for Gaia: the $R_z - R_i$ parameter. It was computed by taking the value of the reflectance of every re-sampled normalised spectra at the central wavelength of the i′ and z′ SDSS filters, namely 748.0 nm and 893.2 nm:

$$R_z - R_i = R(\lambda = 893.2 \text{ nm}) - R(\lambda = 748.0 \text{ nm}). \tag{2.1}$$

It distinguishes from the $z-i$ parameter, as the $R_z - R_i$ parameter was not calculated after an integration of the reflectance spectra into the SDSS filters.

We observed a general agreement in gri-slope between the two surveys, as displayed in Fig. 2.3. The difference between the median slope of both surveys is of only 0.52. This slight difference can be due to the fact that no data filtering has been applied here, and slope values calculated on noisier data may increase the dispersion.

After Galinier et al. (2023) was published, we realised that integrating Gaia reflectance spectra in the SDSS filters was needed to compare the DR3 with the SDSS.

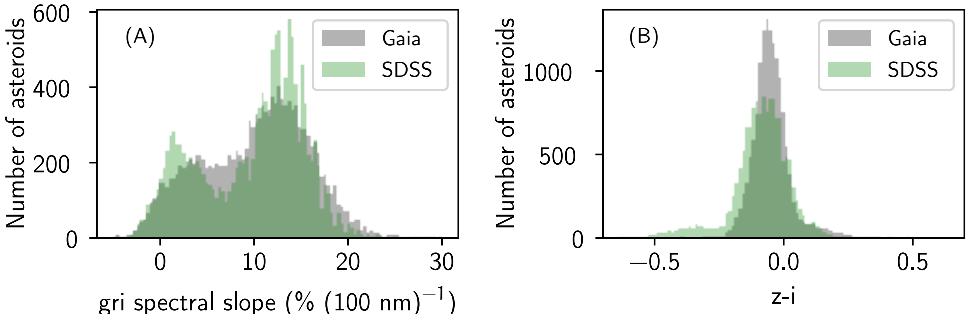

Figure 2.3: Comparison of the gri slope and $z-i$ parameter for the sub-sample of 14 129 asteroids observed both by Gaia and SDSS.

Therefore, the Gaia reflectance spectra of the 14 129 asteroids observed both by Gaia and the SDSS were converted into SDSS colours. This was achieved by integrating the spectra in the SDSS z and i filters using the python tool a Spectral Kit for Asteroids (ska), that allows to convert spectra in chosen photometric systems. Then, the $z-i$ parameter was calculated for these objects.

In Fig.2.3 is presented the $z-i$ parameter histogram for both datasets. To evaluate the value of the small shift in $z-i$ observed between the SDSS and Gaia, the median $z-i$ value was calculated for both datasets, and their difference was found to be of 0.025. It is a reasonable difference, solving the shift in $z-i$ issue identified in Galinier et al. (2023). The small shift still observed between the two datasets can potentially be explained by the use of different solar analogues between the two surveys, as solar colours are needed to convert colour indices to reflectances for the SDSS.

2.1.6 Comparison with SMASS

Finally, studying the spectra of asteroids classified S-types with VISNIR spectroscopy, I noticed that some S-type asteroids show DR3 mean reflectance spectra with slightly higher reflectance values than their SMASS spectra, in the RP part. Such discrepancy is visible for asteroid (25) Phocaea for example, displayed in Fig.2.4. The BP part of the DR3 spectrum of (25) Phocaea is in great accordance with SMASS, while its RP part shows higher reflectance values.

I studied this reddening effect more thoroughly, by comparing Gaia DR3 SSO spectra, to spectra acquired by the SMASS and classified by Bus and Binzel (2002a). Prior to doing any analysis, I filtered out asteroids having a Gaia DR3 spectrum with an average SNR$\leqslant$30 (arbitrary choice), to ensure the analysis on relatively high SNR asteroids. I also deleted asteroids having flagged bands outside of the first two and last two wavelength bands, that I did not take into account for this study. This filtering procedure gave 18 739 spectra, hence 31% of the DR3 dataset. I studied the observed RP reddening effect on a sample of 1187 asteroids observed both by SMASS and contained in the filtered Gaia DR3 dataset.

To do so, I calculated a "global slope" (between 462 and 946 nm) and a "BP slope" (between 462 and 726 nm) on each asteroid spectrum, calculating the slope with a linear regression (scipy function *stats.linregress*). Histograms representing the global slope and the BP slope for the Gaia and the SMASS datasets is displayed in Fig.2.5. We can observe on panel (A) that the global slope is shifted towards higher values for

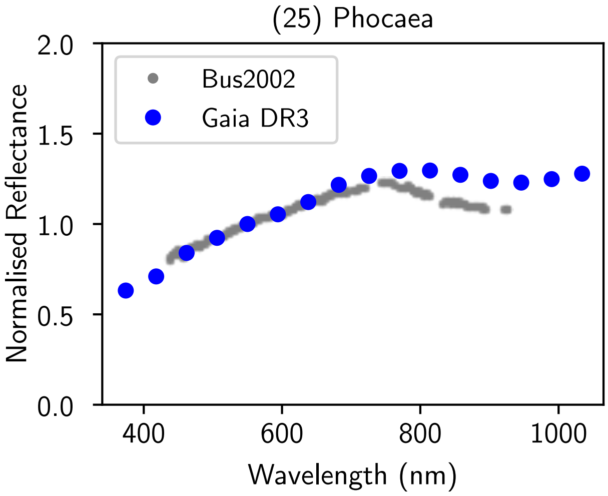

Figure 2.4: Normalised reflectance spectrum of asteroid (25) Phocaea from the DR3 (blue dots), and from Bus and Binzel (2002b) (grey). Every band of this DR3 spectrum is associated to a null flag.

the Gaia DR3 compared to SMASS, when no clear shift is visible for the BP slope on panel (B). This shows that the BP part of Gaia spectra is not affected by the reddening affecting the RP part, as observed for asteroid (25) Phocaea. Whether the BP part of the spectra is affected by another phenomenon when the RP part is highly reddened is left to investigation.

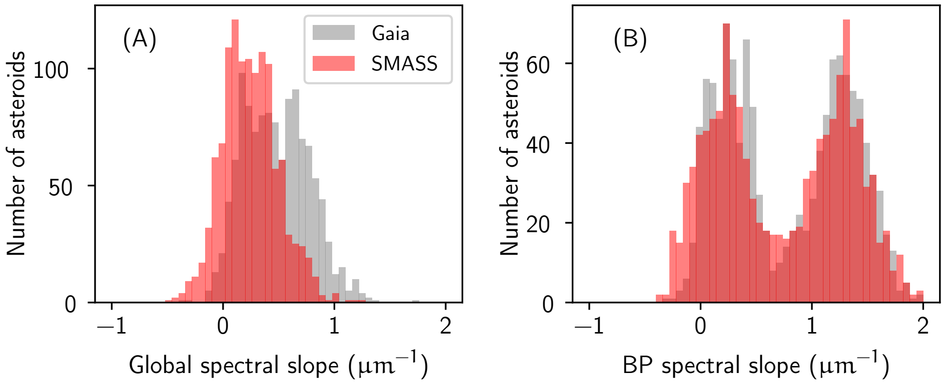

Figure 2.5: Histogram of the global slope (calculated between 462 and 946 nm) and the BP slope (calculated between 462 and 726 nm) for the 1187 asteroids both included in a filtered Gaia DR3 dataset and in SMASS. The Gaia DR3 data are represented in red colors, and the SMASS data in blue.

It can be noted that this phenomenon of high RP reflectance does not necessarily come from an issue in the Gaia DR3 spectra, but might come from geometrical differences in the observation of asteroids between ground-based SMASS and space-acquired Gaia spectra. Gaia observes asteroids at phase angles around 20 degrees (Gaia Collaboration et al., 2023), while SMASS contains observations at various phase angles (Bus and Binzel, 2002b), with asteroids mostly observed at opposition (with a phase angle $\leqslant$20 degrees). Phase reddening is a known geometric effect described in section 1.3.4, that could explain the slope difference between Gaia and SMASS (Fornasier et al., 2020).

In the following, the epoch reflectance spectra that were used to produce the Gaia DR3 mean reflectance spectra are being analysed. In most cases, the published DR3 spectra are in agreement with literature spectra (Gaia Collaboration et al., 2023). Even if discrepancies have been observed with the SMASS survey for example (Anti Pentillä, DPAC communication), these differences can be expected between a ground-based and a space survey, and they are not necessarily due to an issue in the DR3 dataset. The epoch reflectance spectra analysis presented in the following has been conducted to identify any potential issue in the raw data, to search for their cause, and to propose solutions to improve the production of mean reflectance spectra for the DR4. Most of the issues identified here, however, have relatively little impact on the mean reflectance spectra published in the DR3, thanks to the filtering procedure used to produce the spectra.

2.2 EPOCH REFLECTANCE SPECTRA ANALYSIS

To study all these identified issues and to look for potential others, I looked into the dataset of epoch spectra and epoch reflectance spectra used to produce the DR3 mean reflectance spectra. This dataset of 60 518 mean reflectance spectra corresponds to a total of 1 441 520 transits.

To study the potential issues in the DR3 dataset, a sample of bright asteroids were selected, and their DR3 epoch reflectance spectra were visually inspected. Only bright asteroids were studied, as these objects have the highest SNR spectra. In order to have a representation of several asteroid type in this study, I used the spectral taxonomic class prototypes of the Mahlke taxonomy, listed in Mahlke et al. (2022). These prototypes have all been classified from VISNIR spectroscopy, taking their albedo into account. Choosing this taxonomic scheme was arbitrary, and the prototypes of the Bus-DeMeo taxonomy would also have been adapted for this study. However, choosing the Mahlke taxonomy allowed to study asteroids covering a wide range of albedos.

Considering only the objects with a MPC number lower than 1500 among these prototypes, a list of 37 objects was obtained. These asteroids and their taxonomy in the Mahlke scheme are given in Table A.1 in Appendix A, along with their average SNR in the DR3 dataset. Every class of the Mahlke et al. (2022) taxonomy is represented in this sample, except for the O and Q-types, containing objects with MPC numbers outside of my selection. However, the number of identified O-types being of 1 and the Q-types not being abundant among Main Belt objects, the amount of classes represented by this list was considered enough to study Gaia DR3 issues.

I completed my sample with asteroids belonging to the S-complex. These objects were originally studied in the context of a project that was not developed, which aim was to train a random forest algorithm to automatically identify issues in the Gaia DR3 epoch reflectance spectra. To test this algorithm, I started with analysing by eye the epoch reflectance spectra of S-complex asteroids, since they are numerous in the Main Belt. The objects were randomly selected among S-complex asteroids from the literature having a MPC number lower than 1500, and well distributed across the main belt. The list 33 S-types considered are displayed in Table.A.2 in Appendix A, along with the method of determination of their spectral type and the associated reference.

I tried to train the random forest algorithm to recognize S-complex epoch reflectance spectra that showed a mismatch between their BP and RP parts. To do so, I visually analysed the 684 epoch reflectance spectra of the 33 S-types, flagging every spectrum showing a mismatch. However, this training set was too small to be representative of all the S-complex spectra, and the differences in SNR and shapes between the spectra made the results of this automatic procedure not satisfying. This machine learning project was therefore abandoned. However, I decided to include the already visually analysed 684 epoch reflectance spectra of S-type asteroids to the sample of Mahlke's taxonomy prototypes, to increase the number of transits considered in the study of DR3 issues.

In total, 1513 epoch reflectance spectra of 70 asteroids were visually analysed. A flag digit associated to every identified issue was associated to the transit_id of each analysed epoch spectrum. The flags associated to each issue identified by visual analysis are the following:

- 0: good spectrum
- 1: RP mismatch with BP
- 2: "wiggly BP" effect
- 4: "fake band" around 650 nm
- 8: "RP reddening"
- 16: "bad red slope"
- 32: problematic points, or high frequency spectral variations

When several problems were identified on a single epoch reflectance spectrum, the flags number were summed up. An example of issues identified on different epoch reflectance spectra is shown in Fig.2.6. On this figure, the displayed spectrum of asteroid (2) Pallas (panel A) shows a mismatch between its BP and RP spectra, and a high rise of the reflectance after 900 nm. The spectrum of asteroid (24) Themis (panel B) shows a sinusoidal increase and decrease of the reflectance in its BP part, the so-called "wiggly BP" effect. Asteroid (1) Ceres' spectrum (panel C) shows a drop in the reflectance around 650 nm designated as a "fake band", a high red rise on the RP part after 900 nm, and a strong peak around 400 nm. This peak is not associated to any flag number, but its presence was acknowledged and studied. The spectrum of asteroid (234) Barbara (panel D) shows an unexpected shape of its RP spectrum (designated as "bad red slope"), and a slight BP - RP misalignment. The spectrum of asteroid (588) Achilles (panel E) is affected by high frequency variations around 550 nm. This wavelength being the normalisation wavelength, this leads to a misalignment of this epoch reflectance spectrum with the others. Finally, asteroid (153) Hilda (panel F) shows problematic points in its RP part, between 800 and 1000 nm.

In the list of 1513 analysed transits, 804 were flagged by a 0 digit, corresponding to 53% of spectra with no identified potential issue. The first issue discussed in the following is the mismatch between the BP and RP epoch reflectance spectra, illustrated in Fig.2.6 panel A. Among the analysed transits, 1316 were flagged by an even digit, meaning that 87% of spectra in this sample are well aligned. As mentioned above, these issues were studied to improve the production of mean reflectance spectra for the DR4, but their presence did not necessarily impact the mean reflectance spectra published in the DR3.

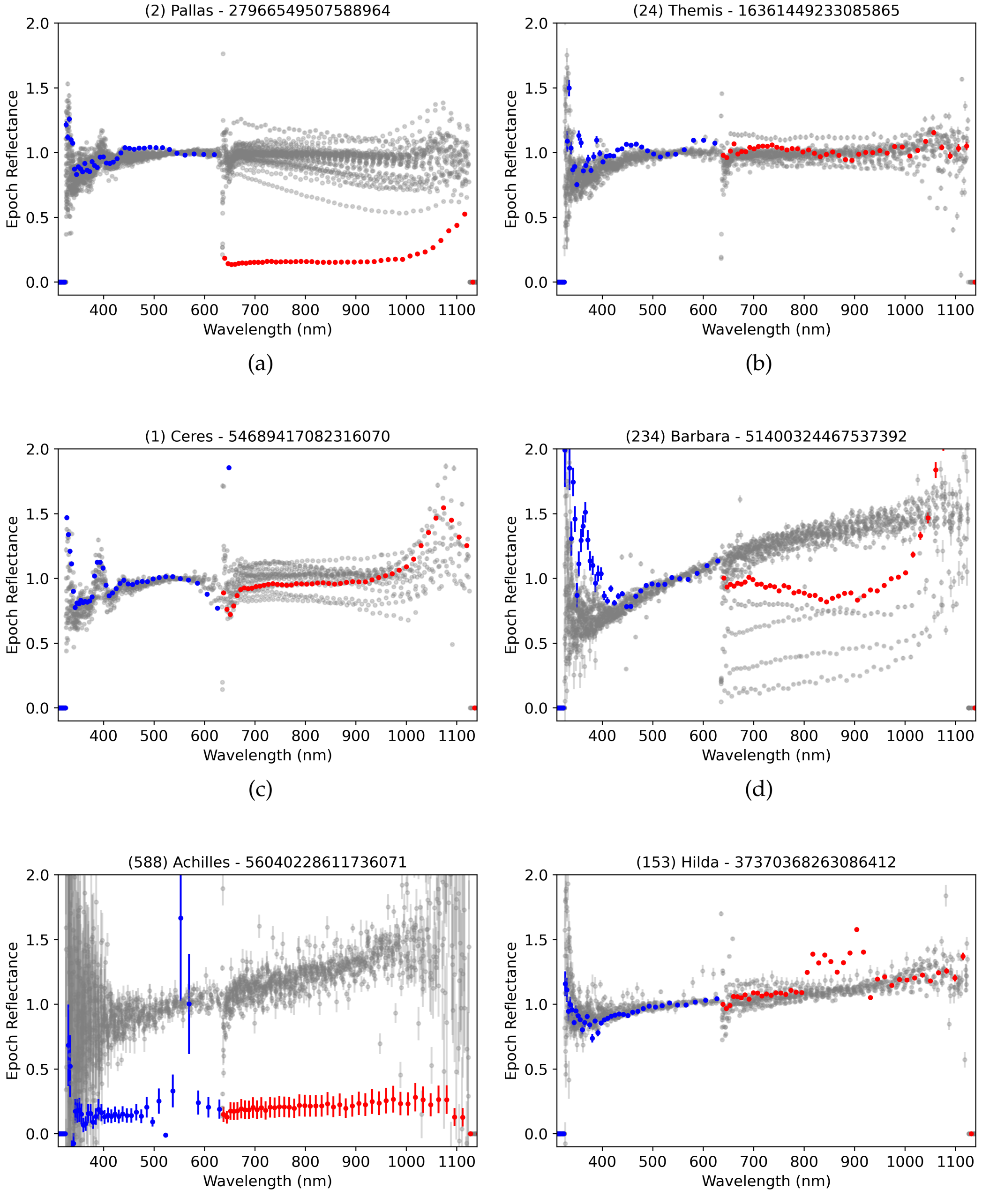

(a) (b)

(c) (d)

(e) (f)

Figure 2.6: Example of normalised epoch reflectance spectra showing flagged issues. In grey dots are displayed every epoch reflectance spectra of a given object, and the BP and RP analysed epoch reflectance spectra are plotted as blue and red dots respectively. Each highlighted epoch spectrum is associated to a transit_id and corresponds to a given asteroid, which number and name are given in the title of each figure.

2.2.1 Analysis of the BP-RP epoch reflectance spectra mismatch

As explained in Chapter 1, BP and RP epoch spectra are acquired independently. Full epoch reflectance spectra are produced by aligning the epoch reflectance spectra thanks to the overlap between the wavelength range covered by both photometers. When a source that has a non-negligible proper motion transits on the focal plane of Gaia, going from the BP to the RP CCDs (see Fig.1.25), a loss of light flux may occur between the two instruments. On the focal plane of Gaia, this motion can be translated along the AL and AC directions and is associated to along-scan and across scan velocities $\frac{\mathrm{dal}}{\mathrm{dt}}$ and $\frac{\mathrm{dac}}{\mathrm{dt}}$.

We studied the effect of the across and along scan velocities of an object on the matching of the BP and RP parts of its epoch reflectance spectra. To do so, we first plotted the epoch reflectance spectra of the 37 asteroids of our list, colour-coding each epoch spectrum with the absolute value of its along scan and across scan velocities. An example of such plot is displayed in Fig.2.7 for asteroid (13) Egeria. It can be noticed in the left panel that the across scan velocity, the BP-RP matching and the quality of the RP spectra appear correlated: well matched spectra correspond to lower values of the absolute across scan velocity, and the BP and RP spectra start getting mismatched as the across-scan velocity increases. Such correlation is not observed for the along scan velocity, as seen in panel (B).

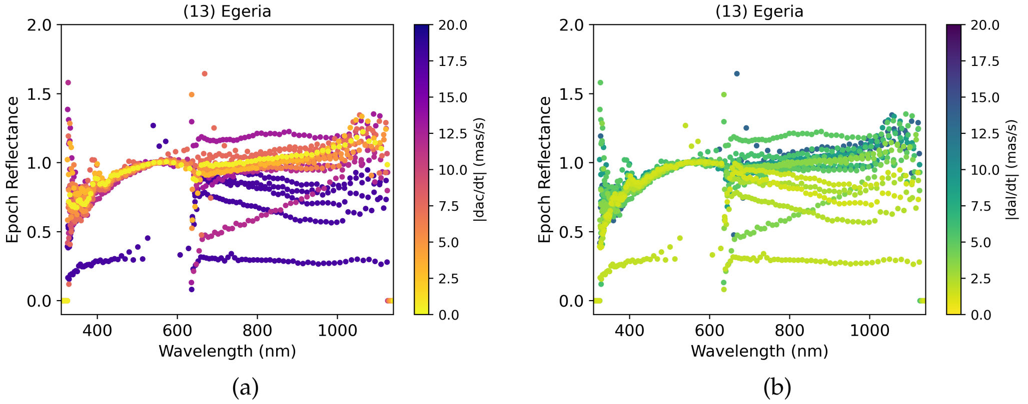

(a) (b)

Figure 2.7: Every epoch reflectance spectra of asteroid (13) Egeria, colour-coded with the absolute value of the across scan velocity (left panel) and along scan velocity (right panel). the error bars are not represented here.

We used the flags assigned to the transits to study the effect of the across scan velocity on the matching of the BP and RP epoch reflectance spectra. We calculated the proportion of aligned spectra (even flag) and badly aligned spectra (odd flag) at each speed range, binning the speed values with bin widths of $1\ \mathrm{mas} \times \mathrm{s}^{-1}$.

In Fig.2.8 is plotted the fraction of aligned and badly aligned spectra with respect to the across scan velocity. It is clear that the higher the across scan velocity of the source, the least aligned the BP and RP spectra are. We observed that when the across scan velocity gets higher than about $14\ \mathrm{mas} \times \mathrm{s}^{-1}$, the proportion of badly matched spectra becomes higher than the proportion of well-matched. Thus, filtering out transits associated with an absolute value of the across scan velocity higher than $10\ \mathrm{mas} \times \mathrm{s}^{-1}$ would allow to keep around 70% of the good transits.

Moreover, this effect appears to affect not only the matching between the BP and RP spectra, but also the shape of the epoch reflectance spectra, as can be seen on Fig.2.7 with the epoch reflectance spectra of (13) Egeria acquired at high across scan velocity (close to 20 $mas \times s^{-1}$). Such spectra were flagged for showing a "bad red slope", that is a slope in the RP part different from the one of the literature, or the one of good transits. Hence, filtering out transits with a $|\frac{dac}{dt}| > 10\ mas \times s^{-1}$ would help solving this issue as well.

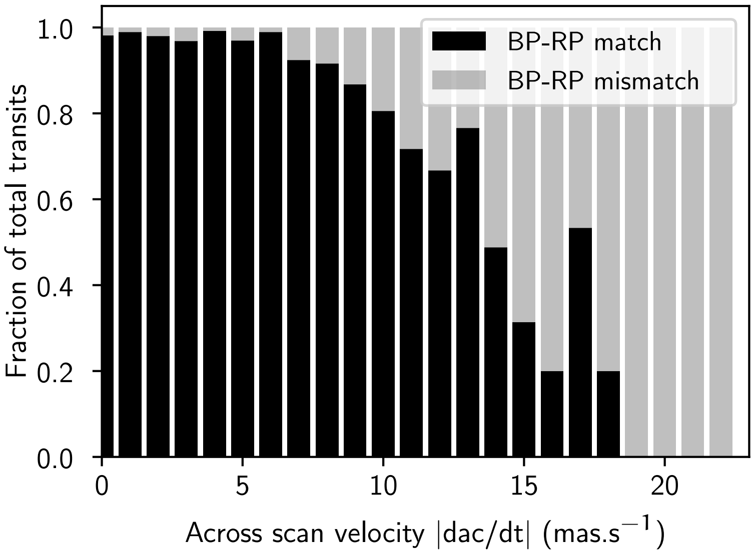

Figure 2.8: Proportion of matched (black) and mismatched (grey) BP-RP epoch reflectance spectra with respect to the absolute value of the across scan velocity.

Among the 1 441 520 transits corresponding to the 60 518 asteroids of the DR3, 929 061 transits remain after filtering out transits with $|\frac{dac}{dt}| > 10\ mas \times s^{-1}$. This corresponds to a total of 60 481 asteroids. Performing this filtering thus allows to remove badly aligned spectra while keeping most of the asteroids published in the DR3. This shows that most mean reflectance spectra published in the DR3 are not significantly affected by this BP-RP mismatch phenomenon. Published spectra found to be highly affected by it are mostly low SNR spectra, such as those of the two asteroids shown in Fig.2.9. Asteroid (40244) 1998 WP4 (left panel) shows an average SNR of 21.72 in the DR3, and its mean reflectance spectrum was produced on 10 transits all acquired at $|\frac{dac}{dt}| > 11.41\ mas \times s^{-1}$. The average SNR of asteroid (42531) McKenna (right panel) is 20.41, and its spectrum was produced on 7 epoch spectra acquired at $|\frac{dac}{dt}| > 10.86\ mas \times s^{-1}$. These two objects are removed by the filtering criterion on the across-scan velocity.

2.2.2 "Wiggly BP"

We then investigated the BP epoch reflectance showing increases and decreases in a sinusoidal pattern, designated as "wiggly BP". This effect appears to be present on most spectra with a transit_id lower than 19×10^{15}. These transit_ids correspond to observations made at the beginning of the Gaia mission, before the first decontamination operation that took place on September 23, 2014. Indeed, Gaia's optics suffered from a continuous contamination by water ice from water vapour degassed after launch, low-

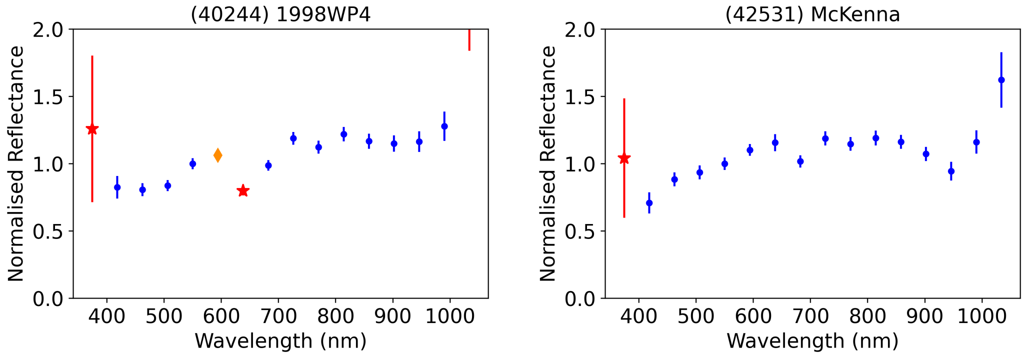

(a)

(b)

Figure 2.9: DR3 mean reflectance spectra of asteroids (40244) 1998 WP4 and (42531) McKenna, that get filtered out because of the high across scan velocity values at which were acquired their respective epoch spectra. The 16 data bands of the Gaia DR3 spectrum are given a colour and a symbol according to the value of the flag associated to the band: blue circle if flag=0, orange diamond if flag=1 and red star if flag=2. The colours and symbols of the DR3 spectra data bands will respect this same convention in the following.

ering the quantity of light received by the optics (Gaia Collaboration et al., 2016). This time-variable transmission degradation is wavelength-dependent, and more important at short wavelength. This could explain why the "wiggly" effect is more apparent on BP than on RP spectra.

To get rid off this problem and to restore the quality of the observations, a payload decontamination was performed in the beginning of the Gaia mission, by heating Gaia's focal plane and selected telescope mirrors to sublimate the water ice (Gaia Collaboration et al., 2016). Therefore, filtering out the transits acquired before this first decontamination phase (hence keeping only transits having a transit_id above 19×10^{15}) removes spectra affected by the "wiggly BP" issue, increasing the quality of the mean reflectance spectra produced.

After filtering out epoch spectra having $|\frac{\mathrm{dac}}{\mathrm{dt}}| > 10\ \mathrm{mas} \times \mathrm{s}^{-1}$ and those acquired before the first decontamination phase, 898 500 transits remain, corresponding to 60 462 asteroids. Few objects had thus a mean spectra produced from epoch reflectance spectra highly affected by these issues. Moreover, a limit of three transits was defined in order to produce the mean reflectance spectrum of an object in the DR3 (see Chapter 1). Adding this supplementary filtering step, a total of 60 233 asteroids spectra is produced.

2.2.3 High frequency variations

The high frequency variations observed in some epoch reflectance spectra did not appear correlated to any parameter we tested. This issue is also visible on the epoch spectra of objects (see Fig.2.10), if the object has a good enough SNR. The strong flux measured and its randomness in the data can be interpreted as the effect of cosmic rays (according to communications with Dafydd Evans and Francesca de Angeli), and the affected transits should be filtered out. Actually, the MAD-clipping procedure defined for the production of the DR3 spectra (see Chapter 1) is efficient in filtering out these damaged spectra, so this issue likely does not affect the published DR3 mean reflectance spectra.

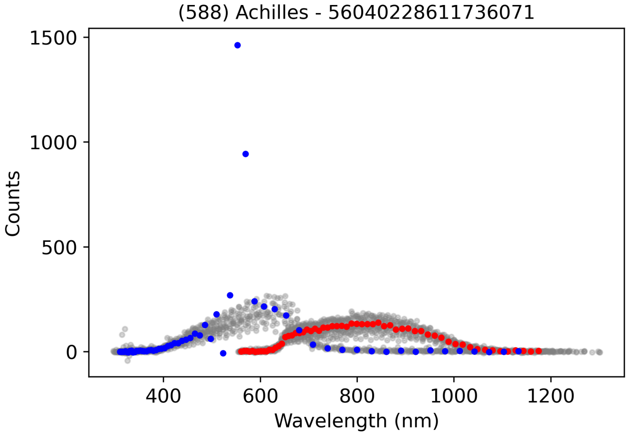

Figure 2.10: BP (blue) and RP (red) epoch spectrum of asteroid (588) Achilles, on which the effect of a cosmic ray is visible in the BP part.

2.2.4 Analysis of the "RP reddening"

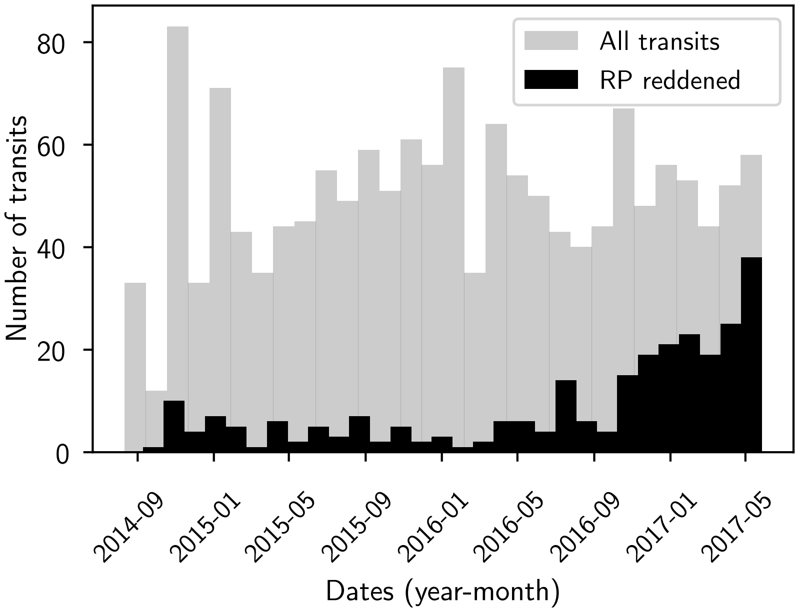

Figure 2.11: Histogram of the transits showing a RP reddening phenomenon (black colour) compared to all analysed transits (grey colour), with respect to the date at which the spectra were acquired. 266 transits were flagged as affected by a RP reddening.

The "RP reddening" issue is characterised by an increase of the reflectance longward 900 nm. It affects mostly the last two wavelength bands of the DR3 mean reflectance spectra, but understanding this effect would allow to correct the spectra from it for the DR4. It is often accompanied by a drop of the reflectance around 650 nm (a "fake band"), and by a peak around 400 nm. This correlation is visible on the epoch spectrum of asteroid (1) Ceres displayed in panel C of Fig.2.6. Brighter asteroids appear to be more evidently affected by these issues.

In the following, the reddening of the RP spectrum is the main focus of the study, not considering whether or not it is accompanied by a peak around 400 nm or a fake band. On the histogram of Fig.2.11 is shown the number of transits with respect to the date at which the epoch spectra were taken, for the 1513 transits visually analysed. The dark area on the histogram corresponds to the 266 epoch spectra on which was identified a RP reddening. This effect seems to appear at the end 2016, and to be increasing with time.

2.3 "RP REDDENING" ANALYSIS: C-, X-, AND S-COMPLEX STUDY

In order to see if this reddening phenomenon affects the same way the epoch spectra of every taxonomic type, we studied asteroids spectra assigned to the three main asteroid taxonomic complexes defined in the Bus-DeMeo taxonomy: the C-, X-, and S-complex. This taxonomic scheme was chosen because it covers the NIR wavelength range, and it contains the X spectroscopic complex that represents the third biggest population of asteroids in the Main Belt. The other taxonomic types were not considered in this study, because of the low number of objects they represented.

For this study, we selected a new sample of 210 asteroids with a MPC lower than 1500, having a DR3 spectrum, and being classified in DeMeo et al. (2009) or in DeMeo et al. (2019) from NIR spectroscopy. This choice was made in order to study the reddening effect on bright asteroids characterised in the literature. The studied samples for the S, C and X-complexes respectively contain 93, 43 and 28 objects. This corresponds to a respective total of 1409, 709 and 415 transits, after filtering out the epoch spectra associated to a $|\frac{dac}{dt}| > 10\ mas \times s^{-1}$ and those acquired before the first decontamination operation.

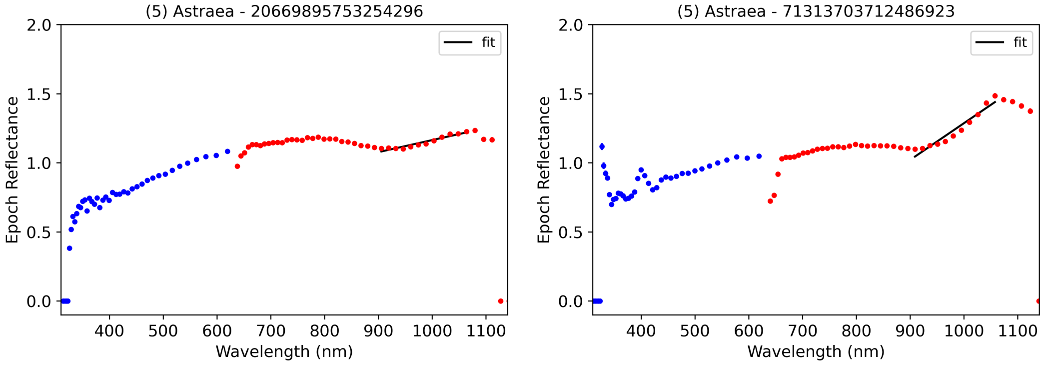

(a) (b)

Figure 2.12: BP and RP epoch reflectance spectra of asteroid (5) Astraea, taken respectively on November 6, 2014 and on May 10, 2017. The linear spline fitting the red slope is displayed in black colors.

2.3.1 "Red slope"

For each epoch spectrum considered, a linear least square regression was performed between 900 and 1070 nm in order to calculate the "red slope". Fig.2.12 shows the red slope fit for two transits of asteroid (5) Astraea. These transits were taken respectively on November 6, 2014 and on May 10, 2017 ; and it is obvious that the reddening effect is more important in 2017. It can be noticed as well that the red slope is accompanied by a peak at 400 nm for the transit of 2017 (right panel).

The red slope was calculated for every transit considered, for the S, C and X-complex. As it appears the red slope increases with time (represented by the transit_id), for each complex, the red slope was plotted with respect to the transit_id on Fig.2.13. To limit the influence of outliers on the calculation, the smoothed moving average of the red slope was calculated with a window of 10, considering a determined range of slope values going from -1 to 4 µm^{-1}. We can see on Fig.2.13 that the red slope starts increasing noticeably after transit_id = 50×10^{15} for the three studied taxonomic complexes, corresponding to a date after May 2016.

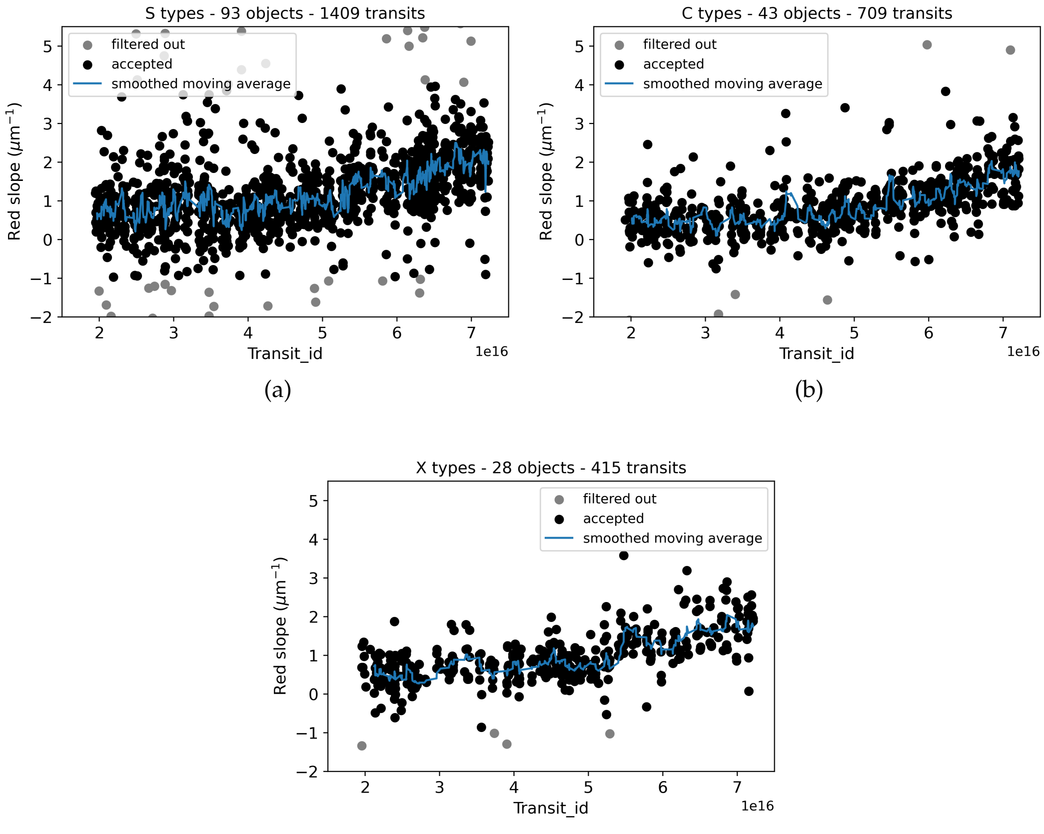

(a)

(b)

(c)

Figure 2.13: Study of the slope of the linear regression fit of the epoch reflectance spectra from 900 to 1070 nm (red slope) for the S, C and X-complexes, after outliers rejection. The rejected outliers are displayed as grey dots, the accepted values as black dots, and the moving average as a blue line.

The smoothed moving average of the red slope for each complex was superimposed for comparison, as displayed in Fig.2.14. It is clear here that the reddening of the RP spectra affects the three taxonomic complexes the same way. This behaviour is quite unexpected, since it has been observed on the mean Gaia DR3 reflectance spectra that the reddening in the RP part seemed to be taxonomic type-dependent (R. Balossi master's thesis), as mentioned before. To further study this phenomenon and to search for its cause, we studied the potential influence of diverse parameters, such as the phase angle.

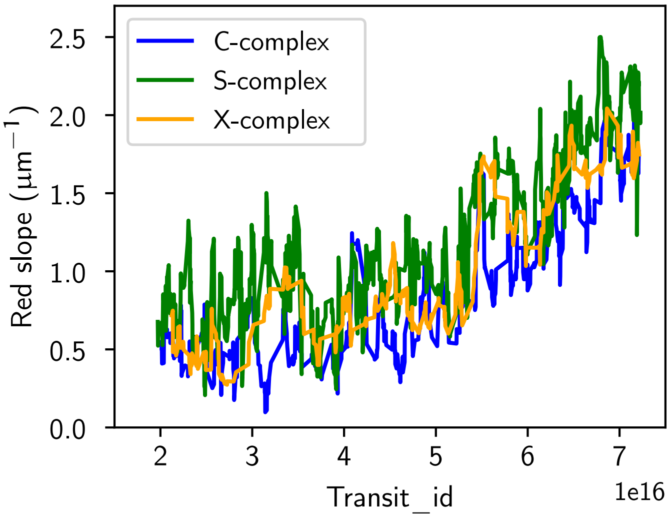

Figure 2.14: Superposition of the smoothed moving average of the red slope, for each taxonomic complex considered. The smoothed moving average corresponding to the S, C and X-complexes is displayed in green, blue and orange colours, respectively.

To evaluate a potential link between phase angle and RP reddening, we plotted the red slope with respect to the phase angle of every transit in Fig.2.15. Bins of phase angle were calculated from 9 deg to 35 deg to normalise by the number of observations, each bin large of 1 deg. We calculated the median red slope inside each bin. From Fig.2.15, the slope increase appears not correlated with the phase angle. The few first and last median values should not be taken into account in the analysis, as the median is calculated on few objects for these phase angle bins.

2.3.2 Payload decontamination

Because of an accumulation of ice on the optics of the Gaia spacecraft, a payload decontamination operation was performed at revolution 4113, on August 22, 2016 (Gaia Collaboration et al., 2016). This third decontamination period might be connected to the RP reddening.

In Fig.2.16 is plotted the 12 epoch reflectance spectra of asteroid (192) Nausikaa aqcuired before the third decontamination period (panel a), and the 4 spectra acquired after (panel b), after filtering out transits associated to a $|\frac{dac}{dt}| > 10 \text{ mas} \times s^{-1}$ and those acquired before the first decontamination operation. We can see that the epoch reflectance spectra show a slightly modified shape after the third payload decontamination, with a reddening of the reflectance at the reddest wavelengths. The BP spectra appear also slightly impacted, and the "fake band" and the peak around 400 nm are

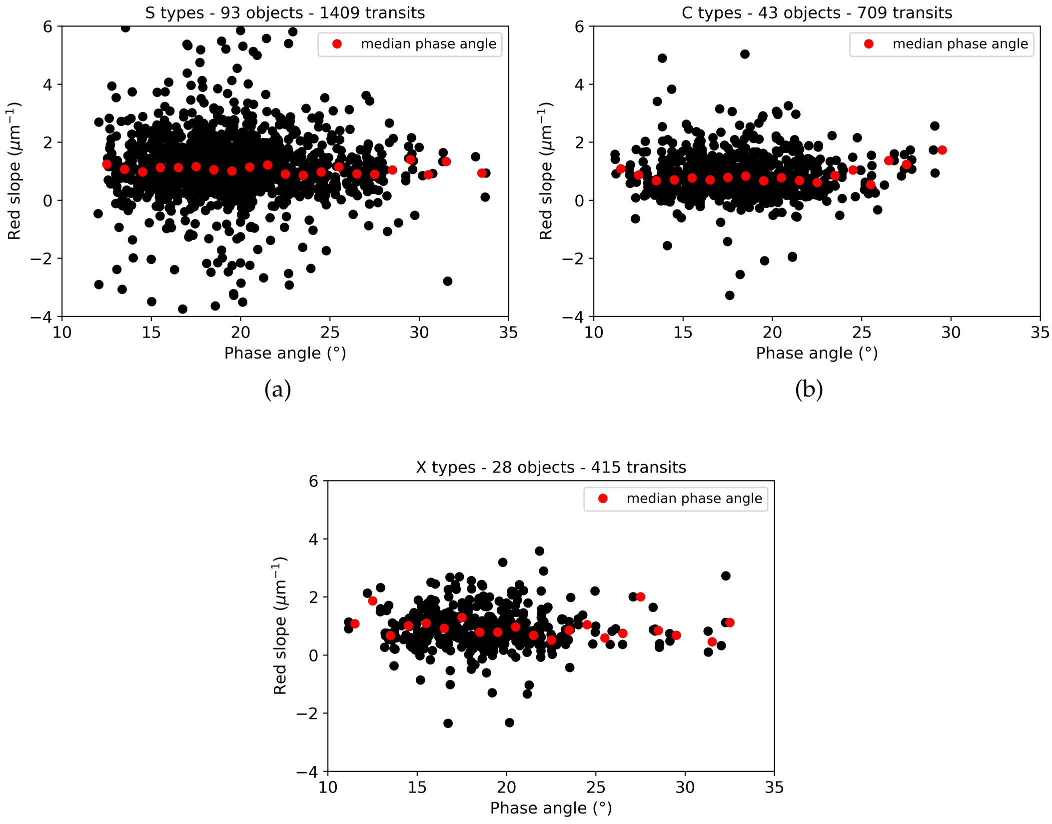

(a) (b)

(c)

Figure 2.15: Study of the influence of the phase angle on the red slope. The median slope calculated on phase angle bins is displayed as red dots.

more obvious. The third payload decontamination may thus be responsible for the observed RP reddening, as it may have affected the spectral response.

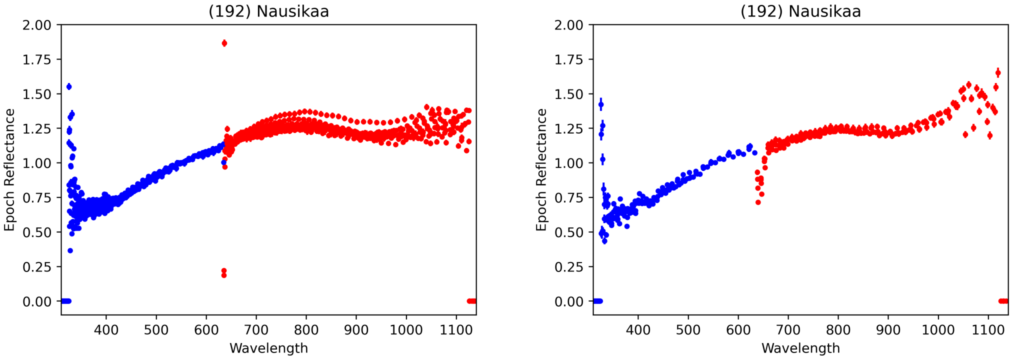

(a) (b)

Figure 2.16: BP and RP epoch reflectance spectra of asteroid (192) Nausikaa, taken before (panel a) and after (panel b) the third payload decontamination.

After filtering out transits taken after the third decontamination period and applying our various filters, a total of 57 194 mean reflectance spectra are produced from three or more epoch reflectance spectra.

2.3.3 Comparison with the literature

In order to see the effect of filtering out transits acquired after the third decontamination period on the possible RP reddening of Gaia SSO mean reflectance spectra, I produced mean reflectance spectra after all the filtering steps, following the procedure used for the DR3 (Gaia Collaboration et al., 2023) (see Chapter 1 section 1.7). The aim was to compare the red slope of Gaia DR3 mean reflectance spectra before and after the application of the filters, with the red slope calculated on literature spectra.

Among the 57 194 mean reflectance spectra produced after filtering, 202 asteroids have a MPC number lower than 1500 and are characterised in DeMeo et al. (2009) and DeMeo et al. (2019). Among these objects, 86 S-complex, 43 C-complex and 26 X-complex asteroids have a VISNIR spectrum in DeMeo et al. (2009). These spectra are the combination of SMASS VIS spectra and NIR spectra acquired with Nasa's IRTF.

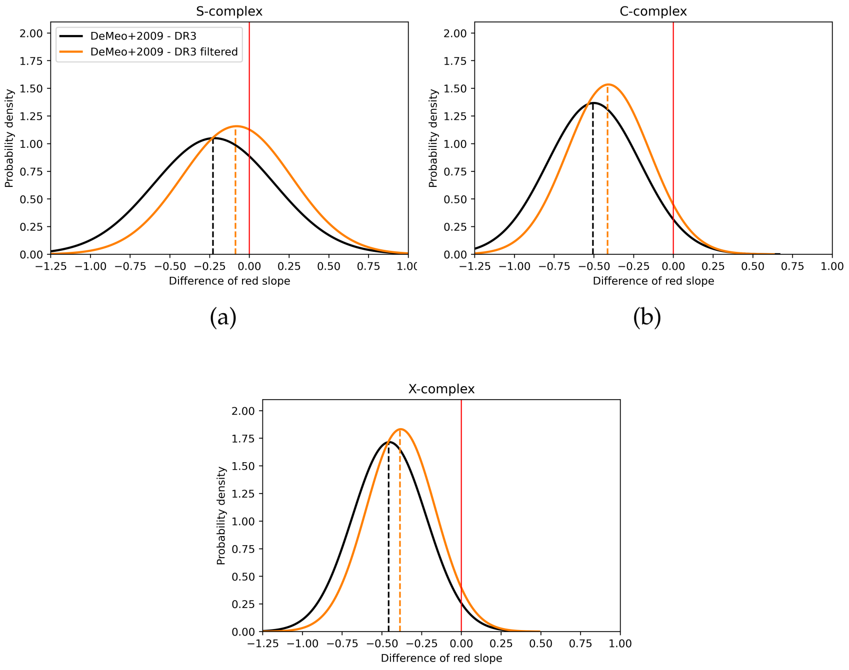

(a) (b)

(c)

Figure 2.17: Gaussian fit of the histogram of the calculated red slope on asteroids members of the S, the C and the X-complex, displayed on panels a), b) and c) respectively. In black, gaussian fit of the histogram of red slope difference between the one calculated on literature spectra from DeMeo et al. (2009) and the one calculated on Gaia DR3 mean reflectance spectra. In orange, red slope difference calculated between the red slope of DeMeo et al. (2009) spectra and the one calculated on filtered Gaia spectra. A line at 0 nm is highlighted in red, and the legend displayed in panel a) applies for panels b) and c).

The red slope was calculated for each of these objects, applying a linear least square regression function to their mean reflectance spectra between 900 and 1034 nm. The limit wavelength to perform the calculation was defined at 1034 nm and not 1070 nm as previously, as the last band of the DR3 spectra is at 1034 nm. The red slope was calculated on the NIR part of the DeMeo et al. (2009) literature spectra, on the DR3 mean reflectance spectra, and on the mean spectra produced after filtering out the transits acquired with $|\frac{dac}{dt}| > 10\ mas \times s^{-1}$, with transit_id $< 19 \times 10^{15}$, and with transit_id $\geqslant 568581 \times 10^{11}$ (spectra acquired after the third decontamination phase). Then, we calculated the difference of red slope between DeMeo et al. (2009) and the DR3, and between DeMeo et al. (2009) and the filtered DR3. We fitted a normal distribution to the obtained histograms of red slope difference, for asteroids of the S, C and X-complexes. The obtained Gaussian fits and are displayed in Fig.2.17, along with an indication of their maximum.

For S-complex asteroids (panel a), the applied filtering almost solves the RP reddening problem, as the difference between the red slope calculated on filtered DR3 spectra and the one calculated on DeMeo et al. (2009) spectra is almost null. For the C and X-complexes (panels b and c), the calculated red slope of the Gaia spectra still appears shifted to higher values, but the difference in red slope is lowered. The calculated difference between the means of the Gaussian before and after filtering is of ≃0.14 for the S-complex, of ≃0.09 for the C-complex and of ≃0.07 for the X-complex. However, as the X-complex is represented by less than half the number of S-complex asteroids, this study would benefit from being carried out on a larger sample of objects.

Finally, our filtering procedure appears to produce mean reflectance spectra less affected by a RP reddening than the DR3 spectra. This effect affecting mostly the last two wavelength bands of the DR3 spectra, not taking these bands into account when exploiting the DR3 is a good temporary solution to conduct large scale study of asteroids population. For the DR4, correcting the epoch reflectance spectra from this reddening effect would be more profitable than filtering them out, as the DR4 will contain 66 months of data, hence about double the amount of data compared to the DR3. Filtering out transits acquired after the third decontamination period is not a viable solution. It might be possible to model the RP reddening by a mathematical function, that would allow to correct the spectra from it. This possibility remains to be studied in the data validation phase of the DR4.

2.4 SOLAR ANALOGUE

After inspecting the diverse potential issues identified in the epoch reflectance spectra of asteroids, we inspected the effect of the solar analogue on the production of mean reflectance spectra. According to Tinaut-Ruano et al. (2023), the mean solar analogue used in the production of the Gaia DR3 spectra induces a change of slope in the NUV wavelength range for most asteroid spectra. We studied the effect of using a new mean solar analogue instead of the mean DR3 solar analogue, on the production of mean reflectance spectra.

This new solar analogue spectrum was calculated as an average spectrum of several stars carefully selected. To produce the mean reflectance spectra from the epoch spectra of asteroids, the spectrum of the new solar analogue was first sampled like each individual epoch spectrum. Then, a ξ factor was calculated to normalise the epoch reflectance spectra to 1 at 550 nm:

$$\xi = \frac{1}{N}\sum_{i\geqslant 525}^{i\leqslant 575}\frac{f(\lambda_i)}{F(\lambda_i)}, \tag{2.2}$$

with $f(\lambda_i)$ the asteroid's epoch spectrum and $F(\lambda_i)$ the solar analogue spectrum, and N the number of reflectance values between 525 and 575 nm, where the normalisation is performed (Gaia Collaboration et al., 2023). Then, each epoch spectrum was divided by the new mean solar analogue spectrum following

$$R(\lambda_i) = \frac{1}{\xi}\frac{f(\lambda_i)}{F(\lambda_i)}. \tag{2.3}$$

2.4.1 Red slope

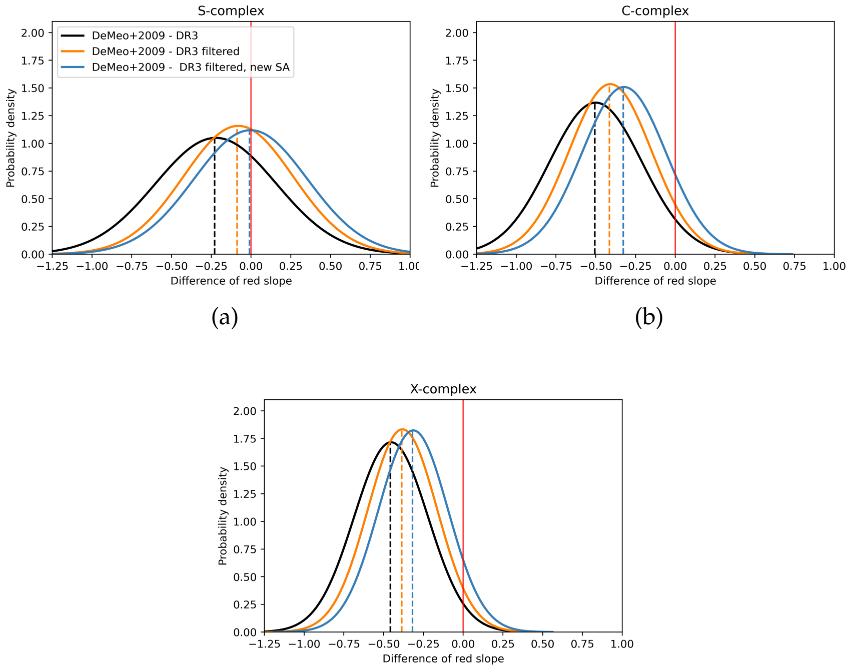

(a) (b)

(c)

Figure 2.18: Gaussian fit of the histogram of the calculated red slope on asteroids members of the S, the C and the X-complex, displayed on panels a), b) and c) respectively. In black, Gaussian fit of the histogram of the red slope difference between the one calculated on literature spectra from DeMeo et al. (2009) and the one calculated on Gaia DR3 mean reflectance spectra. In orange, red slope difference calculated between the red slope of DeMeo et al. (2009) spectra and the one of filtered Gaia spectra. In blue, same difference calculated on filtered Gaia DR3 spectra produced with the new mean solar analogue. A line at 0 nm is highlighted in red, and the legend displayed in panel a) applies for panels b) and c).

First, we studied the impact of the solar analogue on the red slope of the spectra. Using the samples of S, C and X-complex asteroids introduced above, we calculate the red slope of their newly produced DR3 spectra after the whole filtering procedure, and using the new mean solar analogue. We calculated the difference between this red slope and the one calculated on DeMeo et al. (2009) spectra, and we performed a Gaussian fit to the obtained histogram of the differences. We compared this fit to the ones obtained previously, as displayed in Fig.2.18. On this figure, it can be noticed that the choice of solar analogue has an impact on the red slope of asteroids from every complex, and that the new solar analogue further improves the red slope of Gaia mean reflectance spectra. The C and X-complex objects still show lower red slopes than the DeMeo et al. (2009) spectra, for unexplained reasons so far.

2.4.2 NUV slope

After studying the red slope, we studied the impact of the chosen solar analogue on the NUV slope of the mean reflectance spectra. To do so, we used the list of 159 asteroids presented in Tinaut-Ruano et al. (2023) that were selected among asteroids having a Gaia DR3 spectrum, and more than one spectrophotometric observation in the ECAS survey. Among the 159 asteroids, five do not show a reflectance spectrum after applying the different filters: asteroids (37) Fides, (39) Laetitia, (109) Felicitas, (306) Unitas and (433) Eros.

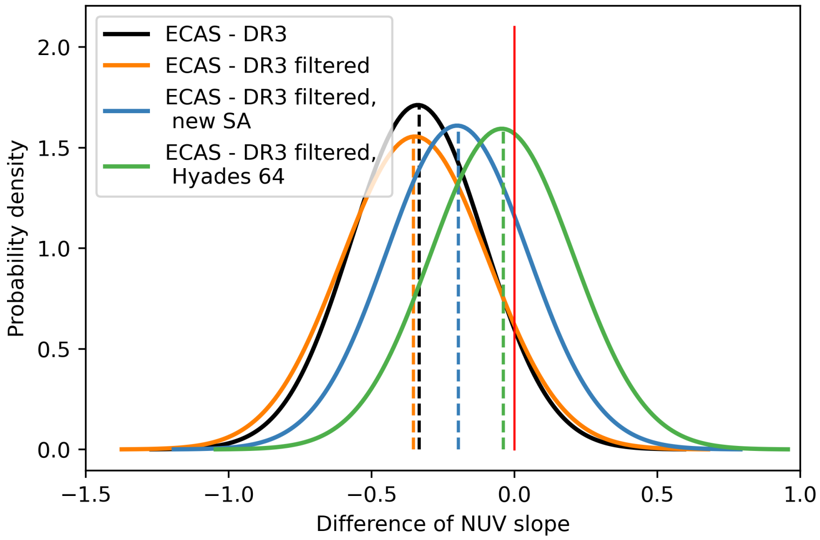

Figure 2.19: Gaussian fit of the histogram of the calculated NUV slope on the 154 asteroids having spectra in the filtered DR3 and in Tinaut-Ruano et al. (2023). In black is displayed the Gaussian fit of the histogram of the NUV slope difference between the one calculated on spectra from the ECAS database and the one calculated on Gaia DR3 mean reflectance spectra, in orange the red slope difference calculated between the red slope of ECAS spectra and the one calculated on filtered Gaia spectra, and in blue the same difference calculated on filtered Gaia DR3 spectra produced with the new mean solar analogue. In green is displayed the Gaussian fit of the histogram of the NUV slope difference between ECAS and the Gaia mean reflectance spectra calculated using Hyades 64 as solar analogue. A line at 0 nm is highlighted in red.

We studied the DR3 spectra, the filtered DR3 spectra, the filtered mean reflectance spectra produced with the new mean solar analogue, and the filtered mean reflectance spectra produced with Hyades 64, that is a solar analogue designated by Tinaut-Ruano et al. (2023) as being highly similar to the solar spectrum in the NUV wavelength range. Using a linear least square regression function, we calculated the NUV slope between 350 and 550 nm of the spectra of each asteroid in the subsample of 154 objects. We then calculated the difference between the NUV slope of ECAS spectra and those of the different Gaia spectra, and we fitted a Gaussian distribution to the obtained histograms of NUV slope. The result of these Gaussian fits is displayed in Fig.2.19.

It is clear from this figure that the choice of solar analogue has a major impact on the NUV slope. The new solar analogue chosen to produce Gaia mean reflectance spectra increases their NUV slope, but not as much as using Hyades 64. It is clear from this plot that Hyades 64 gives NUV slopes closer to the ones calculated on ECAS data, as stated by Tinaut-Ruano et al. (2023).

The choice of solar analogue has thus a large impact on the produced mean reflectance spectra. Even if Hyades 64 shows a great resemblance to the solar spectrum in the NUV wavelength range, it is not necessarily the best solar analogue for the rest of the wavelength range covered by Gaia. Using a single solar analogue to produce Gaia spectra can lead to different issues from the one identified by Tinaut-Ruano et al. (2023), as solar analogues do not show the exact same spectrum as the Sun's. Further studies will be performed to produce the best mean solar analogue spectrum for the DR4, and a synthetic solar spectrum might be used.

2.5 FILTERING METHOD STUDY: MAD-CLIPPING PROCEDURE

As last step, we investigated the filtering method used to produce the mean reflectance spectra published in the DR3. The filtering procedure followed in Gaia Collaboration et al. (2023) is the following: first, a set of fixed wavelength bands is defined to create the 16 Gaia bands, spanning the range from 374 to 1034 nm. Then, 44 nm-wide bins centred on each fixed wavelength band are defined. They are illustrated on Fig.2.20: each epoch reflectance spectrum of asteroid (29) Amphitrite is displayed, and each bin covering a given range of the reflectance spectra is represented in a given color. This specific asteroid is used as an example here, because its RP part was flagged multiple times in the DR3, to indicate its low quality to the community. The asteroid (29) Amphitrite is a perfect example to show the improvements that can be achieved with our filtering procedure, but it is not representative of the mean reflectance spectra published in the DR3.

For this asteroid, we can see in Fig.2.20 that some bins include more variations in reflectance than others, especially in the RP part of the spectrum. Moreover, the bin around 650 nm is exactly at the position of the BP-RP reunion, which can explain why the corresponding band can be affected by the fake band issue.

The next step of the procedure to produce mean SSO spectra is to calculate the median and median absolute deviation (MAD) for each bin. Then, a MAD-clipping approach is repeated twice to filter out data points outside the range (median - 3.7065 MAD, median + 3.7065 MAD), to remove potential outliers (Gaia Collaboration et al., 2023). This threshold was chosen in Gaia Collaboration et al. (2023) because, in a σ-clipping approach, data points outside of the range median $\pm 3\sigma$ are generally

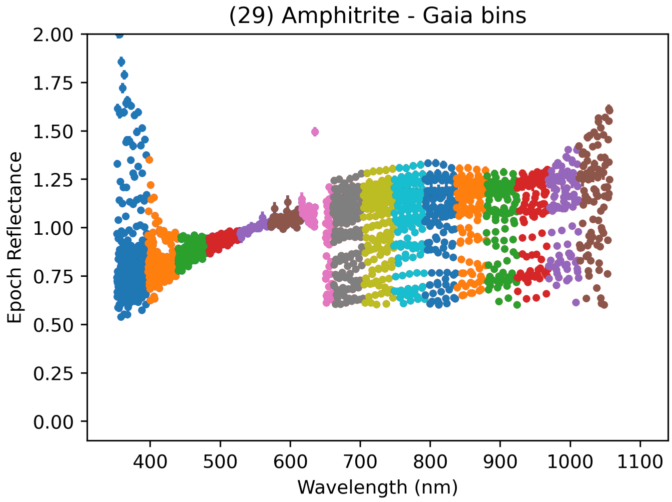

Figure 2.20: Illustration of the Gaia bins chosen for the DR3, on asteroid (29) Amphitrite. Each bin is colour-coded with a colour different from the one of its two direct neighbouring bins.

considered outliers. Here, $\sigma = 2.5$ was found to give more satisfactory results for the production of mean reflectance spectra. For a pure Gaussian distribution, the relation between the MAD and the standard deviation σ is MAD = 0.67449σ, thus the range median±3.7065MAD was chosen for the MAD-clipping approach. For the BP part of the spectrum, only the points inside the range [325-650] nm were considered, and only points spanning the range [650-1125] nm were taken into account for the RP part.

On Fig.2.21 are plotted the result of the median + mad filtering method for asteroid (29) Amphitrite. On the left panel, the median+mad procedure is applied to every epoch reflectance spectra of the asteroid. We can see that some bad spectra are taken into account in the procedure, resulting in a mean spectrum of this asteroid different from its literature spectrum (Fig.2.23, right panel, black dots). When the median+mad procedure is applied to the filtered epoch reflectance spectra only, we can see on the right panel of Fig.2.21 that only good spectra are taken into account. This leads to a mean reflectance spectrum much more similar to the literature Fig.2.23, right panel, orange dots).

The mean reflectance spectra would thus benefit from being produced either averaging only the filtered spectra, or considering every transit, but cleaning the epoch reflectance spectra with the MAD-clipping procedure based on the filtered transits, to avoid taking into account points affected by issues. For most asteroids, the difference between the DR3 and the mean reflectance spectra produced after applying the filtering procedure is hardly distinguishable, showing the efficiency of the MAD-clipping method for most asteroids. However, objects such as (29) Amphitrite see their mean reflectance spectra highly gain in quality thanks to the filters we put in place, which is a great improvement for the DR4.

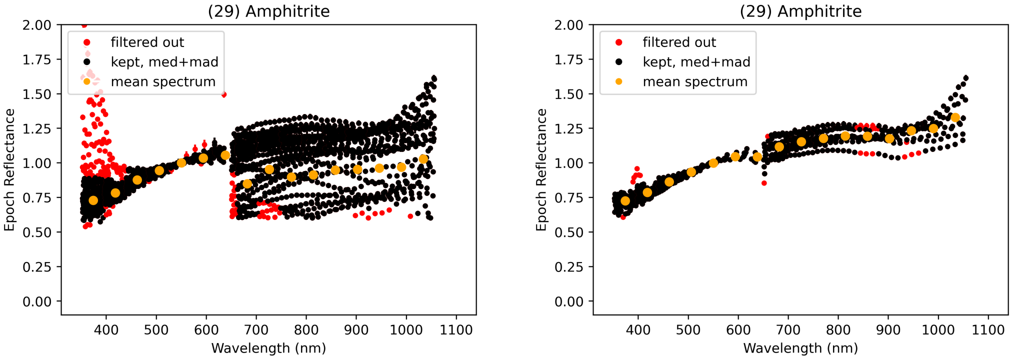

(a)

(b)

Figure 2.21: Comparison of the results of the med+mad filtering method applied to (29) Amphitrite, without transits filtering (left panel) and computed using only the filtered spectra (right panel). On orange is overplotted the derived mean Gaia reflectance spectrum.

2.6 CONCLUSIONS AND PERSPECTIVES

In this chapter, I presented a study of different potential issues identified on the mean reflectance SSO spectra published in the DR3. For the bad BP RP mismatch, we found that the highest the across-scan velocity of the object transiting on Gaia's focal plane, the least well-matched its BP and RP spectra are. Filtering out transits associated to an across-scan velocity $|\frac{dac}{dt}| > 10 \text{ mas} \times s^{-1}$ allows to keep around 70% of the good transits, removing most mismatched spectra. This effect affecting not only the matching between the BP and RP spectra, but also the shape of the epoch reflectance spectra, correcting the spectra from it instead of filtering out transits acquired at high across scan velocity is not a possible solution.

For the "wiggly BP" effect, corresponding reflectance increasing and decreasing unexpectedly in a sinusoidal pattern in the BP part, we realised all that spectra affected by this phenomenon were acquired before the first payload decontamination. They can be filtered out, removing very little asteroids from the dataset.

For the "RP reddening" phenomenon, we found that an increase in the RP reflectance after 900 nm started towards the end of 2016, a period when the third payload decontamination happened. This decontaminatio might be responsible for the noticed reddening, as this effect is visible and follows the same trend for asteroids independently of their taxonomic type. Spectra acquired after this payload decontamination can be filtered out, improving the produced mean reflectance spectra. However, the DR4 will publish new spectra acquired after May 2016. It would therefore be better to correct the epoch reflectance spectra from this effect, rather than filtering them out. This possibility will be investigated during the validation phase for the DR4.

From these analysis, three main filters were thus identified as improving the quality of the reflectance spectra: filtering out transits associated to an across-scan velocity $|\frac{dac}{dt}| > 10 \text{ mas} \times s^{-1}$, filtering out those with a transit_id $< 19 \times 10^{15}$ and those acquired after the third payload decontamination. In Fig.2.22 are illustrated the different steps of the filtering procedure and their effects on the epoch reflectance spectra of asteroids (13) Egeria (right panels) and (29) Amphitrite (right panels). Few epoch reflectance spectra remain for both asteroids after the filtering procedure, but they are enough to produce a mean reflectance spectrum of improved quality.

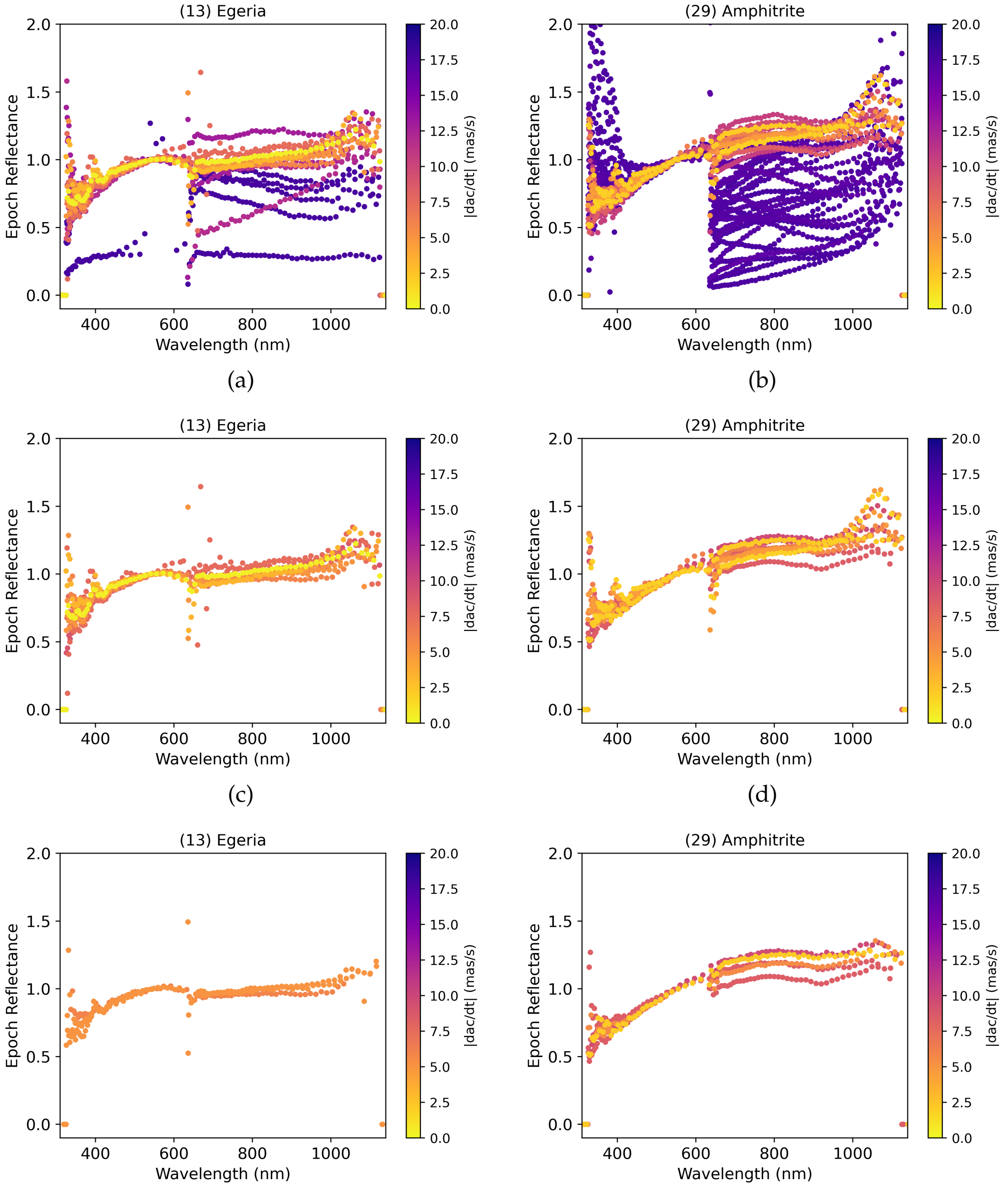

(a) (b)

(c) (d)

(e) (f)

Figure 2.22: Effects of the filtering procedure on the epoch reflectance spectra of (13) Egeria and (29) Amphitrite. Panels a and b: every epoch reflectance spectra colour-coded with the absolute value of the across scan velocity. Panels c and d: epoch reflectance spectra accepted after the first two steps of our filtering procedure. Panels e and f: data points accepted after filtering out spectra acquired after the third decontamination period. The error bars are not represented for clarity.

The comparison between the produced mean reflectance spectra of these two asteroids after application of the filtering procedure, and their DR3 and SMASS spectra (Bus and Binzel, 2002a) is shown in Fig.2.23. The produced mean spectrum of asteroid (13) Egeria is only slightly modified with respect to the DR3, while the spectrum of (29) Amphitrite is highly improved.

As previously mentioned, asteroid (29) Amphitrite has been identified from visual comparisons with literature spectra as one of the Gaia DR3 spectra the most impacted by the mismatch between the BP and RP spectra, and its RP part was flagged multiple times in the DR3. Indeed, it was calculated on a majority of transits with a $|\frac{dac}{dt}| > 10\ mas \times s^{-1}$ (panel (b) of Fig.2.22). It was chosen here to show the improvements achieved by our filtering procedure, but it is not representative of most Gaia DR3 spectra, as can be seen with the spectrum of (13) Egeria in panel (a) of Fig.2.23 for example, that was already good in the DR3.

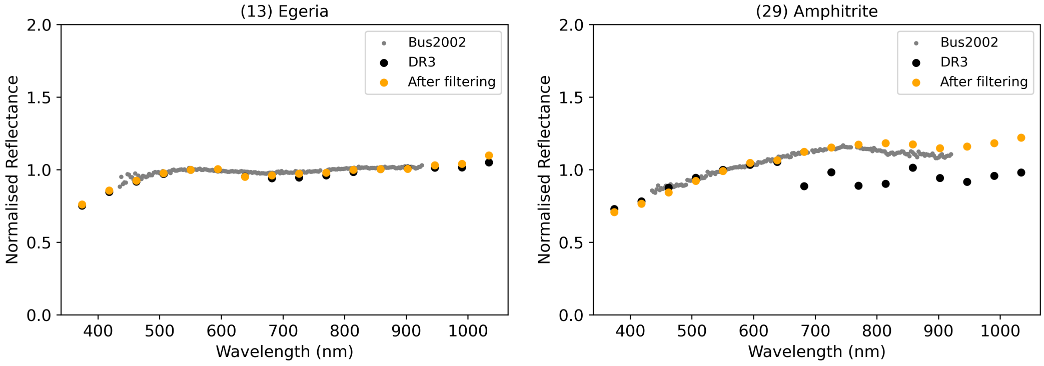

(a) (b)

Figure 2.23: Effects of the filtering procedure on the mean reflectance spectra of (13) Egeria and (29) Amphitrite. Produced mean reflectance spectra after filtering (orange dots), DR3 spectrum (black dots) and literature spectrum from Bus and Binzel (2002a) (grey dots).

Among the other mentioned potential issues, the "fake band" issue (a drop of the reflectance around 650 nm) was barely studied here and would require further investigation. Because this feature appears mostly on bright (and therefore large size) asteroids, it may come from an inaccurate application of the geometric calibrations on asteroids with non-negligible angular extension, such as (4) Vesta or (1) Ceres. Moreover, from the visual inspection of epoch reflectance spectra affected by a "RP reddening", it appeared that this effect, the "fake band", and the presence of a peak around 400 nm might be correlated. The correlation between these effects remains to be confirmed, and solving the RP reddening effect may help solving these other two issues. However, the peak at 400 nm does not affect the DR3 mean reflectance spectra, thanks to the chosen binning.

Cosmic rays are a potential source of high frequency variations observed in some epoch spectra. These spectra are filtered out by the MAD-clipping procedure developed for the production of the DR3 spectra. This procedure produced good quality DR3 spectra for most of the known bright asteroids, despite the identified potential problems affecting the asteroids' epoch spectra.

The impact of the choice of solar analogue on the red and NUV slopes of asteroid mean reflectance spectra has also been studied. Hyades 64 is a star found by Tatsumi et al. (2022) to be similar to the solar spectrum from 350 to 550 nm. Using it to calculate Gaia mean reflectance spectra produces spectra with similar NUV slopes to those calculated on ECAS spectra. However, this solar analogue being optimal for the NUV wavelength range does not guarantee it is similar to the Sun's spectrum for the whole wavelength range covered by Gaia. Using an improved mean solar analogue to produce Gaia DR4 spectra remains the considered option by the DPAC members, and using a modelled synthetic solar spectrum has also been evoked.

The potential issue of the RP part of some spectra "too high" compared to SMASS spectra is left for future investigations. This difference between the two datasets might be due to a bad normalisation of the RP spectra, as the normalisation factor applied to the RP part is the same as the one calculated for BP part. It could also come from a difference of phase angle between ground-based and space-based observations, and SMASS spectra may actually be the ones "too low". On the other hand, the BP part of Gaia and SMASS spectra show a good agreement.

As a remark, the sample chosen to identify and study the potential issues on the epoch reflectance spectra is composed of bright asteroids with a high SNR. This choice probably introduces biases in our study, as bright asteroids are also extended objects, which makes the RP signal larger than the one of a point source and can lead to a reddening of the spectra. Such bright objects were needed to identify clearly potential issues clearly, because of the high SNR or their epoch spectra. However, the effects of our filtering procedure and of the change of solar analogue on dimmer asteroids with lower SNR spectra has to be studied. The filtering procedure reducing the number of epoch reflectance spectra used to produce mean spectra, the mean spectra of dimmer asteroids produced on a few filtered spectra could suffer from the lower number of spectra. Consequently, the impact of our filtering procedure needs to be studied by considering the entire DR3 dataset, in order to make decisions regarding the production of good quality mean reflectance spectra for DR4.

All the above mentioned issues will be further studied during the data production and validation cycles for the DR4, that will be based on 66 months of observations. The filters we have found to improve Gaia spectra will need to be validated on this new set of spectra, once the calibrated epoch spectra produced for the DR4 are available.

Finally, the issues potentially affecting SSO's epoch reflectance spectra do not necessarily lead to a damaged DR3 mean reflectance spectrum, thanks to the quantity of epochs taken into account in the production of mean spectra, and because the MAD-clipping procedure is efficient at filtering out bad epoch spectra, in most cases. The DR3 dataset therefore remains an unprecedented homogeneous dataset allowing to study surface properties of asteroids and to characterise the Main Belt population as a whole. Moreover, the knowledge of the impact of these potential issues on the DR3 spectra allowed me to exploit the dataset keeping a critical eye and paying attention not to interpret potential issues as compositional features of asteroid's surfaces. This dataset was used in this thesis to look for differentiation in the Main Belt, starting with the search for spectral analogues of the meteorite Erg Chech 002.

3

THE METEORITE ERG CHECH 002

The Gaia DR3 dataset offers a unique opportunity to study the Main Belt population of small bodies. Spectra of objects never characterised before have been published in the DR3, and they can be exploited to try linking ungrouped meteorites with asteroids, and to look for evidence of differentiation in the Main Belt.

In this chapter, I first present the unique differentiated meteorite Erg Chech 002 in section 3.1. Using the Gaia DR3 visible (VIS) reflectance spectra and literature spectra presented in section 3.2, I detail a search for spectral analogues of this meteorite in section 3.3. Potential analogues of the meteorite found are presented in section 3.4, and the results from the study in the visible wavelength range are discussed in section 3.5. To confirm these results, I present ground-based observations in the near-infrared wavelength range of some candidate analogues of the meteorite in section 3.6. The analysis of these observations is detailed in section 3.7. The discussion on the connection between Erg Chech 002 meteorite (EC 002) and asteroids, along with the prospects of discovering evidence of differentiated planetesimals in the Main Belt, is presented in sections 3.8 and 3.9, respectively. The first sections of this chapter, about the search for potential analogues of the meteorite in the visible wavelength range, were published in Galinier et al. (2023).

3.1 THE UNGROUPED ACHONDRITE ERG CHECH 002

Erg Chech 002 (hereafter EC 002) is a meteorite that was found in the Sahara desert in May 2020 and has been classified as ungrouped achondrite (Barrat et al., 2021) (see Chapter 1 for the description of meteorite types). A photograph of one of its fragments is shown in Fig.3.1. This meteorite is unbrecciated, meaning that it does not present a mixing of different rock types. It has a coarse-grained texture with grains of average size of about 1.5 mm, and it contains a variety of minerals typical of differentiated meteorites, such as pyroxene, pigeonite, augite, plagioclase feldspar, olivine, and chromite or other spinels (Barrat et al., 2021; Connelly et al., 2023). It has an andesitic composition, typically found on Earth with rocks produced by volcanism in subduction zones (Gill, 2012).

Its age has been inferred by various authors using diverse dating techniques, and is found to be model-dependent (Connelly et al., 2023). It ranges between 4565 and 4569 Myr (Barrat et al., 2021; Fang et al., 2022; Reger et al., 2023; Anand et al., 2022; Zhu et al., 2022; Krestianinov et al., 2023; Connelly et al., 2023), and Zhu et al. (2023)

Figure 3.1: Fragment of the meteorite Erg Chech 002. *Credit*: Anthony Irving (University of Washington), The Meteoritical Society.

recommends to trust the age of ~ 4566.6 Myr. This age lead EC 002 to be designated as "the oldest andesite of the Solar System" (Barrat et al., 2021).

The formation mechanisms deduced from the petrology and composition of this meteorite are consistent with the partial melting of a chondritic source (Yamaguchi et al., 2021; Nicklas et al., 2021; Collinet and Grove, 2020; Chaussidon et al., 2021). Thermal models and laboratory analysis of EC 002 indicate that it probably formed in the primitive igneous crust of an early accreted and differentiated planetesimal, without being fully melted during its core/mantle differentiation, so that enough chondritic material was preserved to form EC 002 (Barrat et al., 2021; Anand et al., 2022; Neumann et al., 2023; Sturtz et al., 2022). This planetesimal was likely part of the NC reservoir of objects (Barrat et al., 2021), defined in Chapter 1. Sturtz et al. (2022) deduced from their thermal model that the parent body of EC 002 must have had a few km-thick chondritic crust, with a total radius between 70 and 130 km. Episodes of partial melting at the base of the crust could have been induced by the heat released by the radioactive decay of ^{26}Al, which would have lead to the formation of EC 002 within the first million years of the Solar System. A violent event such as a collision would have been responsible for the separation of the crust from the original parent body, as suggested by evidence of rapid cooling of the meteorite (Reger et al., 2023; Neumann et al., 2023).

The parent bodies of andesitic meteorites and planetesimals with andesitic crusts are unknown to date in the current Main Belt. Barrat et al. (2021) searched for objects with similar spectral properties to EC 002 among the main belt asteroid population. To do so, they compared laboratory spectra of a powder and three slab samples of EC 002, to astronomical spectra of asteroids with strong pyroxene signatures. They used spectrophotometric data from the Sloan Digital Sky Survey (SDSS), and visible and NIR astronomical spectra of asteroids with strong pyroxene signatures available at the time of the study. On Fig.3.2 is displayed the VISNIR spectrum of a powder sample of EC 002, along with the mean spectra of the O and V spectroscopic types from DeMeo et al. (2009), extracted from Fig.S11 of Barrat et al. (2021). These two classes show the closest spectra to the one of EC 002, and yet it is clear from their comparison and the position and depth of their bands that these asteroid classes are not representative of the meteorite's composition.

EC 002 is spectroscopically unique. Its spectrum shows the presence of two strong absorption bands centred around 950 nm (Band I) and 2000 nm (Band II), that were

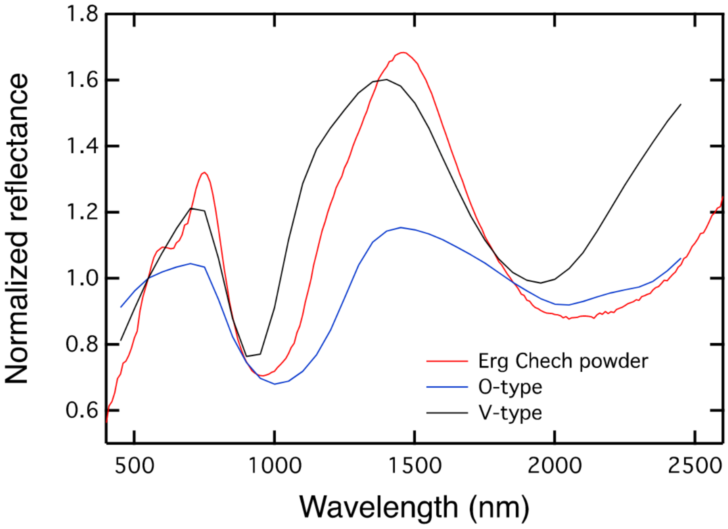

Figure 3.2: Figure from the supplementary material of Barrat et al. (2021), showing the reflectance spectrum of a powder sample of EC 002 compared to the spectra of the V and O-types of DeMeo et al. (2009).

linked to Ca-rich pyroxene. It also shows the presence of a small band centred around 650 nm, whose origin is not discussed in Barrat et al. (2021). We can make hypothesis regarding the origin of this band, given the mineralogical composition of EC 002.

The chemical and mineralogical analysis done by the authors show that the pyroxenes of EC 002 are quite rich in Cr-bearing species (as shown in Table S2 of their supplementary material); and Cr-rich high-Ca pyroxene can lead to the apparition of absorption features near 450 and 650 nm (Moskovitz et al., 2008; Cloutis et al., 2018; Cloutis, 2002). Thus, the presence of chromium-bearing pyroxene is a possible explanation for the band around 650 nm of EC 002. Another possibility is the presence of iron in EC 002's pyroxenes: charge transfer between Fe^{3+} and Fe^{2+} can impact the region around 650 nm (Moskovitz et al., 2008). Either contribution of Cr-bearing or iron-bearing pyroxenes could be responsible for the presence of this band (Moskovitz et al., 2008; Cloutis et al., 2018; Cloutis, 2002).

Barrat et al. (2021) concluded, from the peculiarity of EC 002's spectrum and the absence of match between the meteorite and asteroids, that the entire original population of planetesimals and their fragments showing EC 002-like compositions must have disappeared. They speculate that the disappearance of such objects could be either due to their accretion to other asteroids to form larger planetary embryos, or to their destruction. This disappearance could also result from their erasure by subsequent stages of melting and planetary accretion and differentiation (Collinet and Grove, 2020).

This theory being valid until proven otherwise, we used the recent publication of an unprecedented sample of asteroid spectra by the Gaia DR3 (Gaia Collaboration et al., 2023) to search for analogues of EC 002 in the Main Belt. I present in Sect. 3.2 the dataset of asteroid and meteorite spectra used, and the methods and results of our search for analogues of the meteorite in the asteroid population are presented in sections 3.3 and 3.4. We performed observations in the NIR wavelength range of some of the potential analogues of the meteorite that we found, and these observations, their

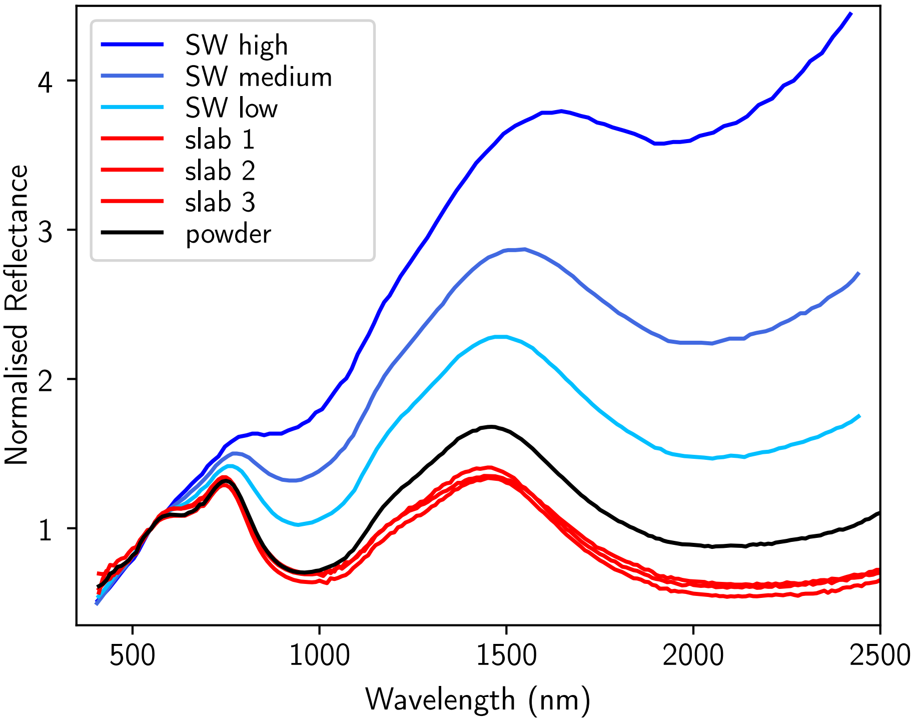

Figure 3.3: VISNIR spectra of the powder (black lines) and three slabs samples (red lines) of EC 002 acquired by Barrat et al. (2021), along with the modelled space weathered spectra of the powder sample (from light to dark blue with increasing space weathering) corresponding to SW low, medium and high.

analysis and the conclusion of the whole study are presented from section 3.6 to the end of this chapter.

3.2 DATA

In order to search for analogues of EC 002 among the asteroid population, we used the DR3 dataset of mean reflectance spectra. A complete description of the dataset and of its production and analysis is given in Chapters 1 and 2.

To perform our analysis, we used the EC 002 spectra that were published by Barrat et al. (2021). They acquired visible and NIR reflectance spectra of one powder sample and three raw slabs samples of EC 002. The spectra of the laboratory samples of the meteorite were kindly provided to us by Jean-Alix Barrat and his co-authors (J. A. Barrat, P. Beck, private communication). Since asteroid surfaces can be altered by space weathering and in order to compare the meteorite spectrum with asteroid spectra, Barrat et al. (2021) applied the Hapke (2001) space weathering model to the powder sample of the meteorite, to simulate the inclusion of nanophase iron inside the silicate host medium. Barrat et al. (2021) published three space-weathered spectra of EC 002 corresponding to three different levels of space weathering – low, medium, and high. We digitised these space weathered spectra from the supplementary material of Barrat et al. (2021) using the SAO Image DS9 software. These seven spectra were used in our study to search for asteroids with similar features to EC 002. They are displayed in Fig.3.3.

3.3 METHODS

In order to identify a spectral link between EC 002 and the asteroids, we compared the laboratory and space-weathered modelled spectra of EC 002 to Gaia DR3 spectra. Since the source of this meteorite is unknown, this object could originate from a family of fragments generated by a recent collision. These fragments would have suffered limited space weathering because of their young age, showing a spectrum similar to the one of EC 002. This explains why we searched for potential spectral matches of the unweathered meteorite.

Moreover, we tried to detect asteroids with similar spectral features to those of EC 002 (similar spectral slope, pyroxene absorption band around 950 nm, and presence of a small 650 nm band), and these features are more easily detected without space weathering. It is also reasonable to believe that asteroids have surface grains. Given that they influence the spectroscopic properties of a medium (see Chapter 1), we used the spectra of the powder and the raw slab samples of EC 002.

On the other hand, EC 002 has the composition of a partial melt of an ordinary chondrite (Barrat et al., 2021). Once weathered, ordinary chondrites are spectrally similar to S-type asteroids (Chapman, 1996). If the asteroids matching EC 002 suffered from space weathering, it is not unreasonable to expect a S-type-like space weathering (as expressed by the space weathering trend assumed by Barrat et al., 2021). Hence, we used as well the modelled space-weathered spectra of EC 002 to look for spectral analogues amongst the asteroid population. To summarise, we searched for asteroids spectrally matching the powder, raw slabs samples, and modelled space-weathered spectra of EC 002 using two spectral matching methods described below.

3.3.1 Identification of potential analogues of EC 002 with spectral parameters comparison

The first method consists in comparing the spectral parameters derived from the reflectance spectra of the meteorite and of the asteroids. These parameters are the slope of the reflectance spectrum between 468.6 and 748 nm, and a measure of the depth of the silicate band centred around 950 nm (Band I depth). This method was inspired by the works of Barrat et al. (2021), DeMeo and Carry (2013) and Parker et al. (2008) using the SDSS asteroid spectrophotometric data. Ivezić et al. (2001) and Nesvorný et al. (2005) identified two parameters on asteroids spectra that express most of the data variability: the a* parameter and the i-z colour. The a* parameter closely represents the slope of the reflectance spectrum in the g′, r′ and i′ SDSS bands (Ivezić et al., 2001), these bands being respectively centred at 468.6 nm, 616.6 nm and 748.0 nm (Fukugita et al., 1996). The i-z colour is sensitive to the depth of a potential 950 nm band, the colour being the difference of magnitude between the i′ and z′ bands. These parameters are useful to characterise a visible asteroid spectrum.

DeMeo and Carry (2013) used slightly different spectral parameters to characterise the asteroids: the so-called z-i parameter, which is a difference of reflectance centred at distinct wavelengths, and the gri-slope. To evaluate these, the SDSS observed magnitudes of asteroids are converted into reflectance values at the centre of each SDSS filter following

$$R_f = 10^{-0.4[(M_f - M_i) - (M_{f,\odot} - M_{i,\odot})]}, \qquad (3.1)$$

with M_f and $M_{f,\odot}$ the respective magnitudes of the object and of the Sun at the central wavelength of a given filter f. M_i and $M_{i,\odot}$ are the respective magnitudes of the object and of the Sun at the normalisation wavelength, that is the central wavelength of the g′ filter (468.6 nm) in Fukugita et al. (1996). The gri-slope is defined as the slope of the derived reflectance spectra over the g′, r′ and i′ filters. The z-i parameter still measures the depth of a potential 950 nm band, and is here defined as $z - i = R(\lambda = 893.2\ nm) - R(\lambda = 748.0\ nm)$.

3.3.1.1 *Spectral parameters of Gaia DR3 mean reflectance spectra*

In order to compare Gaia reflectance spectra with what has been done in the work of Barrat et al. (2021), we evaluated the gri-slope and an equivalent of the z-i parameter for Gaia DR3 spectra. First, each Gaia DR3 spectrum was interpolated using a cubic smoothing spline (python package *csaps*, default smoothing parameter) and re-sampled between 450 and 900 nm. For this procedure, only Gaia bands with flags equal to zero (good quality bands) were considered, and the first and last Gaia bands were not taken into account to limit the impact of low quality bands on the calculated reflectance values. The re-sampled Gaia spectra were then normalised at 468.6 nm, and the spectral gri-slope was computed by linearly fitting the spectrum between 468.6 and 748.0 nm (first-degree polynomial fit, numpy package *polyfit*). The $R_z - R_i$ parameter was computed by taking the value of the reflectance of every re-sampled normalised spectra at the central wavelength of the i′ and z′ SDSS filters, namely 748.0 nm and 893.2 nm:

$$R_z - R_i = R(\lambda = 893.2\ nm) - R(\lambda = 748.0\ nm). \quad (3.2)$$

An illustration of the gri-slope and $R_z - R_i$ parameters on the Gaia DR3 reflectance spectrum of V-type asteroid (1459) Magnya is provided in Fig.3.4.

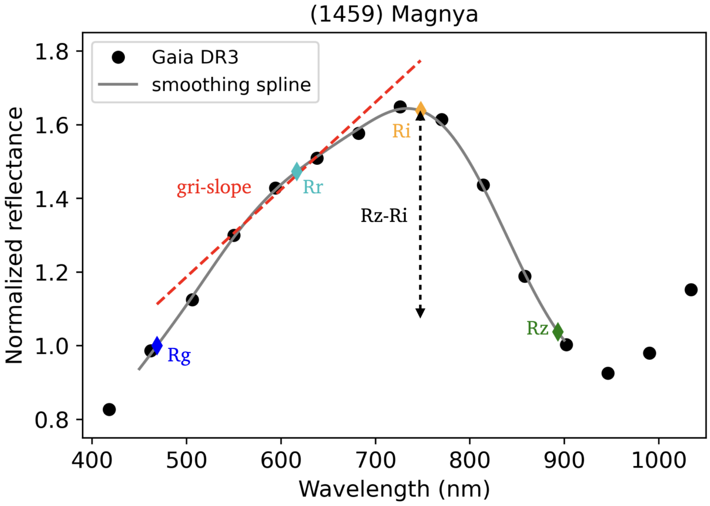

Figure 3.4: Gri-slope and $R_z - R_i$ parameters on the Gaia DR3 reflectance spectrum of (1459) Magnya (black dots). The cubic smoothing spline of the DR3 spectrum is in grey lines. The reflectance values at wavelengths corresponding to the central wavelength of the SDSS filters are indicated as coloured diamonds, with $R_g = R(\lambda = 468.6\ nm)$ the normalisation wavelength, $R_r = R(\lambda = 616.6\ nm)$, $R_i = R(\lambda = 748.0\ nm)$, and $R_z = R(\lambda = 893.2\ nm)$.

The difference between the z-i of DeMeo and Carry (2013) and our $R_z - R_i$ is that Gaia reflectance spectra were not integrated in the SDSS filters, they are reflectance values at wavelengths corresponding to the central wavelength of the g′, r′, i′ and z′ SDSS filters. The asteroids plotting in an area close to the meteorite in the $R_z - R_i$ vs. gri slope diagram are defined as potentially matching the spectrum of EC 002.

3.3.1.2 *Spectral parameters of EC 002 laboratory samples spectra*

First, we studied the four laboratory samples (one powder and three slabs) of the meteorite EC 002, without taking space weathering into account. The spectrum of each sample was interpolated between 450 and 900 nm using a cubic smoothing spline, and they were normalised to unity at 468.6 nm. Then, their $R_z - R_i$ parameter was calculated using Eq.3.2, and their gri-slope was evaluated between 468.6 and 748.0 nm applying a first degree polynomial fit. They are plotted as coloured squares in the $R_z - R_i$ vs gri-slope parameters space in Fig.3.5.

In order to identify the asteroids with spectral parameters similar to EC 002, we calculated the average of the gri-slope and $R_z - R_i$ values for the four samples. The corresponding point is considered as the "barycentre" of the non-space-weathered samples (orange diamond in Fig.3.5). Then, we determined a 3σ confidence ellipse around this barycentre. Given the distribution of the data in the $R_z - R_i$ vs gri-slope space, the confidence ellipse is not axis aligned. The equation of the confidence ellipse centred on a barycentre of coordinates (x_c, y_c) and oriented with an angle α is:

$$\left(\frac{\cos^2\alpha}{a^2}+\frac{\sin^2\alpha}{b^2}\right)(x-x_c)^2+\left(\frac{\sin^2\alpha}{a^2}+\frac{\cos^2\alpha}{b^2}\right)(y-y_c)^2+ \\ 2(x-x_c)(y-y_c)\sin\alpha\cos\alpha\left(\frac{1}{b^2}-\frac{1}{a^2}\right)=s, \tag{3.3}$$

with x the gri-slope of a reflectance spectrum, $y = R_z - R_i$, and s the scale of the ellipse that represents a chosen confidence level. The parameters a and b are respectively the semi-major and semi-minor axis of the ellipse. χ-square probabilities showed that for a 3σ ellipse, the s value is 9.210, defining a 99% confidence level. We used this value of s here.

In order to determine the orientation of the ellipse, we calculated the covariance matrix of the four laboratory samples of the meteorite. The covariance matrix contains information about the directions in which the data varies the most, represented by the eigenvectors of the matrix. The length of the major and minor axis of the ellipse are given by its eigenvalues, as they represent the variance (hence the spread) of the data in the direction of the eigenvectors. The semi-major and semi-minor axis of the ellipse are thus defined as:

$$\begin{cases} a &= \sqrt{s\lambda_1} \\ b &= \sqrt{s\lambda_2}, \end{cases} \tag{3.4}$$

with λ_1 and λ_2 the eigenvalues of the covariance matrix, λ_1 being the largest. The angle α of the ellipse is defined as $\alpha = \arctan\frac{v_1(y)}{v_1(x)}$ with v_1 the eigenvector of the covariance matrix associated to the largest eigenvalue. The ellipse is represented in orange colour in Fig.3.5. If an asteroid falls inside the 3σ ellipse in the spectral parameter space, it is considered a candidate match of the laboratory samples of EC 002.

3.3.1.3 *Spectral parameters of EC 002 modelled space-weathered samples spectra*

After studying non-space-weathered samples of EC 002, we analysed the modelled spectra of EC 002 from Barrat et al. (2021) on which was applied the Hapke (2001) space weathering model. The gri-slope and $R_z - R_i$ parameters were calculated for these spectra, following the aforementioned procedure. Their position in this parameters space is indicated as blue squares in Fig.3.5.

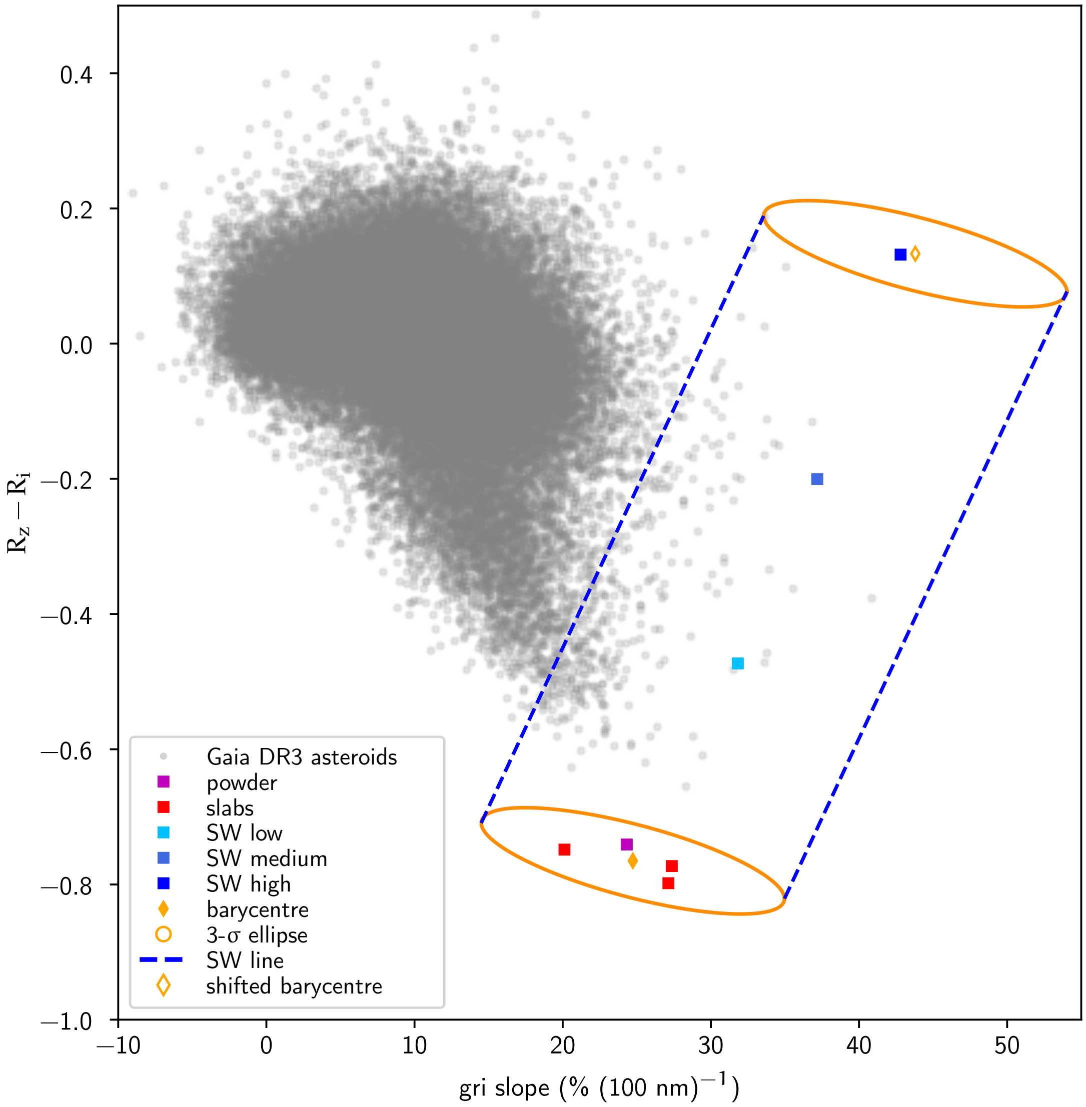

Figure 3.5: Distribution of depth of the band around 1000 nm with respect to the spectral slope of every Gaia asteroid (grey dots). Red squares: raw slabs of the meteorite EC 002. Purple square : powder sample of the meteorite. Full orange diamond: barycentre of these 4 samples, and empty orange diamond: shifted barycentre along the "space weathering line". The squares going from light blue to dark blue represent the modelled space-weathered spectra of EC 002, with different space weathering intensity. The orange ellipses are the 3-σ ellipse respectively around the barycentre and shifted following the space weathering behaviour of EC 002. The two dashed blue lines delimit a "possible matches area", within which can be found candidate asteroids matching EC 002.

In order to study more stages of space weathering of the meteorite, we fitted a straight line to the points corresponding to the powder sample and to the three space-weathered samples in the $R_z - R_i$ vs. gri-slope plot. This line will be referred in the following as the "space weathering line". The equation of this line is $y = 0.047x - 1.92$, and the coefficient of determination of the fit is $R^2 = 0.986$, proof of a good quality fit. A parallel line to this space weathering line centred on the barycentre of the non-weathered samples was calculated, and the 3σ ellipse was moved along this line from the lowest to the highest space weathering points, in order to define a "possible matches area" within which objects could present spectral parameters similar to those of EC 002 with different levels of space weathering. This area is occupies the space within the two ellipses and the dashed blue lines in Fig.3.5.

The spectra of the asteroids located inside this "possible matches area" were visually inspected, to determine the quality of the potential matching with the meteorite's spectra. We relied on visual inspection rather than on an automated method to assess the quality of the matches, mostly because the 650 nm band on the meteorite spectrum was never detected by algorithms. This band being a characteristic feature of the meteorite spectrum, we chose the method where its presence was the most surely detected. The relatively small number of objects to inspect made this choice possible.

3.3.2 Identification of potential analogues of EC 002 with a curve matching method

The second method we used in order to find spectral analogues of EC 002 is a curve matching method, between the meteorite and the asteroids reflectance spectra. This method is widely used in the literature (see, e.g. Popescu et al., 2012; DeMeo et al., 2022). It consists in evaluating how similar two spectra are relying on the measure of a best-fit coefficient. In this work, among the possible existing coefficients, we used the following definition of the reduced χ^2:

$$\chi^2_{red} = \frac{1}{\nu} \sum_{i}^{N} \frac{(A_i - f.M_i)^2}{\sigma_i^2}, \tag{3.5}$$

with M_i the meteorite spectrum, A_i a Gaia asteroid reflectance spectrum and σ_i its associated uncertainties, ν the number of degrees of freedom, and f a normalisation factor allowing the best overlap between the meteorite and Gaia reflectance spectra. The f-value was determined by minimising the χ^2_{red} such that the partial derivative of the χ^2_{red} with respect to f is zero. This leads to:

$$f = \frac{\sum_i^N \frac{M_i.A_i}{\sigma_i^2}}{\sum_i^N \frac{M_i^2}{\sigma_i^2}}. \tag{3.6}$$

In order to compare EC 002 with asteroids, we started by sampling the meteorite spectra at Gaia's wavelengths. We considered only the good quality bands (flag=0) in Gaia spectra, and did not take into account the first and last bands of the Gaia spectra. The "cleaned" Gaia spectra were thus composed of 14 bands spanning the wavelength range from 418 to 990 nm, provided that they had a null flag.

Then, the meteorite spectra were interpolated with a cubic smoothing spline (python package *csaps*, smoothing parameter of 0.0001), sampled as each cleaned Gaia spec-

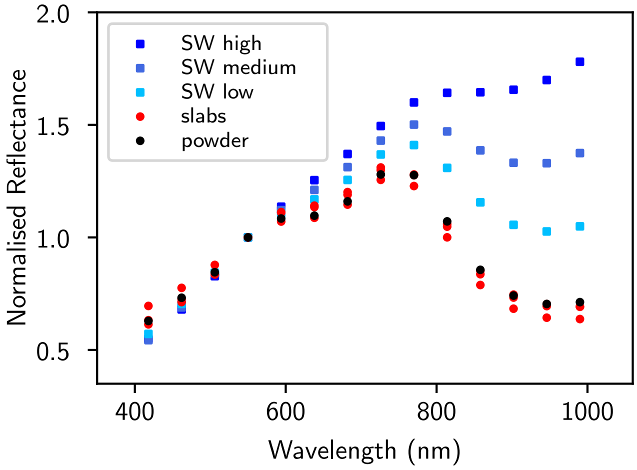

Figure 3.6: Spectra of a powder, three raw slab samples and three modelled spectra of space-weathered of EC 002 sampled and normalised as Gaia data, not taking into account the first and last Gaia bands.

trum, and normalised at 550 nm. Figure 3.6 shows the spectra of EC 002 after re-sampling and normalisation. For each sample of the meteorite, the χ^2_{red} (Eq.3.5) was calculated between each cleaned asteroid spectrum and the re-sampled and normalised meteorite spectrum.

Such definition of the reduced χ^2 is used for example in Press et al. (1986), Alí-Lagoa et al. (2014), Emery et al. (2014), Hanuš et al. (2015), and Hanuš et al. (2018) to determine the uncertainties of some parameters in the context thermophysical modelling of asteroids. In Hanuš et al. (2015) is shown that solutions of the model obtained within $\chi^2_{red} < 1 + \sigma$ are considered indistinguishable, with $\sigma = \frac{\sqrt{2\nu}}{\nu}$ and ν the number of degrees of freedom (number of data points minus number of free parameters). We adapted this formula for a 3σ confidence: an asteroid is considered matching the meteorite's spectrum at 3σ if the following condition is respected: $\chi^2_{red} < 1 + 3\sigma$. We considered ν=16, hence $\chi^2_{red} < 2.06 \simeq \chi^2_{red} < 2$. For each meteorite sample, the best matches were selected according to this criterion and their spectra were visually inspected.

We later realised that this choice of χ^2 metric was not the most adapted to our case. An alternative choice of χ^2 will be discussed in section 3.5.

3.4 RESULTS

In this section we describe the results obtained with (i) the spectral parameters comparison between EC 002 and Gaia asteroids spectra, and (ii) the curve matching method. As shown in the following, some asteroids have been identified as having Gaia reflectance spectra similar to the visible part of EC 002 spectra. The number of matches found with each method and each sample is indicated on Table 3.1, and the detail of the number and name of each asteroid matching, and with which method it was found, is given on Table B.1 in Appendix B.

Table 3.1: Accepted asteroids as candidate matches for the different samples of EC 002, according to the method used.

Sample	Spectral parameter	Curve matching	Total
Powder + slabs	41	18 / 10	51
SW low	56	23 / 15	71
SW medium	12	8 / 5	17
SW high	2	1 / 1	3

Note: The first number in the curve matching column is the number of asteroids found using the curve matching method for a given sample of the meteorite, and the second number corresponds to the number of asteroids not already found with the spectral parameter method. The total number of matches for each sample is indicated in the last column.

3.4.1 Spectral parameters comparison

In the following are described the potential matches of EC 002 obtained with the spectral parameters study. The gri-slope and $R_z - R_i$ spectral parameters were calculated for the powder and raw slab samples of EC 002 (see Table 3.2). The average and standard deviation for the slope and Band I depth are of 24.7 ± 2.9 % (100 nm)$^{-1}$ and -0.76 ± 0.02, respectively. In Fig. 3.7, the corresponding barycentre point is plotted as an orange diamond. We can observe that the points corresponding to the various meteorite samples are located far from any asteroid group in the spectral parameter space, as already observed in Fig. S14 of the supplementary material of Barrat et al. (2021).

Table 3.2: Spectral slope and Band I depth evaluated for different samples of EC 002.

Sample	spectral slope (%(100 nm)$^{-1}$)	$R_z - R_i$
Powder	24.3	-0.74
Raw slab 1	27.4	-0.77
Raw slab 2	20.1	-0.75
Raw slab 3	27.1	-0.80

The "possible matches area", bounded by the two ellipses and the dashed blue lines in Fig. 3.7, contains 305 asteroids, all listed in Table B.2 in Appendix B. Their spectra were visually inspected, and we rejected ~63.8% of the sample following several criteria: (i) we rejected the objects that have known VIS or NIR spectrum in the literature, allowing to distinguish them from EC 002. These objects correspond to 10.2% of the initial sample of 305 asteroids. (ii) We removed the objects having more than three flagged bands in their Gaia DR3 spectrum (1.8% of the sample), and (iii) we rejected the asteroids that had either a too noisy spectrum visually, or that were different from the spectra of EC 002 in either BP or RP parts (51.8% of the sample). Finally, (iv) we rejected the spectra showing a steep increase of their reflectance in the red part (see Chapter 2 for the analysis of this reddening phenomenon).

After visual inspection and application of the criteria presented above, 110 asteroids were retained (displayed in Appendix B Table. B.2). Among these validated asteroids, 106 objects have been given a spectrum for the first time by the Gaia mission, and

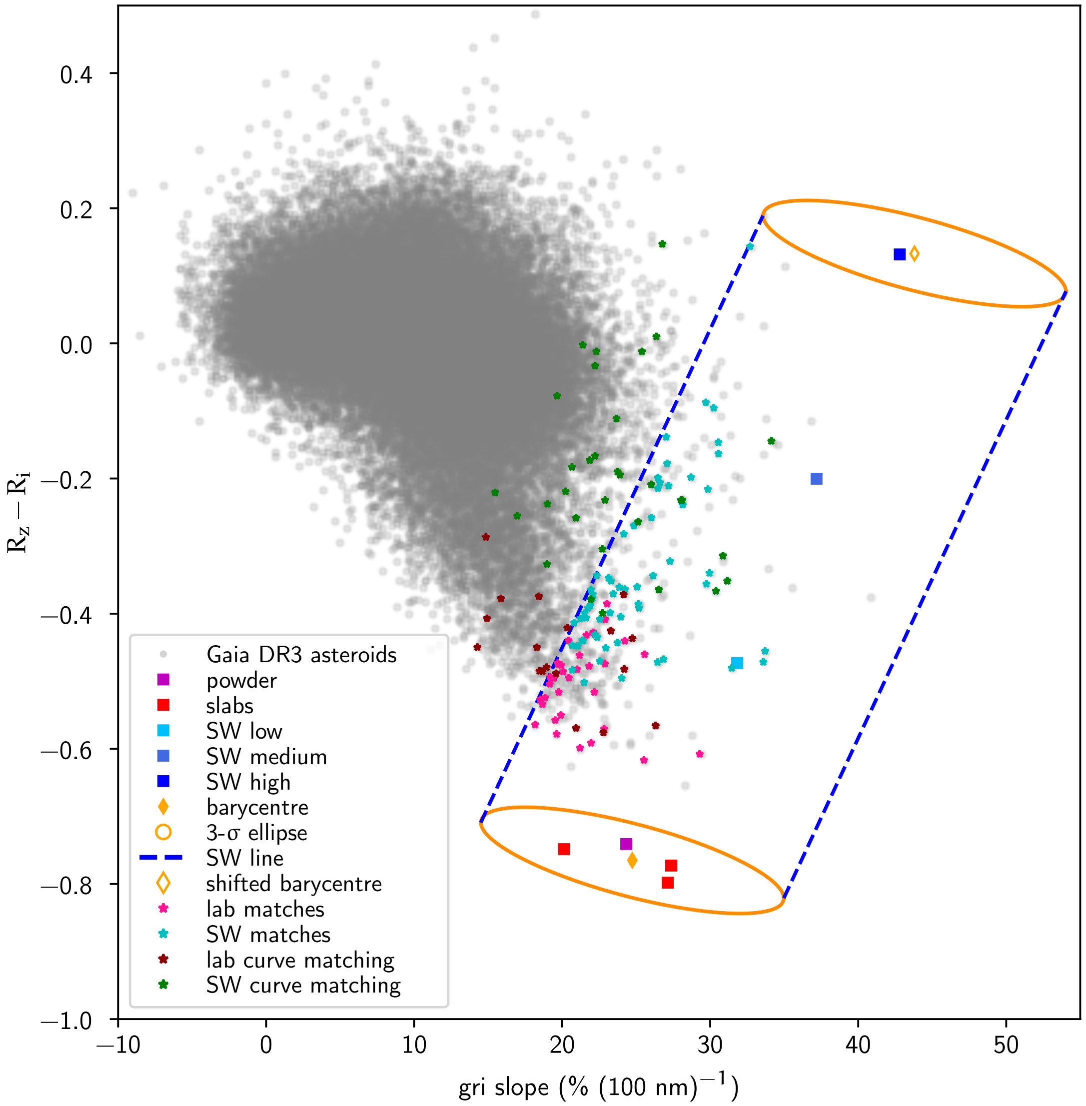

Figure 3.7: Distribution of depth of the band around 1000 nm with respect to the spectral slope of every Gaia asteroid (grey dots). See Fig.3.5 for the legend. Pink stars: asteroids matching the raw slabs and powder sample of EC 002, found within the "possible matches area". Cyan stars: asteroids matching the space-weathered samples, found within the "possible matches area". Dark red stars (resp. green stars): asteroids matching EC 002 (resp. the space-weathered modelled spectra of EC 002) according to the curve matching method.

41 asteroids were identified to have a reflectance spectrum similar to the laboratory spectra of EC 002. These objects are defined as spectral matches, potential analogues of the unweathered meteorite. The spectra of the matches are shown on Fig. B.1 in Appendix B, and their median SNR is of 26.3. The matches of the four laboratory samples were not considered separately here, because these samples show almost indistinguishable spectra in the visible wavelength range.

In addition, 70 asteroids were found matching the space-weathered spectra of EC 002: 56 asteroids match the low space-weathered spectrum, 12 asteroids match the medium space-weathered spectrum, and only two asteroids match the highly space-weathered spectrum. The spectra of these matches are shown respectively on Fig. B.2, Fig. B.3

and Fig. B.4 in Appendix B. The median SNR of the matches is of 23.0 for the low space-weathering, of 18.2 for the median space weathering, of 15.97 for asteroid (9974) Brody, and of 14.05 for asteroid (19754) Paclements.

3.4.2 Curve matching method

We applied the curve matching method to the powder and slabs laboratory spectra of the EC 002 and to the entire dataset of 60 518 Gaia asteroid reflectance spectra. As before, the matches of the four laboratory samples were not considered separately here.

We obtained 58 bodies matching EC 002 respecting χ^2_{red}<2. These objects are listed on Table. B.3. After visual inspection of their spectra and application of the above-mentioned criteria, several objects were rejected (see Table B.3 in Appendix B). Finally, 18 asteroids were retained as potential analogues of the laboratory samples of EC 002. Among these, ten objects were not found with the spectral parameters method: (16856) Banach, (17056) Boschetti, (54062) 2000GX135, (63653) 2001QQ109, (77147) 2001EV6, (77935) 2002GM54, (89556) 2001XS98, (123113) 2000SH361, (124884) 2001TE41, and (164121) 2003YT1. Their spectra are shown in Appendix B Fig. B.5.

The curve matching method was then applied to the space-weathered samples of EC 002. For the low space-weathered spectrum, 269 asteroids had a χ^2_{red}<2. There was 223 asteroids with χ^2_{red}<2 for the medium space-weathered spectrum, and only 12 asteroids for the highly space-weathered spectrum.

Most asteroids were rejected following the criteria exposed earlier. Finally, 23 asteroids were found matching the low space-weathered meteorite spectrum, eight asteroids matching the medium space-weathered spectrum and one asteroid matching the highly space-weathered spectrum. These objects are listed in Table B.4 in Appendix B. The asteroids found as matches with this method and not with the spectral parameters analysis are (10131) Stanga, (15623) 2000 HU30, (18780) Kuncham, (20535) Marshburrows, (22276) Belkin, (22538) Lucasmoller, (32835) 1992EO5, (33423) 1999DK, (33852) Baschnagel, (33934) 2000LA30, (65504) 3544P-L, (74378) 1998XH11, (79827) 1998WU3, (100440) 1996PJ6, and (103308) 2000AH55 for the low space weathering ; asteroids (68089) 2000YS108, (68946) 2002PX138, (93797) 2000WO43, (108899) 2001PP5, (145532) 2006FD42 and (230762) 2003WP192 for the medium space weathering, and asteroid (33809) 1999XK152 for the high space weathering. Their spectra are shown respectively on Fig. B.6, Fig. B.7 and Fig. B.8 in Appendix B.

3.5 DISCUSSION OF THE STUDY IN THE VISIBLE WAVELENGTH RANGE

Asteroids spectroscopically matching EC 002 in the visible wavelength range appear to be extremely rare. We find only 51 asteroids matching the non-space-weathered spectrum of EC 002, and 91 asteroids matching its spectrum on which was modelled the effect of space weathering to various degrees. Considering the entire Gaia dataset of 60 518 asteroids spectra, it means a mere 0.08% of the sample for the non-space-weathered samples and 0.15% of the sample for the space-weathered EC 002. It is in line with the conclusions of Barrat et al. (2021) about the scarcity of analogues of EC 002 among the asteroid population.

We define the best matches of the different samples of EC 002 as the objects found using both methods. For the four laboratory samples, there are seven best matches: (6853) Silvanomassaglia, (10156) 1994VQ7, (20454) Pedrajo, (55549) 2001XC59, (88955) 2001TW42, (205560) 2001SC282, and (310436) 2000AB169. For the spectra on which was applied a low space weathering model, there are eight best matches: asteroids (24684) 1990 EU4, (27876) 1996BM4, (33947) 2000ML1, (43278) 2000ES109, (56561) Jaimenomen, (89952) 2002JB20, (108139) 2001GL11, and (112326) 2002MM4. For the medium space weathering model, asteroids (42822) 1999NT13, (44322) 1998RZ42, and (230762) 2003 WP192 are found by both methods. No asteroid is found by both methods for the highly space-weathered spectrum.

3.5.1 Choice of curve matching coefficient

Both methods give quite different asteroids as matches. That can be explained by our poor choice of curve matching parameter. First, the reduced χ^2 requires the definition of a number of degrees of freedom ν, defined as number of data points minus number of free parameters. We used a value of 16 degrees of freedom arbitrarily, but it is not correct. Andrae et al. (2010) showed that, for non-linear models, it is not possible to determine this parameter, hence we cannot compute the reduced χ^2 as defined here.

Second, we did not filter the objects considering their average SNR values (calculated by Gaia Collaboration et al. (2023)), but we noticed that the objects retained as potential analogues of EC 002 with the curve matching method show a median average SNR value of 17.2. This low value is explained by the fact that the reduced χ^2 we used has been mostly developed in the context of thermophysical modelling of asteroids, to determine the uncertainties of some parameters derived by the models (Press et al., 1986; Alí-Lagoa et al., 2014; Emery et al., 2014; Hanuš et al., 2015; Hanuš et al., 2018). It is not adapted as it is to compare asteroids with meteorites spectra, because of the aforementioned determination of the number of degrees of freedom. As it takes into account the error bars of the data, the largest the error bars of the Gaia DR3 spectrum, the lower the χ^2. Therefore, this χ^2 favours observations with large error bars, hence with low SNR. This noise in the data makes the value of the reduced χ^2 uncertain, according to Andrae et al. (2010). The curve matching using this parameter thus resulting in the filtering out of objects with higher SNR found by the spectral parameter method that appear to be good matches by visual inspection, such as asteroid (5121) Numazawa for example.

Since Galinier et al. (2023) has been published, I performed a deeper study of the Gaia DR3 asteroid spectra, presented on Chapters 2 and 5. These studies showed that DR3 spectra with average $\mathrm{SNR} \leqslant 20$ are often of too low quality to be considered good matches. For the present study, it means that the lower the SNR, the less likely it is that the asteroids we considered as potential matches for EC 002 with the curve matching method are real analogues.

Another curve matching could have been performed using the sum of squared residuals between the meteorite and the asteroids spectra, for example. The sum of the squared residuals is defined as

$$R^2 = \sum_{i}^{N} (A_i - f.M_i)^2, \tag{3.7}$$

with M_i the meteorite spectrum, A_i a Gaia asteroid reflectance spectrum and f a normalisation factor similar to the one in Eq. 3.6 but without consideration of the uncertainties. We calculated it for EC 002 and for the Gaia DR3 asteroids spectra, removing flagged bands and not taking the uncertainties into account.

This parameter gives potential matches of EC 002 among asteroids with a high SNR, and only spectra with a SNR$\geqslant$25 are selected as matches of the powder sample of the meteorite. Because of their higher SNR spectrum, these objects can be more trusted as potential analogues of the meteorite. Actually, most asteroids found as potential matches with this new R^2 plot inside the "possible matches area" of Fig.3.7, and their spectra were therefore already analysed. A limit of the R^2 is that it does not take the error bars of the data into account.

For the rest of this chapter, the asteroids found as potential matches of EC 002 with this R^2 were not analysed, as they overlap with those found with the spectral parameters method. The matches found with χ^2_{red} are still considered potential analogues of the meteorite, despite their low SNR DR3 spectra.

3.5.2 Proper orbital elements and asteroid families

If we still consider asteroids matching the spectra of EC 002 with the curve matching method as potential analogues, all matched asteroids with the non-space-weathered meteorite spectra are located in the Inner Main Belt (Fig. 3.8), between the secular resonance ν_6 and the 3:1 MMR with Jupiter. These two resonances are known to deliver efficiently material to the Near Earth space (Morbidelli et al., 2002; Granvik et al., 2016), and could be the source of EC 002, if some of these asteroids are really linked to the meteorite.

The asteroids matched with the space-weathered meteorite are more scattered across the Main Belt, even though most objects can be found in the Inner Main Belt as well, in particular close to the Vesta family (Fig. 3.9).

Some of the potential analogues of EC 002 are members of known collisional families, according to the membership of Nesvorny et al. (2015). Among the 142 matches of the different samples of EC 002, 23.9% of the asteroids belong to the Vesta family, 9.8% belong to the Flora family and a mere 7.7% belong to other families (mainly Nysa-Polana).

The presence of asteroids matching with EC 002 inside the Vesta family could have two main explanations. If these objects are true analogues of EC 002, they could be interlopers of the Vesta family, as EC 002 is chemically distinct from the HEDs (Barrat et al., 2021), which have been successfully linked to (4) Vesta and its family members, as described in Chapter 1. These asteroids could also be true members of the Vesta family, compositionally similar to HEDs, but with a Gaia reflectance spectrum in the visible wavelength range similar to that of EC 002.

In fact, distinguishing between the reflectance spectra of EC 002 and of HEDs in the visible range is difficult, and relies mainly on the position of the band around 1000 nm. However, the last Gaia bands can show a fast increase in reflectance (Gaia Collaboration et al., 2023; Galinier et al., 2023), and the position of the first silicate band of V-type asteroids might show a shift towards longer wavelengths, as evoked in Chapter 2. These two issues make it difficult to distinguish between a V-type spectrum and an

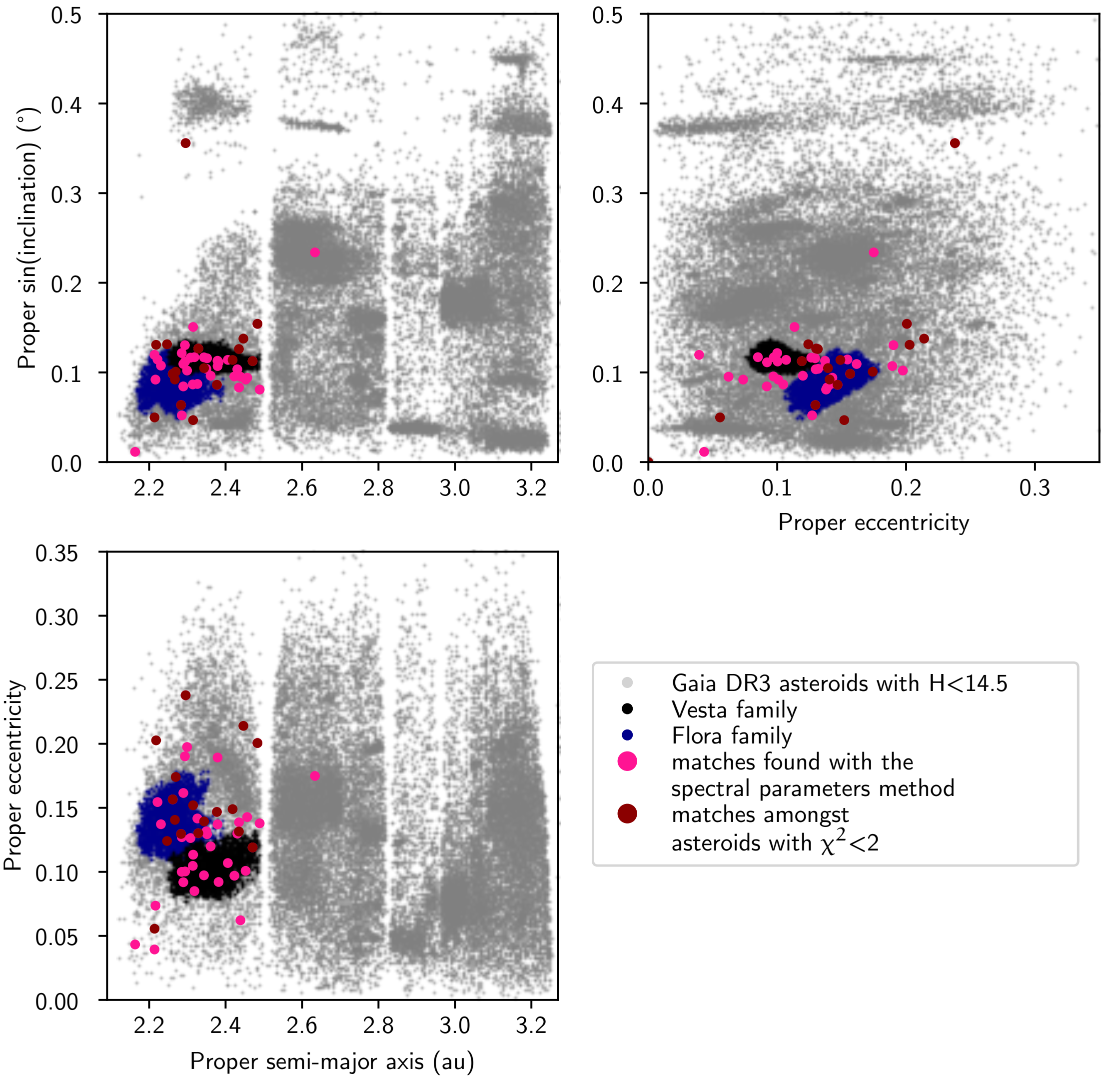

Figure 3.8: Proper orbital element plots of Gaia asteroids with absolute magnitude $H<14.5$ (light grey dots). Vesta and Flora family members are indicated respectively with black and blue dots. Asteroids that were found to be spectroscopically matching with EC 002 after visual inspection are plotted with dots circles indicated in the legend above. Proper orbital elements retrieved from the Belgrade catalogue `http://asteroids.matf.bg.ac.rs/fam/properelements.php`.

EC 002-like spectrum. Therefore, the objects identified here as potential analogues of the meteorite and belonging to the Vesta family might be V-types.

The Flora family is a large collisional family adjacent to the ν_6 secular resonance (Nesvorny et al., 2015), thus making it a potential important source of near-Earth asteroids (La Spina et al., 2004; Kryszczyńska, 2013) and meteorites (Nesvorný et al., 2002). This family is mainly constituted of S-type asteroids (Oszkiewicz et al., 2015; Nesvorny et al., 2015, and references therein), which have been linked to ordinary chondrites (Chapman, 1996). Considering that EC 002 formed by partial melting of a body of such non-carbonaceous chondritic composition (Barrat et al., 2021; Anand et al., 2022; Neumann et al., 2023; Sturtz et al., 2022), if the asteroids belonging to the Flora family are (i) true EC 002 analogues, and (ii) true members of the Flora

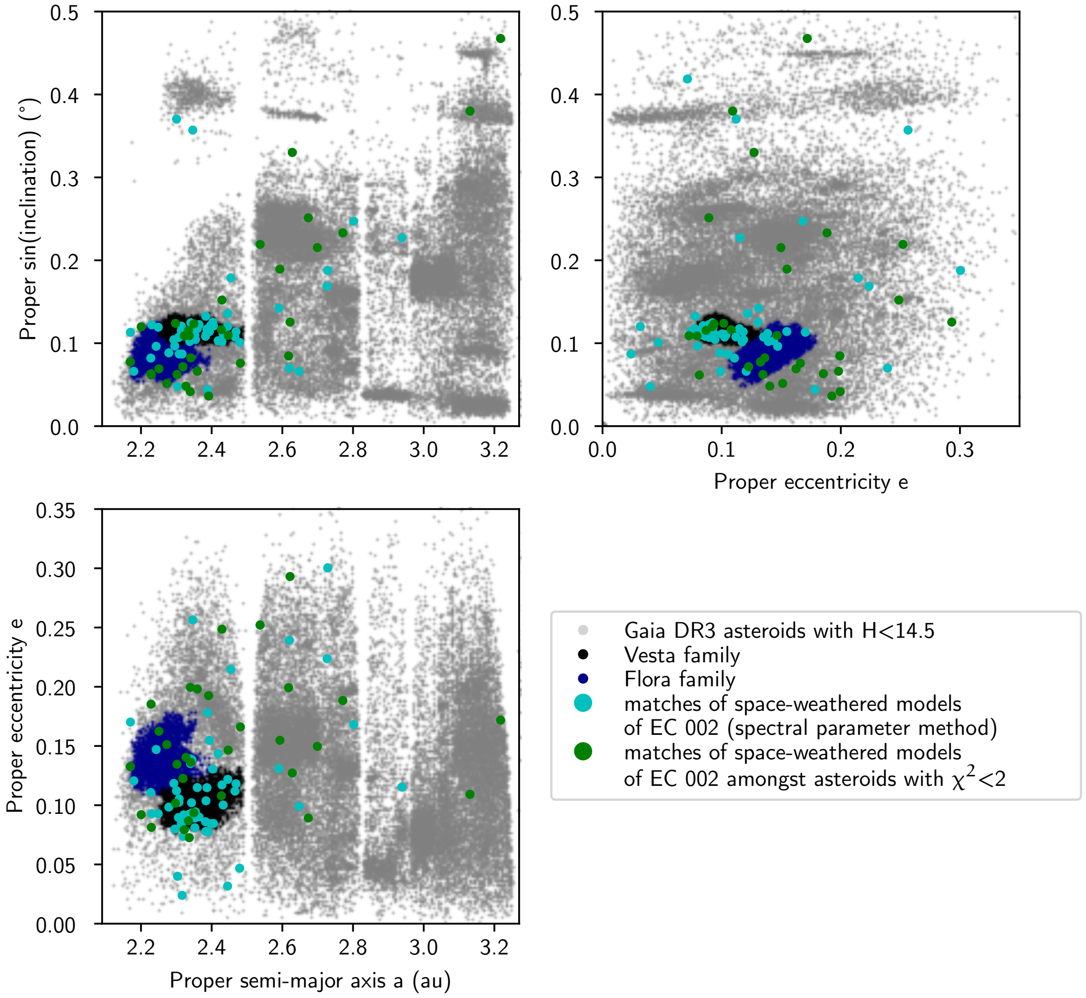

Figure 3.9: Same as Fig. 3.8, but with cyan dots indicating asteroids that have spectral parameters compatible with the space-weathered models of EC 002 derived by Barrat et al. (2021) in the spectral parameters space. The green dots are asteroids matching the weathered models of the meteorite spectra using the curve matching method.

family, this would confirm the spectroscopic diversity within this family pointed out by several studies (Oszkiewicz et al., 2015, and references there in). In addition, this would potentially point towards a differentiation of the family parent body, as has been already proposed (Oszkiewicz et al., 2015). However, these asteroids could also be S-complex asteroids belonging to the Flora family, or interlopers V-type asteroids sharing similar proper orbital elements to the family members; as many V-type asteroids orbit in the Inner Main Belt, part or not of the Vesta family (Oszkiewicz et al., 2023).

Given the small number of asteroids belonging to the other asteroid families, it is difficult to assume that the parent body of EC 002 belonged to any of these families. The other asteroids potentially matching with EC 002 do not belong to known families. However, as described in Chapter 1, current family catalogues are based on algorithms such as the HCM that determine an object's membership of a family based on its proper orbital elements only, in order to distinguish between different families and clearly identify their cores (Milani et al., 2014; Nesvorny et al., 2015; Tsirvoulis et al., 2018). This results in background asteroids interlopers within families, and true family members lost in family halos (Parker et al., 2008; Brož and Morbidelli, 2013). Therefore, the asteroids potentially matching with EC 002 and not designated as family members in Nesvorny et al. (2015) could still be members of some of the known families.

In addition, the study of the dynamical behaviour of family and non-family members by Dermott et al. (2018) lead to the conclusion that most asteroids in the IMB are or were originally part of the main known families, showing evidence that some families are very dispersed. Some of these dispersed families have been detected using the V-shape method, and more are probably left to be identified (Dermott et al., 2018; Bolin et al., 2017; Delbo et al., 2017; Delbo et al., 2019; Ferrone et al., 2023). Hence, it is possible that the asteroids matching with EC 002 that are not listed as family members are part of old families of the IMB that escaped identification so far.

3.5.3 The band around 650 nm

A characteristic feature of the EC 002 reflectance spectrum is the presence of an absorption band at 650 nm. We tried to take this band into account in the search for asteroids spectra matching the meteorite's. Unfortunately, this feature cannot be used as an absolute diagnostic feature in Gaia DR3 asteroid spectra, because it is the region where the BP and RP spectra overlap. Since the spectrophotometers are independently calibrated (De Angeli et al., 2023), their overlapping region can be affected by artefacts (Gaia Collaboration et al., 2023) and must be handled with care (see the "fake band" in Chapter 2).

There is however an object displaying an absorption band near 650 that has been identified in the Main Belt: asteroid (10537) 1991 RY16 (Moskovitz et al., 2008). Its spectrum as been designated as unique, and this asteroid is thought to be coming from a partially or fully differentiated parent body (Moskovitz et al., 2008). Interestingly, its visible reflectance spectra and the one of EC 002 are quite similar, as can be seen in Fig.3.10.

According to Moskovitz et al. (2008), the absorption band around 650 nm of asteroid (10537) 1991 RY16 has several possible explanations. First, this band can be due to iron charge transfers between Fe^{3+} and Fe^{2+}. Indeed, crystal field transitions in the pyroxene structure can lead to absorption features, that could result in an absorption band around 650 nm. Another possibility is the presence of chromium, especially in its Cr^{3+} form, as chromium-bearing pyroxenes create large absorption features around 630 nm, when present in large quantities (Moskovitz et al., 2008). This is the most plausible explanation for the presence of the band (Cloutis et al., 2018). Finally, when chromium is present in spinel, it can exhibit absorption features due to electronic transitions of Cr^{3+}. Transitions of Fe^{2+} and Cr^{3+} however often result in the appearance of other absorption bands, such as features around 550, 590, 690, or 2000 nm (Cloutis et al., 2004). The last possibility would be a combination of all these effects generating the 650 nm band in the spectrum of (10537) 1991 RY16.

This asteroid has been found the closest match to the ungrouped achondrite North-West Africa (NWA) 7325 by Cloutis et al. (2018), based on the spectral features of both bodies. It is however not a satisfactory match, since the absorption bands are more consistent with low-calcium pyroxene in the asteroid, and the meteorite shows high-calcium pyroxene contents (Cloutis et al., 2018). From their visible spectra and the

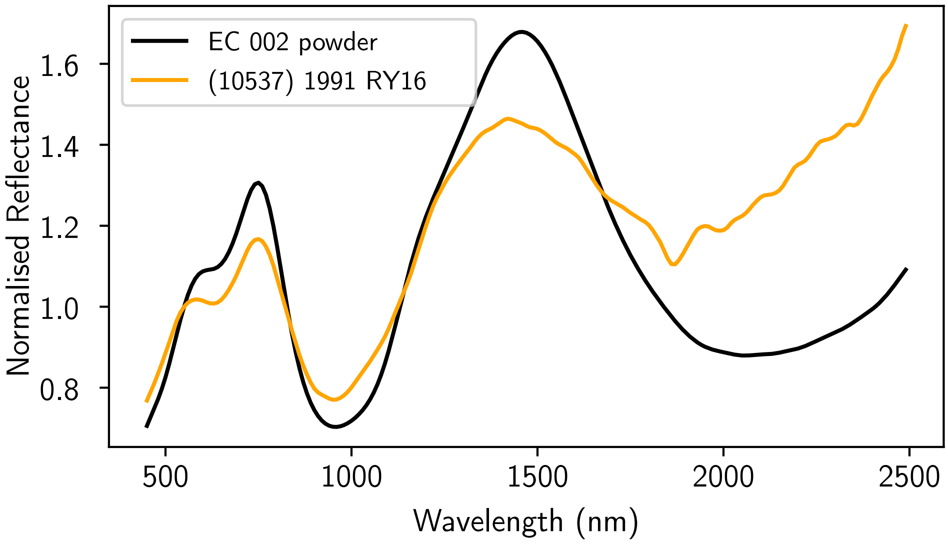

Figure 3.10: VISNIR spectra of the powder sample of EC 002 (black lines) and of asteroid (10537) 1991 RY16 (orange lines) retrieved from Fig.1 of Moskovitz et al. (2008). Both spectra were normalised at 550 nm. The two spectra show a similar shape, both showing a band around 650 nm and similar Band I centre. Their Band II centre appears shifted.

presence of the 650 nm band, (10537) 1991 RY16 could be a better match for EC 002, especially knowing that EC 002 contains low-Ca pyroxene (Barrat et al., 2021). This asteroid will thus be considered for the rest of the analysis.

To summarise, we searched for analogues of the andesitic meteorite EC 002 among the asteroid population, using Gaia visible reflectance spectra. We studied four different laboratory samples of the meteorite (three raw slabs and one powder spectrum), and three modelled space-weathered spectra. Only 0.08% of Gaia asteroids were found to be matching the laboratory samples of the meteorite, and 0.15% were found matching the modelled space-weathered spectra. Acquiring and studying the NIR spectra of these objects could help determining if they are real analogues of EC 002 or not. Therefore, we performed observations of a selected sample of objects, potentially analogues of the meteorite.

3.6 OBSERVATIONS IN THE NIR WAVELENGTH RANGE

We obtained 23 hours and 20 minutes of observations with the Nasa Infrared Telescope Facility (IRTF) in the second semester of 2023. Among the 51 potential analogues of the meteorite without space weathering, 25 were observable at that time. Among the 71 asteroids matching the low space weathered modelled spectrum of EC002, 19 were observable ; and only 4 and one asteroids were observable respectively among the 17 and 3 asteroids matching with the medium and low space weathered modelled meteorite spectra.

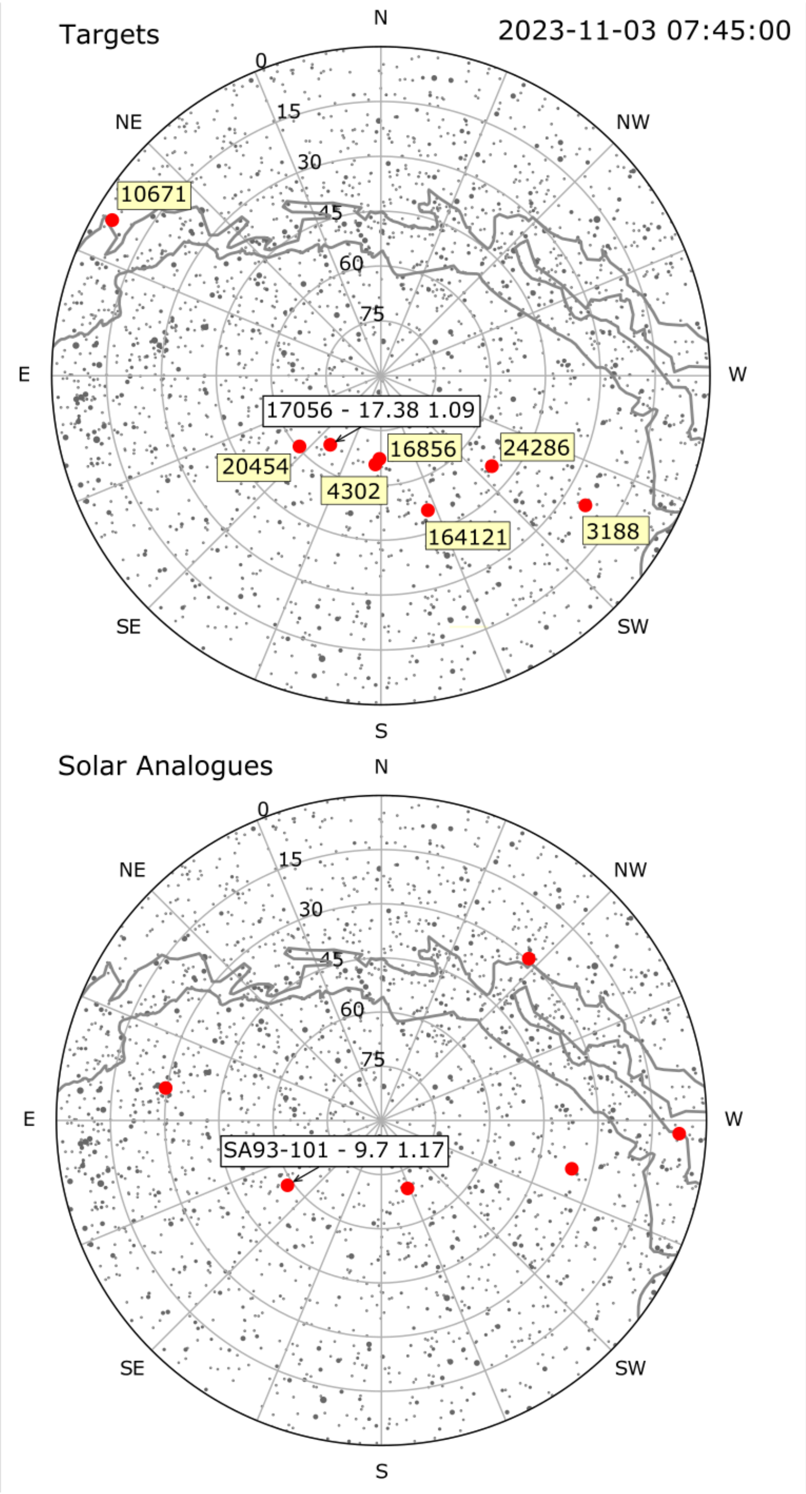

Figure 3.11: Observable asteroids with the IRTF on the night of November 11, 2023. This is a snapshot of the sky as seen by the IRTF at the beginning of our observation run, the date and time being indicated in UTC on the top right corner. The potential analogues of EC 002 without space weathering observable on that night are displayed as red dots, and their numbers are indicated in yellow boxes. In the white box is indicated the name of the pointed target, along with its V magnitude, and an idea of the seeing of the observation.

3.6.1 Target selection

To prepare the observations, we had to determine a list of objects observable on each of our allocated nights. To do so, we checked the position of each potential analogue of EC 002 on the sky observable from Mauna Kea, and having a V magnitude lower than 18. We used a code developed by Marco Delbo, allowing to place the objects on the sky as seen from the IRTF at a given time on a given night, along with theposition of the Milky Way and the Moon.

For example, on the night of November 2, 2023, there was 14 potential analogues of EC 002 observable. Among the 8 asteroids potentially matching the non-space-weathered spectrum of the meteorite and displayed in the top plot of Fig.3.11, (16856) Banach, (17056) Boschetti, (20454) Pedrajo had not been observed already and showed good observation conditions (low seeing, far from the Milky Way). Among the four asteroids potentially matching the low space weathered meteorite spectrum, we could characterise (27884) 1996 EZ1 and (17739) 1998 BY15. Only one asteroid potentially matching the medium space weathered meteorite was observable, asteroid (31060) 1996 TB6; and asteroid (9974) Brody was observable as a potential match of the highly space weathered meteorite. (16856) Banach and (9974) Brody were discarded because of the low average SNR of their DR3 spectrum. The final list of observable asteroids on that day consisted of (17056) Boschetti, (20454) Pedrajo, (27884) 1996 EZ1, (17739) 1998 BY15, and (31060) 1996 TB6.

During the observations, a solar analogue star had to be observed in similar conditions (similar airmass and time) to those of each observed asteroid. Solar analogues are commonly defined as stars with solar-like temperatures (temperatures within $\simeq 500K$), solar metallicities (metallicity within a factor 2 of the Sun's), and without any close companion (Marsset et al., 2020). In practice, solar analogue stars are observed in order to remove the solar contribution from the asteroid spectra (solar slope) during the data reduction phase, by calculating the ratio between the light reflected by the asteroid and the stellar spectrum, to obtain the asteroid reflectance spectrum. Observing the solar analogue in the same conditions as the asteroid's and through the same instrumentation allows to cancel most variations due to the detector response function and to the optical transmission function in the asteroid spectrum (Marsset et al., 2020; Binzel et al., 2019). For our purpose, solar analogue stars are required to have a spectrum similar to the Sun's in the NIR wavelength range.

For the night of November 2, the solar analogue SA93-101 was selected as the best solar analogue given its position in the sky throughout the night. The position and V magnitude of this solar analogue are indicated in the bottom plot of Fig.3.11. In general, a G2V-type star (the solar type) has to be observed close to the target to correct for telluric lines when producing the asteroids spectra, and a solar analogue star observed around 1 airmass is used to correct the slope of the spectra. On the night of November 2, no such G2V star was needed, as the solar analogue was located close to the target.

During the second semester of 2023 we observed 20 asteroids in total with the IRTF, with asteroid (24286) 1999 XU188 that we observed twice. The complete list of objects observed, the date of the observation and associated parameters is displayed in Table 3.3. Most observed asteroids were matches with the non-space-weathered powder spectrum of the meteorite, 7 were matched with the low space-weathered modelled spectrum, and only one was matched with the medium space weathering. A brief description of the telescope and instruments we used is provided in the following.

3.6.2 Instruments

Nasa IRTF is a 3 meters telescope located in Mauna Kea, Hawaii, used since May 2000. It is optimised for the spectroscopic characterisation of faint targets in the infrared wavelength range. Half of its time is dedicated to the observation of Solar System objects, and it was used to perform large asteroids surveys, such as SMASS and MITHNEOS, resulting in a large database of asteroids spectra (Binzel et al., 2019).

Among the instruments mounted on the IRTF, SpeX and MORIS were used for our observations. SpeX is a near-infrared spectrograph and imager covering the wavelength range from 700 to 5300 nm, with a medium resolution (resolving power R $\simeq$ 50 - 2500) (Rayner et al., 2003). This instrument provides a range of observing modes, among which the low resolution prism mode (R $\simeq$ 200) used for the spectroscopic observations of faint targets (Marsset et al., 2020; Rayner et al., 2003). This mode spans the wavelength range from 700 to 2 520 nm (SpeX manual), which covers features in the spectra diagnostic of the presence of ice or minerals. It allows the spectroscopic characterisation and investigation of the surface composition of asteroids. We used a spectroscopic slit of 0.8 x 15 arcsec.

The MIT Optical Rapid Imaging System (MORIS) is an Andor CCD guiding camera mounted on SpeX (Gulbis et al., 2011), which allows to guide the telescope on objects having V magnitudes as low as 20, as it guides on the full visible signal of the target. For our observations, a dichroic reflector of 0.7 nm was used for the spectrograph, in order to redirect the light of faint targets to the CCDs of MORIS.

The spectra were acquired in ABBA pairs of exposures, to take into account background flux from the night sky. This background flux can then be subtracted to the asteroids' spectra in the processing, by alternating image frames between the A and B positions on the slit (Binzel et al., 2019). Observation of solar analogue stars was done in ABBA cycles as the asteroids', and the guiding was achieved by the GuideDog instrument, which allows a guiding on the spillover flux surrounding a target in the slit of the spectrograph. Once per night, we took calibration frames, that are useful for the bias and flat-field corrections (Popescu et al., 2014a). The image of a surface uniformly illuminated by a lamp was taken, in order to do flat field corrections, to get rid off systematic errors and to reduce distortions in the optical path in order to get a uniform output. An argon lamp was used for the wavelength calibrations, as argon gas has a characteristic spectrum that provides clear spectroscopic emission lines to take as reference wavelengths.

We tried to observe objects far from the Milky Way, and close to the zenith at their highest altitude, so that the atmospheric turbulence and the airmass (the length of the path in the atmosphere the light has to go through) are minimised. The airmass at the moment of the observations is indicated in Table.3.3.

3.6.3 Reduction

The observations were reduced using Spextool, an Interactive Data Language (IDL) spectral reduction tool provided by the IRTF. This tool allows the production of re-

Table 3.3: Table of observations of potential analogues of EC 002. Thee table includes object number, the match type (space weathering or not), the proper orbital elements of the asteroids (semi-major axis, eccentricity and inclination), the geometric albedo, the magnitude in the V band, the date of the observations, and the airmass.

Asteroid	Match type	a_p (au)	e_p	$\sin(i_p)$ (°)	pV	Vmag	Date (UT)	Airmass
1643	no SW	2.4892	0.1379	0.0809	0.18	17.4	28-01-2024	1.1
1946	no SW	2.2936	0.1902	0.1304	0.362	16.3	28-01-2024	1.111
3188	no SW	2.2894	0.0919	0.0844	0.425	16	29-07-2023	1.43
3869	no SW	2.4524	0.1008	0.092	0.16	17.9	08-03-2023	1.8
4302	no SW	2.4565	0.1428	0.0941	0.26	17	08-12-2023	1.1
6003	low SW	2.3444	0.0935	0.1116	-	17.4	08-03-2023	1.3
6789	low SW	2.338	0.1392	0.1021	-	16.8	08-12-2023	1.251
8827	no SW	2.3142	0.1047	0.0866	-	16.9	08-12-2023	1.26
10671	no SW	2.4351	0.1387	0.0832	0.25	16.8	18-12-2023	1.029
12551	no SW	2.423	0.097	0.0955	-	16.5	02-02-2023	1.22
14511	low SW	2.3833	0.0779	0.1325	0.287	17	03-10-2023	1.286
15989	no SW	2.3262	0.1417	0.0871	0.609	17	28-01-2024	1.185
17056	no SW	2.2142	0.0556	0.0498	0.34	17.4	03-11-2023	1.073
18780	low SW	2.2293	0.0813	0.0617	-	17.1	03-10-2023	1.407
20454	no SW	2.4707	0.1191	0.1126	0.257	17.6	03-11-2023	1.068
24286 (a)	no SW	2.2992	0.1975	0.1021	-	17.2	29-07-2023	1.42
24286 (b)	-	2.2992	0.1975	0.1021	-	17.2	03-10-2023	1.291
27884	low SW	2.3643	0.0901	0.1224	0.389	17.3	03-11-2023	1.084
30426	low SW	2.4184	0.1436	0.103	0.301	17.6	08-12-2023	1.08
31060	medium SW	2.7283	0.3004	0.1878	0.38	15.5	03-11-2023	1.119
45787	low SW	2.4325	0.1002	0.1112	0.613	17.6	08-12-2023	1.16

Note: SW stands for space weathering.

flectance spectra after a flat-field correction, where the contribution of the background sky is removed thanks to the ABBA cycle procedure, and a wavelength calibration (Rayner et al., 2003). The data reduction is done in three steps (Popescu et al., 2014a): first, the raw asteroid and solar analogue spectra are retrieved. Then, the asteroid spectrum is divided by the corresponding solar analogue spectrum, and the reflectance spectrum is normalised. Finally, telluric lines are corrected. The asteroid reflectance spectrum $R(\lambda)$ is thus obtained Eq. 3.8:

$$R(\lambda) = \frac{A(\lambda)}{S_L(\lambda)} \times Poly\left(\frac{S_L(\lambda)}{S_T(\lambda)}\right), \tag{3.8}$$

where $A(\lambda)$ is the wavelength-calibrated raw spectrum of the asteroid, $S_L(\lambda)$ is the wavelength-calibrated raw spectrum of the local G2V star observed within ~300" of the asteroid, and $S_T(\lambda)$ is the wavelength-calibrated raw spectrum of the selected well-studied solar analogue star observed at a similar airmass to the asteroid. In general, the local solar analog star guarantees the accuracy of telluric line removal, but the difference between the spectrum of the local star and that of the Sun may require a correction of the spectrum's slope defined as $Poly\left(\frac{S_L(\lambda)}{S_T(\lambda)}\right)$. The $Poly()$ function represents a polynomial fit of the ratio of the stars spectra. The regions of the spectra affected by telluric features, corresponding to $1300 < \lambda < 1500$, $1780 < \lambda < 2100$, and $\lambda > 2400$ nm, are excluded. Finally, for the asteroid spectrum to be aligned with the calibration star spectra, the asteroid's spectra were shifted to sub-pixel accuracy (Avdellidou et al., 2022; Galinier et al., 2024). In case the local G2V star was not observed, the asteroid's spectrum was directly divided by the well-studied solar analogue's spectrum, following $R(\lambda) = \frac{A(\lambda)}{S_T(\lambda)}$. This insures the correction of telluric lines (Avdellidou et al., 2022).

3.7 ANALYSIS OF THE OBSERVATIONS

In the following, the NIR asteroid spectra are classified using two online classifiers based on the Bus-DeMeo and the Mahlke taxonomic schemes respectively, in order to get a first idea of the composition of these objects. Then, these NIR spectra are combined with the Gaia DR3 visible spectra, and the obtained full spectra are compared with EC 002's laboratory spectra through the calculation of specific spectral parameters, characteristic of the objects' composition.

3.7.1 Classification of the observed spectra

As presented in Chapter 1, classifying asteroid spectra allows to get a first idea of their potential composition, prior to comparing them with meteorites spectra. Therefore, the 21 NIR spectra of the 20 asteroids were classified using online classifiers, Modeling for ASTeroids (M4AST) and CLAssification of a Solar System bodY (classy). These spectra were classified considering their NIR part only.

M4AST is a public software tool developed by Popescu et al. (2012) that provides a set of tools for analysing asteroid reflectance spectra, such as a classifier, a comparison with laboratory and meteorite spectra, a mineralogical analysis and space weathering models. It was used here to classify the observed asteroid spectra in the Bus-DeMeo taxonomic scheme (DeMeo et al., 2009), using a mean squared error parameter to

Table 3.4: Classification of the observed asteroids with online classifiers, M4AST and *classy*. The first best three classes given by M4AST are indicated, the first class written being the best one. The two observed spectra of (24286) 1999 XU188 are designated as (a) and (b).

Asteroid	M4AST	classy
(1643) Brown	V, R, Sv	V
(1946) Walraven	V, R, Sv	V
(3188) Jekabsons	V, Sv, R	V
(3869) Norton	V, Sv, R	V
(4302) Markeev	V, R, Sv	V
(6003) 1988 VO1	V, Sv, R	V
(6789) Milkey	V, R, Sv	V
(8827) Kollwitz	V, R, Sv	V
(10671) Mazurova	R, V, D	V
(12551) 1998 QQ39	D Sq T	S
(14511) Nickel	V, Sv, R	V
(15989) Anusha	V, R, Sv	V
(17056) Boschetti	V, Sv, R	V
(18780) Kuncham	Sr, Sq, S	S
(20454) Pedrajo	V, Sv, R	V
(24286) 1999 XU188 (a)	V, R, Sv	V
(24286) 1999 XU188 (b)	V, Sv, R	V
(27884) 1996 EZ1	D A Sa	Z
(30426) Philtalbot	V, Sv, R	V
(31060) 1996 TB6	A, Sa, D	A
(45787) 2000 OJ24	V, Sv, R	V

perform the curve matching between the Bus-DeMeo template spectra and the observed spectra. Using this tool was justified by the fact that the spectra cover the NIR wavelength range, as the Bus-DeMeo taxonomy. M4AST gives the first three best taxonomic classes corresponding to an asteroid spectrum, which are indicated for each characterised asteroid in column M4AST in Table.3.4 from the best to the third best class.

The tool *classy* was designed by Mahlke et al. (2022) to analyse and classify asteroid spectra in various taxonomic schemes. It was used here to classify our observed reflectance spectra in the scheme of Mahlke et al. (2022), as it covers the NIR wavelength range and it offers a comparison with the results obtained with the Bus-DeMeo scheme. The results are indicated in Table.3.4. We can notice that every asteroid is classified the same way with both methods and taxonomic schemes: most asteroids are classified as V-type as first best classes. The exceptions are asteroids (10671) Mazurova, classified as R as first best class with M4AST. However, this asteroid showing a noisy spectrum, it is more likely to be a V-type from visual comparison with Bus-DeMeo template spectra. It will be considered a V-type in the following. Given their taxonomic type, these objects are likely of basaltic-rich composition.

Asteroid (18780) Kuncham is found Sr, Sq, or S-type with M4AST, and S-type with *classy*. It will be considered a S-complex object in the following, and it is likely a silicate-rich asteroid. Finally, (31060) 1996 TB6 is an A-type asteroid, that designates it as olivine-rich. According to their classification, none of these objects appear a good analogue of andesitic EC 002.

All the observed asteroids are highlighted in the spectral parameters plot in Fig.3.12. Their position in the spectral parameters space is coherent with their assigned classification from their NIR spectra. The two asteroids (12551) 1998 QQ39 and (27884) 1996

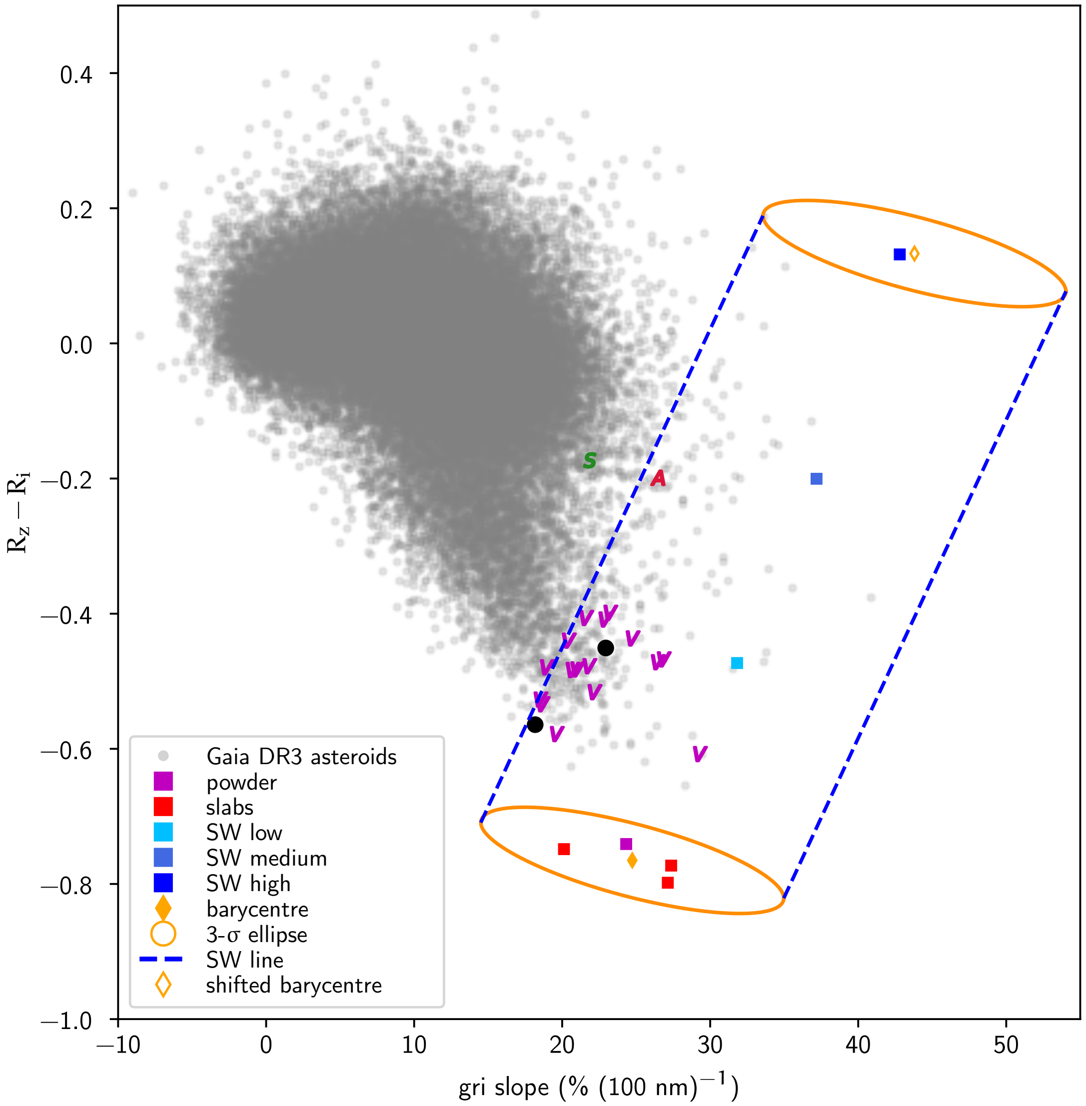

Figure 3.12: Distribution of depth of the band around 1000 nm with respect to the spectral slope of every Gaia asteroid (grey dots). See Fig.3.5 for the legend. The asteroids classified here as V-types are highlighted with a magenta V, and the asteroids respectively classified as S and A are shown with a green S and a red A. The two asteroids (12551) 1998 QQ39 and (27884) 1996 EZ1 are shown as black dots, as their NIR spectra did not allow a good classification.

EZ1 show peculiar spectra, the second one appearing very red. They are shown as black dots in Fig.3.12, and should be classified as V-types according to their DR3 spectra. These objects will be further discussed in the following section.

3.7.2 Producing VISNIR spectra

First, the visible Gaia DR3 spectra were combined with the observed NIR spectra. To do so, NIR spectra were resampled between 690 and 2400 nm, with 5 nm steps, and were normalised at 1000 nm. The spectra were not taken into account after 2400 nm, as they can show large errors due to the detector limits after this wavelength. Connecting the DR3 and the NIR spectra using a rescaling of the NIR spectrum to match the visible spectrum in a given wavelength interval in an automated way (Christou et al., 2021; Popescu et al., 2019) was attempted, but it did not give satisfactory results for most asteroids. It resulted in a shift towards high reflectance values for most NIR spectra, leading to a change in the depth of the band around 1000 nm and in the band area ratio.

As these parameters are important for the meteorite and asteroid comparison, the DR3 and NIR spectra were merged by applying a multiplicative factor α to the NIR spectra normalised at 1000 nm, to align them with their corresponding DR3 spectra normalised at 550 nm. The α factor was chosen arbitrarily, depending on the satisfaction of the visual alignment of the VIS and NIR spectra. The arbitrarily aligned spectra are displayed in Fig.3.13. In some cases, the factor was left to unity, when the alignment was visually satisfying (asteroid (1643) Brown for example), or when no value of the factor seemed to improve the alignment (asteroid (12551) 1998 QQ39 for example).

The spectra of (12551) 1998 QQ39 and (27884) 1996 EZ1 show an unexpected discontinuity between their VIS and NIR part. There is no clear explanation regarding these spectral discontinuity, as their DR3 spectra appear good. There is a possibility that these targets have been mistaken with another object during the observations, so they were discarded out of the analysis. Their taxonomic type defined above should thus not be trusted.

3.7.3 Spectral features analysis: BIC and BAR

According to Gaffey (2011), linking asteroids with meteorites spectra with the means of curve matching is not the most reliable technique, because the best match of a spectrum may not always be a good match. Indeed, many phenomena influence the slope and features of spectra, such as grain size, the geometry of the observations (phase angle), the shape of the body or its temperature. Curve matching might thus find similarities between spectra not always representative of the compositions of the bodies, because of the actions of these phenomena (Gaffey, 2011).

As previously discussed, taking into account the effects on space weathering on asteroids spectra is important to link them with meteorites, as it darkens and reddens silicate materials' spectra. However, determining the corrections to apply to an asteroid spectrum to take space weathering into account is not trivial, as it appears to affect asteroids differently depending on their mineralogic composition (Gaffey, 2011; Marchi et al., 2010; Fulvio et al., 2012; Brunetto et al., 2015; Zhang et al., 2022, e.g).

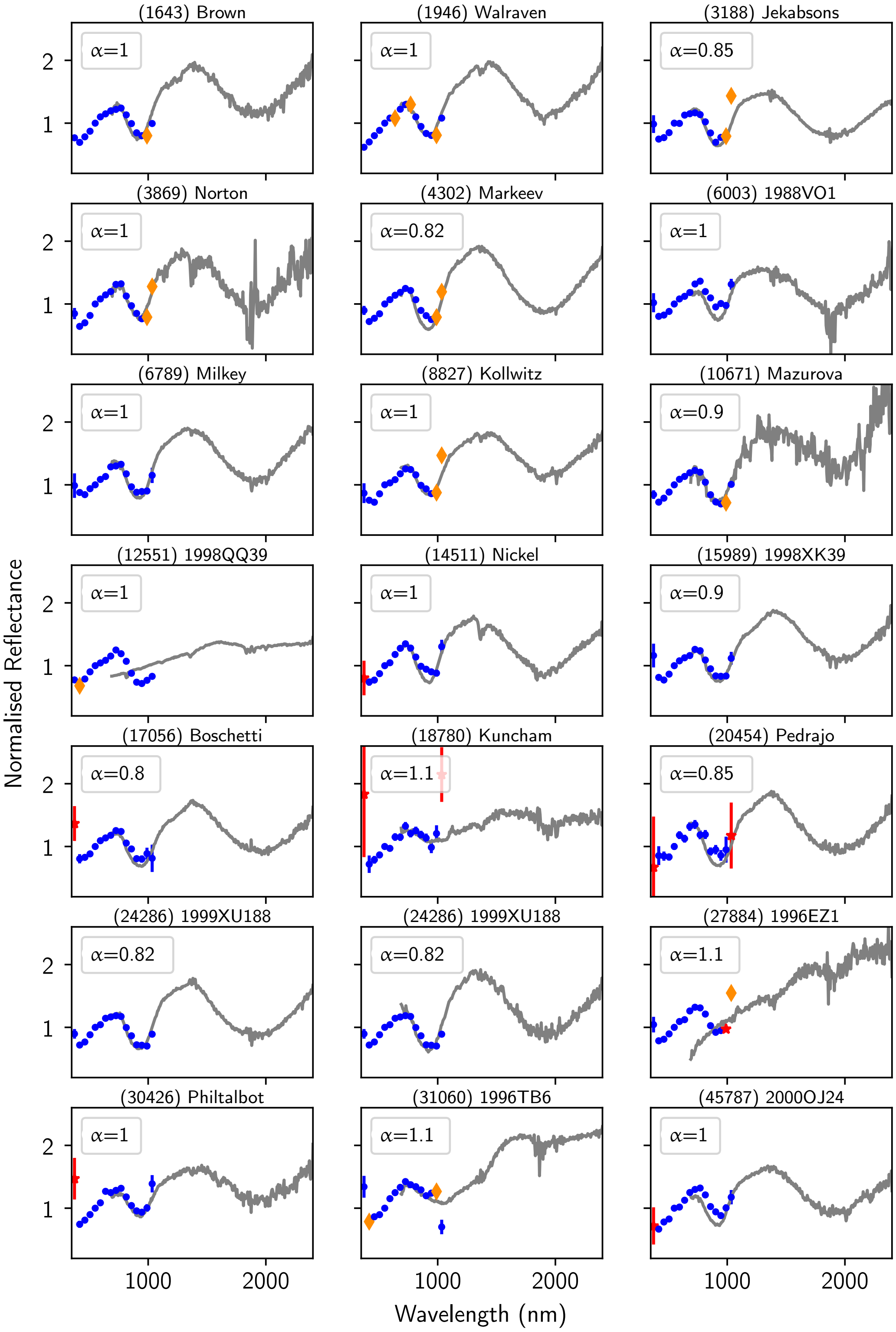

Figure 3.13: NIR (grey lines) and DR3 spectra of the observed asteroids. Their designation is in the title, and the multiplicative factor applied to each NIR spectrum to align it with the VIS spectrum is in the legend of each sub-figure. The 16 bands of Gaia spectra are assigned a colour and symbol according to their flag value: blue circle if flag=0,orange diamond if flag=1 and red star if flag=2.

A way to link asteroids and meteorites is to focus on the diagnostic features of the spectra. The presence and position of the bands around 1000 and 2000 nm (Band I Centre (BIC) and Band II Centre (BIIC)), and the BAR of spectra presenting strong features appear insensitive to space weathering (Brunetto et al., 2006; Gaffey, 2010). The band centres are directly related to the mineral composition of an object (Gaffey, 2011).

To compare the spectra of the asteroids we observed with the ones of EC 002, the centre of the band around 1000 nm (BIC) and the BAR for the EC 002 spectra was calculated for the 18 observed asteroid spectra that do not show a discrepancy between their VIS and NIR spectra. According to Gaffey (2011), the band centre is located at the maximum absorption in the feature. It should not be confused with the band minimum, that is aligned with the band centre in case the background continuum is flat, but that is shifted in case the continuum has a slope (as it is our case here). In order to calculate the BIC, I made the assumption of a linear continuum of the spectra following Gaffey (2011), that was removed using a convex hull fit (*scipy* ConvexHull function). Mathematically, the convex hull of a shape is the smallest convex set that contains the shape. Here, straight line segments are used to connect the local spectra maxima, in order to fit the continuum of the spectrum. Then, the reflectance spectra are divided by their continuum, after interpolating the convex hull at the wavelength of the spectra. The obtained continuum-less spectra have values equal to 1 when the continuum and the spectra match, and lower than 1 at the position of absorption features.

The convex hull fit was performed on the full VISNIR spectra arbitrarily linked (see Fig.3.13). The first two and last two bands of the DR3 spectra were not taken into account, often affected by systematic issues (Gaia Collaboration et al., 2023; Galinier et al., 2023), thus the visible spectra were considered between 462 and 946 nm only. The part of the NIR spectra after 2400 nm was not taken into account. An example of spectrum before and after continuum removal is displayed in Fig.3.14 for (1643) Brown.

The Band I Center was calculated by fitting a second order polynomial (using *nympy*'s *polyfit* function) to the first absorption band on the continuum-removed spectra. For V-type asteroids such as (1643) Brown, the curve was fitted from 750 to 1100 nm, as this wavelength range appeared to give the best fits. The Band I Center was then calculated using the parameters of the polynomial fit: its equation being $y = ax^2 + bx + c$, the band centre was determined as the continuum-removed band minimum $y0 = \frac{-b}{2a}$. An example of band fitting is shown in Fig.3.15 for (1643) Brown. The parameters of the fit are displayed in the red square in the figure.

In order to determine the band area ratio, the continuum-removal spectra were flipped upside-down by calculating 1 - continuum-removed spectrum. The first ten data points of the spectra were not considered, as they are not exactly at zero, and considering them would increase the first absorption band's area. Defining the wavelength limit separating the two bands at 1350 nm for V-type asteroids gave satisfactory results, as can be seen on Fig.3.16 for (1643) Brown. The band areas were computed by calculating the area under each band using the trapeze methods, integrating along the parametric curve (*numpy*'s *trapz* function).

For (1643) Brown, the obtained parameter values are BIC = 930.7 nm and BAR = 2.1. This procedure was applied to every V-type spectra, but could not be applied

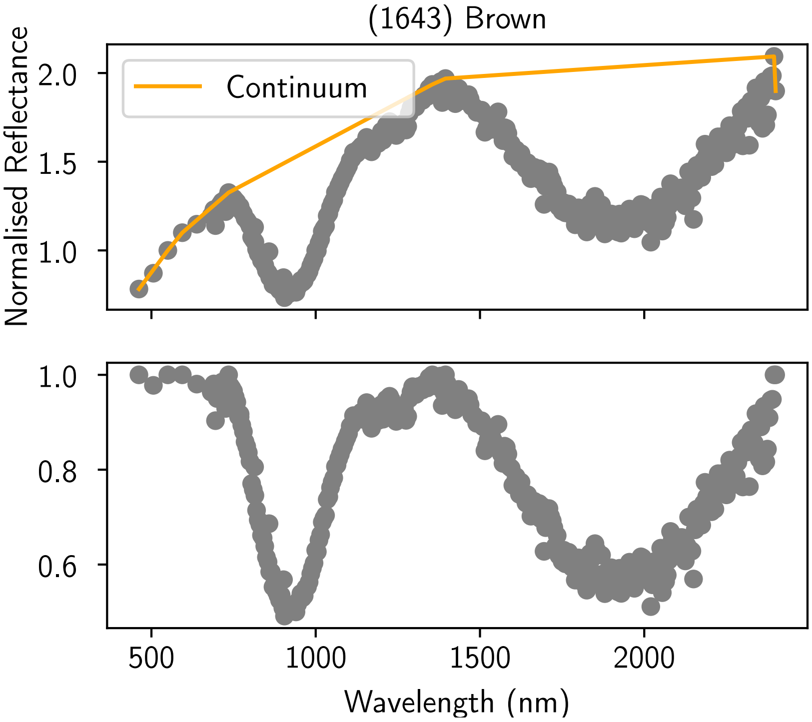

Figure 3.14: VISNIR spectrum of (1643) Brown, before and after continuum removal with a convex hull fit. The spectrum is displayed in grey dots, the continuum fit in orange lines.

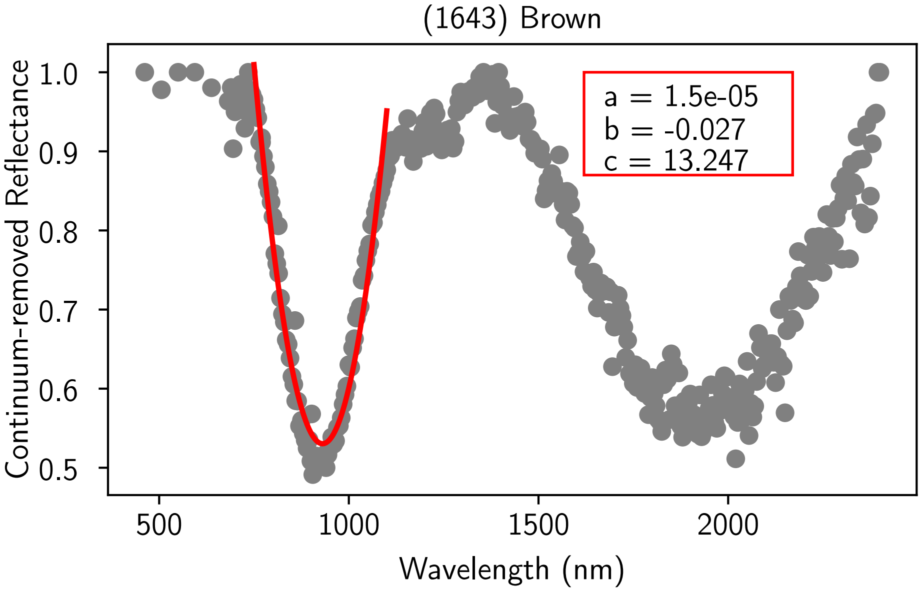

Figure 3.15: Second order polynomial fit of the 1 micron band on the continuum-removed spectrum of (1643) Brown. The polynomial fit parameters are displayed in the red box, the equation of the fit being $y = ax^2 + bx + c$.

identically to other spectral types, because of their shape differences. The method was thus adapted for asteroids (18780) Kuncham and (31060) 1996 TB6.

To fit the second degree polynomial to the first absorption band of S-complex asteroid (18780) Kuncham, the wavelength range from 750 to 1200 nm was considered.

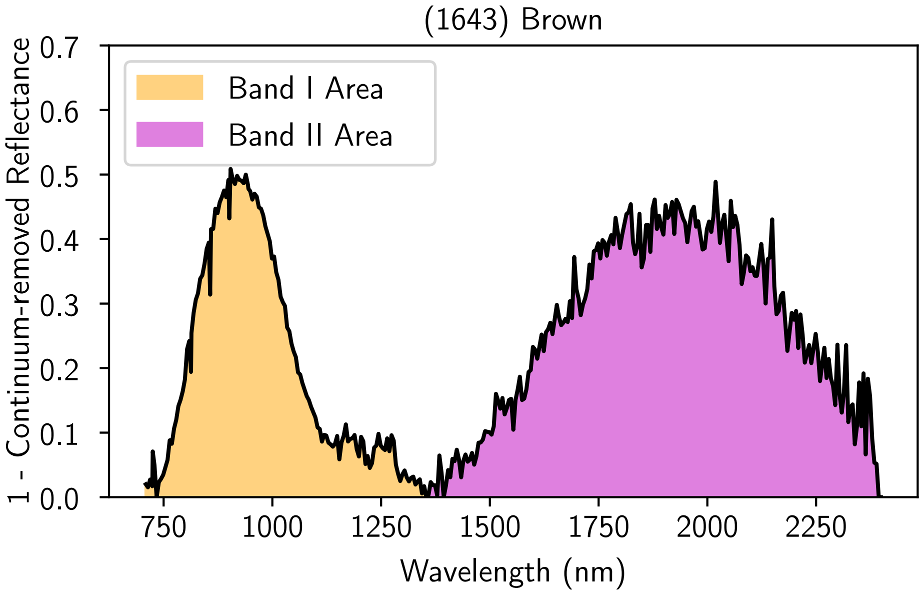

Figure 3.16: Band areas of the first and second bands of the continuum-removed spectrum of (1643) Brown.

The Gaia visible part of this spectrum was not taken into account in the calculatation of the band area ratio, because since it is noisy, the flipped continuum-removed spectrum is not exactly at zero in the visible wavelength range. Considering this part of the spectrum would like to an increase band I area. The limit between the two bands was defined at 1550 nm. For the A-type asteroid (31060) 1996 TB6, the second degree polynomial was fitted to the first absorption band considering the wavelength range from 700 to 1500 nm, given that the Band I of A-types is wider than the one of V-types. To calculate the band area ratio, the limit between the two bands was defined at 1700 nm. Each step for both asteroids is presented in Fig.3.17. As a remark, the noisy spectrum of (18780) Kuncham might have an influence on the BIC and BAR calculation.

On Table.3.5 are displayed the calculated BIC and BAR for each considered spectrum. Since the goal is to compare the acquired asteroid VISNIR spectra to the ones of EC 002, the same BIC and BAR parameters were calculated for the powder and three slabs spectra of the meteorite. For each spectrum, the wavelength range from 750 to 1150 nm was considered to perform the polynomial fit, and the wavelength separating the first from the second absorption band was set at 1450 nm. The BIC and BAR values obtained for each sample are, for the powder, slab 1, slab 2 and slab 3 respectively: BIC=990.1 nm and BAR=0.96; BIC=994.0 nm and BAR=1.15; BIC=992.4 and BAR=1.05; and BIC=992.4 and BAR=1.16.

Following what was done in the supplementary material of Barrat et al. (2021) (see their Fig. S13), I calculated also the BIC and BAR for some of the taxonomic end members of the DeMeo et al. (2009) classification presenting spectra with features. The spectral templates for the A, Sa, K, O, Sq, S, R, Sr, Sv and V-types of DeMeo et al. (2009) were used, covering the wavelength range from 450 to 2400 nm. On Table.3.6 is given the wavelength range considered to perform the polynomial fit of the 1 micron band for each template spectrum considered, along with the considered limit in wavelength to calculate the BAR, and the obtained BIC and BAR values for each template.

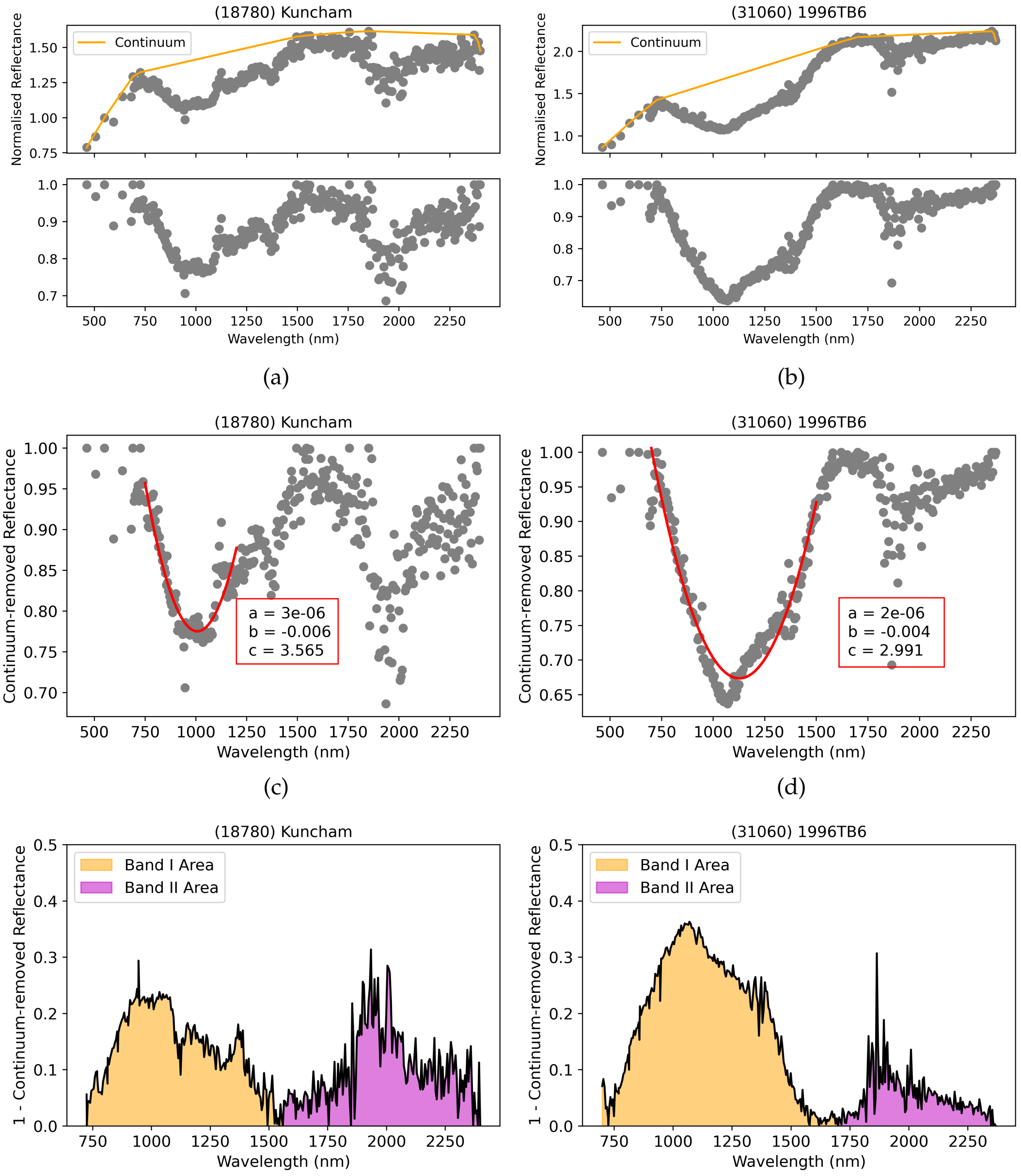

(a) (b)

(c) (d)

(e) (f)

Figure 3.17: Illustration of the continuum-removal (panels a and b), the Band I Center calculation with polynomial fitting (panels c and d) and the and Band Area Ratio calculation (panels e and f)for asteroids (18780) Kuncham (left panels) and (31060) 1996 TB6 (right panels).

Finally, the BIC and BAR parameters were also calculated on the VISNIR spectrum of asteroid (10537) 1991 RY16 of Moskovitz et al. (2008) (Fig.3.10), as it presents a unique spectrum in the asteroid population. The wavelength range considered for the Band I fitting was [750,1050] nm, and the wavelength limit to calculate the BAR was set to 1400 nm for this object. The obtained parameters are BIC=972.7 nm, and BAR=0.92.

The respective position of the considered templates spectra, of the observed asteroids, of (10537) 1991 RY16, and of EC 002 laboratory spectra in the BIC vs BAR plot is displayed in Fig.3.18. Uncertainty in the calculation of the BIC and BAR depends on the SNR of each spectrum and has not been calculated in this preliminary analysis,

Table 3.5: BIC and BAR calculated for every considered asteroid. (a) and (b) designate the two acquired spectra of asteroid (24286) 1999 XU188.

Asteroid	BIC (nm)	BAR
(1643) Brown	930.7	2.14
(1946) Walraven	932.5	2.19
(3188) Jekabsons	928.6	2.24
(3869) Norton	932.1	3.77
(4302) Markeev	930.0	2.34
(6003) 1988 VO1	921.7	3.12
(6789) Milkey	927.8	2.15
(8827) Kollwitz	936.5	2.03
(10671) Mazurova	941.4	2.21
(14511) Nickel	925.3	2.6
(15989) Anusha	939.8	2.02
(17056) Boschetti	942.8	1.91
(18780) Kuncham	1007.1	0.75
(20454) Pedrajo	932.6	2.07
(24286) 1999 XU188 (a)	935.1	2.44
(24286) 1999 XU188 (b)	928.3	1.97
(30426) Philtalbot	933.2	2.63
(31060) 1996 TB6	1126.8	0.19
(45787) 2000 OJ24	920.4	2.27

Table 3.6: Considered wavelength range (Range) for the second degree polynomial fit of the first absorption band, and wavelength limit (Limit) considered to calculate the band area ratio of each taxonomic end-member of DeMeo et al. (2009) considered. The BIC and BAR obtained for each template are given.

Type	Range (nm)	Limit (nm)	BIC (nm)	BAR
A	[700,1500]	1550	1119.3	0.02
Sa	[700,1500]	1550	1114.0	0.02
K	[710,1300]	1600	936.3	0.04
O	[710,1300]	1400	1034.9	0.36
Sq	[710,110]	1500	993.8	0.26
S	[710,110]	1500	964.6	0.51
R	[710,110]	1450	959.8	0.69
Sr	[710,110]	1500	951.9	0.66
Sv	[720,110]	1300	936.3	1.33
V	[750,1100]	1350	933.7	1.69

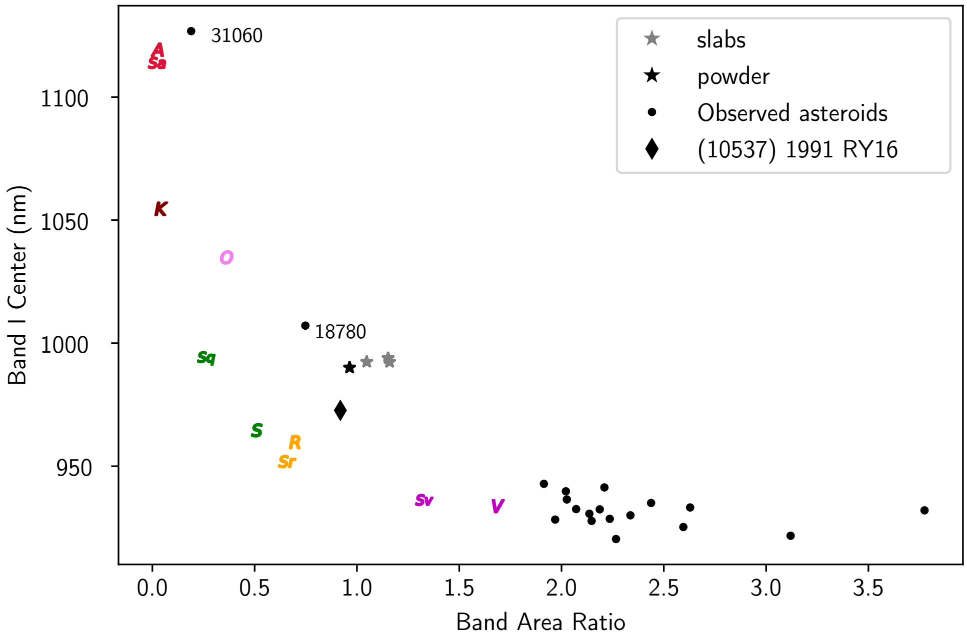

Figure 3.18: Band I Center as a function of the BII/BI area ratio. The BIC and BAR of the meteorite powder and slab spectra are displayed as black and grey stars respectively, and the observed asteroids as black dots. The numbers of asteroids (18780) Kuncham and (31060) 1996 TB6 are highlighted next to their corresponding data point. The BIC and BAR of the taxonomic end-members of DeMeo et al. (2009) are highlighed in colours, the letter corresponding to the taxonomic type. Finally, asteroid (10537) 1991 RY16 is plotted as a black diamond.

but will be in a future publication. On this plot, we can observe that the parameters of the meteorite plot quite far from taxonomic end-members, as noted by Barrat et al. (2021). Most asteroids that we observed plot far from the meteorite in this space as well, with most objects showing parameters corresponding to basaltic V-type objects, and asteroid (31060) 1996 TB6 plotting in the A-type region. Comparing this figure with Fig.S13 of Barrat et al. (2021), we can deduce that the 16 V-type asteroids have a composition closer to HED meteorites than to EC 002. The A-type asteroid (31060) 1996 TB6 has a composition consistent with a high content in olivine.

The asteroid we observed that is the closest to the meteorite in this space is (18780) Kuncham. However, this object was observed because it was a potential match for the low SW EC 002 spectrum, and it shows noisy Gaia and NIR spectra. Its slope is not compatible with a low space-weathered EC 002 spectrum, and it is therefore unlikely to be a good match for the meteorite.

In the BIC vs BAR space, asteroid (10537) 1991 RY16 appears close to the meteorite spectra. It shows slightly lower BIC and BAR values, but it plots quite far from the S, R, Sv and V-types taxonomic end-members as well, confirming the unique character of this asteroid's spectrum (Moskovitz et al., 2008).

3.8 DISCUSSION

We observed 20 asteroids potential analogues for EC 002, for a total of 21 spectra. Among these objects, 16 appear to be basaltic V-types, one is an A-type, and one belongs to the S-complex. Two objects show a discrepancy between their Gaia VIS spectrum and their acquired NIR spectrum, and were not considered in the analysis.

The objects observed are highlighted in the proper orbital elements space in Fig.3.19. In the background are plotted the asteroids having a spectrum in the DR3 dataset and showing a H magnitude lower than 14.5, as done in Galinier et al. (2023) and shown in Fig.3.8 and 3.9. All of the objects we observed are all located in the Inner Main Belt, except for A-type asteroid (31060) 1996 TB6 orbiting in the Middle Main Belt. Among the observed objects, four are found to be (4) Vesta family members by Nesvorny et al. (2015), Milani et al. (2014), Vinogradova (2019), and Brož and Morbidelli (2013): asteroids (6003) 1988 VO1, (20454) Pedrajo, (27884) 1996 EZ1 and (45787) 2000 OJ24. These asteroids are V-types according to their NIR spectrum, except for (27884) 1996 EZ1 that shows a discrepancy between its VIS and NIR spectrum.

Two objects are found part of the (8) Flora family: (6789) Milkey (Nesvorny et al., 2015) and (15989) Anusha (Nesvorny et al., 2015; Vinogradova, 2019). They are both V-types from their NIR spectrum. The other asteroids we observed were not found to belong to any family, but might still be family members that drifted too far from the family cores to be identified as such by the HCM (Dermott et al., 2018).

Out of the 20 observed asteroids, 16 have been predicted by Oszkiewicz et al. (2023) to be V-types from the study of their DR3 spectra, using various machine learning methods. We confirm here that asteroids (1643) Brown, (3188) Jekabsons, (4302) Markeev, (6003) 1988 VO1, (6789) Milkey, (8827) Kollwitz, (10671) Mazurova, (14511) Nickel, (15989) Anusha, (17056) Boschetti, (20454) Pedrajo, (24286) 1999 XU188, (30426) Philtalbot, and (45787) 2000 OJ24 are V-types, which is coherent with their position in the spectral parameters space highlighted in Fig.3.12. We cannot conclude on (12551) 1998 QQ39 and (27884) 1996 EZ1. Asteroid (1946) Walraven shows three flagged bands in the DR3, and was not considered in the sample of objects studied by Oszkiewicz et al. (2023) for this reason. (3869) Norton was not characterised either, and asteroids (18780) Kuncham and (31060) 1996 TB6 were rightly not classified V-types.

Comparing the BIC and BAR parameters of the observed objects with the meteorite's samples, none of the asteroids we observed appears to be a good match of the meteorite. This result can have several explanations. First, distinguishing EC 002's spectrum from the one of a basaltic body in the visible wavelength range is difficult, which explains why our selection of potential analogues is mostly made of V-type objects. Looking for potential analogues of this meteorite exploiting the DR3 dataset is also made difficult by some issues that can affect the DR3 spectra, such as the "fake band" that can appear around 650 nm (see Chapter 2), exactly at the location of a band in EC 002's spectrum. This artificial band in the DR3 spectrum can make an asteroid look like a potential analogue of the meteorite, when it is in fact of basaltic composition.

It is established that laboratory spectra of meteorites do not necessarily match with the spectra of asteroids of analogue composition (Brunetto et al., 2015, and references therein). The reason is that the reflectance spectra of asteroids are affected by the exposure of their surface to weathering agents in space, such as solar wind ions and micrometeorites. The Hapke (2001) model was developed by studying the space weath-

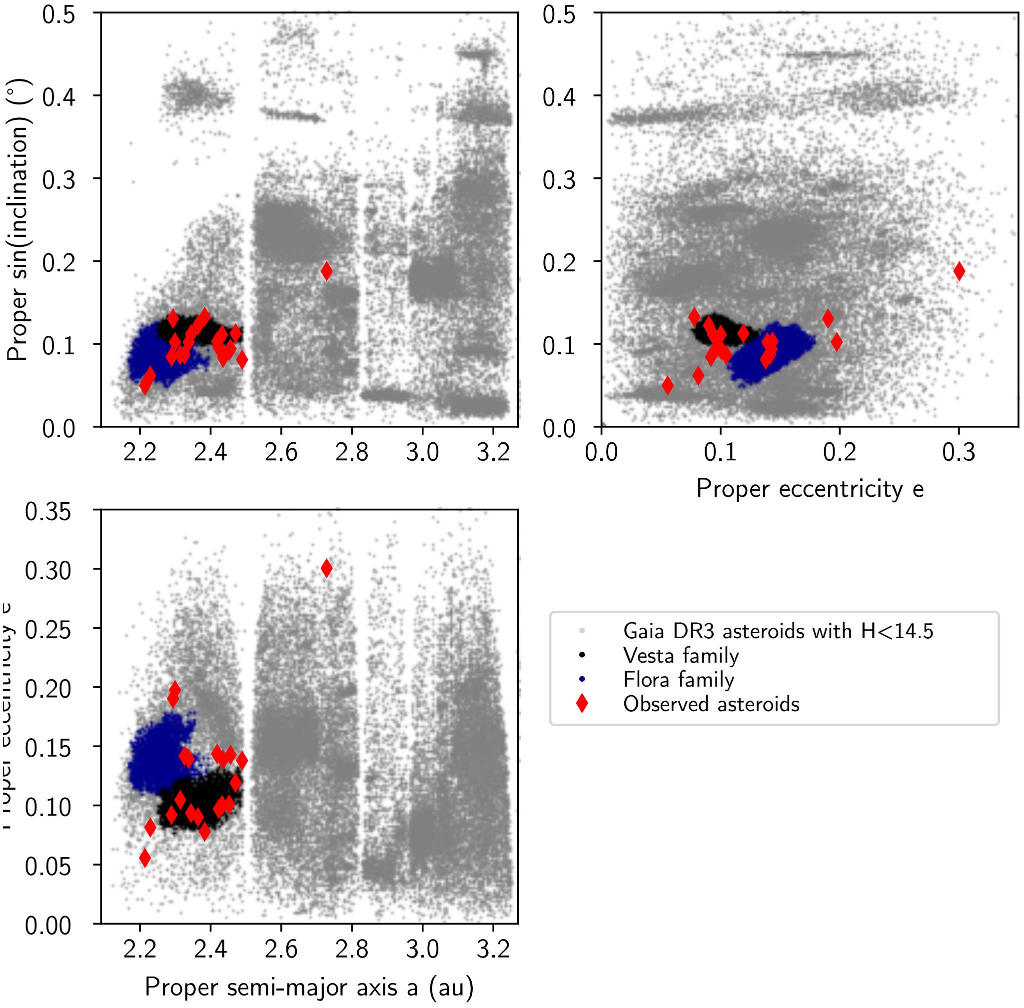

Figure 3.19: Proper orbital element plots of Gaia asteroids with absolute magnitude H<14.5 (light grey dots). Vesta and Flora family members are indicated respectively with black and blue dots. Asteroids potential analogues of the meteorite EC 002 that we observed are highlighted as red diamonds.

ering of the Moon, and it successfully recreates it. For its appliance to an object to be relevant, the mineralogy of the object needs to be dominated by silicates with grains larger than the wavelength (Pierre Beck, private communication). Such model applied to ordinary chondrites, along with laboratory experiments, allowed to successfully link this meteorite type to a subset of S-type asteroids, as previously mentioned (Chapman, 1996; Pieters et al., 2000; Gaffey, 2011).

EC 002 is an achondrite with andesitic composition, corresponding to the partial melt of an ordinary chondrite and which contains silicates with large grains (Barrat et al., 2021). Therefore, using the Hapke model makes sense to simulate the effect of space weathering on an asteroid of the same composition as EC 002, as what was implemented by Barrat et al. (2021).

However, the chemical composition of EC 002 makes it distinct from an ordinary chondrite. As space weathering depends on the composition of the bodies (Zhang et al., 2022; Nesvorný et al., 2005; Lazzarin et al., 2006; Hiroi et al., 2013; Vernazza et al., 2013; Lantz et al., 2017; Kitazato et al., 2021; Vernazza et al., 2009b; Avdellidou et al., 2022), it is possible that some chemical elements in EC 002 would react differently from ordinary chondrites to the inclusion of nanophase iron in the medium, influencing the spectral changes induced by space weathering. Space weathering experiments conducted on the meteorite samples or on simulants could help verifying the accuracy of the weathered modelled spectra of EC 002.

Finally, we may not have found any analogue of EC 002 because, as theorised by Barrat et al. (2021), the original population of asteroids having EC 002-like compositions and their fragments have disappeared. However, if this is the case, what are the odds that the last fragment of the oldest differentiated planetesimal fell on Earth, in the Sahara desert? The fact that the parent body of such meteorite is still in space, unnoticed, seems more likely than having found the last piece of the most ancient planetesimal by pure luck.

In the end, the asteroid showing the BIC and BAR parameters the closest to those of EC 002 is (10537) 1991 RY16. The VISNIR spectrum of this object suggests it is composed of a mixture of pyroxenes and olivine, which made Moskovitz et al. (2008) suggest it originated from a partially or fully differentiated body. This interpretation is in agreement with the origin scenarios of EC 002. Moskovitz et al. (2008) hypothesise that (10537) 1991 RY16 might be "an isolated fragment from a completely eroded parent body" (direct quote from their abstract), which is in line with the theory about the lost parent body of EC 002.

Moreover, (10537) 1991 RY16 might not be the only object showing such peculiar spectrum. Leith et al. (2017) did NIR observations of potential basaltic asteroids, and found other two objects showing a spectrum not belonging neither to the V nor to the R-type: (7472) Kumakiri and (14390) 1990 QP10. Their Gaia DR3 and literature spectra are displayed in Fig.3.20, along with the one of (10537) 1991 RY16 (Moskovitz et al., 2008). On this figure, we can see that the DR3 spectrum of (10537) 1991 RY16 clearly shows the band centred around 650 nm, in agreement with its literature spectrum. This band could also be present as well on the spectra of (7472) Kumakiri and (14390) 1990 QP10, but since these spectra are noisier, band identification is less straightforward.

These objects are all located in the Outer Main Belt. (10537) 1991 RY16 is in the so-called "pristine zone" close to the 5:2 MMR with Jupiter, and the other two have semi-major axis of about 3 and 3.3 au. (7472) Kumakiri is located close to the 7:3 MMR, and (14390) 1990 QP10 is close to the 2:1 MMR.

Leith et al. (2017) hypothesise that these three objects are fragments of differentiated planetesimals, which have been destroyed or ejected from the Solar System since. They are found to show more compositional diversity than (4) Vesta family members, suggesting that they may have formed at a different time or location in the solar nebula. This goes in the direction of these bodies being potentially similar to EC 002.

In the beginning of my PhD, I looked for objects spectrally similar to (10537) 1991 RY16 in the DR3 dataset, using curve matching techniques. However, the potential presence of an artificial band around 650 nm made the identification of such objects difficult, and I abandoned this project to focus on EC 002. There might however be a population of asteroids sharing spectral characteristics with (10537) 1991 RY16, that could be explored with different techniques from the curve matching (exploiting the position of the objects in the Principal Component space for example). If such potential objects are found, they would need to be confirmed with VIS and NIR observations, and it would then be possible to look for their meteoritical analogues and to conclude

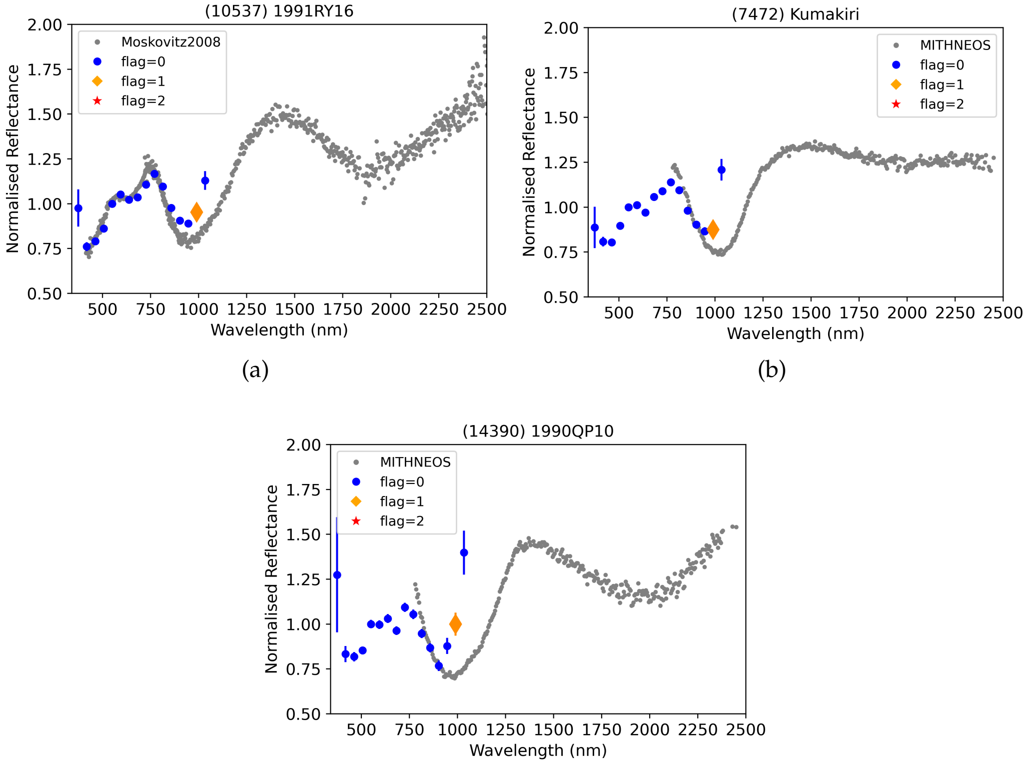

(a)

(b)

(c)

Figure 3.20: Literature (grey dots) and Gaia DR3 spectra of asteroids (10537) 1991 RY16, (7472) Kumakiri and (14390) 1990 QP10. The 16 bands of the Gaia asteroid spectra are given a colour and a symbol according to the value of the flag associated to the band: blue circle if flag=0, orange diamond if flag=1 and red star if flag=2.

on their potential similarities with EC 002. This study could also help understanding how andesitic bodies evolve when exposes to space weathering agents.

3.9 CONCLUSIONS AND PERSPECTIVES

The meteorite Erg Chech 002 is the oldest andesite of the Solar System, found to be about 4566.6 Myr old. Its formation scenario is compatible with the partial melting of a chondritic source, in the crust of an early accreted and differentiated planetesimal of the NC reservoir. The spectrum of this meteorite is unique, showing wide silicate bands around 1000 and 2000 nm, and a small band around 650 nm, likely due to chromium-bearing pyroxene.

Barrat et al. (2021) looked for spectral analogues of this meteorite using asteroid spectra and photometric data available in the literature at that time, and did not find any satisfactory match. We used the Gaia DR3 dataset of more than 60 000 asteroid reflectance spectra spanning the visible wavelength range to look for spectral analogues of the EC 002 among the asteroid population. We studied four different laboratory samples of the meteorite: three raw slabs and one powder spectrum; and three modelled space-weathered spectra of EC 002 were also analysed. As first method, we evaluated and compared the spectral parameters of each sample of the meteorite with the ones of the asteroids, studying the slope and the Band I depth of each asteroid spectrum. We used a curve matching method in a second time.

We obtained with the spectral parameter method 41 objects as potential analogues to the laboratory samples of EC 002, and 70 objects matching the space-weathered spectra of EC 002, after visual analysis and cross-matching with the literature. These objects are mostly located in the Inner Main Belt, around the Vesta and Flora families.

The curve matching method gave 18 objects matching the laboratory samples of the meteorite, also concentrated in the IMB. We also found 23 asteroids as potential analogues of the low space-weathered EC 002, eight asteroids matching the medium space-weathered meteorite and only one asteroid matching the highly space-weathered EC 002. Because of the χ^2_{red} parameter used, only objects with a low SNR were found with this method. In the end, a total of 51 asteroids were found as potential analogues of the not-space-weathered EC 002, and 91 asteroids were found matching the modelled space-weathered spectra of the meteorite. These results were published in Galinier et al. (2023).

To determine if the candidate analogues we found for EC 002 were real compositional analogues of the meteorite, we observed 20 of these candidates in the NIR, using the SpeX instrument on the IRTF. From their NIR spectra, 16 of these asteroids appear to be spectroscopic V-types, one asteroid is an A-type, and one is a S-complex object. The last two were showing a discrepancy between the VIS and NIR parts of their spectrum, and were not considered in this study.

To compare the meteorite's with the asteroids' spectra, I relied on their spectral features, that were found insensitive to the effects of space weathering. I calculated the Band I Centre and Band Area Ratio for the 19 observed asteroid spectra considered, for the laboratory spectra of the meteorite, and for some taxonomic end-members of the (DeMeo et al., 2009) classification scheme showing spectra with features. I also calculated these parameters for asteroid (10537) 1991 RY16, that shows a so-called unique spectrum with a band around 650 nm reminiscent of EC 002. The analysis of the position of these objects in the BIC vs BAR space revealed that none of the observed asteroids appears to be a good match for the meteorite. The 16 V-type asteroids are more consistent with a basaltic composition and plot in a similar area than HEDs in the BIC vs BAR plot, and the A-type asteroid is likely olivine-rich. The S-complex asteroid, even though the closest to EC 002 in the BIC vs BAR plot, shows a spectrum with shallower bands and a less pronounced slope than EC 002.

The object that appears to be matching the spectra of EC 002 best is Outer Main Belt asteroid (10537) 1991 RY16. This asteroid shares spectral characteristics with EC 002, such as a band around 650 nm and two broad bands centred around 1000 and 2000 nm. Theories regarding the origin of this asteroid suggest that it could be a fragment of a differentiated planetesimal, like what has been hypothesised for EC 002. Other asteroids may present similar spectral characteristics, such as (7472) Kumakiri and (14390) 1990 QP10.

Authors suggested that the planetesimals at the origin of these asteroids and the one at the origin of EC 002 had likely disappeared from the Main Belt, due to their accretion to other bodies or to their destruction. However, the odds of detecting the very few last asteroids leftovers from these differentiated planetesimals, and of finding a meteorite on Earth corresponding to the last fragment of a distinct planetesimal that shows a surprisingly similar spectrum to the ones of the asteroids, are in my opinion very low. A link might exist between all these objects, and more asteroids presenting similar spectral characteristics to (10537) 1991 RY16 should be looked for and observed in the widest wavelength range possible.

Finally, understanding how space weathering affects andesitic material specifically could help looking for asteroids with similar composition. Indeed, the Hapke model is justified and might be adapted to describe the weathering of EC 002-like material, but as space weathering affects materials differently, it could be interesting to perform experiments on EC 002-like simulants.

Linking differentiated meteorites with asteroids is a way of searching for evidence of differentiation in the Main Belt. Another way is to study asteroid collisional families, looking for objects showing compositions of the different layers of a differentiated planetesimal: igneous crust, olivine-rich mantle, and metallic core. In the following, I present a search for potential olivine-rich asteroid families, using the Gaia DR3 dataset.

4

THE FAMILY (36256) 1999 XT17

In the previous chapter, potential analogues of the differentiated ungrouped achondrite Erg Chech 002 have been identified in the Main Belt. After searching for evidence of differentiation by trying to link a meteorite to asteroids, I focused on the analysis of asteroid collisional families, using the Gaia DR3 spectral dataset.

As stated in the introductory Chapter 1, spectroscopic surveys shed light on the scarcity of A or Sa-type asteroids in the Main Belt (e.g DeMeo et al., 2019). This spectroscopic type is considered representative of olivine-rich bodies, thought to have been generated in the mantle of differentiated planetesimals (McConnell et al., 1967). The observed lack of mantle-like asteroids is known as the "missing mantle problem" (Chapman, 1986; Burbine et al., 1996).

Spectrophotometric surveys in the visible wavelength range such as the SDSS allowed to detect candidate A-type asteroids across the Main Belt (Carvano et al., 2010; DeMeo and Carry, 2013). DeMeo et al. (2019) performed spectroscopic observations in the NIR wavelength range of 72 A-type candidates, and confirmed 21 of them. The confirmed A-types were found evenly distributed in the Main Belt, showing no statistically significant concentration in an asteroid family (see Sanchez et al., 2014; DeMeo et al., 2019). DeMeo et al. (2019) conclude that the few olivine-rich asteroids detected are fragments of bodies that formed outside the Main Belt, and were dynamically implanted in it.

To discuss the affirmation made by DeMeo et al. (2019) stating that there is no statistically significant concentration of olivine-rich bodies in any asteroid family, we looked for a potential concentration of A-types in the 122 asteroid families of Nesvorny et al. (2015) obtained with a HCM algorithm (see Chapter 1). To select the family most likely to contain a high abundance of A-types, we used a dataset of asteroid spectral classes built from the literature and presented in the following. Along with ground-based spectra, we used the 60 518 asteroid reflectance spectra included in the DR3 (Gaia Collaboration et al., 2023) and a newly acquired NIR reflectance spectrum to characterise asteroids of the selected family. The family selection and characterisation, the methods used, and the obtained results are presented and discussed in the following. This chapter comprises studies and results that were published in Galinier et al. (2024).

4.1 FAMILY SELECTION

To select the family most likely to contain a large number of A-type asteroids, we built a database of asteroids that have been characterized with spectroscopy or photometry in the literature. To do so, I gathered the taxonomic classes of asteroids derived from spectroscopic observations from the following references: Tatsumi et al. (2022), Migliorini et al. (2021), Arredondo et al. (2021b), Gartrelle et al. (2021), Hasegawa et al. (2021), De Prá et al. (2020a), De Prá et al. (2020b), Lucas et al. (2019), DeMeo et al. (2019), Devogèle et al. (2019), Morate et al. (2019), Popescu et al. (2019), Perna et al. (2018), Migliorini et al. (2018), De Prá et al. (2018), Devogèle et al. (2018), Morate et al. (2018), Borisov et al. (2017), Migliorini et al. (2017), Leith et al. (2017), Lucas et al. (2017), de León et al. (2016), Morate et al. (2016), Ribeiro et al. (2014), DeMeo et al. (2014), Thomas et al. (2014), Popescu et al. (2014b), Oszkiewicz et al. (2014), Sanchez et al. (2013), Gietzen et al. (2012), de Sanctis et al. (2011), de León et al. (2010), DeMeo et al. (2009), Clark et al. (2009), Mothé-Diniz et al. (2008a), Roig et al. (2008), Licandro et al. (2008a), Mothé-Diniz and Nesvorný (2008), Alvarez-Candal et al. (2006), Lazzarin et al. (2005), Marchi et al. (2005b), Mothé-Diniz et al. (2005b), Duffard et al. (2004a), Binzel et al. (2004), Lazzarin et al. (2004), Bus and Binzel (2002a), and Carvano et al. (2001). Only asteroids classified in the Bus or Bus-DeMeo taxonomic schemes were accounted for here. We used as well the taxonomic classes of asteroids obtained from spectrophotometric observations from the following references: Carvano et al. (2010), Popescu et al. (2018a), Sergeyev and Carry (2021), Sergeyev et al. (2022), and DeMeo and Carry (2013). This list of articles reunites a total of 445 611 asteroids.

The dataset was exploited by a code developed by Marco Delbo, that organises the information as follows: the classification of asteroids from visible-light photometry is displayed in a column, their classification from NIR photometry in another column, and the classification from spectroscopy in the Bus and Bus-DeMeo taxonomic schemes in other two distinct columns. If an asteroid has been classified several time from the same technique in the same taxonomic scheme, its type gets over-written. Therefore, the order in which the articles are prioritised matter. The code was tested with different rankings of the papers, and the results found were not significantly different from one ranking to another.

Using this dataset, we calculated the proportion of potential A-type asteroids in each asteroid family defined by Nesvorny et al. (2015). We calculated the ratio between the number of objects classified at least once as A or Ad-type in different taxonomies and methods, and the total number of asteroids with any other spectral type in each family. We then looked into the families having a potential A-type abundance of above 10%. This percentage was chosen arbitrarily, to focus on a few member of promising families. Only three families were found to match this criteria: families (10811) Lau (Family Identifier Number (FIN) 619 in Nesvorny et al. (2015)), (36256) 1999 XT17 (FIN 629), and (7468) Anfimov (FIN 635). They were found to contain 13, 23 and 28% of potential A-type members, respectively.

We analysed the literature data for these families and examined the Gaia DR3 spectra (Gaia Collaboration et al., 2023) of their members, to see if new studies of these families could be carried out by exploiting the DR3. We found that one, 15, and 7 asteroids of these respective families show a spectrum in the DR3 dataset. Since only asteroid (10811) Lau itself shows a DR3 spectrum for the (10811) Lau family, we did not consider it.

We then studied the mean average SNR (Gaia Collaboration et al., 2023) of the DR3 spectra of each family member, to assess the quality of their DR3 spectra. The mean average SNR of the (7468) Anfimov family is of 23, with asteroids (7468) Anfimov and (18853) 1999 RO92 having the highest SNR spectra, respectively of 47.41 and

32.21. These two objects have already been classified as A from VISNIR spectroscopic observations (DeMeo et al., 2019; Mahlke et al., 2022). As the other members of this family all show spectra with a SNR<30, we discarded it as well.

The family (36256) 1999 XT17 shows a mean average SNR of 40, with nine objects having a SNR⩾28. Since a SNR⩾21 is generally considered a threshold for reliable spectral classification in the VIS wavelength range (Delbo' et al., 2012), we chose to focus on this family to look for a potential concentration of A-type asteroids.

In the following is presented the characterisation of the (36256) 1999 XT17 family using literature data, the DR3 dataset, and a newly acquired NIR spectrum.

4.2 CHARACTERISATION OF THE (36256) 1999 XT17 FAMILY

The (36256) 1999 XT17 family counts only 58 members, and is reported as a S-complex family in Nesvorny et al. (2015). It is located in the so-called "pristine zone" of the Main Belt (Brož et al., 2013), extending between 2.825 and 2.955 au and bounded by the 5:2 and 7:3 MMRs with Jupiter. This zone and the location of the (36256) 1999 XT17 family are highlighted in Fig.4.1.

Among the 58 members of the 1999 XT17 family, 21 asteroids that do not have a DR3 spectrum are classified in the literature from spectrophotometric data in the VIS or NIR wavelength range. Among these, asteroid 76627 is classified Ad from MOVIS NIR colours (Popescu et al., 2018a). The Moving Objects VISTA (MOVIS) colour catalogue is built on the third data release of the VISTA Hemisphere Survey (VHS) of the Visible and Infrared Survey Telescope for Astronomy (VISTA), that detected 39 947 objects, among which 38 428 Main Belt asteroids. This NIR survey collected data in five broadband filters, the Z, Y, J, H and Ks filters, respectively centred at 879, 1021, 1253, 1646 and 2148 nm (Sutherland et al., 2015). This catalogue has been used to study asteroid families from their (J-Ks), (Y-J) and (H-K) colours (Popescu et al., 2016; Morate et al., 2018). Popescu et al. (2018a) defined the Ad-type for objects showing the reddest (J-Ks) colour, a moderate (H-K) colour, and a moderate to high (Y-J) colour. This class corresponds to objects having the reddest NIR spectra, that could be A or D-types in common taxonomic schemes (Bus and Binzel, 2002a; DeMeo et al., 2009; Mahlke et al., 2022). The colours being not always enough to distinguish between an A or a D-type, the class was called Ad (Popescu et al., 2018a).

From VIS spectrophotometry, asteroids 58777 and 201232 are classified A-types (Carvano et al., 2010; Sergeyev et al., 2022), while 254896 is found both A-type (Carvano et al., 2010) and S-type (Sergeyev et al., 2022), and asteroid 62676 is classified S-type (Sergeyev et al., 2022) and X-type (Carvano et al., 2010). The 7 asteroids 40427, 204222, 222898, 223304, 271103, 285502, and 362895 are classified as S-complex members (Carvano et al., 2010; DeMeo and Carry, 2013; Sergeyev and Carry, 2021; Sergeyev et al., 2022). The remaining objects are classified as L, K, C, D, V or X-types (not considering objects classified as U here, U being "Undertermined").

In the literature, 7 objects out of the 15 members of the 1999 XT17 family that have a spectrum in the DR3 dataset have been classified. Among them, only asteroid 36256 has been characterised using NIR spectroscopy. This object is found A-type by DeMeo et al. (2019) and Mahlke et al. (2022), in their respective taxonomic schemes. Asteroids 25356 and 40671 are found Ad-types by Popescu et al. (2018a) from MOVIS NIR colours; and asteroids 27565, 34902, 36256, 66676, and 99004 are found part of the S-complex from spectrophotometric observations (Carvano et al., 2010; DeMeo and Carry, 2013; Sergeyev and Carry, 2021; Sergeyev et al., 2022). To complete the literature, we performed NIR spectroscopic observations at NASA's IRTF of asteroid (33763) 1999 RB84.

4.2.1 NIR observation of (33763) 1999 RB84

We used NASA's IRTF to acquire the NIR spectrum of asteroid (33763) 1999 RB84. To do so, we used the SpeX (Rayner et al., 2003) and MORIS instruments (Gulbis et al., 2011) on June 13, 2023 to observe this asteroid at 9.4° phase angle (see Chapter 3 section 3.6 for a more thorough description of the instruments and of the observations procedure). SpeX was used in PRISM mode with a slit of 0.8×15 arcsec, covering a wavelength range from 700 to 2500 nm with a spectral resolution of ~200 in a single configuration. The asteroid's magnitude was 17.4, and the exposure time for a single frame was 180 sec. We acquired 6 cycles of "AB-BA" frame pairs, for a total exposure

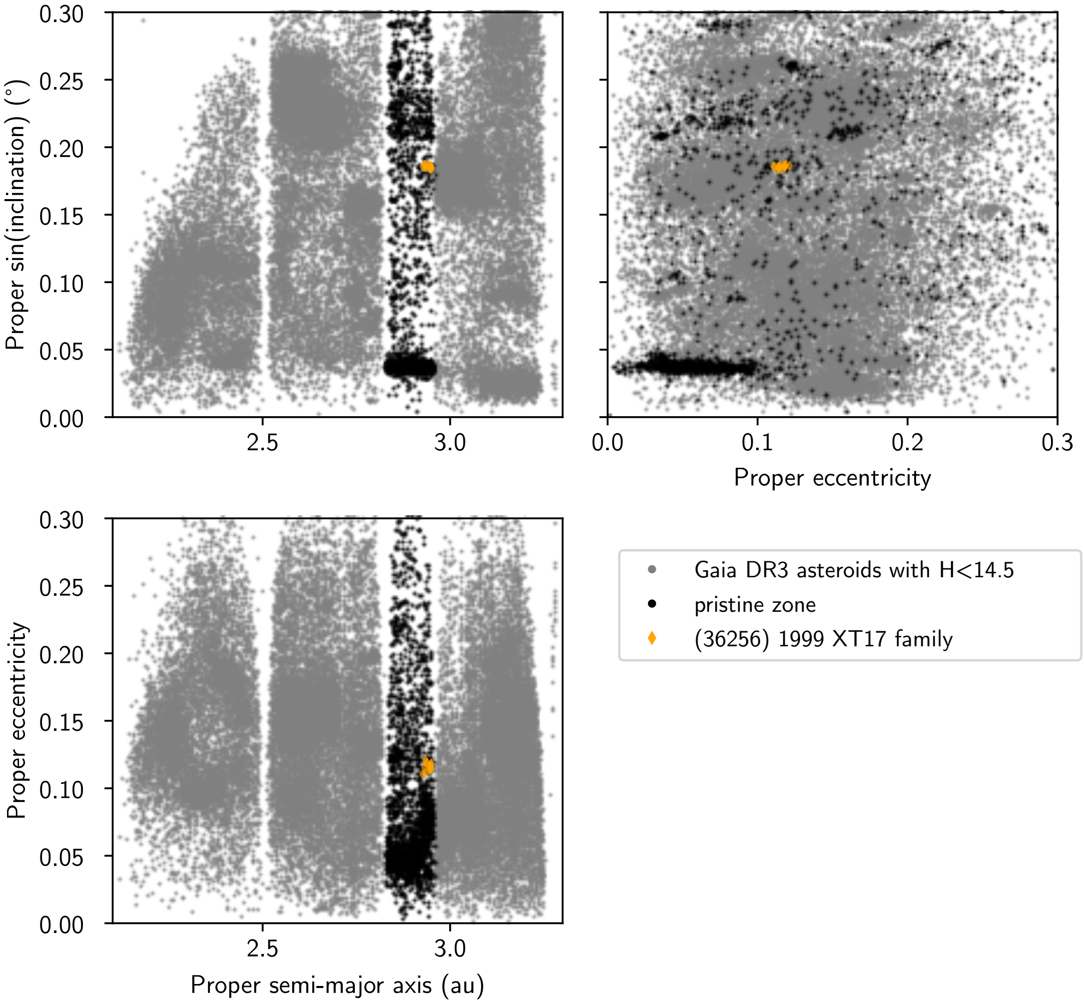

Figure 4.1: Proper orbital elements plots where are highlighted the pristine zone (black dots) and the family (36256) 1999 XT17 (orange diamonds).

time of 18 min, during which the asteroid was shifted along the spectrograph's slit. Following well established procedures (Reddy et al., 2009) described in section 3.6, we calculated the asteroid's reflectance spectrum. To do so, we used the wavelength-calibrated raw spectrum of the local G2V star HD137782 observed within ~300" of the asteroid, and the wavelength-calibrated raw spectrum of the trusted solar analogue star SA107684 that was observed at a similar airmass of the asteroid.

The reduced NIR spectrum of asteroid (33763) 1999 RB84 is displayed in Fig.4.2, linked to its DR3 spectrum. From the overall shape and the red slope of the spectrum from 1100 to 1700 nm, this spectrum is characteristic of an A-type asteroid.

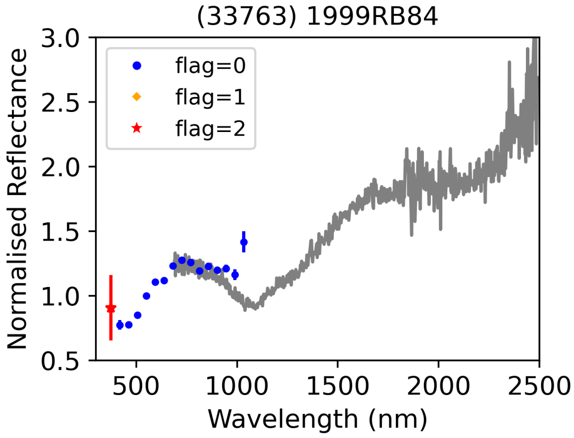

Figure 4.2: Full VISNIR spectrum of (33763) 1999 RB84. The coloured part is the VIS Gaia DR3 spectrum, and in grey is displayed the acquired NIR spectrum.

4.2.2 Classification of family members

Using data from the literature, from the DR3, and our own observed spectrum; we classified each (33763) 1999 XT17 family member in the Bus-DeMeo taxonomic scheme (DeMeo et al., 2009),following the method presented in Avdellidou et al. (2022). The classification algorithm works as follows. First, if the NIR spectrum of an asteroid is available, it gets cleaned from potential telluric lines, and smoothed with the use of a cubic spline. A spline is also applied to any available visible-light spectrum, considered only from 450 to 900 nm. The first two and last four bands of the Gaia DR3 spectra were not taken into account here (Gaia Collaboration et al., 2023; Oszkiewicz et al., 2023).

In case SDSS data is available, the apparent magnitudes from the SDSS are converted to reflectance values (see equation 3.1 in Chapter 3), so they can be compared with taxonomic templates spectra. The u SDSS filter was not considered here, as it can be affected by large errors (DeMeo and Carry, 2013). The normalisation wavelength was chosen at the centre of the i filter, and the solar magnitudes in the g, r, i and z SDSS filters used here are, respectively, 5.12,4.68,4.57, and 4.54.

After calculating the equivalent reflectance spectra from SDSS data and smoothing the NIR and VIS spectra available, a curve matching is performed between each spectrum and the taxonomic templates of the Bus-DeMeo taxonomy, for each asteroid. The Bus-DeMeo taxonomic scheme was chosen here because of its extension to the NIR.

This curve matching relies on the calculation of a reduced χ^2 figure of merit. First, the template spectra are interpolated with a cubic interpolation, and sampled like the spectrum they are being compared to. A scaling factor f is calculated and applied to the template spectra:

$$f = \frac{\sum_{i=1}^{N}(R_i \times R_i^{templ})}{\sum_{i=1}^{N}(R_i^{templ})^2}, \tag{4.1}$$

with N the number of data points, R_i the reflectance value of the considered spectrum at a given index corresponding to the wavelength λ_i, and R_i^{templ} the reflectance value of the interpolated template spectrum at this same index.

Then, a reduced χ^2 is calculated independently, for each considered spectrum of a given asteroid. For example, asteroid 36256 has a VIS Gaia DR3 spectrum, a NIR spectrum, and has been characterised with SDSS spectrophotometry. For this object, three independent reduced χ^2 were calculated between the three spectra and the Bus-DeMeo templates, using the following equation:

$$\chi^2_{red} = \frac{1}{N}\sum_{i=1}^{N}(R_i - f \times R_i^{templ})^2. \tag{4.2}$$

The reduced χ^2_{red} obtained for each data set are then weighted with their errors and summed, giving a global χ^2_{red} value. The two lowest values of the global χ^2_{red} give the best two classes of a given asteroid.

The literature data considered here were the NIR spectrum of asteroid 36256 published in DeMeo et al. (2019), the spectra of asteroids 36256 and 99004 derived from visible-light spectrophotometric data from the SDSS (DeMeo and Carry, 2013), and the spectra derived from MOVIS colours of asteroids 25356 and 40671 (Popescu et al., 2018a). Our own observed NIR spectrum of asteroid 33763 is used as well. The best two classes obtained for the 15 asteroids of the 1999 XT17 family having a DR3 spectrum are presented in Table 4.1. Out of the 15 asteroids, 12 were classified A-type as first or second best class. The remaining three objects, asteroids 34902, 83124, and 88057, were classified as S-complex objects. Fig.4.3 shows the Gaia DR3 spectra of the 15 family members, supplementary data when available, such as data from the MOVIS catalogue (Popescu et al., 2018a).

Using literature data[1], the uncertainty-weighted average of the geometric visible albedo of the potential A-type family members is of 0.22, with an rms value of 0.07. This value is within the range of the A-types' p_V (Mahlke et al., 2022).

4.2.3 Comparison with meteorites

To gain insights on the composition of these family members, we compared the two VISNIR spectra of asteroids (36256) 1999 XT17 and (33763) 1999 RB84 with those of the samples available in NASA's RELAB database. This database holds spectroscopic data of various terrestrial rocks and meteorites of different mineralogies acquired in the laboratory, and covering wavelengths ranges from the near-UV to the far-infrared.

To compare asteroids with meteorites, we used the exponential space-weathering model derived by Brunetto et al. (2006) to correct the asteroids spectra from effects

---

[1] `mp3c.oca.eu`

Table 4.1: Members of the (36256) 1999 XT17 family with a Gaia DR3 spectrum. Here is given the diameter D of family members, their geometric visible albedo p_V, the average signal-to-noise ratio of their DR3 spectrum, their H magnitude, and the two best spectral classes given by our classification algorithm. The physical properties data were obtained from `mp3c.oca.eu`.

Asteroid Number	D (km)	p_V	Avg SNR	H	spectral class
15610	5.84	0.30	35.32	13.3	A, L
16789	6.62	0.18	38.25	13.5	A, Sv
20975	5.24	0.28	36.01	13.6	A, Sv
25356	-	-	66.49	12.8	A, Sa
27565	5.92	0.19	20.74	13.6	A, L
33763	-	-	48.07	13.4	A, Sa
34902	4.15	0.15	14.7	14.4	Sq, Sr
36256	10.21	0.19	66.56	12.4	A, Sa
40671	-	-	28.09	13.6	A, Sa
57276	7.20	0.31	128.7	12.9	A, Sv
66676	6.55	0.22	52.28	13.3	L, A
83124	-	-	14.88	14.7	S, Sr
88057	-	-	20.75	14.5	K, S
99004	3.83	0.10	13.93	14.6	L, A
140349	3.69	0.20	13.86	14.7	Sv, A

of space weathering (as done for example in DeMeo et al., 2022; Mahlke et al., 2023). Indeed, Brunetto et al. (2006) carried out ion irradiation experiments on various meteorites and silicate materials, in order to reproduce the effects of solar-wind ion bombardment on them. Solar wind is considered the main source of weathering of asteroids surfaces, since it happens over timescales of 10^4 to 10^6 years (Vernazza et al., 2009a; Brunetto et al., 2015). They found that the reddening and darkening process of solar-wind ion bombardment affects mostly the slopes and continuum of the spectra, but does not significantly change the position and relative intensities of mafic silicate absorption bands, although the area of each band diminishes. From their experiments and previously existing models, Brunetto et al. (2006) calculated the ratio between the spectra of irradiated and non-irradiated samples, and they derived an exponential space-weathering function $W(\lambda)$:

$$W(\lambda) = K\exp(\frac{C_s}{\lambda}), \tag{4.3}$$

with λ the wavelength, K a normalising scale factor that depends on the normalisation of the spectra, and C_s the strength of the exponential curve, representing the strength of the space weathering. This function describes how the continuum of a spectrum is affected by space weathering, and it is used by fitting it to the spectra. It is adapted to study the weathering of mafic silicate material (Brunetto et al., 2006).

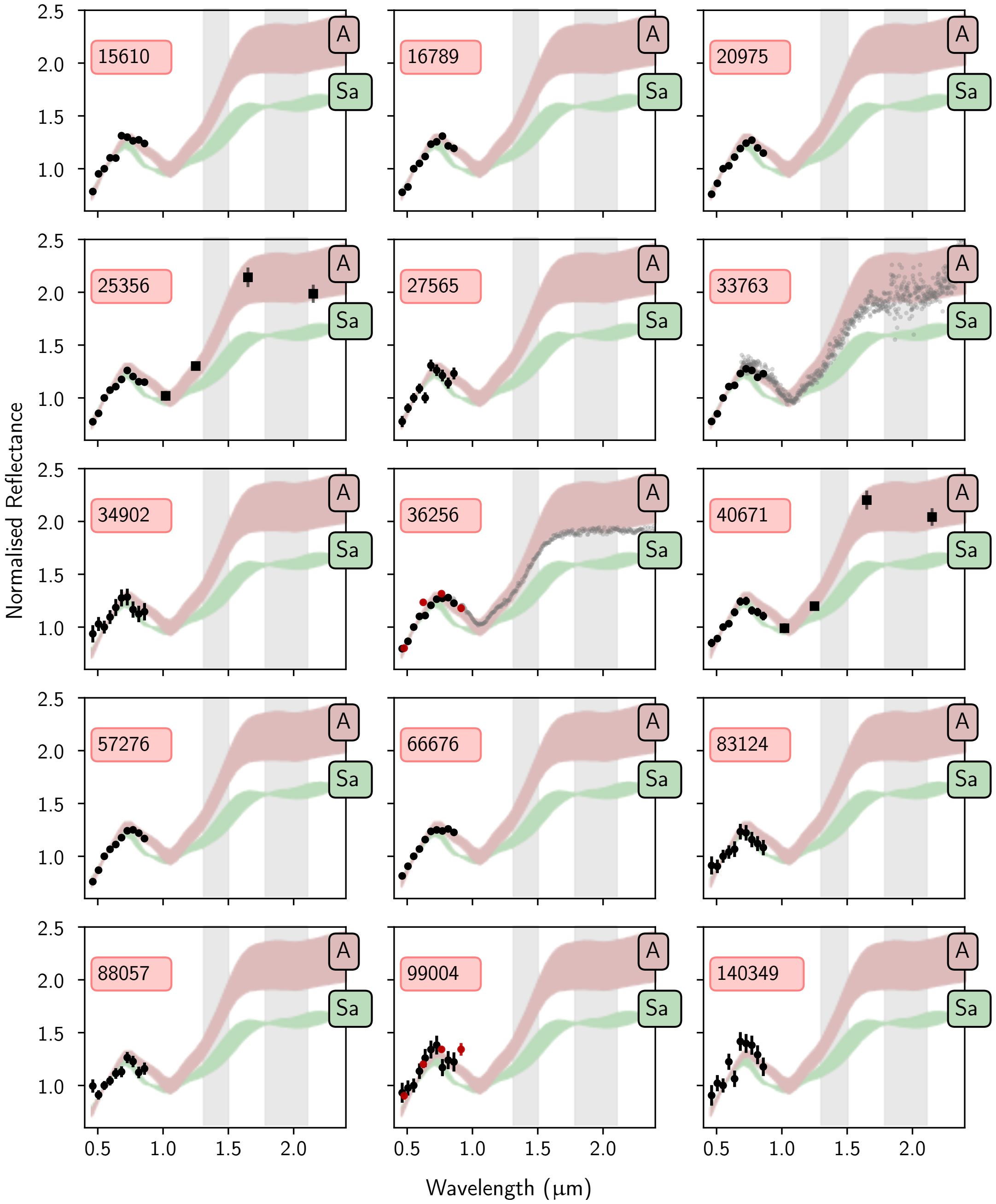

Figure 4.3: Available data of the members of the family (36256) 1999 XT17 in the Gaia DR3: Gaia spectra (black dots), SDSS data from DeMeo and Carry (2013) (red dots), MOVIS data from Popescu et al. (2018a) (black squares), and NIR spectra from DeMeo et al. (2019) and from our own observations (grey stars). The shaded coloured areas represent the reflectance spectra from the A and S-type taxonomic templates of the Bus-DeMeo scheme (DeMeo et al., 2009), and the grey areas represent zones affected by telluric lines.

For asteroids 36256 and 33763, we calculated the ratio between their VISNIR spectra, and the spectrum of every sample available in the RELAB database. To do so, we resampled the asteroids and the meteorites spectra from 450 to 2500 nm for asteroid 36256, and from 450 to 1800 nm for asteroid 33763. A narrower wavelength range was adopted for the latter, to filter out the noisier part of its NIR spectrum affected by a positive slope (see Fig.4.2). Then, we fitted the exponential space-weathering model of Brunetto et al. (2006) to each calculated ratio, to compute de-weathered asteroids spectra.

We used a curve matching method to find the best meteoritical analogues of asteroids 36256 and 33763, following established methods (see e.g. Avdellidou et al., 2022; DeMeo et al., 2022; Mahlke et al., 2023). We calculated the Φ_{comb} parameter of Popescu et al. (2012) between the RELAB samples and the de-weathered asteroids spectra. This coefficient is defined as follows:

$$\Phi_{comb} = \frac{\rho_{x_i,m_i}}{\Phi_{std}} \tag{4.4}$$

with ρ_{x_i,m_i} the correlation coefficient, and Φ_{std} the minimisation of the standard deviation of the errors. The correlation coefficient quantifies the level of dependence between x_i an asteroid spectrum and m_i a meteorite spectrum:

$$\rho_{x_i,m_i} = \frac{cov(x_i, m_i)}{\sigma_{x_i}\sigma_{m_i}}. \tag{4.5}$$

$cov(x_i, m_i)$ is the covariance matrix characterising the dependence of the two variables, and σ_{x_i} and σ_{m_i} are the errors associated to each reflectance spectrum. The higher the correlation coefficient, the better the match.

The minimisation of the standard deviation of the errors between an asteroid and a meteorite spectrum is defined as

$$\Phi_{std} = \frac{1}{N}\sqrt{\sum_{i}^{N}(e_i - \bar{e})^2}, \tag{4.6}$$

with $e_i = (x_i - m_i)$ the error between the asteroid and the meteorite spectrum, $\bar{e}$ the mean value of the set $\{e_i\}$, and N the number of wavelengths. The lower is Φ_{std}, the better is the match. Hence, the highest values of Φ_{comb} gives the best matches between a meteorite and an asteroid spectrum. This coefficient has been found to give satisfactory results by Popescu et al. (2012) and Mahlke et al. (2022).

Calculating the Φ_{comb} coefficient, we obtained as best matches mostly olivine assemblages and olivine-rich meteorites for both asteroids, confirming previous findings on other A-types (DeMeo et al., 2022). Among the meteorites found as best spectral matches, we found the CK6 meteorite LEW 87009, the R-chondrite Rumuruti, the shergottite ALHA77005, the pallasites Esquel and Thiel Mountains, and the brachinite EET99402 for asteroids 36256 and 33763.

We used the equivalent geometric visible albedo presented in Beck et al. (2021) to try discriminating between these best spectral matches. We followed the method as implemented in Avdellidou et al. (2022): we determined the equivalent geometric visible albedo of the RELAB meteorite samples, and we compared it to the mean albedo of the family, $p_V = 0.22$. To do so, we calculated the reflectance at 550 nm of the meteorites observed at a phase angle of 30°, and we derived their reflectance value at a phase angle of 0°, using Eq. 2 of Beck et al. (2021):

$$\frac{R_{\lambda,g=0^\circ}}{R_{\lambda,g=30^\circ}} = C_1 + C_2 exp\left(-\left[\frac{ln(\frac{R_{\lambda,g=30^\circ}}{C_3})}{C_4}\right]^2\right), \tag{4.7}$$

with $C_1 = 5.48 \pm 1.14$, $C_2 = -4.40 \pm 1.14$, $C_3 = 0.388 \pm 0.019$, and $C_4 = 6.08 \pm 0.95$ (Beck et al., 2021). The comparison between this equivalent geometric visible albedo to the family's mean p_V gives an indication of which meteorite samples might be the best matches for the family members.

Among the best meteorite analogues obtained with the curve matching method, we found that the CK6 meteorite LEW87009, the R-chondrites Rumuruti and LAP04840, the R4 chondrite MIL07440, the olivine of the shergottite ALHA77005, and the brachinites NWA4882 and ALH84025, show an equivalent geometric albedo close to $p_V = 0.22$. These meteorites are therefore the best matches found for asteroids (36256) 1999 XT17 and (33763) 1999 RB84.

4.3 DISCUSSION ON THE METHODS

4.3.1 Family selection

To select the families showing a potential abundance of A-type asteroids, we used a list of bibliographic references listed in section 4.1, and the families of Nesvorny et al. (2015). One can wonder what happens when using another dataset of references, or when using different definition of the families.

As a test, I used the Solar system Open Database Network (SsODNet), a data aggregator containing more than 1 300 00 objects (Berthier et al., 2023), to perform the family selection as presented in section 4.1. In May 2024, this database contains 197 families registered from diverse sources (e.g Vinogradova, 2019; Nesvorny et al., 2015; Brož and Morbidelli, 2013; Milani et al., 2014). In this database, the taxonomic data are ranked as follows: if an asteroid has been classified from VISNIR spectroscopy accounting for the albedo, its derived taxonomic type prevails. If it has been classified on the basis of VISNIR spectroscopy, its type takes precedence over any type obtained from NIR spectroscopy, which in turn takes precedence over VIS spectroscopy. A ranking is also made according to the scheme used for classification: asteroids types obtained with the Mahlke scheme prevail over those classified in the Bus-DeMeo scheme, themselves prevailing over the Bus scheme, and so on (see Berthier et al. (2023) for details). Finally, asteroid classes obtained from spectroscopic data prevail over those obtained from photometric data.

As previously, I calculated the ratio between the proportion of potential A-types and the proportion of asteroids classified otherwise, for each family contained in the database. I obtained six families with a potential A-types proportion above 10%. The families (7468) Anfimov and (36256) 1999 XT17 are found as candidate A-type-rich families with this method as well, showing proportions of potential A-types of respectively 25.9 % and 19 %. This result shows that, even with another dataset of literature spectra, another ranking of the references, taking into account every taxonomic scheme to date, and considering other definition families, the family (36256) 1999 XT17 still appears as a potential A-type family.

Among the six families obtained, family (11882) 1990 RA3 is found to contain a proportion of potential A-types of 25 %. This family defined in Milani et al. (2014) contains 13 objects in SsODNet, but only one of these objects has a spectrum in the DR3 dataset: asteroid (36560) 2000 QP107.

Families (2076) Levin, (1019) Strackea and (1067) Lunaria respectively show a proportion of potential A-types of 13.3%, 10.3%, and 10 %. Family (2076) Levin contains 48 asteroids in Milani et al. (2014), 5 of which have a spectrum in the DR3 dataset. Family (1067) Lunaria (Vinogradova, 2019) contains 44 asteroids, 14 of which have a DR3 spectrum. Finally, family (1019) Strackea (Vinogradova, 2019) contains 326 asteroids, 78 of which have a spectrum in the DR3 dataset. These families could be analysed in the future.

4.3.2 Classification algorithm

We investigated the possibility that our A-type classification based on Gaia data is affected by an issue in the DR3, which tends to overestimate the reflectance values mostly in the reddest bands (see Chapter 2). Due to this reddening, a non-A-type asteroid could potentially be classified as such, since this class shows a red slope in the VIS wavelength range.

To investigate this issue, we tested our algorithm by classifying asteroids with a spectrum in DR3, and that were classified on the basis of VISNIR observations by DeMeo et al. (2009), DeMeo et al. (2014), and DeMeo et al. (2019). Indeed, VISNIR spectroscopy allows to classify asteroids more accurately than visible-light spectra only, and comparing the our classification of asteroids with asteroids classified from VISNIR spectra in the same taxonomic scheme allows to evaluate the performances of our algorithm.

The list of asteroids characterised both in the DR3 and by DeMeo et al. (2009), DeMeo et al. (2014), and DeMeo et al. (2019) contains 389 objects. We applied our classification method to their DR3 spectra, considering the wavelength range from 450 to 900 nm. This range was chosen to eliminate bands potentially affected by systematic errors, and to limit the effect of a potential DR3 reddening. Moreover, we did not consider the bands in the DR3 spectra flagged with a non-zero number, as done in Galinier et al. (2023).

We studied the performances of our algorithm for the classification of A-types only, using the confusion matrix presented in Table 4.2. In the list of 389 asteroids, 21 are classified as A-types in the literature. We found that eight asteroids that are not A-type in DeMeo et al. (2009), DeMeo et al. (2014), and DeMeo et al. (2019) are classified A-type by our method. This corresponds to a False Positive Rate (FPR) of around 2.2%. Among these false positives, three asteroids are classified as A-type by Mahlke et al. (2022) in his own taxonomic scheme. If we consider this information, the FPR goes down to less than 1.5%. Therefore, we concluded that the aforementioned DR3 reddening unlikely affects our classification of A-types.

Among the 21 A-type asteroids of the list, 15 get correctly classified as A-types as first or second best class with the Bus-DeMeo templates. This corresponds to a True Positive Rate (TPR) of above 71%. The accuracy of the classification corresponds to the sum of the true positives and the true negatives, divided by the total population. The accuracy for the A-type classification here is therefore of $\frac{15+360}{389} = 96\%$.

Among the six A-type asteroids of the literature that did not get classified as A-type here (false negative rate of 28.6%), four asteroids have a SNR<21. Therefore, the classification of low SNR asteroids should be taken with caution: it is not impossible that a low SNR asteroid that was not found A by our method is a true A. Similarly,

Table 4.2: Confusion matrix of the classification of A-type asteroids by our algorithm. The list of 389 asteroids both classified by DeMeo et al. (2009), DeMeo et al. (2014), and DeMeo et al. (2019) and having a DR3 spectrum considered for this study contains 21 A-type asteroids.

True Predicted	A-type	Non-A-type
A-type	15	8
Non-A-type	6	360

asteroids found A by our method and that show a SNR<21 might not be true A. This will be further discussed in Chapter 5.

We did not aim to extensively study the performances of this classification algorithm on other taxonomic types for the scope of this project. In Chapter 5 will be presented a more extensive study of the classification of Gaia DR3 spectra and their limitations.

4.4 DYNAMICAL ASPECTS AND FAMILY FORMATION SCENARIOS

In total, assuming that our classification and the literature classes assigned from spectrophotometry are correct, then 36 members of the (36256) 1999 XT17 family have a classification. Out of these, 16 asteroids are classified as A-type, making a proportion of 44.4% of potential A-types in this family. Among these, four asteroids are confirmed A-types from the combination of DR3 and NIR data: asteroids 36256 and 33763 are confirmed from NIR spectroscopy, and asteroids 25356 and 40671, from the combination of their Gaia DR3 spectrum and their MOVIS Ad colour (Popescu et al., 2018a). Their spectra are displayed in Fig.4.3.

The second most abundant class in this family is the S-complex, with a proportion of potential S-complex asteroids of 30.5%. In the following, assuming these are true S-complex objects, we explore the possibility that some are interlopers in the (36256) 1999 XT17 family.

As mentioned before, the (36256) 1999 XT17 family orbits in the so-called "pristine zone" of the Main Belt. We studied the identified S-complex families in the pristine zone, wondering if they could be the source of interlopers in the (36256) 1999 XT17 family. According to Nesvorny et al. (2015), other five families showing a S-complex composition are detected in the pristine zone: (158) Koronis, (832) Seraphina, (918) Itha, (10811) Lau, and (15477) 1999 CG1. However, none of these families is in close vicinity to the 1999 XT17 family, as visible in the proper orbital elements plots of Fig.4.4. These families are unlikely to be the source of contamination for the (36256) 1999 XT17 family.

While the pristine zone is relatively empty compared to other regions of the Main Belt (Nesvorny et al., 2015), it was shown that this region is contaminated by "Eos family fugitives" (Tsirvoulis et al., 2018; Brož and Morbidelli, 2019). The (36256) 1999 XT17 family is located just inwards the 7:3 MMR with Jupiter, a region populated as well by Eos family members that drifted away from the family core by the action of non-gravitational forces (Nesvorny et al., 2015). In Fig.4.5 taken from Fig.3 of Tsirvoulis et al. (2018) is shown the V-shape of the (221) Eos family as identified by Milani et al.

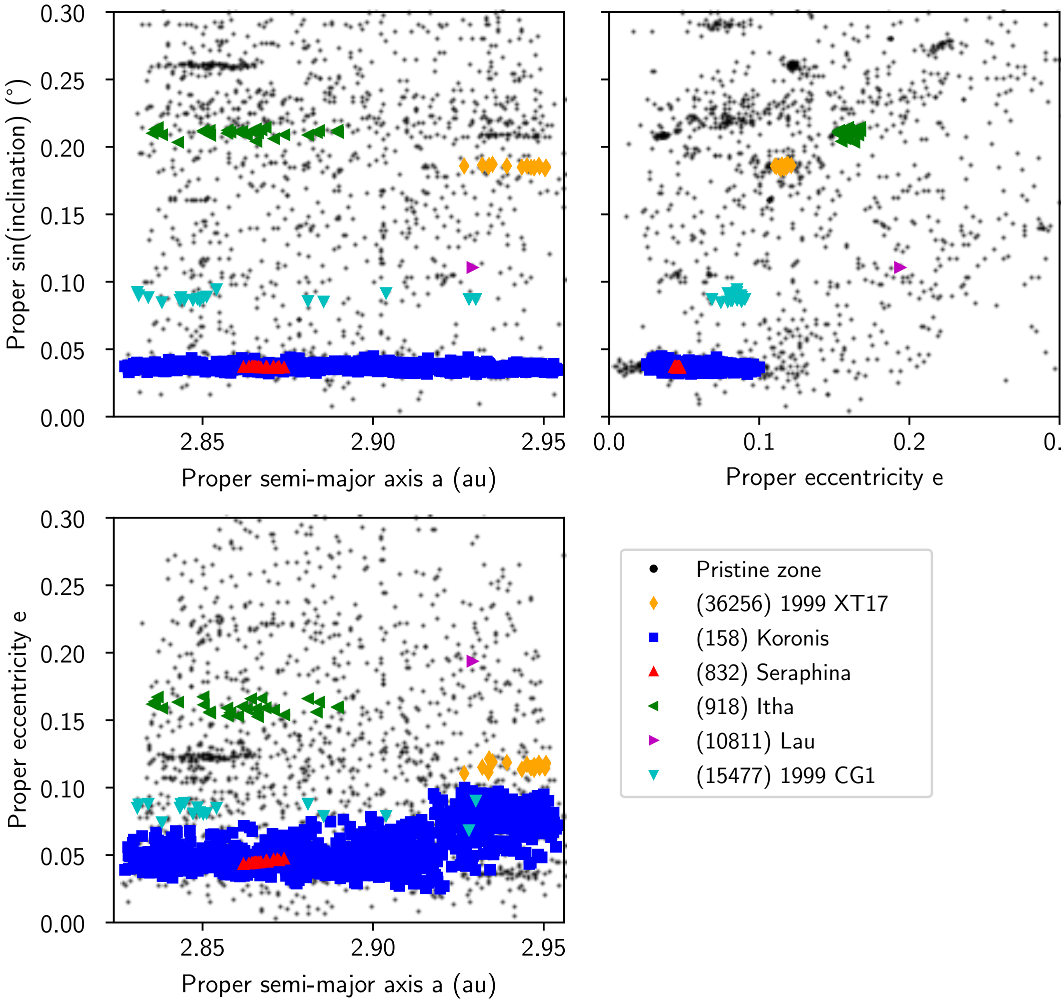

Figure 4.4: Proper orbital elements plots of the pristine zone (black dots) on which are highlighted S-complex families identified by Nesvorny et al. (2015). Only the asteroids having a Gaia DR3 spectrum are highlighted in this plot.

(2014). Tsirvoulis et al. (2018) selected asteroids in a region of the pristine zone delimited by $2.82 < a_p < 2.96$, $0.03 < e_p < 0.1$ and $0.12 < \sin(i_p) < 0.2$, with a_p,e_p and i_p the proper orbital elements of the objects. It is visible in Fig.4.5 that the asteroids in the selected region are in continuity with the V-shape of Eos, so they have been identified by Tsirvoulis et al. (2018) as Eos fugitives that have crossed MMR 7:3 quickly enough that their eccentricity did not reach planet-crossing values. According to Nesvorny et al. (2015), such resonance crossing can lead to a discontinuity in eccentricity between family fugitives and core members, while affecting little the objects' proper inclination.

We displayed the (36256) 1999 XT17 and the (221) Eos family as defined by Nesvorny et al. (2015) in the absolute magnitude versus proper semi-major axis space, and in the proper orbital elements space in Fig.4.6. Tsirvoulis et al. (2018) and Brož and Morbidelli (2019) discovered that the (36256) 1999 XT17 family members share similar inclinations as the Eos family core, but show slightly larger eccentricities. Brož and Morbidelli (2019) concluded that the (36256) 1999 XT17 is a remnant of the original velocity field of the Eos family, and may further contaminate the pristine zone. In the proper elements space (top panels of Fig.4.6), we can see this discontinuity in eccen-

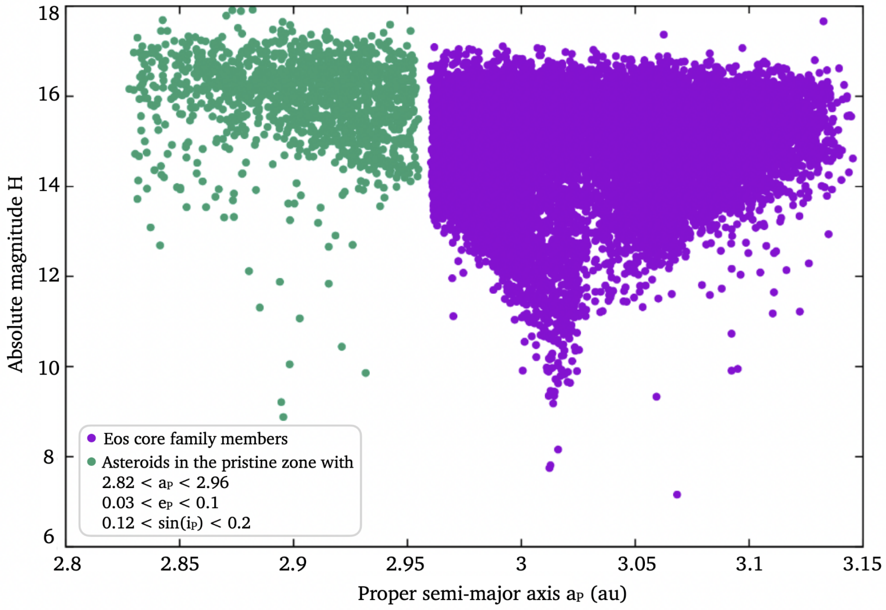

Figure 4.5: Figure 3 from Tsirvoulis et al. (2018): (221) Eos family V-shape and identified population of Eos fugitives in the pristine zone. The Eos family core as identified by Milani et al. (2014) is displayed in purple dots, and the asteroids in the pristine zone in the region delimited by $2.82 < a_p < 2.96$, $0.03 < e_p < 0.1$ and $0.12 < \sin(i_p) < 0.2$ in green dots.

tricity between the members of the (36256) 1999 XT17 and the core of the Eos family, while both clusters show similar proper inclination values. On the V-shape plot (down panel), it can be noticed as well that the (36256) 1999 XT17 family members having $H \lesssim 14$ lay outside the V-shape of Eos. These objects were all classified A-types here, and they have a SNR> 28.

Every (36256) 1999 XT17 family member we classified as belonging to the secondary S-complex lays inside the Eos family V-shape. These objects present similar inclination values to the Eos family core, and show a discontinuity in eccentricity. They could therefore be Eos fugitives that were merged with asteroids of the (36256) 1999 XT17 family by the HCM (Nesvorny et al., 2015).

Indeed, the fact that the pristine zone presents a lower number density of asteroid than the rest of the belt had an impact in the definition of asteroid families with the HCM (Nesvorny et al., 2015). Many families are detected in this little populated zone (about 20 families with $i_p < 17.5°$), much more than in denser wider zones of the belt. From this observation, Nesvorny et al. (2015) concluded that the family identification from the HCM is likely incomplete. Furthermore, this method is unable to detect that objects orbiting on one side of a resonance belong to a family of asteroids on the other side of the resonance, since the distance represented by the resonance is greater than the chosen d_{cut} (see section 1.2 Chapter 1 for details about the HCM). Therefore, it is probable that the Eos fugitives were identified as a new family by the HCM, and that they were merged with the (36256) 1999 XT17 family due to their similar proper elements.

Spectroscopically, Eos is mostly composed of K-type asteroids (Brož and Morbidelli, 2019), so it should be possible to distinguish Eos fugitives from (36256) 1999 XT17 family members. However, the distinction between S and K-types is non trivial in the

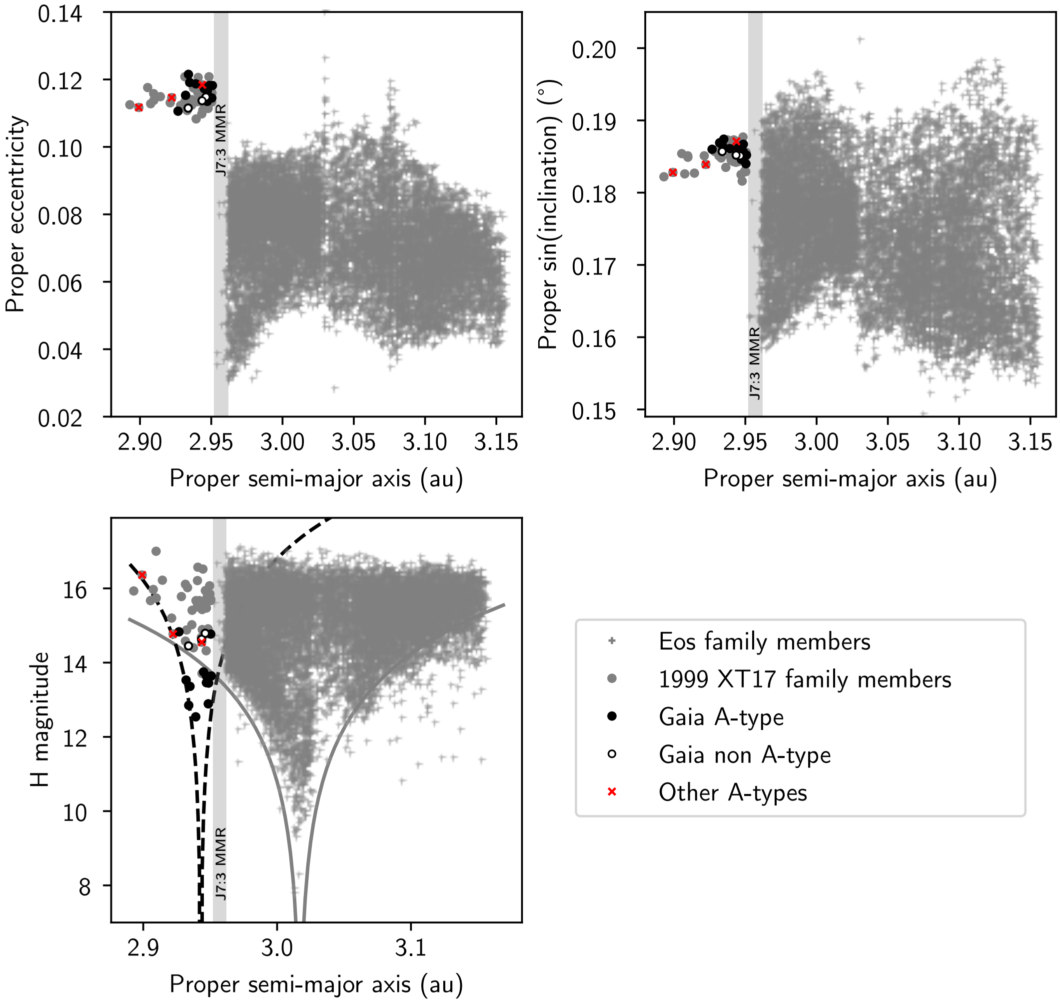

Figure 4.6: V-shape (down panel) and proper orbital elements plots (top panels) of the (36256) 1999 XT17 and the (221) Eos family, according to Nesvorny et al. (2015). The Eos family members are displayed as grey crosses, and those of the 1999 XT17 family as circles. Black filled circles are 1999 XT17 family members that were classified as A-types by our algorithm, while the empty circles are members that were not classified as A. Family members that were classified A-types in the literature and have no DR3 spectra are marked with a red "X". Among the latter group, asteroid 76627 overlaps in the plot with asteroid 88052 (non A-type), due to their similar proper orbital elements and H magnitudes. The position of the 7:3 mean motion resonance with Jupiter is highlighted with a shade of light-grey. The V-shapes of the two families are drawn by eye following the equation $H = 5\log_{10}(|a - a_c|/C_0)$ with $a_C = 2.942$ au and $C_0 = 1.8 \times 10^{-5}$ au for the 1999 XT17 family, and $a_C = 3.017$ au and $C_0 = 2.25 \times 10^{-4}$ au for the Eos family.

visible (Vokrouhlický et al., 2006), so it is not impossible that the S-complex asteroids detected in the 1999 XT17 family are in fact K-type Eos fugitives.

The cluster of asteroids laying outside Eos' V-shape (down panel of Fig.4.6) contains ten asteroids, nine of which classified A-types from their DR3 spectra with a SNR>28, and four being confirmed A-types from NIR data (DeMeo et al., 2019; Popescu et al., 2018a). Moreover, the link established between asteroids 36256 and 33763 and olivine-rich samples from the RELAB database confirms the likely high olivine content of these bodies. Since they are outside the V-shape of Eos, they are less likely to be part of Eos family fugitives. We therefore argue that the A-type members of the (36256) 1999 XT17 family originate from the breakup of a common parent body.

If the true (36256) 1999 XT17 family is composed only by A-types, it could originate from the breakup of an olivine-rich asteroid that was once itself part of a differentiated planetesimal. The latter could have been catastrophically disrupted in another region, and a fragment of it could then have been implanted in its current location through dynamical processes (Bottke et al., 2006b; Raymond and Izidoro, 2017). The (36256) 1999 XT17 family is small, containing just a few dozen asteroids, the largest of which (asteroid 36256 itself) has a small diameter of only 10 km, and the rest have diameters around 5 km. These facts could provide corroborating evidence for this theory. This was recently shown to be a valid scenario for the parent body of the enstatite meteorites of subtype EL, identified as the (161) Athor family (Avdellidou et al., 2022). It has been proposed that this family was delivered to the IMB from the terrestrial region during the early evolution phases of our Solar System (Avdellidou et al., 2022).

On the other hand, some olivine-rich Main Belt asteroids could be the result of direct accretion of grains from an oxidized region of the solar nebula, instead of magmatic differentiation, as understood from the study of R-chondrites (Schulze et al., 1994; Sunshine et al., 2007). The olivine-rich parent body at the origin of the (36256) 1999 XT17 family could have formed through such processes, if such processes are able to form large enough bodies. These olivine-rich asteroids could also be fragments of an early Mars' crust implanted in the Main Belt, resulting from a mega impact on an early Mars (Polishook et al., 2017; Hyodo and Genda, 2018).

We go on to explore the hypothesis that the (36256) 1999 XT17 family is totally or partially differentiated. As stated above, the second most abundant class in this family according to the literature is the S-complex. S-complex asteroids are typically associated to ordinary chondrites (Vernazza et al., 2015; Reddy et al., 2015; DeMeo et al., 2022), that are undifferentiated meteorites (see Vernazza et al., 2015, and references therein). Based on the hypothesis that these objects are correctly classified and belong to the (36256) 1999 XT17 family, it is possible that their parent body was only partially differentiated. It could have built an olivine mantle without heating enough for the crust to melt, which could have preserved its undifferentiated nature (Weiss and Elkins-Tanton, 2013). Unfortunately, spectrophotometry is often not precise enough to distinguish between the A and S classes in a reliable way (DeMeo et al., 2019). Further spectroscopic observations in the NIR would allow to validate the spectral types, and could help us distinguish between our hypotheses.

Moreover, Migliorini et al. 2024 (EGU 2024 poster: [2]) studied VISNIR spectra of brachinite meteorites and S-type asteroids, to assess the potential detection limit of olivine from spectroscopy. They found that olivine-rich bodies, depending on the olivine abundance and on the iron content, show spectra matching with pyroxene-rich S-type asteroids and not with A-type asteroids spectra. There is thus a possibility that the missing mantle problem comes from the fact that A-type asteroids are not the only olivine-rich bodies in the Main Belt, but are the only one confirmed as such from VISNIR spectroscopy.

Finally, spectroscopic studies that attempted to map the olivine-rich asteroids in the Main Belt concluded that there is no prominent concentration of olivine-rich objects in any asteroid family (DeMeo et al., 2019). Here, we identified the first concentration

---

[2] `https://doi.org/10.5194/egusphere-egu24-7979`

of A-type objects in an asteroid family, using the Gaia DR3 dataset. This identification makes the (36256) 1999 XT17 family the first olivine-rich family in the Main Belt.

4.5 CONCLUSIONS

The (36256) 1999 XT17 family, orbiting in the pristine zone of the Main Belt, appears to show the first concentration of A-type asteroids in an asteroid family to date. This family contains 16 potential A-type asteroids, among which four are confirmed by NIR data. The comparison of the VISNIR spectra of asteroids 36256 and 33763 with meteorites confirms that these objects should be mostly composed of pure olivine.

The other dominant spectroscopic class of asteroids in this family is the S-complex. These objects could be: (i) true S-complex bodies and true family members, (ii) true S-complex bodies interlopers in the family, (iii) K-type Eos fugitives interlopers in the family, or (iv) A-type asteroids misclassified as S-complex and true family members. Considering these scenarios, we propose two main hypotheses for the origin of the (36256) 1999 XT17 family. First, if the true family members are only A-types, the parent body of the family could have been a pure olivine-rich object, formed in the mantle of a partially or totally differentiated planetesimal. This parent body could have been disrupted at a different location in the Solar System, before getting implanted at its current location in the pristine zone. Second, if the family is composed of A-type and S-complex asteroids, it could come from a partially differentiated object that broke in situ. NIR observations are needed to confirm the spectral type of this family's members, and to help conclude between our different scenarios.

Finally, the Gaia DR3 dataset could allow to study other families presenting a high potential A-type asteroids content from the literature, such as the family (1019) Strackea (Vinogradova, 2019). There is a possibility that the family (36256) 1999 XT17 is not the only olivine-rich family in the Main Belt. The search for other A-type asteroids using the Gaia DR3 dataset is one of the goals of the next chapter.

5

CLASSIFICATION OF GAIA DR3 SPECTRA

In the previous chapters, I presented different ways to search for evidence of differentiation in the Main Belt. In Chapter 3, I searched for potential analogues of the andesite meteorite Erg Chech 002, using the Gaia DR3 dataset (Galinier et al., 2023). I found no convincing match of the meteorite in the DR3 dataset, and few potential matches in the literature.

Then, in Chapter 4, I searched for evidence of differentiation in asteroid collisional families, in the form of a potential concentration of olivine-rich asteroids. I found that the family (36256) 1999 XT17 contains a high number of potential A-type asteroids, making it the first potential olivine-rich family even discovered in the Main Belt (Galinier et al., 2024).

In the present chapter, I aimed to study the Main Belt as a whole, in particular to look for potential differentiated asteroid families. To do so, I classified the DR3 asteroids reflectance spectra into the taxonomic scheme developed by Bus and Binzel, 2002a. As stated in Chapter 1, classifying asteroids based on their reflectance spectra allows to get an idea of their surface composition. Such information is useful to constrain the formation and evolution of bodies in the Solar System, and to study populations of objects, such as asteroid families. In this chapter, I tried to optimise the classification of DR3 spectra paying a particular attention to the A-class, characteristic of olivine-rich compositions.

Studying the classification of Gaia DR3 reflectance spectra is also important to prepare for the DR4, as the DPAC plans to produce a Gaia taxonomic scheme to accompany this data release. This Gaia taxonomy will probably be produced using unsupervised machine learning methods. In this chapter, I performed a supervised classification of DR3 asteroids spectra as a preliminary study, and I did not aim to develop a new Gaia taxonomic scheme.

To assess the limits of my classification method and the ones intrinsic to the DR3 spectra, I worked on chosen samples of objects already characterised with spectroscopy in the literature, presented in section 5.1. In section 5.2, I introduce the classification algorithm, and the different methods used to evaluate its performances. Various tests and choices made to test the and improve the classification method are presented in section 5.3, and the obtained most satisfactory classification of DR3 spectra is presented in section 5.4. A supplementary classification step in presented in section 5.5, developed to improve the classification of A-type asteroids. A justification and verification of the choices made during the development of the classification method are given in Appendix C.2.

In a second part, presented in section 5.6, the developed classification method is applied to classify Main Belt asteroids. First, it is used to characterise again the family (36256) 1999 XT17 in section 5.6.1, in order to further test the performances of the classification method, and to confirm the results obtained in Chapter 4. It is then used in section 5.6.2 to classify a subsample of 18 739 Main Belt asteroids having a DR3 spectrum with SNR⩾30. Then, a search for potential new A-type asteroids and A-type-rich families in the Main Belt is detailed in section 5.6.3.

5.1 DATA

The Gaia DR3 contains mean reflectance spectra of asteroids with an average SNR as low as 13, and which lower quality bands are flagged (Gaia Collaboration et al., 2023). To assess the accuracy of the classification of DR3 spectra, I first filtered out potentially low-quality spectra in the DR3 dataset. I filtered out asteroids having flagged bands from 462 to 946 nm, without considering the first two and last two bands of the spectra for the classification, as they are often affected by systematic issues (Gaia Collaboration et al., 2023; Galinier et al., 2023). Then, I considered only asteroids having a Gaia DR3 spectrum with an average SNR⩾30. This procedure filtered out 69% of the DR3 dataset, leaving 18 739 spectra to be studied. The DR3 dataset after this filtering procedure will be referred to as the "filtered Gaia DR3 dataset" in the following.

Before classifying Gaia DR3 spectra and in order to test the classification algorithm, I classified the spectra characterised in the visible wavelength range by the SMASS, and classified by Bus and Binzel (2002a). Later on, to further test the accuracy of the classification method, I used a list of asteroids with a "confirmed" spectral type, i.e. which have been classified from VISNIR or NIR observations in the literature. A description of this list will be provided in the following.

5.2 METHODS

To classify asteroid reflectance spectra, I used a curve matching algorithm, that I present in section 5.2.1. To verify the accuracy of the classification performed, I used confusion matrices, presented in section 5.2.2. Finally, to further study the classification of DR3 spectra and to compare it with the literature, I used the Principal Component Analysis (PCA) presented, in section 5.2.3.

5.2.1 Classification algorithm: curve matching

Assigning an asteroid to a taxonomic class in an existing scheme (supervised classification) is done via the comparison of the object's spectrum with spectra characteristic of each taxonomic classes: the template spectra. A template spectrum is usually defined as the average spectrum of the asteroids belonging to a given class, or the average spectrum of the asteroids having the most reliable spectra in that class (Bus and Binzel, 2002a; DeMeo et al., 2009; Mahlke et al., 2022).

Asteroids can be classified in a given taxonomic scheme, by comparing their spectrum with template spectra using curve matching methods. Such method rely on the calculation of a χ^2 figure or merit, quantifying the level of similarity between a spectrum and the template of a taxonomic class. The value of the figure of merit indicates the classes that best correspond to an asteroid, based on its spectrum.

Different mathematical definition of such figure of merit exist. Here, in order to classify Gaia DR3 reflectance spectra, I used the Φ_{comb} coefficient of Popescu et al. (2012). This coefficient was originally developed to perform curve matching between meteorite and asteroid spectra, and it was found to give satisfactory results (Popescu et al., 2012; Mahlke et al., 2023). This similarity criterion is defined as

$$\Phi_{comb} = \frac{\rho_{X,T}}{\Phi_{std}} \tag{5.1}$$

with X an asteroid spectrum and T a template spectrum sampled at the same wavelengths λ_i , consisting of N data points x_i and t_i $\forall i \in \{1, \ldots, N\}$. $\rho_{X,T}$ is the correlation coefficient of the two spectra, and it quantifies their level of dependence following

$$\rho_{X,T} = \frac{cov(X,T)}{\sigma_X \sigma_T}. \tag{5.2}$$

$cov(X,T)$ is the covariance matrix characterising the dependence of the two variables, and σ_X and σ_T are the respective standard deviations associated to each reflectance spectrum. High values of $\rho_{X,T}$ indicate a high level of dependence between the spectra, hence a good spectral match.

The second parameter used in the calculation of Φ_{comb}, Φ_{std}, quantifies the similarity between a template and an asteroid spectrum, by minimising the standard deviation of the errors between the two spectra:

$$\Phi_{std} = \frac{1}{N}\sqrt{\sum_i^N (e_i - \bar{e})^2}. \tag{5.3}$$

$e_i = (x_i - t_i)$ represents the error (or residuals) between the asteroid and the template spectrum, and $\bar{e}$ is the mean residual value. The lower Φ_{std}, the better the match. Therefore, the most probable class of an asteroid is given by the highest values of Φ_{comb}, after calculating it between an asteroid spectrum and every template spectra representing the classes defined a given taxonomic scheme.

In the following, the taxonomic classes corresponding to the two highest values of Φ_{comb} will be considered, as done by Popescu et al. (2012). The highest value of Φ_{comb} gives the "first best class" of an asteroid, and the second highest value, the "second best class".

5.2.2 Confusion matrix

I used confusion matrices to evaluate the accuracy of the classification model. Such matrix allows to visualise the performances of a classification algorithm, showing the proportions of well and badly-classified objects. Each row of the confusion matrix corresponds to the "true" class of an object, considered here as its class from the literature. Each column corresponds to the "predicted" class, assigned to the object by the classification algorithm. Each cell of the confusion matrix thus contains the proportion of objects of a given true class, estimated by the algorithm to belong to a predicted class. The elements in central diagonal cells are true positives, i.e objects classified the same in the literature and by the algorithm. The more diagonal the matrix, the better the classification.

The asteroids that are classified differently in the literature and by the classification algorithm are either false positives, or false negatives. False positives are asteroids that are classified in a class but do not belong to this class in the literature. They appear in column cells outside of the diagonal. False negatives are asteroids that belong to a class in the literature, but are not classified as such. They appear in row cells outside of the diagonal.

I ordered the classes in the confusion matrix according to the prominence of the feature of their associated spectra, based on the Bus and Binzel (2002a) taxonomy (see Fig.1.13). That way, classes representing similar spectra appear next to each other. In the following, only the first best class of objects, associated to the highest value of Φ_{comb}, will be represented in the confusion matrix. The second best class will be exploited in a second time, for the development of a secondary classification step in section 5.5.

5.2.3 Principal Component Analysis

The PCA is a dimension-reduction technique allowing the analysis and interpretation of large datasets, while preserving the maximum amount of information. It has been widely used as an unsupervised method to classify asteroids and to define taxonomies (e.g Tholen, 1989; Bus and Binzel, 2002b; Bus and Binzel, 2002a; DeMeo et al., 2009). It relies on the linear transformation of the data into a new coordinate system, representing in few dimensions most of the variation of the data. The principal components are the new variables representing the system, ranked by the quantity of variance they contain.

For asteroids spectra, as explained in Bus and Binzel (2002a), the first principal component (hence the one that contains the most variance) is the spectral slope γ. It is calculated in Bus and Binzel (2002a) by fitting a line of equation $R_i = 1.0 + \gamma(\lambda_i - 0.55)$ to each asteroid spectrum, with R_i the reflectance value at a given wavelength λ_i (in microns), the spectra being normalised at 550 nm. Bus and Binzel (2002a) then divide each spectrum by this spectral slope, and apply the PCA to the dataset of slope-less asteroids spectra. The first principal components derived from this operation, called PC2′ by Bus and Binzel (2002a), is sensitive to the strength of a potential band around 1000 nm. The stronger the band, the more negative the value of PC2′. This method enables the visualisation of a complex spectral data set of asteroids in two dimensions, the spectral slope and the depth of a potential 1 micron band. Bus and Binzel (2002a) used this representation to assign classes to asteroids from their SMASS spectra.

In this work, I did not use the PCA to classify asteroids spectra. Instead, I used it to visualise the results of the classification of Gaia DR3 spectra and to compare it with the literature, as described in Appendix C.2.3.

5.3 BUILDING THE CLASSIFICATION

In the following, I present the trial-and-error approach and the choices that lead to a satisfactory classification of Gaia DR3 reflectance spectra. In section 5.3.1, I check the performances of the classification algorithm, applying it to asteroids spectra of the

SMASS dataset. Then, in section 5.3.2, I study the influence of the choice of templates on the classification of Gaia DR3 spectra, and I define Gaia templates based on the ones of the Bus taxonomy. In section 5.3.3, I study the influence of the literature classes considered as "true" on the classification. Finally, in section 5.4, I present the final results of the classification of Gaia DR3 reflectance spectra.

5.3.1 Testing the algorithm: classification of SMASS spectra using Bus templates

First and foremost, I tested the performances of the algorithm on visible spectra observed by the SMASS and classified by Bus and Binzel (2002a). Using SMASS spectra to test the algorithm allowed me to: (i) test the limitations of the classification algorithm in the visible wavelength range, which is of interest since both Gaia and SMASS cover this range ; and (ii) test the classification of SMASS spectra using template spectra derived from this dataset. The Bus and Binzel (2002a) taxonomic templates, displayed

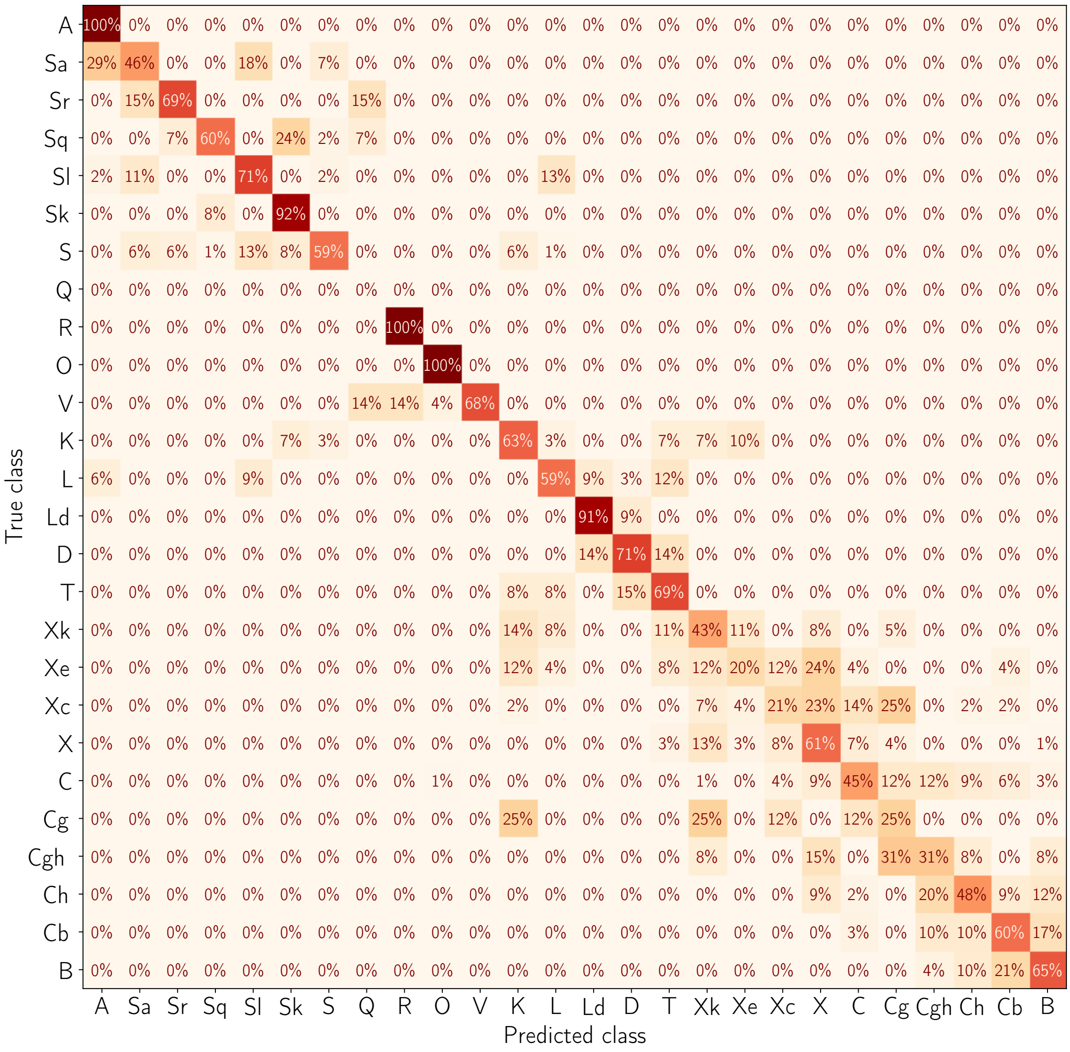

	A	Sa	Sr	Sq	Sl	Sk	S	Q	R	O	V	K	L	Ld	D	T	Xk	Xe	Xc	X	C	Cg	Cgh	Ch	Cb	B
A	100%	0%	0%	0%	0%	0%	0%	0%	0%	0%	0%	0%	0%	0%	0%	0%	0%	0%	0%	0%	0%	0%	0%	0%	0%	0%
Sa	29%	46%	0%	0%	18%	0%	7%	0%	0%	0%	0%	0%	0%	0%	0%	0%	0%	0%	0%	0%	0%	0%	0%	0%	0%	0%
Sr	0%	15%	69%	0%	0%	0%	0%	15%	0%	0%	0%	0%	0%	0%	0%	0%	0%	0%	0%	0%	0%	0%	0%	0%	0%	0%
Sq	0%	0%	7%	60%	0%	24%	2%	7%	0%	0%	0%	0%	0%	0%	0%	0%	0%	0%	0%	0%	0%	0%	0%	0%	0%	0%
Sl	2%	11%	0%	0%	71%	0%	2%	0%	0%	0%	0%	0%	13%	0%	0%	0%	0%	0%	0%	0%	0%	0%	0%	0%	0%	0%
Sk	0%	0%	0%	8%	0%	92%	0%	0%	0%	0%	0%	0%	0%	0%	0%	0%	0%	0%	0%	0%	0%	0%	0%	0%	0%	0%
S	0%	6%	6%	1%	13%	8%	59%	0%	0%	0%	0%	6%	1%	0%	0%	0%	0%	0%	0%	0%	0%	0%	0%	0%	0%	0%
Q	0%	0%	0%	0%	0%	0%	0%	0%	0%	0%	0%	0%	0%	0%	0%	0%	0%	0%	0%	0%	0%	0%	0%	0%	0%	0%
R	0%	0%	0%	0%	0%	0%	0%	0%	100%	0%	0%	0%	0%	0%	0%	0%	0%	0%	0%	0%	0%	0%	0%	0%	0%	0%
O	0%	0%	0%	0%	0%	0%	0%	0%	0%	100%	0%	0%	0%	0%	0%	0%	0%	0%	0%	0%	0%	0%	0%	0%	0%	0%
V	0%	0%	0%	0%	0%	0%	0%	14%	14%	4%	68%	0%	0%	0%	0%	0%	0%	0%	0%	0%	0%	0%	0%	0%	0%	0%
K	0%	0%	0%	0%	0%	7%	3%	0%	0%	0%	0%	63%	3%	0%	0%	7%	7%	10%	0%	0%	0%	0%	0%	0%	0%	0%
L	6%	0%	0%	0%	9%	0%	0%	0%	0%	0%	0%	0%	59%	9%	3%	12%	0%	0%	0%	0%	0%	0%	0%	0%	0%	0%
Ld	0%	0%	0%	0%	0%	0%	0%	0%	0%	0%	0%	0%	0%	91%	9%	0%	0%	0%	0%	0%	0%	0%	0%	0%	0%	0%
D	0%	0%	0%	0%	0%	0%	0%	0%	0%	0%	0%	0%	0%	14%	71%	14%	0%	0%	0%	0%	0%	0%	0%	0%	0%	0%
T	0%	0%	0%	0%	0%	0%	0%	0%	0%	0%	0%	8%	8%	0%	15%	69%	0%	0%	0%	0%	0%	0%	0%	0%	0%	0%
Xk	0%	0%	0%	0%	0%	0%	0%	0%	0%	0%	0%	14%	8%	0%	0%	11%	43%	11%	0%	8%	0%	5%	0%	0%	0%	0%
Xe	0%	0%	0%	0%	0%	0%	0%	0%	0%	0%	0%	12%	4%	0%	0%	8%	12%	20%	12%	24%	4%	0%	0%	0%	4%	0%
Xc	0%	0%	0%	0%	0%	0%	0%	0%	0%	0%	0%	2%	0%	0%	0%	0%	7%	4%	21%	23%	14%	25%	0%	2%	2%	0%
X	0%	0%	0%	0%	0%	0%	0%	0%	0%	0%	0%	0%	0%	0%	0%	3%	13%	3%	8%	61%	7%	4%	0%	0%	0%	1%
C	0%	0%	0%	0%	0%	0%	0%	0%	0%	1%	0%	0%	0%	0%	0%	0%	1%	0%	4%	9%	45%	12%	12%	9%	6%	3%
Cg	0%	0%	0%	0%	0%	0%	0%	0%	0%	0%	0%	25%	0%	0%	0%	0%	25%	0%	12%	0%	12%	25%	0%	0%	0%	0%
Cgh	0%	0%	0%	0%	0%	0%	0%	0%	0%	0%	0%	0%	0%	0%	0%	0%	8%	0%	0%	15%	0%	31%	31%	8%	0%	8%
Ch	0%	0%	0%	0%	0%	0%	0%	0%	0%	0%	0%	0%	0%	0%	0%	0%	0%	0%	0%	9%	2%	0%	20%	48%	9%	12%
Cb	0%	0%	0%	0%	0%	0%	0%	0%	0%	0%	0%	0%	0%	0%	0%	0%	0%	0%	0%	0%	3%	0%	10%	10%	60%	17%
B	0%	0%	0%	0%	0%	0%	0%	0%	0%	0%	0%	0%	0%	0%	0%	0%	0%	0%	0%	0%	0%	0%	4%	10%	21%	65%

Figure 5.1: Confusion matrix corresponding to the classification of SMASS spectra, using Bus and Binzel (2002a) templates.

in Fig.1.13 in Chapter 1, are calculated as the average of asteroids spectra from the SMASS, belonging to each of the 26 spectral class defined in the Bus taxonomy. These spectra are normalised at 550 nm, and are represented by nine reflectance values and their associated uncertainties, spanning the wavelength range from 440 to 920 nm.

To evaluate the performances of the algorithm on SMASS data, I used a sample of 1187 asteroids both classified by Bus and Binzel (2002a), and contained in the filtered Gaia DR3 dataset. In this sample, 467 asteroids belong to the S-complex, 307 to the C-complex and 226 to the X-complex (see Chapter 1 for the definition of taxonomies and complexes). The others asteroids are 52 B-types, 43 L-types, 30 K-types, 28 V-types, 13 T-types, 11 Ld-types, 10 A-types, 3 R-types, and one O-type. As a note, there is no Q-type asteroid in the sample considered here.

To perform the classification, I sampled the 1187 SMASS spectra like the Bus and Binzel (2002a) templates using a spline function (python function *csaps*), and I classified them using the Φ_{comb} coefficient. The results of the classification algorithm are displayed as a confusion matrix in Fig.5.1. This confusion matrix is quite diagonal, indicating that most asteroids are well classified by the algorithm. Some inevitable spillovers can be observed between the sub-classes of a given complex (for example, Xe and Xk-type asteroids assigned to different sub-classes of the X-complex), but the classification is overall satisfactory.

In Bus and Binzel (2002a), spectral classes are assigned to asteroids on the base of their principal components. This can explain why the classification obtained by our curve-matching technique is slightly different from the one of Bus and Binzel (2002a). This technique is indeed not able to distinguish well between sub-classes of a given complex, or between classes that are spatially close in the principal component space. Despite these differences, the results obtained by the classification technique were judged satisfactory enough, and the curve-matching algorithm was used to classify Gaia DR3 spectra.

5.3.2 Study of the templates: classification of Gaia DR3 spectra

In the following, I explored the influence of the choice of templates on the classification of Gaia DR3 spectra. I started with classifying Gaia spectra using Bus templates, and the bad classification results lead me to define Gaia templates. I then evaluated the results of the classification obtained with the Gaia templates.

5.3.2.1 *Classification of Gaia DR3 spectra using Bus templates*

To compare the classification of DR3 spectra using Bus templates with the one obtained with SMASS spectra, I used the same sample of 1187 asteroids both classified by Bus and Binzel (2002a) and having a spectrum in the DR3. To perform the classification, I sampled the Bus templates like the DR3 spectra, using a spline fit. Sampling the Gaia spectra like the SMASS templates was a possible choice, but re-sampling more than a thousand asteroids requires more computational time than re-sampling only a few templates. I then applied the curve matching classification algorithm to the DR3 spectra, not taking into account their first and last two bands (Gaia Collaboration et al., 2023; Galinier et al., 2023; Oszkiewicz et al., 2023; Galinier et al., 2024).

The result of this classification is shown as a confusion matrix in Fig.5.2. Most objects are not correctly classified here: most S-complex asteroids are found L; the K, L, Ld, D and T-types are all found D-types; and asteroids belonging to the X and C-complexes are mostly either found T, Xk, X or Ch-types.

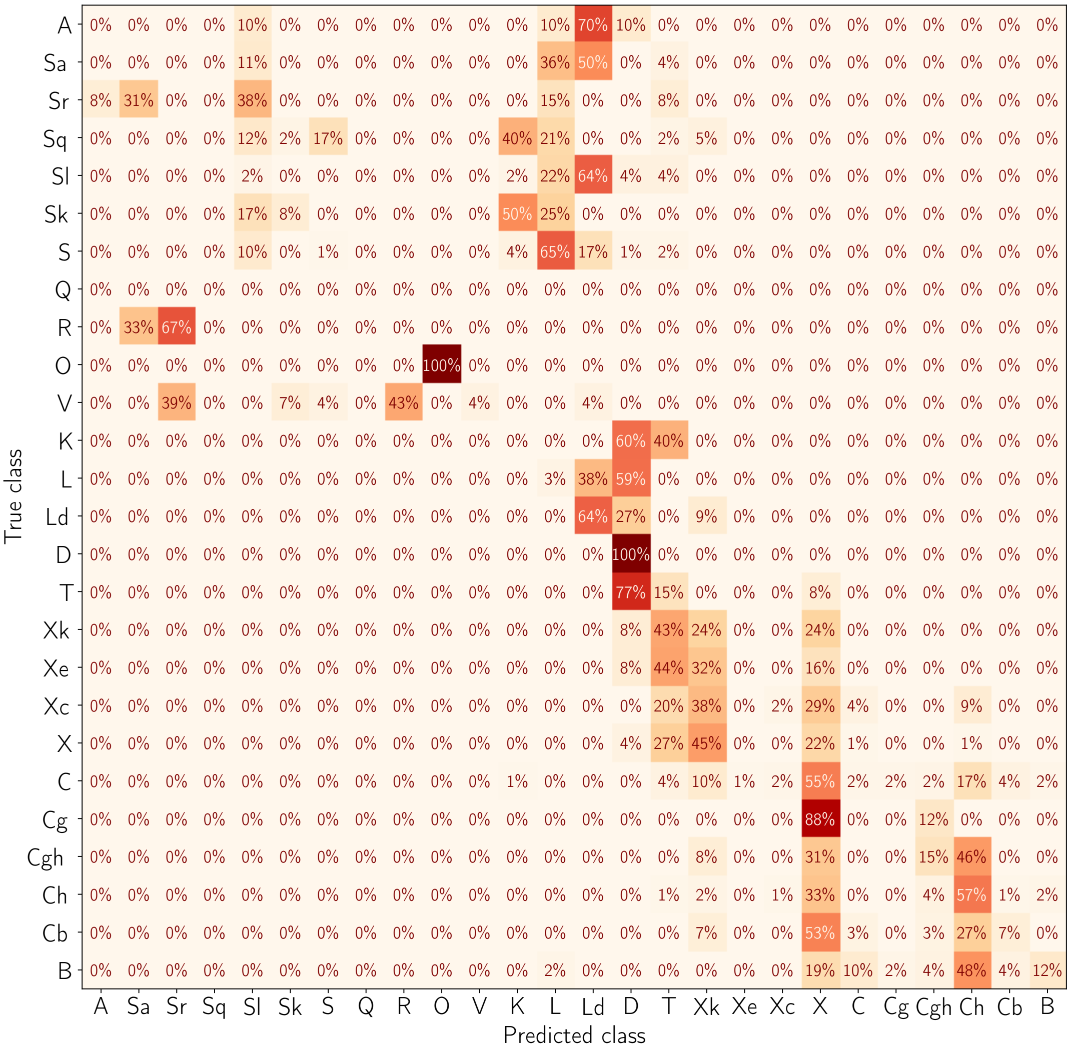

True class \ Predicted class	A	Sa	Sr	Sq	Sl	Sk	S	Q	R	O	V	K	L	Ld	D	T	Xk	Xe	Xc	X	C	Cg	Cgh	Ch	Cb	B
A	0%	0%	0%	0%	10%	0%	0%	0%	0%	0%	0%	0%	10%	70%	10%	0%	0%	0%	0%	0%	0%	0%	0%	0%	0%	0%
Sa	0%	0%	0%	0%	11%	0%	0%	0%	0%	0%	0%	0%	36%	50%	0%	4%	0%	0%	0%	0%	0%	0%	0%	0%	0%	0%
Sr	8%	31%	0%	0%	38%	0%	0%	0%	0%	0%	0%	0%	15%	0%	0%	8%	0%	0%	0%	0%	0%	0%	0%	0%	0%	0%
Sq	0%	0%	0%	0%	12%	2%	17%	0%	0%	0%	0%	40%	21%	0%	0%	2%	5%	0%	0%	0%	0%	0%	0%	0%	0%	0%
Sl	0%	0%	0%	0%	2%	0%	0%	0%	0%	0%	0%	2%	22%	64%	4%	4%	0%	0%	0%	0%	0%	0%	0%	0%	0%	0%
Sk	0%	0%	0%	0%	17%	8%	0%	0%	0%	0%	0%	50%	25%	0%	0%	0%	0%	0%	0%	0%	0%	0%	0%	0%	0%	0%
S	0%	0%	0%	0%	10%	0%	1%	0%	0%	0%	0%	4%	65%	17%	1%	2%	0%	0%	0%	0%	0%	0%	0%	0%	0%	0%
Q	0%	0%	0%	0%	0%	0%	0%	0%	0%	0%	0%	0%	0%	0%	0%	0%	0%	0%	0%	0%	0%	0%	0%	0%	0%	0%
R	0%	33%	67%	0%	0%	0%	0%	0%	0%	0%	0%	0%	0%	0%	0%	0%	0%	0%	0%	0%	0%	0%	0%	0%	0%	0%
O	0%	0%	0%	0%	0%	0%	0%	0%	0%	100%	0%	0%	0%	0%	0%	0%	0%	0%	0%	0%	0%	0%	0%	0%	0%	0%
V	0%	0%	39%	0%	0%	7%	4%	0%	43%	0%	4%	0%	0%	4%	0%	0%	0%	0%	0%	0%	0%	0%	0%	0%	0%	0%
K	0%	0%	0%	0%	0%	0%	0%	0%	0%	0%	0%	0%	0%	0%	60%	40%	0%	0%	0%	0%	0%	0%	0%	0%	0%	0%
L	0%	0%	0%	0%	0%	0%	0%	0%	0%	0%	0%	0%	3%	38%	59%	0%	0%	0%	0%	0%	0%	0%	0%	0%	0%	0%
Ld	0%	0%	0%	0%	0%	0%	0%	0%	0%	0%	0%	0%	0%	64%	27%	0%	9%	0%	0%	0%	0%	0%	0%	0%	0%	0%
D	0%	0%	0%	0%	0%	0%	0%	0%	0%	0%	0%	0%	0%	0%	100%	0%	0%	0%	0%	0%	0%	0%	0%	0%	0%	0%
T	0%	0%	0%	0%	0%	0%	0%	0%	0%	0%	0%	0%	0%	0%	77%	15%	0%	0%	0%	8%	0%	0%	0%	0%	0%	0%
Xk	0%	0%	0%	0%	0%	0%	0%	0%	0%	0%	0%	0%	0%	0%	8%	43%	24%	0%	0%	24%	0%	0%	0%	0%	0%	0%
Xe	0%	0%	0%	0%	0%	0%	0%	0%	0%	0%	0%	0%	0%	0%	8%	44%	32%	0%	0%	16%	0%	0%	0%	0%	0%	0%
Xc	0%	0%	0%	0%	0%	0%	0%	0%	0%	0%	0%	0%	0%	0%	0%	20%	38%	0%	2%	29%	4%	0%	0%	9%	0%	0%
X	0%	0%	0%	0%	0%	0%	0%	0%	0%	0%	0%	0%	0%	0%	4%	27%	45%	0%	0%	22%	1%	0%	0%	1%	0%	0%
C	0%	0%	0%	0%	0%	0%	0%	0%	0%	0%	0%	1%	0%	0%	0%	4%	10%	1%	2%	55%	2%	2%	2%	17%	4%	2%
Cg	0%	0%	0%	0%	0%	0%	0%	0%	0%	0%	0%	0%	0%	0%	0%	0%	0%	0%	0%	88%	0%	0%	12%	0%	0%	0%
Cgh	0%	0%	0%	0%	0%	0%	0%	0%	0%	0%	0%	0%	0%	0%	0%	0%	8%	0%	0%	31%	0%	0%	15%	46%	0%	0%
Ch	0%	0%	0%	0%	0%	0%	0%	0%	0%	0%	0%	0%	0%	0%	0%	1%	2%	0%	1%	33%	0%	0%	4%	57%	1%	2%
Cb	0%	0%	0%	0%	0%	0%	0%	0%	0%	0%	0%	0%	0%	0%	0%	0%	7%	0%	0%	53%	3%	0%	3%	27%	7%	0%
B	0%	0%	0%	0%	0%	0%	0%	0%	0%	0%	0%	0%	2%	0%	0%	0%	0%	0%	0%	19%	10%	2%	4%	48%	4%	12%

Figure 5.2: Confusion matrix corresponding to the classification of Gaia DR3 spectra, using Bus and Binzel (2002a) templates.

The bad results of this classification can be due to differences between the Bus templates and the DR3 dataset. Indeed, the Bus templates were defined on SMASS data (Bus and Binzel, 2002a), and a difference in the red part of DR3 and SMASS spectra has been noted in Chapter 2. More generally, it is possible that the specificities of the DR3 reflectance spectra, explored in Chapter 2, make them difficult to compare to templates defined on another dataset. Therefore, I worked on a definition of templates based on Gaia DR3 reflectance spectra, to try improving the classification of DR3 spectra.

5.3.2.2 *Definition of Gaia templates*

To classify Gaia DR3 spectra in the Bus taxonomy using Gaia templates, I needed to produce a Gaia template for each of the 26 classes defined by Bus and Binzel (2002a). To do so, I used the taxonomic classes prototypes given in Bus and Binzel (2002a).

Table 5.1: Asteroids used in the definition of Gaia templates, defined as classes prototypes in the Bus and Binzel (2002a) taxonomy.

Spectral type	Asteroid number
A	246, 289, 863
Sa	63, 244, 625
Sr	984, 1494, 2956
Sq	33, 720
Sl	151, 192, 354
Sk	3, 11, 43
S	5, 7, 20
R	349, 1904, 5111
O	3628, 4341
V	4, 1929, 2912
K	221, 579, 606
L	42, 236, 908
Ld	269, 1406, 2850
D	1542, 2246, 4744
T	96, 596, 3317
Xk	21, 99, 114
Xe	64, 77, 434
Xc	65, 131, 209
X	22, 55, 69
C	1, 10, 52
Cg	175, 1300
Cgh	106, 706, 776
Ch	19, 48, 49
Cb	150, 210
B	2, 24, 85

These objects, listed in Table II of Bus and Binzel (2002a), are defined as good representatives of each class.

To produce the Gaia templates, the DR3 spectra corresponding to the asteroids designated as prototypes of each Bus class were averaged for each class. The average reflectance value and its associated error were calculated for each Gaia wavelength band, without taking into account the error bars of the DR3 spectra, since most of them are smaller than the difference between two spectra, for high SNR asteroids.

Not every prototype was used in the definition of the Gaia templates. Indeed, prototype asteroids that do not have a spectrum in the DR3, such as Q-type asteroid (5660) 1974 MA, could not be used to produce the Gaia templates. Moreover, since the goal was to produce template spectra representative of each class of the Bus taxonomy, a quality check of the DR3 spectra of the prototypes was performed. If the DR3 spec-

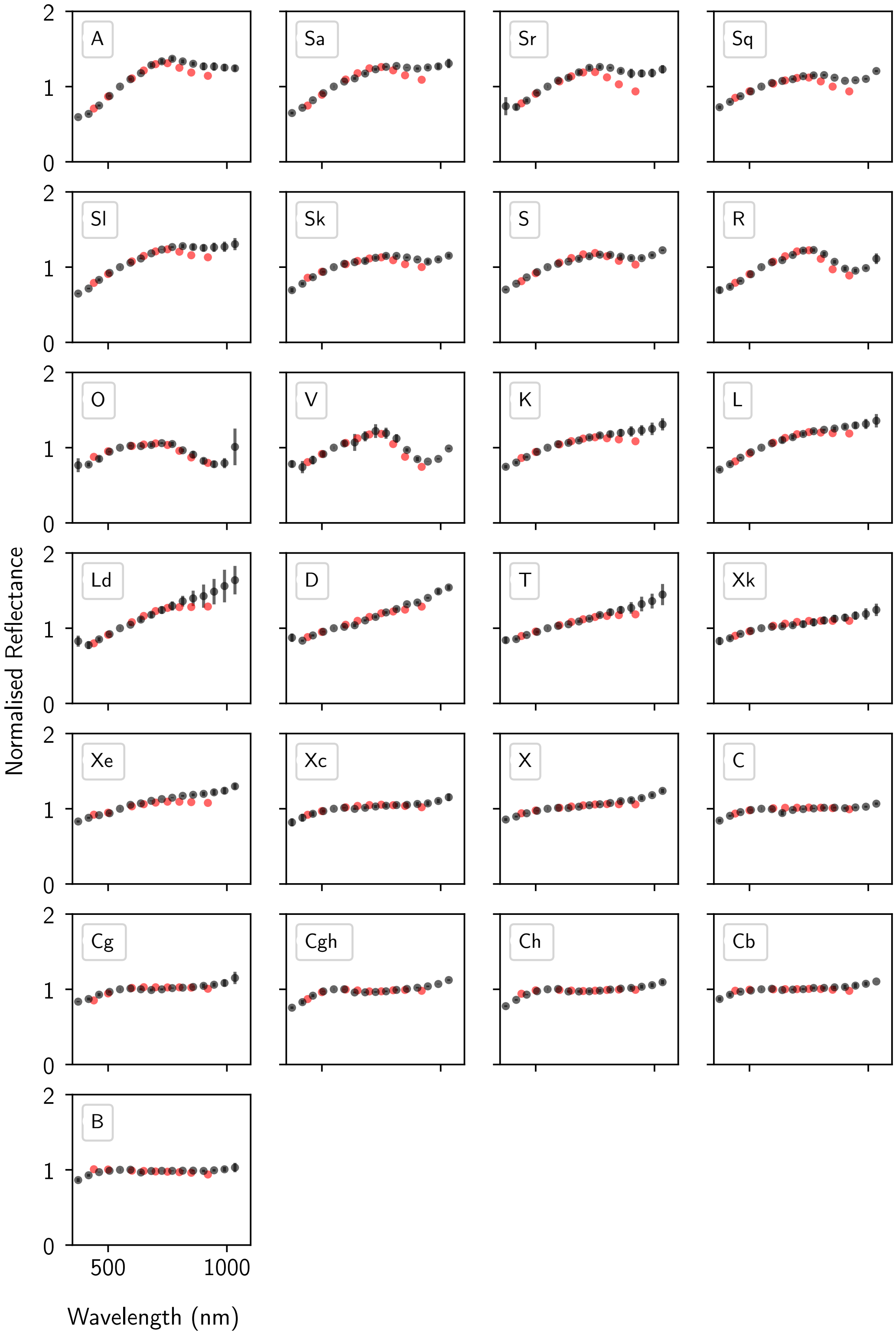

Figure 5.3: Gaia templates (black dots), defined as the average of the prototypes of each taxonomic class of Bus and Binzel (2002a). The Bus templates are displayed as red dots for comparison. The type corresponding to each template spectrum is indicated on the top left of each sub-figure.

trum of a prototype showed several flagged bands, was visually noisy, or differed too greatly from the Bus template spectrum in its class, it was discarded. Asteroids (1483) Hakoila, (2102) Tantalus and (5143) Heracles were therefore not included in the template calculations.

Discarding Q-type (2102) Tantalus lead to a definition of the Q-type template based on a single asteroid, (1862) Apollo. Since this type is not a main focus of this thesis, I decided not to define a Q-type template, and to consider Q-types as part of the S-complex in the following. This decision is supported by the fact that there is an observed continuum between S-complex and Q-type asteroids, and Q-type objects could be "unweathered" S-type asteroids (Binzel et al., 2010). For future works, the Q class should however be considered, as this class is of importance for the study of the evolutionary processes of NEOs for example (Devogèle et al., 2019; Binzel et al., 2019).

Here, I did not try correcting Gaia DR3 spectra from any of potential issue identified in Chapter 2. Instead, I tried taking these issues into account in the definition of the Gaia templates. This is why asteroid (4) Vesta was kept for the definition of the V-type template spectrum, even if its DR3 spectrum shows a "fake band" around 650 nm, that we know absent from its literature reflectance spectra. Since Vesta has a characteristic V-type spectrum, and since the "fake band" has been observed in other DR3 spectra, I decided to keep Vesta's spectrum in the definition of the templates.

Every asteroid used in the definition of the Gaia template spectra for each class is given in Table 5.1, and the obtained Gaia template spectra and their comparison with the Bus templates is shown in Fig.5.3. Large discrepancies between the Gaia and Bus templates can be noted in the red part mostly for the A, S-complex, Ld, and Xe-classes, which is consistent with what has been noted in Chapter 2. The first two and last two bands of these templates will not be taken into account to classify asteroids.

5.3.2.3 *Classification of Gaia DR3 spectra using Gaia templates*

Using the defined Gaia templates, I classified the DR3 spectra of the 1187 asteroids both observed by SMASS and Gaia, considering the wavelength range from 462 to 946 nm. The result of this classification is shown in Fig.5.4. The confusion matrix is quite diagonal, and the classification of DR3 spectra is highly improved compared to Fig.5.2. Therefore, defining Gaia templates improves the classification of Gaia DR3 spectra.

As for the classification of SMASS spectra with Bus templates, the sub-classes of the C, S and X-complexes are not well distinguished when classifying Gaia spectra with Gaia templates, and the C and X-complexes show some overlapping. Such phenomenon is to be expected, since these classes were defined by Bus and Binzel (2002a) using the PCA, and because there is a spectral continuum between the classes. Moreover, it can be tricky distinguishing a subclass from another one based only on visible-light reflectance data, and using a curve matching technique. It is possible that the sampling in 16 large bands of the DR3 mean reflectance spectra does not allow to distinguish clearly the discrete spectral features associated to each subclass.

To get a clearer idea of the performance of the classification algorithm, I decided to merge the sub-classes of each complex into their corresponding complex: the asteroids assigned to the Sa, Sr, Sq, Sl and Sk class were grouped as S-complex asteroids after performing the classification, and the same was done for the X- and C-complex. The confusion matrix resulting from this grouping is shown in Fig.5.5. From this matrix, it becomes clearer that the classification of Gaia DR3 spectra with Gaia templates pro-

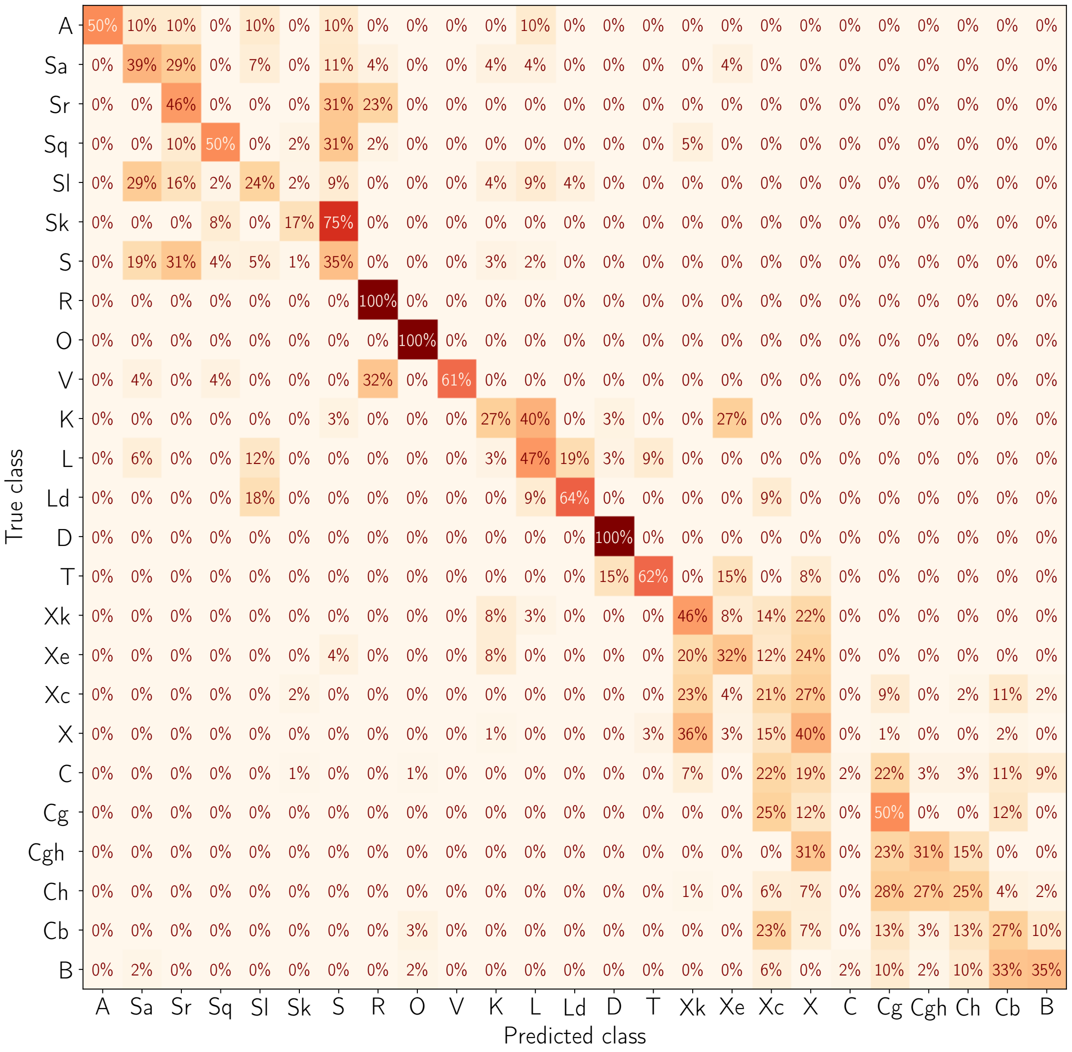

Figure 5.4: Confusion matrix corresponding to the classification of Gaia DR3 spectra using Gaia templates.

duces satisfactory results, although there is still room for improvement. For example, half of the A-types are classified as S-complex or L-type asteroids here, and 32% of V-types are classified as R-types.

Thus far, classification accuracy has been determined by comparing predicted taxonomic types with the "true" types of Bus and Binzel (2002a). These types were assigned based on SMASS spectra, that cover the visible wavelength range. Later observations in the NIR of objects classified by Bus and Binzel (2002a) have shown that, in some cases, the type assigned to asteroids on the basis of their visible spectrum is not correct. These differences are to be expected, and the NIR wavelength range is often used to confirm spectral types assigned from visible data.

For example, asteroid (2732) Witt was found A by Bus and Binzel (2002a), but was later assigned to the L-class by DeMeo et al. (2019) and to the S-class by Mahlke et al. (2022) from the study of their NIR spectrum. Here, this asteroid is classified as L-type, and not A-type, on the basis of its DR3 spectrum. This classification is coherent with NIR observations of the literature, and this asteroid should therefore be considered as well classified. Therefore, considering as "true" classes assigned from visible spectra

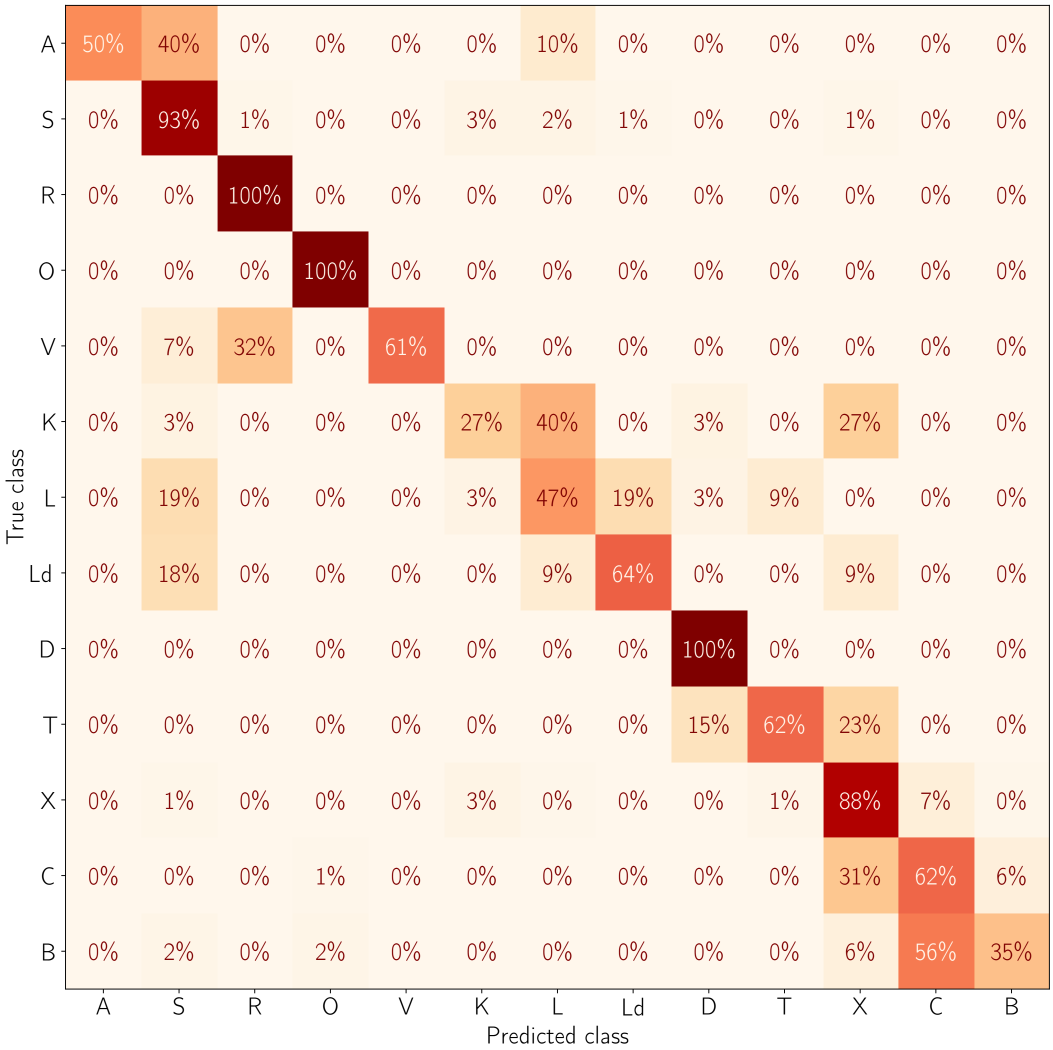

	A	S	R	O	V	K	L	Ld	D	T	X	C	B
A	50%	40%	0%	0%	0%	0%	10%	0%	0%	0%	0%	0%	0%
S	0%	93%	1%	0%	0%	3%	2%	1%	0%	0%	1%	0%	0%
R	0%	0%	100%	0%	0%	0%	0%	0%	0%	0%	0%	0%	0%
O	0%	0%	0%	100%	0%	0%	0%	0%	0%	0%	0%	0%	0%
V	0%	7%	32%	0%	61%	0%	0%	0%	0%	0%	0%	0%	0%
K	0%	3%	0%	0%	0%	27%	40%	0%	3%	0%	27%	0%	0%
L	0%	19%	0%	0%	0%	3%	47%	19%	3%	9%	0%	0%	0%
Ld	0%	18%	0%	0%	0%	0%	9%	64%	0%	0%	9%	0%	0%
D	0%	0%	0%	0%	0%	0%	0%	0%	100%	0%	0%	0%	0%
T	0%	0%	0%	0%	0%	0%	0%	0%	15%	62%	23%	0%	0%
X	0%	1%	0%	0%	0%	3%	0%	0%	0%	1%	88%	7%	0%
C	0%	0%	0%	1%	0%	0%	0%	0%	0%	0%	31%	62%	6%
B	0%	2%	0%	2%	0%	0%	0%	0%	0%	0%	6%	56%	35%

Figure 5.5: Confusion matrix corresponding to the classification of Gaia DR3 spectra using Gaia templates, with sub-classes grouped as complexes.

can make us think that an asteroid is misclassified because of its DR3 spectrum, when the literature class it is being compared to is actually the incorrect one. In order to discard this source of error, I defined a list of asteroids with a "confirmed" spectral type, i.e. which have been classified from VISNIR (visible and near-infrared) or NIR observations.

5.3.3 "True" classes on the basis of VISNIR and NIR spectroscopy

To build this list of objects, I searched in the literature for asteroids classified from observations in the VISNIR or NIR wavelength range, in the Bus or Bus-DeMeo scheme. The papers used to build this VISNIR list are the following: Duffard et al. (2004b), Lazzarin et al. (2004), Lazzarin et al. (2005), Marchi et al. (2005a), Licandro et al. (2008b), Mothé-Diniz et al. (2008b), Clark et al. (2009), DeMeo et al. (2009), de León et al. (2010), de Sanctis et al. (2011), Gietzen et al. (2012), Sanchez et al. (2013), DeMeo et al. (2014), Borisov et al. (2017), Leith et al. (2017), Lucas et al. (2017), Migliorini et al. (2017), De Prá et al. (2018), Devogèle et al. (2018), Migliorini et al. (2018), Binzel et al. (2019), De-

Meo et al. (2019), Lucas et al. (2019), Arredondo et al. (2021a), Gartrelle et al. (2021), Hasegawa et al. (2021), and Migliorini et al. (2021).

Building this list of asteroids with a "confirmed" spectral type required several steps, described in Appendix C section C.1. The final list of asteroids classified on the basis of NIR or VISNIR spectra contains 754 asteroids, of which 517 have a spectrum in the Gaia DR3 filtered dataset. This list of 517 objects is given in Table C.1 in Appendix C, and will be referred to as the "NIR list" in the following. The proportions of each asteroid type in this list is:

- S-complex: 199 asteroids, 38.49 %
- C-complex: 79 asteroids, 15.28 %
- X-complex: 60 asteroids, 11.61 %
- D: 46 asteroids, 8.9 %
- V: 42 asteroids, 8.12 %
- L: 33 asteroids, 6.38 %
- K: 18 asteroids, 3.48 %
- A: 14 asteroids, 2.71 %
- Q: 13 asteroids, 2.51 %
- T: 8 asteroids, 1.55 %
- B: 3 asteroids, 0.58 %
- Ld 3 asteroids, 0.58 %
- R: 1 asteroids, 0.19 %
- O: 1 asteroid, 0.19 %

Considering the wavelength range from 462 to 946 nm, I classified the 517 asteroids of the NIR list on the basis of their Gaia DR3 spectrum, using the defined Gaia templates. The confusion matrix corresponding to this classification is displayed in Fig.5.6, with the subclasses of each complex grouped into complexes.

It can be noticed in Fig.5.6 that 57% of A-type asteroids are found to be part of the S-complex. An analysis of the S-complex sub-classes indicates that these A-types are found Sa at 21%, Sr at 29%, and Sl at 7%. This result is not surprising, given the spectroscopic similarity between these classes, translating a compositional gradient. However, every Sa-type asteroid is also found Sr with this classification. I therefore deleted the Sr class, to try improving the classification of A types.

Among the subclasses of the S-complex, the Sl class defined by Bus and Binzel (2002a) was later deleted by DeMeo et al. (2009), from the study of asteroids NIR spectra. I chose to delete this class as well, hoping to retrieve more A-type asteroids.

The R and O-type asteroids get correctly classified here. However, 43% of V-types get incorrectly classified as R-types, and 33% of B-types get classified as O. The R-type asteroids being extremely rare and the O-class having been created for the single

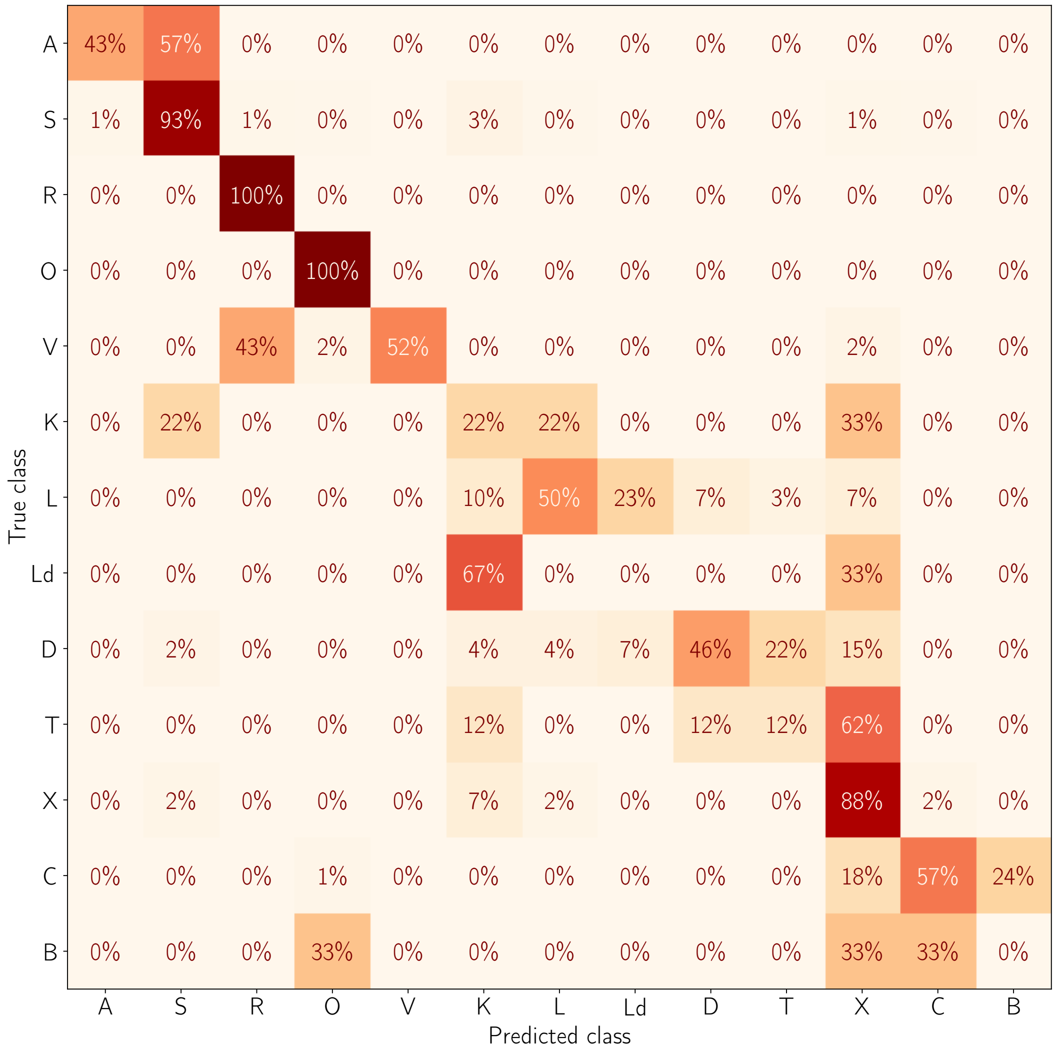

True class \ Predicted class	A	S	R	O	V	K	L	Ld	D	T	X	C	B
A	43%	57%	0%	0%	0%	0%	0%	0%	0%	0%	0%	0%	0%
S	1%	93%	1%	0%	0%	3%	0%	0%	0%	0%	1%	0%	0%
R	0%	0%	100%	0%	0%	0%	0%	0%	0%	0%	0%	0%	0%
O	0%	0%	0%	100%	0%	0%	0%	0%	0%	0%	0%	0%	0%
V	0%	0%	43%	2%	52%	0%	0%	0%	0%	0%	2%	0%	0%
K	0%	22%	0%	0%	0%	22%	22%	0%	0%	0%	33%	0%	0%
L	0%	0%	0%	0%	0%	10%	50%	23%	7%	3%	7%	0%	0%
Ld	0%	0%	0%	0%	0%	67%	0%	0%	0%	0%	33%	0%	0%
D	0%	2%	0%	0%	0%	4%	4%	7%	46%	22%	15%	0%	0%
T	0%	0%	0%	0%	0%	12%	0%	0%	12%	12%	62%	0%	0%
X	0%	2%	0%	0%	0%	7%	2%	0%	0%	0%	88%	2%	0%
C	0%	0%	0%	1%	0%	0%	0%	0%	0%	0%	18%	57%	24%
B	0%	0%	0%	33%	0%	0%	0%	0%	0%	0%	33%	33%	0%

Figure 5.6: Confusion matrix corresponding to the classification of Gaia DR3 spectra of asteroids classified in the literature from VISNIR and NIR spectroscopy, using Gaia templates. The sub-classes are grouped as complexes.

asteroid (3628) Boznemcova (Bus and Binzel, 2002a), I decided to no further include the R- and O-class here.

K-type asteroids get incorrectly classified as S, L and X-complex (Xe-class at 22% more specifically). The K-class is on the edge of the S-complex (Vokrouhlický et al., 2006) and K-type objects can get misclassified as S from their visible spectrum (Granahan et al., 1993). This can explain the 22% of K-types classified as S. It can be noticed as well that the K, L and Ld classes show a high degree of mixing. This is to be expected for classes L and Ld, given that the Ld class of Bus and Binzel (2002a) is an extension of the L-class, that was subsequently deleted by DeMeo et al. (2009). Here, the 67% of Ld-type asteroids classified K represent only two objects, so I decided to discard the Ld class. The high degree of mixing between the L and K-classes is expected from the great spectral diversity of objects in the L class (e.g DeMeo et al., 2009; Mahlke et al., 2022), hence the mixing of these classes from their DR3 spectra is not surprising.

T-type asteroids are mostly classified as X-types here, while the T-class is mostly populated with D-types. From Fig.15 of Bus and Binzel (2002a), the T-class plots between the X-complex and the D-type in the principal component space, which is coherent with the classification results obtained here. As these spectra are featureless, the classification of T-types mostly relies on the value of their spectral slope, that could be affected by Gaia systematics. The RP reddening issue identified in Chapter 2 is hard to take into account, even with the definition of Gaia templates, as it varies from an object to another according to the date at which the epoch reflectance spectra included in the production of the mean spectra were observed. I therefore chose to discard the T-class, as decided as well by Mahlke et al. (2022) in the definition of his taxonomic scheme.

X-types get mostly correctly classified, but this class is polluted by other classes, such as the K, T, C and B-class. Looking into the sub-classes in more details, 33% of B-types are found Xc, as well as many C-types. This is not surprising given the spectroscopic similarities between these classes, but I decided to discard the Xc-class to try improving the classification. 33% of B-types are also incorrectly found Cgh, so I discarded the Cgh-class. The K and X-class mix mostly because of the Xe-class, so I discarded it as well.

As a summary, I chose to discard the Sr, Sl, Q, R, O, Ld, T, Xc, Xe, and Cgh classes of the definition of Gaia templates. These decisions were all taken to try improving the classification of Gaia DR3 spectra. To validate these choices, the 517 asteroids of the NIR list were classified considering only the templates of the A, Sa, Sq, Sk, S, V, K, L, D, Xk, X, C, Cg, Ch, Cb, and B classes.

5.4 FINAL CLASSIFICATION

The results of the classification obtained considering only the aforementioned templates is presented in Fig.B.9 in Appendix C. This classification gave better results, but I noticed in Fig.B.9 that 27% of C-complex asteroids are found B, and none of the three B-types considered here is successfully classified B. After studying their DR3 spectra and their classification (see Appendix C.1.1), the B class was merged into the C-complex.

Finally, from the study of C-complex asteroids and based on the taxonomic scheme of Mahlke et al. (2022), it appears possible to distinguish C-type from Ch-type asteroids. It would be interesting to make such distinction, to study the hydration of carbonaceous asteroids and to address questions regarding the origin of water on Earth. Studying primitive material is out of the scope of this thesis, but I wanted to see if distinguishing C from Ch-types with the DR3 data was achievable. Therefore, I took the Ch-class out of the C-complex.

The confusion matrix displayed in Fig.5.7 shows the result of the classification based on the templates of the A, Sa, Sq, Sk, S, V, K, L, D, Xk, X, C, Cg, Ch, Cb, and B classes, and after grouping the Sa, Sq, Sk and S classes into the S-complex, the Xk and X classes into the X-complex, and the C, Cg, Cb and B classes into the C-complex. The Ch-class is considered independant of the C-complex here, in an attempt to distinguish hydrated from non-hydrated carbonaceous asteroids.

It can be noticed in Fig.5.7 that the S-types are successfully classified at 93%, and the V-types at 88%. Thus, deleting the R-class allowed to improve the classification of V-types. There is a spectral continuity between the V and S classes (a Sv class was in

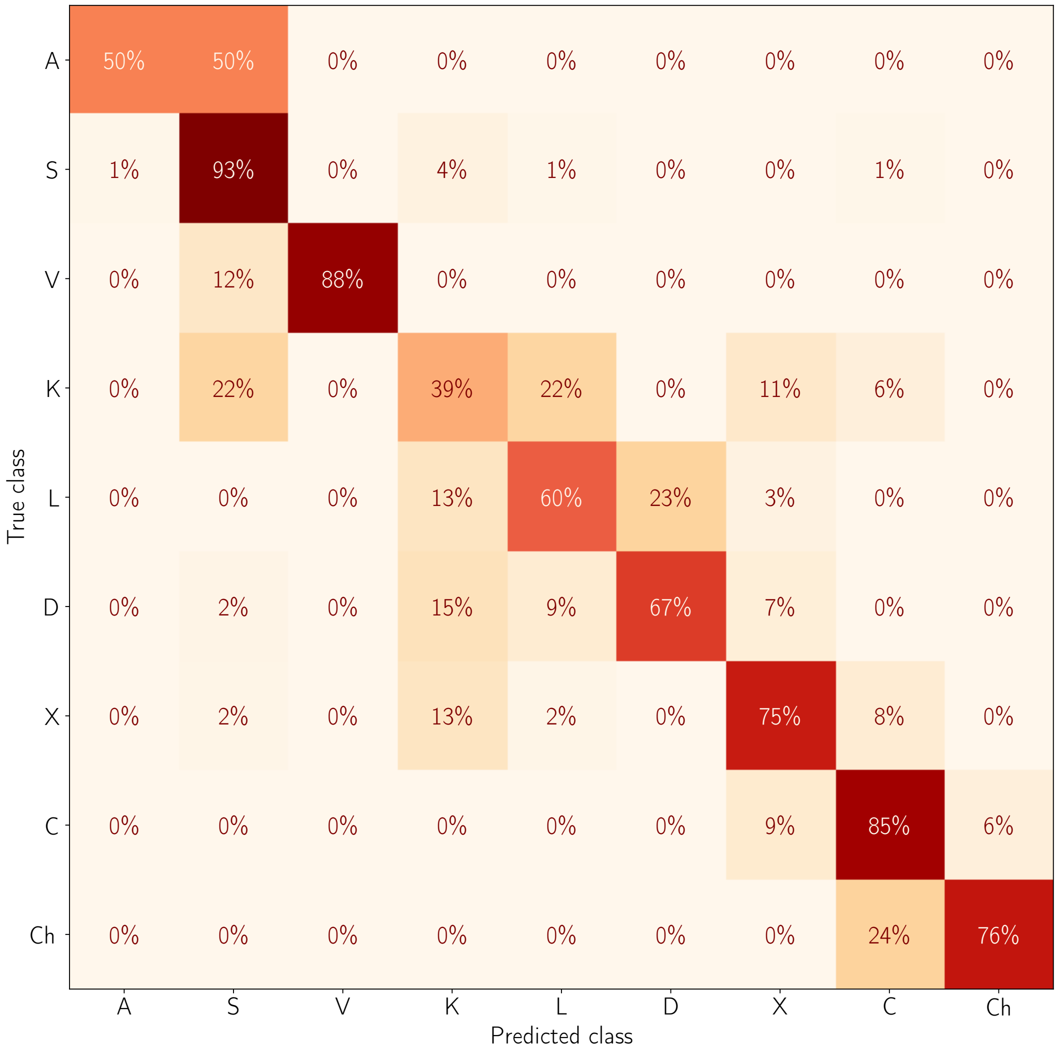

Figure 5.7: Confusion matrix corresponding to the classification of Gaia DR3 spectra of asteroids classified in the literature from VISNIR and NIR spectroscopy, using Gaia templates. The sub-classes are grouped as complexes and the B-class is included in the C-complex. An exception is the Ch-class, considered here outside of the C-complex. The templates of the classes Sr, Sl, Q, R, O, Ld, T, Xc, Xe, and Cgh are not considered.

fact defined by DeMeo et al. (2009) to represent it), so losing 12% of V-types to the S-complex makes sense.

The K class does not give exceedingly satisfactory results here. However, a thorough analysis of the 18 K-type asteroids of the NIR list, presented in Appendix C.1.2, indicates that this bad classification is to be expected, and appears not to come from the quality of the DR3 spectra. The mixing of K and L-classes is also expected, as already discussed.

The reason why 15% of D-types get classified K can be explained by the study of the D and K-type templates displayed in Fig.5.3. The Gaia K-type template shows a reddening of its RP part compared to the Bus template, which makes the K and D-templates more similar. This could explain the loss of literature D-types to the K-class. Another possible explanation is that some of these D-types have a DR3 spectrum more similar to K-type asteroids than to D-types. The classification of D-types is further analysed in Appendix C.2.3.

The confusion matrix of Fig.5.7 shows that hydrated and non-hydrated carbonaceous asteroids can be distinguished on the base of their DR3 spectra, to an extent. However, some C-type DR3 spectra can be affected by a "fake band" issue at the location of a real hydration band, because of a mismatch between the BP and RP. The C and Ch-types can thus be subject to a certain level of mixing, and the distinction of an hydrated band with this algorithm is to be verified.

Finally, the best results for the classification of Gaia DR3 visible reflectance spectra are obtained by (i) defining Gaia templates, (ii) using templates only for the A, Sa, Sq, Sk, S, V, K, L, D, Xk, X, C, Cg, Ch, Cb and B classes, as determined by a trial-and-error approach of removing classes and analysing the classification results at each step, and (ii) grouping afterwards the Sa, Sq, Sk and S classes into a S-complex; the Xk and X classes into a X-complex; and the C, Cg, Cb and B classes into a C-complex. This classification is referred to as the "Gaia classification" in the following. Some of the choices that lead to these results are discussed in Appendix C.

Analysing the confusion matrix of Fig.5.7, the classification of A-types remains to be discussed. It can be noticed that half of the A-type asteroids are classified correctly, which is better than in Fig.5.6. Thus, deleting the Sr and Sl-classes improved the classification of A-types, and did not impact the classification of S-types.

Moreover, only 1% of S-types are classified A. This 1% of false positives corresponds to two objects here. The first object is asteroid (1600) Vyssotsky, found A by Carvano et al. (2001), Bus and Binzel (2002a), and Lazzaro et al. (2004) from VIS spectroscopy, and Sw by Lucas et al. (2019) and S by Mahlke et al. (2022) from VISNIR spectroscopy. It is not surprising to find this object classified as A-type here, given that Gaia covers only the visible wavelength range.

The other non-A-type classified A-type is asteroid (1709) Ukraina, found S by DeMeo et al. (2019), and thus identified as S in the NIR list. However, this asteroid is found A by Mahlke et al. (2022) with his own taxonomic scheme. Therefore, classifying this object as A-type here is not incorrect. To summarise, the A-class obtained using the Gaia templates and this classification algorithm is very restrictive, and most asteroids found A-types here should be reliable.

Unfortunately, with this classification method, half of the literature A-types are "lost" in the S-complex. The mixing of A-types and S-complex asteroids is not surprising, because a continuum exists between S, Sa and A-type asteroids, translating a gradient of olivine content in these bodies. However, this classification of A-types can be improved.

In the following section, I present an attempt at retrieving some of these false negative A-types, while trying to limit the amount of false positives in the A-class. To do so, I exploit the BP part of Gaia DR3 mean reflectance spectra.

5.5 IMPROVING THE CLASSIFICATION OF A-TYPES

5.5.1 A-types and BP slope

As shown in Chapter 2, Gaia DR3 spectra appear reddened compared to SMASS spectra, when considering their global spectral slope. Such reddening affecting the spectrum of a S-type asteroid could potentially make it look like an A-type. Such issue could lead to a contamination of the A-class by S-type asteroids, but it does not seem to be the case here.

On the contrary, the BP part of DR3 spectra does not appear affected by the reddening affecting their RP part, and the BP slope of DR3 spectra calculated between 462 and 726 nm is in great agreement with the one calculated on SMASS spectra (see Chapter 2 section 2.1.6). Therefore, given that A-type spectra show a redder slope in this wavelength range than S-type spectra, this slope could help distinguishing false positive and false negative A-types, and could help retrieving A-types "lost" in the S-complex.

The NIR list contains 14 A-types, of which only half are found A as first best class with the Gaia classification, the other half being found S (see Fig.5.7). Among the 199 S-types of this list, two are found A-types. This gives a total of 9 asteroids classified A as first best class.

To try improving this result and to evaluate if S-types and A-types can really be distinguished from the bluer part of their spectra, the "BP slope" (between 462 and 726 nm) and the global spectral slope (between 462 and 946 nm) were calculated on the Gaia DR3 spectra of the 14 A-types, and of the 199 S-complex asteroids of the NIR list, using a linear regression.Then, ranges of slope were defined both for the global and the BP slope, going from 0 to 2.6 % $(100\ \mathrm{nm})^{-1}$, taking a step of 0.2 % $(100\ \mathrm{nm})^{-1}$. The amount of S-complex and A-type asteroids per slope range was calculated, and the obtained histograms are displayed in Fig.5.8.

The global slope histogram (panel A) shows that, at best, there is a 50% probability that an asteroid showing a DR3 spectrum with the highest global slope is an A-type. Panel (B), on the other hand, shows that the probability of an asteroid being an A-type increases with the BP slope, reaching 100% for the highest BP slope values. Exploiting the BP slope could thus allow us to retrieve A-types lost in the S-complex, to an extent.

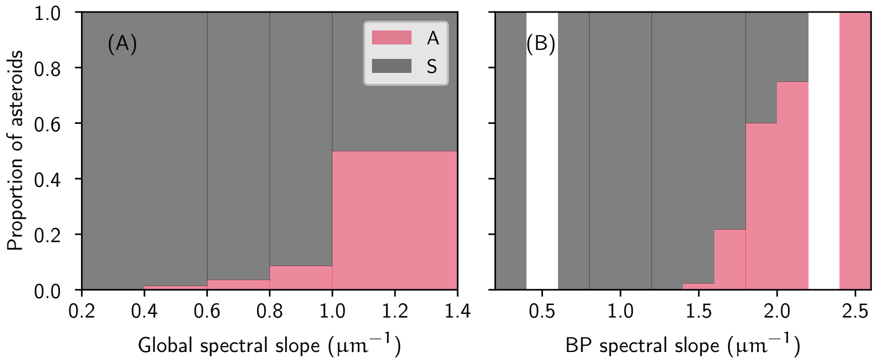

Figure 5.8: Proportion of asteroids in the NIR list classified as A or S-complex from the literature, depending on their Global spectral slope of BP slope value. Ranges of slopes go from 0 to a 2.6 by steps of 0.2. No asteroid shows BP slope values between 0.4 and 0.6 % $(100\ \mathrm{nm})^{-1}$ and between 2.2 and 2.4 % $(100\ \mathrm{nm})^{-1}$ in the chosen sample, which is why these regions are white in panel (B).

5.5.2 BP classification

So far, only the first best class of asteroids has been considered in the study of the classification of DR3 spectra. However, the second best class given by the algorithm gives more information about the spectra, and could be of use to retrieve lost A-types.

Indeed, 24 asteroids of the NIR list are classified as A-type as second best class by the algorithm, and only 3 of these objects are classified A in the literature. My goal here was to try retrieving these 3 A-types, keeping a low amount of false positives in the A-class.

In total, considering the 9 asteroids classified A as first best class, and the 24 asteroids classified A as second best class; 33 asteroids are classified A as first or second best class by the classification method. Among these, 10 objects are A-types in the literature. Given that the BP slope appears to help distinguishing A-types from S-types, I classified the 33 asteroids found A as first or second best class, considering only the BP part of their spectra.

The overlap region between the BP and the RP parts of the DR3 spectra is around 650 nm. Since this region can be affected by systematic issues such as a fake band (see Chapter 2), I applied the curve matching algorithm to the spectra, considering the wavelength range between 462 and 594 nm (instead of from 462 to 726 nm). After this BP classification, 12 asteroids were classified A-types out of the 33 considered, 9 of which being A-types in the literature. This choice of wavelength range was found to give better results at retrieving A-types than doing a BP classification considering the range from 462 to 726 nm.

In detail, 8 of the 9 asteroids that were found A-types as first best class after the Gaia classification, are still found A after the BP classification. Seven of them are literature A-types, and one asteroid, (1709) Ukraina, is a S in DeMeo et al. (2009). It was however mentioned earlier that this asteroid is found A by Mahlke et al. (2022), making this asteroid a good potential A. Therefore, objects classified A-type as first best class by the Gaia classification, and still classified A-type after the BP classification can be considered best potential A-types. This designation will be used in the following.

Four of the 24 asteroids found A-type as second best class after the Gaia classification are found A-type after the BP classification. Two of them are literature A-types, and the other two, (2150) Nyctimene and (6485) Wendeesther, are not. This step thus allows to retrieve two A-types out of the three of the literature, and only adds two false positives. Finally, asteroid (1600) Vyssotsky, that was incorrectly found A-type as first best class after the Gaia classification (false positive), is found non-A after the BP classification step.

Therefore, out of the 10 literature A-types in the list of 33 asteroids found A as first or second best class, 9 are successfully retrieved with the BP classification step. Only 3 asteroids found A-type here are non-A in the NIR list, and one of these three objects is an A-type according to Mahlke et al. (2022).

This BP classification step thus allows to improve the classification of A-type asteroids, allowing to retrieve more A-types (reducing the amount of false negative), and to eliminate most literature non-A-types (reducing the amount of false positive). It did not allow to retrieve every literature A-type, but it appears efficient to find reliable A-type candidates. This secondary BP classification step will thus be used in the following, to try detecting A-type asteroids in the Main Belt.

As the Gaia classification is restrictive regarding the assignment to the A-class, the objects classified A-type as first best class after the Gaia classification, and non-A after the BP classification, can still be considered potential A-types. Similarly, objects classified A-type as second best class after the Gaia classification, and classified A-type after the BP classification, are also considered potential A-types. These designations will be used in the following.

A discussion about the choices made during the exploration and development of the classification of Gaia DR3 spectra is provided in Appendix C.2. There, I discuss and test the impact of the choice of templates on the classification of Gaia DR3 asteroids spectra. Then, I explore the limit in SNR needed to classify Gaia DR3 asteroid spectra reliably. Finally, I use the PCA to analyse the classification results and to compare them to the literature, and I comment on the classification of low SNR DR3 spectra.

These validation tests allowed me to conclude that classifying Gaia DR3 spectra with a curve matching algorithm gives satisfactory results. As described in Appendix C.2.2, taking into account spectra with an average SNR$\geqslant$30 guarantees that about 80% of asteroids are classified coherently with the literature. The 20% of asteroids badly classified can be so because (i) their Gaia DR3 spectrum is not of good quality, (ii) the class assigned from literature spectra and considered as "true" here is incorrect, (iii) the define templates do not represent all the spectral variations within an asteroid class.

Appendix C.2.3 shows that visualising the position of asteroids in the principal component space gives further information about their composition. Classifying low SNR asteroids with a curve matching method does not give satisfactory results, but the PCA applied on low SNR DR3 spectra showed that rough information about the asteroids' composition can still be deduced from their spectra. PCA can thus be a useful tool to complete the information obtained with the curve matching classification, especially when studying populations of objects with spectral types on the edge of other types.

The Gaia classification of A-type asteroids gives only 50% of true positives for the first best class. This very restrictive assignment to the A-class means that asteroids found A as first best class are reliable potential A. The use of a secondary classification based on the BP part of the DR3 spectra of asteroids found A as first or second best class allows to retrieve more A-types. In the following, the Gaia and BP classification steps are applied to the whole filtered Gaia DR3 dataset, to characterise the Main Belt as a whole, and to search for potential new A-type asteroids and olivine-rich families.

5.6 APPLICATION OF THE CLASSIFICATION METHOD

First, in section 5.6.1, the (36256) 1999 XT17 family is characterised with the Gaia and BP classification procedure. As it has been found a A-type family in Galinier et al. (2024), it is a good start to test the performances of the two steps classification algorithm, and it confirms the results described in Chapter 4. Then, the Gaia classification is applied to the filtered Gaia DR3 dataset in section 5.6.2, and asteroids identified A-types as first or second best class are analysed in section 5.6.3.

5.6.1 Gaia classification of the (36256) 1999 XT17 family

I studied the family (36256) using the two steps classification procedure based on Gaia templates. As explained in Chapter 4, 15 members of the family (36256) have a spectrum in the DR3, and 6 of them show an average SNR⩽21. As described in Appendix C.2.2, the lower the SNR, the most uncertain the classification. Therefore, I filtered out these low SNR asteroids before performing the classification. Only one object in this family has an average 21⩽SNR⩽30: asteroid (40671) 1999 RE202. It has a SNR of 28.09 and it is found Ad by Popescu et al. (2018a) from MOVIS colour measurements. Since this object show a SNR close to 30, it was reasonable to classify it.

Table 5.2: Members of the (36256) 1999 XT17 family with a Gaia DR3 spectrum having a SNR⩾21.

Asteroid Number	D (km)	p_V	Average SNR	H	spectral class 1	spectral class 2	BP spectral class
15610	5.84	0.30	35.32	13.3	S	A	A
16789	6.62	0.18	38.25	13.5	A	S	S
20975	5.24	0.28	36.01	13.6	S	A	S
25356	-	-	66.49	12.8	S	S	A
33763	-	-	48.07	13.4	S	A	A
36256	10.21	0.19	66.56	12.4	S	A	A
40671	-	-	28.09	13.6	S	S	S
57276	7.20	0.31	128.7	12.9	S	A	A
66676	6.55	0.22	52.28	13.3	S	L	S

The 9 family members having a SNR⩾21 were thus classified with the two steps classification, and the obtained results are displayed in Table 5.2. Only one asteroid is found A as best first spectral class after the Gaia classification: asteroid (16789) 1997 AU3. It is considered a potential A-type, as the Gaia classification is restrictive.

The 4 asteroids (15610) 2000 GY126, (33763) 1999 RB84, (36256) 1999 XT17, and (57276) 2001 QP139 are found A as second best class, and A-type after the BP classification. Among these, asteroids 33763 and 36256 are confirmed A-types from NIR spectroscopy. This makes the other two asteroids potential A-types.

Asteroid (20975) 1981 ER4 is found A as second best type, but non-A after the BP classification. It is therefore a less probable A-type. A peculiar case is the one of asteroid (25356) 1999 SK6: it is found A-type only after the BP classification, and it is found S-complex by the Gaia classification. The BP classification being efficient at retrieving A-types, and this object being found Ad by Popescu et al. (2018a) from NIR photometry, this makes (25356) 1999 SK6 a potential A-type.

Finally, asteroids (40671) 1999 RE202 and (66676) 1999 TS27 are found S-complex. Asteroid (40671) 1999 RE202 is however found Ad by Popescu et al. (2018a), making this asteroid a potential A-type, but not on the basis of its DR3 spectrum.

According to this 2 steps classification, asteroids (16789) 1997 AU3, (15610) 2000 GY126, and (57276) 2001 QP139 are good potential A-types. Given their classification in Popescu et al. (2018a), asteroids (25356) 1999 SK6 and (40671) 1999 RE202 can be considered potential A-types. The asteroid (20975) 1981 ER4 is found A as second best class only, making it a less probable A-type candidate. Finally, asteroid (66676) 1999 TS27 is not an A-type on the basis of its DR3 spectrum.

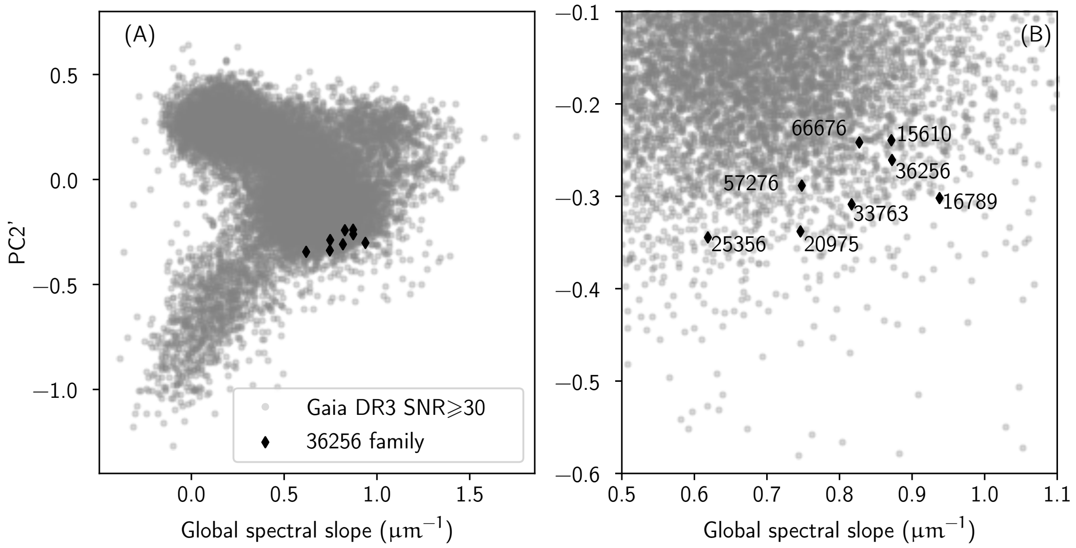

Figure 5.9: Plot of the principal component PC2′ with respect to the global spectral slope, calculated for the 18 739 filtered Gaia DR3 asteroids. The eight asteroids of family 36256 having a SNR⩽30 are highlighted as black diamonds, and their names are given in panel (B). Panel (B) is a zoom of panel (A)

The eight asteroids of this family having a SNR⩾30 are highlighted in the principal component plot in Fig.5.9. Asteroid (40671) 1999 RE202 is not on this plot, because the PCA has been applied only to the filtered Gaia DR3 dataset. It can be observed that the asteroids of this family are all clustered in the PCA space, close to the limit between the S-complex and the A-types. This explains their classification, and the fact they are clustered likely indicates a common composition.

Overall, the results obtained with this two steps classification scheme are consistent with those obtained with the algorithm based on Bus-DeMeo templates. The main difference is that the two steps classification scheme is more restrictive, allowing to confirm the best potential A-types found with the algorithm based on Bus-DeMeo templates used in Galinier et al. (2024), but likely losing A-types in the process. The whole analysis exposed in Chapter 4 holds, making the (36256) 1999 XT17 family the first potential A-type family discovered in the Main Belt.

5.6.2 Classification of Gaia DR3 asteroid spectra

The 18 739 asteroids of the filtered Gaia DR3 dataset were classified with the Gaia classification algorithm. As a reminder, this filtered Gaia DR3 dataset is composed of Gaia DR3 reflectance spectra having no flagged band in the considered wavelength range from 462 to 946 nm, and having a SNR⩾30. Applying these filters insures that the first best class obtained with the Gaia classification is coherent with the literature at about 80%, as described in Appendix C.2.2.

The following proportion of asteroids was found for each considered class, considering only their best first class: 44.43 % S-complex, 18.29 % C-complex, 15.18 % X-complex, 9.4 % K-types, 4.48 % V-types, 3.96 % Ch-types, 3.86 % D-types, 4.01 % L-types, and 0.35 % A-types. These proportions have been calculated for the inner, middle and outer Main Belt, and the corresponding histograms for each taxonomic type of asteroids are reported in Fig.5.10. These proportions appear coherent with the literature, with a dominance of S-type asteroids in the Inner and Middle Main Belt, and a dominance of carbonaceous asteroids in the Outer Main Belt. The vast majority of V-types are found in the IMB, corresponding to the Vesta family, and the concentration of K-types in the OMB corresponds to the Eos family. The proportion of S, K and X-types might be a little overestimated, which is expected given the performances of our algorithm (see Fig.5.7). Moreover, the large proportion of S-types compared to C-types is likely due to selection biases: this study has been performed on asteroids with high SNR spectra, which are often larger and/or brighter bodies. Since C-type asteroids are darker than S-types, many C-types have likely been filtered out on the basis of their lower SNR.

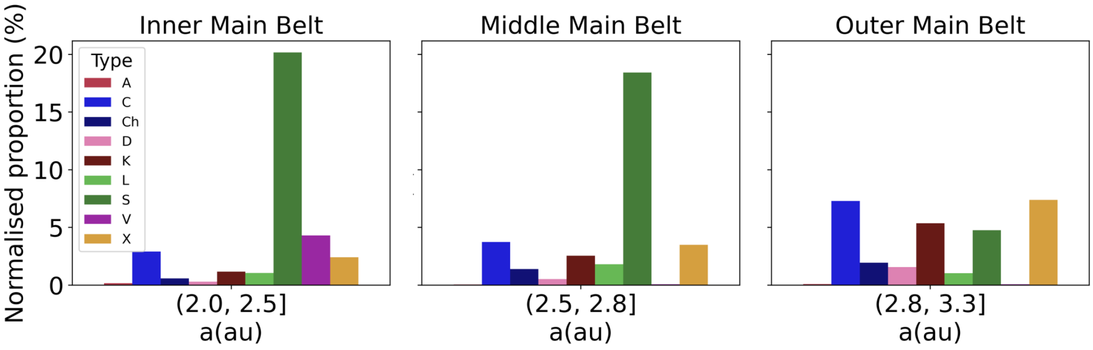

Figure 5.10: Histograms of the proportion of asteroids of each taxonomic type according to the Gaia classification, normalised by the total number of asteroids considered (18 739); in the inner, middle and outer Main Belt. The interval of semi-major axis considered for each part are given.

The point of interest here is that the proportion of asteroids found A-type as first best class is of 0.35 %, which is about twice as much as the 0.16% found by DeMeo et al. (2019). This proportion remains lower than the one of other asteroid types, but it could be larger in reality, given that the classification algorithm is restrictive in the assignment of objects to the A-class.

In the following, the BP classification is applied to the asteroids found A-type as first or second best class by the Gaia classification, and the results of the two steps classification are analysed. Then, the potential A-types found with this method are briefly analysed.

5.6.3 Gaia A-type asteroids

5.6.3.1 *A-types classification*

In the filtered Gaia DR3 dataset of 18 739 asteroids, the 0.35% of asteroids found A-types as first best class represents 65 objects, and 372 asteroids are classified A as second best class. To distinguish potential A-type asteroids from non-A-types among these objects, the BP classification step was applied to the 437 asteroids found A as first or second best class. The results obtained after the two steps classification are summarized as a flow chart in Fig.5.11.

Out of the 65 asteroids found A as first best class, 40 are found A again after the BP classification step. They are the best potential A-types. Among these, 17 are A-types in the literature, over 26 objects characterised. This high proportion of literature A-types confirms that the other objects classified as A here are the best potential A-types in the DR3 dataset.

Out of the 25 asteroids found A as first best class and non-A after the BP classification, 13 were never classified before the Gaia DR3, and 9 are characterised only from photometry. These objects are all potential A-types.

Out of the 372 asteroids found A as second best class by the Gaia classification, only 33 are classified A after the BP classification. Among these, only 7 have already been characterised from spectroscopy, 3 being A-types. The 11 asteroids never characterised before and the 15 objects characterised only with photometry are all potential A-types.

Finally, 339 asteroids out of the 372 second best class A-types are found non-A after the BP classification step. Although two asteroids out of these 339 are A from spectroscopy in the literature, most objects of this sub-sample can be considered the least probable A-types, and they probably belong to the S-complex.

In total, the two steps classification algorithm allowed to obtain a list of 40 best potential A-types (asteroids found A as best first class by the Gaia classification and A by the BP classification), and 58 potential A-types (asteroids found A as first best class after one of the two classification steps). The lists of best potential and potential A-types are given in Tables C.3 and C.4 in Appendix C. They represent a total of 98 potential A-types, which corresponds to 0.52% of the filtered Gaia DR3 dataset. This proportion is more than three times what has been found by DeMeo et al. (2019).

5.6.3.2 *A-types repartition in the Main Belt*

The positions in the proper orbital elements space of the 40 best potential A-types and the 58 potential A-types found with the two steps classification method is displayed in Fig.5.12. I highlighted in this figure the positions of 71 asteroids found A-types with spectroscopy in the literature included in the *rocks* database, and having a spectrum in the DR3. In total, between the asteroids found A by the algorithm and the ones found A with spectroscopy in the literature, 157 A-type asteroids are found in the Main Belt.

On Fig.5.12, we can notice that potential and confirmed A-type asteroids are scattered throughout the Main Belt, as found by DeMeo et al. (2019). The different regions of the Main Belt will be studied independently in the following.

The Hungaria region, populated with objects having a $1.78 < a < 2.$, counts 16 A-types. None of these objects is found to be belonging to the Hungaria family in

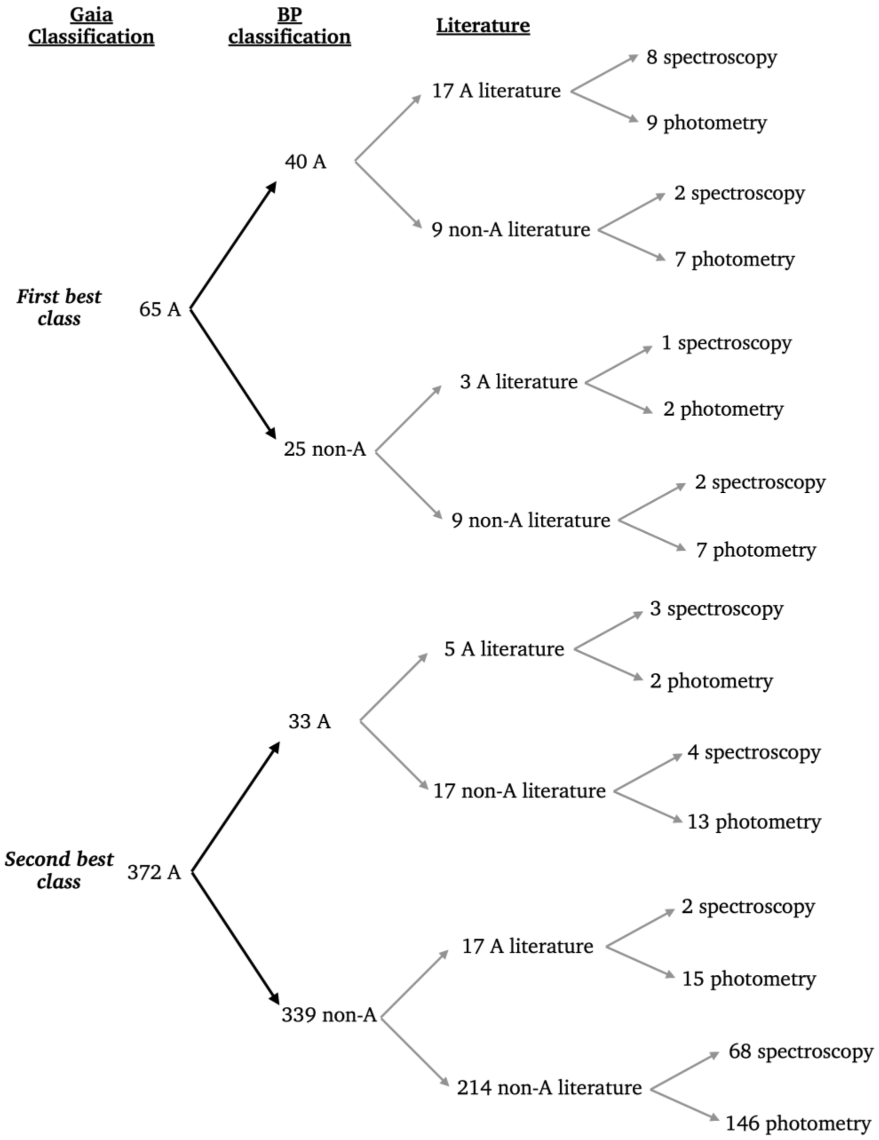

Figure 5.11: Flow chart of the classification of A-type asteroids, after the two steps classification using Gaia templates.

the family identification of Nesvorny et al. (2015), which is consistent with this group being mostly composed of E-type asteroids (Tholen, 1989; Mahlke et al., 2022).

The IMB, defined by $2. < a < 2.5$ shows a slightly greater concentration of potential A-types than the rest of the belt, with 63 A-types. The IMB is mainly populated by S-complex objects, and by (4) Vesta's large V-type family (Gradie et al., 1989; Gaffey et al., 1993; Binzel and Xu, 1993). A-type asteroids have spectra on the verge of S-complex and V-type spectra, as can be seen on the PC plot of Fig.B.9, thus some asteroids found potential A-types might be S-complex or V-type asteroids. There is always an ambiguity considering only visible-light reflectance spectra, that can be lifted with observations in the NIR wavelength range.

If these objects are true A-types, or asteroids showing olivine-rich compositions, then they might bring evidence that some asteroid families of the IMB are differentiated. In the catalogue of Nesvorny et al. (2015), 22 of these objects are family mem-

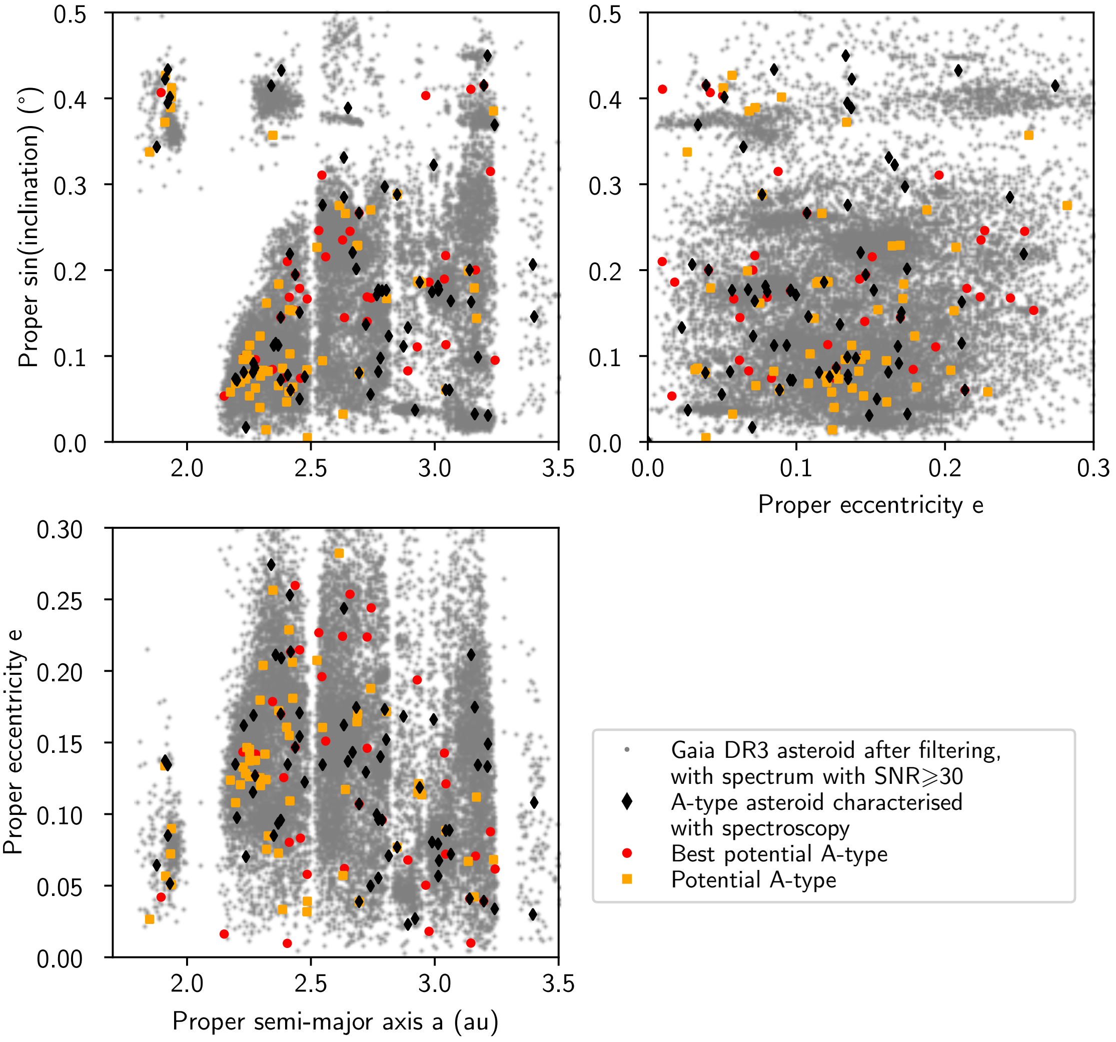

Figure 5.12: Proper orbital elements plot of the 40 best potential A-types (asteroids found A as best first class after both classification steps, red dots) and 58 potential A-types (asteroids found A as first best class after one of the two classification steps, orange squares). The 71 asteroids having a spectrum in the DR3 and found A with spectroscopy in the literature are highlighted as black diamonds.

bers: 12 belong to the (8) Flora family, four to the (298) Baptistina family, three to the (4) Vesta family, and three to the (44) Nysa-Polana family. The other A-types that are not found to belong to any family, could still be part of a family but not have been assigned as such by the HCM (Nesvorny et al., 2015). I will focus here on the Flora family, showing the highest number of potential A-type asteroids.

The Flora family is a S-type family, that has been linked to undifferentiated LL-chondrites (Brož et al., 2024). Looking at the V-shape of asteroids with a spectrum in the filtered Gaia DR3 dataset and designated as Flora family members in Nesvorny et al. (2015), displayed in Fig.5.13, a clear dominance of S-complex asteroids is noticeable. Other asteroid types, such as X or V-types, do not appear to be follow the V-shape of the family. These objects are likely interlopers in the dynamical Flora family, and part of the background or of other surrounding families. Concluding regarding the belonging of the A-type asteroids to the Flora family is made difficult by their low number; but they could be part of the V-shape of Flora.

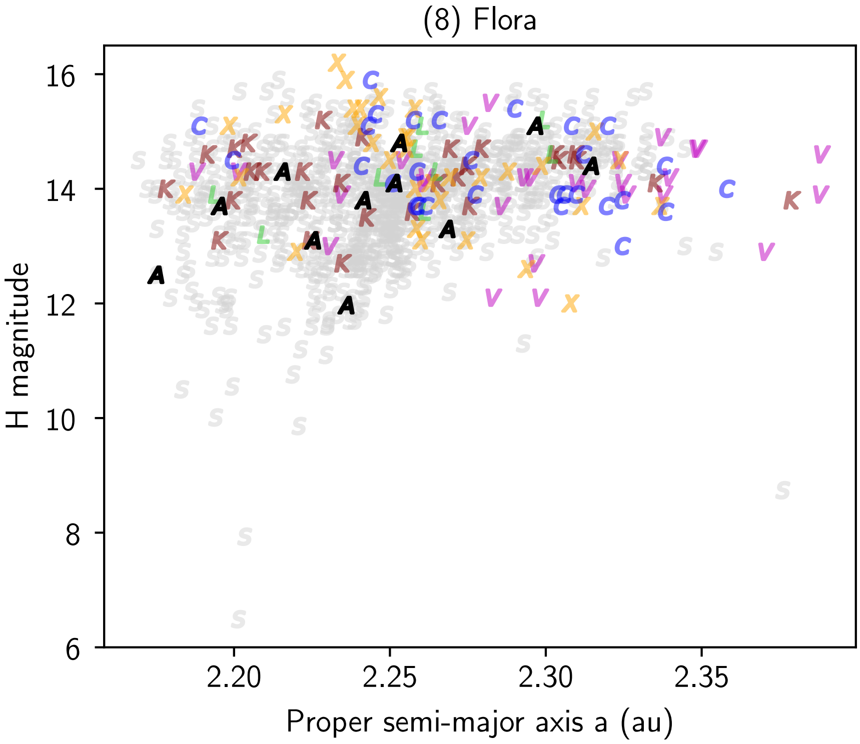

Figure 5.13: V-shape of the Flora family, using the membership of Nesvorny et al. (2015). Only the asteroids classified are considered, each taxonomic type is given a colour and a symbol corresponding to the type. Best potential A-types asteroids, potential A-types and A-types from spectroscopy in the literature are highlighted in black colour.

The MMB, corresponding to $2.5 < a < 2.82$, count 36 potential A-types. Two are part of the (15) Eunomia family according to Nesvorny et al. (2015), and three others are part of the respective (3) Juno, (145) Adeona and (1726) Hoffmeister families. With such a low number of A-types, these families are likely not differentiated. However, on Fig.5.12, a small cluster of $\simeq 5$ A-types is noticeable close to $a = 2.8$, at $\sin(i) \simeq 0.19$ and $e \simeq 0.1$. Further analysis is needed to determine if these objects are part of an already existing family, or could constitute a new family.

The OMB and the pristine zone, extending further than 2.82 au, counts 40 potential A-types. Among these, 5 belong to the small (36256) 1999 XT17 family, that is an A-type family as discussed in the previous section. Other 5 belong to the large (221) Eos family, a well-studied family known to be mostly composed of K-type asteroids (Vokrouhlický et al., 2006; Brož and Morbidelli, 2013; Brož and Morbidelli, 2019). The families (702) Alauda, (24) Themis, and (7468) Anfimov contain each 2 A-types; and (10) Hygiea, (158) Koronis, (10811) Lau and (709) Fringilla each contain one. The Lau and Anfimov families each contains 100% of A-types here, but it is because only asteroid (10811) Lau itself is characterised in the Gaia DR3, and only two asteroids are contained in the Anfimov family after filtering the DR3.

Finally, this rapid analysis of the Main Belt using the classification of DR3 spectra shows that the family (36256) 1999 XT17 remains the best A-type family candidate.

5.7 PERSPECTIVES AND CONCLUSIONS

In this chapter, I presented the steps and tests involved in developing a method to classify and exploit the Gaia DR3 spectral dataset. I considered only asteroids having a SNR$\geqslant$30 to perform this study, and with no flagged bands in the considered wavelength range, from 462 to 946 nm. I found that the best classification of DR3 spectra is obtained by defining Gaia templates, and using a two-step classification, that classifies asteroids in an adaptation of Bus' taxonomic scheme (Bus and Binzel, 2002a). The second step of the classification is based on the BP part of the DR3 spectrum and spans the short wavelength range from 462 to 594 nm. It was developed specifically in an attempt to retrieve more A-type asteroids, and to filter out S-type asteroids misclassified as A. It showed satisfactory results, mostly at filtering out incorrectly classified literature S-types, and it allowed to obtain a list of 98 potential A-types in the DR3 dataset. These objects are scattered across the Main Belt as expected from A-types (DeMeo et al., 2019), while showing a slightly larger concentration in the Inner Main Belt. Among these, 12 asteroids are already known A from spectroscopy in the literature, and 8 are found non-A. If we take into account our own observed spectrum of asteroid (33763) 1999 RB84, it leaves us with 77 potential A-types never characterised with spectroscopy before, considering only the filtered Gaia DR3 dataset with objects having a SNR$\leqslant$30. This represents 0.4% of the filtered Gaia DR3 dataset, and 2.5 times the 0.16% found by DeMeo et al. (2019).

The results obtained using this classification algorithm are consistent with those obtained with the algorithm based on Bus-DeMeo templates (Avdellidou et al., 2022), and that make family (36256) 1999 XT17 the first potential A-type family discovered in the Main Belt. Other families could be studied with this algorithm, such as those in the Inner Main Belt, where most of the A-type candidates orbit. More generally, every asteroid family could be systematically explored with the Gaia DR3 data, as this dataset contains many objects characterized with spectroscopy for the first time. Families already defined could be further characterised, or regions of the Main Belt could be explored using Gaia data alone. That way, families defined from the proper orbital elements of the objects using HCM algorithms (Nesvorny et al., 2015; Milani et al., 2014; Vinogradova, 2019) could be compared with spectroscopic clusters observed thanks to the classification of Gaia DR3 spectra.

Before doing so, this algorithm could be further improved. Indeed, it is based on a χ^2-like parameter developed by Popescu et al. (2012), that would benefit from the comparison to other χ^2 metrics. Studying the impact of metrics such as the Wasserstein distance or the Kullback-Leibler divergence on the classification could help improving it. The few tests I performed in that direction showed that the Φ_{comb} coefficient of Popescu et al. (2012) gave better classification results. However, these tests were performed on the classification improved while using the Φ_{comb} coefficient. Starting the work from scratch again with another metric could give more satisfactory results, and could highlight the potential limitations of the Φ_{comb} coefficient.

The Gaia template spectra I defined here are each based on 3 objects at most. They are simple, and they do not represent the complexity and diversity of the DR3 asteroids spectra, but they gave results satisfactory enough to characterise asteroids from their Gaia DR3 spectra. However, the effect of template definition on the classification needs to be further studied. Templates defined on a larger number of objects, as Mahlke et al. (2022) did for the development of his classification, would probably give different results, as the choice of the few asteroids used to define each Gaia template has a major impact on the final template. A different selection of objects could drastically modify the classification results. Since the aim here was not to define a new Gaia classification scheme, but to classify the DR3 asteroid spectra in an existing scheme, the way in which the templates were defined is less important than the quality of the classification obtained by using them. Defining templates using a few objects, but selecting them to achieve the best classification, would be enough for the scope of this work. For example, it is possible that defining another B-class template spectrum would allow to keep the B-type as an independent class, instead of merging it to the C-complex. The impact of template spectra on the classification should thus be further studied, in order to improve the classification of DR3 spectra, and to prepare for the Gaia classification that will be released with the DR4.

I focused here on the classification of DR3 spectra in the Bus taxonomic scheme, as this scheme was developed on spectra spanning the visible wavelength range. The classification of DR3 data could be done using other taxonomic schemes, such as the Mahlke et al. (2022) scheme for example. This is the latest taxonomic scheme defined, and some asteroids found non-A in other taxonomic schemes are found A in Mahlke et al. (2022). It would be interesting to look for potential A-type asteroids in the DR3 spectral dataset with the use of this taxonomic scheme, for example.

Finally, the "BP classification step" could be further studied and exploited. The study was focused on A-types here, but the wavelength range from 462 to 594 nm could be useful to distinguish D-types from L-types for example, as D-types generally show redder slopes. It could also be of use to study objects with a steep red slope belonging to the Z-class of Mahlke et al. (2022), such as asteroid (269) Justitia.

To summarise, this chapter presents the first results of a work in progress. Here, I determined that asteroids can be classified into an existing taxonomic scheme from their DR3 reflectance spectra, by defining Gaia templates. I found that grouping subclasses into their main complex improves classification, implying that some discrete features observed in literature spectra and allowing subclasses to be distinguished may not be clearly visible in the DR3 dataset. These results will be useful for the definition of a Gaia taxonomic scheme, that will be published with the DR4.

The developed classification method allowed me to study the Main Belt as a whole, and to detect new potential A-type asteroids, that need to be confirmed with NIR observations. The classification of DR3 mean reflectance spectra can be further used to characterise asteroid families, and to help disentangle between family members and interlopers. I will continue to work on this project in the future, to characterise asteroid families and more specifically to search for more of differentiation in the Main Belt.

6

CONCLUSIONS AND PERSPECTIVES

Over the past three years, I have analysed and exploited ESA's Gaia DR3 spectral dataset of Solar System small bodies, which contains 60 518 reflectance spectra of Solar System small bodies, with the aim of searching for evidence of differentiation in the Main Belt. I sought answers to the following questions: is there evidence of differentiation in the Main Belt? Where are mantle-like olivine-rich bodies? What happened to the early-differentiated planetesimals?

Indeed, early-formed planetesimals are thought to have differentiated, and evidence confirming it should be observable today in the Main Belt, as asteroids are the remnants of these objects (Bottke et al., 2005; Morbidelli et al., 2009; Klahr and Schreiber, 2020; Delbo et al., 2017; Delbo et al., 2019; Ferrone et al., 2023; Bourdelle de Micas et al., 2022). In the Main Belt, the Vesta family shows basaltic compositions characteristic of the crust of differentiated planetesimals, and is the only confirmed differentiated family (McCord et al., 1970; Russell et al., 2012). Metallic asteroids, generated in the core of differentiated bodies, have been detected in the Main Belt with spectroscopic surveys and density measurements (Weiss and Elkins-Tanton, 2013; Fornasier et al., 2010; Harris and Drube, 2014), and metallic meteorites have been retrieved (Scott and Wasson, 1975; Goldstein et al., 2009). Olivine-rich asteroids and meteorites are known, and they can be generated in the mantle or core-mantle boundary of differentiated bodies (Buseck, 1977; Keil, 2014; DeMeo et al., 2019).

Planetesimals that have been catastrophically disrupted should be observable today in the form of asteroid collisional families. Members of these families should show compositions characteristic of the different layers of the differentiated parent body. However, years of spectroscopic and spectrophotometric surveys showed that most collisional families of asteroids detected in the Main Belt are homogeneous (Mothé-Diniz et al., 2005a; Jurić et al., 2002; Parker et al., 2008; Masiero et al., 2011; Oszkiewicz et al., 2014). Moreover, there is an observed scarcity of olivine-rich asteroids in the Main Belt, known as the "missing-mantle problem" (Chapman, 1986; Burbine et al., 1996). DeMeo et al. (2019) found that olivine-rich asteroids with a diameter above 2 km account for less than 0.16% of the Main Belt and are evenly distributed in the proper orbital element space, showing no statistically significant concentration in any asteroid family.

To address these questions, I started with analysing the Gaia DR3 spectral dataset. In the context of the preparation for the DR4 and as DPAC member, I analysed the epoch reflectance spectra used to produce the mean reflectance spectra published in the DR3. Results of this analysis are presented in Chapter 2, and filtering procedures have been proposed to resolve potential issues affecting asteroid epoch reflectance spectra. These procedures will be further validated before being implemented to produce improved asteroid reflectance spectra for the DR4.

Knowledge of the potential issues affecting the Gaia DR3 asteroid spectra enabled me to exploit this large and homogeneous dataset with a critical eye, and led me to develop analysis techniques specifically adapted to this dataset. Since it contains thousands of objects characterized spectroscopically for the first time, it is a powerful tool for studying object populations in the Main Belt.

6.1 CONCLUSIONS

In this thesis, I searched for evidence of differentiation in the Main Belt in two main ways. First, in Chapter 3, I searched for potential spectral analogues of the differentiated meteorite Erg Chech 002 in the Main Belt asteroid population. Then, in Chapter 4, I characterised the asteroid family (36256) 1999 XT17, which appears to show a potential concentration of olivine-rich objects. Finally, in Chapter 5, I developed a method for classifying DR3 asteroid spectra, optimised for the search for olivine-rich asteroids.

Among the many ungrouped meteorites, Erg Chech 002 is known as the oldest andesite of the Solar System (Barrat et al., 2021). The peculiarities of this differentiated meteorite, and the fact that it does not match with any known spectral type of asteroid, lead us to search for its potential spectral analogues in the DR3 spectral dataset. Since thousands of new objects have been characterise with spectroscopy with Gaia, analogues of this meteorite could potentially be found in the dataset.

In Chapter 3, I presented two methods used to detect asteroids showing visible DR3 spectra potentially similar to the meteorite's. First, the spectral slope and the depth of the silicate band were calculated and compared between the meteorite and DR3 asteroid spectra. Then, a curve matching method was used to determine which spectra from the DR3 dataset were most similar to those of the meteorite.

A total of 51 asteroids were found to be potential analogues of the laboratory sample spectra of EC 002, which constitutes a mere 0.08% of the full DR3 dataset. On the other hand, 91 asteroids (0.15% of the DR3 dataset) were found matching the spectra of the meteorite on which was applied a space weathering model, simulating an increasing exposure to space weathering agents (Galinier et al., 2023).

To confirm or disprove that these asteroids are EC 002 analogues, we characterized 20 of the candidate analogues with spectroscopic observations in the near-infrared wavelength range with the IRTF. The results of these observations are presented for the first time in this manuscript. A confirmed spectral similarity between the meteorite and asteroids would likely suggest a similar surface composition, which would imply that the asteroids found as analogues are fragments of early differentiated planetesimals.

An analysis and classification of the observed potential analogues showed 16 V-type basaltic asteroids, one A-type olivine-rich body, and one object belonging to the stony S-complex. None of the observed asteroids was found to show an EC 002-like andesitic composition.

However, a few objects have been found in the literature with near-infrared spectra similar to the laboratory spectrum of EC 002, such as Outer Main Belt asteroid (10537) 1991 RY16 (Moskovitz et al., 2008; Leith et al., 2017). Theories regarding its origin suggest that it could be a fragment of a differentiated planetesimal (Moskovitz et al., 2008), which is in line with the formation theories of EC 002. Other asteroids, such as (7472) Kumakiri and (14390) 1990 QP10, also show a peculiar spectrum compared to the known spectroscopic types (Leith et al., 2017), and they may present spectral characteristics similar to those of EC 002.

It has been suggested that the planetesimals at the origin of EC 002, and those at the origin of these asteroids have likely disappeared from the Main Belt, due to their accretion to other bodies, or to their destruction (Barrat et al., 2021; Moskovitz et al., 2008). However, the spectral similarities between the asteroids and the meteorite could suggest a link, and the asteroids (10537) 1991 RY16, (7472) Kumakiri and (14390) 1990 QP10 could be the first detected objects of a new class of andesitic bodies, remnants of differentiated planetesimals in the Main Belt.

In Chapter 4, I presented a search for a potential concentration of olivine-rich A-type asteroids in asteroid collisional families, that could indicate that the family is differentiated. Exploiting the DR3 spectral dataset, a NIR spectrum we observed, and spectroscopic and spectrophotometric data of the literature, we characterised the small family (36256) 1999 XT17. This small family of 57 members (Nesvorny et al., 2015) is located in the pristine zone of the Main Belt, and appeared from literature data to be a good candidate olivine-rich family.

We classified the available spectra of the members of this family using a curve-matching algorithm, and obtained 12 asteroids classified A-type as first or second best class, among the 15 members with DR3 spectra. Taking into account literature data, 36 members of the (36256) 1999 XT17 family have a classification, and 16 of these are classified as A-type. This makes a proportion of 44.4% of potential A-type asteroids among the characterised members of this family. Four of these objects are confirmed by the combination of DR3 and near-infrared data, and two of these have a composition matching with pure olivine assemblages and olivine-rich meteorites. These elements could indicate that the other family members classified A-types from their DR3 spectra are also true olivine-rich A-types.

Therefore, the (36256) 1999 XT17 family appears to be the first olivine-rich A-type family ever detected (Galinier et al., 2024). This detection challenges the affirmation made by DeMeo et al. (2019), stating that there is no statistically significant concentration of olivine-rich bodies in any asteroid family.

The family members of (36256) 1999 XT17 show proper orbital elements and a size distribution in continuity with the neighbouring (221) Eos family. It therefore is possible that this family, defined by Nesvorny et al. (2015) from a dynamical aspect, is a mixture of Eos family fugitives that managed to cross the 7:3 MMR, and independent members of the true olivine-rich (36256) 1999 XT17 family.

If the true family members are all A-type asteroids, then this family could derive from the disruption of a purely olivine-rich parent body, that could have formed in the mantle of a partially or totally differentiated planetesimal. This parent body could have been implanted at its current location in the pristine zone, after being disrupted at a different location in the Solar System (Avdellidou et al., 2022). If the family is composed of A-type and S-complex asteroids, it could come from a partially differentiated object that broke in situ.

Finally, I developed in Chapter 5 a method to classify DR3 asteroids reflectance spectra in the taxonomic scheme of Bus and Binzel (2002a). One objective of this work was to do a preliminary analysis of the limits imposed by the DR3 dataset regarding the classification of asteroids, to pave the way for the Gaia classification scheme that will be published with the DR4. For the scope of this thesis, another objective was to search for new A-type asteroids in the DR3 dataset, and to search for other potential families showing a concentration of olivine-rich bodies in the Main Belt.

To classify DR3 spectra, I worked on a chosen sample of spectra with a average SNR⩾30. This SNR limit was found to provide satisfactory classification results. I used a classification algorithm based on curve matching between asteroids and taxonomic templates spectra, and I obtained good classification results by defining and using Gaia templates. I optimised the classification of DR3 spectra by grouping taxonomic classes, as subtleties between spectroscopic subclasses seem poorly detected with this classification method.

To optimise the classification of A-type asteroids, I developed a secondary classification step based on the slope of the DR3 reflectance spectra in the blue part. This secondary classification seems effective in recovering false-negative A-types classified as S-types, while discriminating S-types wrongly classified as A-types due to their high spectral slope.

After validating its performances, this two steps classification algorithm was applied to the Gaia DR3 dataset. Among the 18 739 asteroids having a DR3 spectrum with an average SNR⩾30 and only validated bands in the considered wavelength range from 462 to 946 nm, 98 asteroids were found A-types. Among these, 12 asteroids are already classified A-types from spectroscopy in the literature, and 8 are found non-A-types. If we take into account our own NIR spectrum of asteroid (33763) 1999 RB84, confirming that this object is an A-type, I found 77 potential A-types never characterised with spectroscopy before the Gaia DR3. They represents 0.4% of the 18 739 asteroids of the filtered Gaia DR3 dataset, which makes an amount of A-type asteroids in the Main Belt 2.5 times higher than the 0.16% found by DeMeo et al. (2019) for objects with a diameter larger than 2 km.

In total, considering as well the asteroids found A-types with spectroscopy in the literature, 157 A-type asteroids are found in the Main Belt. These objects are evenly distributed, confirming previous observations (DeMeo et al., 2019), but they show a slightly larger concentration in the Inner Main Belt. If the A-type asteroids detected are confirmed, they might bring evidence that some asteroid families of the IMB are differentiated. In the Middle and Outer Main Belt, small clusters of A-types can be observed, but no family defined by Nesvorny et al. (2015) appears obviously olivine-rich, at the exception of (36256) 1999 XT17.

Finally, the results found in this thesis seem to indicate that remains of early-differentiated planetesimals are rare in the Main Belt. As suggested by various authors, these objects might have mostly been destroyed, or might have disappeared by accreting to other bodies (see for example Barrat et al., 2021; DeMeo et al., 2019). However, some evidence of differentiation seems to be detectable in the Main Belt, in the form of asteroids showing peculiar spectra resembling the ones of the andesitic meteorite Erg Chech 002, or in the form of olivine-rich asteroid families.

6.2 PERSPECTIVES

First, to further search for potential analogues of the meteorite Erg Chech 002 in the Main Belt and to confirm or invalidate its possible link with asteroids such as (10537) 1991 RY16, it could be interesting to search for other asteroids sharing its spectral characteristics. This object could be the first representative of a class of andesitic bodies, and detecting and characterising these objects could help linking Erg Chech 002 and other ungrouped meteorites. However, the Gaia DR3 dataset might not be the most suited for such work. Indeed, the spectrum of (10537) 1991 RY16 shows a characteristic band around 650 nm. In this region, Gaia DR3 spectra can be affected by a drop in the reflectance, due to the merging between the spectra acquired by two independent spectrophotometers onboard Gaia. This "fake band" could hide a real compositional band, or could be mistaken for it.

This "fake band" issue has not been completely understood yet, but further studies will be performed to try solving this issue in preparation for the DR4. If it is the case, the DR4 dataset could be a great opportunity to search for asteroids showing visible spectra similar to the one of (10537) 1991 RY16. If such asteroids are detected, they will then need to be confirmed with near-infrared observations.

In continuity with the work on EC 002, the DR3 dataset could be used to try linking other ungrouped meteorite with asteroids, but this work requires to know how space weathering and grain size would affect the spectra of such meteorites in space. It would thus be interesting to perform space weathering experiments on the meteorite Erg Chech 002 and on other ungrouped meteorites, to make sure that the Hapke model used by Barrat et al. (2021) represents accurately the effects of space weathering on andesitic bodies.

To confirm that the family (36256) 1999 XT17 shows a concentration of olivine-rich asteroids, near-infrared observations of its members should be performed. Such characterisation of the family could help determine which members of the (36256) 1999 XT17 family defined with the HCM algorithm are true family members, and which are part of the Eos fugitives. This could help to conclude on the origin of its parent body, that could be a piece of the mantle of a differentiated or partially differentiated planetesimal.

Only this family has been fully characterised using the Gaia DR3 in this thesis. The classification of DR3 spectra presented in Chapter 5 could however be used to systematically explore every asteroid family, as this dataset contains many objects characterized with spectroscopy for the first time. Regions of the Main Belt could be explored without a-priori knowledge of the asteroid families from a dynamical point of view, and the spectroscopic clusters found could be compared to the known definition of families a-posteriori. This work could help finding interlopers in asteroid families, and could allow to separate families merged together by clustering algorithms. Moreover, the family definition of Nesvorny et al. (2015) has been extensively used in this thesis, but other family catalogues could be used as well to search for a potential concentration of A-types (Milani et al., 2014; Vinogradova, 2019).

Finally, potential A-type asteroids found from the classification of Gaia DR3 spectra have to be confirmed with NIR observations. This would be interesting both to validate the classification method developed in Chapter 5, and to further study and characterise A-type asteroids in the Main Belt. Actually, an observation campaign of A-types has been performed (Avdellidou et al. in prep.), and the results of these observations can be compared with the ones obtained with the two steps classification method as a preliminary check. The algorithm developed here could also be further improved, and tests regarding the choice of curve-matching metric, the definition of templates, and the taxonomic scheme used could be performed.

Moreover, studies have shown that the olivine content in the surface composition of asteroids has to be high compared to the iron content, to be detected with spectroscopy (Cloutis et al., 1990). There is a known compositional gradient in the asteroid population, and taxonomic classes are useful to study it, but they cannot represent each mineralogical subtlety. S-complex asteroids are thought to be undifferentiated bodies from their link with ordinary chondrites. However, there is a large spectral diversity within the S-complex, and OCs are linked only to a subclass of the S-complex, according to Gaffey (2011). Some of these objects could actually be olivine-rich, with and olivine/iron content ratio preventing the olivine from being detected[1]. The position of S-complex objects in the principal component space (or in other representation based on asteroids characteristics) could help detecting olivine-rich S-complex objects, which could change our analysis of asteroid families. S-complex objects dominating in the Main Belt, the "missing mantle problem" could actually not be one.

Finally, many authors have already used the Gaia DR3 spectral dataset to carry out specific projects. For example, Hasegawa et al. (2022) studied the space weathering process on the surface of asteroid (596) Scheila, using Gaia spectra. They found that space weathering process do not affect the surface colour of dark asteroids over the course of 10 years, suggesting a link between D, T and low albedo X-complex asteroids with red asteroids (belonging to the Z-class in Mahlke et al. (2022)). Oszkiewicz et al. (2023) analysed the DR3 asteroid spectra to study basaltic asteroids, and they found three times more V-type asteroids in the DR3 than the V-types known from the literature. They identified about 350 possible V-type asteroids, and they confirmed from the DR3 dataset that vestoids (Vesta's family members) show distinct spectral characteristics from Middle and Outer Main Belt V-types. Delbo et al. (2023) used the DR3 SSO reflectance spectra to characterise C-complex families in the IMB, and found that the Polana and Eulalia families can be distinguished from their DR3 spectra in the NUV wavelength range. These families appear similar to Bennu and Ryugu, suggesting a link between these objects and these families. On other aspects, Tinaut-Ruano et al. (2024) explored the NUV region of the Gaia DR3 spectra to study primitive asteroids, and they discovered the first observational evidence linking an absorption at NUV wavelengths to the presence of hydrated iron-rich phyllosilicates at the surface of an asteroid. Finally, Bourdelle de Micas et al. (2024) used the DR3 asteroids spectra to characterise a primordial family, and found it to be dominated by S-complex asteroids, with a mineralogy consistent with pyroxene-rich minerals and ordinary chondrites.

These authors, amongst others, developed a specific method depending on the requirements of their projects, and their exploitation of the Gaia DR3 spectral data lead to new discoveries. During this thesis, I similarly developed methods to search for evidence of differentiation with the DR3 dataset, but I also worked on the improvements of the Gaia mean reflectance spectra themselves, and I propose here a classification method allowing to study the Main Belt as a whole. I therefore conclude that the Gaia spectral data are a powerful tool to study asteroid populations, and the following data releases could help answering the long standing questions regarding the evolution of early differentiated planetesimals.

---

[1] `https://doi.org/10.5194/egusphere-egu24-7979`

Part II

APPENDIX

A

GAIA DR3 BP-RP SPECTRA

Table A.1: Asteroids selected among the class prototypes of Mahlke et al. (2022).

Asteroid	Spectral type	Average SNR
(1) Ceres	C	2593.3
(2) Pallas	B	3840.51
(3) Juno	S	828.09
(4) Vesta	V	1658.82
(5) Astraea	S	619.4
(10) Hygiea	C	2183.68
(13) Egeria	Ch	1348.17
(14) Irene	S	462.24
(16) Psyche	M	1511.04
(19) Fortuna	Ch	1352.18
(22) Kalliope	M	1594.91
(24) Themis	C	967.58
(41) Daphne	Ch	1334.77
(64) Angelina	E	247.45
(65) Cybele	P	1123.76
(87) Sylvia	P	1244.2
(153) Hilda	P	688.72
(203) Pompeja	Z	927.46
(214) Aschera	E	473.11
(216) Kleopatra	M	1336.55
(221) Eos	K	618.07
(234) Barbara	L	399.67
(246) Asporina	A	268.67

– *continued on next page*

– continued.

Asteroid	Spectral type	Average SNR
(269) Justitia	Z	305.46
(289) Nenetta	A	171.37
(349) Dembowska	R	400.17
(354) Eleonora	A	427.5
(397) Vienna	L	328.98
(434) Hungaria	E	337.65
(531) Zerlina	B	131.9
(579) Sidonia	K	588.7
(588) Achilles	D	127.34
(599) Luisa	L	355.19
(653) Berenike	K	353.39
(908) Buda	Z	295.84
(911) Agamemnon	D	238.8
(1143) Odysseus	D	206.83

Table A.2: Selected S-type asteroids.

Asteroid	Type	Method	reference
(57) Mnemosyne	S	Spec VISNIR	Mahlke et al. (2022)
(67) Asia	S	Spec VISNIR	Mahlke et al. (2022)
(138) Tolosa	S	Spec VISNIR	Mahlke et al. (2022)
(149) Medusa	S	Spec VISNIR	Mahlke et al. (2022)
(192) Nausikaa	S	Spec VISNIR	Mahlke et al. (2022)
(202) Chryseis	S	Phot VIS	Sergeyev et al. (2022)
(215) Oenone	S	Phot VIS	Sergeyev et al. (2022)
(235) Carolina	S	Spec VISNIR	Mahlke et al. (2022)
(270) Anahita	S	Spec VISNIR	Mahlke et al. (2022)
(277) Elvira	S, K	Spec VIS	Mothé-Diniz et al. (2005a)
(290) Bruna	S	Spec VISNIR	Mahlke et al. (2022)
(292) Ludovica	S	Spec VISNIR	Mahlke et al. (2022)
(346) Hermentaria	S	Spec VISNIR	Mahlke et al. (2022)
(532) Herculina	S	Spec VISNIR	Mahlke et al. (2022)
(584) Semiramis	S	Spec VISNIR	Mahlke et al. (2022)
(662) Newtonia	S, M	Spec VIS, Spec VISNIR	Lazzaro et al. (2004), Mahlke et al. (2022)
(695) Bella	S	Spec VISNIR	Mahlke et al. (2022)
(787) Moskva	S	Spec VISNIR	Mahlke et al. (2022)
(819) Barnardiana	S	Spec VISNIR	Mahlke et al. (2022)
(945) Barcelona	S	Spec VISNIR	Mahlke et al. (2022)
(951) Gaspra	S	Spec VISNIR	Mahlke et al. (2022)
(964) Subamara	S	Phot VIS	DeMeo and Carry (2013)
(984) Gretia	Sa, A	Spec VISNIR	DeMeo et al. (2009), Mahlke et al. (2022)
(985) Rosina	S	Spec VISNIR	Mahlke et al. (2022)
(1060) Magnolia	S	Spec VISNIR	Mahlke et al. (2022)
(1065) Amundsenia	S	Spec VISNIR	Mahlke et al. (2022)
(1069) Planckia	S	Spec VISNIR	Mahlke et al. (2022)
(1129) Neujmina	S, K	Spec VISNIR	Mothé-Diniz et al. (2008b)
(1248) Jugurtha	S	Spec VISNIR	Mahlke et al. (2022)
(1252) Celestia	S	Spec VISNIR	Mahlke et al. (2022)
(1322) Coppernicus	S	Spec VISNIR	Mahlke et al. (2022)
(1329) Eliane	S	Spec VISNIR	Mahlke et al. (2022)
(1478) Vihuri	S, L	Spec VIS, Spec VISNIR	Xu et al. (1995), Mahlke et al. (2022)

B

THE METEORITE ERG CHECH 002

Table B.1: Accepted asteroids as candidate matches for the different samples of EC 002

Asteroid	Method
Powder + raw slabs	
(1643) Brown	Spectral parameters
(1946) Walraven	Spectral parameters
(2432) Soomana	Spectral parameters
(3188) Jekabsons	Spectral parameters
(3651) Friedman	Spectral parameters
(3869) Norton	Spectral parameters
(4302) Markeev	Spectral parameters
(5121) Numazawa	Spectral parameters
(6853) Silvanomassaglia	Spectral parameters + CM
(6876) Beppeforti	Spectral parameters
(8587) Ruficollis	Spectral parameters
(8827) Kollwitz	Spectral parameters
(9197) Endo	Spectral parameters
(9433) 1997 CF3	Spectral parameters
(10156) 1994 VQ7	Spectral parameters + CM
(10671) Mazurova	Spectral parameters
(10902) 1997 WB22	Spectral parameters
(11155) Kinpu	Spectral parameters
(12551) 1998 QQ39	Spectral parameters
(13839) 1999 XF29	Spectral parameters
(15989) 1998 XK39	Spectral parameters
(16856) Banach	CM
(17056) Boschetti	CM

– continued on next page

– continued.

Asteroid	Method
(17240) Gletorrence	Spectral parameters
(20454) Pedrajo	Spectral parameters + CM
(24286) 1999 XU188	Spectral parameters
(24892) 1997 AD3	Spectral parameters + CM
(26573) 2000 EG87	Spectral parameters
(27262) 1999 XT184	Spectral parameters
(28162) 1998 VD14	Spectral parameters
(30769) 1984 ST2	Spectral parameters
(33418) Jacksonweaver	Spectral parameters
(36431) 2000 PJ12	Spectral parameters
(44150) 1998 HC108	Spectral parameters
(47232) 1999 VQ36	Spectral parameters
(49101) 1998 RE76	Spectral parameters
(54062) 2000 GX135	CM
(55549) 2001 XC59	Spectral parameters + CM
(56904) 2000 QP171	Spectral parameters
(63653) 2001 QQ109	CM
(77147) 2001 EV6	CM
(77935) 2002 GM54	CM
(87093) 2000 LW6	Spectral parameters
(88955) 2001 TW42	Spectral parameters + CM
(89556) 2001 XS98	CM
(90604) 4813 P-L	Spectral parameters
(123113) 2000 SH361	CM
(124884) 2001 TE41	CM
(164121) 2003 YT1	CM
(205560) 2001 SC282	Spectral parameters + CM
(310436) 2000 AB169	Spectral parameters + CM
SW low	
(4088) Baggesen	Spectral parameters
(6003) 1988 VO1	Spectral parameters
(6789) Milkey	Spectral parameters
(8243) Devonburr	Spectral parameters
(8483) Kinwalaniihsia	Spectral parameters
(8692) 1992 WH	Spectral parameters

– continued on next page

– continued.

Asteroid	Method
(9753) 1990 QL3	Spectral parameters
(10131) Stanga	CM
(11920) 1992 UY2	Spectral parameters
(14511) Nickel	Spectral parameters
(15088) Licitra	Spectral parameters
(15623) 2000 HU30	CM
(17739) 1998 BY15	Spectral parameters
(17821) Bolsche	Spectral parameters
(17882) Thielemann	Spectral parameters
(17943) 1999 JZ6	Spectral parameters
(18344) 1989 TN11	Spectral parameters
(18780) Kuncham	CM
(19978) 1989 TN6	Spectral parameters
(20289) Nettimi	Spectral parameters
(20535) Marshburrows	CM
(21318) 1996 XU26	Spectral parameters
(22276) Belkin	CM
(22538) Lucasmoller	CM
(23766) 1998 MZ23	Spectral parameters
(24569) 9609 P-L	Spectral parameters
(24684) 1990 EU4	Spectral parameters + CM
(26084) 1981 EK17	Spectral parameters
(26851) Sarapul	Spectral parameters
(27876) 1996 BM4	Spectral parameters + CM
(27884) 1996 EZ1	Spectral parameters
(28132) Karenzobel	Spectral parameters
(29171) 1990 QK3	Spectral parameters
(30426) Philtalbot	Spectral parameters
(30834) 1990 VR6	Spectral parameters
(32835) 1992 EO5	CM
(33423) 1999 DK	CM
(33852) Baschnagel	CM
(33934) 2000 LA30	CM
(33947) 2000 ML1	Spectral parameters + CM
(35364) Donaldpray	Spectral parameters

– continued on next page

– continued.

Asteroid	Method
(39940) 1998 FR99	Spectral parameters
(41894) 2000 WH121	Spectral parameters
(43278) 2000 ES109	Spectral parameters + CM
(44162) 1998 HC148	Spectral parameters
(45787) 2000 OJ24	Spectral parameters
(48039) 2001 DT69	Spectral parameters
(51659) Robohachi	Spectral parameters
(53417) 1999 NP38	Spectral parameters
(53661) 2000 DU62	Spectral parameters
(53899) 2000 FM49	Spectral parameters
(56561) Jaimenomen	Spectral parameters + CM
(58640) 1997 WH18	Spectral parameters
(61098) 2000 LY28	Spectral parameters
(64458) 2001 VF35	Spectral parameters
(65504) 3544 P-L	CM
(74107) 1998 QM37	Spectral parameters
(74378) 1998 XH11	CM
(75323) 1999 XY47	Spectral parameters
(79827) 1998 WU3	CM
(87216) 2000 OG38	Spectral parameters
(89776) 2002 AL90	Spectral parameters
(89952) 2002 JB20	Spectral parameters + CM
(92593) 2000 PN16	Spectral parameters
(100440) 1996 PJ6	CM
(103308) 2000 AH55	CM
(108139) 2001 GL11	Spectral parameters + CM
(112326) 2002 MM4	Spectral parameters + CM
(122122) 2000 JM16	Spectral parameters
(128450) 2004 NX24	Spectral parameters
(134916) 2000 YP53	Spectral parameters
SW medium	
(13133) Jandecleir	Spectral parameters
(18143) 2000 OK48	Spectral parameters
(31060) 1996 TB6	Spectral parameters
(42822) 1999 NT13	Spectral parameters + CM

– continued on next page

– continued.

Asteroid	Method
(44322) 1998 RZ42	Spectral parameters + CM
(49141) 1998 SM41	Spectral parameters
(51379) 2001 BY7	Spectral parameters
(52408) 1993 TJ34	Spectral parameters
(68089) 2000 YS108	CM
(68946) 2002 PX138	CM
(90843) 1995 YZ22	Spectral parameters
(93797) 2000 WO43	CM
(99714) 2002 JQ41	Spectral parameters
(108899) 2001 PP5	CM
(122125) 2000 JO17	Spectral parameters
(145532) 2006 FD42	CM
(230762) 2003 WP192	Spectral parameters + CM
SW high	
(9974) Brody	Spectral parameters
(19754) Paclements	Spectral parameters
(33809) 1999 XK152	CM

Note: Asteroids showing a spectrum matching the powder and raw slabs samples of the meteorite are 51 in number, while 71 asteroids match the low space-weathered spectrum of EC 002, 17 asteroids match its medium space-weathered spectrum and three asteroids match its highly space-weathered spectrum. CM stands for curve matching.

Table B.2: Asteroids within the "possible matches area".

Asteroid	Acceptance	Notes	Type	Method	Ref.
(289) Nenetta	0	longer band I centre	A	Spec. VISNIR	5
(863) Benkoela	0	longer band I centre	A	Spec. VISNIR	5
(956) Elisa	0	-	V	Spec. VIS and NIR	3, 6
(1459) Magnya	0	VISNIR different	V	Spec. VISNIR	5
(1468) Zomba	0	NIR different	V	Spec. VISNIR	20
(1488) Aura	0	different red part	A	Phot. VIS	24
(1643) Brown	1	-	S	Phot. VIS	24
(1709) Ukraina	0	A type spectrum	A	Spec. VISNIR	25
(1908) Pobeda	0	longer band I centre	S	Phot. VIS	24
(1946) Walraven	1	-	V	Spec. VIS	4
(2168) Swope	0	-	V	Spec. NIR	16,22
(2371) Dimitrov	0	NIR different	V	Spec. VIS and NIR	2, 6
(2432) Soomana	1	-	V	Phot. VIS	10, 23
(2442) Corbett	0	shorter band I centre	V	Spec. VISNIR	5

Table B.2 – continued.

Asteroid	Acceptance	Notes	Type	Method	Ref
(2557) Putnam	0	shorter band I centre	S	Phot. VIS	24
(2851) Harbin	0	-	V	Spec. VISNIR	5
(2912) Lapalma	0	-	V	Spec. VISNIR	5
(3104) Durer	0	different red part	K	Spec. VISNIR	25
(3155) Lee	0	shorter band I centre	V	Spec. VISNIR	5
(3188) Jekabsons	1	-	V	Spec. VIS	21
(3651) Friedman	1	bad two last points	V	Phot. VIS	24
(3817) Lencarter	0	shorter band I centre	-	-	-
(3869) Norton	1	article: related to 4 Vesta	V	Spec. VIS	1
(3882) Johncox	0	-	V	Spec. VISNIR	18
(4055) Magellan	0	-	V	Spec. VISNIR	5
(4088) Baggesen	1	no clear 650 nm band - SW low	-	-	-
(4302) Markeev	1	-	V	Phot. VIS	23
(4402) Tsunemori	0	different band I shape	A	Spec. VISNIR	25
(4692) SIMBAD	0	shorter band I centre	V	Phot. VIS	10, 23
(5037) Habing	0	shorter band I centre	V	Spec. VISNIR	25
(5121) Numazawa	1	-	S	Phot. VIS	24
(5498) Gustafsson	0	linked to howardites	V	Spec. VIS and NIR	6, 8
(5696) Ibsen	0	different red part			
(6003) 1988 VO1	1	SW low	X	Phot. VIS	24
(6046) 1991 RF14	0	shorter band I centre	V	Spec. VISNIR	18
(6159) Andreseloy	0	shorter band I centre	V	Spec. VISNIR	25
(6369) 1983 UC	0	shorter band I centre	-	-	-
(6584) Ludekpesek	0	shorter band I centre	V	Phot. NIR	17
(6728) 1991 UM	0	shorter band I centre	-	-	-
(6789) Milkey	1	SW low	-	-	-
(6853) Silvanomassaglia	1	-	V	Phot. NIR	17
(6876) Beppeforti	1	-	S	Phot. VIS	24, 24
(6877) Giada	0	shorter band I centre	V	Phot. NIR	17
(6964) Kunihiko	0	shorter band I centre	V	Phot. VIS	24
(7294) Barbaraakey	0	flatter red part	S	Phot. VIS	24
(7529) Vagnozzi	0	flatter red part	V	Phot. VIS	24
(7889) 1994 LX	0	noisy	V	Spec. VISNIR	20
(7933) Magritte	0	shorter band I centre	X	Phot. VIS	24
(7942) 1991 OK1	0	shorter band I centre	S	Phot. VIS	24
(8031) Williamdana	0	shorter band I centre	V	Phot. VIS	24
(8243) Devonburr	1	SW low	S	Phot. VIS	24, 24
(8483) Kinwalaniihsia	1	SW low	V	Phot. VIS	24
(8587) Ruficollis	1	-	K	Phot. VIS	24
(8660) Sano	0	longer band I centre	S	Phot. VIS	24
(8669) 1991 NS1	0	shorter band I centre	S	Phot. VIS	24
(8692) 1992 WH	1	SW low	S	Phot. VIS	24
(8827) Kollwitz	1	-	C	Phot. VIS	24
(8838) 1989 UW2	0	longer band I centre	A	Spec. VISNIR	19
(9115) Battisti	0	shorter band I centre	V	Phot. VIS	24

Table B.2 – continued.

Asteroid	Acceptance	Notes	Type	Method	Ref
(9197) Endo	1	VISNIR literature spectrum not good	V	Spec. VISNIR	22
(9432) Iba	0	shorter band I centre	V	Phot. VIS	24
(9433) 1997 CF3	1	-	C	Phot. VIS	24
(9593) 1991 PZ17	0	bump instead of 650 nm band	S	Phot. VIS	24
(9752) 1990 QZ1	0	longer band I centre	S	Phot. VIS	24
(9753) 1990 QL3	1	SW low	-	-	-
(9974) Brody	1	SW high	-	-	-
(10156) 1994 VQ7	1	bad three last points	V	Phot. VIS	24
(10319) Toshiharu	0	shorter band I centre V	V	Phot. VIS	23, 24
(10418) 1998 WZ23	0	shorter band I centre	V	Phot. VIS	24
(10438) Ludolph	0	shorter band I centre	-	-	-
(10578) 1995 LH	0	bad BP RP overlapping	-	-	-
(10671) Mazurova	1	-	S	Phot. VIS	24
(10811) Lau	0	flatter red part	-	-	-
(10902) 1997 WB22	1	-	-	-	-
(11041) Fechner	0	shorter band I centre	V	Phot. VIS	7
(11155) Kinpu	1	-	S	Phot. VIS	24
(11764) Benbaillaud	0	shorter band I centre	V	Spec. VIS	8
(11861) Teruhime	0	longer band I centre	-	-	-
(11890) 1991 FF	0	longer band I centre	C	Phot. VIS	24
(11920) 1992 UY2	1	SW low (noisy)	C	Phot. VIS	24
(12551) 1998 QQ39	1	-	V	Phot. VIS	24
(12860) Turney	0	shorter band I centre	S	Phot. VIS	24, 24
(13133) Jandecleir	1	SW medium	S	Phot. VIS	24
(13704) Aletesi	0	shorter band I centre	C	Phot. VIS	24
(13714) Stainbrook	0	noisy	S	Phot. VIS	24
(13743) Rivkin	0	shorter band I centre	V	Phot. VIS	24
(13839) 1999 XF29	1	-	S	Phot. VIS	24
(14108) 1998 OA13	0	shorter band I centre	-	-	-
(14489) 1994 UW	0	-	V	Phot. VIS	23
(14511) Nickel	1	bump instead of band - SW low	-	-	-
(14562) 1997 YQ19	0	noisy	V	Spec VISNIR	25
(15031) Lemus	0	shorter band I centre	V	Phot. NIR	17
(15088) Licitra	1	SW low	S	Phot. VIS	24
(15759) 1992 GM4	0	shorter band I centre	V	Phot. VIS	24
(15989) 1998 XK39	1	-	V	Phot. VIS	24
(16866) 1998 AR	0	no clear band I	S	Phot. VIS	24
(16962) Elizawoolard	0	shorter band I centre	C	Phot. VIS	24
(17225) Alanschorn	0	shorter band I centre	-	-	-
(17240) Gletorrence	1	-	S	Phot. VIS	24
(17739) 1998 BY15	1	SW low	V	Phot. NIR	17
(17821) Bolsche	1	lower quality spectrum - SW low	C	Phot. VIS	24
(17882) Thielemann	1	SW low	V	Phot. VIS	24
(17904) Annekoupal	0	shorter band I centre	S	Phot. VIS	24
(17943) 1999 JZ6	1	SW low	V	Phot. VIS	24

Table B.2 – continued.

Asteroid	Acceptance	Notes	Type	Method	Ref
(17951) Fenska	0	shorter band I centre	-	-	-
(18102) Angrilli	0	shorter band I centre	-	-	-
(18143) 2000 OK48	1	SW medium	A	Phot. VIS	10, 23, 24
(18280) 4245 T-3	0	more similar to a V type	S	Phot. VIS	24
(18344) 1989 TN11	1	SW low	V	Phot. VIS	24
(19230) Sugazi	0	shorter band I centre	V	Phot. NIR	17
(19281) 1996 AP3	0	-	V	Spec. VISNIR	18
(19487) Rosscoleman	0	shorter band I centre	-	-	-
(19589) Kirkland	0	noisy	V	Phot. VIS	24
(19754) Paclements	1	SW high or medium	S	Phot. VIS	10, 23, 24
(19978) 1989 TN6	1	SW low	V	Phot. VIS	10, 23
(20079) 1994 EP	0	shorter band I centre	V	Phot. VIS	24
(20157) 1996 TS18	0	shorter band I centre	S	Phot. VIS	24
(20237) Clavius	0	no clear band I	-	-	-
(20289) Nettimi	1	SW low (noisy)	-	-	-
(20454) Pedrajo	1	noisy	S	Phot. VIS	24
(20955) 2387 T-3	0	shorter band I centre	S	Phot. VIS	24
(21318) 1996 XU26	1	SW low	-	-	-
(21435) Aharon	0	noisy	-	-	-
(21891) Andreabocelli	0	shorter band I centre	-	-	-
(22113) 2000 RH9	0	shorter band I centre	V	Phot. VIS	10, 23
(22197) 3555 P-L	0	shorter band I centre	C	Phot. VIS	24
(22322) Bodensee	0	shorter band I centre	V	Phot. VIS	24
(23306) Adamfields	0	shorter band I centre	S	Phot. VIS	24
(23502) 1992 DE3	0	shorter band I centre	-	-	-
(23595) 1995 VR11	0	shorter band I centre	C	Phot. VIS	24
(23766) 1998 MZ23	1	SW low	S	Phot. VIS	24
(24286) 1999 XU188	1	-	S	Phot. VIS	24
(24569) 9609 P-L	1	SW low or medium	S	Phot. NIR	17
(24684) 1990 EU4	1	SW low	S	Phot. NIR	17
(24892) 1997 AD3	1	-	-	-	-
(25434) Westonia	0	shorter band I centre	V	Phot. VIS	23, 24
(25752) 2000 BE8	0	noisy + bad BP-RP alignment	-	-	-
(25808) 2000 CK103	0	flatter red part	S	Phot. VIS	24
(26084) 1981 EK17	1	SW low	S	Phot. VIS	24
(26417) Michaelgord	0	bad BP-RP overlapping	V	Phot. VIS	10, 23, 24
(26573) 2000 EG87	1	-	V	Phot. VIS	24
(26851) Sarapul	1	SW low	-	-	-
(27106) Jongoldman	0	shorter band I centre	V	Phot. VIS	24
(27162) 1999 AM6	0	shorter band I centre	S	Phot. VIS	24
(27262) 1999 XT184	1	bad RP	X	Phot. VIS	24
(27390) Kyledavis	0	shorter band I centre	-	-	-
(27399) Gehring	0	shorter band I centre	C	Phot. VIS	24
(27876) 1996 BM4	1	SW low	S	Phot. VIS	24
(27884) 1996 EZ1	1	SW low	S	Phot. VIS	24

Table B.2 – continued.

Asteroid	Acceptance	Notes	Type	Method	Ref
(28132) Karenzobel	1	SW low	S	Phot. VIS	24
(28162) 1998 VD14	1	-	-	-	-
(28291) 1999 CX52	0	shorter band I centre	V	Spec. VIS	9
(29171) 1990 QK3	1	bump instead of band - SW low	-	-	-
(29269) 1993 FD25	0	shorter band I centre	C	Phot. VIS	24
(30426) Philtalbot	1	SW low	V	Phot. VIS	23
(30751) 1981 EL29	0	shorter band I centre	S	Phot. VIS	24
(30769) 1984 ST2	1	-	-	-	-
(30781) 1988 CR2	0	shorter band I centre	C	Phot. VIS	24
(30820) 1990 RU2	0	more similar to a V type	S	Phot. VIS	24
(30834) 1990 VR6	1	SW low	V	Phot. VIS	10, 23
(30892) 1993 FR18	0	shorter band I centre	A	Phot. VIS	23
(31060) 1996 TB6	1	SW medium	SQ	Phot. VIS	7
(31414) Rotarysusa	0	shorter band I centre	V	Spec. VISNIR	25
(31544) 1999 DZ5	0	shorter band I centre	V	Phot. VIS	24
(31572) 1999 FM22	0	shorter band I centre	V	Phot. VIS	24
(31622) 1999 GL19	0	shorter band I centre	-	-	-
(32168) 2000 NP9	0	shorter band I centre	-	-	-
(32449) Crystalmiller	0	shorter band I centre	S	Phot. VIS	24
(32590) Cynthiachen	0	shorter band I centre SW low	V	Phot. VIS	10, 23
(33418) Jacksonweaver	1	-	V	Phot. VIS	10, 23
(33562) Amydunphy	0	different red part	V	Phot. NIR	17
(33881) 2000 JK66	0	-	V	Spec. VISNIR	20
(33947) 2000 ML1	1	SW low	S	Phot. VIS	24
(34698) 2001 OD22	0	shorter band I centre	V	Spec. NIR	16
(34706) 2001 OP83	0	Vesta family	V	Spec. NIR	14
(35193) 1994 CG14	0	no clear band I	C	Phot. VIS	24
(35364) Donaldpray	1	SW low	V	Phot. VIS	10
(36360) 2000 OH3	0	shorter band I centre	S	Phot. VIS	24
(36363) 2000 OB5	0	shorter band I centre	S	Phot. VIS	24
(36431) 2000 PJ12	1	-	V	Phot. VIS	7
(36798) 2000 SA43	0	shorter band I centre + noisy	S	Phot. VIS	24
(37306) 2001 KW46	0	no clear band I	-	-	-
(37386) 2001 WG29	0	shorter band I centre	V	Phot. NIR	17
(39940) 1998 FR99	1	SW low (bad BP)	-	-	-
(40056) 1998 KT44	0	shorter band I centre	C	Phot. VIS	24
(41574) 2000 SQ1	0	no clear band I	-	-	-
(41765) 2000 VV35	0	shorter band I centre	X	Phot. VIS	24
(41894) 2000 WH121	1	SW low	-	-	-
(42644) 1998 FE67	0	bump instead of band	V	Phot. NIR	17
(42822) 1999 NT13	1	SW medium	S	Phot. VIS	24, 24
(43278) 2000 ES109	1	SW low	C	Phot. VIS	24
(43302) 2000 GE114	0	shorter band I centre	V	Phot. VIS	24
(43388) 2000 WA61	0	shorter band I centre	V	Phot. NIR	17
(44150) 1998 HC108	1	-	V	Phot. VIS	10, 23

Table B.2 – continued.

Asteroid	Acceptance	Notes	Type	Method	Ref
(44162) 1998 HC148	1	SW low	C	Phot. VIS	24
(44322) 1998 RZ42	1	SW medium	S	Phot. VIS	24
(44711) Carp	0	no clear band I	S	Phot. VIS	24
(44940) 1999 VH53	0	shorter band I centre	C	Phot. VIS	24, 24
(45417) 2000 AZ151	0	shorter band I centre	-	-	-
(45787) 2000 OJ24	1	SW low	-	-	-
(46701) Interrante	0	shorter band I centre	V	Phot. VIS	23
(47232) 1999 VQ36	1	good agreement [500 - 950] nm	C	Phot. VIS	24
(47398) 1999 XC116	0	bump instead of band	V	Phot. VIS	23
(47463) 1999 XE258	0	shorter band I centre	-	-	-
(48039) 2001 DT69	1	SW low	V	Phot. VIS	23
(48114) 2001 FW77	0	different blue part	S	Phot. VIS	10, 23
(48323) 2002 NN33	0	low quality spectrum	S	Phot. VIS	24
(48632) 1995 SV29	0	more similar to a V type	V	Phot. VIS	10
(49101) 1998 RE76	1	-	V	Phot. VIS	10, 23
(49141) 1998 SM41	1	SW medium (or A type?)	A	Phot. VIS	10, 23
(49901) 1999 XK164	0	shorter band I centre	S	Phot. VIS	24
(50139) 2000 AH129	0	no clear band I	-	-	-
(50236) 2000 BB3	0	shorter band I centre SW low	V	Phot. VIS	24
(51379) 2001 BY7	1	SW medium (noisy)	C	Phot. VIS	24
(51443) 2001 FN27	0	bump instead of band	V	Phot. NIR	17
(51659) Robohachi	1	SW low (noisy)	S	Phot. VIS	24
(52216) 5014 T-3	0	shorter band I centre	V	Phot. VIS	24
(52408) 1993 TJ34	1	SW medium	-	-	-
(52995) 1998 UJ32	0	shorter band I centre	V	Phot. NIR	17
(53417) 1999 NP38	1	SW low	-	-	-
(53425) 1999 SO4	0	noisy	S	Phot. VIS	10, 23
(53593) 2000 CJ58	0	shorter band I centre	S	Phot. VIS	24
(53661) 2000 DU62	1	SW low	S	Phot. VIS	24
(53899) 2000 FM49	1	SW low or medium	-	-	-
(54061) 2000 GX134	0	shorter band I centre	-	-	-
(55549) 2001 XC59	1	noisy but plausible	S	Phot. VIS	24
(55831) 1995 XL	0	bad BP-RP alignment	S	Phot. NIR	17
(56348) 2000 AH69	0	shorter band I centre	C	Phot. VIS	24
(56561) Jaimenomen	1	SW low	-	-	-
(56585) 2000 JZ29	0	shorter band I centre	Q	Phot. VIS	24
(56696) 2000 LQ26	0	shorter band I centre	V	Phot. VIS	10, 23
(56904) 2000 QP171	1	-	C	Phot. VIS	24
(57857) 2001 XJ203	0	shorter band I centre	-	-	-
(58640) 1997 WH18	1	SW low	-	-	-
(59228) 1999 CH	0	shorter band I centre	V	Phot. VIS	10, 23
(59530) 1999 JU24	0	shorter band I centre	-	-	-
(59686) 1999 JS108	0	shorter band I centre	-	-	-
(60285) 1999 XR106	0	shorter band I centre	S	Phot. VIS	24
(60584) 2000 EW132	0	shorter band I centre	S	Phot. VIS	24

Table B.2 – continued.

Asteroid	Acceptance	Notes	Type	Method	Ref
(61098) 2000 LY28	1	SW low	V	Phot. VIS	24
(61203) 2000 OY4	0	-	V	Phot. VIS	24
(61682) 2000 QV124	0	shorter band I centre	C	Phot. VIS	24
(63366) 2001 HK4	0	different red part	V	Phot. VIS	10
(63438) 2001 MY28	0	no clear band I	-	-	-
(64252) 2001 TL168	0	shorter band I centre	A	Phot. VIS	24
(64458) 2001 VF35	1	SW low	V	Phot. NIR	17
(64948) 2001 YH124	0	noisy	S	Phot. VIS	24
(65707) 1992 PY1	0	bad quality spectrum	-	-	-
(66679) 1999 TD29	0	shorter band I centre	V	Phot. VIS	24
(68765) 2002 EE99	0	shorter band I centre	-	-	-
(69595) 1998 FK11	0	shorter band I centre	V	Phot. VIS	24
(69628) 1998 FD62	0	shorter band I centre	S	Phot. VIS	24
(74107) 1998 QM37	1	SW low? Bad BP-RP overlapping?	-	-	-
(75323) 1999 XY47	1	SW low	-	-	-
(75441) 1999 XB129	0	shorter band I centre	S	Phot. VIS	24
(77584) 2001 KP14	0	noisy	S	Phot. VIS	24
(77590) 2001 KM17	0	shorter band I centre	V	Phot. NIR	17
(78034) 2002 JF82	0	shorter band I centre	V	Phot. VIS	7
(79137) 1991 PD15	0	no band I	-	-	-
(80356) 1999 XM124	0	no clear band I	Ad	Phot. NIR	17
(80863) 2000 DT27	0	more similar to a V type	V	Phot. VIS	10
(85301) 1994 UM5	0	shorter band I centre	-	-	-
(87093) 2000 LW6	1	-	V	Phot. VIS	23
(87216) 2000 OG38	1	SW low (bad BP spectrum)	-	-	-
(88912) 2001 TS8	0	no clear band I	V	Phot. VIS	24
(88955) 2001 TW42	1	-	S	Phot. VIS	24
(89776) 2002 AL90	1	SW low	-	-	-
(89952) 2002 JB20	1	SW low	S	Phot. VIS	24
(90604) 4813 P-L	1	bad red part	S	Phot. VIS	24
(90843) 1995 YZ22	1	SW medium	-	-	-
(90855) 1996 GZ8	0	bump instead of band	C	Phot. VIS	24
(91343) 1999 JP30	0	shorter band I centre	V	Phot. NIR	17
(92593) 2000 PN16	1	SW low	-	-	-
(98482) 2000 UL101	0	noisy	S	Phot. VIS	24
(98745) 2000 YB47	0	shorter band I centre	V	Phot. NIR	17
(99714) 2002 JQ41	1	SW medium	S	Phot. VIS	24
(102071) 1999 RK139	0	shorter band I centre	V	Phot. VIS	10, 23
(102107) 1999 RL164	0	shorter band I centre	V	Phot. VIS	10
(102195) 1999 ST10	0	noisy	-	-	-
(102469) 1999 TC237	0	bap BP RP overlapping?	V	Phot. VIS	23
(108139) 2001 GL11	1	SW low	V	Phot. VIS	7
(108199) 2001 HX21	0	no clear band I	-	-	-
(112326) 2002 MM4	1	SW low	V	Phot. VIS	23
(114486) 2003 AJ57	0	-	-	-	-

Table B.2 – continued.

Asteroid	Acceptance	Notes	Type	Method	Ref
(119385) 2001 TU7	0	lower quality spectrum	V	Phot. NIR	17
(122122) 2000 JM16	1	SW low	V	Phot. VIS	23
(122125) 2000 JO17	1	SW medium	S	Phot. VIS	10, 23
(125002) 2001 TJ154	0	shorter band I centre	-	-	-
(127422) 2002 OX11	0	low quality spectrum	S	Phot. VIS	10, 23
(128450) 2004 NX24	1	SW low	-	-	-
(130988) 2000 WT141	0	NEA	V	Spec. VIS	13
(133245) 2003 RL2	0	shorter band I centre	-	-	-
(134693) 1999 XP67	0	noisy	-	-	-
(134916) 2000 YP53	1	bad RP spectrum, SW low	-	-	-
(149372) 2002 XC71	0	bad agreement before 700 nm	-	-	-
(150544) 2000 SG164	0	noisy	X	Phot. VIS	23
(158242) 2001 TM24	0	bad BP-RP alignment	V	Phot. VIS	23
(163804) 2003 QQ88	0	noisy	S	Phot. VIS	7
(179587) 2002 LS2	0	-	S	Phot. VIS	15
(180757) 2004 NE33	0	-	-	-	-
(190138) 2005 RW27	0	shorter band I centre	-	-	-
(190664) 2000 YX90	0	bad BP-RP overlapping	-	-	-
(205560) 2001 SC282	1	noisy but plausible	-	-	-
(230762) 2003 WP192	1	SW medium	-	-	-
(310436) 2000 AB169	1	noisy but plausible	-	-	-

Note: The information in the table are the number and name of the 305 asteroids, if they are accepted or not as a match for EC 002 (1 if accepted, 0 if not), some notes about the visual inspection, the spectral type of the asteroid if determined and the method and relevant references associated (Ref column). The taxonomic scheme used for the type of each asteroid is the one used in the reference papers associated. Spec. stands for Spectroscopy and Phot. for Photometry.

Table B.3: Asteroids found as a match to the powder and raw slab samples of EC 002 with a curve-matching method.

Asteroid	Acceptance	Notes	Type	Method	Ref.
(6853) Silvanomassaglia	1	-	V	Phot. NIR	17
(10156) 1994 VQ7	1	-	V	Phot. VIS	24
(13743) Rivkin	0	shorter band I centre	V	Phot. VIS	24
(16856) Banach	1	-	S	Phot. VIS	24
(17056) Boschetti	1	-	S	Phot. VIS	24
(20289) Nettimi	0	noisy and unclear band I	-	-	-
(20454) Pedrajo	1	-	S	Phot. VIS	24
(23522) 1992 WC9	0	shorter band I centre	V	Phot. NIR	17
(24143) 1999 VY124	0	noisy	C	Phot. VIS	24
(24892) 1997 AD3	1	-	-	-	-
(26399) Rileyennis	0	shorter band I centre	-	-	-
(26420) 1999 XL103	0	shorter band I centre	V	Phot. VIS	23
(27106) Jongoldman	0	shorter band I centre	V	Phot. VIS	24
(27627) 2038 P-L	0	shorter band I centre	V	Phot. VIS	24

Table B.3 – continued.

(30000) Camenzind	0	shallow slope	V	Phot. VIS	10, 23, 24
(30081) Zarinrahman	0	shorter band I centre	S	Phot. VIS	24
(38690) 2000 QS29	0	unclear band I	S	Phot. VIS	24
(40693) 1999 RX229	0	unclear band I	C	Phot. VIS	24
(44691) 1999 RF221	0	shallow slope	C	Phot. VIS	24
(47327) 1999 XZ25	0	shorter band I centre	V	Phot. VIS	10, 23
(48632) 1995 SV29	0	shorter band I centre	V	Phot. VIS	10
(50488) 2000 DA86	0	shallow slope	-	-	-
(51659) Robohachi	0	noisy	S	Phot. VIS	24
(51688) 2001 KW12	0	shorter band I centre	S	Phot. VIS	24
(53561) 2000 CM22	0	noisy and unclear band I	S	Phot. VIS	24
(54062) 2000 GX135	1	noisy but plausible	C	Phot. VIS	24
(55549) 2001 XC59	1		S	Phot. VIS	24
(55866) 1997 PV4	0	shallow slope	V	Phot. VIS	24
(59686) 1999 JS108	0	shorter band I centre	-	-	-
(61169) 2000 NY20	0	band red and blue parts	X	Phot. VIS	24
(63653) 2001 QQ109	1	-	-	-	-
(64181) 2001 TS64	0	shorter band I centre	V	Phot. VIS	23
(68814) 2002 GP66	0	shallow slope	-	-	-
(77147) 2001 EV6	1	bad two last points	S	Phot. VIS	24
(77590) 2001 KM17	0	shorter band I centre	V	Phot. NIR	17
(77935) 2002 GM54	1	noisy but plausible	V	Phot. VIS	24
(78034) 2002 JF82	0	shorter band I centre	V	Phot. VIS	7
(80924) 2000 DJ73	0	noisy and unclear band I	C	Phot. VIS	24
(81448) 2000 GV123	0	shallow slope	S	Phot. VIS	24
(87010) 2000 JR55	0	shallow slope	C	Phot. VIS	24, 24
(88955) 2001 TW42	1	-	S	Phot. VIS	24
(89556) 2001 XS98	1	except for last points	-	-	-
(93893) 2000 WL141	0	unclear band I	S	Phot. VIS	10, 23, 24
(96353) 1997 VF3	0	flatter spectrum	C	Phot. VIS	24
(99722) 2002 JW46	0	flatter spectrum	S	Phot. VIS	24
(102107) 1999 RL164	0	shorter band I centre	V	Phot. VIS	10
(103308) 2000 AH55	0	unclear band I	-	-	-
(119144) 2001 PH32	0	unclear band I	V	Phot. VIS	10, 23
(123113) 2000 SH361	1	-	V	Phot. VIS	23
(124884) 2001 TE41	1	-	V	Phot. VIS	10, 23
(130988) 2000 WT141	0	NEA	V	Spec. VIS	13
(147124) 2002 TH129	0	less pronounced band	-	-	-
(149372) 2002 XC71	0	bad agreement before 700 nm	-	-	-
(153408) 2001 QV137	0	shorter band I centre	-	-	-
(164121) 2003 YT1	1	RP noisy but plausible	V	Spec. VISNIR	12
(194248) 2001 TA199	0	flatter spectrum	-	-	-
(205560) 2001 SC282	1	noisy but plausible	-	-	-
(310436) 2000 AB169	1	noisy but plausible	-	-	-

Table B.3 – continued.

Note: The information in the table are the number and name of the 58 asteroids, if they are accepted or not as a good match for EC 002 (1 if accepted, 0 if not), some notes about the visual inspection, the spectral type of the asteroid if determined and the method and relevant references associated (Ref. column). The taxonomic scheme used for the type of each asteroid is the one used in the reference papers associated. Spec. stands for Spectroscopy and Phot. for Photometry.

Note: The references are (1) Xu et al. (1995), (2) Bus and Binzel (2002a), (3) Lazzaro et al. (2004), (4) Alvarez-Candal et al. (2006), (5) DeMeo et al. (2009), (6) Moskovitz et al. (2010), (7) Carvano et al. (2010), (8) de Sanctis et al. (2011), (9) Solontoi et al. (2012), (10) DeMeo and Carry (2013), (11) Jasmim et al. (2013), (12) Sanchez et al. (2013), (13) Ribeiro et al. (2014), (14) Lindsay et al. (2015), (15) Carry et al. (2016), (16) Hardersen et al. (2018), (17) Popescu et al. (2018a), (18)Medeiros et al. (2019), (19) **DeMeo2019**, (20) Binzel et al. (2019), (21) Matlovič et al. (2020), (22) Migliorini et al. (2021), (23) Sergeyev and Carry (2021), (24) Sergeyev et al. (2022), (25) Mahlke et al. (2022)

Table B.4: Accepted asteroids as candidate matches to the three space-weathered modelled samples of EC 002.

Asteroid	Type	Method	Ref
SW low			
(10131) Stanga	S	Phot. VIS	24
(15623) 2000 HU30	S	Phot. NIR	17
(18780) Kuncham	S	Phot. VIS	24
(20535) Marshburrows	L	Phot. VIS	24
(22276) Belkin	S	Phot. VIS	24
(22538) Lucasmoller	S	Phot. VIS	24
(24684) 1990 EU4	S	Phot. NIR	17
(27876) 1996 BM4	S	Phot. VIS	24
(32835) 1992 EO5	V	Phot. VIS	24
(33423) 1999 DK	A	Phot. VIS	23
(33852) Baschnagel	V	Phot. VIS	24
(33934) 2000 LA30	S	Phot. VIS	24
(33947) 2000 ML1	S	Phot. VIS	24
(43278) 2000 ES109	C	Phot. VIS	24
(56561) Jaimenomen	-	-	-
(65504) 3544 P-L	V	Phot. NIR	17
(74378) 1998 XH11	S	Phot. NIR	17
(79827) 1998 WU3	-	-	-
(89952) 2002 JB20	S	Phot. VIS	24
(100440) 1996 PJ6	-	-	-
(103308) 2000 AH55	-	-	-
(108139) 2001 GL11	V	Phot. VIS	7
(112326) 2002 MM4	V	Phot. VIS	23
SW medium			
(42822) 1999 NT13	S	Phot. VIS	24
(44322) 1998 RZ42	S	Phot. VIS	24
(68089) 2000 YS108	-	-	-
(68946) 2002 PX138	S	Phot. VIS	24
(93797) 2000 WO43	S	Phot. VIS	10
(108899) 2001 PP5	-	-	-
(145532) 2006 FD42	-	-	-
(230762) 2003 WP192	-	-	-
SW high			
(33809) 1999 XK152	C	Phot. VIS	24

Note: This selection has been done after visual inspection of 269 asteroids for the low space-weathered sample, 223 asteroids for the medium space weathering and 12 asteroids for the high space weathering. The references associated with the numbers in the Ref. column are given in appendix. The taxonomic scheme used for the type of each asteroid is the one used in the reference papers associated. SW stands for space weathering.

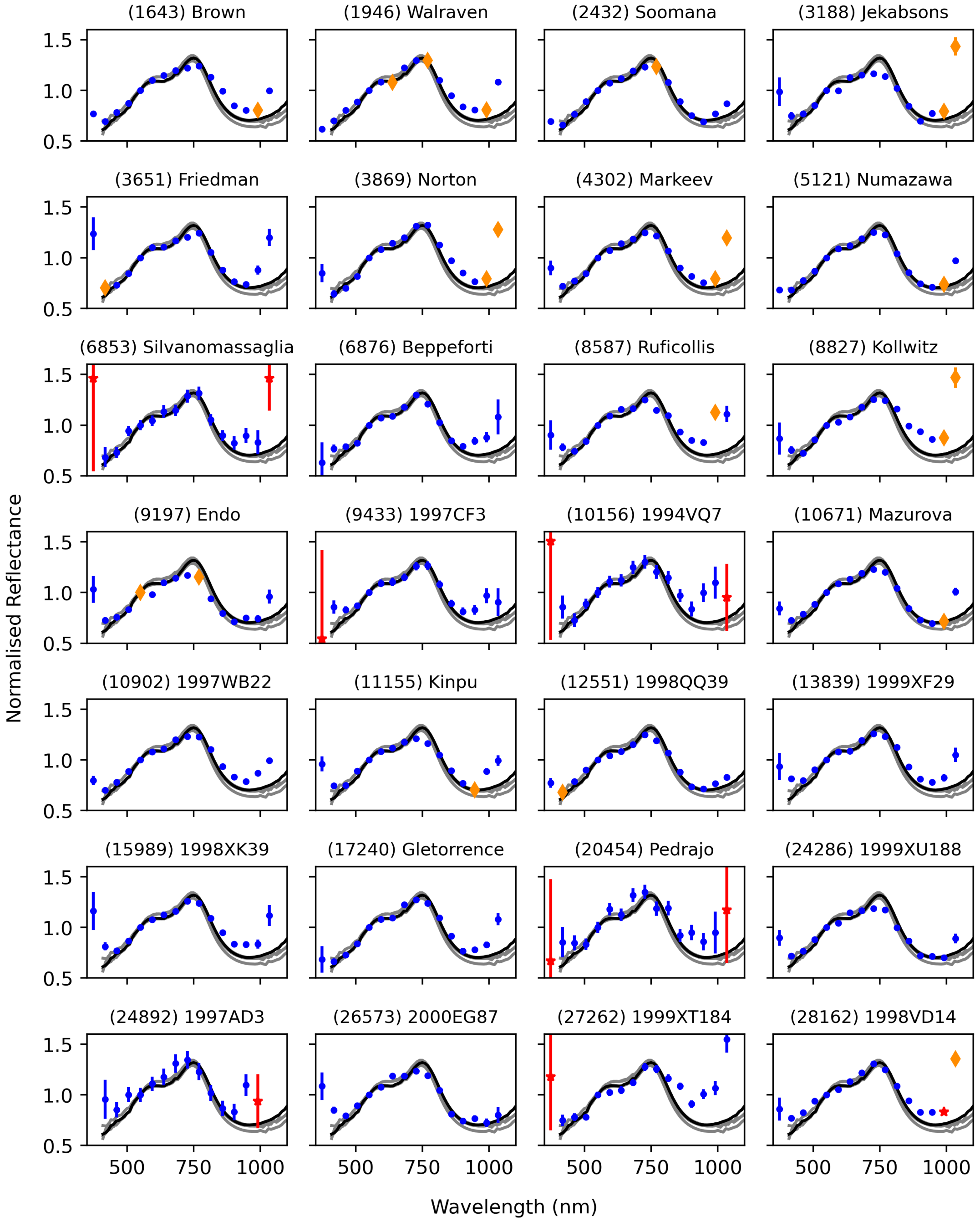

Figure B.1: Spectra of the 41 asteroids found in the 'possible matches area', validated as matches of EC 002 after visual inspection. The spectra are normalised at 550 nm. Black continuous line: spectrum of the powder sample of the meteorite, grey lines: spectra of the raw slab samples. The 16 bands of the Gaia asteroid spectra are given a colour and a symbol according to the value of the flag associated to the band: blue circle if flag=0, orange diamond if flag=1 and red star if flag=2. This way of showing the asteroid spectra applies for every figure hereafter.

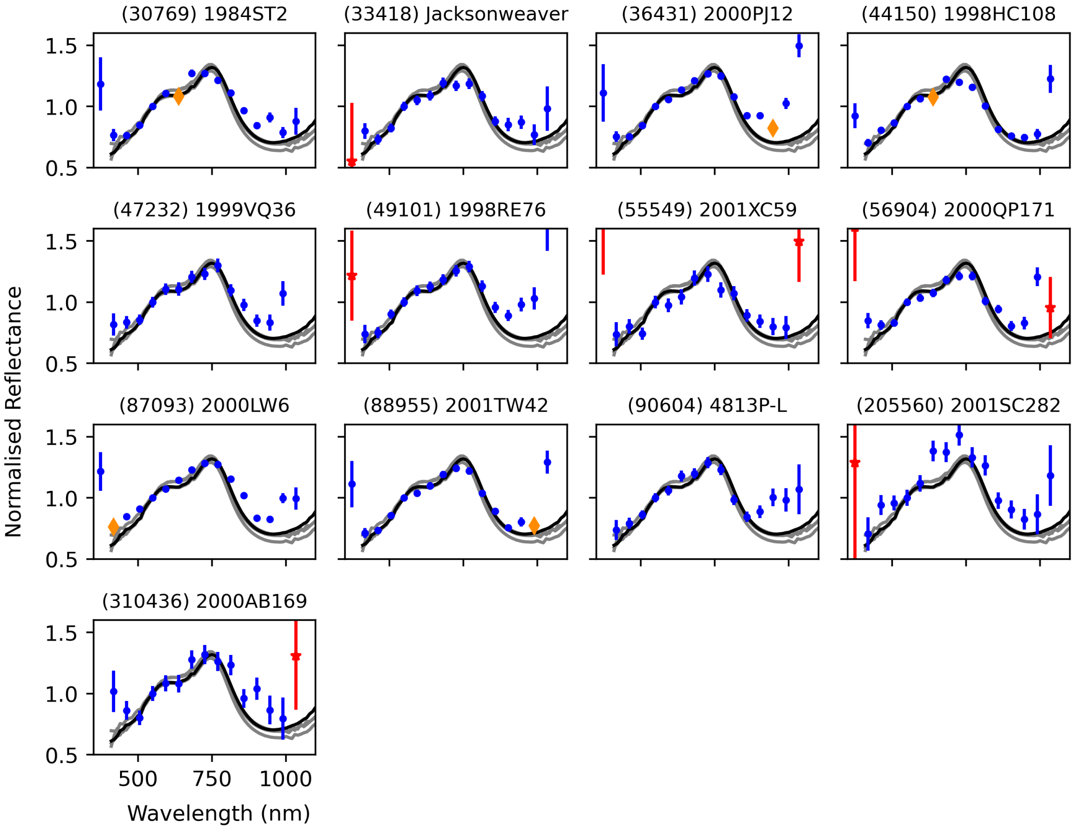

Figure B.1: continued.

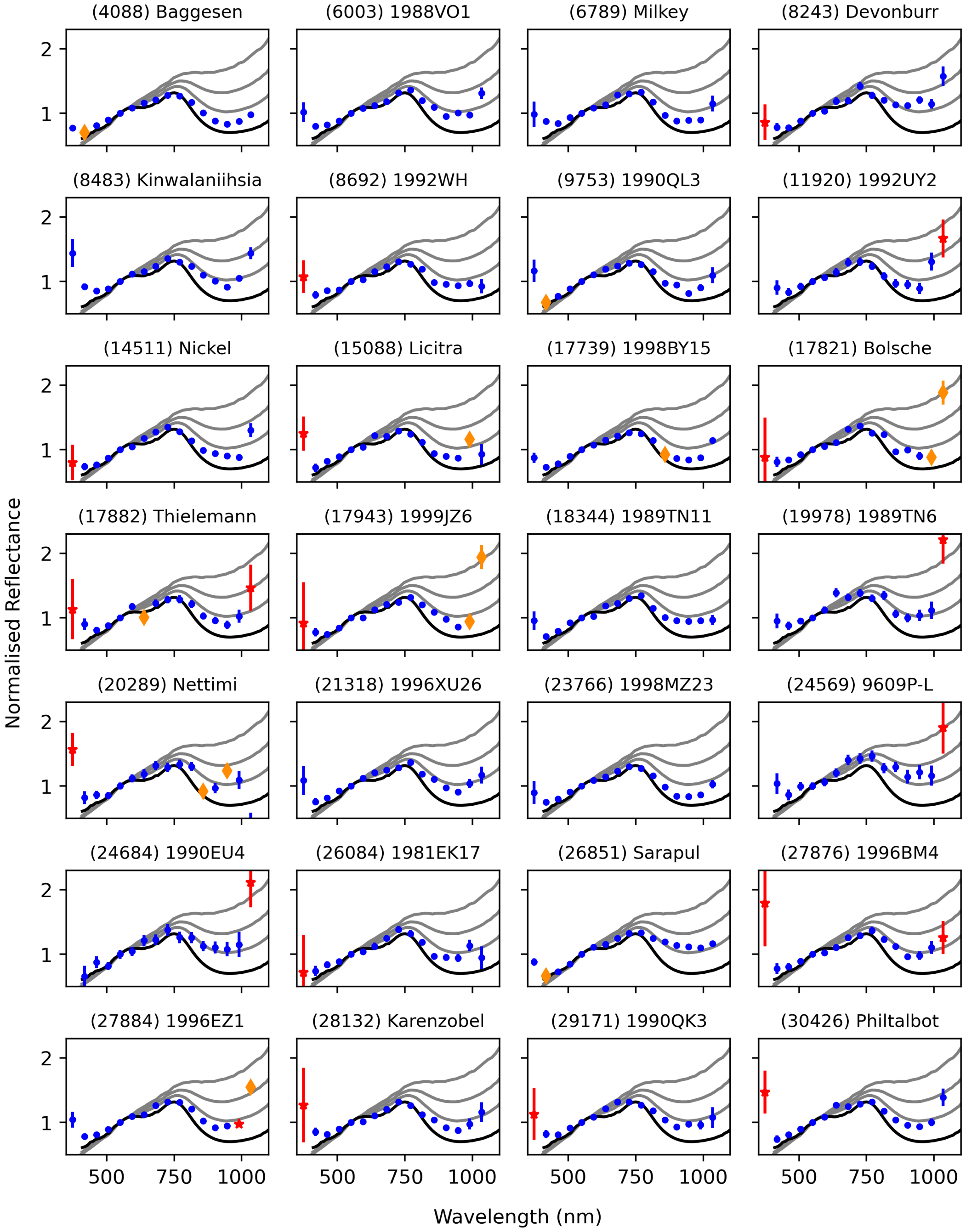

Figure B.2: Same as Fig. B.1 but with the 56 asteroids visually validated as matches of the low space-weathered EC 002. The space-weathered spectra of EC 002 are shown in grey lines.

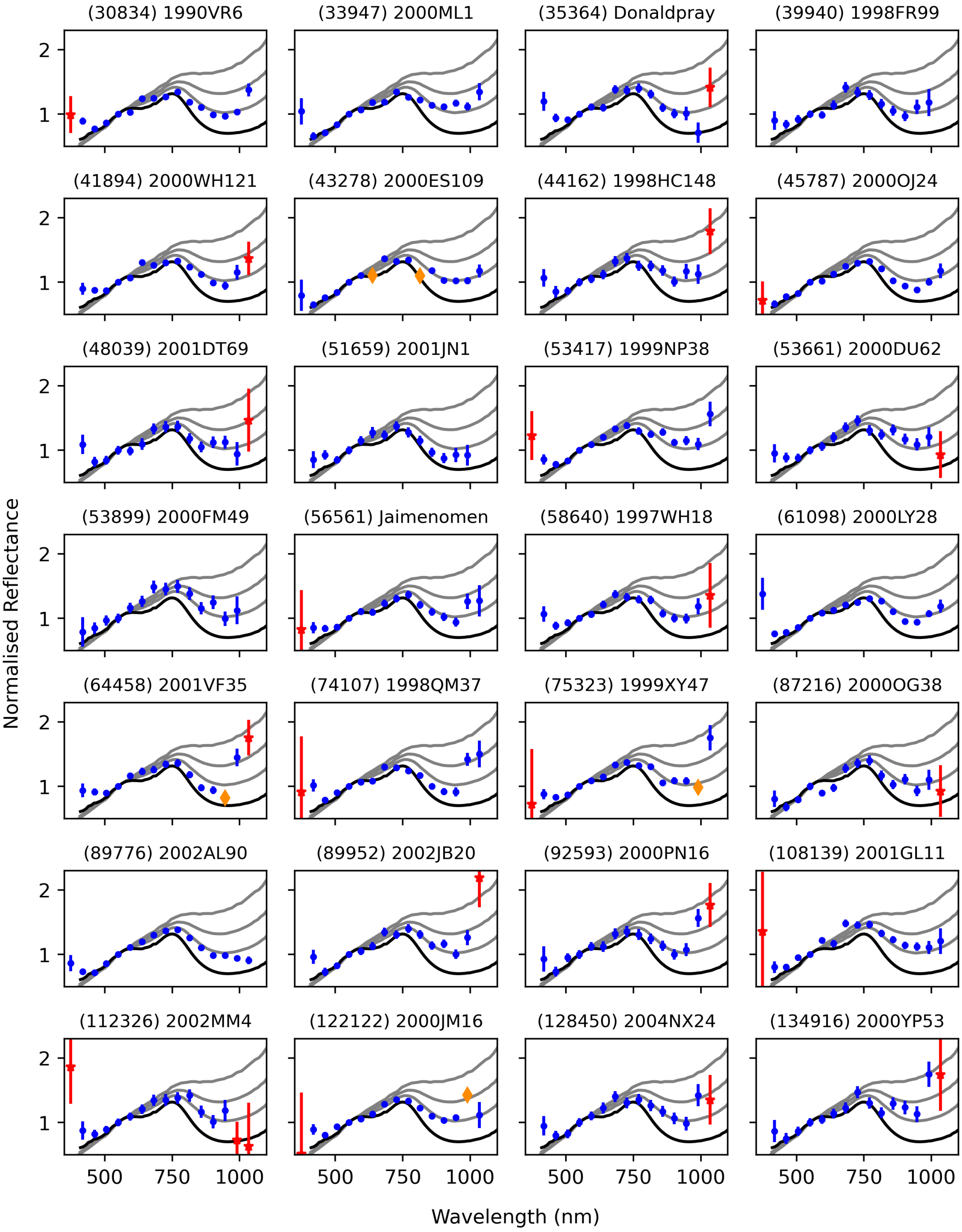

Figure B.2: continued.

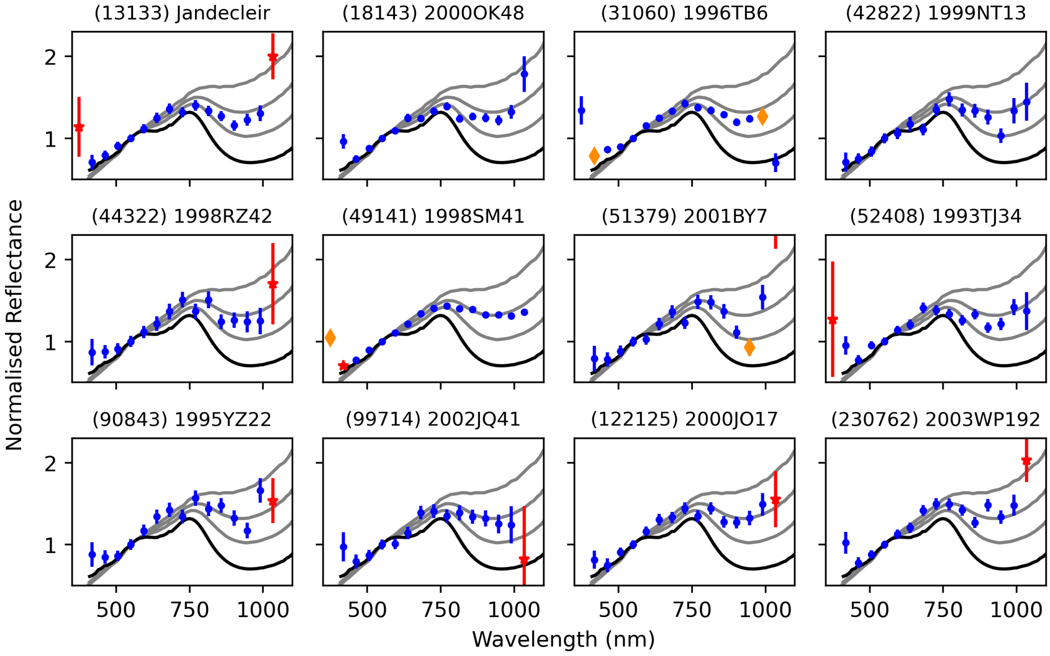

Figure B.3: Same as Fig. B.2 but with the 12 asteroids visually validated as matches of the medium space-weathered EC 002.

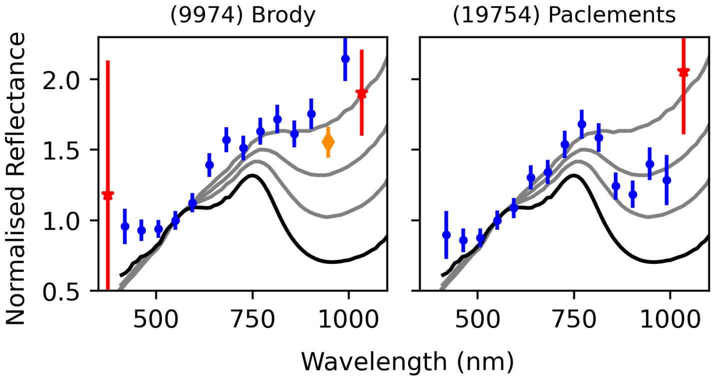

Figure B.4: Same as Fig. B.2 but with the two asteroids visually validated as matches of the high space-weathered EC 002.

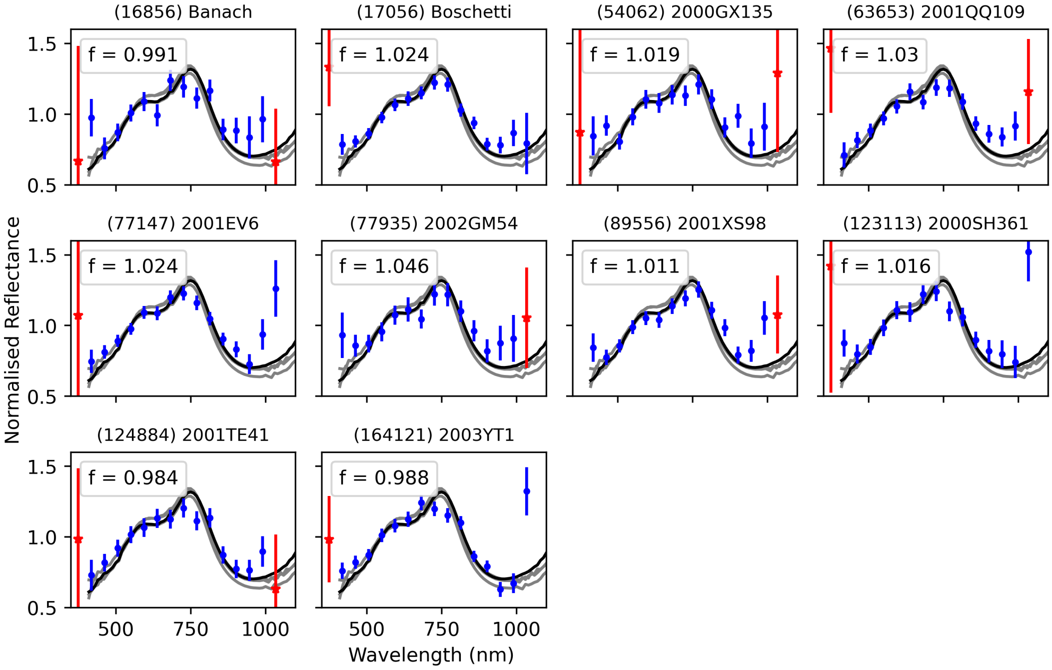

Figure B.5: Spectra of the ten asteroids found with the curve matching method only, validated as matches of EC 002 after visual inspection. The spectra are normalised with a scaling factor f, here the meteorite spectrum was divided by the scaling factor. The spectra of the powder sample of the meteorite is shown in black continuous line, and the raw slab samples spectra are shown in grey lines. As previously, the 16 bands of the Gaia asteroid spectra are shown with a colour and a symbol associated to their flag number.

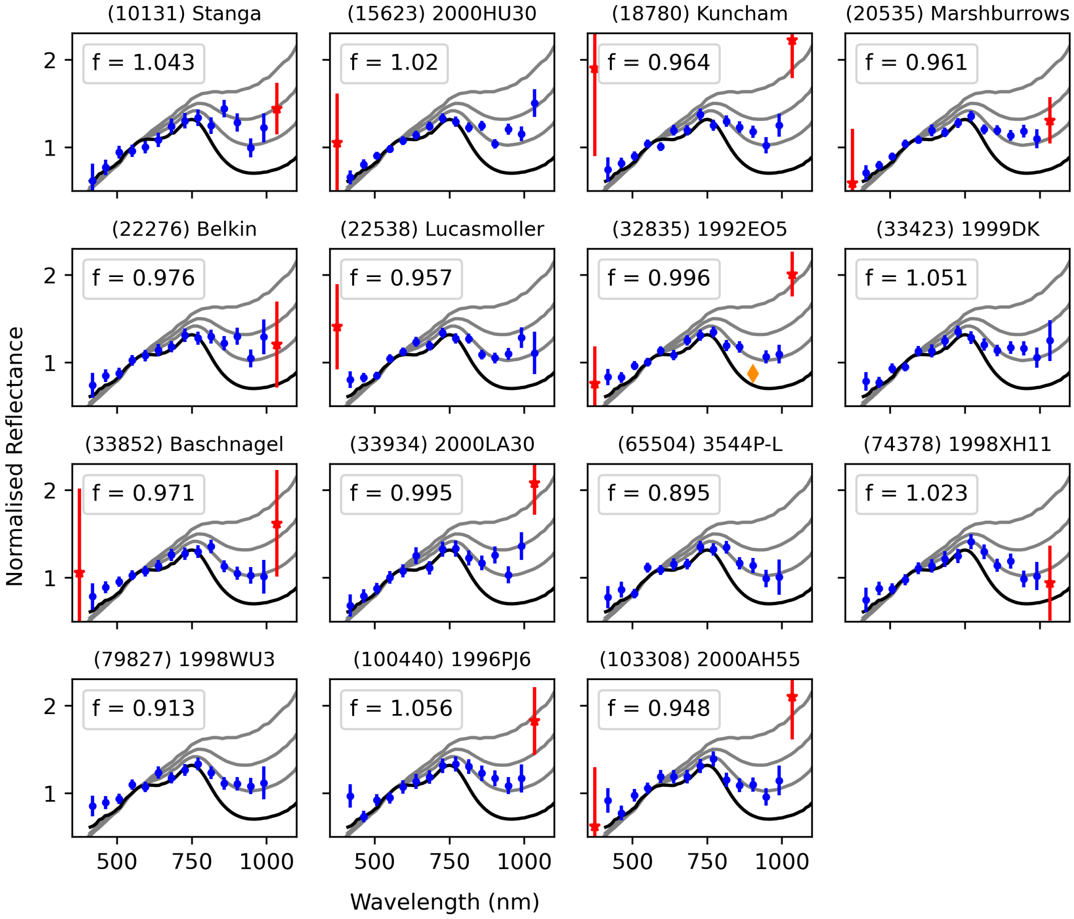

Figure B.6: Same as Fig. B.5 but with the 15 asteroids visually validated as matches of the low space-weathered EC 002. Here the spectra of the powder sample of the meteorite is shown in black continuous line, and the space-weathered spectra are shown in grey lines.

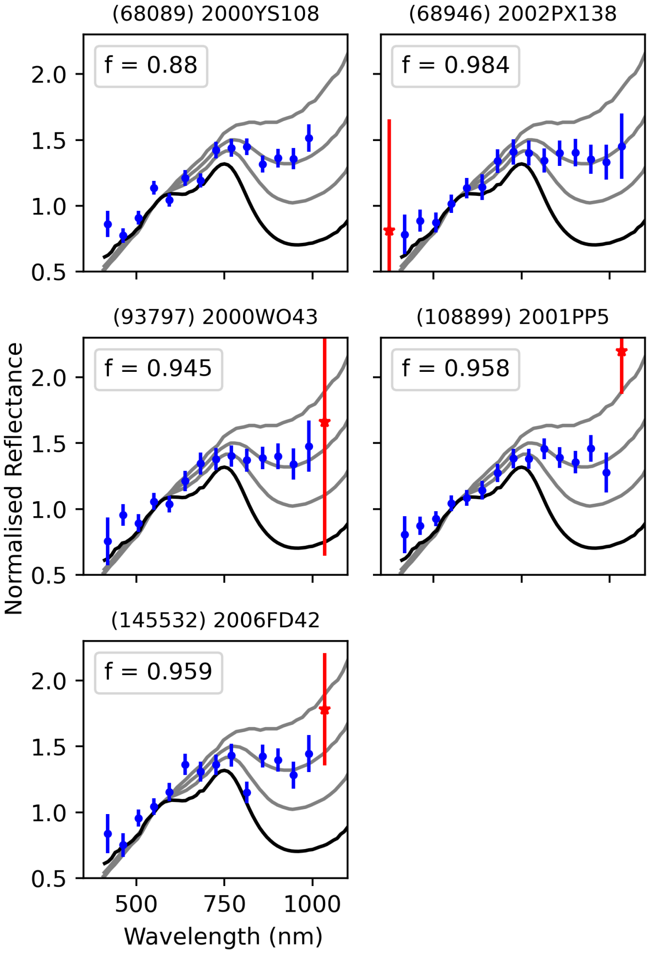

Figure B.7: Same as Fig. B.6 but with the 8 asteroids visually validated as matches of the medium space-weathered EC 002.

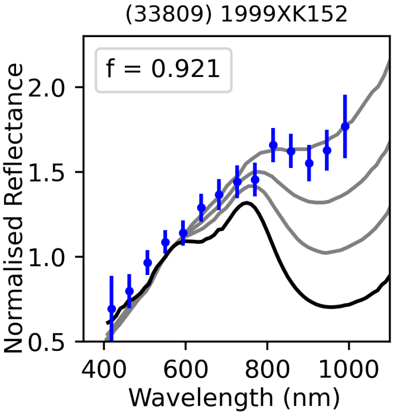

Figure B.8: Same as Fig. B.6 but with the asteroid visually validated as match of the high space-weathered EC 002.

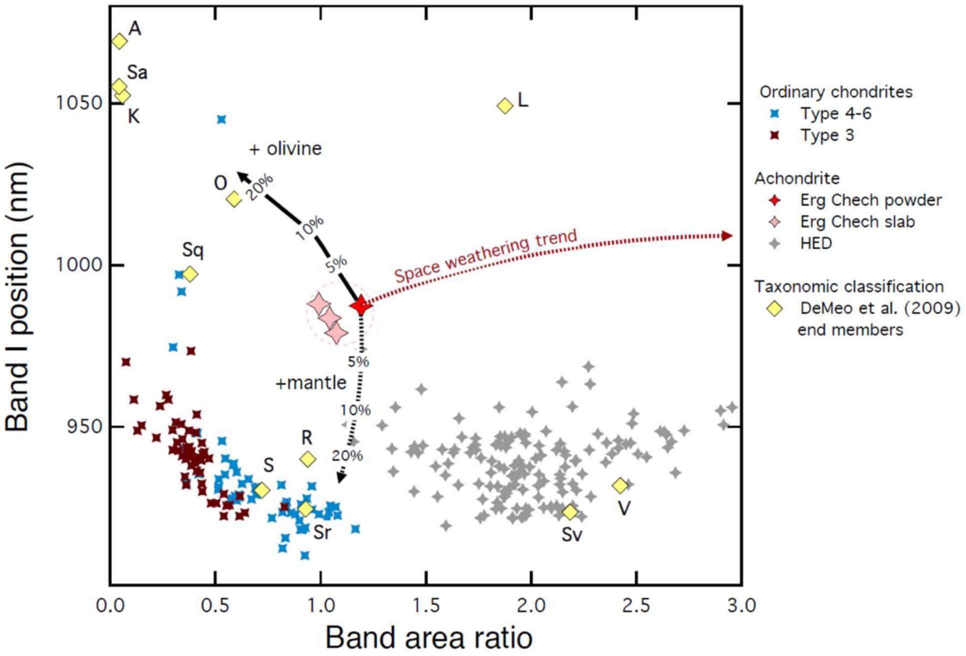

Figure B.9: Fig.S13 from Barrat et al. (2021), showing the Band I Center (BIC) as a function of the Band Area Ratio (BAR) of the silicate features of the spectra. The BIC and BAR were calculated for EC 002 laboratory samples, for Ordinary Chondrite meteorites, for HEDs, and for some of the DeMeo et al. (2009) taxonomic end-members showing silicate features. Trends calculated based on mixtures of EC 002 with olivine or mantle material, and calculated on modelled space-weathered spectra are shown.

C

CLASSIFICATION OF GAIA DR3 SPECTRA

C.1 BUILDING THE NIR LIST

To build the NIR list, I searched in the literature for asteroids classified from observations in the VISNIR or NIR wavelength range. I only considered asteroids classified in the Bus or Bus-DeMeo scheme, since Gaia DR3 spectra are being classified in the Bus taxonomic scheme. The fact that some subclasses of the S, C and X-complexes differ between the Bus and the Bus-DeMeo scheme (see Chapter 1) do not matter here, as I decided to group the subclasses of each complex into their main complex. Asteroids classified in the Tholen (1989) or Mahlke et al. (2022) scheme were not considered here, as these schemes differ from the Bus scheme because of their including of albedo data. The papers used to build this VISNIR list are the following: Duffard et al. (2004b), Lazzarin et al. (2004), Lazzarin et al. (2005), Marchi et al. (2005a), Licandro et al. (2008b), Mothé-Diniz et al. (2008b), Clark et al. (2009), DeMeo et al. (2009), de León et al. (2010), de Sanctis et al. (2011), Gietzen et al. (2012), Sanchez et al. (2013), DeMeo et al. (2014), Borisov et al. (2017), Leith et al. (2017), Lucas et al. (2017), Migliorini et al. (2017), De Prá et al. (2018), Devogèle et al. (2018), Migliorini et al. (2018), Binzel et al. (2019), DeMeo et al. (2019), Lucas et al. (2019), Arredondo et al. (2021a), Gartrelle et al. (2021), Hasegawa et al. (2021), and Migliorini et al. (2021).

Firstly, I discarded every asteroid on this list that has been observed several times and shows major differences in classification between sources. For example, asteroid (3199) Nefertiti is found K, A, and Sq by different sources (e.g DeMeo et al., 2009; de León et al., 2010; Thomas and Binzel, 2010; Binzel et al., 2019), so its classification is uncertain. As my goal here was to define a list of asteroids having spectral types that can be considered "true", this asteroid was discarded. Same for asteroid (85989) 1999 JD6, found Cg, K or L by different sources (e.g Lazzarin et al., 2005; de León et al., 2010; Binzel et al., 2019).

Secondly, asteroids classified by different sources as belonging to different subclasses of the same complex were defined as belonging to the complex. For example, asteroid (1920) Sarmiento, both classified as Xe and Xn type by Lucas et al. (2019), was defined as an X-complex asteroid here. Such decisions were repeated to produce the "NIR list", that contains 517 asteroids having a spectrum in the Gaia DR3 filtered dataset. The MPC number of the asteroids belonging to this NIR list, their spectral type and the associated references are given in Table C.1.

Table C.1: Asteroids observed in the NIR or VISNIR wavelength range, used to test my classification algorithm. The MPC number of the asteroids along with their spectroscopic type is given, with the associated reference. When an asteroid was classified differently by different authors, the different classes and the associated reference are displayed in the last column.

Asteroid	Type	Reference or Type (Reference)
3	Sq	DeMeo et al. (2009)
5	S	DeMeo et al. (2009)
6	S	Gietzen et al. (2012)
7	S	DeMeo et al. (2009)
8	Sw	DeMeo et al. (2009)
10	C	DeMeo et al. (2009)
12	D	Devogèle et al. (2018)
13	Ch	DeMeo et al. (2009)
14	S	DeMeo et al. (2009)
15	K	DeMeo et al. (2009)
16	Xk	DeMeo et al. (2009)
17	S	DeMeo et al. (2009)
18	S	Gietzen et al. (2012), DeMeo et al. (2009)
19	Ch	DeMeo et al. (2009)
20	S	DeMeo et al. (2009)
21	Xc	DeMeo et al. (2009)
22	X	DeMeo et al. (2009)
24	C	DeMeo et al. (2009)
25	S	DeMeo et al. (2009)
26	S	DeMeo et al. (2009)
27	S	DeMeo et al. (2009)
28	S	DeMeo et al. (2009)
30	S	DeMeo et al. (2009)
32	Sw	DeMeo et al. (2009)
33	S	DeMeo et al. (2009)
34	Ch	DeMeo et al. (2009)
37	S	DeMeo et al. (2009)
38	Cgh	DeMeo et al. (2009)
39	Sqw	DeMeo et al. (2009)
40	S	DeMeo et al. (2009)
41	Ch	DeMeo et al. (2009)
42	K	Gietzen et al. (2012), DeMeo et al. (2009)

– *continued on next page*

– continued.

Asteroid	Type	Reference or Type (Reference)
43	Sq	Clark et al. (2009), DeMeo et al. (2009)
48	Ch	DeMeo et al. (2009)
49	Ch	DeMeo et al. (2009)
50	Ch	DeMeo et al. (2009)
51	Cgh	DeMeo et al. (2009)
52	C	DeMeo et al. (2009)
54	Cgh	DeMeo et al. (2009)
55	Xk	DeMeo et al. (2009)
56	Xk	DeMeo et al. (2009)
57	S	DeMeo et al. (2009)
58	Ch	DeMeo et al. (2009)
61	S	DeMeo et al. (2009)
63	Sw	Gietzen et al. (2012), DeMeo et al. (2009)
64	Xe	DeMeo et al. (2009)
65	Xk	DeMeo et al. (2009)
66	Ch	DeMeo et al. (2009)
67	S	DeMeo et al. (2009)
69	Xk	DeMeo et al. (2009)
70	Cgh	DeMeo et al. (2009)
73	S	DeMeo et al. (2009)
75	K	Clark et al. (2009)
76	C	DeMeo et al. (2009)
77	Xe	DeMeo et al. (2009)
78	Ch	DeMeo et al. (2009)
82	S	DeMeo et al. (2009)
84	Ch	DeMeo et al. (2009)
85	C	DeMeo et al. (2009)
87	X	DeMeo et al. (2009)
89	K	Clark et al. (2009)
90	C	DeMeo et al. (2009)
92	Xk	DeMeo et al. (2009)
93	C	DeMeo et al. (2009)
96	T	DeMeo et al. (2009)
97	Xc	DeMeo et al. (2009)
99	K	K (Clark et al., 2009), Xk (DeMeo et al., 2009)

– continued on next page

– continued.

Asteroid	Type	Reference or Type (Reference)
101	S	DeMeo et al. (2009)
103	S	DeMeo et al. (2009)
105	Ch	DeMeo et al. (2009)
106	Cgh	DeMeo et al. (2009)
108	Sw	DeMeo et al. (2009)
110	Xk	DeMeo et al. (2009)
111	Ch	DeMeo et al. (2009)
112	X	Arredondo et al. (2021a)
114	K	Xk (Clark et al., 2009) K (DeMeo et al., 2009)
115	S	DeMeo et al. (2009)
119	S	DeMeo et al. (2009)
122	S	Devogèle et al. (2018)
128	C	DeMeo et al. (2009)
130	Ch	DeMeo et al. (2009)
131	K	DeMeo et al. (2009)
132	Xe	DeMeo et al. (2009)
133	S	DeMeo et al. (2009)
142	C	Arredondo et al. (2021a)
147	C	DeMeo et al. (2009)
150	C	DeMeo et al. (2009)
151	Sw	DeMeo et al. (2009)
153	X	DeMeo et al. (2009)
158	S	DeMeo et al. (2009)
160	Xk	DeMeo et al. (2009)
167	Sw	Gietzen et al. (2012)
170	S	DeMeo et al. (2009)
172	L	Devogèle et al. (2018)
173	Xk	Clark et al. (2009)
175	Cg	DeMeo et al. (2009)
179	S	Clark et al. (2009)
180	Sr	Gietzen et al. (2012), DeMeo et al. (2009)
181	Xk	DeMeo et al. (2009)
186	K	Clark et al. (2009)
188	S	DeMeo et al. (2009)
191	Cb	DeMeo et al. (2009)

– continued on next page

– continued.

Asteroid	Type	Reference or Type (Reference)
192	Sw	DeMeo et al. (2009)
199	D	DeMeo et al. (2009)
201	Xk	DeMeo et al. (2009)
203	D	Hasegawa et al. (2021)
205	Ch	DeMeo et al. (2009)
210	Cb	DeMeo et al. (2009)
214	Cgh	DeMeo et al. (2009)
216	Xe	DeMeo et al. (2009)
221	K	Mothé-Diniz et al. (2008b), Clark et al. (2009), (DeMeo et al., 2009)
225	B	De Prá et al. (2018)
226	S	DeMeo et al. (2009)
229	Xc	De Prá et al. (2018)
233	Xk	Clark et al. (2009), DeMeo et al. (2009)
234	L	Gietzen et al. (2012), DeMeo et al. (2009)
236	L	DeMeo et al. (2009)
237	Sr	DeMeo et al. (2009)
243	Sw	DeMeo et al. (2009)
244	Sw	DeMeo et al. (2009)
246	A	Gietzen et al. (2012), DeMeo et al. (2009)
250	Xk	Clark et al. (2009), DeMeo et al. (2009)
258	S	DeMeo et al. (2009)
264	S	DeMeo et al. (2009)
266	Ch	DeMeo et al. (2009)
267	D	DeMeo et al. (2009), Gartrelle et al. (2021)
269	D	Gietzen et al. (2012), DeMeo et al. (2009), Hasegawa et al. (2021)
278	S	DeMeo et al. (2009)
279	D	DeMeo et al. (2009)
288	S	DeMeo et al. (2009)
295	Sw	DeMeo et al. (2009)
308	T	DeMeo et al. (2009)
322	D	DeMeo et al. (2009)
334	Xc	De Prá et al. (2018)
336	D	Gartrelle et al. (2021)
337	Xk	DeMeo et al. (2009)

– continued on next page

– continued.

Asteroid	Type	Reference or Type (Reference)
339	K	Mothé-Diniz et al. (2008b)
345	Ch	DeMeo et al. (2009)
346	S	DeMeo et al. (2009)
349	R	Gietzen et al. (2012), DeMeo et al. (2009), Leith et al. (2017)
352	Sw	DeMeo et al. (2009)
354	A	Gietzen et al. (2012), DeMeo et al. (2009)
359	Xk	DeMeo et al. (2009)
368	D	Gartrelle et al. (2021)
371	S	DeMeo et al. (2009)
378	S	DeMeo et al. (2009)
387	L	DeMeo et al. (2009)
397	L	Clark et al. (2009)
401	Cb	De Prá et al. (2018)
402	L	Clark et al. (2009), DeMeo et al. (2009)
403	S	DeMeo et al. (2009)
417	Xk	Clark et al. (2009)
433	S	Sw (DeMeo et al., 2009) S (de León et al., 2010)
434	Xe	Xe (DeMeo et al., 2009) Xe, K (Lucas et al., 2017)
441	Xc	Clark et al. (2009)
444	C	DeMeo et al. (2009)
446	A	DeMeo et al. (2009)
450	Xk	Mothé-Diniz et al. (2008b)
453	Sw	DeMeo et al. (2009)
456	S	DeMeo et al. (2009)
458	L	Devogèle et al. (2018)
460	L	DeMeo et al. (2009)
472	S	Clark et al. (2009)
485	S	DeMeo et al. (2009)
495	C	Arredondo et al. (2021a)
512	Sqw	DeMeo et al. (2009)
513	K	Mothé-Diniz et al. (2008b), DeMeo et al. (2009)
528	Cb	De Prá et al. (2018)
532	S	DeMeo et al. (2009)
547	Xk	Clark et al. (2009)

– continued on next page

– continued.

Asteroid	Type	Reference or Type (Reference)
557	C	Arredondo et al. (2021a)
559	Xk	Clark et al. (2009)
570	D	DeMeo et al. (2009)
579	K	Mothé-Diniz et al. (2008b), DeMeo et al. (2009)
590	T	Mothé-Diniz et al. (2008b)
596	T	DeMeo et al. (2009)
599	L	Clark et al. (2009), DeMeo et al. (2009)
606	L	DeMeo et al. (2009)
611	L	Devogèle et al. (2018)
625	Sw	DeMeo et al. (2009)
631	S	DeMeo et al. (2009)
633	S	Mothé-Diniz et al. (2008b)
639	S	Mothé-Diniz et al. (2008b)
653	K	Mothé-Diniz et al. (2008b), DeMeo et al. (2009)
661	K	Mothé-Diniz et al. (2008b), Clark et al. (2009), (DeMeo et al., 2009)
669	Ld	Mothé-Diniz et al. (2008b)
670	S	DeMeo et al. (2009)
673	L	DeMeo et al. (2009)
675	Sw	DeMeo et al. (2009)
679	L	Clark et al. (2009), DeMeo et al. (2009)
686	L	Clark et al. (2009)
688	C	DeMeo et al. (2009)
699	S	S (DeMeo et al., 2009) Sq (de León et al., 2010)
706	Cgh	DeMeo et al. (2009)
716	S	DeMeo et al. (2009)
720	Sq	DeMeo et al. (2009)
721	D	Gartrelle et al. (2021)
729	L	DeMeo et al. (2009)
739	Xc	DeMeo et al. (2009)
742	K	Mothé-Diniz et al. (2008b), Clark et al. (2009), (DeMeo et al., 2009)
750	C	Arredondo et al. (2021a)
752	X	Arredondo et al. (2021a)
753	S	Devogèle et al. (2018)
757	Xk	Clark et al. (2009)

– continued on next page

– continued.

Asteroid	Type	Reference or Type (Reference)
766	Ld	Mothé-Diniz et al. (2008b)
776	Cgh	DeMeo et al. (2009)
785	Cb	DeMeo et al. (2009)
789	Xk	DeMeo et al. (2009)
790	X	De Prá et al. (2018)
793	S	DeMeo et al. (2009)
798	T	Mothé-Diniz et al. (2008b)
808	Sr	DeMeo et al. (2009)
809	V	Duffard et al. (2004b)
824	L	DeMeo et al. (2009)
832	S	DeMeo et al. (2009)
847	S	DeMeo et al. (2009)
863	A	DeMeo et al. (2009)
884	D	Gartrelle et al. (2021)
908	D	DeMeo et al. (2009), DeMeo et al. (2014)
909	X	De Prá et al. (2018)
913	Sw	DeMeo et al. (2009)
925	S	DeMeo et al. (2009)
929	S	DeMeo et al. (2009)
940	Cgh	De Prá et al. (2018)
944	D	DeMeo et al. (2009)
956	V	Duffard et al. (2004b)
973	T	Clark et al. (2009)
984	Sa	DeMeo et al. (2009)
985	S	DeMeo et al. (2009)
1012	C	Arredondo et al. (2021a)
1019	Sw	Lucas et al. (2017)
1020	Sr	DeMeo et al. (2009)
1036	S	Sr (Gietzen et al., 2012) S (Palomba et al., 2014) S (de León et al., 2010)
1065	S	DeMeo et al. (2009)
1094	Xk	DeMeo et al. (2009)
1103	X	Xk (Clark et al., 2009) Xc, Xe (Lucas et al., 2017)
1112	T	Mothé-Diniz et al. (2008b)
1126	Sw	DeMeo et al. (2009)

– continued on next page

– continued.

Asteroid	Type	Reference or Type (Reference)
1129	K	Mothé-Diniz et al. (2008b)
1131	S	DeMeo et al. (2009)
1139	Sw	DeMeo et al. (2009)
1143	D	DeMeo et al. (2009)
1144	D	De Prá et al. (2018)
1147	Sw	DeMeo et al. (2009)
1148	K	Mothé-Diniz et al. (2008b), DeMeo et al. (2009)
1167	D	Gartrelle et al. (2021)
1177	X	De Prá et al. (2018)
1183	C	Arredondo et al. (2021a)
1190	C	Arredondo et al. (2021a)
1204	Sw	DeMeo et al. (2009)
1228	Sr	DeMeo et al. (2009)
1256	D	Gartrelle et al. (2021)
1267	C	Arredondo et al. (2021a)
1269	D	De Prá et al. (2018), Gartrelle et al. (2021)
1280	C	De Prá et al. (2018)
1300	Cgh	DeMeo et al. (2009)
1329	Sqw	DeMeo et al. (2009)
1332	L	DeMeo et al. (2009)
1350	S	DeMeo et al. (2009)
1364	Ld	Mothé-Diniz et al. (2008b)
1372	L	Devogèle et al. (2018)
1374	Sq	DeMeo et al. (2009)
1388	L	Mothé-Diniz et al. (2008b)
1413	D	Mothé-Diniz et al. (2008b)
1416	D	Mothé-Diniz et al. (2008b)
1433	S	DeMeo et al. (2009)
1439	X	De Prá et al. (2018)
1459	V	Vw (DeMeo et al., 2009) V (Leith et al., 2017)
1471	D	DeMeo et al. (2009)
1493	C	Arredondo et al. (2021a)
1494	Sqw	DeMeo et al. (2009)
1509	Sw	Lucas et al. (2017)
1542	D	DeMeo et al. (2009), Gartrelle et al. (2021)

– continued on next page

– continued.

Asteroid	Type	Reference or Type (Reference)
1545	L	Clark et al. (2009)
1565	S	S (DeMeo et al., 2009) Sq (de León et al., 2010)
1583	D	Gartrelle et al. (2021)
1600	Sw	Lucas et al. (2019)
1620	S	Sqw (Gietzen et al., 2012) S (DeMeo et al., 2009)
1627	S	de León et al. (2010)
1640	S	DeMeo et al. (2009)
1642	S	DeMeo et al. (2009)
1650	C	Arredondo et al. (2021a)
1659	S	DeMeo et al. (2009)
1662	Sr	DeMeo et al. (2009)
1667	Sw	DeMeo et al. (2009)
1685	Sq	DeMeo et al. (2009)
1702	D	Gartrelle et al. (2021)
1709	S	DeMeo et al. (2019)
1727	Sw	Lucas et al. (2017)
1740	C	Arredondo et al. (2021a)
1746	D	Gartrelle et al. (2021)
1750	Srw	Lucas et al. (2017)
1751	S	DeMeo et al. (2009)
1807	Sqw	DeMeo et al. (2009)
1839	S	DeMeo et al. (2009)
1848	S	DeMeo et al. (2009)
1858	S	DeMeo et al. (2009)
1862	Q	DeMeo et al. (2009), de León et al. (2010)
1864	S	Sq (DeMeo et al., 2009) Sr (de León et al., 2010)
1866	S	Sw (DeMeo et al., 2009) S (de León et al., 2010)
1902	X	De Prá et al. (2018)
1903	K	Mothé-Diniz et al. (2008b), Clark et al. (2009), (DeMeo et al., 2009)
1904	V	DeMeo et al. (2009)
1920	X	Xe, Xn (Lucas et al., 2019)
1923	X	Arredondo et al. (2021a)
1929	V	de Sanctis et al. (2011), DeMeo et al. (2009)
1980	S	Srw (Gietzen et al., 2012) Sw, (DeMeo et al., 2009) Sl (de León et al., 2010)

– continued on next page

– continued.

Asteroid	Type	Reference or Type (Reference)
2007	C	Arredondo et al. (2021a)
2011	V	de Sanctis et al. (2011)
2035	Xe	DeMeo et al. (2009)
2036	S	DeMeo et al. (2019)
2042	Sr	DeMeo et al. (2009)
2045	V	Duffard et al. (2004b) V DeMeo et al. (2009)
2047	Q	Q, Sq (Lucas et al., 2017)
2064	S	Sqw (DeMeo et al., 2009) S (de León et al., 2010)
2066	C	Arredondo et al. (2021a)
2074	Sw	DeMeo et al. (2009), Lucas et al. (2017)
2081	C	Arredondo et al. (2021a)
2083	X	Xe, Xc (Lucas et al., 2019)
2085	L	DeMeo et al. (2009)
2107	Sw	DeMeo et al. (2009)
2131	Sw	Lucas et al. (2017)
2139	C	Arredondo et al. (2021a)
2150	Sw	Lucas et al. (2019)
2157	S	DeMeo et al. (2009)
2168	V	Migliorini et al. (2021)
2207	D	Gartrelle et al. (2021)
2208	D	Gartrelle et al. (2021)
2246	D	DeMeo et al. (2009), Gartrelle et al. (2021)
2266	D	Gartrelle et al. (2021)
2276	C	Arredondo et al. (2021a)
2311	D	Gartrelle et al. (2021)
2315	D	Mothé-Diniz et al. (2008b)
2335	S	S (DeMeo et al., 2009) Sa (de León et al., 2010)
2353	S	DeMeo et al. (2009)
2354	L	DeMeo et al. (2009), Devogèle et al. (2018)
2357	D	Gartrelle et al. (2021)
2358	Xk	Mothé-Diniz et al. (2008b)
2378	Cgh	DeMeo et al. (2009)
2386	S	DeMeo et al. (2009)
2396	S	DeMeo et al. (2009)
2401	S	DeMeo et al. (2009)

– continued on next page

– continued.

Asteroid	Type	Reference or Type (Reference)
2442	V	DeMeo et al. (2009)
2443	T	Mothé-Diniz et al. (2008b)
2448	L	DeMeo et al. (2009)
2452	V	Migliorini et al. (2021)
2468	V	Duffard et al. (2004b)
2501	A	DeMeo et al. (2009)
2521	S	DeMeo et al. (2009)
2566	V	DeMeo et al. (2009)
2579	V	DeMeo et al. (2009)
2606	Xk	Clark et al. (2009)
2674	D	Gartrelle et al. (2021)
2715	Sw	DeMeo et al. (2009)
2732	L	DeMeo et al. (2009)
2763	V	Duffard et al. (2004b)
2851	V	Duffard et al. (2004b) V DeMeo et al. (2009)
2873	Sq	DeMeo et al. (2009)
2875	S	DeMeo et al. (2009)
2893	D	Gartrelle et al. (2021)
2911	Sw	DeMeo et al. (2009)
2957	K	DeMeo et al. (2009)
2965	Sv	DeMeo et al. (2009)
2977	S	DeMeo et al. (2009)
3043	Sw	Lucas et al. (2019)
3064	C	Arredondo et al. (2021a)
3130	C	Arredondo et al. (2021a)
3200	B	DeMeo et al. (2009)
3202	D	De Prá et al. (2018)
3225	S	Lucas et al. (2017)
3228	C	Arredondo et al. (2021a)
3247	C	Arredondo et al. (2021a)
3248	D	DeMeo et al. (2009), Gartrelle et al. (2021)
3283	D	Gartrelle et al. (2021), DeMeo et al. (2014)
3309	Sw	Lucas et al. (2017)
3317	D	DeMeo et al. (2009)
3318	D	Mothé-Diniz et al. (2008b)

– continued on next page

– continued.

Asteroid	Type	Reference or Type (Reference)
3331	V	Migliorini et al. (2021)
3363	Sr	DeMeo et al. (2009)
3385	S	DeMeo et al. (2019)
3395	S	DeMeo et al. (2009)
3430	S	DeMeo et al. (2009)
3469	D	Mothé-Diniz et al. (2008b)
3498	V	Duffard et al. (2004b)
3511	Srw	DeMeo et al. (2009)
3566	C	Arredondo et al. (2021a)
3573	S	DeMeo et al. (2019)
3577	D	De Prá et al. (2018)
3628	O	DeMeo et al. (2009)
3635	S	Srw (DeMeo et al., 2009) S (de León et al., 2010) Srw (Lucas et al., 2017)
3701	S	DeMeo et al. (2009)
3734	L	DeMeo et al. (2009)
3782	V	Duffard et al. (2004b)
3788	S	DeMeo et al. (2009)
3843	X	De Prá et al. (2018)
3844	L	DeMeo et al. (2009)
3858	Srw	DeMeo et al. (2009)
3890	V	Duffard et al. (2004b)
3903	S	DeMeo et al. (2009)
3910	S	DeMeo et al. (2009)
3920	Sqw	DeMeo et al. (2009)
3944	V	de Sanctis et al. (2011)
3949	Sq	DeMeo et al. (2009)
3999	C	Arredondo et al. (2021a)
4038	Vw	DeMeo et al. (2009)
4125	A	Lucas et al. (2019)
4147	V	de Sanctis et al. (2011)
4173	C	Arredondo et al. (2021a)
4219	C	Arredondo et al. (2021a)
4352	S	DeMeo et al. (2009)
4407	Sqw	DeMeo et al. (2009)

– continued on next page

– continued.

Asteroid	Type	Reference or Type (Reference)
4434	V	Duffard et al. (2004b)
4451	Svw	DeMeo et al. (2009)
4490	A	Lucas et al. (2019)
4531	X	Xe, Xc (Lucas et al., 2019)
4558	Sr	DeMeo et al. (2009)
4570	Sw	DeMeo et al. (2009)
4587	Sr	de León et al. (2010), Lazzarin et al. (2005)
4674	Sw	Lucas et al. (2017)
4713	Sw	DeMeo et al. (2009), Lucas et al. (2019)
4736	X	Xe, Xc (Lucas et al., 2017)
4737	L	DeMeo et al. (2009)
4744	D	Gartrelle et al. (2021)
4764	X	Xk, Xe (Lucas et al., 2019)
4796	V	Duffard et al. (2004b)
4815	V	Duffard et al. (2004b)
4917	L	Devogèle et al. (2018)
4954	Sr	Gietzen et al. (2012)
4995	S	DeMeo et al. (2009)
5013	Sw	DeMeo et al. (2009)
5111	V	DeMeo et al. (2009)
5175	Q	Q, Sq (Lucas et al., 2017)
5230	S	DeMeo et al. (2009)
5261	Sa	DeMeo et al. (2009)
5379	Sr	DeMeo et al. (2009)
5401	Sw	DeMeo et al. (2009)
5407	S	DeMeo et al. (2009), Sanchez et al. (2013)
5477	S	Lucas et al. (2019)
5577	Q	Q, Sq (Lucas et al., 2017)
5587	Sr	DeMeo et al. (2009)
5685	S	DeMeo et al. (2009)
5758	V	Migliorini et al. (2021)
5817	Sr	DeMeo et al. (2009)
5840	L	DeMeo et al. (2009)
5905	Q	Q, Sq (Lucas et al., 2017)
6039	D	De Prá et al. (2018)

– continued on next page

– continued.

Asteroid	Type	Reference or Type (Reference)
6067	S	DeMeo et al. (2019)
6159	V	Duffard et al. (2004b)
6271	D	Lucas et al. (2019)
6386	S	DeMeo et al. (2009), de León et al. (2010)
6406	V	de Sanctis et al. (2011)
6411	B	DeMeo et al. (2009)
6447	X	Xe, Xc (Lucas et al., 2017)
6471	C	Arredondo et al. (2021a)
6485	Q	Q, Sq (Lucas et al., 2019)
6550	V	Migliorini et al. (2017)
6661	C	Arredondo et al. (2021a)
6769	C	Arredondo et al. (2021a)
7057	S	DeMeo et al. (2019)
7086	Q	Q, Sq (Lucas et al., 2017)
7148	V	de Sanctis et al. (2011)
7341	Q	Q (DeMeo et al., 2009) Sq (de León et al., 2010)
7394	D	De Prá et al. (2018)
7763	L	DeMeo et al. (2009)
7783	X	Xn, Xe (Lucas et al., 2019)
8212	S	Arredondo et al. (2021a)
8334	S	DeMeo et al. (2009)
8444	S	DeMeo et al. (2009)
8693	V	de Sanctis et al. (2011)
8838	A	DeMeo et al. (2019)
8927	C	Arredondo et al. (2021a)
9069	Q	Q, Sq (Lucas et al., 2017)
9476	Cg	Arredondo et al. (2021a)
9554	Q	Q, Sq (Lucas et al., 2019)
9873	S	Sq, S (Lucas et al., 2017) Sw (Lucas et al., 2019)
10037	V	Duffard et al. (2004b)
10320	V	Duffard et al. (2004b)
10349	V	Duffard et al. (2004b)
10544	V	Migliorini et al. (2017)
11952	S	DeMeo et al. (2019)
12421	Cg	Arredondo et al. (2021a)

– continued on next page

– continued.

Asteroid	Type	Reference or Type (Reference)
13245	C	Cb, C (Lucas et al., 2019)
13724	S	DeMeo et al. (2019)
15898	Q	QS (Migliorini et al., 2018)
16520	A	DeMeo et al. (2019)
17239	S	Migliorini et al. (2021)
17408	S	Sr, S (Lucas et al., 2017)
17889	A	DeMeo et al. (2019)
18853	A	DeMeo et al. (2019)
19164	S	S, Sq (Lucas et al., 2017)
19165	V	Migliorini et al. (2017)
19570	S	DeMeo et al. (2019)
20188	V	Migliorini et al. (2021)
20786	Sq	DeMeo et al. (2009)
21088	Sl	de León et al. (2010)
21238	V	de Sanctis et al. (2011) V Leith et al. (2017) V Migliorini et al. (2018)
21809	A	DeMeo et al. (2019)
24726	X	Arredondo et al. (2021a)
26145	V	Migliorini et al. (2017)
26471	S	Sq, S (Lucas et al., 2017)
26807	X	Arredondo et al. (2021a)
29731	S	DeMeo et al. (2019)
30856	S	S, Sr (Lucas et al., 2019)
31793	Q	Q, Sq (Lucas et al., 2019)
33745	Q	S/Q (DeMeo et al., 2019)
35102	S	DeMeo et al. (2019)
35925	A	DeMeo et al. (2019)
36118	V	Migliorini et al. (2021)
36256	A	DeMeo et al. (2019)
44028	S	DeMeo et al. (2019)
47035	Sr	Sanchez et al. (2013)
53431	S	S, Sr (Lucas et al., 2019)
53433	S	Sr, S (Lucas et al., 2019)
53435	S	Srw (DeMeo et al., 2009) S (de León et al., 2010)
54789	X	(Lazzarin et al., 2005)

– continued on next page

– continued.

Asteroid	Type	Reference or Type (Reference)
55854	C	Cgh, Ch (Lucas et al., 2017)
61985	V	(Migliorini et al., 2021)

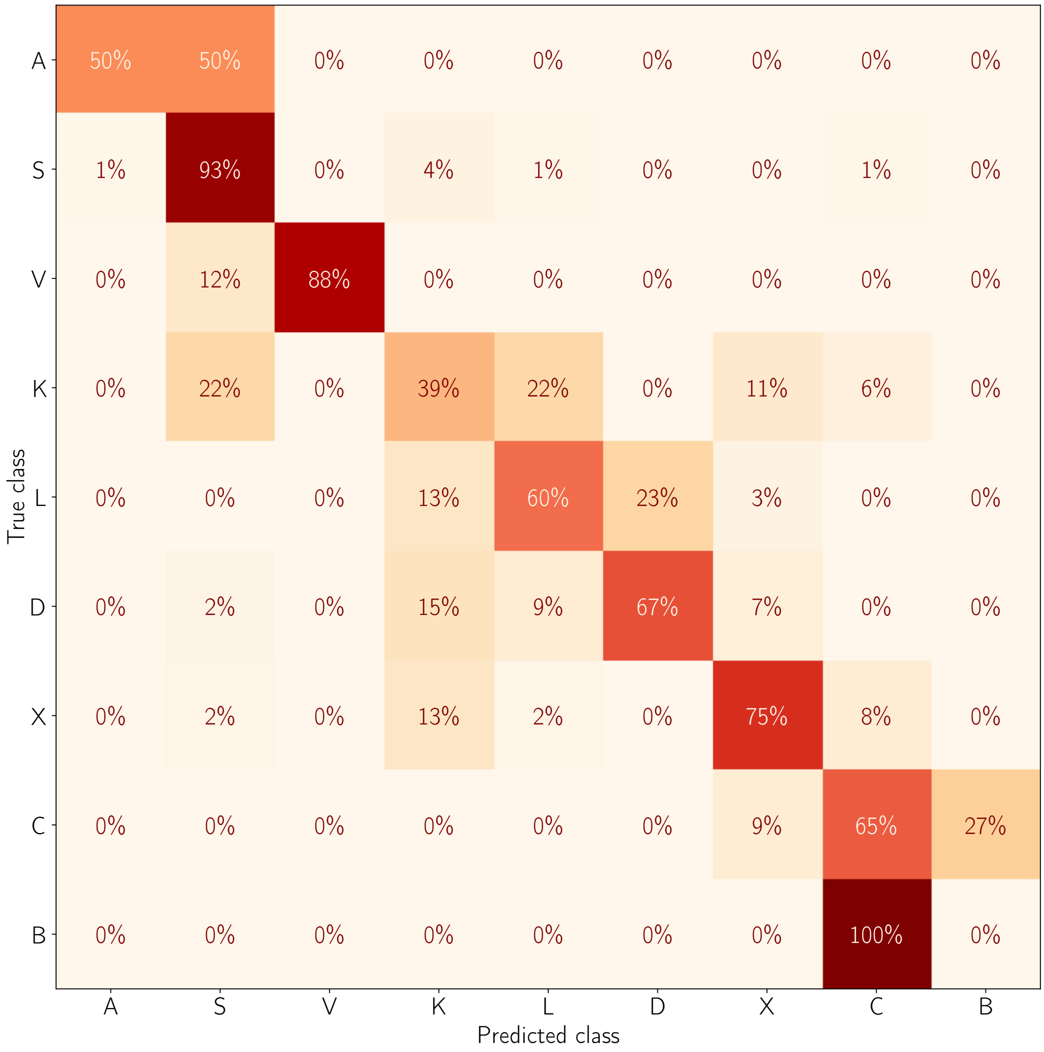

	A	S	V	K	L	D	X	C	B
A	50%	50%	0%	0%	0%	0%	0%	0%	0%
S	1%	93%	0%	4%	1%	0%	0%	1%	0%
V	0%	12%	88%	0%	0%	0%	0%	0%	0%
K	0%	22%	0%	39%	22%	0%	11%	6%	0%
L	0%	0%	0%	13%	60%	23%	3%	0%	0%
D	0%	2%	0%	15%	9%	67%	7%	0%	0%
X	0%	2%	0%	13%	2%	0%	75%	8%	0%
C	0%	0%	0%	0%	0%	0%	9%	65%	27%
B	0%	0%	0%	0%	0%	0%	0%	100%	0%

Figure B.9: Confusion matrix corresponding to the classification of Gaia DR3 spectra of asteroids classified in the literature from VISNIR and NIR spectroscopy, using Gaia templates. The sub-classes are grouped as complexes, and only the templates of the A, Sa, Sq, Sk, S, V, K, L, D, Xk, X, C, Cg, Ch, Cb, and B classes are considered.

C.1.1 B-types

The spectra of the three B-type asteroids considered in the NIR list are displayed in Fig.B.9, along with the spectrum of the Gaia B-type template. (225) Henrietta is classified Cg here, probably because of the important RP reddening affecting its spectrum. (3200) Phaeton is classified Cb due to its noisy spectrum, and (6411) Tamaga is classified Ch probably because of the slight misalignment of its BP and RP spectrum. This misalignment introduces a small fake band around 650 nm (see Chapter 2), making this B-type resemble more a Ch-type. Because of potential issues in the DR3 dataset, distinguishing featureless spectra with the curve-matching algorithm appears tricky. Therefore, the B-class was merged to the C-complex. This decision is supported by the fact that these types correspond to primitive material, and a gradient of composition exists between them (Tinaut-Ruano et al., 2024).

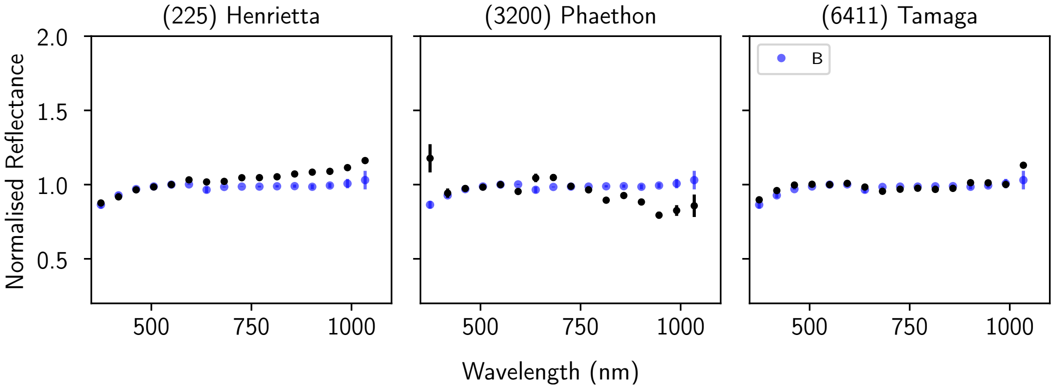

Figure B.9: Gaia DR3 spectra of the three B-type asteroids contained in the NIR list (black dots). The Gaia B-type template is displayed as blue dots, for reference.

C.1.2 K-types

The designation of the 18 K-types of the NIR list classified here are displayed in Table.C.2, along with their classification from visible or VISNIR spectra by different authors. These references were retrieved using the python tool *rocks*. By studying this table, the classification of asteroids (15) Eunomia, (42) Isis, (75) Euridyke, (89) Julia, (131) Vala and (1148) Raharu as non-K from their DR3 spectrum is coherent with other classifications based on visible-light spectra. The classification of asteroid (186) Celuta as S-type is in agreement with its classification by Mahlke et al. (2022), and the classification of (339) Dorothea as X is not surprising, given the diversity in classification of this asteroid depending on the study (this asteroid should actually have been excluded from the NIR list). The classification as L-type of (1148) Rarahu, (1903) Adzhimushkaj and (2957) Tatsuo is expected as well, because of the aforementioned spectral degeneracy of the L-class. (221) Eos is classified as X here (in fact, as Xk), which is not surprising given that Xk-types are leaning towards K-types. In the end, the classification as non-K of K-type asteroids considered here can be explained by the spectral variability of these objects, and by the spectral continuum between the K, S, L and X-classes (Granahan et al., 1993; Vokrouhlický et al., 2006; DeMeo et al., 2009; Mahlke et al., 2022). Similarly, this continuum explain why S, L, and X-types get classified K here. Improving the classification of K-type objects is out of the scope of this work, but this study allowed to determine that the misclassification of K-type objects appears not to come from the DR3 data.

Table C.2: K-type asteroids classified with the Gaia classification algorithm. Their assigned class is given in the Type column, and their literature class in the Class column, along with the wavelength range and associated reference (Ref. column). The taxonomic schemes used in the literature are the Bus (Bus and Binzel, 2002a), Bus-DeMeo (DeMeo et al., 2009), or Mahlke (Mahlke et al., 2022) schemes.

Asteroid	Type	Class	Wavelength range	Ref
(15) Eunomia	S	S	VIS	Bus and Binzel, 2002a
		S	VIS	Mothé-Diniz et al., 2005a
		K	VISNIR	DeMeo et al., 2009
		K	VISNIR	Mahlke et al., 2022
(42) Isis	S	L	VIS	Bus and Binzel, 2002a
		K	VISNIR	DeMeo et al., 2009
		K	NIR	Gietzen et al., 2012
		Sq	VISNIR	Bourdelle de Micas et al., 2022
		M	VISNIR	Mahlke et al., 2022
(75) Eurydike	X	Xk	VIS	Bus and Binzel, 2002a
		K	VISNIR	Clark et al., 2009
		M	VISNIR	Mahlke et al., 2022
(89) Julia	L	K	VIS	Bus and Binzel, 2002a
		Ld/S	VIS	Lazzaro et al., 2004
		S	VIS	Birlan et al., 2004
		K	VISNIR	Clark et al., 2009
		S	VISNIR	Mahlke et al., 2022
(114) Kassandra	K	Xk	VIS	Bus and Binzel, 2002a
		K	VISNIR	DeMeo et al., 2009
		Xk	VISNIR	Clark et al., 2009
		M	VISNIR	Mahlke et al., 2022
(131) Vala	C	Xc	VIS	Bus and Binzel, 2002a
		K	VISNIR	DeMeo et al., 2009
		K	VISNIR	Bourdelle de Micas et al., 2022
		S	VISNIR	Mahlke et al., 2022
(186) Celuta	S	K	VIS	Bus and Binzel, 2002a
		K	VISNIR	Clark et al., 2009
		K	VISNIR	Bourdelle de Micas et al., 2022
		S	VISNIR	Mahlke et al., 2022
(221) Eos	K	K	VIS	Bus and Binzel, 2002a
		K	VIS	Mothé-Diniz et al., 2005a
		K	VISNIR	Mothé-Diniz et al., 2008b
		K	VISNIR	Clark et al., 2009
		K	VISNIR	DeMeo et al., 2009

Table C.2 – continued.

Asteroid	Type	Class	Wavelength range	Ref
		K	VISNIR	Mahlke et al., 2022
(339) Dorothea	X	K	VIS	Bus and Binzel, 2002a
		T/K	VIS	Lazzaro et al., 2004
		T	VISNIR	Mothé-Diniz et al., 2005a
		K	VISNIR	Mothé-Diniz et al., 2008b
		B	VISNIR	Mahlke et al., 2022
(513) Centesima	K	K	VIS	Bus and Binzel, 2002a
		K	VIS	Mothé-Diniz et al., 2005a
		K	VISNIR	Mothé-Diniz et al., 2008b
		K	VISNIR	DeMeo et al., 2009
		S	VISNIR	Mahlke et al., 2022
(579) Sidonia	K	K	VIS	Bus and Binzel, 2002a
		D/K	VIS	Lazzaro et al., 2004
		D	VIS	Mothé-Diniz et al., 2005a
		K	VISNIR	Mothé-Diniz et al., 2008b
		K	VISNIR	DeMeo et al., 2009
		K	VISNIR	Mahlke et al., 2022
(653) Berenike	K	K	VIS	Bus and Binzel, 2002a
		K	VIS	Mothé-Diniz et al., 2005a
		K	VISNIR	Mothé-Diniz et al., 2008b
		K	VISNIR	DeMeo et al., 2009
		K	VISNIR	Mahlke et al., 2022
(661) Cloelia	K	K	VIS	Bus and Binzel, 2002a
		K	VIS	Mothé-Diniz et al., 2005a
		K	VISNIR	Mothé-Diniz et al., 2008b
		K	VISNIR	Clark et al., 2009
		K	VISNIR	DeMeo et al., 2009
		K	VISNIR	Mahlke et al., 2022
(742) Edisona	K	K	VIS	Bus and Binzel, 2002a
		K	VIS	Mothé-Diniz et al., 2005a
		K	VISNIR	Mothé-Diniz et al., 2008b
		K	VISNIR	Clark et al., 2009
		K	VISNIR	DeMeo et al., 2009
		K	VISNIR	Mahlke et al., 2022
(1129) Neujmina	S	K	VIS	Mothé-Diniz et al., 2005a
		K	VISNIR	Mothé-Diniz et al., 2008b

Table C.2 – continued.

Asteroid	Type	Class	Wavelength range	Ref
(1148) Rarahu	L	K	VIS	Bus and Binzel, 2002a
		Ld	VIS	Mothé-Diniz et al., 2005a
		K	VISNIR	Mothé-Diniz et al., 2008b
		K	VISNIR	DeMeo et al., 2009
		K	VISNIR	Mahlke et al., 2022
(1903) Adzhimushkaj	L	K	VIS	Bus and Binzel, 2002a
		K	VIS	Mothé-Diniz et al., 2005a
		K	VISNIR	Mothé-Diniz et al., 2008b
		K	VISNIR	Clark et al., 2009
		K	VISNIR	DeMeo et al., 2009
		K	VISNIR	Mahlke et al., 2022
(2957) Tatsuo	L	K	VIS	Bus and Binzel, 2002a
		K	VIS	Mothé-Diniz et al., 2005a
		K	VISNIR	DeMeo et al., 2009
		K	VISNIR	Mahlke et al., 2022

C.2 VALIDATION AND DISCUSSION

In the following, I discuss the impact of the choice of templates on the classification of Gaia DR3 asteroids spectra. Then, I discuss the limit in SNR needed to classify Gaia DR3 asteroid spectra reliably. Finally, I use PCA to visually analyse the results of the classification an to compare them to the literature, and I comment on the classification of low SNR DR3 spectra.

C.2.1 Templates

First, one could wonder why considering subclasses in the templates, only to group asteroids classified as these subclasses into complexes afterwards. To assess whether or not considering subclasses improves the classification, I classified the 517 asteroids from the NIR list considering only the templates of the A, S, V, K, L, D, X, C, Ch, and B-classes. The results of this classification is displayed in Fig.B.9.

We can notice that this definition of templates leads to a higher proportion of true positives in the A-class. However, 10% of S-types are found A-types here, which corresponds to 22 objects. Among these, only one asteroid is found Sa in the literature. Therefore, not defining templates of the sub-classes of the S-complex leads to a greater contamination of the A-class. For the scope of this thesis, I favoured the definition of the A-class that lead to the least contamination, so I decided to keep the Sa, Sq and Sk templates and to merge these classes into the S-complex afterwards.

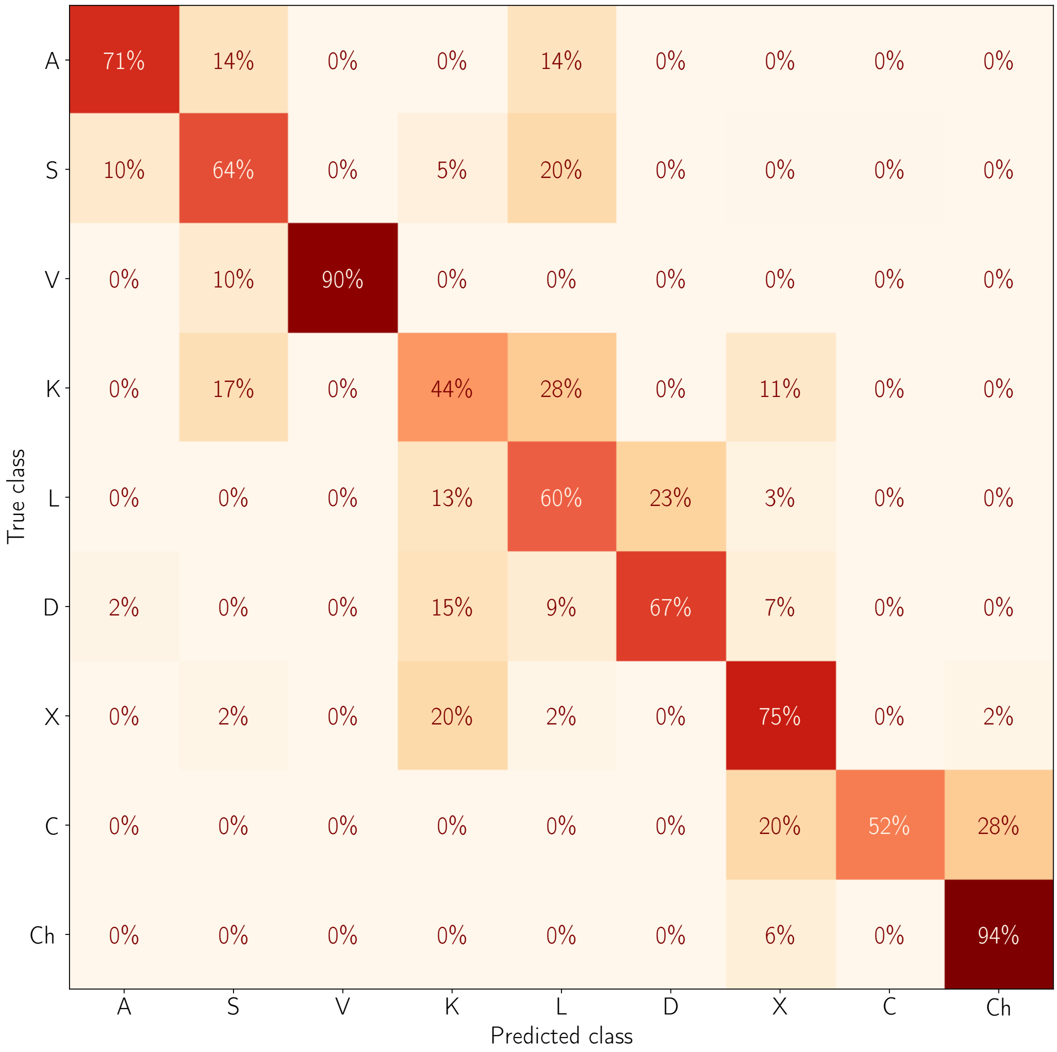

Figure B.9: Confusion matrix corresponding to the classification of Gaia DR3 spectra of asteroids classified in the literature from VISNIR and NIR spectroscopy, using Gaia templates of the A, S, V, K, L, D, X, C, Ch, and B-classes only. The sub-classes are not considered in the classification, and the B-class is merged into the C-complex.

Moreover, the classification without defining templates for the subclasses leads some A and S-type asteroids to be found L, creating a larger amount of false positives in the L-class. The C-class also shows more false negatives in this case. Overall, defining templates of some sub-classes before grouping them into complexes gives better results than the classification performed without defining subclasses. As seen earlier however, not all subclass was found to improve the classification, and I deleted some of them using a trial-and-error approach.

On the first hand, the definition of template spectra is highly dependent on the asteroids chosen to define them. Indeed, each Gaia template spectra was calculated by averaging the spectra of three objects, at most. Changing these objects would change the templates, which would change the results of the classification, and thus would impact the choices made about which subclass to keep and which to delete to improve the overall classification of Gaia DR3 spectra. It is possible that another choice of asteroid spectra would produce templates that would improve the classification notably, since the template spectra are defined on such little number of object. However, I did not perform tests in that direction.

On the other hand, defining template spectra on a larger number of objects could produce templates more representative of the spectral variation within a class. Here, my goal was to test the limits of the classification of DR3 spectra, and the simple definition of the templates was enough to show that Gaia DR3 spectra can be classified in a Bus-like taxonomic scheme. However, the impact of a more complex definition of the templates should be tested.

Finally, classifying Gaia DR3 spectra in another taxonomic scheme, such as the Tholen, 1989 or Mahlke et al., 2022 schemes, could also allow to resolve some classes that are grouped, by considering the asteroid's geometric albedo. This parameter could help distinguishing between asteroids with featureless spectra, mostly. As these spectral types are not of direct interest here, and as the defined templates allow to produce a A-class not too contaminated by false positives, and to distinguish roughly between the other classes, I continued my studies with the previously defined Gaia templates.

C.2.2 SNR limit

To produce the "filtered Gaia DR3 dataset", I considered only DR3 spectra having an average SNR⩾30. In the following, I tested the performances of the classification algorithm on a wider range of SNR.

To determine the SNR limit at which asteroids start getting misclassified, I considered as well-classified the asteroids assigned to the same class in the literature and with the Gaia classification. Therefore, before performing this SNR test, I excluded asteroids classified as R, O, Q, Cgh, T, and Ld from the NIR list. Indeed, the templates for these classes are not taken into account for the Gaia classification, so the asteroids assigned to these classes in the literature are inevitably classified differently with the Gaia classification. Since my goal here was to study the impact of the SNR on the classification, I discarded these spectral types to remove a bias.

I classified selected asteroids from the NIR list with SNRs ranging from 10 to 100, using a step of 10. Gaia DR3 spectra have $SNR > 13$ (Gaia Collaboration et al., 2023), so asteroids with 10⩽SNR⩽20 have in fact 13<SNR⩽20. I obtained 70 asteroids with SNR⩽30, and 184 with 30⩽SNR⩽100.

The proportion of well and badly classified spectra was calculated for each SNR range, and the results are shown in Fig.B.9. We can notice that the proportion of well-classified asteroids increases with the SNR, as expected, reaching a plateau around SNR⩾50, where about 80% of asteroids get well-classified. Actually, 79.9% of asteroids (147 out of 184) with a SNR⩾30 are well-classified. For 13<SNR⩽20, 18 asteroids are well-classified and 20 are not. For 20⩽SNR⩽30, 21 asteroids are well classified and 11 are not.

Therefore, taking a SNR limit above 30 allows the classification to be about 80% correct. The 20% of badly classified asteroids having a SNR⩾30 does not seem to come from the quality of the spectrum's signal, and may come from differences between the DR3 and literature spectra. Such difference does not mean that the classification of DR3 spectra is erroneous, as discussed in Appendix C.1.2 with the K-type classification for example. In addition, the classification considered here as "true" comes from ground-based VISNIR or NIR observations. Classes assigned from spectra cov-

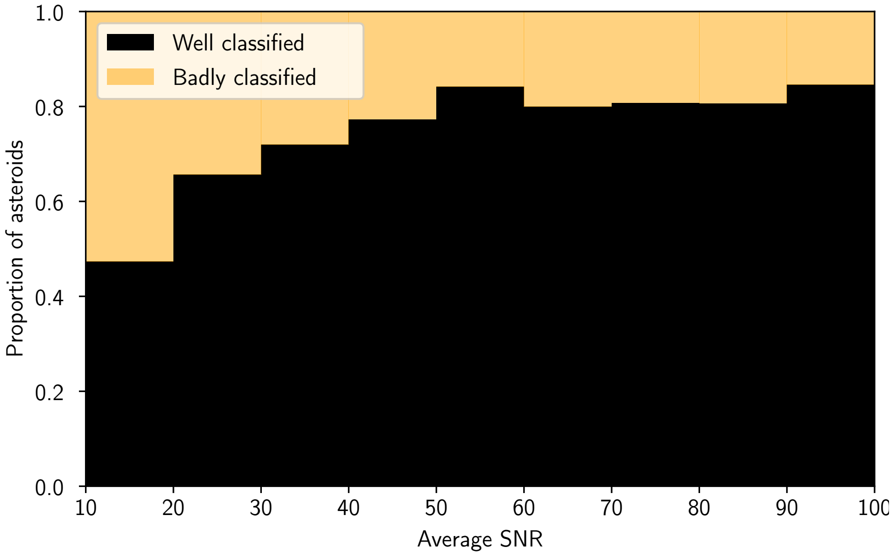

Figure B.9: Proportion of well and badly classified asteroids with my classification algorithm for ranges of SNR going from 10 to a hundred by steps of 10.

ering this wider wavelength range are more reliable, which motivated the definition of the NIR list to test the Gaia classification, but it is logical not to obtain the same classification results as the literature using visible-light spectra.

C.2.3 Principal Component Analysis and curve matching

The PCA is used here to compare the results of the Gaia classification with the literature, as the classifications developed by Bus and Binzel (2002a) and DeMeo et al. (2009) are based on PCA.

First, I applied the PCA to the filtered Gaia DR3 dataset, following the procedure described in Bus and Binzel (2002a). Before applying the PCA, Gaia DR3 spectra were resampled between 460 and 960 nm, in 10 nm increments. The resampled spectra were then normalised at 550 nm, and their global spectral slope was calculated using a linear regression, considering the range from 462 to 946 nm. The slope line was translated so it passes through 1 at 550 nm, and every spectrum was divided by its own slope. The PCA was then applied to the "slope-less" 18 739 spectra of the filtered DR3 dataset, using the *PCA* function from *scikit learn*. A spectral slope and a PC2′ value were obtained for each considered asteroid. PC2′ is the first principal component after removal of the slope, and it corresponds to the depth of a potential band around 1000 nm (Bus and Binzel, 2002a),

C.2.3.1 *Comparison with the literature*

The result of the PCA on the filtered DR3 dataset is shown in Fig.B.9. On panel (A) is highlighted the spectral type from the literature of the 517 asteroids of the NIR list, and on panel (B) is indicated the first best class of these same objects obtained with the Gaia classification.

First, the general shape of the PC2′ vs global spectral slope plot strongly resembles the one obtained by Bus and Binzel (2002a) using SMASS data. The C and X-types

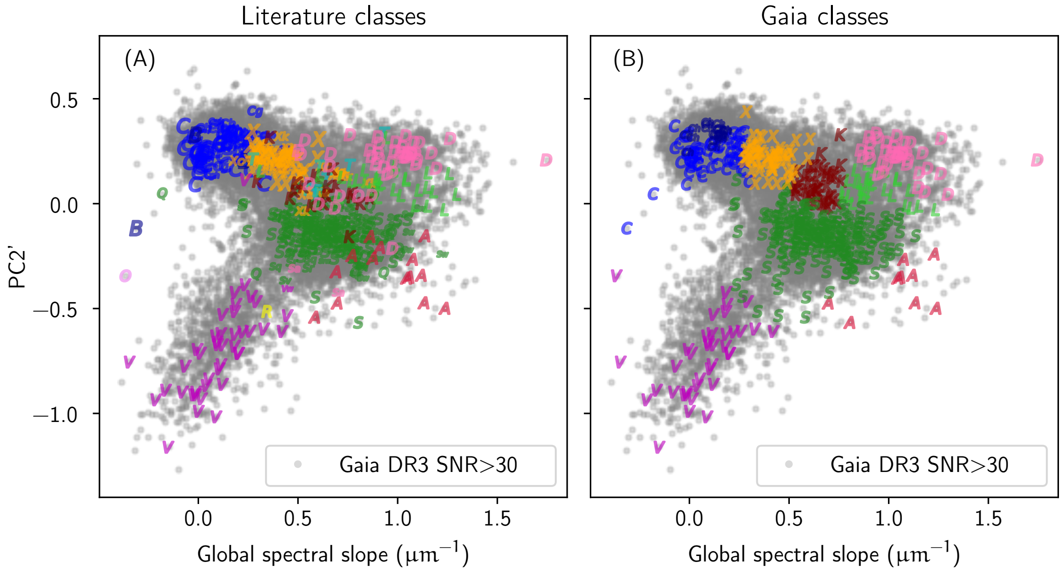

Figure B.9: Plot of the principal component PC2′ with respect to the global spectral slope, calculated for the 18 739 filtered Gaia DR3 asteroids. The 517 asteroids highlighted are the objects classified from NIR observations. Each coloured letter represents the assigned spectral type from the literature in panel (A), and the first best spectral type assigned with the Gaia classification in panel (B).

groupings are recognisable, as well as the S, V, and D-types groupings. On panel (A), we can note that T-type asteroids from the literature are quite scattered over the regions dominated by X, K, L and D-types. This explains why T-type asteroids were not classified as such with the Gaia classification, and it confirms the decision of not taking this class into account in the definition of Gaia templates. Gaia DR3 spectra are not suited for the identification of T-types.

By comparing the results of the classification (panel B) to the literature (panel A), we can see that many literature D-types do not get identified as such with the Gaia classification. Given their location in the PCA plot, this phenomenon must be due to their DR3 spectrum, rather than to the definition of the K and D-type templates.

The limit between the S and the V-types groupings from the literature (panel A) is located at slightly higher values of PC2′ and global spectral slope than the limit obtained with the Gaia classification (panel B). This gives further information about the V-types that get classified as S with the Gaia classification. Data visualisation on the PCA plot could therefore be of use to study a V-type asteroid family, for example, to help distinguishing V-types classified as S from interloper S-types, using their location in the PCA space.

As expected, asteroids having a spectrum at the frontier between several classes (such as the X, K, L, D and S class) are difficult to classify from their visible spectrum. Therefore, visualising where asteroids plot in the PCA space can be interesting to study an asteroid family, for example, rather than using classification results alone. Indeed, a family such as Eos contains K, D, T and Xk-type members mostly, but that can show spectra on the verge of S-types (Vokrouhlický et al., 2006). In Fig.B.9 is shown the position of Eos family members (according to Nesvorny et al. (2015)) in the principal component space, along with their spectral type assigned with the Gaia classification. We can see that family members are grouped in this space, even if the members were

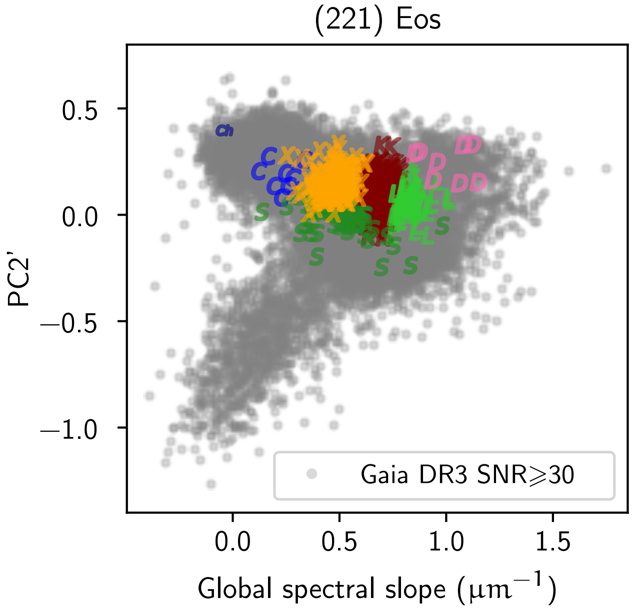

Figure B.9: Plot of the principal component PC2′ with respect to the global spectral slope, calculated for the 18 739 filtered Gaia DR3 asteroids. The classes and positions of Eos family members according to Nesvorny et al. (2015), that have a spectrum in the filtered Gaia DR3 dataset, are highlighted. Each coloured letter represents the spectral type assigned to the family members from the Gaia classification.

assigned to different classes by the curve matching algorithm. Therefore, visualising the position of family members on the principal component space gives information on the gradient of composition in this family, that is complementary to the classification obtained with the curve matching method.

Finally, panel (B) of Fig.B.9 shows again that the Gaia classification is restrictive on the identification of A-types. It identifies as A only the objects with a $-0.6 < \mathrm{PC2}' < 0$ and with a global spectral slope $\geqslant 0.5$ % (100 nm)$^{-1}$. As seen on panel (A), A-type asteroids can be located among the S-complex on the PCA plot, at lower slope values. As shown in section 5.5, the secondary BP classification step is of help to retrieve some of these lost A-types.

C.2.3.2 *PCA and SNR*

To further study the performances of the classification of DR3 spectra with different ranges of SNR, I applied the PCA to the 14 132 asteroids having a 20⩽SNR⩽30, and to the 22 066 asteroids having a SNR⩽20, without considering objects with flagged bands outside of the first two and last two bands.

On Fig.B.9 and Fig.B.9 are shown the results of the PCA in both cases. On panel (A) are highlighted the class assigned to asteroids of the NIR list from the literature, and on panel (B) their class assigned by the Gaia classification. In the NIR list, 36 asteroids have a 20⩽SNR⩽30, and 33 have a SNR⩽20.

On Fig.B.9, the different zones occupied by the S-complex, the C and X-complex, and the V-types are still distinguishable. The Gaia classification shows differences with the literature, but it appears that asteroids with 20⩽SNR⩽30 can be characterised roughly from the PCA plot. The C and X-complexes are little distinct in this SNR range

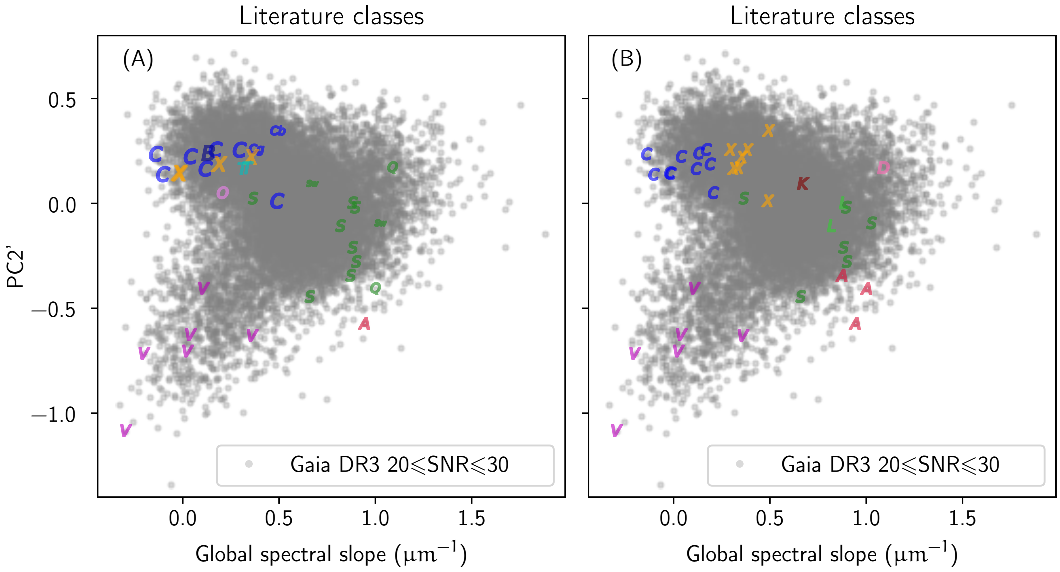

Figure B.9: Plot of the principal component PC2′ with respect to the global slope, calculated for the 14 132 filtered Gaia DR3 asteroids with 20⩽SNR⩽30. The 36 asteroids highlighted are the objects classified from NIR observations. Each coloured letter represents the assigned spectral type from the literature in panel (A), and the first best spectral type assigned with the Gaia classification in panel (B).

according to panel (A), but the more carbonaceous composition of asteroids plotting in this region of the principal component space can be deduced. Similarly, asteroids plotting towards the S-complex or the V-types region, respectively, can be identified as more stony or basaltic.

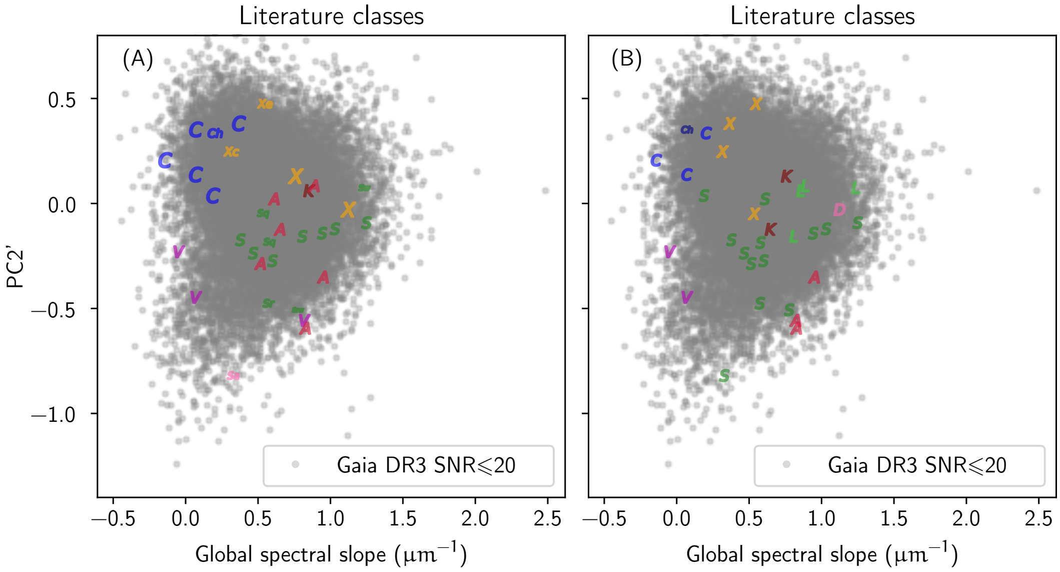

Figure B.9: Plot of the principal component PC2′ with respect to the global slope, calculated for the 22 066 filtered Gaia DR3 asteroids with SNR⩽20. The 33 asteroids highlighted are the objects classified from NIR observations. Each coloured letter represents the assigned spectral type from the literature in panel (A), and the first best spectral type assigned with the Gaia classification in panel (B).

On the PCA plot of asteroids with SNR⩽20 displayed in Fig.B.9, the asteroid groupings previously identified are much less evident, and a greater mixing of classes occurs. At such low SNRs, it is possible to deduce if an object is likely more stony or carbonaceous from its DR3 spectrum, but without further precision. The taxonomic type obtained for these objects using a curve matching classification method should not be trusted as such, but could be translated into a carbonaceous/stony information.

C.3 A-TYPES

Table C.3: List of the 40 asteroids found A-type as first best class after the Gaia classification, and after the BP classification. The asteroid number and name is given in the first column, accompanied with its assigned type from the literature, the method and wavelength range used, and the corresponding reference, when existing. The python package *rocks* was used to produce this table.

Asteroid	Type	Method	Ref
(246) Asporina	A	Spec VISNIR	Mahlke et al. (2022)
(446) Aeternitas	A	Spec VISNIR	Mahlke et al. (2022)
(863) Benkoela	A	Spec VISNIR	Mahlke et al. (2022)
(1488) Aura	A	Phot VIS	Sergeyev et al. (2022)
(1709) Ukraina	A	Spec VISNIR	Mahlke et al. (2022)
(1908) Pobeda	S	Phot VIS	Sergeyev et al. (2022)
(2501) Lohja	A	Spec VISNIR	Mahlke et al. (2022)
(3104) Durer	K	Spec VISNIR	Mahlke et al. (2022)
(3995) Sakaino	S	Spec VISNIR	Mahlke et al. (2022)
(4350) Shibecha	-	-	-
(4720) Tottori	S	Phot VIS	Sergeyev et al. (2022)
(7529) Vagnozzi	V	Phot VIS	Sergeyev et al. (2022)
(8660) Sano	A	Phot VIS	Sergeyev et al. (2022)
(8838) 1989 UW2	A	Spec VISNIR	DeMeo et al. (2019)
(8843) 1990 OH	S	Phot VIS	Sergeyev et al. (2022)
(10811) Lau	-	-	-
(11861) Teruhime	-	-	-
(11890) 1991 FF	-	-	-
(12729) Berger	-	-	-
(13704) Aletesi	A	Phot VIS	Sergeyev et al. (2022)
(14683) Remy	V	Phot VIS	Sergeyev et al. (2022)
(16261) Iidemachi	A	Phot VIS	Sergeyev and Carry (2021)
(16520) 1990 WO3	A	Spec VISNIR	Mahlke et al. (2022)
(16866) 1998 AR	-	-	-

– continued on next page

– continued.

Asteroid	Type	Method	Ref
(17152) 1999 JA118	-	-	-
(19687) 1999 RP199	-	-	-
(20237) Clavius	-	-	-
(22790) 1999 KP4	A	Phot VIS	Sergeyev et al. (2022)
(25808) 2000 CK103	A	Phot VIS	Sergeyev and Carry (2021)
(26851) Sarapul	-	-	-
(34003) Ivozell	A	Phot VIS	Sergeyev et al. (2022)
(35925) 1999 JP104	A	Spec VISNIR	Mahlke et al. (2022)
(37306) 2001 KW46	-	-	-
(48196) 2001 JU1	S	Phot VIS	DeMeo and Carry (2013)
(49141) 1998 SM41	A	Phot VIS	DeMeo and Carry (2013), Sergeyev and Carry (2021)
(56145) 1999 CN84	X	Phot VIS	Sergeyev et al. (2022)
(74412) 1999 AZ7	A	Phot VIS	Sergeyev et al. (2022)
(108199) 2001 HX21	-	-	-
(137881) 2000 AR119	-	-	-
(193478) 2000 XN37	-	-	-

Note. Phot. stands for photometry, Spec. for spectroscopy, VIS for visible-light, NIR for near-infrared and VISNIR for visible-near-infrared.

Table C.4: List of the 58 potential A-type asteroids found after the Gaia and the BP classification. The asteroid number and name is given in the first column, accompanied with its assigned type from the literature, the method and wavelength range used, and the corresponding reference. The python package *rocks* was used to produce this table.

Asteroid	Type	Method	Ref
(703) Noemi	S	Phot VIS	Sergeyev et al. (2022)
(1052) Belgica	S	Spec VISNIR	Mahlke et al. (2022)
(1153) Wallenbergia	S	Phot VIS	DeMeo and Carry (2013), Sergeyev and Carry (2021)
(1600) Vyssotsky	S	Spec VISNIR	Mahlke et al. (2022)
(2150) Nyctimene	S	Spec VISNIR	Mahlke et al. (2022)
(2699) Kalinin	S	Phot VIS	Sergeyev and Carry (2021)
(4025) Ridley	S	Spec VISNIR	Mahlke et al. (2022)
(4671) Drtikol	LS	Phot VIS	Carvano et al. (2010)
(4825) Ventura	S	Phot VIS	Sergeyev et al. (2022)

– continued on next page

– continued.

Asteroid	Type	Method	Ref
-			
(5099) Iainbanks	-	-	-
(6485) Wendeesther	S	Spec VISNIR	Mahlke et al. (2022)
(7144) Dossobuono	L	Phot VIS	DeMeo and Carry (2013)
(7468) Anfimov	A	Spec VISNIR	Mahlke et al. (2022)
(8258) McCracken	S	Phot VIS	Sergeyev et al. (2022)
(8310) Seelos	S	Phot VIS	DeMeo and Carry (2013)
(9106) Yatagarasu	S	Phot VIS	DeMeo and Carry (2013)
(9690) Houtgast	Ad	Phot NIR	Popescu et al. (2018a)
(11262) Drube	-	-	-
(11362) 1998 EN9	-	-	-
(11366) 1998 GL9	-	-	-
(11711) Urquiza	-	-	-
(11733) 1998 KJ52	-	-	-
(13063) Purifoy	S	Phot VIS	Sergeyev et al. (2022)
(13699) Nickthomas	S	Phot VIS	DeMeo and Carry (2013), Carvano et al. (2010), Erasmus et al. (2018), Erasmus et al. (2019), Sergeyev and Carry (2021)
(14095) 1997 PE2	S	Phot VIS	DeMeo and Carry (2013), Sergeyev and Carry (2021), Sergeyev et al. (2022)
(14221) 1999 WL	-	-	-
(15522) Trueblood	-	-	-
(15610) 2000 GY126	-	-	-
(16539) 1991 PY12	-	-	-
(16789) 1997 AU3	-	-	-
(17015) Shriyareddy	-	-	-
(17991) Joshuaegan	S	Phot VIS	Sergeyev et al. (2022)
(18392) 1992 PT4	A	Phot VIS	Carvano et al. (2010)
(20782) Markcroce	-	-	-
(21086) 1992 AO1	-	-	-
(21809) 1999 TG19	A	Spec VISNIR	Mahlke et al. (2022)
(29550) Yaribartolini	SV	Phot VIS	Carvano et al. (2010)
(29801) 1999 CX84	-	-	-

– continued on next page

– continued.

Asteroid	Type	Method	Ref
-			
(31831) 1999 YL	-	-	-
(32046) 2000 JR28	S	Phot VIS	Sergeyev et al. (2022)
(33763) 1999 RB84	-	-	-
(34670) 2000 YL11	-	-	-
(36256) 1999 XT17	A	Spec VISNIR	Mahlke et al. (2022)
(41424) 2000 CK40	A	Phot VIS	Sergeyev et al. (2022)
(43752) Maryosipova	S	Phot VIS	Sergeyev et al. (2022)
(46793) Phinney	-	-	-
(49692) 1999 UB7	A	Phot VIS	Sergeyev et al. (2022)
(50926) 2000 GF65	S	Phot VIS	Sergeyev et al. (2022)
(52726) 1998 GY6	A	Spec VIS	Solontoi et al. (2012)
(56041) Luciendumont	-	-	-
(56321) 1999 VB53	-	-	-
(57276) 2001 QP139	-	-	-
(59530) 1999 JU24	-	-	-
(59811) 1999 RV17	S	Phot VIS	Sergeyev et al. (2022)
(61091) 2000 LU27	S	Phot VIS	Sergeyev et al. (2022)
(68765) 2002 EE99	-	-	-
(70373) 1999 RY207	S	Phot VIS	Sergeyev et al. (2022)
(89776) 2002 AL90	V	Spec VIS	Oszkiewicz et al. (2023)

Note. Phot. stands for photometry, Spec. for spectroscopy, VIS for visible-light, NIR for near-infrared and VISNIR for visible-near-infrared.

BIBLIOGRAPHY

Adams, J. B. and T. B. McCord (Jan. 1971). "Optical properties of mineral separates, glass, and anorthositic fragments from Apollo mare samples." In: *Lunar and Planetary Science Conference Proceedings* 2, p. 2183.

Alí-Lagoa, V., L. Lionni, M. Delbo, B. Gundlach, J. Blum, and J. Licandro (Jan. 2014). "Thermophysical properties of near-Earth asteroid (341843) 2008 EV_5 from WISE data." In: *Astronomy & Astrophysics* 561, A45. DOI: 10.1051/0004-6361/201322215.

Alvarez-Candal, A., R. Duffard, D. Lazzaro, and T. Michtchenko (Dec. 2006). "The inner region of the asteroid Main Belt: a spectroscopic and dynamic analysis." In: *Astronomy & Astrophysics* 459.3, pp. 969–976. DOI: 10.1051/0004-6361:20065518.

Amelin, Yuri, Angela Kaltenbach, Tsuyoshi Iizuka, Claudine H. Stirling, Trevor R. Ireland, Michail Petaev, and Stein B. Jacobsen (Dec. 2010). "U-Pb chronology of the Solar System's oldest solids with variable $^{238}U/\ ^{235}U$." In: *Earth and Planetary Science Letters* 300.3-4, pp. 343–350. DOI: 10.1016/j.epsl.2010.10.015.

Ammannito, E. et al. (Dec. 2013). "Olivine in an unexpected location on Vesta's surface." In: 504, p. 122. DOI: 10.1038/nature12665.

Anand, Aryavart, Pascal M. Kruttasch, and Klaus Mezger (Nov. 2022). "^{53}Mn-^{53}Cr chronology and $\varepsilon^{54}Cr$-$\Delta^{17}O$ genealogy of Erg Chech 002: The oldest andesite in the solar system." In: 57.11, pp. 2003–2016. DOI: 10.1111/maps.13916.

Andrae, Rene, Tim Schulze-Hartung, and Peter Melchior (Dec. 2010). "Dos and don'ts of reduced chi-squared." In: *arXiv e-prints*, arXiv:1012.3754. arXiv: 1012.3754 [astro-ph.IM].

Armitage, Philip J. (Sept. 2011). "Dynamics of Protoplanetary Disks." In: 49.1, pp. 195–236. DOI: 10.1146/annurev-astro-081710-102521.

Armitage, Philip J. (Jan. 2019). "Physical Processes in Protoplanetary Disks." In: *Saas-Fee Advanced Course* 45, p. 1. DOI: 10.1007/978-3-662-58687-7_1.

Arredondo, Anicia, Humberto Campins, Noemi Pinilla-Alonso, Julia de León, Vania Lorenzi, and David Morate (Apr. 2021a). "Near-infrared spectroscopy of the Sulamitis asteroid family: Surprising similarities in the inner belt primitive asteroid population." In: 358, p. 114210. DOI: 10.1016/j.icarus.2020.114210.

Arredondo, Anicia, Humberto Campins, Noemi Pinilla-Alonso, Julia de León, Vania Lorenzi, David Morate, Juan Luis Rizos, and Mário De Prá (Nov. 2021b). "Spectral diversity of the inner belt primitive asteroid background population." In: 368, p. 114619. DOI: 10.1016/j.icarus.2021.114619.

Avdellidou, C., M. Delbo, A. Morbidelli, K. J. Walsh, E. Munaibari, J. Bourdelle de Micas, M. Devogèle, S. Fornasier, M. Gounelle, and G. van Belle (Sept. 2022). "Athor asteroid family as the source of the EL enstatite meteorites." In: *Astronomy & Astrophysics* 665, p. L9. DOI: 10.1051/0004-6361/202244590.

Barrat, J. A., R. C. Greenwood, K. Keil, M. L. Rouget, J. S. Boesenberg, B. Zanda, and I. A. Franchi (Nov. 2016). "The origin of aubrites: Evidence from lithophile trace element abundances and oxygen isotope compositions." In: 192, pp. 29–48. DOI: 10.1016/j.gca.2016.07.025.

Barrat, Jean-Alix, Marc Chaussidon, Akira Yamaguchi, Pierre Beck, Johan Villeneuve, David J. Byrne, Michael W. Broadley, and Bernard Marty (Mar. 2021). "A 4,565-My-old andesite from an extinct chondritic protoplanet." In: *Proceedings of the National Academy of Science* 118.11, p. 2026129118. DOI: 10.1073/pnas.2026129118.

Barrat, Jean-Alix, Akira Yamaguchi, Brigitte Zanda, Claire Bollinger, and Marcel Bohn (Nov. 2010). "Relative chronology of crust formation on asteroid Vesta: Insights from the geochemistry of diogenites." In: 74.21, pp. 6218–6231. DOI: 10.1016/j.gca.2010.07.028.

Beck, Andrew W., Kees C. Welten, Harry Y. McSween, Christina E. Viviano, and Marc W. Caffee (June 2012). "Petrologic and textural diversity among the PCA 02 howardite group, one of the largest pieces of the Vestan surface." In: 47.6, pp. 947–969. DOI: 10.1111/j.1945-5100.2012.01360.x.

Beck, P., B. Schmitt, S. Potin, A. Pommerol, and O. Brissaud (Jan. 2021). "Low-phase spectral reflectance and equivalent "geometric albedo" of meteorites powders." In: 354, p. 114066. DOI: 10.1016/j.icarus.2020.114066.

Benedix, G. K., T. J. McCoy, K. Keil, D. D. Bogard, and D. H. Garrison (July 1998). "A petrologic and isotopic study of winonaites: evidence for early partial melting, brecciation, and metamorphism." In: 62.14, pp. 2535–2553. DOI: 10.1016/S0016-7037(98)00166-5.

Berthier, J., B. Carry, M. Mahlke, and J. Normand (Mar. 2023). "SsODNet: Solar system Open Database Network." In: *Astronomy & Astrophysics* 671, A151. DOI: 10.1051/0004-6361/202244878.

Bertka, Constance M. and Yingwei Fei (Mar. 1997). "Mineralogy of the Martian interior up to core-mantle boundary pressures." In: 102.B3, pp. 5251–5264. DOI: 10.1029/96JB03270.

Binzel, R. P. et al. (May 2019). "Compositional distributions and evolutionary processes for the near-Earth object population: Results from the MIT-Hawaii Near-Earth Object Spectroscopic Survey (MITHNEOS)." In: 324, pp. 41–76. DOI: 10.1016/j.icarus.2018.12.035.

Binzel, Richard P., Alessandro Morbidelli, Sihane Merouane, Francesca E. DeMeo, Mirel Birlan, Pierre Vernazza, Cristina A. Thomas, Andrew S. Rivkin, Schelte J. Bus, and Alan T. Tokunaga (Jan. 2010). "Earth encounters as the origin of fresh surfaces on near-Earth asteroids." In: 463.7279, pp. 331–334. DOI: 10.1038/nature08709.

Binzel, Richard P., Andrew S. Rivkin, J. Scott Stuart, Alan W. Harris, Schelte J. Bus, and Thomas H. Burbine (Aug. 2004). "Observed spectral properties of near-Earth objects: results for population distribution, source regions, and space weathering processes." In: 170.2, pp. 259–294. DOI: 10.1016/j.icarus.2004.04.004.

Binzel, Richard P. and Shui Xu (1993). "Chips off of Asteroid 4 Vesta: Evidence for the Parent Body of Basaltic Achondrite Meteorites." In: *Science* 260.5105, pp. 186–191. DOI: 10.1126/science.260.5105.186. eprint: https://www.science.org/doi/pdf/10.1126/science.260.5105.186.

Birlan, Mirel, Maria Antonietta Barucci, Pierre Vernazza, Marcello Fulchignoni, Richard P. Binzel, Schelte J. Bus, Irina Belskaya, and Sonia Fornasier (June 2004). "Near-IR spectroscopy of asteroids 21 Lutetia, 89 Julia, 140 Siwa, 2181 Fogelin and 5480 (1989YK8), potential targets for the Rosetta mission; remote observations campaign on IRTF." In: 9.5, pp. 343–351. DOI: 10.1016/j.newast.2003.12.005.

Bizzarro, Martin, Joel A. Baker, Henning Haack, and Kasper L. Lundgaard (2005). "Rapid Timescales for Accretion and Melting of Differentiated Planetesimals Inferred from 26Al-26Mg Chronometry." In: *The Astrophysical Journal* 632.1, p. L41. DOI: 10.1086/497638. URL: https://dx.doi.org/10.1086/497638.

Bland, P. A., M. E. Zolensky, G. K. Benedix, and M. A. Sephton (2006). "Weathering of Chondritic Meteorites." In: *Meteorites and the Early Solar System II*. Ed. by Dante S. Lauretta and Harry Y. McSween, p. 853.

Bland, Philip A. (Oct. 2004). "Fireball cameras: The Desert Fireball Network." In: *Astronomy and Geophysics* 45.5, pp. 5.20–5.23. DOI: 10.1046/j.1468-4004.2003.45520.x.

Bolin, B. T., M. Delbo, A. Morbidelli, and K. J. Walsh (Jan. 2017). "Yarkovsky V-shape identification of asteroid families." In: *Icarus* 282, pp. 290–312. DOI: 10.1016/j.icarus.2016.09.029.

Bolin, B. T., A. Morbidelli, and K. J. Walsh (Apr. 2018). "Size-dependent modification of asteroid family Yarkovsky V-shapes." In: *Astronomy & Astrophysics* 611, A82. DOI: 10.1051/0004-6361/201732079.

Borisov, G., A. Christou, S. Bagnulo, A. Cellino, T. Kwiatkowski, and A. Dell'Oro (Apr. 2017). "The olivine-dominated composition of the Eureka family of Mars Trojan asteroids." In: 466.1, pp. 489–495. DOI: 10.1093/mnras/stw3075.

Bottke William F., Jr., David Vokrouhlický, David P. Rubincam, and David Nesvorný (May 2006a). "The Yarkovsky and Yorp Effects: Implications for Asteroid Dynamics." In: *Annual Review of Earth and Planetary Sciences* 34, pp. 157–191. DOI: 10.1146/annurev.earth.34.031405.125154.

Bottke, W. F., D. D. Durda, D. Nesvorný, R. Jedicke, A. Morbidelli, D. Vokrouhlický, and H. F. Levison (Dec. 2005). "Linking the collisional history of the main asteroid belt to its dynamical excitation and depletion." In: *Icarus* 179, p. 63. DOI: 10.1016/j.icarus.2005.05.017.

Bottke, W. F., D. Nesvorný, R. E. Grimm, A. Morbidelli, and D. P. O'Brien (Feb. 2006b). "Iron meteorites as remnants of planetesimals formed in the terrestrial planet region." In: 439, pp. 821–824. DOI: 10.1038/nature04536.

Bottke, William Frederick (2002). *Asteroids III*. University of Arizona Press.

Bourdelle de Micas, J., S. Fornasier, C. Avdellidou, M. Delbo, G. van Belle, P. Ochner, W. Grundy, and N. Moskovitz (Sept. 2022). "Composition of inner main-belt planetesimals." In: *Astronomy & Astrophysics* 665, A83. DOI: 10.1051/0004-6361/202244099.

Bourdelle de Micas, J., S. Fornasier, M. Delbo, S. Ferrone, G. van Belle, P. Ochner, and C. Avdellidou (Feb. 2024). "Compositional characterization of a primordial S-type asteroid family of the inner main belt." In: *Astronomy & Astrophysics* 682, A64. DOI: 10.1051/0004-6361/202347391.

Bourdelle de Micas, Jules (Dec. 2022). "La composition des astéroïdes primordiaux, vestiges de la population des planétésimaux et membres des familles les plus anciennes." Theses. Université Paris sciences et lettres. URL: https://theses.hal.science/tel-04198803.

Bouvier, Audrey and Meenakshi Wadhwa (Sept. 2010). "The age of the Solar System redefined by the oldest Pb-Pb age of a meteoritic inclusion." In: *Nature Geoscience* 3.9, pp. 637–641. DOI: 10.1038/ngeo941.

Brož, M. and A. Morbidelli (Jan. 2019). "A study of 3-dimensional shapes of asteroid families with an application to Eos." In: 317, pp. 434–441. DOI: 10.1016/j.icarus.2018.08.022.

Brož, M., A. Morbidelli, W. F. Bottke, J. Rozehnal, D. Vokrouhlický, and D. Nesvorný (Mar. 2013). "Constraining the cometary flux through the asteroid belt during the late heavy bombardment." In: *Astronomy & Astrophysics* 551, A117. DOI: 10.1051/0004-6361/201219296.

Brož, M., P. Vernazza, M. Marsset, F. E. DeMeo, R. P. Binzel, D. Vokrouhlický, and D. Nesvorný (Mar. 2024). "Young asteroid families as the primary source of meteorites." In: *arXiv e-prints*, arXiv:2403.08552. DOI: 10.48550/arXiv.2403.08552. arXiv: 2403.08552 [astro-ph.EP].

Brož, M. and D. Vokrouhlický (Oct. 2008). "Asteroid families in the first-order resonances with Jupiter." In: 390.2, pp. 715–732. DOI: 10.1111/j.1365-2966.2008.13764.x.

Brož, M and A Morbidelli (Apr. 2013). "The Eos family halo." In: *Icarus* 223.2, pp. 844–849.

Brunetto, R., M. J. Loeffler, D. Nesvorný, S. Sasaki, and G. Strazzulla (2015). "Asteroid Surface Alteration by Space Weathering Processes." In: *in Asteroids IV (P. Michel, et al. eds)*. Ed. by P. Michel, F. E. DeMeo, and W. F. Bottke, pp. 597–616. DOI: 10.2458/azu_uapress_9780816532131-ch031.

Brunetto, R., J. de León, and J. Licandro (Sept. 2007). "Testing space weathering models on A-type asteroid (1951) Lick." In: *Astronomy & Astrophysics* 472.2, pp. 653–656. DOI: 10.1051/0004-6361:20077722.

Brunetto, Rosario, Pierre Vernazza, Simone Marchi, Mirel Birlan, Marcello Fulchignoni, Vincenzo Orofino, and Giovanni Strazzulla (Oct. 2006). "Modeling asteroid surfaces from observations and irradiation experiments: The case of 832 Karin." In: 184.2, pp. 327–337. DOI: 10.1016/j.icarus.2006.05.019.

Burbine, T. H., P. C. Buchanan, R. P. Binzel, S. J. Bus, T. Hiroi, J. L. Hinrichs, A. Meibom, and T. J. Mccoy (n.d.). "Vesta, Vestoids, and the howardite, eucrite, diogenite group: Relationships and the origin of spectral differences." In: *Meteoritics & Planetary Science* 36.6 (), pp. 761–781. DOI: https://doi.org/10.1111/j.1945-5100.2001.tb01915.x.

Burbine, Thomas H. and Richard P. Binzel (Oct. 2002). "Small Main-Belt Asteroid Spectroscopic Survey in the Near-Infrared." In: 159.2, pp. 468–499. DOI: 10.1006/icar.2002.6902.

Burbine, Thomas H., Anders Meibom, and Richard P. Binzel (Sept. 1996). "Mantle material in the main belt: Battered to bits?" In: 31.5, pp. 607–620. DOI: 10.1111/j.1945-5100.1996.tb02033.x.

Burns, Roger G. (1993). *Mineralogical Applications of Crystal Field Theory*.

Bus, Schelte J. and Richard P. Binzel (July 2002a). "Phase II of the Small Main-Belt Asteroid Spectroscopic Survey. A Feature-Based Taxonomy." In: 158.1, pp. 146–177. DOI: 10.1006/icar.2002.6856.

Bus, Schelte J. and Richard P. Binzel (July 2002b). "Phase II of the Small Main-Belt Asteroid Spectroscopic Survey. The Observations." In: 158.1, pp. 106–145. DOI: 10.1006/icar.2002.6857.

Buseck, P. R. (June 1977). "Pallasite meteorites—mineralogy, petrology and geochemistry." In: 41.6, pp. 711,723–721,740. DOI: 10.1016/0016-7037(77)90044-8.

Cantillo, D. C., V. Reddy, B. Sharkey, N. C. Pearson, T. Campbell, A. Satpathy, M. De Florio, A. Battle, R. Furfaro, and J. Sanchez (Aug. 2023). "Can Grain Size Affect Taxonomy of Low-Albedo Near-Earth Objects?" In: *LPI Contributions*. Vol. 2851. LPI Contributions, p. 2030.

Carporzen, L., B. P. Weiss, L. T. Elkins-Tanton, D. L. Shuster, D. Ebel, and J. Gattacceca (Apr. 2011). "From the Cover: Magnetic evidence for a partially differentiated carbonaceous chondrite parent body." In: *Proceedings of the National Academy of Science* 108.16, pp. 6386–6389. DOI: 10.1073/pnas.1017165108.

Carrasco, J. M., M. Weiler, C. Jordi, C. Fabricius, F. De Angeli, D. W. Evans, F. van Leeuwen, M. Riello, and P. Montegriffo (Aug. 2021). "Internal calibration of Gaia BP/RP low-resolution spectra." In: *Astronomy & Astrophysics* 652, A86. DOI: 10.1051/0004-6361/202141249.

Carrasco, J. M. et al. (Nov. 2016). "Gaia Data Release 1. Principles of the photometric calibration of the G band." In: *Astronomy & Astrophysics* 595, A7. DOI: 10.1051/0004-6361/201629235.

Carry, B. (Dec. 2012). "Density of asteroids." In: 73.1, pp. 98–118. DOI: 10.1016/j.pss.2012.03.009.

Carry, B, E Solano, S Eggl, and F E DeMeo (Apr. 2016). "Spectral properties of near-Earth and Mars-crossing asteroids using Sloan photometry." In: *Icarus* 268, pp. 340–354.

Carvano, J. M. and J. A. G. Davalos (Aug. 2015). "Shape and solar phase angle effects on the taxonomic classification of asteroids." In: *Astronomy & Astrophysics* 580, A98, A98. DOI: 10.1051/0004-6361/201526268.

Carvano, J. M., P. H. Hasselmann, D. Lazzaro, and T. Mothé-Diniz (Feb. 2010). "SDSS-based taxonomic classification and orbital distribution of main belt asteroids." In: *Astronomy & Astrophysics* 510, A43. DOI: 10.1051/0004-6361/200913322.

Carvano, Jorge Márcio, Daniela Lazzaro, Thais Mothé-Diniz, Cláudia A. Angeli, and Marcos Florczak (Jan. 2001). "Spectroscopic Survey of the Hungaria and Phocaea Dynamical Groups." In: 149.1, pp. 173–189. DOI: 10.1006/icar.2000.6512.

Ceplecha, Z. and J. Rajchl (Jan. 1965). "Programme of fireball photography in Czechoslovakia." In: *Bulletin of the Astronomical Institutes of Czechoslovakia* 16, p. 15.

Chapman, C. R. (1986). In: *Proceedings of the NASA and CNR, International Workshop on Catastrophic Disruption of Asteroids and Satellites*, 103–114.

Chapman, C. R., D. Morrison, and B. Zellner (May 1975). "Surface properties of asteroids - A synthesis of polarimetry, radiometry, and spectrophotometry." In: *Icarus* 25, p. 104. DOI: 10.1016/0019-1035(75)90191-8.

Chapman, Clark R. (Nov. 1996). "S-Type Asteroids, Ordinary Chondrites, and Space Weathering: The Evidence from Galileo's Fly-bys of Gaspra and Ida." In: 31.6, pp. 699–725. DOI: 10.1111/j.1945-5100.1996.tb02107.x.

Chaussidon, M., J. A. Barrat, A. Yamaguchi, P. Beck, J. Villeneuve, D. J. Byrne, M. W. Broadleye, and B. Marty (Mar. 2021). "26Al Chronology of Erg Chech 002, the Oldest Andesite in the Solar System." In: *52nd Lunar and Planetary Science Conference*. Lunar and Planetary Science Conference, p. 2222.

Christou, Apostolos A., Galin Borisov, Aldo Dell'Oro, Alberto Cellino, and Maxime Devogèle (Jan. 2021). "Composition and origin of L5 Trojan asteroids of Mars: Insights from spectroscopy." In: 354, p. 113994. DOI: 10.1016/j.icarus.2020.113994.

Clark, B. E., B. Hapke, C. Pieters, and D. Britt (2002). "Asteroid Space Weathering and Regolith Evolution." In: *Asteroids III*, p. 585.

Clark, Beth Ellen, Maureen E. Ockert-Bell, Ed A. Cloutis, David Nesvorny, Thais Mothé-Diniz, and Schelte J. Bus (July 2009). "Spectroscopy of K-complex asteroids: Parent bodies of carbonaceous meteorites?" In: 202.1, pp. 119–133. DOI: 10.1016/j.icarus.2009.02.027.

Cloutis, E. A., M. J. Gaffey, D. G. W. Smith, and R. St. J. Lambert (June 1990). “Metal Silicate Mixtures: Spectral Properties and Applications to Asteroid Taxonomy.” In: 95, pp. 8323–8338. DOI: `10.1029/JB095iB06p08323`.

Cloutis, E. A., P. Hudon, T. Hiroi, M. J. Gaffey, and P. Mann (Nov. 2012). “Spectral reflectance properties of carbonaceous chondrites: 8. “Other” carbonaceous chondrites: CH, ungrouped, polymict, xenolithic inclusions, and R chondrites.” In: 221.2, pp. 984–1001. DOI: `10.1016/j.icarus.2012.10.008`.

Cloutis, Edward A. (June 2002). “Pyroxene reflectance spectra: Minor absorption bands and effects of elemental substitutions.” In: *Journal of Geophysical Research (Planets)* 107.E6, p. 5039. DOI: `10.1029/2001JE001590`.

Cloutis, Edward A., Michael J. Gaffey, Timothy L. Jackowski, and Kevin L. Reed (Oct. 1986). “Calibrations of phase abundance, composition, and particle size distribution for olivine-orthopyroxene mixtures from reflectance spectra.” In: 91, pp. 11,641–11,653. DOI: `10.1029/JB091iB11p11641`.

Cloutis, Edward A., Paul S. Hardersen, David L. Bish, Daniel T. Bailey, Michael J. Gaffey, and Michael A. Craig (Feb. 2010). “Reflectance spectra of iron meteorites: Implications for spectral identification of their parent bodies.” In: 45.2, pp. 304–332. DOI: `10.1111/j.1945-5100.2010.01033.x`.

Cloutis, Edward A., Vishnu Reddy, and David T. Blewett (Sept. 2018). “The ungrouped achondrite Northwest Africa (NWA) 7325: Spectral reflectance properties and implications for parent body identification.” In: 311, pp. 384–393. DOI: `10.1016/j.icarus.2018.04.027`.

Cloutis, Edward A., J. M. Sunshine, and R. V. Morris (Apr. 2004). “Spectral reflectance-compositional properties of spinels and chromites: Implications for planetary remote sensing and geothermometry.” In: 39.4, pp. 545–565. DOI: `10.1111/j.1945-5100.2004.tb00918.x`.

Colas, F. et al. (Dec. 2020). “FRIPON: a worldwide network to track incoming meteoroids.” In: *Astronomy & Astrophysics* 644, A53. DOI: `10.1051/0004-6361/202038649`.

Collinet, Max and Timothy L Grove (2020). “Widespread production of silica-and alkali-rich melts at the onset of planetesimal melting.” In: *Geochimica et Cosmochimica Acta* 277, pp. 334–357.

Connelly, J. N., J. Bollard, E. Amsellem, M. Schiller, K. K. Larsen, and M. Bizzarro (Aug. 2023). “Evidence for Very Early Planetesimal Formation and ^{26}Al/^{27}Al Heterogeneity in the Protoplanetary Disk.” In: 952.2, p. L33. DOI: `10.3847/2041-8213/ace42e`.

Connelly, James N., Martin Bizzarro, Alexander N. Krot, Åke Nordlund, Daniel Wielandt, and Marina A. Ivanova (Nov. 2012). “The Absolute Chronology and Thermal Processing of Solids in the Solar Protoplanetary Disk.” In: *Science* 338.6107, p. 651. DOI: `10.1126/science.1226919`.

Crowley, C. et al. (Nov. 2016). “Gaia Data Release 1. On-orbit performance of the Gaia CCDs at L2.” In: *Astronomy & Astrophysics* 595, A6. DOI: `10.1051/0004-6361/201628990`.

Cruikshank, Dale P. and William K. Hartmann (1984). “The Meteorite-Asteroid Connection: Two Olivine-Rich Asteroids.” In: *Science* 223.4633, pp. 281–283. DOI: `10.1126/science.223.4633.281`. eprint: `https://www.science.org/doi/pdf/10.1126/science.223.4633.281`.

D'Angelo, Gennaro, Stuart J. Weidenschilling, Jack J. Lissauer, and Peter Bodenheimer (Oct. 2014). "Growth of Jupiter: Enhancement of core accretion by a voluminous low-mass envelope." In: 241, pp. 298–312. DOI: 10.1016/j.icarus.2014.06.029.

Daubrée, Auguste (1867). *Classification adoptée pour la collection de météorites du Muséum*. Gauthier-Villars.

David, M., R. Blomme, Y. Frémat, Y. Damerdji, C. Delle Luche, E. Gosset, D. Katz, and Y. Viala (Feb. 2014). "A multi-method approach to radial-velocity measurement for single-object spectra." In: *Astronomy & Astrophysics* 562, A97. DOI: 10.1051/0004-6361/201322721.

De Angeli, F. et al. (June 2023). "Gaia Data Release 3. Processing and validation of BP/RP low-resolution spectral data." In: *Astronomy & Astrophysics* 674, A2. DOI: 10.1051/0004-6361/202243680.

De Prá, M. N., J. Licandro, N. Pinilla-Alonso, V. Lorenzi, E. Rondón, J. Carvano, D. Morate, and J. De León (Mar. 2020a). "The spectroscopic properties of the Lixiaohua family, cradle of Main Belt Comets." In: 338, p. 113473. DOI: 10.1016/j.icarus.2019.113473.

De Prá, M. N., N. Pinilla-Alonso, J. M. Carvano, J. Licandro, H. Campins, T. Mothé-Diniz, J. De León, and V. Alí-Lagoa (Sept. 2018). "PRIMASS visits Hilda and Cybele groups." In: 311, pp. 35–51. DOI: 10.1016/j.icarus.2017.11.012.

De Prá, M. N., N. Pinilla-Alonso, J. Carvano, J. Licandro, D. Morate, V. Lorenzi, J. de León, H. Campins, and T. Mothé-Diniz (Nov. 2020b). "A comparative analysis of the outer-belt primitive families." In: *Astronomy & Astrophysics* 643, A102. DOI: 10.1051/0004-6361/202038536.

DeMeo, F. E., R. P. Binzel, S. M. Slivan, and S. J. Bus (July 2009). "An extension of the Bus asteroid taxonomy into the near-infrared." In: *Icarus* 202, p. 160. DOI: 10.1016/j.icarus.2009.02.005.

DeMeo, F. E. and B. Carry (Sept. 2013). "The taxonomic distribution of asteroids from multi-filter all-sky photometric surveys." In: 226.1, pp. 723–741. DOI: 10.1016/j.icarus.2013.06.027.

DeMeo, Francesca E., Richard P. Binzel, Benoît Carry, David Polishook, and Nicholas A. Moskovitz (Feb. 2014). "Unexpected D-type interlopers in the inner main belt." In: 229, pp. 392–399. DOI: 10.1016/j.icarus.2013.11.026.

DeMeo, Francesca E., David Polishook, Benoît Carry, Brian J. Burt, Henry H. Hsieh, Richard P. Binzel, Nicholas A. Moskovitz, and Thomas H. Burbine (Apr. 2019). "Olivine-dominated A-type asteroids in the main belt: Distribution, abundance and relation to families." In: 322, pp. 13–30. DOI: 10.1016/j.icarus.2018.12.016.

DeMeo, Francesca E. et al. (July 2022). "Connecting asteroids and meteorites with visible and near-infrared spectroscopy." In: 380, p. 114971. DOI: 10.1016/j.icarus.2022.114971.

Delbo, M., C. Avdellidou, and K. J. Walsh (Dec. 2023). "Gaia view of primitive inner-belt asteroid families. Searching for the origins of asteroids Bennu and Ryugu." In: *Astronomy & Astrophysics* 680, A10, A10. DOI: 10.1051/0004-6361/202346452. arXiv: 2308.13828 [astro-ph.EP].

Delbo, M., G. Libourel, J. Wilkerson, N. Murdoch, P. Michel, K. T. Ramesh, C. Ganino, C. Verati, and S. Marchi (Apr. 2014). "Thermal fatigue as the origin of regolith on small asteroids." In: 508, p. 233. DOI: 10.1038/nature13153.

Delbo, M., K. Walsh, B. Bolin, C. Avdellidou, and A. Morbidelli (Sept. 2017). "Identification of a primordial asteroid family constrains the original planetesimal population." In: *Science* 357, pp. 1026–1029. DOI: 10.1126/science.aam6036.

Delbo, Marco, Chrysa Avdellidou, and Alessandro Morbidelli (Apr. 2019). "Ancient and primordial collisional families as the main sources of X-type asteroids of the inner main belt." In: *Astronomy & Astrophysics* 624, A69. DOI: 10.1051/0004-6361/201834745.

Delbo', Marco, Julie Gayon-Markt, Giorgia Busso, Antony Brown, Laurent Galluccio, Christophe Ordenovic, Philippe Bendjoya, and Paolo Tanga (Dec. 2012). "Asteroid spectroscopy with Gaia." In: 73.1, pp. 86–94. DOI: 10.1016/j.pss.2012.07.029.

Delbo', Marco and Paolo Tanga (Feb. 2009). "Thermal inertia of main belt asteroids smaller than 100 km from IRAS data." In: 57.2, pp. 259–265. DOI: 10.1016/j.pss.2008.06.015. arXiv: 0808.0869 [astro-ph].

Delbo', Marco, Aldo dell'Oro, Alan W. Harris, Stefano Mottola, and Michael Mueller (Sept. 2007). "Thermal inertia of near-Earth asteroids and implications for the magnitude of the Yarkovsky effect." In: 190.1, pp. 236–249. DOI: 10.1016/j.icarus.2007.03.007.

Delsanti, Audrey and David Jewitt (2006). "The solar system beyond the planets." In: *Solar System Update*. Springer, pp. 267–293.

Demidova, SI, MA Nazarov, CA Lorenz, G Kurat, F Brandstätter, and Th Ntaflos (2007). "Chemical composition of lunar meteorites and the lunar crust." In: *Petrology* 15, pp. 386–407.

Dermott, Stanley F., Apostolos A. Christou, Dan Li, Thomas. J. J. Kehoe, and J. Malcolm Robinson (2018). "The common origin of family and non-family asteroids." In: *Nature Astronomy* 2.7, pp. 549–554. ISSN: 2397-3366. DOI: 10.1038/s41550-018-0482-4. URL: https://doi.org/10.1038/s41550-018-0482-4.

Devillepoix, H. A. R. et al. (Oct. 2020). "A Global Fireball Observatory." In: 191, p. 105036. DOI: 10.1016/j.pss.2020.105036.

Devogèle, M. et al. (Apr. 2018). "New polarimetric and spectroscopic evidence of anomalous enrichment in spinel-bearing calcium-aluminium-rich inclusions among L-type asteroids." In: 304, pp. 31–57. DOI: 10.1016/j.icarus.2017.12.026.

Devogèle, Maxime et al. (Nov. 2019). "Visible Spectroscopy from the Mission Accessible Near-Earth Object Survey (MANOS): Taxonomic Dependence on Asteroid Size." In: 158.5, p. 196. DOI: 10.3847/1538-3881/ab43dd.

Dodd, R. T. (Feb. 1969). "Metamorphism of the ordinary chondrites: A review." In: 33.2, 161,IN1,165–164,IN5,203. DOI: 10.1016/0016-7037(69)90138-0.

Duffard, René, Daniela Lazzaro, Javier Licandro, Maria Cristina De Sanctis, Maria Teresa Capria, and Jorge M. Carvano (Sept. 2004a). "Mineralogical characterization of some basaltic asteroids in the neighborhood of (4) Vesta: first results." In: 171.1, pp. 120–132. DOI: 10.1016/j.icarus.2004.05.004.

Duffard, René, Daniela Lazzaro, Javier Licandro, Maria Cristina De Sanctis, Maria Teresa Capria, and Jorge M. Carvano (Sept. 2004b). "Mineralogical characterization of some basaltic asteroids in the neighborhood of (4) Vesta: first results." In: 171.1, pp. 120–132. DOI: 10.1016/j.icarus.2004.05.004.

Duncan, M. J. and H. F. Levison (June 1997). "A scattered comet disk and the origin of Jupiter family comets." In: *Science* 276, pp. 1670–1672. DOI: 10.1126/science.276.5319.1670.

Durech, J., V. Sidorin, and M. Kaasalainen (Apr. 2010). "DAMIT: a database of asteroid models." In: *Astronomy & Astrophysics* 513, A46. DOI: 10.1051/0004-6361/200912693.

Elkins-Tanton, Linda T., Benjamin P. Weiss, and Maria T. Zuber (May 2011). "Chondrites as samples of differentiated planetesimals." In: *Earth and Planetary Science Letters* 305.1-2, pp. 1–10. DOI: 10.1016/j.epsl.2011.03.010.

Emery, J. P., D. M. Burr, and D. P. Cruikshank (Jan. 2011). "Near-infrared Spectroscopy of Trojan Asteroids: Evidence for Two Compositional Groups." In: 141.1, p. 25. DOI: 10.1088/0004-6256/141/1/25.

Emery, J. P., Y. R. Fernández, M. S. P. Kelley, K. T. Warden, C. Hergenrother, D. S. Lauretta, M. J. Drake, H. Campins, and J. Ziffer (May 2014). "Thermal infrared observations and thermophysical characterization of OSIRIS-REx target asteroid (101955) Bennu." In: 234, pp. 17–35. DOI: 10.1016/j.icarus.2014.02.005.

Encke, Johann Franz (2023). *Berliner Astronomisches Jahrbuch für 1854*. BoD–Books on Demand.

Erasmus, N., A. McNeill, M. Mommert, D. E. Trilling, A. A. Sickafoose, and K. Paterson (June 2019). "A Taxonomic Study of Asteroid Families from KMTNET-SAAO Multiband Photometry." In: 242.2, p. 15. DOI: 10.3847/1538-4365/ab1344.

Erasmus, N., A. McNeill, M. Mommert, D. E. Trilling, A. A. Sickafoose, and C. van Gend (July 2018). "Taxonomy and Light-curve Data of 1000 Serendipitously Observed Main-belt Asteroids." In: 237.1, p. 19. DOI: 10.3847/1538-4365/aac38f.

Fang, Linru, Paul Frossard, Maud Boyet, Audrey Bouvier, Jean-Alix Barrat, Marc Chaussidon, and Frederic Moynier (Mar. 2022). "Half-life and initial Solar System abundance of ^{146}Sm determined from the oldest andesitic meteorite." In: *Proceedings of the National Academy of Science* 119.12, e2120933119. DOI: 10.1073/pnas.2120933119.

Feierberg, Michael A, Harold P Larson, and Clark R Chapman (1982). "Spectroscopic evidence for undifferentiated S-type asteroids." In: *Astrophysical Journal, Part 1, vol. 257, June 1, 1982, p. 361-372.* 257, pp. 361–372.

Ferrone, S., M. Delbo, C. Avdellidou, R. Melikyan, A. Morbidelli, K. Walsh, and R. Deienno (Aug. 2023). "Identification of a 4.3 billion year old asteroid family and planetesimal population in the Inner Main Belt." In: *Astronomy & Astrophysics* 676, A5. DOI: 10.1051/0004-6361/202245594.

Fieber-Beyer, Sherry K., Michael J. Gaffey, Michael S. Kelley, Vishnu Reddy, Chalbeth M. Reynolds, and Tony Hicks (June 2011). "The Maria asteroid family: Genetic relationships and a plausible source of mesosiderites near the 3:1 Kirkwood Gap." In: 213.2, pp. 524–537. DOI: 10.1016/j.icarus.2011.03.009.

Fienga, A., C. Avdellidou, and J. Hanuš (Feb. 2020). "Asteroid masses obtained with INPOP planetary ephemerides." In: 492.1, pp. 589–602. DOI: 10.1093/mnras/stz3407.

Forgács-Dajka, E., Zs. Sándor, and J. Sztakovics (Jan. 2022). "A survey on Hungaria asteroids involved in mean motion resonances with Mars." In: *Astronomy & Astrophysics* 657, A135. DOI: 10.1051/0004-6361/202141719.

Fornasier, S., B. E. Clark, E. Dotto, A. Migliorini, M. Ockert-Bell, and M. A. Barucci (Dec. 2010). "Spectroscopic survey of M-type asteroids." In: 210.2, pp. 655–673. DOI: 10.1016/j.icarus.2010.07.001.

Fornasier, S. et al. (Dec. 2020). “Phase reddening on asteroid Bennu from visible and near-infrared spectroscopy.” In: *Astronomy & Astrophysics* 644, A142, A142. DOI: `10.1051/0004-6361/202039552`. arXiv: `2011.09339 [astro-ph.EP]`.

Fu, Roger R., Benjamin P. Weiss, David L. Shuster, Jérôme Gattacceca, Timothy L. Grove, Clément Suavet, Eduardo A. Lima, Luyao Li, and Aaron T. Kuan (Oct. 2012). “An Ancient Core Dynamo in Asteroid Vesta.” In: *Science* 338.6104, p. 238. DOI: `10.1126/science.1225648`.

Fukugita, M., T. Ichikawa, J. E. Gunn, M. Doi, K. Shimasaku, and D. P. Schneider (Apr. 1996). “The Sloan Digital Sky Survey Photometric System.” In: 111, p. 1748. DOI: `10.1086/117915`.

Fulvio, D., R. Brunetto, P. Vernazza, and G. Strazzulla (Jan. 2012). “Space weathering of Vesta and V-type asteroids: new irradiation experiments on HED meteorites.” In: *Astronomy & Astrophysics* 537, p. L11. DOI: `10.1051/0004-6361/201118486`.

Gaffey, M. J. (Feb. 1976). “Spectral reflectance characteristics of the meteorite classes.” In: 81.B5, pp. 905–920. DOI: `10.1029/JB081i005p00905`.

Gaffey, M. J., E. A. Cloutis, M. S. Kelley, and K. L. Reed (2002). “Mineralogy of Asteroids.” In: *Asteroids III*. Ed. by W. F. Bottke Jr., A. Cellino, P. Paolicchi, and R. P. Binzel, pp. 183–204.

Gaffey, Michael J. (Oct. 2010). “Space weathering and the interpretation of asteroid reflectance spectra.” In: 209.2, pp. 564–574. DOI: `10.1016/j.icarus.2010.05.006`.

Gaffey, Michael J. (Sept. 2011). “Mineralogy of Asteroids.” In: *XV Special Courses at the National Observatory of Rio de Janeiro*. Ed. by Eduardo Telles, Renato Dupke, and Daniela Lazzaro. Vol. 1386. American Institute of Physics Conference Series, pp. 129–169. DOI: `10.1063/1.3636041`.

Gaffey, Michael J., Jeffrey F. Bell, R. Hamilton Brown, Thomas H. Burbine, Jennifer L. Piatek, Kevin L. Reed, and Damon A. Chaky (Dec. 1993). “Mineralogical Variations within the S-Type Asteroid Class.” In: 106.2, pp. 573–602. DOI: `10.1006/icar.1993.1194`.

Gaffey, Michael J., Kevin L. Reed, and Michael S. Kelley (Nov. 1992). “Relationship of E-type Apollo asteroid 3103 (1982 BB) to the enstatite achondrite meteorites and the Hungaria asteroids.” In: 100.1, pp. 95–109. DOI: `10.1016/0019-1035(92)90021-X`.

Gaia Collaboration et al. (Nov. 2016). “The Gaia mission.” In: *Astronomy & Astrophysics* 595, A1. DOI: `10.1051/0004-6361/201629272`.

Gaia Collaboration et al. (June 2023). “Gaia Data Release 3. Reflectance spectra of Solar System small bodies.” In: *Astronomy & Astrophysics* 674, A35. DOI: `10.1051/0004-6361/202243791`.

Galinier, M., M. Delbo, C. Avdellidou, and L. Galluccio (Mar. 2024). “Discovery of the first olivine-dominated A-type asteroid family.” In: *Astronomy & Astrophysics* 683, p. L3. DOI: `10.1051/0004-6361/202349057`.

Galinier, M., M. Delbo, C. Avdellidou, L. Galluccio, and Y. Marrocchi (Mar. 2023). “Gaia search for early-formed andesitic asteroidal crusts.” In: *A&A* 671, A40. DOI: `10.1051/0004-6361/202245311`.

Gardiol, D., A. Cellino, and M. Di Martino (Jan. 2016). “PRISMA, Italian network for meteors and atmospheric studies.” In: *International Meteor Conference Egmond, the Netherlands, 2-5 June 2016*. Ed. by A. Roggemans and P. Roggemans, p. 76.

Gartrelle, Gordon M., Paul S. Hardersen, Matthew R. M. Izawa, and Matthew C. Nowinski (July 2021). “Same family, different neighborhoods: Visible near-infrared

(0.7-2.45 µm) spectral distinctions of D-type asteroids at different heliocentric distances." In: 363, p. 114295. DOI: 10.1016/j.icarus.2020.114295.

Gietzen, Katherine M., Claud H. S. Lacy, Daniel R. Ostrowski, and Derek W. G. Sears (Nov. 2012). "IRTF observations of S complex and other asteroids: Implications for surface compositions, the presence of clinopyroxenes, and their relationship to meteorites." In: 47.11, pp. 1789–1808. DOI: 10.1111/maps.12013.

Gill, James B (2012). *Orogenic andesites and plate tectonics*. Vol. 16. Springer Science & Business Media.

Goldstein, J. I., E. R. D. Scott, and N. L. Chabot (Nov. 2009). "Iron meteorites: Crystallization, thermal history, parent bodies, and origin." In: *Chemie der Erde / Geochemistry* 69.4, pp. 293–325. DOI: 10.1016/j.chemer.2009.01.002.

Goodrich, Cyrena A. (Sept. 1992). "Ureilites - A critical review." In: *Meteoritics* 27.4, pp. 327–352.

Gradie, Jonathan C., Clark R. Chapman, and Edward F. Tedesco (Jan. 1989). "Distribution of taxonomic classes and the compositional structure of the asteroid belt." In: *Asteroids II*. Ed. by Richard P. Binzel, Tom Gehrels, and Mildred Shapley Matthews, pp. 316–335.

Granahan, James C., Greg Smith, and Jeffrey F. Bell (Mar. 1993). "New K Type Asteroids." In: *Lunar and Planetary Science Conference*. Lunar and Planetary Science Conference, p. 557.

Granvik, M., A. Morbidelli, R. Jedicke, B. Bolin, W. F. Bottke, E. Beshore, D. Vokrouhlický, M. Delbò, and P. Michel (Feb. 2016). "Super-catastrophic disruption of asteroids at small perihelion distances." In: 530, pp. 303–306. DOI: 10.1038/nature16934.

Greenstreet, Sarah, Henry Ngo, and Brett Gladman (Jan. 2012). "The orbital distribution of Near-Earth Objects inside Earth's orbit." In: 217.1, pp. 355–366. DOI: 10.1016/j.icarus.2011.11.010.

Greenwood, Richard C., Thomas H. Burbine, and Ian A. Franchi (May 2020). "Linking asteroids and meteorites to the primordial planetesimal population." In: 277, pp. 377–406. DOI: 10.1016/j.gca.2020.02.004.

Greenwood, Richard C., Thomas H. Burbine, Martin F. Miller, and Ian. A. Franchi (Apr. 2017). "Melting and differentiation of early-formed asteroids: The perspective from high precision oxygen isotope studies." In: *Chemie der Erde / Geochemistry* 77.1, pp. 1–43. DOI: 10.1016/j.chemer.2016.09.005.

Gulbis, A. A. S. et al. (Apr. 2011). "First Results from the MIT Optical Rapid Imaging System (MORIS) on the IRTF: A Stellar Occultation by Pluto and a Transit by Exoplanet XO-2b." In: 123.902, p. 461. DOI: 10.1086/659636.

Hanuš, J, M Delbo, J Durech, and V Alí-Lagoa (July 2018). "Thermophysical modeling of main-belt asteroids from WISE thermal data." In: *Icarus* 309, pp. 297–337.

Hanuš, J., M. Delbo', J. Ďurech, and V. Alí-Lagoa (Aug. 2015). "Thermophysical modeling of asteroids from WISE thermal infrared data - Significance of the shape model and the pole orientation uncertainties." In: 256, pp. 101–116. DOI: 10.1016/j.icarus.2015.04.014.

Hapke, Bruce (May 2001). "Space weathering from Mercury to the asteroid belt." In: 106.E5, pp. 10039–10074. DOI: 10.1029/2000JE001338.

Hardersen, Paul S., Vishnu Reddy, Edward Cloutis, Matt Nowinski, Margaret Dievendorf, Russell M. Genet, Savan Becker, and Rachel Roberts (2018). "Basalt or Not? Near-infrared Spectra, Surface Mineralogical Estimates, and Meteorite Analogs for 33 Vsubp/sub-type Asteroids." In: *The Astronomical Journal* 156.1, p. 11. DOI: 10.3847/1538-3881/aac3d2. URL: https://doi.org/10.3847/1538-3881/aac3d2.

Harris, Alan W. and Line Drube (Apr. 2014). "How to Find Metal-rich Asteroids." In: 785.1, p. L4. DOI: 10.1088/2041-8205/785/1/L4.

Hasegawa, Sunao, Michal Marsset, Francesca E. DeMeo, Schelte J. Bus, Jooyeon Geem, Masateru Ishiguro, Myungshin Im, Daisuke Kuroda, and Pierre Vernazza (July 2021). "Discovery of Two TNO-like Bodies in the Asteroid Belt." In: 916.1, p. L6. DOI: 10.3847/2041-8213/ac0f05.

Hasegawa, Sunao et al. (Nov. 2022). "Spectral Evolution of Dark Asteroid Surfaces Induced by Space Weathering over a Decade." In: 939.1, p. L9. DOI: 10.3847/2041-8213/ac92e4.

Henrard, J. and A. Lemaitre (Sept. 1983). "A mechanism of formation for the Kirkwood gaps." In: 55.3, pp. 482–494. DOI: 10.1016/0019-1035(83)90117-3.

Herschel, William (1832). "Observations on the two lately discovered celestial bodies." In: *Abstracts of the Papers Printed in the Philosophical Transactions of the Royal Society of London*. 1. The Royal Society London, pp. 80–82.

Hilton, James L (2007). "When did the asteroids become minor planets?" In: *US Naval Observatory. Retrieved on*, pp. 04–08.

Hiroi, T., S. Sasaki, T. Misu, and T. Nakamura (Mar. 2013). "Keys to Detect Space Weathering on Vesta: Changes of Visible and Near-Infrared Reflectance Spectra of HEDs and Carbonaceous Chondrites." In: *44th Annual Lunar and Planetary Science Conference*. Lunar and Planetary Science Conference, p. 1276.

Hiroi, Takahiro, Faith Vilas, and Jessica M. Sunshine (Jan. 1996). "Discovery and Analysis of Minor Absorption Bands in S-Asteroid Visible Reflectance Spectra." In: 119.1, pp. 202–208. DOI: 10.1006/icar.1996.0012.

Hyodo, Ryuki and Hidenori Genda (Apr. 2018). "Implantation of Martian Materials in the Inner Solar System by a Mega Impact on Mars." In: 856.2, p. L36. DOI: 10.3847/2041-8213/aab7f0.

Ivezic, Zeljko, M. Juric, Robert H. Lupton, S. Tabachnik, and T. Quinn (Dec. 2002). "Asteroids Observed by The Sloan Digital Sky Survey." In: *Survey and Other Telescope Technologies and Discoveries*. Ed. by J. Anthony Tyson and Sidney Wolff. Vol. 4836. Society of Photo-Optical Instrumentation Engineers (SPIE) Conference Series, pp. 98–103. DOI: 10.1117/12.457304.

Ivezić, Željko et al. (Nov. 2001). "Solar System Objects Observed in the Sloan Digital Sky Survey Commissioning Data." In: 122.5, pp. 2749–2784. DOI: 10.1086/323452.

Jasmim, F. L., D. Lazzaro, J. M. F. Carvano, T. Mothé-Diniz, and P. H. Hasselmann (Apr. 2013). "Mineralogical investigation of several Q_p asteroids and their relation to the Vesta family." In: *Astronomy & Astrophysics* 552, A85. DOI: 10.1051/0004-6361/201220494.

Javoy, M. et al. (May 2010). "The chemical composition of the Earth: Enstatite chondrite models." In: *Earth and Planetary Science Letters* 293.3-4, pp. 259–268. DOI: 10.1016/j.epsl.2010.02.033.

Johnson, Torrence V. and Fraser P. Fanale (Jan. 1973). "Optical Properties of Carbonaceous Chondrites and Their Relationship to Asteroids." In: 78.35, pp. 8507–8518. DOI: 10.1029/JB078i035p08507.

Jordi, C., M. Gebran, J. M. Carrasco, J. de Bruijne, H. Voss, C. Fabricius, J. Knude, A. Vallenari, R. Kohley, and A. Mora (Nov. 2010). "Gaia broad band photometry." In: *Astronomy & Astrophysics* 523, A48. DOI: 10.1051/0004-6361/201015441.

Jurić, Mario et al. (Sept. 2002). "Comparison of Positions and Magnitudes of Asteroids Observed in the Sloan Digital Sky Survey with Those Predicted for Known Asteroids." In: 124.3, pp. 1776–1787. DOI: 10.1086/341950.

Keil, Klaus (Sept. 2012). "Angrites, a small but diverse suite of ancient, silica-undersaturated volcanic-plutonic mafic meteorites, and the history of their parent asteroid." In: *Chemie der Erde / Geochemistry* 72.3, pp. 191–218. DOI: 10.1016/j.chemer.2012.06.002.

Keil, Klaus (Oct. 2014). "Brachinite meteorites: Partial melt residues from an FeO-rich asteroid." In: *Chemie der Erde / Geochemistry* 74.3, pp. 311–329. DOI: 10.1016/j.chemer.2014.02.001.

Keil, Klaus and Timothy J. McCoy (May 2018). "Acapulcoite-lodranite meteorites: Ultramafic asteroidal partial melt residues." In: *Chemie der Erde / Geochemistry* 78.2, pp. 153–203. DOI: 10.1016/j.chemer.2017.04.004.

Kirkwood, Daniel (Apr. 1891). "On the Origin of Gaps in the Zone of Asteroids." In: *Sidereal Messenger* 10, pp. 194–196.

Kita, Noriko T. and Takayuki Ushikubo (July 2012). "Evolution of protoplanetary disk inferred from ^{26}Al chronology of individual chondrules." In: 47.7, pp. 1108–1119. DOI: 10.1111/j.1945-5100.2011.01264.x.

Kitazato, K. et al. (Jan. 2021). "Thermally altered subsurface material of asteroid (162173) Ryugu." In: *Nature Astronomy* 5, pp. 246–250. DOI: 10.1038/s41550-020-01271-2.

Klahr, Hubert and Andreas Schreiber (2015). "Linking the Origin of Asteroids to Planetesimal Formation in the Solar Nebula." In: *Proceedings of the International Astronomical Union* 10.S318, 1–8. DOI: 10.1017/S1743921315010406.

Klahr, Hubert and Andreas Schreiber (Sept. 2020). "Turbulence Sets the Length Scale for Planetesimal Formation: Local 2D Simulations of Streaming Instability and Planetesimal Formation." In: *The Astrophysical Journal* 901.1, p. 54. DOI: 10.3847/1538-4357/abac58.

Kleine, Thorsten, Ulrik Hans, Anthony J. Irving, and Bernard Bourdon (May 2012). "Chronology of the angrite parent body and implications for core formation in protoplanets." In: 84, pp. 186–203. DOI: 10.1016/j.gca.2012.01.032.

Knežević, Z. and A. Milani (June 2003). "Proper element catalogs and asteroid families." In: *Astronomy & Astrophysics* 403, pp. 1165–1173. DOI: 10.1051/0004-6361:20030475.

Kohley, Ralf, Philippe Garé, Cyril Vétel, Denis Marchais, and François Chassat (Sept. 2012). "Gaia's FPA: sampling the sky in silicon." In: *Space Telescopes and Instrumentation 2012: Optical, Infrared, and Millimeter Wave*. Ed. by Mark C. Clampin, Giovanni G. Fazio, Howard A. MacEwen, and Jr. Oschmann Jacobus M. Vol. 8442. Society of Photo-Optical Instrumentation Engineers (SPIE) Conference Series, 84421P. DOI: 10.1117/12.926144.

Kokubo, Eiichiro and Shigeru Ida (Jan. 2000). "Formation of Protoplanets from Planetesimals in the Solar Nebula." In: 143.1, pp. 15–27. DOI: 10.1006/icar.1999.6237.

Krestianinov, Evgenii et al. (Aug. 2023). "Igneous meteorites suggest Aluminium-26 heterogeneity in the early Solar Nebula." In: *Nature Communications* 14, 4940, p. 4940. DOI: 10.1038/s41467-023-40026-1.

Kruijer, T. S., T. Kleine, C. Burkhardt, and G. Budde (Mar. 2017). "Dating the Formation of Jupiter through W and Mo Isotope Analyses of Meteorites." In: *48th Annual Lunar and Planetary Science Conference*. Lunar and Planetary Science Conference, p. 1386.

Kryszczyńska, A. (Mar. 2013). "Do Slivan states exist in the Flora family? . II. Fingerprints of the Yarkovsky and YORP effects." In: *Astronomy & Astrophysics* 551, A102. DOI: 10.1051/0004-6361/201220490.

La Spina, A., P. Paolicchi, A. Kryszczyńska, and P. Pravec (Mar. 2004). "Retrograde spins of near-Earth asteroids from the Yarkovsky effect." In: 428.6981, pp. 400–401. DOI: 10.1038/nature02411.

Lantz, C., R. Brunetto, M. A. Barucci, S. Fornasier, D. Baklouti, J. Bourçois, and M. Godard (Mar. 2017). "Ion irradiation of carbonaceous chondrites: A new view of space weathering on primitive asteroids." In: 285, pp. 43–57. DOI: 10.1016/j.icarus.2016.12.019.

Lazzarin, M., S. Marchi, M. A. Barucci, M. Di Martino, and C. Barbieri (June 2004). "Visible and near-infrared spectroscopic investigation of near-Earth objects at ESO: first results." In: 169.2, pp. 373–384. DOI: 10.1016/j.icarus.2003.12.023.

Lazzarin, M., S. Marchi, S. Magrin, and J. Licandro (June 2005). "Spectroscopic investigation of near-Earth objects at Telescopio Nazionale Galileo." In: 359.4, pp. 1575–1582. DOI: 10.1111/j.1365-2966.2005.09006.x.

Lazzarin, M., S. Marchi, L. V. Moroz, R. Brunetto, S. Magrin, P. Paolicchi, and G. Strazzulla (Aug. 2006). "Space Weathering in the Main Asteroid Belt: The Big Picture." In: 647.2, pp. L179–L182. DOI: 10.1086/507448.

Lazzaro, D., C. A. Angeli, J. M. Carvano, T. Mothé-Diniz, R. Duffard, and M. Florczak (Nov. 2004). "S ^{3}OS ^{2}: the visible spectroscopic survey of 820 asteroids." In: 172.1, pp. 179–220. DOI: 10.1016/j.icarus.2004.06.006.

Leith, Thomas B., Nicholas A. Moskovitz, Rhiannon G. Mayne, Francesca E. DeMeo, Driss Takir, Brian J. Burt, Richard P. Binzel, and Dimitra Pefkou (Oct. 2017). "The compositional diversity of non-Vesta basaltic asteroids." In: 295, pp. 61–73. DOI: 10.1016/j.icarus.2017.05.007.

Li, Jian-Yang et al. (Nov. 2013). "Global photometric properties of Asteroid (4) Vesta observed with Dawn Framing Camera." In: 226.2, pp. 1252–1274. DOI: 10.1016/j.icarus.2013.08.011.

Licandro, J., A. Alvarez-Candal, J. de León, N. Pinilla-Alonso, D. Lazzaro, and H. Campins (Apr. 2008b). "Spectral properties of asteroids in cometary orbits." In: *Astronomy & Astrophysics* 481.3, pp. 861–877. DOI: 10.1051/0004-6361:20078340.

Licandro, J., A. Alvarez-Candal, J. de León, N. Pinilla-Alonso, D. Lazzaro, and H. Campins (Sept. 2008a). "Spectral properties of asteroids in cometary orbits." In: *Astronomy & Astrophysics* 487.3, pp. 1195–1196. DOI: 10.1051/0004-6361:20078340e.

Lindegren, L. et al. (Aug. 2018). "Gaia Data Release 2. The astrometric solution." In: *Astronomy & Astrophysics* 616, A2. DOI: 10.1051/0004-6361/201832727.

Lindsay, S. S., F. Marchis, J. P. Emery, J. E. Enriquez, and M. Assafin (Feb. 2015). "Composition, mineralogy, and porosity of multiple asteroid systems from visible and near-infrared spectral data." In: 247, pp. 53–70. DOI: 10.1016/j.icarus.2014.08.040.

Lucas, M. P., J. P. Emery, N. Pinilla-Alonso, S. S. Lindsay, and V. Lorenzi (July 2017). "Hungaria asteroid region telescopic spectral survey (HARTSS) I: Stony asteroids abundant in the Hungaria background population." In: 291, pp. 268–287. DOI: 10.1016/j.icarus.2016.11.002.

Lucas, Michael P., Joshua P. Emery, Eric M. MacLennan, Noemi Pinilla-Alonso, Richard J. Cartwright, Sean S. Lindsay, Vishnu Reddy, Juan A. Sanchez, Cristina A. Thomas, and Vania Lorenzi (Apr. 2019). "Hungaria asteroid region telescopic spectral survey (HARTSS) II: Spectral homogeneity among Hungaria family asteroids." In: 322, pp. 227–250. DOI: 10.1016/j.icarus.2018.12.010.

Lucey, P. G., J. L. Hinrichs, and M. S. Robinson (Mar. 1998). "Dependence of Spectral Properties of Olivine and Pyroxene on Temperature: Implications for NEAR Observations of Eros." In: *Lunar and Planetary Science Conference*. Lunar and Planetary Science Conference, p. 1357.

Lupishko, D. F. and I. N. Belskaya (Apr. 1989). "On the surface composition of the M-type asteroids." In: 78.2, pp. 395–401. DOI: 10.1016/0019-1035(89)90186-3.

MacLennan, Eric M., Joshua P. Emery, Michael P. Lucas, Lucas M. MCClure, and Sean S. Lindsay (June 2024). "Space weathering, grain size, and metamorphic heating effects on ordinary chondrite spectral reflectance parameters." In: 59.6, pp. 1329–1352. DOI: 10.1111/maps.14150.

Mahlke, M., B. Carry, and P. A. Mattei (Sept. 2022). "Asteroid taxonomy from cluster analysis of spectrometry and albedo." In: *Astronomy & Astrophysics* 665, A26. DOI: 10.1051/0004-6361/202243587.

Mahlke, M., J. Eschrig, B. Carry, L. Bonal, and P. Beck (Aug. 2023). "Spectral analogues of Barbarian asteroids among CO and CV chondrites." In: *Astronomy & Astrophysics* 676, A94. DOI: 10.1051/0004-6361/202346032.

Mainprice, David, Andréa Tommasi, Hélène Couvy, Patrick Cordier, and Daniel J. Frost (Feb. 2005). "Pressure sensitivity of olivine slip systems and seismic anisotropy of Earth's upper mantle." In: 433.7027, pp. 731–733. DOI: 10.1038/nature03266.

Mansour, J. A., M. Popescu, J. de León, and J. Licandro (Feb. 2020). "Distribution and spectrophotometric classification of basaltic asteroids." In: 491.4, pp. 5966–5979. DOI: 10.1093/mnras/stz3284.

Marchi, S., R. Brunetto, S. Magrin, M. Lazzarin, and D. Gandolfi (Dec. 2005a). "Space weathering of near-Earth and main belt silicate-rich asteroids: observations and ion irradiation experiments." In: *Astronomy & Astrophysics* 443.3, pp. 769–775. DOI: 10.1051/0004-6361:20053525.

Marchi, S., M. C. De Sanctis, M. Lazzarin, and S. Magrin (Oct. 2010). "On the Puzzle of Space Weathering Alteration of Basaltic Asteroids." In: 721.2, pp. L172–L176. DOI: 10.1088/2041-8205/721/2/L172.

Marchi, S., M. Lazzarin, P. Paolicchi, and S. Magrin (May 2005b). "New V-type asteroids in near-Earth space." In: 175.1, pp. 170–174. DOI: 10.1016/j.icarus.2004.11.015.

Marchi, S. et al. (May 2012). "The Violent Collisional History of Asteroid 4 Vesta." In: *Science* 336.6082, p. 690. DOI: 10.1126/science.1218757.

Marsset, Michaël et al. (Apr. 2020). "Twenty Years of SpeX: Accuracy Limits of Spectral Slope Measurements in Asteroid Spectroscopy." In: 247.2, p. 73. DOI: 10.3847/1538-4365/ab7b5f.

Masiero, J. R. et al. (Nov. 2011). "Main Belt Asteroids with WISE/NEOWISE. I. Preliminary Albedos and Diameters." In: *ApJ* 741, p. 68. DOI: 10.1088/0004-637X/741/2/68.

Matlovič, Pavol, Julia de Leon, Hissa Medeiros, Marcel Popescu, Juan Luis Rizos, and Jad-Alexandru Mansour (Nov. 2020). "Spectral characterisation of 14 V-type candidate asteroids from the MOVIS catalogue." In: *Astronomy & Astrophysics* 643, A107. DOI: 10.1051/0004-6361/202039263.

McConnell Robert K., Jr., Leslie A. McClaine, D. William Lee, James R. Aronson, and Ronald V. Allen (Jan. 1967). "A Model for Planetary Idneous Differentiation." In: *Reviews of Geophysics and Space Physics* 5, pp. 121–172. DOI: 10.1029/RG005i002p00121.

McCord, T. B., J. B. Adams, and T. V. Johnson (June 1970). "Asteroid Vesta: Spectral Reflectivity and Compositional Implications." In: *Science* 168, p. 1445. DOI: 10.1126/science.168.3938.1445.

McEachern, Firth M., Matija Ćuk, and Sarah T. Stewart (Dec. 2010). "Dynamical evolution of the Hungaria asteroids." In: 210.2, pp. 644–654. DOI: 10.1016/j.icarus.2010.08.003.

McSween, Harry Y. et al. (Nov. 2013). "Dawn; the Vesta-HED connection; and the geologic context for eucrites, diogenites, and howardites." In: 48.11, pp. 2090–2104. DOI: 10.1111/maps.12108.

Medeiros, H., J. de León, D. Lazzaro, M. Popescu, V. Lorenzi, N. Pinilla-Alonso, Z. Landsman, J. L. Rizos, and D. Morate (Sept. 2019). "Compositional characterization of V-type candidate asteroids identified using the MOVIS catalogue." In: 488.3, pp. 3866–3875. DOI: 10.1093/mnras/stz2001.

Michel, Patrick, Willy Benz, and Derek C. Richardson (Oct. 2004a). "Catastrophic disruption of asteroids and family formation: a review of numerical simulations including both fragmentation and gravitational reaccumulations." In: 52.12, pp. 1109–1117. DOI: 10.1016/j.pss.2004.07.008.

Michel, Patrick, Willy Benz, and Derek C. Richardson (Apr. 2004b). "Catastrophic disruption of pre-shattered parent bodies." In: 168.2, pp. 420–432. DOI: 10.1016/j.icarus.2003.12.011.

Michel, Patrick, Fabbio Migliorini, Alessandro Morbidelli, and Vincenzo Zappalà (June 2000). "The Population of Mars-Crossers: Classification and Dynamical Evolution." In: 145.2, pp. 332–347. DOI: 10.1006/icar.2000.6358.

Migliorini, Alessandra, M. C. De Sanctis, D. Lazzaro, and E. Ammannito (Jan. 2017). "Spectral characterization of V-type asteroids outside the Vesta family." In: 464.2, pp. 1718–1726. DOI: 10.1093/mnras/stw2441.

Migliorini, Alessandra, M. C. De Sanctis, D. Lazzaro, and E. Ammannito (Mar. 2018). "Spectroscopy of five V-type asteroids in the middle and outer main belt." In: 475.1, pp. 353–358. DOI: 10.1093/mnras/stx3193.

Migliorini, Alessandra, M. C. De Sanctis, T. A. Michtchenko, D. Lazzaro, M. Barbieri, D. Mesa, M. Lazzarin, and F. La Forgia (June 2021). "Characterization of V-type asteroids orbiting in the middle and outer main belt." In: 504.2, pp. 2019–2032. DOI: 10.1093/mnras/stab332.

Migliorini, F., A. Morbidelli, V. Zappala, B. J. Gladman, M. E. Bailey, and A. Cellino (Nov. 1997). "Vesta fragments from v6 and 3:1 resonances: Implications for V-type NEAs and HED meteorites." In: 32.6, pp. 903–916. DOI: 10.1111/j.1945-5100.1997.tb01580.x.

Migliorini, F., V. Zappalà, R. Vio, and A. Cellino (Dec. 1995). "Interlopers within asteroid families." In: 118.2, pp. 271–291. DOI: 10.1006/icar.1995.1191.

Milani, A., A. Cellino, Z. Knežević, B. Novaković, F. Spoto, and P. Paolicchi (Sept. 2014). "Asteroid families classification: Exploiting very large datasets." In: *Icarus* 239, p. 46. DOI: 10.1016/j.icarus.2014.05.039.

Montegriffo, P. et al. (June 2023). "Gaia Data Release 3. External calibration of BP/RP low-resolution spectroscopic data." In: *Astronomy & Astrophysics* 674, A3. DOI: 10.1051/0004-6361/202243880.

Morate, David, Julia de León, Mário De Prá, Javier Licandro, Antonio Cabrera-Lavers, Humberto Campins, and Noemí Pinilla-Alonso (Feb. 2018). "Visible spectroscopy of the Sulamitis and Clarissa primitive families: a possible link to Erigone and Polana." In: *Astronomy & Astrophysics* 610, A25. DOI: 10.1051/0004-6361/201731407.

Morate, David, Julia de León, Mário De Prá, Javier Licandro, Antonio Cabrera-Lavers, Humberto Campins, Noemí Pinilla-Alonso, and Víctor Alí-Lagoa (Feb. 2016). "Compositional study of asteroids in the Erigone collisional family using visible spectroscopy at the 10.4 m GTC." In: *Astronomy & Astrophysics* 586, A129. DOI: 10.1051/0004-6361/201527453.

Morate, David, Julia de León, Mário De Prá, Javier Licandro, Noemí Pinilla-Alonso, Humberto Campins, Anicia Arredondo, Jorge Marcio Carvano, Daniela Lazzaro, and Antonio Cabrera-Lavers (Oct. 2019). "The last pieces of the primitive inner belt puzzle: Klio, Chaldaea, Chimaera, and Svea." In: *Astronomy & Astrophysics* 630, A141. DOI: 10.1051/0004-6361/201935992.

Morbidelli, A., K. Baillié, K. Batygin, S. Charnoz, T. Guillot, D. C. Rubie, and T. Kleine (Jan. 2022). "Contemporary formation of early Solar System planetesimals at two distinct radial locations." In: *Nature Astronomy* 6, pp. 72–79. DOI: 10.1038/s41550-021-01517-7.

Morbidelli, A., B. Bitsch, A. Crida, M. Gounelle, T. Guillot, S. Jacobson, A. Johansen, M. Lambrechts, and E. Lega (Mar. 2016). "Fossilized condensation lines in the Solar System protoplanetary disk." In: 267, pp. 368–376. DOI: 10.1016/j.icarus.2015.11.027.

Morbidelli, A., R. Jedicke, W. F. Bottke, P. Michel, and E. F. Tedesco (Aug. 2002). "From Magnitudes to Diameters: The Albedo Distribution of Near Earth Objects and the Earth Collision Hazard." In: *Icarus* 158, p. 329. DOI: 10.1006/icar.2002.6887.

Morbidelli, A., H. F. Levison, K. Tsiganis, and R. Gomes (May 2005). "Chaotic capture of Jupiter's Trojan asteroids in the early Solar System." In: 435.7041, pp. 462–465. DOI: 10.1038/nature03540.

Morbidelli, Alessandro, William F. Bottke, David Nesvorný, and Harold F. Levison (Dec. 2009). "Asteroids were born big." In: 204.2, pp. 558–573. DOI: 10.1016/j.icarus.2009.07.011.

Morbidelli, Alessandro and Jacques Henrard (June 1991). "Secular Resonances in the Asteroid Belt - Theoretical Perturbation Approach and the Problem of Their Location." In: *Celestial Mechanics and Dynamical Astronomy* 51.2, pp. 131–167. DOI: 10.1007/BF00048606.

Morrison, D. (June 1977). "Asteriod Sizes and Albedos." In: 31.2, pp. 185–220. DOI: 10.1016/0019-1035(77)90034-3.

Moskovitz, Nicholas A., Robert Jedicke, Eric Gaidos, Mark Willman, David Nesvorný, Ronald Fevig, and Željko Ivezić (Nov. 2008). "The distribution of basaltic asteroids in the Main Belt." In: 198.1, pp. 77–90. DOI: 10.1016/j.icarus.2008.07.006.

Moskovitz, Nicholas A., Mark Willman, Thomas H. Burbine, Richard P. Binzel, and Schelte J. Bus (Aug. 2010). "A spectroscopic comparison of HED meteorites and V-type asteroids in the inner Main Belt." In: 208.2, pp. 773–788. DOI: 10.1016/j.icarus.2010.03.002.

Moskovitz, Nicholas and Eric Gaidos (June 2011). "Differentiation of planetesimals and the thermal consequences of melt migration." In: 46.6, pp. 903–918. DOI: 10.1111/j.1945-5100.2011.01201.x. arXiv: 1101.4165 [astro-ph.EP].

Mothé-Diniz, T., J. M. Carvano, S. J. Bus, R. Duffard, and T. H. Burbine (May 2008a). "Mineralogical analysis of the Eos family from near-infrared spectra." In: 195.1, pp. 277–294. DOI: 10.1016/j.icarus.2007.12.005.

Mothé-Diniz, T., J. M. Carvano, S. J. Bus, R. Duffard, and T. H. Burbine (May 2008b). "Mineralogical analysis of the Eos family from near-infrared spectra." In: 195.1, pp. 277–294. DOI: 10.1016/j.icarus.2007.12.005.

Mothé-Diniz, T. and D. Nesvorný (Aug. 2008). "Visible spectroscopy of extremely young asteroid families." In: *Astronomy & Astrophysics* 486.2, pp. L9–L12. DOI: 10.1051/0004-6361:200809934.

Mothé-Diniz, T., F. Roig, and J. M. Carvano (Mar. 2005a). "Reanalysis of asteroid families structure through visible spectroscopy." In: 174.1, pp. 54–80. DOI: 10.1016/j.icarus.2004.10.002.

Mothé-Diniz, T., F. Roig, and J. M. Carvano (Mar. 2005b). "Reanalysis of asteroid families structure through visible spectroscopy." In: 174.1, pp. 54–80. DOI: 10.1016/j.icarus.2004.10.002.

Mustard, John F. and John E. Hays (Jan. 1997). "Effects of Hyperfine Particles on Reflectance Spectra from 0.3 to 25 μm." In: 125.1, pp. 145–163. DOI: 10.1006/icar.1996.5583.

Nesvorný, D., M. Brož, and V. Carruba (2015). "Identification and Dynamical Properties of Asteroid Families." In: *Asteroids IV*, pp. 297–321. DOI: 10.2458/azu_uapress_9780816532131-ch016.

Nesvorny, D., M. Broz, and V. Carruba (2015). "Identification and Dynamical Properties of Asteroid Families." In: *in Asteroids IV (P. Michel, et al. eds)*. Ed. by P. Michel, F. E. DeMeo, and W. F. Bottke, pp. 297–321. DOI: 10.2458/azu_uapress_9780816532131-ch016.

Nesvorný, D., A. Morbidelli, D. Vokrouhlický, W. F. Bottke, and M. Brož (May 2002). "The Flora Family: A Case of the Dynamically Dispersed Collisional Swarm?" In: 157.1, pp. 155–172. DOI: 10.1006/icar.2002.6830.

Nesvorný, David, William F. Bottke, David Vokrouhlický, Alessandro Morbidelli, and Robert Jedicke (2005). "Asteroid families." In: *Proceedings of the International Astronomical Union* 1.S229, 289–299. DOI: 10.1017/S1743921305006800.

Neumann, W., D. Breuer, and T. Spohn (July 2012). "Differentiation and core formation in accreting planetesimals." In: *Astronomy & Astrophysics* 543, A141. DOI: 10.1051/0004-6361/201219157.

Neumann, Wladimir, Robert Luther, Mario Trieloff, Philip M. Reger, and Audrey Bouvier (Oct. 2023). "Fitting Thermal Evolution Models to the Chronological Record of Erg Chech 002 and Modeling the Ejection Conditions of the Meteorite." In: 4.10, 196, p. 196. DOI: 10.3847/PSJ/acf465.

Nicklas, R. W., J. M. D. Day, K. G. Gardner-Vandy, and A. Udry (Mar. 2021). "Multi-Stage Differentiation History of Andesitic Achondrite Erg Chech 002." In: *52nd Lunar and Planetary Science Conference*. Lunar and Planetary Science Conference, p. 1074.

Novaković, Bojan, Alberto Cellino, and Zoran Knežević (Nov. 2011). "Families among high-inclination asteroids." In: 216.1, pp. 69–81. DOI: 10.1016/j.icarus.2011.08.016.

Novaković, Bojan, David Vokrouhlický, Federica Spoto, and David Nesvorný (Aug. 2022). "Asteroid families: properties, recent advances, and future opportunities."

In: *Celestial Mechanics and Dynamical Astronomy* 134.4, p. 34. DOI: `10.1007/s10569-022-10091-7`.

O'Brien, David P. and Richard Greenberg (Nov. 2005). "The collisional and dynamical evolution of the main-belt and NEA size distributions." In: 178.1, pp. 179–212. DOI: `10.1016/j.icarus.2005.04.001`.

Oszkiewicz, D. A., P. Kankiewicz, I. Włodarczyk, and A. Kryszczyńska (Dec. 2015). "Differentiation signatures in the Flora region." In: *Astronomy & Astrophysics* 584, A18. DOI: `10.1051/0004-6361/201526219`.

Oszkiewicz, D. A., T. Kwiatkowski, T. Tomov, M. Birlan, S. Geier, A. Penttilä, and M. Polińska (Dec. 2014). "Selecting asteroids for a targeted spectroscopic survey." In: *Astronomy & Astrophysics* 572, A29. DOI: `10.1051/0004-6361/201323250`.

Oszkiewicz, Dagmara, Hanna Klimczak, Benoit Carry, Antti Penttilä, Marcel Popescu, Joachim Krüger, and Marcelo Aron Keniger (Feb. 2023). "Spectral analysis of basaltic asteroids observed by the Gaia space mission." In: 519.2, pp. 2917–2928. DOI: `10.1093/mnras/stac3442`.

Overholt, Andrew C. and Adrian L. Melott (Sept. 2013). "Cosmogenic nuclide enhancement via deposition from long-period comets as a test of the Younger Dryas impact hypothesis." In: *Earth and Planetary Science Letters* 377, pp. 55–61. DOI: `10.1016/j.epsl.2013.07.029`.

Palomba, E. et al. (Sept. 2014). "Composition and mineralogy of dark material units on Vesta." In: *Icarus* 240, p. 58. DOI: `10.1016/j.icarus.2014.04.040`.

Papike, J. J., J. M. Karner, C. K. Shearer, and P. V. Burger (Dec. 2009). "Silicate mineralogy of martian meteorites." In: 73.24, pp. 7443–7485. DOI: `10.1016/j.gca.2009.09.008`.

Parker, A., Ž. Ivezić, M. Jurić, R. Lupton, M. D. Sekora, and A. Kowalski (Nov. 2008). "The size distributions of asteroid families in the SDSS Moving Object Catalog 4." In: 198.1, pp. 138–155. DOI: `10.1016/j.icarus.2008.07.002`.

Pentikäinen, Hanna, Antti Penttilä, Karri Muinonen, and Jouni Peltoniemi (Oct. 2014). "Spectroscopic investigations of meteorites." In: 146, pp. 391–401. DOI: `10.1016/j.jqsrt.2014.02.007`.

Perna, D., M. A. Barucci, M. Fulchignoni, M. Popescu, I. Belskaya, S. Fornasier, A. Doressoundiram, C. Lantz, and F. Merlin (Aug. 2018). "A spectroscopic survey of the small near-Earth asteroid population: Peculiar taxonomic distribution and phase reddening." In: 157, pp. 82–95. DOI: `10.1016/j.pss.2018.03.008`.

Perryman, Michael AC (2009). *Astronomical applications of astrometry: ten years of exploitation of the Hipparcos satellite data*. Cambridge University Press.

Piazzi, Giuseppe (1801). *Risultati delle osservazioni della nuova stella scoperta il di'I. gennajo all'Osservatorio reale di Palermo*.

Pieters, C. M. et al. (Nov. 2012). "Distinctive space weathering on Vesta from regolith mixing processes." In: 491.7422, pp. 79–82. DOI: `10.1038/nature11534`.

Pieters, Carle M. and Sarah K. Noble (Oct. 2016). "Space weathering on airless bodies." In: *Journal of Geophysical Research (Planets)* 121.10, pp. 1865–1884. DOI: `10.1002/2016JE005128`.

Pieters, Carlé M., Larry A. Taylor, Sarah K. Noble, Lindsay P. Keller, Bruce Hapke, Richard V. Morris, Carl C. Allen, David S. McKay, and Susan Wentworth (Sept. 2000). "Space weathering on airless bodies: Resolving a mystery with lunar samples." In: 35.5, pp. 1101–1107. DOI: `10.1111/j.1945-5100.2000.tb01496.x`.

Piralla, Maxime, Johan Villeneuve, Nicolas Schnuriger, David V. Bekaert, and Yves Marrocchi (Apr. 2023). "A unified chronology of dust formation in the early solar system." In: 394, 115427, p. 115427. DOI: 10.1016/j.icarus.2023.115427.

Pitjeva, EV and NP Pitjev (2018). "Masses of the Main Asteroid Belt and the Kuiper Belt from the motions of planets and spacecraft." In: *Astronomy Letters* 44, pp. 554–566.

Polishook, D., S. A. Jacobson, A. Morbidelli, and O. Aharonson (Aug. 2017). "A Martian origin for the Mars Trojan asteroids." In: *Nature Astronomy* 1, p. 0179. DOI: 10.1038/s41550-017-0179.

Popescu, M., M. Birlan, and D. A. Nedelcu (Aug. 2012). "Modeling of asteroid spectra - M4AST." In: *Astronomy & Astrophysics* 544, A130. DOI: 10.1051/0004-6361/201219584.

Popescu, M., M. Birlan, D. A. Nedelcu, J. Vaubaillon, and C. P. Cristescu (Dec. 2014a). "Spectral properties of the largest asteroids associated with Taurid Complex." In: *Astronomy & Astrophysics* 572, A106. DOI: 10.1051/0004-6361/201424064.

Popescu, M., M. Birlan, D. A. Nedelcu, J. Vaubaillon, and C. P. Cristescu (Dec. 2014b). "Spectral properties of the largest asteroids associated with Taurid Complex." In: *Astronomy & Astrophysics* 572, A106. DOI: 10.1051/0004-6361/201424064.

Popescu, M., J. Licandro, J. M. Carvano, R. Stoicescu, J. de León, D. Morate, I. L. Boacă, and C. P. Cristescu (Sept. 2018a). "Taxonomic classification of asteroids based on MOVIS near-infrared colors." In: *Astronomy & Astrophysics* 617, A12. DOI: 10.1051/0004-6361/201833023.

Popescu, M., J. Licandro, D. Morate, J. de León, D. A. Nedelcu, R. Rebolo, R. G. McMahon, E. Gonzalez-Solares, and M. Irwin (June 2016). "Near-infrared colors of minor planets recovered from VISTA-VHS survey (MOVIS)." In: *Astronomy & Astrophysics* 591, A115. DOI: 10.1051/0004-6361/201628163.

Popescu, M. et al. (July 2019). "Near-Earth asteroids spectroscopic survey at Isaac Newton Telescope." In: *Astronomy & Astrophysics* 627, A124. DOI: 10.1051/0004-6361/201935006.

Popescu, Marcel, D. Perna, M. A. Barucci, S. Fornasier, A. Doressoundiram, C. Lantz, F. Merlin, I. N. Belskaya, and M. Fulchignoni (June 2018b). "Olivine-rich asteroids in the near-Earth space." In: 477.2, pp. 2786–2795. DOI: 10.1093/mnras/sty704.

Press, William H., Brian P. Flannery, and Saul A. Teukolsky (1986). *Numerical recipes. The art of scientific computing*.

Raymond, Sean N. and Andre Izidoro (Sept. 2017). "The empty primordial asteroid belt." In: *Science Advances* 3.9, e1701138. DOI: 10.1126/sciadv.1701138.

Rayner, J. T., D. W. Toomey, P. M. Onaka, A. J. Denault, W. E. Stahlberger, W. D. Vacca, M. C. Cushing, and S. Wang (Mar. 2003). "SpeX: A Medium-Resolution 0.8-5.5 Micron Spectrograph and Imager for the NASA Infrared Telescope Facility." In: 115.805, pp. 362–382. DOI: 10.1086/367745.

Recio-Blanco, A., P. de Laverny, C. Allende Prieto, D. Fustes, M. Manteiga, B. Arcay, A. Bijaoui, C. Dafonte, C. Ordenovic, and D. Ordoñez Blanco (Jan. 2016). "Stellar parametrization from Gaia RVS spectra." In: *Astronomy & Astrophysics* 585, A93. DOI: 10.1051/0004-6361/201425030.

Reddy, V., T. L. Dunn, C. A. Thomas, N. A. Moskovitz, and T. H. Burbine (2015). "Mineralogy and Surface Composition of Asteroids." In: *in Asteroids IV (P. Michel, et al. eds)*. Ed. by P. Michel, F. E. DeMeo, and W. F. Bottke, pp. 43–63. DOI: 10.2458/azu_uapress_9780816532131-ch003.

Reddy, V., J. P. Emery, M. J. Gaffey, W. F. Bottke, A. Cramer, and M. S. Kelley (Jan. 2009). "Composition of 298 Baptistina: Implications for the K/T impactor link." In: 44.12, pp. 1917–1927. DOI: 10.1111/j.1945-5100.2009.tb02001.x.

Reger, Philip M., Yvonne Roebbert, Wladimir Neumann, Abdelmouhcine Gannoun, Marcel Regelous, Winfried H. Schwarz, Thomas Ludwig, Mario Trieloff, Stefan Weyer, and Audrey Bouvier (Feb. 2023). "Al-Mg and U-Pb chronological records of Erg Chech 002 ungrouped achondrite meteorite." In: 343, pp. 33–48. DOI: 10.1016/j.gca.2022.12.025.

Ribeiro, A. O., F. Roig, M. Cañada-Assandri, J. M. F. Carvano, F. L. Jasmin, A. Alvarez-Candal, and R. Gil-Hutton (Mar. 2014). "The first confirmation of V-type asteroids among the Mars crosser population." In: 92, pp. 57–64. DOI: 10.1016/j.pss.2014.01.015.

Righter, Kevin and Michael J. Drake (n.d.). "A magma ocean on Vesta: Core formation and petrogenesis of eucrites and diogenites." In: *Meteoritics & Planetary Science* 32.6 (), pp. 929–944. DOI: https://doi.org/10.1111/j.1945-5100.1997.tb01582.x.

Roig, F., D. Nesvorný, R. Gil-Hutton, and D. Lazzaro (Mar. 2008). "V-type asteroids in the middle main belt." In: 194.1, pp. 125–136. DOI: 10.1016/j.icarus.2007.10.004.

Rubin, A. E. and D. W. Mittlefehldt (Feb. 1993). "Evolutionary History of the Mesosiderite Asteroid: A Chronologic and Petrologic Synthesis." In: 101.2, pp. 201–212. DOI: 10.1006/icar.1993.1018.

Ruf, Alexander, Louis d'Hendecourt, and Philippe Schmitt-Kopplin (June 2018). "Data-Driven Astrochemistry: One Step Further within the Origin of Life Puzzle." In: *Life* 8.2, p. 18. DOI: 10.3390/life8020018.

Russell, C. T. et al. (May 2012). "Dawn at Vesta: Testing the Protoplanetary Paradigm." In: *Science* 336.6082, p. 684. DOI: 10.1126/science.1219381.

Ruzicka, Alex, Jeffrey Grossman, Audrey Bouvier, and Carl B. Agee (May 2017). "The Meteoritical Bulletin, No. 103." In: 52.5, pp. 1014–1014. DOI: 10.1111/maps.12888.

Sanchez, J. A. et al. (Jan. 2014). "Olivine-dominated asteroids: Mineralogy and origin." In: *Icarus* 228, p. 288. DOI: 10.1016/j.icarus.2013.10.006.

Sanchez, Juan A., René Michelsen, Vishnu Reddy, and Andreas Nathues (July 2013). "Surface composition and taxonomic classification of a group of near-Earth and Mars-crossing asteroids." In: 225.1, pp. 131–140. DOI: 10.1016/j.icarus.2013.02.036.

Sanchez, Juan A., Vishnu Reddy, Andreas Nathues, Edward A. Cloutis, Paul Mann, and Harald Hiesinger (July 2012). "Phase reddening on near-Earth asteroids: Implications for mineralogical analysis, space weathering and taxonomic classification." In: 220.1, pp. 36–50. DOI: 10.1016/j.icarus.2012.04.008. arXiv: 1205.0248 [astro-ph.EP].

Schulze, H., A. Bischoff, H. Palme, B. Spettel, G. Dreibus, and J. Otto (Mar. 1994). "Mineralogy and Chemistry of Rumuruti: The First Meteorite Fall of the New R Chondrite Group." In: *Meteoritics* 29.2, p. 275. DOI: 10.1111/j.1945-5100.1994.tb00681.x.

Scott, E. R. D. and J. T. Wasson (Aug. 1975). "Classification and properties of iron meteorites." In: *Reviews of Geophysics and Space Physics* 13, pp. 527–546. DOI: 10.1029/RG013i004p00527.

Sears, Derek W. G. and Robert T. Dodd (1988). "Overview and classification of meteorites." In: *Meteorites and the Early Solar System*. Ed. by John F. Kerridge and Mildred Shapley Matthews, pp. 3–31.

Sergeyev, A. V., B. Carry, C. A. Onken, H. A. R. Devillepoix, C. Wolf, and S. W. Chang (Feb. 2022). "Multifilter photometry of Solar System objects from the SkyMapper Southern Survey." In: *Astronomy & Astrophysics* 658, A109. DOI: `10.1051/0004-6361/202142074`.

Sergeyev, Alexey V. and Benoit Carry (Aug. 2021). "A million asteroid observations in the Sloan Digital Sky Survey." In: *Astronomy & Astrophysics* 652, A59. DOI: `10.1051/0004-6361/202140430`.

Sokolova, M., M. Sergienko, Y. Nefedyev, A. Andreev, and L. Nefediev (Oct. 2018). "Genetic analysis of parameters of near earth asteroids for determining parent bodies of meteoroid streams." In: *Advances in Space Research* 62.8, pp. 2355–2363. DOI: `10.1016/j.asr.2017.11.020`.

Solontoi, Michael R., Mark Hammergren, Geza Gyuk, and Andrew Puckett (Aug. 2012). "AVAST survey 0.4-1.0 μm spectroscopy of igneous asteroids in the inner and middle main belt." In: 220.2, pp. 577–585. DOI: `10.1016/j.icarus.2012.05.035`.

Starukhina, L. V. and T. B. McCord (Mar. 2012). "Asteroid Shielding from Solar Wind: Calculation of the Parameters of Magnetospheres." In: *43rd Annual Lunar and Planetary Science Conference*. Lunar and Planetary Science Conference, p. 1288.

Stern, S Alan and Joshua E Colwell (1997). "Collisional erosion in the primordial Edgeworth-Kuiper belt and the generation of the 30-50 AU Kuiper gap." In: *The Astrophysical Journal* 490.2, p. 879.

Sturtz, Cyril, Angela Limare, Marc Chaussidon, and Édouard Kaminski (Oct. 2022). "Structure of differentiated planetesimals: A chondritic fridge on top of a magma ocean." In: 385, p. 115100. DOI: `10.1016/j.icarus.2022.115100`.

Sunshine, Jessica M., Schelte J. Bus, Catherine M. Corrigan, Timothy J. McCoy, and Thomas H. Burbine (Aug. 2007). "Olivine-dominated asteroids and meteorites: Distinguishing nebular and igneous histories." In: 42.2, pp. 155–170. DOI: `10.1111/j.1945-5100.2007.tb00224.x`.

Sunshine, Jessica M., Schelte J. Bus, Timothy J. McCoy, Thomas H. Burbine, Catherine M. Corrigan, and Richard P. Binzel (Aug. 2004). "High-calcium pyroxene as an indicator of igneous differentiation in asteroids and meteorites." In: 39.8, pp. 1343–1357. DOI: `10.1111/j.1945-5100.2004.tb00950.x`.

Sutherland, Will et al. (Mar. 2015). "The Visible and Infrared Survey Telescope for Astronomy (VISTA): Design, technical overview, and performance." In: *Astronomy & Astrophysics* 575, A25. DOI: `10.1051/0004-6361/201424973`.

Tarduno, John A., Rory D. Cottrell, Francis Nimmo, Julianna Hopkins, Julia Voronov, Austen Erickson, Eric Blackman, Edward R. D. Scott, and Robert McKinley (Nov. 2012). "Evidence for a Dynamo in the Main Group Pallasite Parent Body." In: *Science* 338.6109, p. 939. DOI: `10.1126/science.1223932`.

Tatsumi, E., F. Tinaut-Ruano, J. de León, M. Popescu, and J. Licandro (Aug. 2022). "Near-ultraviolet to visible spectroscopy of the Themis and Polana-Eulalia complex families." In: *Astronomy & Astrophysics* 664, A107. DOI: `10.1051/0004-6361/202243806`.

Terai, Tsuyoshi and Fumi Yoshida (July 2018). "Size Distribution of Small Hilda Asteroids." In: 156.1, p. 30. DOI: `10.3847/1538-3881/aac81b`.

Tholen, D. J. (1989). “Asteroid taxonomic classifications.” In: *in Asteroids II (R. P.Binzel et al. eds)*. Ed. by R. P. Binzel, T. Gehrels, and M. S. Matthews, p. 1139.

Thomas, Cristina A. and Richard P. Binzel (Feb. 2010). “Identifying meteorite source regions through near-Earth object spectroscopy.” In: 205.2, pp. 419–429. DOI: 10.1016/j.icarus.2009.08.008.

Thomas, Cristina A., Joshua P. Emery, David E. Trilling, Marco Delbó, Joseph L. Hora, and Michael Mueller (Jan. 2014). “Physical characterization of Warm Spitzer-observed near-Earth objects.” In: 228, pp. 217–246. DOI: 10.1016/j.icarus.2013.10.004.

Tinaut-Ruano, F., E. Tatsumi, P. Tanga, J. de León, M. Delbo, F. De Angeli, D. Morate, J. Licandro, and L. Galluccio (Jan. 2023). “Asteroids’ reflectance from Gaia DR3: Artificial reddening at near-UV wavelengths.” In: *Astronomy & Astrophysics* 669, p. L14. DOI: 10.1051/0004-6361/202245134.

Tinaut-Ruano, F., J. de León, E. Tatsumi, D. Morate, M. Mahlke, P. Tanga, and J. Licandro (June 2024). “Asteroid reflectance spectra from Gaia DR3: Near-UV in primitive asteroids.” In: *Astronomy & Astrophysics* 686, A76. DOI: 10.1051/0004-6361/202348752.

Tóth, Juraj et al. (Dec. 2015). “All-sky Meteor Orbit System AMOS and preliminary analysis of three unusual meteor showers.” In: 118, pp. 102–106. DOI: 10.1016/j.pss.2015.07.007.

Trigo-Rodríguez, J. M., A. J. Castro-Tirado, J. Llorca, J. Fabregat, V. J. Martínez, V. Reglero, M. Jelínek, P. Kubánek, T. Mateo, and A. de Ugarte Postigo (Dec. 2004). “The Development of the Spanish Fireball Network Using a New All-Sky CCD System.” In: *Earth Moon and Planets* 95.1-4, pp. 553–567. DOI: 10.1007/s11038-005-4341-9.

Trigo-Rodríguez, Josep M., Albert Rimola, Safoura Tanbakouei, Victoria Cabedo Soto, and Martin Lee (Feb. 2019). “Accretion of Water in Carbonaceous Chondrites: Current Evidence and Implications for the Delivery of Water to Early Earth.” In: 215.1, 18, p. 18. DOI: 10.1007/s11214-019-0583-0. arXiv: 1902.00367 [astro-ph.EP].

Tsirvoulis, G., A. Morbidelli, M. Delbo, and K. Tsiganis (Apr. 2018). “Reconstructing the size distribution of the primordial Main Belt.” In: 304, pp. 14–23. DOI: 10.1016/j.icarus.2017.05.026.

Turrini, D., V. Svetsov, G. Consolmagno, S. Sirono, and S. Pirani (Dec. 2016). “Olivine on Vesta as exogenous contaminants brought by impacts: Constraints from modeling Vesta’s collisional history and from impact simulations.” In: 280, pp. 328–339. DOI: 10.1016/j.icarus.2016.07.009.

Van Schmus, W. R. and J. A. Wood (Jan. 1967). “A chemical-petrologic classification for the chondritic meteorites.” In: 31.5, 747,IN7,755–754,IN10,765. DOI: 10.1016/S0016-7037(67)80030-9.

Vernazza, P., R. P. Binzel, A. Rossi, M. Fulchignoni, and M. Birlan (Apr. 2009a). “Solar wind as the origin of rapid reddening of asteroid surfaces.” In: 458, p. 993. DOI: 10.1038/nature07956.

Vernazza, P., R. Brunetto, R. P. Binzel, C. Perron, D. Fulvio, G. Strazzulla, and M. Fulchignoni (Aug. 2009b). “Plausible parent bodies for enstatite chondrites and mesosiderites: Implications for Lutetia’s fly-by.” In: *Icarus* 202, pp. 477–486. DOI: 10.1016/j.icarus.2009.03.016.

Vernazza, P., R. Brunetto, G. Strazzulla, M. Fulchignoni, P. Rochette, N. Meyer-Vernet, and I. Zouganelis (June 2006). “Asteroid colors: a novel tool for magnetic field detection? The case of Vesta." In: *Astronomy & Astrophysics* 451.3, pp. L43–L46. DOI: 10.1051/0004-6361:20065176.

Vernazza, P., B. Carry, J. Emery, J. L. Hora, D. Cruikshank, R. P. Binzel, J. Jackson, J. Helbert, and A. Maturilli (June 2010). "Mid-infrared spectral variability for compositionally similar asteroids: Implications for asteroid particle size distributions." In: 207.2, pp. 800–809. DOI: 10.1016/j.icarus.2010.01.011.

Vernazza, P., B. Zanda, R. P. Binzel, T. Hiroi, F. E. DeMeo, M. Birlan, R. Hewins, L. Ricci, P. Barge, and M. Lockhart (Aug. 2014). "Multiple and Fast: The Accretion of Ordinary Chondrite Parent Bodies." In: *The Astrophysical Journal* 791.2, p. 120. DOI: 10.1088/0004-637X/791/2/120.

Vernazza, P., B. Zanda, T. Nakamura, E. R. D. Scott, and S. Russell (2015). "The Formation and Evolution of Ordinary Chondrite Parent Bodies." In: *Asteroids IV*, pp. 617–634. DOI: 10.2458/azu_uapress_9780816532131-ch032.

Vernazza, P. et al. (July 2013). "Paucity of Tagish Lake-like parent bodies in the Asteroid Belt and among Jupiter Trojans." In: 225.1, pp. 517–525. DOI: 10.1016/j.icarus.2013.04.019.

Vernazza, P. et al. (Oct. 2021). "VLT/SPHERE imaging survey of the largest main-belt asteroids: Final results and synthesis." In: *Astronomy & Astrophysics* 654, A56. DOI: 10.1051/0004-6361/202141781.

Vernazza, Pierre and Pierre Beck (Nov. 2016). "Composition of Solar System Small Bodies." In: *arXiv e-prints*, arXiv:1611.08731. DOI: 10.48550/arXiv.1611.08731. arXiv: 1611.08731 [astro-ph.EP].

Vilas, Faith and Michael J. Gaffey (Nov. 1989). "Phyllosilicate Absorption Features in Main-Belt and Outer-Belt Asteroid Reflectance Spectra." In: *Science* 246.4931, pp. 790–792. DOI: 10.1126/science.246.4931.790.

Vilas, Faith, Stephen M. Larson, Erin C. Hatch, and Kandy S. Jarvis (Sept. 1993). "CCD Reflectance Spectra of Selected Asteroids. II. Low-Albedo Asteroid Spectra and Data Extraction Techniques." In: 105.1, pp. 67–78. DOI: 10.1006/icar.1993.1111.

Vinogradova, T. A. (Apr. 2019). "Empirical method of proper element calculation and identification of asteroid families." In: 484.3, pp. 3755–3764. DOI: 10.1093/mnras/stz228.

Vokrouhlický, D., M. Brož, A. Morbidelli, W. F. Bottke, D. Nesvorný, D. Lazzaro, and A. S. Rivkin (May 2006). "Yarkovsky footprints in the Eos family." In: 182.1, pp. 92–117. DOI: 10.1016/j.icarus.2005.12.011.

Wadhwa, M., G. Srinivasan, and R. W. Carlson (2006). "Timescales of Planetesimal Differentiation in the Early Solar System." In: *Meteorites and the Early Solar System II*. Ed. by Dante S. Lauretta and Harry Y. McSween, p. 715.

Walsh, K. J., M. Delbó, W. F. Bottke, D. Vokrouhlický, and D. S. Lauretta (July 2013). "Introducing the Eulalia and new Polana asteroid families: Re-assessing primitive asteroid families in the inner Main Belt." In: *Icarus* 225, p. 283. DOI: 10.1016/j.icarus.2013.03.005.

Warren, Paul H. (Nov. 2011). "Stable-isotopic anomalies and the accretionary assemblage of the Earth and Mars: A subordinate role for carbonaceous chondrites." In: *Earth and Planetary Science Letters* 311.1, pp. 93–100. DOI: 10.1016/j.epsl.2011.08.047.

Watters, T. R. and M. Prinz (Jan. 1979). "Aubrites: their origin and relationship to enstatite chondrites." In: *Lunar and Planetary Science Conference Proceedings* 1, pp. 1073–1093.

Weisberg, M. K., T. J. McCoy, and A. N. Krot (2006). “Systematics and Evaluation of Meteorite Classification.” In: *Meteorites and the Early Solar System II*. Ed. by Dante S. Lauretta and Harry Y. McSween, p. 19.

Weiss, Benjamin P. and Linda T. Elkins-Tanton (May 2013). “Differentiated Planetesimals and the Parent Bodies of Chondrites.” In: *Annual Review of Earth and Planetary Sciences* 41, pp. 529–560. DOI: `10.1146/annurev-earth-040610-133520`.

Weryk, R. J., M. D. Campbell-Brown, P. A. Wiegert, P. G. Brown, Z. Krzeminski, and R. Musci (July 2013). “The Canadian Automated Meteor Observatory (CAMO): System overview.” In: 225.1, pp. 614–622. DOI: `10.1016/j.icarus.2013.04.025`.

Windmill, Richard J, Ian A Franchi, Jan L Hellmann, Jonas M Schneider, Fridolin Spitzer, Thorsten Kleine, Richard C Greenwood, and Mahesh Anand (Mar. 2022). “Isotopic evidence for pallasite formation by impact mixing of olivine and metal during the first 10 million years of the Solar System.” In: *PNAS Nexus* 1.1, pgac015. ISSN: 2752-6542. DOI: `10.1093/pnasnexus/pgac015`. eprint: `https://academic.oup.com/pnasnexus/article-pdf/1/1/pgac015/47087252/pgac015.pdf`.

Woitke, P., J. Drażkowska, H. Lammer, K. Kadam, and P. Marigo (Apr. 2024). “CAI formation in the early Solar System.” In: *arXiv e-prints*, arXiv:2404.15715, arXiv:2404.15715. DOI: `10.48550/arXiv.2404.15715`. arXiv: `2404.15715 [astro-ph.EP]`.

Xu, Shui, Richard P. Binzel, Thomas H. Burbine, and Schelte J. Bus (May 1995). “Small Main-belt Asteroid Spectroscopic Survey: initial results.” In: 115.1, pp. 1–35. DOI: `10.1006/icar.1995.1075`.

Yamaguchi, A., J. A. Barrat, M. Chaussidon, P. Beck, J. Villeneuvee, D. J. Byrne, M. W. Broadley, and B. Marty (Mar. 2021). “Petrology and Geochemistry of Erg Chech 002, the Oldest Andesite in the Solar System.” In: *52nd Lunar and Planetary Science Conference*. Lunar and Planetary Science Conference, p. 1892.

Yomogida, K. and T. Matsui (Apr. 1984). “Multiple parent bodies of ordinary chondrites.” In: *Earth and Planetary Science Letters* 68.1, pp. 34–42. DOI: `10.1016/0012-821X(84)90138-9`.

Zappala, Vincenzo, Alberto Cellino, Paolo Farinella, and Zoran Knezevic (Dec. 1990). “Asteroid Families. I. Identification by Hierarchical Clustering and Reliability Assessment.” In: 100, p. 2030. DOI: `10.1086/115658`.

Zellner, B. (Sept. 1973). “Polarimetric Albedos of Asteroids.” In: *Bulletin of the American Astronomical Society*. Vol. 5, p. 388.

Zellner, B., D. J. Tholen, and E. F. Tedesco (Mar. 1985). “The eight-color asteroid survey: Results for 589 minor planets.” In: 61.3, pp. 355–416. DOI: `10.1016/0019-1035(85)90133-2`.

Zhang, P. et al. (Mar. 2022). “Diverse space weathering effects on asteroid surfaces as inferred via laser irradiation of meteorites.” In: *Astronomy & Astrophysics* 659, A78. DOI: `10.1051/0004-6361/202142590`.

Zhu, K., A. Bischoff, J. A. Barrat, L. Chen, and W. B. Hsu (Aug. 2023). “Ureilites and Erg Chech 002 Represent the Heaviest and Lightest Ca Isotope Reservoirs in the Inner Solar System.” In: *LPI Contributions*. Vol. 2990. LPI Contributions, p. 6180.

Zhu, Ke, Harry Becker, Shi-Jie Li, Yan Fan, Xiao-Ning Liu, and Tim Elliott (Sept. 2022). “Radiogenic chromium isotope evidence for the earliest planetary volcanism and crust formation in the Solar system.” In: 515.1, pp. L39–L44. DOI: `10.1093/mnrasl/slac061`.

Zuber, Maria T. (July 2001). “The crust and mantle of Mars.” In: 412.6843, pp. 220–227.

de León, J., J. Licandro, M. Serra-Ricart, N. Pinilla-Alonso, and H. Campins (July 2010). "Observations, compositional, and physical characterization of near-Earth and Mars-crosser asteroids from a spectroscopic survey." In: *Astronomy & Astrophysics* 517, A23. DOI: `10.1051/0004-6361/200913852`.

de León, J. et al. (Mar. 2016). "Visible spectroscopy of the Polana-Eulalia family complex: Spectral homogeneity." In: 266, pp. 57–75. DOI: `10.1016/j.icarus.2015.11.014`.

de Sanctis, M. C., A. Migliorini, F. Luzia Jasmin, D. Lazzaro, G. Filacchione, S. Marchi, E. Ammannito, and M. T. Capria (Sept. 2011). "Spectral and mineralogical characterization of inner main-belt V-type asteroids." In: *Astronomy & Astrophysics* 533, A77. DOI: `10.1051/0004-6361/201117136`.

Ďurech, J. et al. (Aug. 2011). "Combining asteroid models derived by lightcurve inversion with asteroidal occultation silhouettes." In: *Icarus* 214, pp. 652–670. DOI: `10.1016/j.icarus.2011.03.016`.